Diogo Miguel Rodrigues Marinho da Mata

Compósitos CNTs/biocerâmico para estimulação elétrica óssea in situ

Diogo Miguel Rodrigues Marinho da Mata

Compósitos CNTs/biocerâmico para estimulação elétrica óssea in situ

Tese apresentada à Universidade de Aveiro para cumprimento dos requisitos necessários à obtenção do grau de Doutor em Ciência e Engenharia dos Materiais, realizada sob a orientação científica do Doutor Rui Ramos Ferreira e Silva, Professor Associado do Departamento de Engenharia de Materiais e Cerâmica da Universidade de Aveiro e co-orientação da Doutora Maria Ascensão Ferreira da Silva Lopes, Professora Auxiliar do Departamento de Engenharia Metalúrgica e de Materiais da Faculdade de Engenharia da Universidade do Porto

À minha mãe e irmã. À Ana pelo incansável apoio.

À memória do meu pai.

o júri

presidente

Prof. Doutor Amadeu Mortágua Velho da Maia Soares
professor catedrático do Depart. de Biologia da Universidade de Aveiro

Prof. Doutora Ana Cristina Moreira Freire
professora associada do Depart. de Química e Bioquímica da Universidade do Porto

Prof. Doutor João Pedro Santos Hall Agorreta Alpuim
professor auxiliar do Depart. de Física da Universidade do Minho

Prof. Doutora Maria Helena Figueira Vaz Fernandes
professora associada do Depart. de Eng. de Materiais e Cerâmica da Universidade de Aveiro

Prof. Doutora Maria Ascensão Ferreira Silva Lopes
professora auxiliar do Depart. de Eng. Metalúrgica e de Materiais da Universidade do Porto

Prof. Doutor Rui Ramos Ferreira e Silva
professor associado do Depart. de Eng. de Materiais e Cerâmica da Universidade de Aveiro

palavras-chave

resumo

A presente tese tem como objetivo o desenvolvimento de um substituo ósseo condutor elétrico e biocompatível, formulado com nanotubos de carbono (CNTs), que permite a regeneração in situ do osso sob a aplicação externa de estímulos elétricos pulsados.

Os CNTs foram produzidos por deposição química em fase de vapor (CVD) por um método semi-contínuo com um rendimento ~500 mg/dia. Os parâmetros de deposição foram otimizados de modo a obterem-se CNTs com elevada pureza ~99.96% e morfologias controladas, requisitos fundamentais para a aplicação biomédica em estudo.

A funcionalização química dos CNTs foi igualmente otimizada para maximizar a sua processabilidade e biocompatíbilidade. Os CNTs foram funcionalizados pela reação de adição Diels-Alder de 1,3 butadieno. O comportamento biológico dos CNTs funcionalizados foi avaliado *in vitro* com a linha celular osteoblástica MG63 e *in vivo*, por implantação subcutânea em ratos. Os materiais não induziram uma resposta inflamatória manifesta, mas os CNTs funcionalizados apresentaram uma biocompatibilidade *in vitro* e *in vivo* superior aos não funcionalizados.

Compósitos de matriz cerâmica, biovidro (Vidro) e hidroxiapatite (HA), reforçada com nanotubos de carbono (CNT/Vidro/HA), foram processados por via líquida. A incorporação de 4.4 vol% de CNTs permitiu um aumento de 10 ordens de grandeza da condutividade elétrica da matriz. Estudos *in vitro* com células MG63 mostraram que os compósitos de CNT/Vidro/HA garantem a adesão e proliferação das células ósseas, e estimulam a expressão do seu fenótipo, nomeadamente a fosfatase alcalina (ALP).

As interações entre os materiais compósitos e o meio de cultura (α-MEM), sob a aplicação de um campo elétrico externo, foram estudadas pela técnica do eléctrodo vibratório de varrimento. Observou-se um aumento da condutividade elétrica do meio de cultura e do confinamento de campos elétricos na presença de amostras CNT/Vidro/HA submersas no meio, relativamente às de Vidro/HA. A estimulação elétrica *in vitro* das células MG63 nos compósitos condutores promoveu um aumento da actividade metabólica e do teor de DNA de 130% e 60%, relativamente à condição não estimulada, após apenas 3 dias de estimulação diária de 15 µA por 15 min. Além disso, a expressão genética osteoblástica para o Runx2, osteocalcina (OC) e ALP foi aumentada em 80 %, 50 % e 25 %, após 5 dias de estimulação. Por outro lado, para materiais dielétricos, a estimulação apresentou-se menos eficiente, originando uma resposta celular igual ou inferior à situação não estimulada.

Os substitutos ósseos condutores elétricos permitem a entrega *in situ* dos estímulos às células e consequente controlo da taxa de crescimento do novo tecido ósseo. Estes novos biomateriais condutores funcionais poderão tornar a electroterapia selectiva do osso clinicamente relevante, ao possibilitarem a diminuição dos tempos pós-operatórios.

abstract

The present thesis aims to develop a biocompatible and electroconductor bone graft containing carbon nanotubes (CNTs) that allows the in situ regeneration of bone cells by applying pulsed external electrical stimuli.

The CNTs were produced by chemical vapor deposition (CVD) by a semi-continuous method with a yield of ~500 mg/day. The deposition parameters were optimised to obtain high pure CNTs ~99.96% with controlled morphologies, fundamental requisites for the biomedical application under study.

The chemical functionalisation of CNTs was also optimised to maximise their processability and biocompatibility. The CNTs were functionalised by the Diels-Alder cycloaddition of 1,3-butadiene. The biological behaviour of the functionalised CNTs was evaluated *in vitro* with the osteoblastic cells line MG63 and *in vivo*, by subcutaneous implantation in rats. The materials did not induce an expressed inflammatory response, but the functionalised CNTs showed a superior *in vitro* and *in vivo* biocompatibility than the non-functionalised ones.

Composites of ceramic matrix, of bioglass (Glass) and hydroxyapatite (HA), reinforced with carbon nanotubes (CNT/Glass/HA) were processed by a wet approach. The incorporation of just 4.4 vol% of CNTs allowed the increase of 10 orders of magnitude of the electrical conductivity of the matrix. *In vitro* studies with MG63 cells show that the CNT/Glass/HA composites guarantee the adhesion and proliferation of bone cells, and stimulate their phenotype expression, namely the alkaline phosphate (ALP).

The interactions between the composite materials and the culture medium (α-MEM), under an applied electrical external field, were studied by scanning vibrating electrode technique. An increase of the culture medium electrical conductivity and the electrical field confinement in the presence of the conductive samples submerged in the medium was demonstrated.

The *in vitro* electrical stimulation of MG63 cells on the conductive composites promotes the increase of the cell metabolic activity and DNA content by 130% and 60%, relatively to the non-stimulated condition, after only 3 days of daily stimulation of 15 µA for 15 min. Moreover, the osteoblastic gene expression for Runx2, osteocalcin (OC) and ALP was enhanced by 80%, 50% and 25%, after 5 days of stimulation. Instead, for dielectric materials, the stimulus delivering was less efficient, giving an equal or lower cellular response than the non-stimulated condition.

The proposed electroconductive bone grafts offer exciting possibilities in bone regeneration strategies by delivering in situ electrical stimulus to cells and consequent control of the new bone tissue formation rate. It is expected that conductive smart biomaterials might turn the selective bone electrotherapy of clinical relevance by decreasing the postoperative healing times.

Foreword

The present thesis focuses on the preparation of electrical conductive carbon nanotube (CNT)/Glass/hydroxyapatite (HA) bone grafts to maximize the *in situ* delivery of electrical stimuli to bone cells. The new bone grafts are expected to turn the Food and Drug Administration (FDA) approved non-invasive stimulation methods (capacitive and inductive coupling) more efficient by becoming the mechanism of stimulus delivering highly selective with the confinement of electric signals at the damaged bone site.

The matrix of the bone graft composite is a calcium phosphate (CaP)-related material, approved by FDA and widely applied in clinics. This matrix is a P_2O_5-bioglass reinforced hydroxyapatite (Glass/HA) presenting higher mechanical properties, bioactivity and osteoconduction than single phase HA, but still being a dielectric material. Biologically safe CNTs become an attractive reinforcing phase to convert the Glass/HA into a "smart" bone graft. Owing to their functional properties, CNTs allow to obtain non-metallic highly thermal and electrical conductive biocomposites at low percolation thresholds, free of corrosion-induced toxicological risks and with minor damage to the matrix biological profile.

The present thesis is organized in 6 chapters. *Chapter 1* is devoted to the bibliographic review of the major topics that compose the present thesis: (1) a brief background in the CNT field; (2) the *in vitro* and *in vivo* electrical stimulation of bone and its clinical limitations; and (3) a state of the art on CNT-bioceramic composites applied to bone tissue engineering, stressing their major processing challenges, attractive properties and *in vitro* and *in vivo* toxicological profiles.

The body of the thesis comprises 8 paper works (3 accepted and 5 submitted), disposed in *Chapters 2 to 5*. *Chapter 2* describes two catalyst-supported chemical vapor deposition (CVD) methods developed for growing carbon nanofilaments, in particular the thermal CVD route of CNT synthesis. The control of CNT biopersistency and biocompatibility by means of chemical functionalization is the subject of *Chapter 3*. The optimization of the production cycle (processing and sintering) of CNT/Glass/HA composites with adequate functional properties and biological profile (*in vitro* biocompatibility assays with MG63 cells) is the core of *Chapter 4*. Finally, *Chapter 5* is the proof of concept that conductive bone grafts act as high efficient electron stimuli delivering systems to MG63 cells while *in vitro* electrically stimulated.

Chapter 6 is the thesis' epilogue that covers an integrated discussion of the major subjects and main conclusions and prospects future research lines.

Index

Chapter I

Bibliographic Review

I.1. Carbon nanotubes (CNTs)

I.1.1. Structure and properties

Carbon is present in all building blocks of life owing to its chemical bonding versatility. Each carbon atom has six electrons which occupy $1s^2$, $2s^2$ and $2p^2$ atomic orbitals. The $2s^2$ and $2p^2$ valence orbitals are filled by four weakly bonded electrons that are free to change position, in crystalline carbon forms they are as $2s^1$, $2p_x^1$, $2p_y^1$ and $2p_z^1$. When these orbitals are combined, $2s^1+2p_x^1$, $2s^1+2p_x^1+2p_y^1$ or $2s^1+2p_x^1+2p_y^1+2p_z^1$, hybridization states are formed, sp, sp^2 and sp^3, respectively. These states promote covalent sigma (σ) bonding with specific structural arrangements: sp - chain structures; sp^2 - planar structures and sp^3 - tetrahedral structures [1].

Those of the most common sp^2 and sp^3-bonded crystalline structures of carbon (i.e. carbon allotrope phases) are the graphite and diamond. According to a recent version of the phase diagram [2], graphite is the most stable form of solid carbon at ambient conditions. The 3D graphite structure concerns multi-layers of graphene stacked on top of each other bonded together by weak non-covalent Van der Waals bonding (Fig.1). In a graphene layer, each carbon atom is covalently sp^2-σ bonded to three neighbored atoms in a hexagonal (hcc) structure (Fig. 1).

Beyond the 3D configuration, sp^2-bonded carbon clusters of few atoms were found to be able to yield highly stable nanostructures by simply elimination of high energy dangling bonds [1]. Following this, carbon clusters had been catching great interest by the scientific community over the last five decades [3]. Relevant landmarks in the carbon field were accomplished with the discovery of novel carbon sp^2 allotropes (Fig. 1) of closed cage nanostructures - fullerenes (0D) [4], carbon nanotubes (1D) [5, 6] or open nanostructures - cones (0D) [7], graphene (2D) [8], and ribbons (2D) [9].
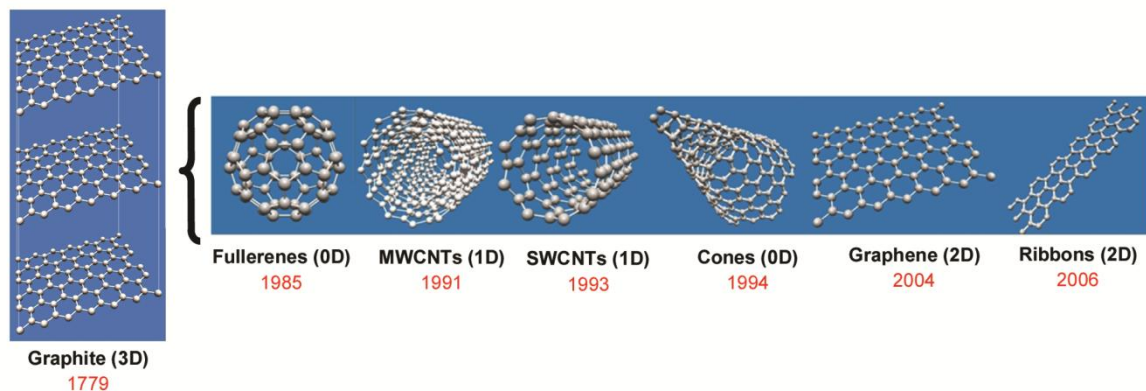
Fig. 1 - Carbon sp^2 allotropes (generated using the nanotube modeler freeware - http://www.jcrystal.com/products/wincnt/index.htm).

These nanostructures are related between them by being formed by a single layer of graphene, the building block of all sp^2-bonded carbon allotropes [10]. Simply, the graphene layer can be modulated (e.g. buckling, rolling) to promote the bonding of carbon atoms of the extremities of the layer and reach a low energy state [10].

Regarding carbon nanotube (CNT) structures, they are formed by concentrically rolled-up graphene layers. Those having several layers are multi-walled CNTs (MWCNTs) and when formed by a single layer they are denominated single-walled CNTs (SWCNTs) (Fig. 1). Both CNT types were discovered by Iijima in 1991 and 1993, respectively [5, 6]. Other nanofilaments, with similar cross-sectional appearance in TEM, were observed some decades earlier, in 1970s, by Baker et al. [11], the carbon nanofibers (CNFs). Yet, these carbon nanofilaments present structural differences. While CNFs are filaments with graphene layers having different angles to the filament axis, the CNTs are filaments with tubular graphene layers parallel to the axis [12, 13].

SWCNTs and MWCNTs do not present a simple and universal rolling direction. They revealed a large number of potential directions, i.e. helicities or chiralities that defines the structural arrangement of the tube. To describe such fundamental structural characteristic of the nanotubes, a SWCNT is adopted for simplification. This structure is formed by rolling-up a single graphene layer (Fig. 2) with hexagonal lattice unit vectors ($|a_1|=|a_2|= 0.246$ nm). Considering this lattice, the unit cell of a nanotube can be define by two vectors, C_h and T [14, 15].
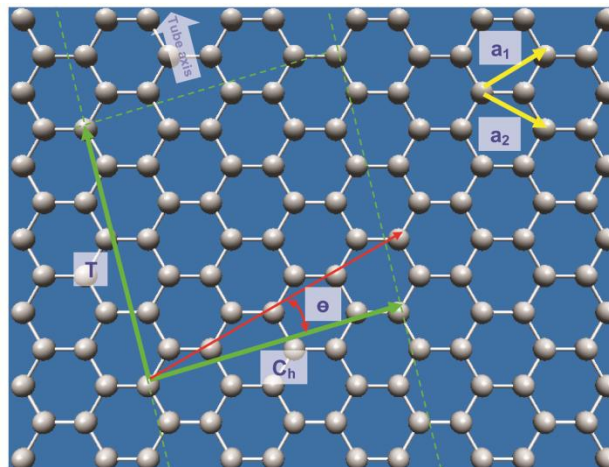
Fig. 2 - The unrolled hexagonal lattice of a SWCNT structure (generated using the nanotube modeler freeware - http://www.jcrystal.com/products/wincnt/index.htm).

The C_h is the chiral vector or rolling vector defining the circumference on the surface of the tube connecting two equivalent carbon atoms positions. This vector can be expressed as,

$$C_h = na_1 + ma_2, \ C_h = (n,m) \qquad (1)$$

where n and m are positive integers ($0 \leq n \leq m$), also known as chiral indices. When $n=m$, the tube is designated armchair, zig-zag when $m=0$, and chiral in all other cases. Examples for each type of CNT structure are given in Fig. 3.
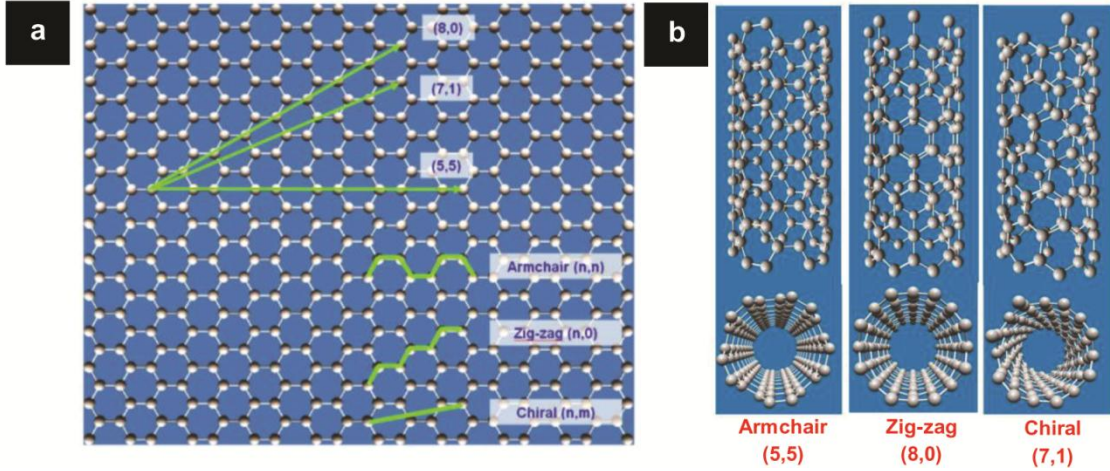
Fig. 3 - (a) Definition of chiral vectors on a hexagonal lattice for an armachair, zig-zag and chiral tube. (b) Respective 3D structures of the CNTs of (a) (generated using the nanotube modeler freeware - http://www.jcrystal.com/products/wincnt/index.htm).

The magnitude of the C_h vector defines one dimension of the unit cell, and might be use to determine the diameter of the tube (d_t), as follows,

$$| C_h |= d_t \pi = 0.246\sqrt{n^2 + nm + m^2} \qquad (2)$$

The T vector, perpendicular to C_h, is defined in the direction of the axis of the tube.

$$T = t_1 a_1 + t_2 n a_2, \ T = (t_1, t_2) \qquad (3)$$

where t_1 and t_2 are positive integers that are related with (n,m), as follows,

$$t_1 = \frac{(2m+n)}{d_R} \qquad (4)$$

$$t_2 = -\frac{(2n+m)}{d_R} \qquad (5)$$

where d_R is given by,

$$d_R = d, \ if \ n - m \neq multiple \ of \ 3d \qquad (6)$$

$$d_R = 3d, \ if \ n - m = multiple \ of \ 3d \qquad (7)$$

where d_R is the highest common divisor of *(n, m)*.

The magnitude of the *T* vector corresponded to the other dimension of the unit cell, i.e. the shorter repeat distance along the axis of the tube, determined as,

$$|T| = \frac{\sqrt{3}C_h}{d_R} \qquad (8)$$

The number of carbon atoms in unit cell of a nanotube is *2N*, where *N* is given by,

$$N = \frac{2(n^2 + m^2 + nm)}{d_R} \qquad (9)$$

The angle between C_h and the zig-zag direction (Fig. 2) is the chiral angle (*Ө*), calculated as follows,

$$\theta = \tan^{-1}\left(\frac{\sqrt{3}m}{m + 2n}\right) \qquad (10)$$

A nule chiral angle, *Ө*=0⁰, corresponds to a zig-zag tube, whereas a armchair tube have a *Ө*=30⁰, and a chiral tube to intermediate angles, 0⁰<*Ө*<30⁰. So, a chiral angle (*Ө*) or a pair of integers *(n,m)* are commonly used to define the type of the nanotube structure.

Besides the evident rolling structural differences between CNTs and graphene, tubes have some other singularities. CNTs are closed cage clusters with extreme curvature sections and thus higher strain energy are predictable than in graphene [1]. Also, the curvature geometry may leads to some overlapping of the orbitals π (2p_z) and σ(2s+2p_x+2p_y) [16], resulting in a small amount of sp³ bonds (2s+2p_x+2p_y+2p_z). Moreover, the circumference of nano-sized dimensions allowed a very limited number of electron states in the circumference direction. Therefore, a quantum confinement of the waveforms in the circumferential directions is expectable with only a few wave vectors needed to describe the periodic boundary conditions [16].

The CNT singularities of curvature and quantum confinement offer them unique properties, different that those of 3D graphite, 2D graphene and that other 1D fibrillar carbon allotropes. Table

1 shows some of the main physical properties of 3D-graphite (highly oriented pyrolytic graphite - HOPG), 2D graphene and several 1D fibrillar carbon allotropes.

Table 1 - Physical properties of carbon sp^2 allotropes.

Properties	Graphite (HOPG)	Graphene	Pitch carbon fibers	SWCNTs	MWCNTs
Mechanical					
Young's Modulus (GPa)	28-31 [17]	1000 [18]	241-542 [19]	1000-1250 [20, 21]	1000-1280 [21, 22]
Flexural strength (GPa)	0.08-0.17 [17]	-	2.09-3.04 [23]	-	14 [22]
Tensile strength (GPa)	0.11 [17]	130 [24]	1.1-3.21 [17, 23]	25-135 [25]	11-63 [25, 26]
Electrical and Electronic					
Conductivity (S.m^{-1})	2×10^5-2.5×10^5 [17]	10^6 [27]	4×10^5-4.5×10^5 [17]	10^6 [21]	10^6 [21]
Current density (A.cm^{-2})	-	10^{11}-10^{12} [28]	-	10^7-10^9 [21]	10^7-10^9 [21]
Band gap (eV)	-	Zero-gap semiconductor (semi-metallic) 0 [29]	-	~0.4-0.7 (non-semiconductive) if n-m is not divisible by 3 0 (metallic) if n-m is divisible by 3 [21]	~0 (metallic) [21]
Thermal and Optical					
Thermal conductivity (W.mK^{-1})	190-390 [17]	4840-5300 [30]	500-1100 [31]	3500-5800 [21, 30]	>3000 [21, 30]
Fluorecence emission (nm)	-	NIR range:900-1500 (oxidized) [32] UV-Visible range: 400-700 (oxidized) [32]	-	NIR range: 800-1600 (pristine, semiconductive) [33] UV-Visible range: 400-550 (functionalised) [34]	UV-Visible range: 400-550 (functionalised) [34]

Comparing the SWCNTs and MWCNTs, it can be seen that the former has slightly higher mechanical and conductive values. This occurs because SWCNTs having smaller diameters and therefore higher curvature confinement than MWCNTs, so the strain energy of CNT curvature [1] and σ-π rehybridization phenomena that promotes a higher π orbitals delocalization outside the tube [1, 35] are more pronounced. Besides this, particularly in phonon transport, MWCNTs seem to have lower efficiency than SWCNTs due to the inter-carbon layers scattering phenomena that ultimately perturbs the magnitude of the thermal conductivity [1].

Nonetheless, graphene has key advantages over CNTs. Graphene is a versatile charge carrier with electrons and holes having similar mobility, as high as 200,000 cm^2.Vs^{-1} and extremely high current densities up to 10^{12} A.cm^{-2} [28, 29]. These electron transporting properties makes graphene the highest performance non metallic conductor at room temperature beyond any 3D and 2D material known [29, 36]. Yet, the conductivity values for graphene are close or slightly lower than CNTs, probably due to the σ-π rehybridization phenomenon referred above. Also, graphene is a zero gap semiconductor with a electronic structure much simpler than SWCNTs due to the absence of confined density of states, making the exploration of the electronic properties of graphene greatly attractive than the latter.

Considering the optical properties, graphene and SWCNTs show similar fluorescence spectroscopy ranging from UV to NIR regions. The optical properties in CNTs depend on the diameter and symmetry of the tubes, so these emissions become more improbable in MWCNTs [35]. Yet, it was found some MWCNT fluorescence emission, but only in the UV-Visible region.

According to Table 1, the electronic, electrical and mechanical properties of CNTs are the most noteworthy and are the ones that have catching more attention caused by the wide range of potential applications (see section I.1.3). To better understand CNT electronic properties, the band structure of the 2D graphene is introduced. The unit cell of the graphene in real space and in reciprocal space is presented (highlighted at red dotted line in Fig. 4a and 4b). These unit cells contain two atoms, the core atoms ($1s^2$). The other four valence electrons form the valence bands, three σ ($2s^1$, $2p_x^1$, $2p_y^1$) and one π ($2p_z^1$). The respective basic vectors of the hexagonal lattice are defined as a_1 and a_2, for the real space,

$$a_1 = \left(\frac{\sqrt{3}}{2}a, \frac{a}{2} \right); \ a_2 = \left(\frac{\sqrt{3}}{2}a, -\frac{a}{2} \right)$$

and b_1 and b_2 for the reciprocal space,

$$b_1 = \left(\frac{2\pi}{\sqrt{3}a}, \frac{2\pi}{a} \right); \ b_2 = \left(\frac{2\pi}{\sqrt{3}a}, -\frac{2\pi}{a} \right)$$

The reciprocal vectors, b_1 and b_2, delineates the Brillouin zone (BZ, grey area in Fig. 4b) with six corners, called K points or Dirac points. The three corners labelled with a black dot are connected to each other by reciprocal vectors, so they are equivalent. The same occurs for the red dotted corners [37]. Two of these K points are represented as K and K' in Fig. 4b (highlighted with green circles).

The two-dimensional energy (E_{2D}) dispersion relations for π band in graphene [16] are given by,

$$E_{2D}(k_x, k_y) = \pm \delta_0 \left\{ 1 + 4 \cos\left(\frac{\sqrt{3}k_x a}{2} \right) \cos\left(\frac{k_y a}{2} \right) + 4 \cos^2\left(\frac{k_y a}{2} \right) \right\}^{1/2} \qquad (11)$$

where (k_x, K_y) is a wavevector K defined in the BZ, δ_0 is the nearest-neighbour tranfer integral and $a=|a_1|=|a_2|= 0.246$ nm.

The allowed K vectors in the Γ-K', Γ-M and Γ-K directions and respective E_{2D} energies are represented in Fig. 4c. At the Dirac points, the conduction/antbonding band (π*) and the valence/bonding band (π) meet at the Fermi energy (E_f), with a 2D linear/3D conical dependence of the energy dispersion (E_{2D}) (Figs. 4b-d). Under this condition, the electrons are able to run freely through the π* band, with this band being completely empty of electrons and the π band completely full. This occurs by an electron-hole conversion mechanism [37]. An electron is defined as a filled state with an energy $E>E_f$, and a hole excitation a empty state with an energy $E<E_f$. For an undoped graphene, when $E_f= 0$ (Figs. 4c and 4d), the electron belongs to the π* band and the

hole to the π band [37]. So, undoped graphene is a zero gap material (metallic) that behaves as "non-semiconductor" due to the linear energy dispersion relation (E_{2D}) at the Dirac points (Fig. 4c).
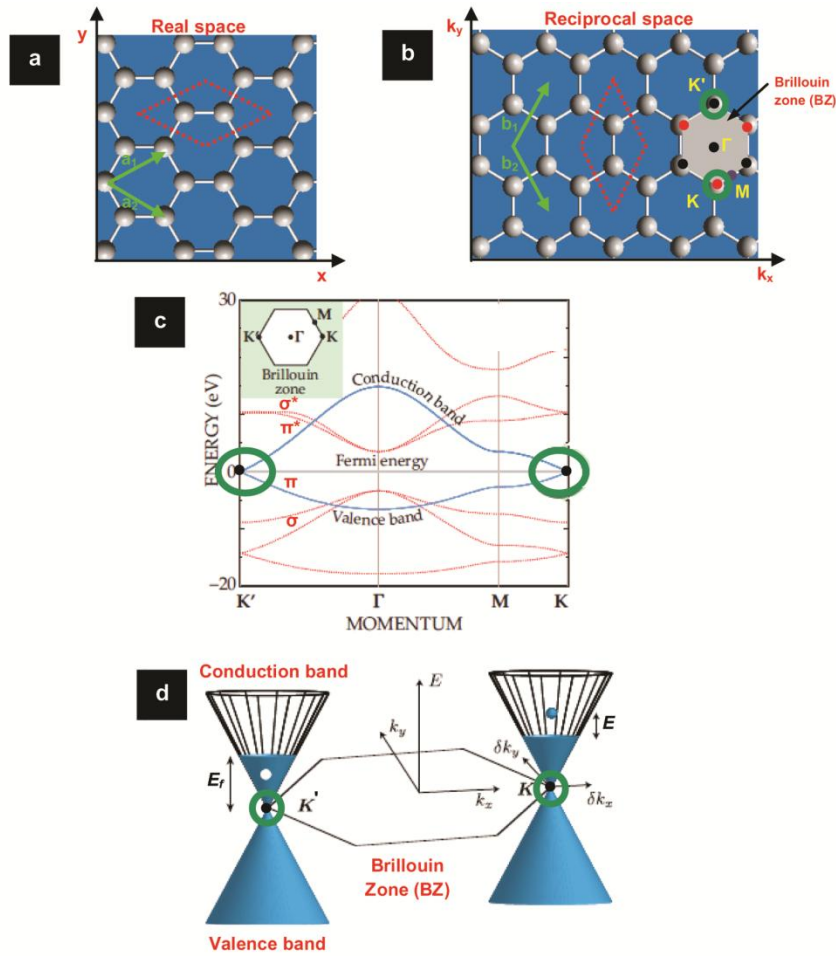
Fig. 4 - (a) Real space and (b) reciprocal space of a hexagonal lattice (unit cells highlighted at dotted red and lattice vectors highlighted at green). The Brillioun zone (BZ) is highlighted by a grey hexagonal area (black spots are equivalent Dirac or K points, as also the red spots ones) with two symmetric Dirac points labeled K and K', and two reference positions in the BZ, Γ and M (c) 2D electronic band structure (E_{2D}, eq. 11) of a graphene layer along the Γ-K', Γ-M and Γ-K directions (adapted from [38]). (d) respective 3D conical band structure of (c) presenting electron (filled circle) and hole (empty circle) excitations (adapted from [37]).

To determine the band structure of the 2D graphene presented above, it was assumed an infinite graphene layer without boundary conditions [16]. However, the number of allowed states or K waveform vectors in the circumferential direction of a CNT is very limited, which might induce the formation of a gap. This means that only specific slices of the conical bands of graphene at the *K* points in reciprocal space are allowed. As proposed by Dresselhaus et al. [14], the allowed *K*-values in the circumferential direction of a CNT can be represented by parallel lines in the 2D graphene BZ (Fig. 5).
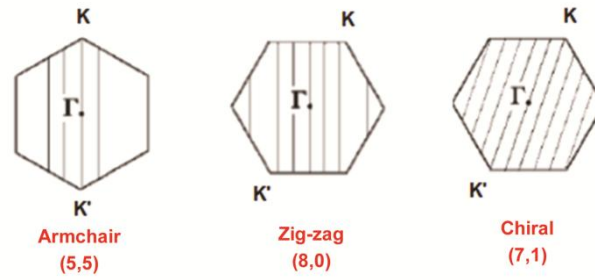
Fig. 5 - Allowed K vectors (solid lines) in the graphene Brillioun zone for the (5,5), (8,0) and (7,1) tubes (adapted from [14]).

A semiconducting CNT presents *K* vectors that do not cross a *K* point, otherwise it is a metallic CNT [14]. The spacing of the lines is inversely proportional to the CNT diameter and their angle depends on the nanotube chirality. So, another form to assess the electronic behavior of a specific tube, contemplates its chiral integers *(n, m)* [14]. The metallic conduction is observed only for,

$$n - m = 3q \qquad (12)$$

where *(n,m)= C_h* and *q* is an integer. So, armchair CNT is metallic, while zig-zag and chiral tubes can be metallic or semiconductive.

In relation to MWCNTs, their electronic properties should be similar to those of several independent SWCNTs concentrically rolled-up, since the neighboring layers should not interact [1]. So, a much complex band structure is expected comparatively to a SWCNT. The several tubes/layers in the MWCNTs might present different chiralities with different electronic behaviors. For example, if one tube is semiconductive and the other is metallic, the low-energy properties are dictated by the metallic tube, with neglected changes of the density of states around the Fermi level. In this sense, MWCNTs are considered as metallic conductors with an electronic behavior between those of a SWCNT and the 3D graphite [1].

Regarding the CNT electrical properties, the electrical conduction appears to be almost ballistic along the tube length [39]. This is attributed to the restriction of allowed electronic states in CNTs that implies that the electron transport should follows discrete electron states [39]. The ballistic conduction means that there are no scattering losses and no overheating. So, high current densities passing through the CNTs structure are allowed [40] (Table 1).

Turning to the mechanical properties (Table 1), CNTs present the highest Young's modulus ever measured [20], but also present extreme flexibility [41], thus giving prove to their high resilience and toughness.

I.1.2. CVD methods and growth mechanisms

Over the past decades, an extensive research work has been carried out to develop cost-effective and high-quality production methods of 1D carbon nanofilaments such as CNFs and CNTs. The earlier reported synthesis of CNFs by a chemical vapour deposition (CVD) method dates back to the 1970's, in investigation works carried out by Baker's group [11] and Endo's group [42]. The CVD growth of MWCNT was first reported by Endo et al., in 1993 [43], following his previously experience in CNFs, two years later to the Iijima's discovery using an arc discharge apparatus. Soon after, in 1996, Dai et al. reported the CVD growth of SWCNTs [44]

CVD methods had cached superior attention over the arc-discharge and laser ablation methods due to their much higher simplicity and higher growth yield. While the latter two use high vacuum conditions, high temperatures (up to 3000°C) and need a continuous replacement of the carbon source (graphite target), the CVD process operates at mild conditions such as amospheric pressure and low temperature (below 1200 °C) with a continuous flowing of a gas carbon source - carbon monoxide (CO) or a hydrocarbon (e.g. C_2H_2, CH_4). Moreover, in CVD methods the dissociation of the gas carbon source is assisted by transition-metal catalyst nanoparticles (e.g. Co, Ni, Cu,Fe) placed on substrates (e.g. Si, glass, metal foils - catalyst-supported methods) [45] or injected directly into the CVD chamber (floating-catalyst methods) [46]. Advantageously, the use of the catalyst is meant to facilitate the control of the nanofilaments structure, such as number of graphene layers, diameter, length and alignment [47, 48].

CVD methods can be also classified accordingly to the activation source of the gas carbon precursor: (1) chemical activation - Combustion flame (CCVD) [49]; (2) electrical activation - Plasma enhanced (PECVD) [50]; and (3) thermal activation - Hot-filament (HFCVD) [51] and hot-wall or Thermal (TCVD) [52]. Although the simplicity of the CCVD method, involving the oxidization of a gas flow mixture of O_2 + hydrocarbon (carbon source) + organometallic (metallic particles source) + carrier gas, it yields a carbon soot with a high amount of carbon by-products and low graphitized filaments [49]. On the other hand, PECVD becomes a very promising method to grow high quality nanofilaments at low temperature (below 500 ºC) on low-melting point substrates such as polymers and glass, highly desirable for electronic applications [53]. Yet, this method is not recommended to large-scale synthesis due to the low yields (limited by the plasma area) and to the great expense of the plasma power source.

Contrarily, the HFCVD methods use inexpensive metallic filaments (e.g. tungsten, W) heated-up at 2000-2500ºC to thermally dissociate the carbon gas precursor at mild pressure (5-100 mbar). These filaments might have different 3D arrangements over large areas allowing the use of growth substrates with a wide range of sizes and geometries. So, the HFCVD methods present higher yields and are more versatile and less costly than PECVD ones. Nevertheless, some limitations of the HFCVD method can be pointed-out. An extra step of carburization of the filaments is needed to avoid the consumption of carbon of the gas mixture during the growth step. Besides this, after the carburization of the filaments they become highly brittle with high appetency to break

under severe conditions, so they limit the range of the growth parameters that might be used. Also, during the growth run, small metallic clusters of the filaments or components near the hot filaments might evaporate and condensate on the substrates, and then catalyze the growth of carbon by-products and/or interfere with the as-placed catalyst particles used to nucleate and grow carbon filaments [54]. Another disadvantage is that the filaments have a upper limit temperature (melting point temperature), so an extra heating source, a heated substrate (600-800ºC), is needed to increase the gas activation temperature.

The TCVD method consists in a simple furnace running in the temperature range of 600-1200 ºC, sufficiently high to fully activate the gas mixture. The slightly higher temperature used in TCVD, compared to HFCVD, is explained by the first being purely thermally activated. Nonetheless, the absence of the filaments has huge advantages, as referred above. In some cases, the gases mixture flows through a quartz tube housed in the furnace at room pressure (~1000 mbar) and reacts with the growth substrates positioned in a quartz boat, at the hot reaction zone (centre of the furnace). This zone is totally clean, containing only the metal catalyst and the substrate, therefore allowing the growth of nanofilaments with high graphitization level and structural control. Following this, the TCVD methods emerged as the most promising approach for mass production of CNTs as they offer the highest degree of growth control and upscaling potential. Various TCVD-based scalable processes had been developed over the last years, including: (1) floating catalyst methods - "HiPCO process" of the Rice University in 1999 [55]; (2) "CoMoCat process" of the Oklahoma University in 2000 [56]; (3) "Nano-agglomerate fluidized process" of the Tsinghua University in 2002 [57]; and (4) catalyst-supported methods - the "Supergrowth process" of the National Institute of Advanced Industrial Science and Technology (AIST) in 2004 [58].

Among these several CVD methods, the catalyst-supported TCVD provides superior versatility and yields, and the purest CNTs (~99.98%) [58, 59]. This approach has two important advantages: allows the grow of highly dense vertically-aligned CNTs (VACNTs) or "forests" (~10^{11} CNTs.cm^{-2}) with a high structural control [59]; the catalyst can be patterned on the substrate to obtain any desired 1D, 2D or 3D shape of VACNTs [58].

Catalyst-supported TCVD

Catalyst-supported TCVD growth of VACNTs was optimised in the present work by employing Al_2O_3(10 nm)/Fe(1 nm)/Si(200 nm)/SiO_2 substrates and C_2H_2-H_2-Ar gas mixtures. A reactor was bulit contemplating a tubular furnace (RT- 1200ºC) housing a 2" inner diameter quartz tube. This tube was coupled to a set of devices such as mass flows, electrovalves and a PC control station for full automatic operation (Fig. 6a).

In a typical growth run, the growth substrates are placed in a quartz boat and pushed to the hot-zone of the furnace (Fig. 6b) followed by an *in situ* annealing in a H$_2$-reductive atmosphere to

convert the Fe film into nano-sized particles, and subsequent Fe-catalyzed growth of VACNTs in C_2H_2-rich atmospheres.
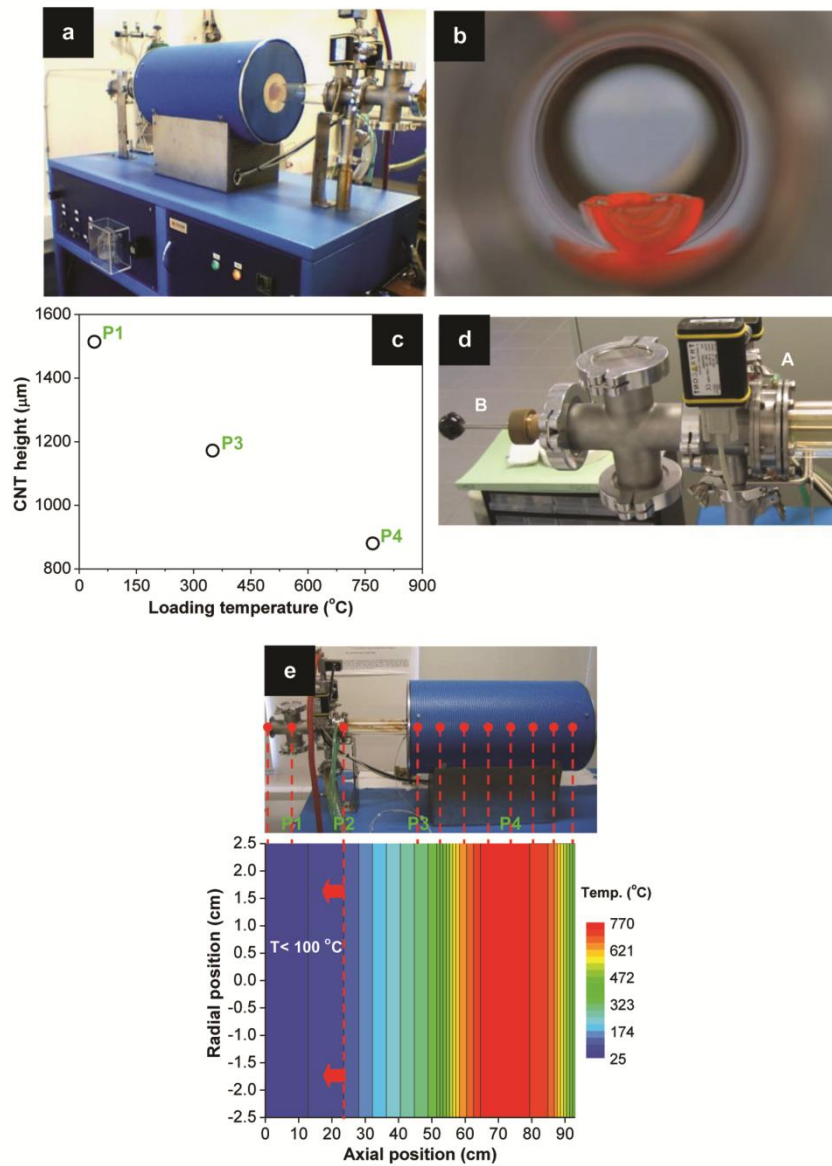
Fig. 6 - (a) Panoramic photograph of the hot-wall CVD reactor setup. (b) Photograph depicting the quartz boat inside the quartz tube at the hot-zone. (c) Plot showing the CNT height dependence on the loading temperature in air. (d) Photograph showing in detail the water-cooled flange (cold-zone) connected to the quartz tube, and also the stainless-steel arm used to push/pull the samples. (e) Temperature profile of the reactor at the set-point temperature of 750ºC.

In conventional hot-wall TCVD reactors, the sample loading/unloading takes place at room temperature. This implies slow heating and cooling steps in each growth run which represent significant shortcomings if high outputs are envisaged. However, these time-consuming steps are required because the sample loading under air atmospheres at temperatures above 300ºC induces

significant cracking of the Fe film and coarsening of the Fe particles, negatively affecting the CNT growth [60]. These observations corroborate data of Fig. 6c that shows the decrease of the CNT height with the increasing loading temperature in air.

To overcome this, a simple solution is suggested by coupling a cold-zone (<300 ºC) to the reactor, a water-cooled flange (labeled with A in Fig. 6d) with high efficient thermal dissipation by conduction. In this way, the furnace can run continuously at the growth temperature and the loading/unloading of samples can be done in a "controlled manner" by using a stainless steel arm (labeled with B in Fig. 6d) to push the samples to the hot-zone under a protective atmosphere.

Fig. 6e shows the temperature profile of the reactor coupled with a cold-zone at a set-point temperature of 750ºC. There is a deviation of 20 ºC between the set-point temperature and the real temperature measured inside the furnace because the temperature is controlled by a K-type thermocouple touching the outer wall of the quartz tube to assure the total cleanness of the reactive zone. The profile of Fig. 6c shows a fast drop of the temperature between position P3 (350ºC) and P2 (100ºC), reaching the minimum value at position P1 (40ºC). The cold-zone (<100 ºC) is defined between P2 and P1.

So, in a semi-continuous process, the growth substrates are loaded into the cold-zone of the reactor, with the furnace already heated at the set-point temperature. The reactor tube is then pumped down and subsequently filled up with Ar. The quartz boat is then pushed to the centre of the hot zone using a stainless steel arm, allowing a fast heating. After the growth process, the quartz boat is pulled to the cold zone for a fast cooling down to room temperature during less than 2 min, becoming the system ready for a new growth run.

This semi-continuous process has a huge advantage compared to a conventional hot-wall CVD setup by increasing fourfold the daily output yield.

Growth mechanisms

The use of catalytic particles in the CVD growth processes of 1D materials has been reported since 1964, with the pioneer studies of Wagner et al. describing the synthesis of Si whiskers [61], and later on, with the growth studies of carbon nanofilaments by Baker et al. and Endo et al. [11, 42]. Thereafter, it has been found that the catalytic particles have key roles in the production of carbon nanofilaments [62]: (1) lowers the nucleation/growth temperature of the carbon filament by promoting the dissolution of the initial elementary amorphous carbon (or methyl radicals) in the particle and subsequent saturation and precipitation in the form of a graphitic carbon phase; (2) works as a transporting medium in the diffusion process that starts with the initial amorphous carbon being dissolved in the particle and ends when the final graphitic carbon phase is precipitated; (3) helps to mold the tubular graphitic structure making more energetically favorable the perpendicular precipitation of graphene layers to the particle surface than the parallel precipitation one.

14

The Vapour-Liquid-Solid (VLS) mechanism suggested earlier by Wagner [61] and then adopted for the growth of nanofilaments has six main steps that are briefly described in Table 2. Small variations to this general VLS mechanism had been defined by the characteristics of the catalytic particles such as the diffusion process in/on the particle, the catalyst-substrate interactions and the physical state of the catalyst particle (Table 2).

Table 2 - VLS growth mechanism of CNTs.

VLS mechanism description (adapted for carbon nanofilaments)	Variations to Wagner's VLS mechanism		CNT type	Ref.
(1) adsorption of the carbon precursor gas (Vapour state) on the metal catalyst surface; (2) dissociation of the precursor molecules; (3) carbon species dissolution in the catalyst particle; (4) diffusion of carbon species inside the particle (Liquid state); (5) carbon supersaturation and graphite-like structure precipitation (Solid state); (6) metal particle reshaping and successive carbon incorporation into the growing structure.	**Physical state of the catalyst**		SWCNTs	[62]
	Small particles Low metal-C eutectic point	Semi liquid (Gorbunov's model)		
	Large particles High metal-C eutectic point	Solid (Baker's model)	MWCNTs	[63]
	Diffusion process		SWCNTs MWCNTs	[64]
	High C solubility of the metal High temperatures	Bulk (Baker's model)		
	Low C solubility of the metal Low temperatures	Surface (Oberlin's model)		[42]
	Substrate-catalyst interaction			[64]
	Weak	Tip-growth (Baker's model)		
	Strong	Base-growth (Baker's model)		[64]

In relation to the physical state of the particle, it depends on the size of the particle and the eutectic point of the metal-carbon solid solution. Metallic particles with diameters below 10 nm have their melting point highly depressed due to the Gibson size effect (Fig. 7a) [48]; and this temperature can be further reduced up to the eutectic point if the metal solubilizes carbon in its structure, which is favorable with the decreasing of the particle size (Fig. 7b).

For example, Baker et al. found that the activation energy (E_{act}) for the growth of carbon filaments matches that of the E_{act} of the bulk diffusion of C in a solid Ni [11] and Fe [63] lattice, so it was concluded that the Ni and Fe particles are in the solid state at ~600ºC. Conversely, others found Ni [66] and Fe [62] particles behaving like a liquid at ~700ºC. *In situ* TEM observations accomplished by Gorbunov et al. [62] depicts this behavior by showing a ~50 nm size Ni particle moving about 200 nm along the surface of the amorphous carbon film of the TEM grid, leaving a graphitic track behind (high magnified image as inset, Fig. 7c). The graphitic track was formed by a low-temperature catalytic graphitization process promoted by the contact between the particle and the amorphous carbon [62]. Small-range movements of liquid-like particles can also take place according to the Ostwald ripenning, where highly mobile small particles tend to be absorbed by larger ones, as occurred with Fe particles at 987ºC, observed by *In situ* TEM (Fig. 7d) [65].
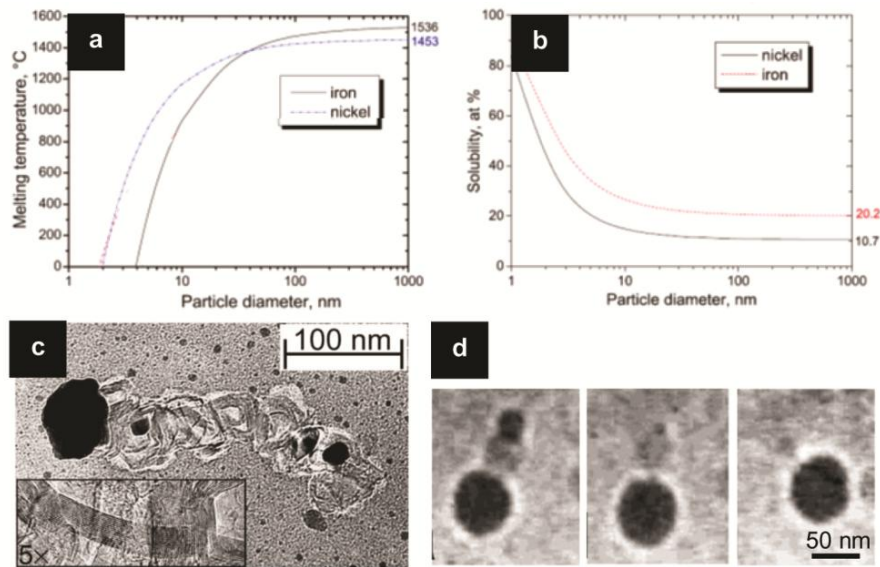
Fig. 7 - Plots showing the dependence of the (a) melting temperature and (b) carbon solubility of Fe and Ni particles on its diameter size (adapted from [48]). (c) *In situ* TEM observations of a liquefied Ni particle at 800 ºC moving on the surface of the amorphous carbon film of a TEM grid leaving a graphitic track behind (high magnified inset picture) (adapted from [62]). (d) Sequence of *in situ* TEM images screening a Ostwald ripenning of nano-sized Fe particles at 987 ºC (adapted from [65]).

According to the growth process described in Table 2, after dissolution (step 3), the carbon species start to diffuse (step 4) inside the particle (bulk diffusion, 8a) or on its surface (surface diffusion, Fig. 8b). The growth conditions that dictates the predominance of one of these mechanisms is the growth temperature and the ability of the metal catalyst to solubilize carbon. For example, at a typical growth temperature of 700ºC, the Cu catalysts admit a surface diffusion [67] whereas the Fe and Ni ones are expectable to assume a bulk diffusion [11, 63, 67]. The driving force involved in both diffusion processes might be temperature [68] or concentration [69] gradients along the surface and/or the bulk of the particle.
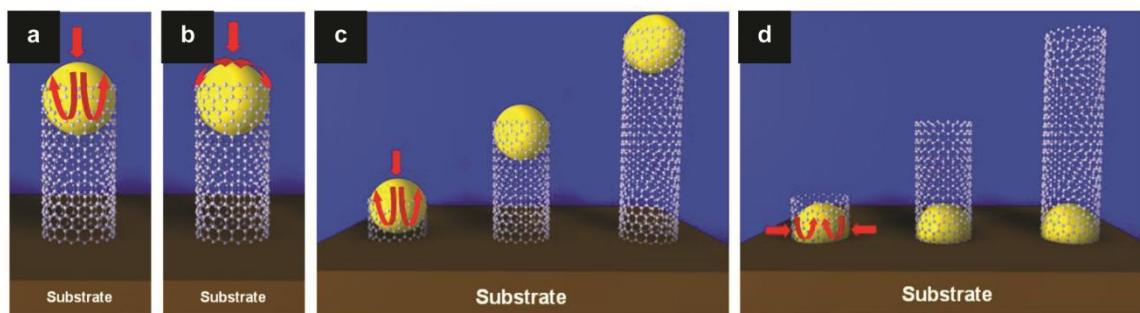
Fig. 8 - Schematic illustration of the growth mechanisms of CNTs regarding the diffusion pathway: (a) bulk and (b) surface diffusion; and the catalyst-substrate interactions: (c) tip and (d) base growth (generated using the Cinema 4D Maxon software).

16

Concerning the catalyst-substrate interaction, it decides the growth mode concerning the position of the catalyst particle in the grown carbon filament structure: the tip growth (top of the structure, Fig 8c) and the base growth (bottom of the structure, Fig. 8d). In the tip growth method, the steps 1 to 3 occur at the "top or front face" of the catalyst particle and after the downward diffusion of the carbon (step 4, highlighted with red arrows in Fig. 8c), it precipitates (step 5) at the "bottom or trailing face" to form the filament. On the other hand, in the base growth the steps 1 to 4 take place at the "lateral face" of the catalyst and in an upward path (highlighted with red arrows in Fig. 8d), respectively, to form a precipitated carbon filament at the "top or front face". These growth modes, the tip and base growth are obtained when the catalyst-substrate present weak and strong interactions, respectively. This interactions can be evaluated by the contact angle formed by the metal particle and the substrate at a given growth temperature. At 700ºC, Ni particles on SiO_2 have large contact angles (weak interaction) [50] while Fe particles on the same substrate present small contact angles (strong interaction) [70], so tip and a base growths are observed, respectively.

Under optimized growth conditions, involving mild growth temperatures (below 750ºC), a high catalyst-substrate interaction is also relevant to avoid an extend coarsening of metal particles during the nucleation and growth steps of carbon nanofilaments [71]. Having in mind the previously mentioned key roles of the catalytic particles during the nucleation and growth steps, the preservation of the shape and size of the catalyst becomes mandatory to grow highly graphitized and millimeter-long structures [71] by: (1) keeping balanced the dissolution-diffusion-precipitation rates in the particle (a constant volume of the particle means a constant atomic ratio of metal/C), to further promote a constant growth rate of filaments for long periods with almost defect-free structures [66]; (2) defining the angle between the precipitated stacked graphene planes and the filament axis, thus dictating the formation of a CNF or a CNT (see section I.1.1) [72]; (3) allowing the strict control of the number of graphene layers and inner and outer diameters of the grown filament, since it was found a close correlation between the initial catalyst particle size distribution and the final filament diameter distribution [59]; (4) permitting the growth of filaments by a base-growth model which allows to obtain almost catalyst-free materials, by leaving the catalyst particles anchored to the substrate after removing the grown materials [58]; (5) allowing the preservation of the particle density [73] and thus a perfect vertical alignment of the grown filaments by Van der Wall interactions of neighbored structures [74].

Moreover, considering a specific catalyst-substrate system, the growth mechanism of carbon nanofilaments is governed by a narrow range of growth conditions that set up the best equilibrium between the dissolution-diffusion-precipitation rates of carbon (i.e. controlled kinetics regime) [71]. Between these three steps and the others showed in Table 2, the diffusion step of carbon in/on the catalytic particle was found to be the slowest (i.e. the limiting step with higher activation energy, E_{act}), as suggested by several kinetic studies [75, 76]. Fig. 9 shows an example of a tight window of growth conditions with a controlled kinetics regime optimized for a Fe catalyst/Al–Si–O substrate system [71].

At the top-left-side of the window, for high concentrations of carbon and low temperatures, filaments cannot grow due to the fast poisoning of the catalyst (covering with a thick carbon layer [77] because of the low rate of carbon dissolution and diffusion, so, only carbon by-products are obtained. On the other hand, at the bottom-right-side of the window, for low concentrations of carbon and high temperatures, there is an inefficient grow of filaments because big particles formed by a strong Ostwald ripening cannot saturate with a small amount of carbon, thus there is no further precipitation. The extreme conditions of the window lead to high values of growth rates and the final length sizes. Both are intimately related dissolution-diffusion-precipitation rates and the latter is also related to the lifetime of the catalyst. Wherefore, these terminally-activated rates and the lifetime of the catalyst have a pronounced dependence on the temperature and the concentration of carbon species. So, high concentrations of carbon and high temperatures conditions gives the much higher growth rates than low concentrations of carbon and low temperatures conditions, but longer filaments are obtained for the latter conditions due to a higher lifetime of the catalyst due to the absence of an excess of carbon species.

Briefly, the control of a catalyst-assisted growth mechanism of carbon nanofilaments is intimately dependent upon the combination of a strongly bonded catalyst-substrate system and a controlled growth kinetics regime.
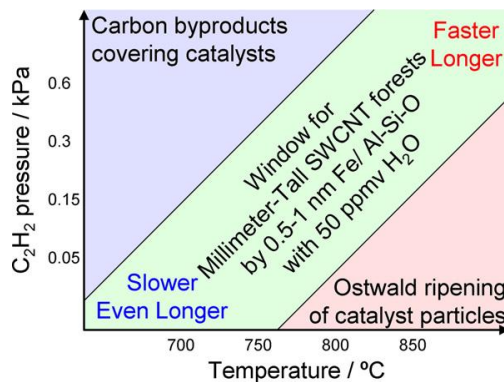
Fig. 9 - Colour mapping showing the growth parameter window (C_2H_2 pressure and temperature) for millimeter-long CNT forests grown on a Fe catalyst/Al–Si–O substrate system (adapted from [71]).

I.1.3. Applications

The supreme properties of CNTs had been promoting huge enthusiasm over the last decades, guiding to the exploration of a wide range of potential applications. Table 3 compiles some of these applications, divided in two main categories: properties and scale.

Table 3 - CNT applications.

Properties	Limited-volume applications	Large-volume applications
Mechanical	▪ Microcatheters [78]; ▪ Probes [79].	▪ Structural composites[80];
Electrical and Electronic	▪ Electrodes[81]; ▪ Sensor devices[82, 83]. ▪ Nanoelectronics[84, 85]. ▪ Electro-stimulated drug-delivery systems [86, 87].	▪ Supercapacitors[80]; ▪ Li-ion batteries [88]; ▪ "Smart" multifunctional composites[89, 90]; ▪ Fuel-cells[91]; ▪ Field emission displays/lighting[92];
Thermal and Optical	▪ Thermal rectifiers[93]; ▪ Flurescent markers for cell targeting[33, 94].	▪ Photovoltaic devices[95]; ▪ Transparent conducting films[96, 97].

Considering the high aspect ratio of CNTs, they are indicated to work as field emission materials [92] in electron microscopes or in field emission displays/lightening, with some advantages over the common Si and W tips such as the higher current densities and resistance to electromigration [80] . Also, the high aspect ratio, high mechanical strength and flexibility convert them into ideal materials to be used as scanning probes (e.g. AFM -atomic force microscopy and STM - scanning tunneling microscopy) [79] and microcatheters [78]. Additionally, CNTs can be applied as electrodes [81], in electrochemistry and in electrocatalysis of fuel cells [91, 98], as simple electron donors in photovoltaic devices [95] or sensor devices (e.g chemical and physical) [82], due to their high surface area, high conductivity and chemical stability in a wide range of potentials. The high surface area of CNTs has also catching some attention for supercapacitors and lithium-ion batteries applications [88]. Finally, CNTs have been applied in several nanoelectronic devices (e.g. FETs - field effect transistors and interconnects) due to their high chemical stability, high current density (over 1000 that for copper) and high thermal conductivity (Table 1) [85]. The latter property allows CNTs to work as thermal rectifiers to prevent overheating in devices [93]. However, one of the biggest problems for the electronic application of CNTs is that their band gap depends on the structure chirality. So far, the strict control of the CNT structure is not possible, but some progresses have been made by engineering the metal catalyst particles involved in the CNT growth mechanisms.

Moreover, low weight structural CNT-based composites have catching huge interest in several areas (e.g. aerospace and automobile). These high-performance composites were possible to be designed due the combination of a high CNT Young's modulus (Table 1) and a low density of 2 g.cm^{-3} [80]. Another use of CNTs in composites is as high electroconductive fillers (Table 1) to produce conductive composites at low percolation threshold owed to the CNT high aspect ratio (length to radius ratio up to 10^4). The low electrical percolation threshold and the high flexibility of CNTs make then promising to produce transparent and flexible conducting composite substrates [97] for the displays industry, in replacement of brittle indium tin oxide (ITO) ones.

In addition, the high surface area and the ability to bond chemical groups make CNTs as ultimate fillers in "smart" multifunctional composites with escalating interest for biological applications. These CNT-based composites had triggered a particular excitement in tissue engineering [90, 99], with major attention in nervous and bone tissues [90, 100], due to the accumulation of several CNT functionalities in an unique scaffold material, such as: electrical

conductivity for cell sensing [83] and control of cell functions under electric stimulation [89], fluorescence for cell tracking [33, 94] and *in situ* delivery of functional biomolecules, from CNT outer wall or hollow core, under (or not) an electro-stimulated release [86, 87].

I.2. Electrotherapy of bone

I.2.1. Physiology of bone and remodelling cycle

Bones are the main component of the human skeleton, which also comprises ligaments, cartilage and tendons and serves a variety of functions: (1) provides structural support for the rest of the body; (2) allows movement and locomotion by providing levers for the muscles; (3) protects vital internal organs and structures; (4) provides maintenance of mineral homeostasis and acid-base balance; and (5) provides the environment for blood cells production [101, 102].

Bone is a supportive connective tissue with a hierarchical structure that defines its unique properties [102]. By weight, mature bone matrix normally is approximately 10% of water, 20% organic matter (consisting mainly of collagen and proteoglycans, and the remainder of cellular components), and 70% inorganic matter (consisting primarily of a calcium-deficient carbonate-substituted apatite crystals, similar in structure and composition to hydroxyapatite HA [103]) [102]. Collagen fibbers with few nanometers in diameter provide flexible strength to the matrix, while the mineral components offer the matrix compression strength.

Every adult skeleton contains 206 major bones that can be described according to their shape or histological organization [104]. Based on the shape, four categories of bones are commonly mentioned: (1) flat bones, that present thin, roughly parallel surfaces (e.g. sternum and ribs); (2) irregular bones, that have different shapes with short, flat, notched or rigid surfaces (e.g. vertebrae and sacrum); (3) short bones, that are small and boxy (e.g. carpal and tarsal bones); (4) long bones (Fig. 10), which are relatively long and slender (e.g. bones of the superior and inferior members) [101].

Regarding the histological organization of an adult long bone (Fig. 10), it contains three principal components: (1) diaphysis (body of the bone); (2) epiphysis (extremities of the bone); and (3) epiphyseal lines (area between diaphysis ad epiphysis). The first is formed by compact bone (also called dense or cortical bone) (Figs. 10a and 10b) organised in a sophisticate tubular Harversian system (Fig. 10c). This system is arranged by a group of concentric lamellas involving centred blood vessels. The compact bone can be seen surrounding the medullar cavity. Also, compact bone is delimited by an external protective bilayer named periosteum (fibrous and cellular layers) and by an internal layer designated endosteum. Secondly, the epiphysis is mainly constituted by cancellous bone (also called trabecular or spongy bone) surrounded by cortical bone (Figs. 10a and 10b). The cancellous bone consists of delicate bars and sheets of bone, *trabeculae*,

which branch and intersect to form a sponge like network [102]. Thirdly, the epiphyseal lines are seen in mature bones and result from the calcification of the epiphyseal plate, where the bone growth process take place.
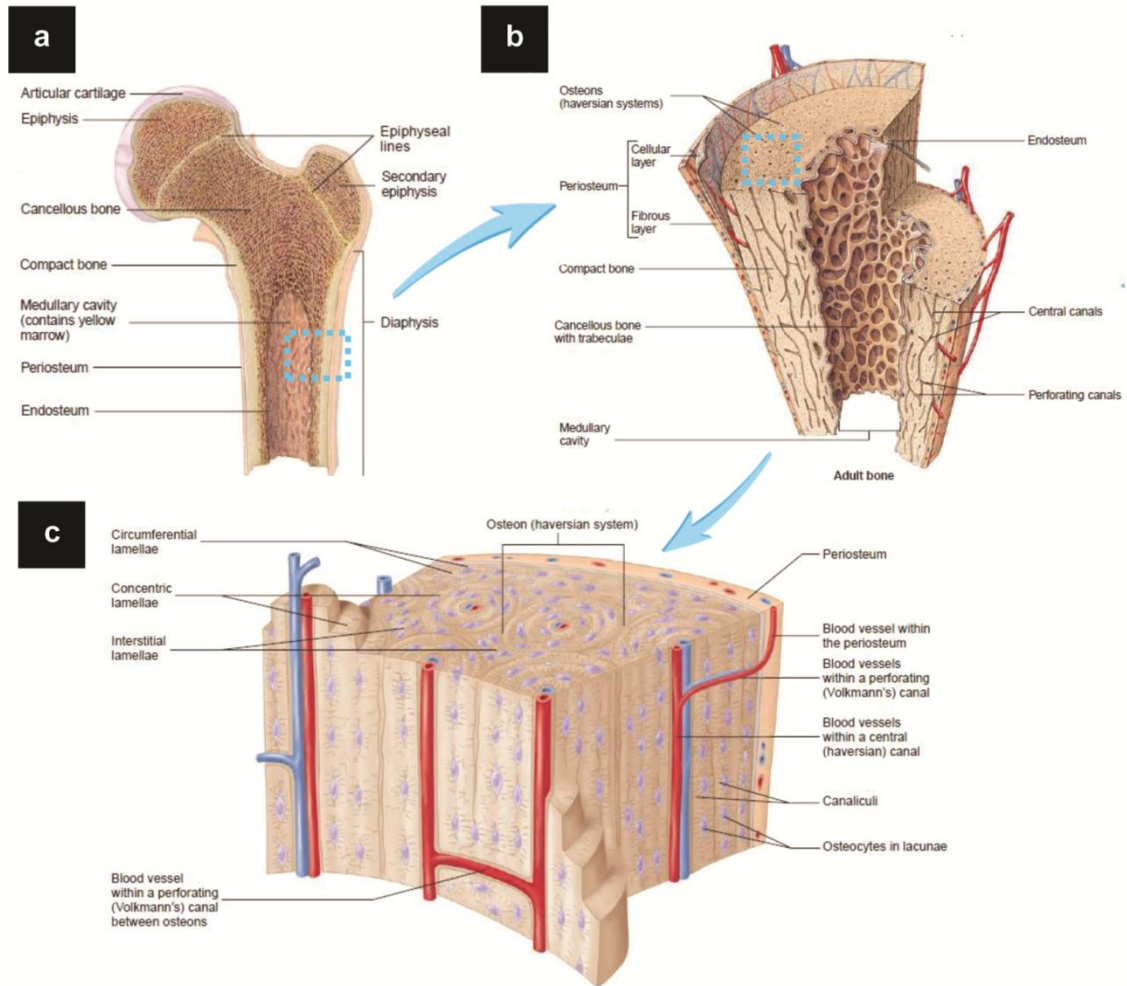
Fig. 10 - Squematic images of the histology of a mature long bone: (a) general view; (b) magnification of the diaphysis section; (c) magnification of the cortical bone section along side with the detailed histology of the Haversian system (adapted from [102]).

Beyond the extracellular bone matrix, bone tissue is formed by specialized cells (Fig. 11), whose main type are: (1) the osteoblasts or bone-forming cells; (2) the osteoclasts or bone-resorbing cells; and (3) the osteocytes [102, 105].
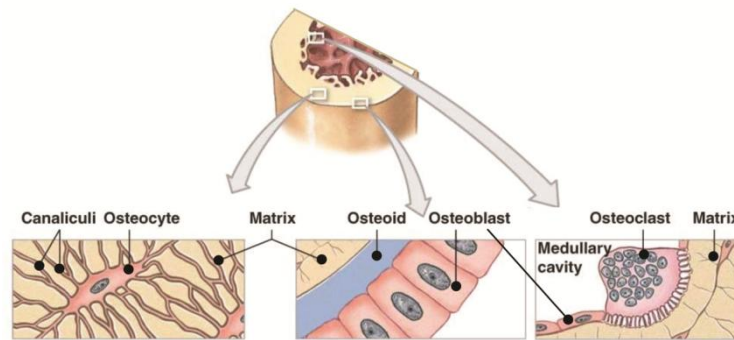
Fig. 11 - Squematic images of the bone cells and their histological organization (adapted from[106]).

Osteoblasts: Derived from osteochondral progenitor cells. They consist of mononuclear, cuboid-shaped cells with an extensive endoplasmic reticulum and numerous ribosomes, usually found lining the bone matrix they are producing. They are responsible to deposit the uncalcified bone matrix, named *osteoid*, and to subsequently provide for its mineralization.

Osteoclasts: Derived from stem cells in red bone marrow. They consist of large cells with several nuclei (with irregular shapes), found attached to the bone matrix in small depressions named *Howship's lacunae*. Responsible for the degradation of the bone matrix. To resorb bone, they polarize, acidify the resorbing lacuna and secrete proteolytic enzymes.

Osteocytes: Represent terminally differentiated osteoblasts. They consist of spider-shaped cells encased in a lacuna, abundantly dispersed in the mineralized matrix and connected to each other and with the surrounding medium through their dendritic processes located in tiny canals called *canaliculi*. They act as mechanosensors, instructing osteoclasts where and when to resorb bone and osteoblasts where and when to form it. They are also responsible for the regulation of phosphate and calcium homeostasis.

Bone remodelling: an overview

Bone is constantly being resorbed by osteoclasts and then replaced by osteoblasts in a process called bone remodelling that is mandatory for the success of the following functions: (1) removal of primary and infantile bone, and deposition of the mechanically competent secondary bone (i.e. bone growth in diameter and length, Fig. 12a); (2) old bone renewing; (3) removal and substitution of ischemic or microfractured bone; and (4) regulation of calcium homeostasis [107].

Bone remodeling (Fig. 12b) is performed by clusters of bone-resorbing osteoclasts and bone-forming osteoblasts arranged within temporary anatomical structures known as "basic multicellular units" (BMUs) [102]. The process is accomplished according to four sequential and highly regulated phases [107]:

1. *Activation phase:* osteoclasts are activated in specific focal sites by mechanisms that are still not understood, but may occur because of microfractures, alteration of mechanical loading sensed by the osteocytes and some factors realeased in the bone microenvironment, e.g. parathyroide hormone (PTH). These converge on lining cells - quiescent osteoblasts that secrete factors able to recruit osteoclast precursors, allowing their differentiation, migration, and fusion toward multinucleated osteoclasts.

2. *Resorption phase*: once differentiated, osteoclasts polarize, adhere to the bone surface and initiate resorption. This is accomplished through the secretion of hydrogen ions and lysosomal enzymes, particularly cathepsin K, which can degrade all the components of bone matrix, including collagen, at low pH. The attachment of osteoclasts to bone may require specific changes in the "lining cells" on the bone surface, which can contract and release proteolytic enzymes to uncover a mineralized surface. Osteoclastic resorption produces irregular scalloped cavities on the trabecular bone surface, called Howship lacunae, or cylindrical Haversian canals in cortical bone. This phase has been estimated to last 2-3 weeks in humans.

3. *Reverse phase*: This phase lasts 9 days, during which osteoclast activity is arrested, likely by promoting osteoclast apoptosis (i.e. cell death). During this phase, reverse cells are seen on the bone surface. The role of these cells is not totally clear, but it is recognised that they are macrophage-like cells possibly responsible for the removal of residues produced during matrix degradation. Moreover, these cells might participate in the release of factors that inhibit osteoclast and/or stimulate osteoblasts.

4. *Formation phase:* This phase takes 4-6 months. Bone matrix resorption leads to the release of several growth factors which are likely responsible for the recruitment of the osteoblasts to the reabsorbed area**.** Once recruited, osteoblasts produce the new bone matrix, initially not calcified (osteoid), and promote its mineralization, thus completing the bone remodelling process. Osteoblasts that remain encased in the new bone matrix eventually differentiate into osteocytes, other osteoblasts become quiescent and form flattened lining cells on the bone surface until a new remodelling cycle is started, while the remaining osteoblasts die by apoptosis.

The bone remodeling cycle is a slow process where resorption is much faster than formation. This process occurs at the endosieum (Figs. 10 and 11) in an inside-out way (see arrows in Fig. 12a). The correct balance between bone formation and resorption is crucial for the proper maintenance of the bone mass. A deregulation of this balance can produce a variety of skeletal disorders (e.g., osteoporosis) [107].
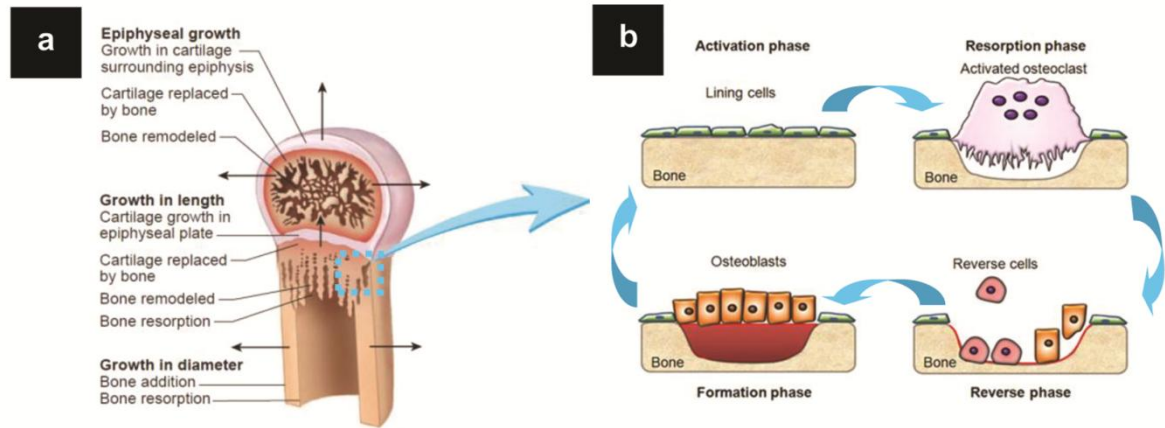
Fig. 12 - Squematic images of the (a) remodelling process involved in the growth of a long bone (adapted from [102]) and of the (b) remodelling cycle (adapted from[102]).
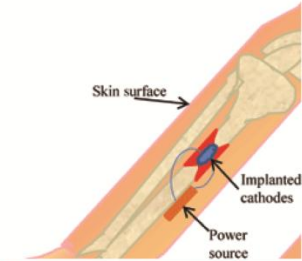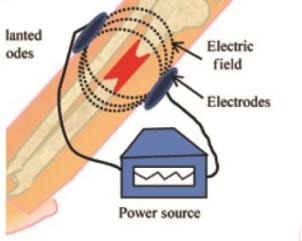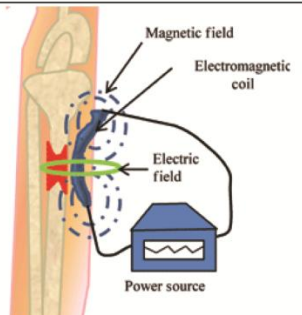
I.2.2. *In vitro* and *in vivo* electrical stimulation of bone and stimulation mechanisms

Endogenous electric signals in living organisms were documented earlier in 1792 by Luigi Galvin [108]. Since then, several works had been reporting electric signals in organs, tissues and cells guiding to the general postulation that living organisms are electrodynamic systems [109].

In 1954, Yasuda firstly found endogenous electric signals in loaded dry bone, i.e. bone piezoelectricity [110]. Years later, it was suggested by Basset and Becker that intrinsic piezoelectric potentials in bone might influence its proliferation and functions [111]. This idea was further supported latter on, by the discovery of the coexistence of two sources of electrical currents in wet bone: piezoelectric currents in mechanically deformed collagen fibres (organic component of bone) [112] and electrokinetic currents originated by strain-induced interaction of charged constituents of extracellular fluids flowing through mineral phase of the matrix (inorganic component of bone) [113]. These electrical currents found in healthy bone are not expected to exist at the fractured bone site, in case of bone tissue damage or loosening. So, it was thought that the use of exogenous electric fields would mimic the mislaid endogenous electric signals and accelerates bone healing [114].

Following this idea, numerous *in vitro* and *in vivo* studies have been accomplished to evaluate the effects of electric fields in bone cell functions and bone tissue growth as well as to optimize the electrical metrics (e.g. frequency, duration, magnitude and waveform). The stimuli are generally applied by three FDA (Food and Drug Administration) approved methods described in Table 4: (1) invasive - direct current by implanting electrodes (DC) earlier found by Dwyer's group; and non-invasive - (2) capacitive (CC) by Brighton's group and (3) inductive (IC) coupling by Bassett's group [115, 116].

Table 4 - Electrical stimulation methods of bone (adapted from [115]).

Stimulation method		Scheme	Description
Invasive	Direct current		A cathode is implanted at the fracture site which is attached to either a subcutaneous power source or an external power source to generate an electric field at the fracture site.
Non-invasive	Capacitive coupling		Two capacitive coupled electrodes are situated on the skin on either sides of the fracture site. An external power source is then attached to the electrodes, which induces an electric field at the fracture site.
	Inductive coupling		An electromagnetic current carrying coil is placed on the skin overlying the fracture site, which is attached to an external power source. The coil generates a magnetic field in the axis of the coil, which induces an electrical field along the same axis but perpendicular to the magnetic field at the fracture site.

Earlier *in vitro* stimulation studies of osteosarcoma cells (ROS 1712.8) using direct electrodes (DC) dates back to 1987, performed by Noda et al. [117]. It was used a 60 Hz sinusoidal electric field with current densities of 300 pA.cm^{-2} for 34 h to show an increment of DNA synthesis. At the same year, Cain et al. [118] reported the inductive coupling stimulation (IC) of primary rat calvarial osteoblast cells to study the PTH-stimulated adenylate cyclase response. Magnetic fields of 0.6 mV.cm^{-1} were used to induce 15Hz pulses of 2 ms. Years later, in 1989, Ozawa et al. [119] reported similar results to Noda et al. with enhancement of DNA synthesis for electrically stimulated osteoblast-like cell line (MC3T3-E1). In this case, capacitively coupled (CC) electrical fields of 32 V.cm^{-1} were used with a waveform having 10 Hz pulses of 3 ms.

In vitro stimulation studies of osteoblast cells have the limitation of evaluate exclusively the formative activity of bone. Yet, living bone has the ability to both resorb and form. So, to make sure that only the formative activity of bone was stimulated, as expected, *in vivo* studies have been also conducted.

In 1968, McElhaney et al. found that in a rat model the remodelling process of bone tissue has a frequency-dependent response when stimulated by capactively coupled (CC) sinusoidal fields. While 30 Hz signals were effective to prevent bone loss, 3 Hz signals were not [120]. Years
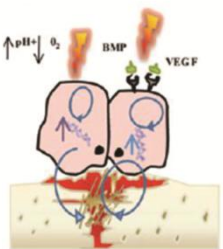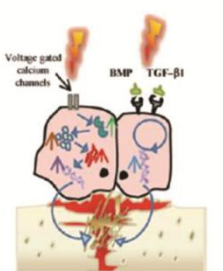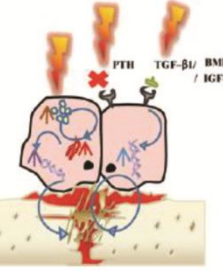
after, in 1971, Lavinei et al. using a rabbit model reported a direct current stimulation (DC) in the range of 2-4 µA for 1-6 weeks. At the 3 week, the stimulated group increased the bone regeneration by roughly a factor of two relatively to the non stimulated condition [121].

Later in 1982, Bassett et al. observed similar results as Lavinei et al. but by using a rat model and pulsed magnetic fields (IC). Electric signals of 2-15 Hz with duration of 200-250 µs were equally effective in promoting bone growth by a factor of two and a half comparatively to the non stimulated condition [122].

These pioneer *in vitro* and *in vivo* studies reporting on the firstly effects of electrical stimulation on osteogenesis shown inconsistencies in the stimulation protocols. Nevertheless, it is able to assess that electrical currents has the potential to control the bone remodelling process.

The mechanisms involved in the regulation of the bone remodelling process are complex and it was found that they are dependent on the applied stimulation method. A recent meta-analysis performed by Griffin et al. [115] compiling 35 *in vitro* studies and 105 clinical studies reporting the evaluation of the electrically induced osteogenesis sheds some light on these mechanisms, briefly described in Table 5.

Table 5 - Electrical stimulation mechanisms of bone (adapted from [115]).

Stimulation method		Scheme	Mechanisms
Invasive	Direct current		Direct current lowers the oxygen level and increases the pH, which causes an increase in osteoblast cell proliferation. This in turn enhances callus formation and maturation, leading to bone healing.
Non-invasive	Capacitive coupling		Capacitive coupling causes an increase in cystolic calcium through voltage gated calcium channels. This then increases intracellular calcium, which in turn enhances activated calmodulin stores. Cell proliferation then increases, which enhances callus formation and maturation, leading to bone healing.
Non-invasive	Inductive coupling		Inductive coupling causes a direct increase in intracellular calcium, which in turn enhances activated calmodulin stores. Cell proliferation is increased, which enhances callus formation and maturation, leading to bone healing.

In respect to non-invasive methods, further details of the stimulation mechanisms are presented. In the normal adult skeleton, bone formation by osteoblasts occurs after the initiation of bone resorption by osteoclasts (remodelling cycle, described in section I.2.1). During remodeling of bone, an increase in the extracellular calcium concentration $[Ca^{2+}]_o$, beneath a resorbing osteoclast, takes place [123]. This local increasesing of calcium plays a critical role in regulating osteoblast proliferation and differentiation via either activation of the systemic hormones (PTH, vitamin D3, prostaglandins) and enhancing in the intracellular calcium concentration $[Ca^{2+}]_i$ into osteoblasts. This calcium influx occurs by transportation through ion channels at osteoblast cell membranes, including mechanosensitive cation channels and voltage-gated Ca^{2+} channels [124-126]

Ion channels are proteins permeable to ions that are embedded in the cell membrane, i.e. lipidic bilayer (Figs. 13a and 13b). Considering a functional voltage-gated Ca^{2+} channel, it is formed by one large subunit that contains four homologous domains such that one showed in Fig. 13a [127]. Each domain is constituted by two basic structures, a voltage sensor (transmembrane segments: S1 to S4) and a pore (transmembrane segments: S5 and S6) [127]. The voltage sensor detects the voltage across the membrane and communicate it to the pore favoring its open or close state (Fig. 13b).
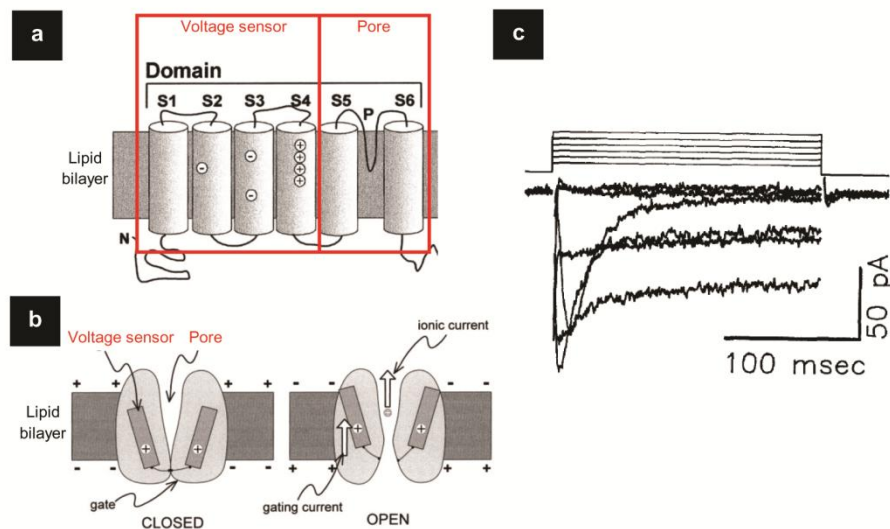
Fig. 13 - (a) Schematic illustration of a domain structure of a voltage-gated Ca^{2+} channel. Four of these domains are assembled into a functional channel (adapted from [127]). (b) schematic view of the gating mechanism of the channel molecule of (a) (light grey area) (adapted from [127]). (c) Voltage-gated Ca^{2+} currents (bottom traces) expressed on of rat calvarial osteoblast cells by depolarization potentials of -80, -50, -30, -10. +10, +30 and +50 mv (top traces) (adapted from [128]).

Voltage-gated Ca^{2+} channels are activated by a electrochemical pathway similar to the initial gating process involved in the production of the action potential via membrane depolarization [126, 129]. When a electrical field with a defined electric dipole orientation is applied to a osteoblast

membrane, resembling a capacitor storing an electric dipole, it will incite a change in the membrane potential (i.e. depolarization), according to the induced external field (Fig. 13b). This reorientation of dipoles within the membrane field produces a conformational change in the ion channel caused by a upward movement of the charged rectangular region inside the channel molecule respecting the membrane potential, allowing the pore opening. Afterwards, the Ca^{2+} ions flow passively with the electrochemical gradient through the channel until the intracellular charge is neutralized and the gate is again closed (Fig. 13b).

Fig. 13c shows a typical current-voltage response for the calcium current expressed on ion channels of rat calvarial osteoblasts cells. In general, Ca^{2+} enters cells via ion channels at rates of ~10^6/s, resulting in a steep $[Ca^{2+}]_i$ gradient or calcium current lasting less than 1 ms [130]. *In vitro* studies have been demonstrated that primary rat calvarial osteoblasts cells express two classes of voltage-gated Ca^{2+} channels [131]: "low voltage threshold" (T-type) and "high voltage threshold" (L-type). L-type Ca^{2+} channels have also been identified in rat osteoblast-like osteosarcoma cells such as ROS 17/2.8, UMR-106.01 and MG-63 [132-134]. L-type Ca^{2+} channels have probably the most relevant role in control of the $[Ca^{2+}]_i$ influx and osteoblast stimulation the since they regulate Ca^{2+}-dependent genes and enzymes [135, 136].

After the increasing of $[Ca^{2+}]_i$ inside osteoblast cells, Ca^{2+} signaling pathways considering Ca^{2+}-binding proteins such as protein kinase C [137] and Ca^{2+}/calmodulin-dependent protein kinase II (CaMKII) [138] are activated. Between these two pathways, the CaMKII-dependent was found to be the key regulator one [139]. Calmodulin (CaM) is a Ca^{2+} binding protein that has the ability to be involved in almost all aspects of cellular function via the diversity of its target proteins, which include many protein kinases (CaMKII) and ion channels [139]. CaM not only mediates the effects of changes in $[Ca^{2+}]i$, but also $[Ca^{2+}]i$ itself by regulating the opening/closening of Ca^{2+} ion channels [140]. CaMKII ultimately leads to the activation of cyclin protein expression and acceleration of the rate of entry of cells into the cell cycle [141]. As so, the intracellular Ca^{2+} signals decoded by CaMKII are thought to play a more significant role in osteoblast proliferation than in differentiation (i.e. gene expression) [140-142]. These cellular processes have been shown to be influenced by the wave frequency of Ca^{2+} signals. Interestingly, the multifunctional CaMKII is also able to decode the frequency of Ca^{2+} signals [138].

Both the magnitude (µM) and duration (ms) of individual Ca^{2+} signals modulates the frequency response of CaMKII that are translated into distinct levels of CaMKII autonomous activity [138]. When high local concentrations of Ca^{2+} and thus Ca^{2+}-CaM are present an autophosphorylation or inactivation process of the CaMKII takes place [138]. The autophosphorylation is an intersubunit reaction between two neighbors molecules of CaM enabling the kinase to remain partially active even after calmodulin dissociates [143].

Figs. 14a and 14b show the frequency response of CaMKII to 100 spikes of Ca^{2+}-CaM that ranged from 1 to 10 ms in duration (fixed magnitude of 2.5 µM) and from 1 to 5 µM CaM in magnitude (fixed duration of 2 ms), respectively. These simulations indicate that

autophosphorylation only occurs at significantly high frequencies (>10 Hz) for brief spikes or when very high local concentrations of Ca^{2+}-CaM are present [138].
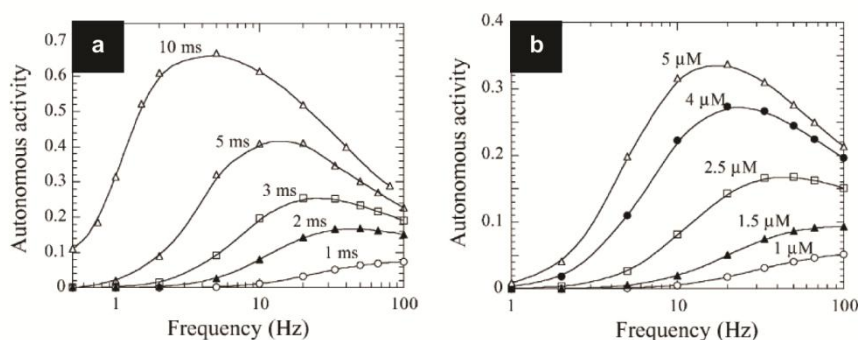
Fig. 14 - Plots depicting the dependence of CaMKII activity on the frequency of 100 spikes of Ca2+-CaM: (a) for a fixed spike magnitude of 2.5 µM and varied burst duration; (b) for a fixed spike duration of 2 ms and varied amplitudes (adapted from [138]).

So, the optimization of the exogenous stimuli frequency and duration would provide three main advantages: (1) controls excess of $[Ca^{2+}]_i$ avoiding autophosphorylation and other perturbations on CaMKII pathway [144]; (2) ensures preferential activation of CaMKII over other Ca^{2+} effectors that require sustained Ca^{2+} or higher frequency Ca^{2+} spikes for activation, thus ensuring some specificity in Ca^{2+}-dependent cascades [138]; (3) avoids any potential harmful effects of excessive Ca^{2+} stimulation such as cell apoptosis [145-147].

Moreover, as voltage-gated Ca^{2+} channels are thought to control osteoblast functions via increasing of $[Ca^{2+}]_i$ and subsequent activation of CaMKII, the optmization of the magnitude parameters of the exogenous stimuli, i.e the electrical current density and the electric field intensity, are also mandatory to ensure the current-voltage gating thresholds of osteoblast cells (Fig. 13c). Alongside with this, the selection of these two stimuli parameters must contemplate the threshold levels of hazard to living organisms. Electrical fields and current densities above 10 V.cm^{-1} and 1 mA.cm^{-2}, respectively, induce cellular and tissue damage from heat generation (Joule's effect) [148, 149].

Moreover, tissue injury originated by pH changes has been correlated to high current densities. While slight increases in pH favour bone formation, substantial pH changes may damage the host bone [163]. The waveform of the exogenous stimulus signal also dictates the increasing of the local pH at the fracture bone site. If alternating electric currents (AC) are used with cyclic reverse of the polarity of the electrodes, the creation of faradic by-products (e.g. hydrogen peroxide, hydroxyl) are avoided, lowering the risk of strong pH changes [154]. Also, AC signals depressed the possibilities for deposition of charged proteins on the electrode surfaces, preventing the loosening of current flow [154].

Table 6 compiles the *in vitro* stimulation conditions of osteoblast cells of some recent studies. The varied stimulation methods and metrics being used since earlier times, referred above, and more recently, presented in Table 6, makes difficult to identify the optimised stimulation conditions, as well as, the correlation of particular cell response to specific field parameters. Yet, these stimulation data give evidences that AC pulses during below 5 ms, with frequencies and current intensities in the range of 10-30 Hz and 10-50 µA, respectively, are preferentially applied. It is relevant to notice that the selection of 5 ms duration time and 10-30Hz frequencies are in accordance with the maximum of CaMKII activity in Fig. 14a. Also, in general, the current selected are within 5-20 µA range found to favour bone cells growth [116].

Table 6 - *In vitro* stimulation conditions of osteoblast cells.

Stimulation method	Signal type/Wave shape/Electric al field (V.m^{-1})	Current (µA)/Current density(µA.cm^{-2})	Frequency(Hz)/Burst duration (ms)/Pulse duration (µs)	Stimulation time (hours.day^{-1})	Osteoblast cell type	Substrate Material	Ref.
DC	AC/-/-	10/-	10/-/-	6	Rat calvarial primary cells	PLA/CNTs (20 wt%)	[150]
DC	AC/Square/-	20/1.5	3000/-/32	6, 24	Rat calvarial primary cells	Coverslip	[151]
DC	AC/-/-	-	0.5/5/-	12	Human bone marrow mesenchymal stem cells	Coverslip	[152]
DC	-/-/200	-	-/-/-	6	Saos-2 cells	PLLA/PPy/HE	[153]
DC	AC/-/-	13,65,130,195/-	20/0.4/-	1	CEL-11372 cells	Anodized nanotubular titanium	[154]
DC	-/-/-	50,100,200/-	-/-/-	4	Rat mandibular cell line	PLA/MWCNTs	[155]
CC	DC/Saw-tooth/-	-	16/-/-	24	Bovine primary cells	Coverslip	[156]
CC, IC	CC: AC/-/2 IC: AC/-/0.16	CC:-/300	CC: 60000/-/- IC: 15/-/-	-	MC3T3-E1 osteoblastic cells	Coverslip	[157]
IC	AC/Sinusoidal/0.6	-	30/-/-	24	ROS 17/2.8 cells	Coverslip	[158]
IC	AC/Square/0.2	-	15/5/200	8	Rat calvarial primary cells	Coverslip	[159]
IC	AC/ Square, Sinusoidal, Triangular, Pulsed/-	-	15/10/200	0.5	Rat calvarial primary cells	Coverslip	[160]
IC	AC/Square/0.2	-	7.5/-/300	2	Human bone marrow mesenchymal stem cells	Coverslip	[161]
IC	AC/-/-	-	15/5/5	24	Human bone marrow-derived stromal cell	Coverslip	[162]

I.2.3. Clinical limitations of electrical stimulation of bone

The clinical use of electrical stimulation to treat nonunions fractures (e.g. femur, tibia, clavicle, radius) is well known for over four decades [116, 164]. Although the general acceptance of

the beneficial effects of electrical stimulation in bone healing, its broadly use in clinical has been limited [165].

Table 7 - Currently clinical available stimulation devices, strengths/weaknesses and success rates [165].

Stimulation method		Device designation	Strengths	Weaknesses	Clinical success rates(%)	Ref.
Invasive	Direct current	OsteoGen® surgically implanted bone growth stimulator	• Patient compliance.	• Invasive (requires surgery for electrode implantation and removal); • Transcutaneous leads have infection risks and mechanical failures; • Electrochemical reactions at the electrode sites; • Limited bone formation near the electrodes; • Damage of the newly formed bone tissue during removal of the electrodes.	63-86	[168, 169]
Non-invasive	Capacitive coupling	OrthoPak 2® bone growth stimulator	• Non-invasive.	• Requires high voltages with large limbs; • Non concentrated delivering of electrical fields at the nonunion site; • Patient compliance.	70-77	[170, 171]
	Inductive coupling	EBI® bone healing system	• Non-invasive.	• Nonweight bearing technique; • Non concentrated delivering of electrical fields at the nonunion site; • Interferences if highly magnetic metal is within the region of the nonunion site; • Patient compliance.	84-87	[172, 173]

This is because clinicians have failed to notice that electrical current densities are more relevant than electric current to promote bone osteogenesis [165]. So, severe patient complications have been occurred from overloaded stimulation leading to osteonecrosis [166]. The restrained use of electrical stimulation is also caused by limitations of the clinical available stimulation devices. Some of the most currently applied FDA approved stimulation devices in the clinic are presented, alongside with respective strengths/weaknesses and clinical success rates (Table 7).

On the whole, the invasive approach is considered the least attractive. This stems from the lowest control of the electrical current density due to the variable spatial position of the electrodes when implanted. Also, it yields limited bone formation near the electrodes and the high risk of inflammation and damage of the newly formed bone tissue when the implanted electrodes are removed [165]. Although preferential, non-invasive methods also present some weaknesses. The electrical stimuli are randomly delivered, targeting non-specified cells, not only those of the injured

bone but also others of the surrounding conductive tissues having similar voltage-gating response [167]. The activation of voltage-dependent pathway signals in the surrounding tissues may lead to an overloaded concentration of the internal Ca^{2+} concentration in cells (see section ver) causing functional disorders (e.g. oxidative stress, cytotoxicity) and its premature apoptosis [147].

Besides the differences of mechanisms (Table 5) and strengths/weaknesses (Table 7) of the three stimulation methods, they show similar clinical success rates with an average value of 75 %, also reported by others [116]. These are considerably high rates but they could be even higher. Accordingly to Brighton et al. [116], the efficiency of all reported stimulation methods in treating nonunions fractures depends on the combination of the following requisites: (1) the treatment time should be from three to six months; (2) the nonunion has to be immobilized during the treatment period; (3) the electric fields must be concentrated exactly in the nonunion site; (4) the gap at the nonunion site needs to be small (one half the diameter of the bone). This last requisite is particularly restrictive, if the gap is too large there will not be enough cells at the nonunion site to form new bone when electrically stimulated and those the union of opposite bone counterparts fail to occur.

Novel solutions based on electrically conductive bone grafts are promising to solve some of the currently drawbacks seen in clinical stimulation of bone by confining electrical fields at the nonunion site, by annulling the imposition of a minimum gap size and ultimately by decreasing of the post-operative healing time of patients. Yet, these materials have not been used. This because most of the conductive bone grafts used in orthopaedics are so only due to the use of metallic phases [174]. These are limited by strong oxidation enhanced by the electrical current. Electrode degradation induces cytotoxicity making these grafts unsuitable under electrical stimulation routines [175, 176].

I.3. CNT-bioceramic bone grafts for bone electrical stimulation

I.3.1. Promises and challenges

When bone is lost due to injury or illness, bone grafts are inserted at the bone damaged site to restore skeletal integrity by offering mechanical and biological functional supports during bone repairing. To ensure these functionalities, bone graft scaffolds should fulfil the following main criteria [174]: (1) biocompatible; (2) biodegradable (with non-cytotoxic degradation by-products) with a resorbtion rate close to that of the new growing bone; (3) highly interconnected porous network for bone ingrowth, vascularization and nutrient delivery; (4) mechanical properties to keep its structural integrity and thus to preserve the porous network during the first stages of the new bone formation.

The clinical applications of bone graft substitutes have a market value set at 1.2 billion Euros according to 2008 reports, with an annual growth rate of 12.9% for 2008-2014 [177]. The current gold standard of bone grafts is the autograft (i.e. transplantation bone from one part of the body to another in the same individual) [178] since it possesses all the characteristics for new bone growth: osteoconductivity (i.e. growth of bone tissue into the structure of a bone graft), osteoinductivity (i.e. process of stimulating osteogenesis), and osteogenicity (i.e. formation of bone) [178]. However, autografts present drawbacks, including donor-site morbidity and supply limitations, restricting them as an option for bone repair. These limitations have been suppressed by the development of new synthetic bone grafts. The currently synthetic materials in the market include: (1) ceramics (hydroxyapatite - HA, tricalcium phosphate - TCP and calcium sulphate); (2) polymers (polylactic acid - PLA, polyglycolic acid - PGA, and co-polymer of both - PLGA); (3) bioactive glass and glass ceramics (Bioglass® and A-W glass-ceramics); (4) composites (HA/TCP and HA/polyethylene) [179-181].

Calcium phosphate (CaP)

Those with higher clinical application for over more than three decades are the calcium phosphate (CaP) family-related materials (Fig. 15). These have tuned physico-chemical properties, by changing the Ca/P molar ratio - 10/6 - hydroxyapatite (HA, $Ca_{10}(PO_4)_6(OH)_2$); 4/2 - tetracalcium phosphates (TTCP, $Ca_4(PO_4)_2O$); 3/2 - α-phase and β-phase tricalcium phosphates (α, β-TCP, $Ca_3(PO_4)_2$) [182]. The success of these bone graft materials is owed to the chemical resemblance with the inorganic component of the natural bone [183], yielding ceramics with high bioactivity (i.e. formation of a carbonate apatite layer on the surface of the bone graft) [184], osteoinduction [185] and osteoconduction [186].
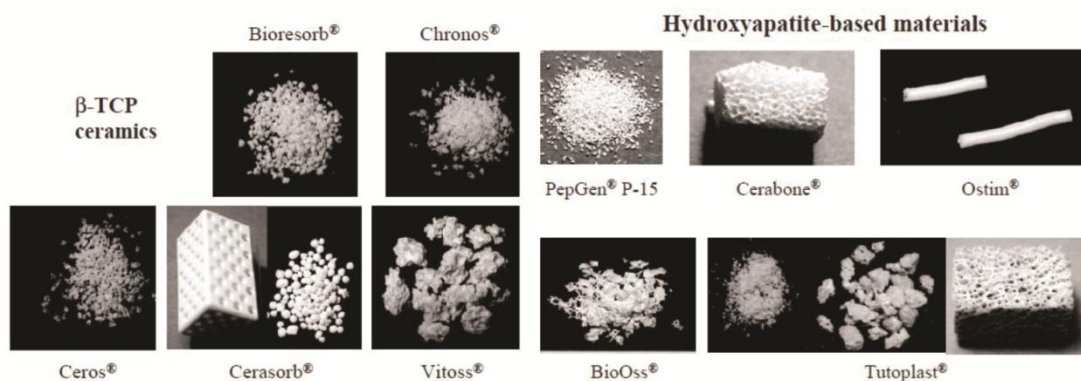
Fig. 15 - Macromorphology of the different CaP-based bone graft materials available in clinic (adapted from [187]).

Even though, these materials do not match two main characteristics of natural bone: mechanical behaviour (toughening and bending strengths [182, 188]) and electrical conductivity [182]. Following this, several fillers have been used to reinforce CaP materials but with lack of success: by falling the matching both requisites referred above; or by matching them, but without preserving the bioactivity of the ceramic matrix. P_2O_5-bioglass reinforced hydroxyapatite (Glass/HA) composites are an example of the first case. This composite present higher mechanical properties [189], bioactivity [190] and osteoconduction [191] than single phase HA but it still being a dielectric material.

Carbon nanotubes (CNTs) as a filler in CaP

Carbon nanotubes (CNTs) have rise as an exciting filler to overcome these drawbacks and also to turn ordinary bone grafts into multifunctional ones, the third generation of improved bone grafts for bone tissue engineering [174, 181, 192]. CNTs are inexpensive fillers, easily mass produced by CVD methods with controlled morphologies and high purities (see chapter I.1.2). Also, CNTs are simply made of carbon, that when incorporated in synthetic HA matrices make them more chemically similar to those of carbonate apatites of natural bone [183]. Moreover, CNT characteristics - non-metallic phases, high aspect-ratio (quasi 1D material) and ultimate mechanical strength and electrical conductivity (Table 1) - make them the highest performance filler to obtain highly tough and conductive biomaterials at low percolation thresholds, without damaging the biological profile of the matrix. Noteworthing, the high surface area and high versatile surface functionalization chemistry of CNTs make them promising delivery vehicles of therapeutic molecules such as glycoproteins and bone morphogenetic proteins (BMP2, BMP4 and BMP7) or antibiotics [193, 194].

CNTs (single- and multi-walled) can be easily tracked and monitorized *in vitro* and *in vivo* by Raman spectroscopy [195] and fluorescence spectrocopy [34, 196, 197]. Of relevance, both Raman scattering and fluorescence are stable with neither blinking nor photobleaching, even after prolonged exposure to excitation [198].

In fluorescence spectrocopy, the photoluminescence of CNTs might occur at different emission wavelengths, ranging from the near-infrared region for pristine SWCNTs [196] to ultraviolet-visible region for chemical functionalized SWCNTs and MWCNTs [34, 197] (Table 1).

For example, *in vitro* CLSM imaging using an argon laser with a wavelength near 488 nm is able to detect and show CNT-NH3+, with the same excitation wavelength (Fig. 16a), interacting with cells (Figs. 16b and c) [197]. Additionally, studies have shown that CNTs are bioactive [200, 201] and present high biocompatibility with bone tissue [202].
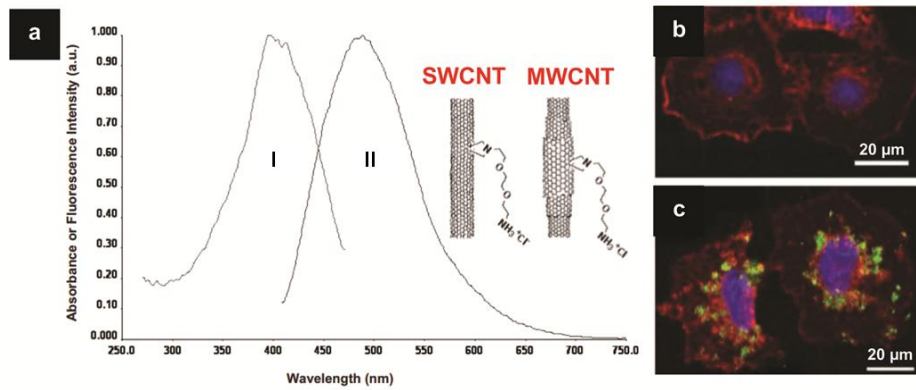
Fig. 16 - (a) Excitation (I) and emission (II) spectra of SWCNTs-NH$_3^+$ and MWCNTs-NH$_3^+$ (adapted from [34]). (b and c) confocal images of A549 cells (plasma membrane stained at red and nucleus stained at blue) in the (b) absence and (c) with SWCNTs-NH$_3$ showed at green ($\lambda_{emissin}$= 510 nm).Scale bar corresponds to 20 µm (adapted from [199]).

SWOT analysis for CNT/Glass/HA composites

However, the risk-to-benefit ratio offered by CNT containing composites should be carefully analysed. Table 8 shows a SWOT analyze of the CNT/Glass/HA composites.

Table 8 - SWOT analysis for CNT/Glass/HA compostes.

CNT/Glass/HA composites	
Strengths	**Weaknesses**
Chemical composition close to carbonate bone apatites	Challenging powder processing and sintering
Non-metallic electroconductive bone grafts (electrical conductor CNT filler)	Non-biodegradability of CNTs
Exposed CNTs in the composite have high surface area and high versatile surface chemistry	Lack of systematic toxicological studies of CNTs.
Visible and near-infrared fluorescence (CNTs)	
Bioactive (CNTs and Glass/HA)	
Biocompatibility with bone (CNTs and Glass/HA)	-
Mimicking of the biofunctionalities of the inorganic (Glass/HA) and organic (CNTs) components of bone	
Opportunities	**Threats**
Smart non-metallic electroconductive bone graft to promote *in situ* electrical stimulation without corrosion related toxicological risks	*In vivo* CNT agglomeration and accumulation may cause unwanted side effects in the long-term.
Controlled delivering of drugs from exposed CNTs in the composite by a electro-stimulated release mechanism.	
Functionalization of exposed CNTs in the composite by functional moieties to maximize its bone grafting performance before implantation by simple immersion of the materials in a solution containing those moities.	-
Enable non-invasive monitoring of carbon nanotube release from the bioceramic upon degradation and biodistribution *in vivo*	

By combining the bioactivity and mechanical strength of Glass/HA composite ceramics with the flexibility and electrical conductivity of CNTs, an unique synthetic bone graft is obtained, mimicking the biofunctionalities of the inorganic and organic components of the natural bone, the apatite-like phase and the collagen I fibres, respectively [188, 203, 204]. This is the central strength of the CNT/Glass/HA composite. The common function among CNTs and collagen I fibres is that both operate as generation source of electrical signals and further pathway delivering to the

surrounding bone tissue. In natural bone, endogenous electrical signals are generated by mechanically deformed piezoelectric collagen I fibres and are then propagated across the conductive living bone (conductive hierarchical structure of blood vessels). On the other hand, in a conductive CNT bone graft it is expected the confinement of electrical signals on its surface and their locally delivery to the neighboured bone tissue. According to literature, these electrical signals embrace a key role in the bone remodelling process by activating voltage-gated ion channels in osteoblastic cell membranes (see section I.2.2). As so, in case of bone damage, by filling the bone loss zone with conductive bone grafts is expectable an acceleration of bone regeneration by *in situ* electrical stimulation promoted by two simple approaches. By considering the conductive bone graft as an electron transportation pathway to endogenous electrical signals, generated by the surrounding healthy bone, at the bone loss zone. Alternatively, the conductive bone grafts can be used to confine exogenous electrical signals applied by electrostimulation apparatus clinically approved *by* FDA (see section I.2.3). The second method as a key advantage over the first one, that is the full control of the level and duration of the delivered stimulus, avoiding the imposition of a mechanical deformation for charge generation, as it is for the piezoelectric bone tissue.

A novel generation of non-metallic electroconductive bone grafts becomes an exciting solution in clinical electrostimulation practices as they are seen as a breakthrough in the delivering mechanisms of stimulus to the damaged bone.
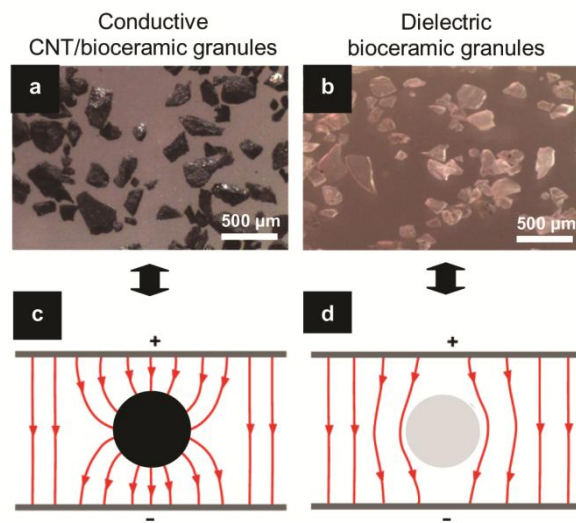
Fig. 17 - Optical images of (a) conductive and (b) dielectric CNT/bioceramic granules. Schematic images of the current density (electric field) lines distributions of a (c) conductive and a (d) dielectric spheres implanted in a homogeneous material

It is expected that conductive bone grafts may be able to increase the electrical conductivity at fracture bone site implying the use of lower applied voltages and to confine exogenous electrical fields on their surface and directly deliver current to cells boosting the spatial and temporal control

of bone tissue regeneration. To further elucidate this behaviour under an *in vivo* scenario, an example is showed considering a capacitive coupling stimulation method with parallel electrodes (Fig. 17). The 2D distributions of the current density (electric field) lines interacting with a conductive and a dielectric bone graft granule implanted in a homogeneous fracture bone site are illustrated in Figs. 17c and 17d [129, 205].

If a conductor is placed between parallel electrodes, positive charges are attracted in one direction and negative charges in the opposite one, originating a small degree of polarization, but there are no fields within the conductor (E=0). Therefore, all the uncompensated charge must reside in the surface layer, where all the external fields are confined at the surface of the conductor in perpendicular angles (Fig. 17c). So, in this case, cells or tissues in contact with the surface of the conductor are crossed by electrical fields. If the charge is reversed, then the polarity of the conductor will change. This causes a small shift in charge, and an alternating electric current is generated locally at the surface of the conductor. Contrarily, in a dielectric material the external fields are parallel to its surface (Fig. 17d), so they are not confined, thus a much lower efficiency of stimuli delivering at the bone fracture site is observed relatively to the conductor material.

Other opportunity of the composite consists in the exploration of the very same current-voltage electrical signal confined on the surface of the CNT composite to control the delivering rate of therapeutic molecules attached to the outer walls of CNTs [206]. The exposed CNTs in the composite can be also functionalized with functional moieties such as antibiotics to avoid infection or bone growth factors to maximize bone bonding and bone functional activity by preimmersing the material in solutions containing those moities [207, 208]. Another opportunity of this composite is that in case of CNT release from the matrix they can be easily tracked and monitored by spectroscopy methodologies.

One of the weaknesses of the CNT composites is that they are very difficult to process due to the high tendency of CNTs to agglomerate by strong van der Waals forces and due to CNT oxidation during dehydroxylation of HA at high temperatures [209] (see section I.3.2). Other weakness is the low *in vivo* biodegradation of CNT structures, though strategies to make them biodegradable are actively pursued. Recently, it has been reported the *in vitro* and *in vivo* degradation of CNTs by human neutrophil cells [210] and by brain cortex tissue in a mouse model [211] leading to new window of opportunities for bioapplications of CNTs.

Other weakness is the lack of systematic toxicological studies of CNTs to evaluate the dependence of their toxicological risks on doses, CNT types and route of administration. It is mandatory a complete toxicological profile of CNTs to make them 'standard' fibrilar nanomaterials. This would help to avoid absolute statements such as "CNTs are toxic" that are damaging to their potential clinical use (see section I.3.3).

The highest threat of CNTs containing composites under an *in vivo* scenario is the release of nanotubes from the composite and extensive agglomeration and accumulation in tissues or organs. This might cause unwanted side effects in the long-term such as triggering an acute inflammation response and formation of granuloma lesions [212] (see section I.3.3).

I.3.2. Processing and properties

The ultimate carbon fibres, CNTs [213], have catching high interest to reinforce bioceramics due to their intrinsic properties (see section I.1.3). To take advantage of these properties, CNTs should be homogeneously distributed in the matrix to maximize the interfacing area with the matrix and achieve low electrical percolation thresholds. Yet, this goal is challenging because CNTs tend to agglomerate due to their high surface area and to high CNT-CNT van der Walls forces and in its turn tends to have typically poor CNT interactions with solvents and matrix components [209]. To maximize these interactions, CNT surface is commonly functionalized either directly by π-bonded chemical groups, non-covalently bonded and covalently bonded (Fig. 18), or indirectly by surfactants [209, 213].
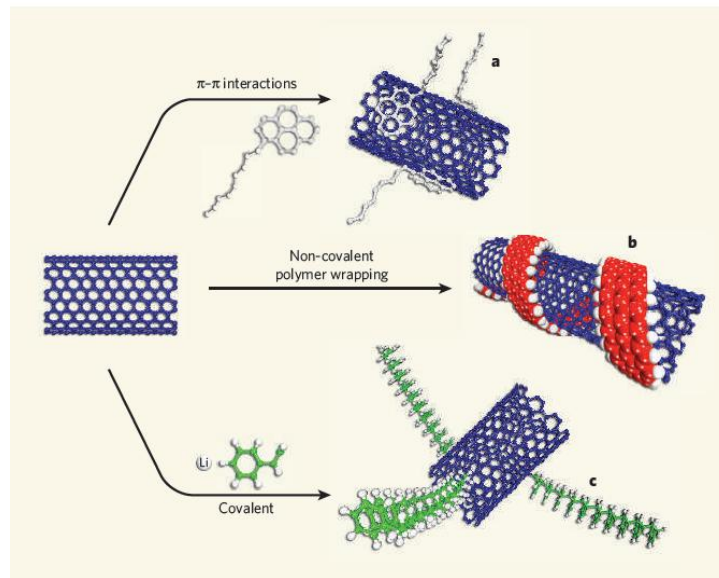
Fig. 18 - CNT functionalization approaches (adapted from [213]).

Also, to take full advantage of these interactions, the powders have been prepared in wet conditions under vigorous mixing (e.g in situ chemical precipitation, mechanical mixing, spray drying). Alternatively, other reinvented methods contemplating in situ CVD growth of CNTs on the HA powder have been also considered. The description and advantages/disadvantages of the main processing methods of CNT-HA systems are presented in Table 9. The first attempt to prepare these powders dates back to 2004 by a chemical precipitation method [214]. This process becomes very promising in preparing powders with high homogeneity and improved adhesion between HA and CNTs, but its complexity restricts its use to laboratory scale. On the other hand, mechanical mixing (e.g. ball milling, ultrasonication and high speed shearing) and spray drying are classified as bulk-scale production routes. Ball milling has been avoided due to strong damage and breakdown to CNTs [215] and to high formation of CNT agglomeration [216]. Ultrasonication and high speed shearing, when not used excessively, do not damage CNTs [217]; and when applied

altogether with an efficient solvent dispersion medium and/or a chemical exfoliator/dispersior, they can yield uniform powders and final highly dense compacts. Spray drying is based in a powder atomization process that originates micro sized agglomerates of homogeneous mixtures of HA and CNTs [218]. Contrarily to standard free powders, these agglomerates make harder the full sintering by pressureless processes.

To avoid the multi-steps involved in conventional powder processing methods and thus preserve the CNT structure, altogether with the assurance of a satisfactory homogeneity and interaction of the CNT/HA powders, an *in situ* CVD growth of CNTs on the HA powder was also explored by Li et al. in 2008 [219]. This investigation followed the pioneer work of Alain Peigney with Al_2O_3-based matrices [220]. In this process, high load of metallic particles such Fe (up to 10 wt.%) are added to ceramic powders to catalyse the *in situ* growth of CNTs on the HA powders. Indeed, these metallic particles were trapped in the final composite which is highly undesirable due to toxicological issues.

Table 9 - Powder processing and consolidation methods for CNT/HA composites, description and strengths/weaknesses.

	Method	Description	Strengths	Weaknesses	Ref.
Powder processing	*In situ* chemical precipitation	CNTs dispersion in a chemical bath along side with HA precipitation in its surface	Powders uniformity and strong CNT-HA interactions	Lab-scale method	[214]
	Mechanical mixing	Mixing of phases under shearing, gridding or sonication forces	Bulk-scale method	CNT damage if used excessively	[215-217]
	Spray drying	Atomization of powders and organic binder conjugates to produce micro-sized agglomerates	Powders uniformity and strong CNT-HA interactions	Agglomerates are unsuitable for pressureless methods consolidation	[218]
	In situ CVD growth	CVD growth of CNTs on metal catalyst/HA powder mixtures	Undamaged CNTs due to lack of manipulation	High load of metallic particles contamination	[219]
Consolidation	Sintering	Sintering in reductive atmospheres	Economic and non geometrically limited	Low densification and low HA and CNT retention	[221]
	Reactive sintering	Sintering in reductive atmospheres with samples embedded in a reactive powder bed	High HA and CNT retention	Low densification, still higher than the sintering method	[222]
	Hot-pressing	Pressure assisted sintering in reductive atmospheres	High HA and CNT retention and high densification	Geometrically limited method and CNT damage	[223]
	Spark plasma sintering	Pressure assisted sintering in reductive atmospheres with a pulsed current passing through the sample	Extremely fast sintering leads to high HA and CNT retention, and helps obtaining nanostructures	Expensive and geometrically limited	[218, 224]

The further consolidation step of the green powders is not straightforward. The HA sintering occurs typically in the temperature range of 900-1300ºC and the CNTs oxidize and burn above 500ºC. As so, inert or vacuum atmospheres free of oxygen should be selected to preserve the CNTs [222]. Besides this, other sources of oxygen might react with CNTs during the high temperature sintering cycle such as the released H_2O from the HA decomposition (or dehydroxylation, above 900ºC) and the oxygen containing chemical groups of the functionalization process intimately attached to the CNT walls [209, 222]. One other challenge concerns the full

densification of the material since CNTs are seen as physical obstacles to matrix grain growth [225].

In very broad terms, the consolidation routes can be divided in two classes depending if they are assisted by pressure or not (Table 9). Pressureless routes are not geometrically limited and less destructive to CNTs than pressure-assisted routes [223]. One of these routes contemplates the sintering in the presence of a reactive powder bed. This bed is composed of a mixture of powder precursors that are decomposed during sintering to form a local gaseous equilibrium near the samples. In the presence of this confined atmosphere, it is possible at some extend to retain the HA phase and therefore to preserve CNTs in the final composite compact [222]. These reactive powder beds allowed much better balance of CNT loading and densification than simple pressureless routes [222]. However, the densification levels are quite disappointing even for reactive sintering, usually below 90% [222], due to the lack of full prevention of the HA dehydroxylation and to inhibition of grain growth by CNTs.

Pressure-assisted routes have been found to be more proficient to densify CNT/HA composites than the pressureless ones. The applied pressure fosters grain contact and accelerates sintering, yielding densifications typically above 95% [224]. So, under pressure conditions, the maximum densification values are obtained at significantly reduced time and temperature sintering parameters [209]. These less severe conditions allows not only a better control of the kinetics of the chemical reactions and thus a maximum prevention of HA dissociation and CNT retention but also allows fine grain size [209]. Spark plasma sintering (SPS) has catching higher attention than hot pressing related methods due to its higher advantage over the second one in the control of the overall sintering processes such as densification, chemical reaction and grain growth, simply because it implies much faster sintering steps (heating and cooling rates up to 400 ºC.min^{-1} and dwell time no longer than 5 min) [224].

The final properties of the CNT/HA composites highly depends in its final degree of densification. This is particularly relevant for mechanical properties where porosity acts as defects leading to stress-concentration, and premature cracking and eventually catastrophic failure [209]. On the other hand, the electrical properties are not as dependent on the final densification as the mechanical ones are, since even with residual porosity, CNTs in the composite can touch each other to form a 3D network, assuring in this way the electrical percolation.

Table 10 compares the mechanical and electrical properties of the natural cortical bone with some examples of bioceramic bone grafts currently applied in clinic and the novel free standing CNT/bioceramic composites.

Hindering their high bioactivity, the listed bioceramic bone grafts in Table 10 have been successfully applied in clinics. However, it must be notice that most of them do not fully match the mechanical properties of the natural cortical bone, particularly those of the fracture toughness and flexural strength, and therefore can not be used in major load-bearing applications. The only one that would be suitable for load bearing is the Cerabone A/W (R), with fracture toughness and

flexural strength values above the lower limit ones of natural bone of 2 MPa.m$^{1/2}$ and 50 MPa, respectively.

Regarding the new CNT/HA composites, it can be seen that the values reported for mechanical properties vary due to the use of different processing routes and characterization methods. Also, the collected literature data indicates a maximum of weight fraction of CNTs to reinforce the ceramic matrix of 4 wt%. To better understand the CNT effect on the mechanical properties of the CNT/bioceramic composites (Table 10), the respective percentages of increasing of the composite mechanical properties relatively to the matrix alone were calculated (the matrix values were collected from the respective paper works) and ploted (Fig. 19). Data depict an average increasing of 50% for the overall properties, a quiet disappointing.

Table 10 - Mechanical and electrical properties of natural cortical bone, clinical available bioceramic bone grafts and novel CNT/HA composites.

	Material	CNT(.wt%)[a]/Powder processing/Consolidation	Young's Modulus, E (GPa)	Hardness (GPa)	Fracture toughness, K_{IC} (MPam$^{1/2}$)	Compressive strength (MPa)	Flexural strength (MPa)	Electrical Conductivity (S. m^{-1})
	Cortical bone	-	6.5-20.7 [226, 227]	0.31-0.58 [228]	2-12 [227]	100-230 [229]	50-150 [227]	5x10^{-3}-6.5x10^{-2} [230]
Bioceramic in clinic	HA	-	70-120 [231]	4.9-7.8 [231]	~1 [231]	100-900 [231]	20-80 [231]	10^{-13}-10^{-8} [232]
	β-TCP	-	33-120 [233, 234]	-	1.2 [233]	-	140-154 [234]	10^{-9} [235]
	45S5 bioglass (R)	-	35 [234]	4.6 [234]	~2 [233]	-	42 [234]	10^{-9} [236]
	P$_2$O$_5$-Glass/HA (Bonelike (R))	-/Mechanical mixing/S	95-100 [189]	5.03-5.83 [237]	0.61-1.31 [237]	-	100-150 [238]	10^{-8} [239]
	Cerabone A/W (R)	-	118 [240]	6.6 [240]	2 [240]	1080 [240]	100-215 [240, 241]	-
CNT/ bioceramics	HA	1.12/Spray drying/SPS [242]	131	6.86	-	-	-	-
		2/In situ CVD/S [219]	-	-	2.35	-	79	-
		2/Chemical precipitation/HP [214]	-	-	-	102	-	-
		3/Mechanical mixing/S [221]	-	-	0.76	-	61	-
		3/Chemical precipitation/HP [243]	-	-	2.6	-	80	-
		4//Spray drying/SPS [218]	130	9	-	-	-	-
		4/Chemical precipitation/HP [244]	-	-	1.23	-	103	-

[a] Volume fractions were converted to weight fractions assuming a CNT density of 1.75 g.cm^{-3}.
S - Pressureless Sintering
HP - Hot pressing
SPS - Spark plasma sintering

Yet, the properties with higher percentage of increasing are those that must be improved in the commercially available bone grafts, the fracture toughness and flexural strength. Considering the absolute values of these properties in Table 1, it is attested only a slight increase of the fracture toughness of the CNT/HA composites relatively to the ones of the commercially available grafts, yet, it still be significantly lower than the natural cortical bone. Nonetheless, these values points out that CNTs can work as efficient toughening agents [245].
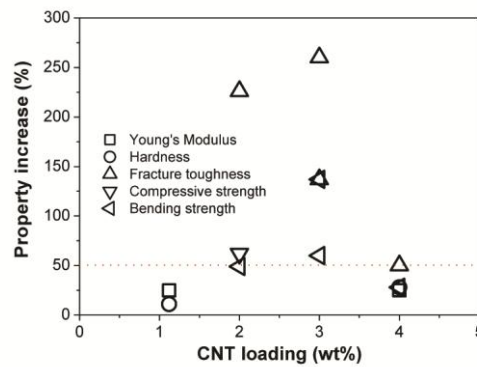
Fig. 19 - Plot summarizing the increase percentage of the mechanical properties of CNT/HA composites relatively to the matrix alone.

Considering the electrical properties, the commercially available bioceramic bone grafts are all dielectric materials. Also, surprisingly, no data on the electrical conductivity of the CNT/HA composites has been reported up to now. Having as reference values in the literature for other CNT-ceramic composites, the electrical percolation threshold is usually obtained below 2 wt.% with a corresponding electrical conductivity value of 100 S.m^{-1} [246, 247], highly above the value of wet bone [230]. This gives clues that high conductive CNT/HA grafts with preserved bioactivity of the ceramic matrix would be promising materials for electrical stimulation of bone. So, the functional properties of CNT/HA grafts such as the electrical conductivity should be investigated.

I.3.3. *In vitro* and *In vivo* toxicological profiles

In view of using CNTs as fillers in HA-based bone grafts that are expected to interface with living bone, in the human body, evidences of the CNT and CNT/HA composite toxicity are mandatory to be assessed, both *in vitro* and *in vivo*. Also, the *in vivo* biodistribution of CNTs and its potential harmful responses are equally relevant to be investigated if bone grafts applications are envisaged. This is because CNTs may be released from the bioceramic matrix into the body at a given rate, depending on the rates of the matrix dissolution and on the osteoclastic degradation/reabsorption.
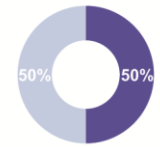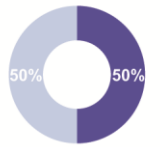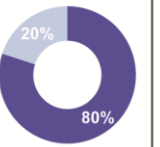
Solo CNTs

The toxicity of CNT is still controversial due to contradictory reports, mostly due to the wide range of variables that dictates the *in vitro* and *in vivo* toxicological profile of CNTs. These variables are commonly classified in two main groups: (1) physico-chemical characteristics of CNTs (morphology, purity, chemical functionalization, agglomeration state); and (2) the applied experimental protocol (type of cell/tissue, dosage, administration route).

To further understand this, several toxicological studies (Table A1, in appendix) were analysed to achieve tendencies/patterns that might help to identify the most relevant toxicity-induced CNT variables. The selected studies are *in vitro* and *in vivo* experiments of SWCNTs and MWCNTs carried out by different investigation groups. A total of ten studies were analysed for each condition. All *in vitro* studies were accomplished with CNTs suspended in the cell culture media allowing the "free interaction" with suspended cells. This approach was selected because it potentiates much more the toxicity of CNTs than the CNT substrates assemblies [248]. Also, all *in vivo* studies compromise the use of a mouse model (Table A1).

Table 11 compiles the toxicity data of Table A1 (in appendix). The data indicate that SWCNTs and MWCNTs have similar *in vitro* and *in vivo* toxicological profiles

Table 11 - Summary of the CNT toxicity data of Table A1.

		In vitro		In vivo	
		SWCNTs	MWCNTs	SWCNTs	MWCNTs
		50% / 50%	50% / 50%	20% / 80%	20% / 80%
■	Toxic	5	5	8	8
■	Non-toxic	5	5	2	2
Total		10 [249-258]	10 [251, 259-267]	10 [268-277]	10 [267, 268, 275, 278-284]

To identify the most relevant toxicity-induced CNT variables in each test condition, the toxicity data of Table 11 were compared with data of Table 12 presenting the four main CNT toxicological variables: (1) chemical functionalization; (2) length size; (3) purity; and (4) dosage.

The cut-off values for each variable were determined accordingly to the literature. Assuming that all CNTs are individually distributed, those with length sizes higher than 2 µm have high potential to be toxic to cells and tissues [285]. Considering the purity level, investigation works had shown that CNTs highly pure, above 99%, are non toxic [286, 287]. Also, CNT dosages above 10 mg.l^{-1} [287-290] or 2 mg.Kg^{-1} [276, 283] substantially increases cellular apoptosis or tissue necrosis.

Regarding the *in vitro* toxicological studies, data indicates that functionalization and dosage are the main variables dictating the SWCNTs toxicity, while purity and dosage are those influencing the MWCNTs. Conversely, the functionalization and the functionalization and dosage are the variables most directly linked to the *in vivo* toxicological profile of SWCNTs and MWCNTs. Overall, there are strong evidences that the *in vitro* and *in vitro* toxicological behaviour of CNTs are preferentially defined by the dosage and functionalization. As so, the high dosage used and the lack of chemical functionalization are the main causes for the high % of toxicity values of Table 11.

Lined with this, the window of opportunity for CNTs in biology and biomedicine concerns their use at low dosages and in the functionalized form.

Table 12 - Organization of the CNT toxicity data of Table A1 according to the toxicity-induced CNT variables: chemical functionalization, length size, purity and dosage.

	In vitro		In vivo	
	SWCNTs	MWCNTs	SWCNTs	MWCNTs
Functionalized / Non-functionalized	30% / 70%	30% / 70%	30% / 70%	20% / 80%
Purity < 99% / Purity > 99%	90% / 10%	60% / 40%	60% / 40%	50% / 50%
Length < 2 µm / Length > 2 µm	80% / 20%	80% / 20%	60% / 40%	80% / 20%
Dosage < 10 mg.l^{-1} or < 2 mg.kg^{-1} / Dosage > 10 mg.l^{-1} or > 2 mg.kg^{-1}	30% / 70%	40% / 60%	50% / 50%	60% / 40%
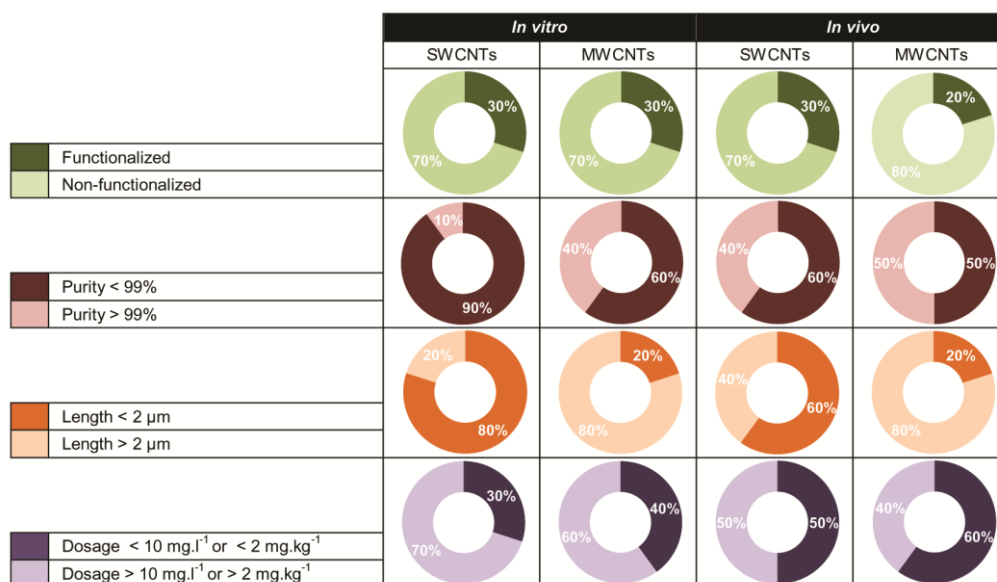
As regards the bone graft qualities of CNTs, they are found promoting the *in vitro* proliferation and differentiation of osteoblastic-like cells [291-293] and the bonding and stimulation of bone tissue *in vivo* [202].

MWCNT/HA composites

Bearing in mind MWCNT involved by a bioactive HA composite matrix, it is expected that their potential toxicity is highly depressed [248]. To look further on this, several *in vitro* and *in vivo* data on bioactivity and toxicity of MWCNT/HA composites are presented in Table A2 (appendix). A total of five studies were analysed for each condition. All *in vitro* studies were accomplished with MWCNT/HA composites interacting with bone forming cells, i.e. osteoblastic-like cells. Also, all *in vivo* studies concern a mouse model with MWCNT/HA composites interfacing subcutaneous tissue, muscle tissue and bone tissue.

Table 13 resumes the toxicity data of Table A2. There is a strong pattern showing MWCNT/HA composites with absence of acute toxicological response either *in vitro* or *in vivo*. Of relevance, all the analysed composites have CNT loadings below 4 wt.%. This indicates that at low CNT contents it is possible to preserve the biocompatibility of the bioceramic matrix and its bone grafting qualities.

Table 13 - Summary of the toxicity data of the CNT/HA composites presented in Table A2.

	In vitro	In vivo
	MWCNT/HA composites	MWCNT/HA composites
	0% ⬤ 100%	0% ⬤ 100%
⬛ Toxic	0	0
⬜ Non-toxic	5	5
Total	5 [294-297]	5 [221, 298-301]

Taking as reference a larger animal model, such as a rabbit, CNT containing composites, in this case 0.5 wt% of ultra-short SWCNTs tubes (UST) reinforcing a poly(propylene fumarate) (PFF) polymeric matrix, also show high biocompatibility with subcutaneous tissue (Fig. 20a) and bone tissue (Fig. 20b) after 12 weeks of implantation [302].

Surprisingly, the UST/PFF composite yielded threefold higher bone growth and had less inflammation compared to the polymer scaffold alone. It is also relevant to notice that even using non-functionalized ultra-short CNTs of length size of 20-80 nm in the initial composite, when they are released from the matrix, they tend to agglomerate in vivo forming roughly 50 μm sized agglomerates. Interestingly, these agglomerates are embedded by the connective tissue and the new bone tissue without negatively affecting their biofunctionalities.
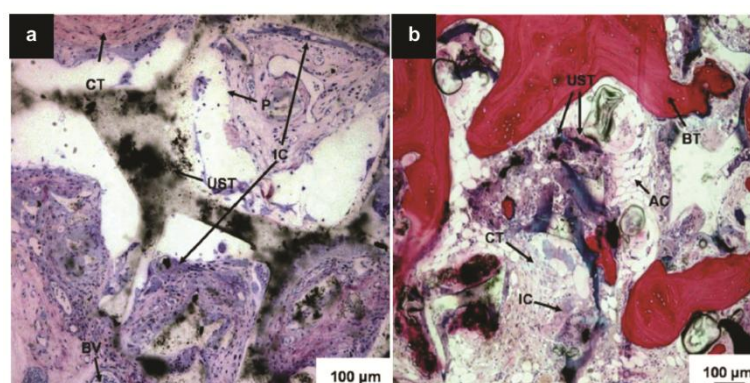
Fig. 20 - Optical images of histological sections of UST/PFF scaffolds implanted (a) subcutaneously and in (b) bone tissue after 12 weeks of implantation. PPF scaffold (P) and bone-like tissue (BT) appear as white and red areas, respectively. US-tubes (UST), connective tissue (CT), adipose cells (AC), and inflammatory cells (IC) are also shown (adapted from [302]).

Additionally, when bone undergoes resorption, the release of CNTs from the HA graft material or from the bone matrix it should not be considered as toxicological problem. This

assumption is based on the fact that the resorption mechanism occurs at the bone interior, in an inside-out way, and the resorption site is constantly delimited by an external protective layer formed by the cortical bone and periosteum (see section I.2.1). However, there is always some probability of CNTs entry in the circulation system by penetrating blood vessels at the bone matrix (Fig. 10). The probability of this event is higher when CNTs are individually by following a "piercing" or "nanosyringe" mechanisms, already reported by Kostarelos' group [199]. Concerning this hypothesis is important to investigate the *in vivo* biodistribution of intravenously administered CNTs.

In vivo biodistribution of CNTs: mouse model

CNTs present high chemical stability *in vivo* thus their persistency in human body is a real concern when bioapplications are envisaged. Table 14 compiles data from some recent *in vivo* studies reporting on the biodistribution of intravenously administered CNTs after 24 h of injection in mice [276, 303-305].

Table 14 - Studies of *in vivo* biodistribution of intravenously administered CNTs in mice.

	CNT type	Diameter (nm)	Lenght (µm)	Chemical functionalization	Dosage (µg/µL)	Organ with higher uptake of CNTs	Ref.
CNT1	SW	1-5	0.1-0.3	PL-PEG	0.005	Liver	[276]
CNT2	MW	10-20	0.01-0.6	Taurine group	0.1	Liver	[303]
CNT3	SW	10-30*	2-3	-	1	Lung	[304]
CNT4	SW	15-30*	0.3-1	DTPA	0.3	Kidney	[305]
CNT5	MW	20-30	0.5-2	DTPA	0.3	Kidney	[305]

SW- single walled
MW- multi walled
NF- non functionalised
PL-PEG- phospholipid-polyethylene glycol
DTPA- diethylentriaminepentaacetic
*bundle diameter (measured by TEM)

The uptake level of CNTs in organs was quantitatively analysed using an ordinal scale (1 to 5) along each study (Table 14). The fraction of CNTs on each organ was calculated by dividing the sum across studies by the total sum. These results were plotted in a pie graph (Fig. 21a). It can be seen that CNTs are preferentially cleared from the systemic blood circulation by high uptake in the reticuloendothelial system (RES), i.e., spleen, liver and lungs, rather than being excreted by the kidneys.

For a more comprehensive analysis of these data, the CNTs of Table 14 were compared by length, stiffness and mobility (Fig. 21b). These characteristics may dictate the success of RES clearance [267, 306-308]. So far, *in vivo* studies did not show obvious breakage or digestion of CNTs inside the phagocytes [33, 309]. More recently it was reported that alveolar macrophages can breakdown CNTs by a cyclic-phagocytise mechanism, but a detailed description was not given [310]. Supposedly, CNT break by oxidation rather than dissolution due to the formation of an oxidative milieu in the phagolysosome, containing acid hydrolase enzymes (lysozymes), hydrogen peroxide and superoxide anions [311, 312]. Some *in-vitro* studies have reported on exposing CNT to simulated phagolysosome medium to address their chemical stability [313, 314]. Of interest, it

was observed that CNTs break more easily in the presence of strong oxidisers such as hydrogen peroxide rather than in acids [313]. Also, the cleavage/oxidation rate of CNTs depends on the density of their side-wall defects induced by the degree and type of the covalent functionalisation [314].
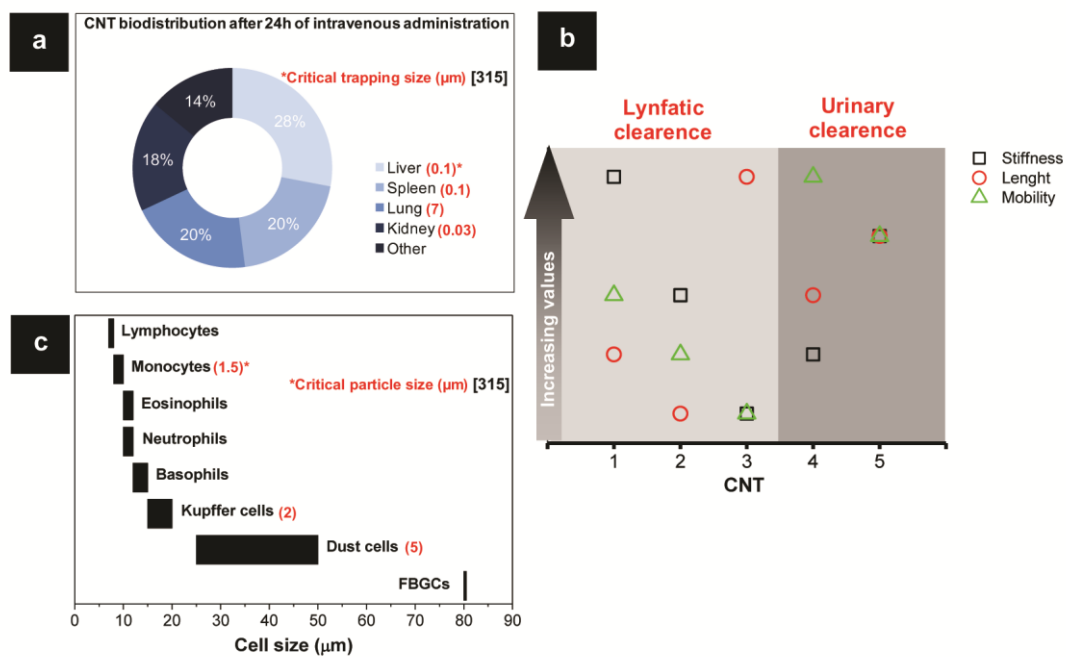
Fig. 21 - CNT biodistribution after 24h of intravenous administration in mice. (a) Pie graph compiling the CNT biodistribution data of the studies of Table 14 alongside with the critical trapping size of each organ. (b) Plot showing the size and the critical particle size of the cells of the lynfatic system. (c) Plot comparing the CNT of Table 1 by length, stiffness and mobility that are the characteristics that may dictate the simple geometrical trapping and the success of RES clearance.

Moreover, the uptake in organs by simple geometrical trapping depends on the CNT characteristics referred above [315]. The critical trapping size of human organs [315] (it is assumed the similarity of sizes for the mice model) is presented in Fig. 21a. This value corresponds to the minimum size of the organ fenestrations above which bigger rigid particles cannot pass through.

Here, MWCNTs were compared considering that stiffness slightly increases with the increasing number of layers [316] and outer diameter [317]. SWCNT, usually present in ropes due to the high surface area, even for functionalised materials [305], have their stiffness depressed with the increasing number of CNTs in a bundle [318]. Also, SWCNT ropes are more compliant than MWCNTs with similar diameters [319]. Moreover, the mobility parameter is determined by the solubility and size of CNTs: for the same solubility degree smaller tubes have higher mobility.

Fig. 21b shows that functionalised, highly mobile CNTs, are easily cleared by the urinary system (dark gray area). Accordingly to the pioneering work of Kostarelos's team [305], CNT4 and CNT5 are able to permeate through the glomerular filtration barrier with a critical trapping size (0.03 µm) close to the diameter of the tubes, and can be eliminated almost intact 24 h post-

administration [305]. It becomes obvious that well individualised hydrophilic CNTs present high mobility and can be easily reoriented in bloodstream. As a result, permeation of carbon nanotubes through the fenestras of the different organs is greatly simplified, helping CNTs riddance from circulation by renal excretion [305, 320]. Fig. 22 corraborates this by showing that the *in vivo* biodistribution of CNTs is modulated by the functionalization degree: low functionalized CNTs are accumulated in the liver (left-side image) while high functionalized materials are easily eliminated by urinary excretion with high accumulation in the bladder (right-side image).

Besides their enhanced mobility, covalently functionalised CNTs, having more side-wall defects, can be more easily cut by macrophages which helps on their complete excretion from the body. This may explain its supremacy over the non covalent functionalisation approach [193].

Conversely, non covalent (coated) or even non functionalised tubes are cleared by the lymphatic system (CNT 1-3) (light gray area). CNTs with decreased mobility, longer sizes and larger stiffness (i.e. with increasing bundle size) are preferentially digested by RES phagocytes in the following order: liver (Kupffer cells), spleen (sinusoidal cells) and lung (dust cells or alveolar magrophages) [315]. Interestingly, this biodistribution data is correlated to the systemic circulation sequence and organs characteristics [315]. Firstly, oxygenated blood leaves the lungs by pulmonary vein route. The biggest CNT aggregates (CNT3) are promptly trapped in this organ with the highest critical trapping size (7 μm). Here, the biggest macrophages, the dust cells (15-50 μm), with the highest critical particle size (5 μm) (i.e. particle size above which the phagocyte cannot be totally engulfed) have the difficult task of eliminating these tubes (Fig. 21c) [315]. Notably, the high uptake in the lung occurs due to the formation of pulmonary intravascular macrophages (PIMs) (20-80 μm) [315], when Kupffer cells are incapable (i.e. in damaged liver circumstances) [321].
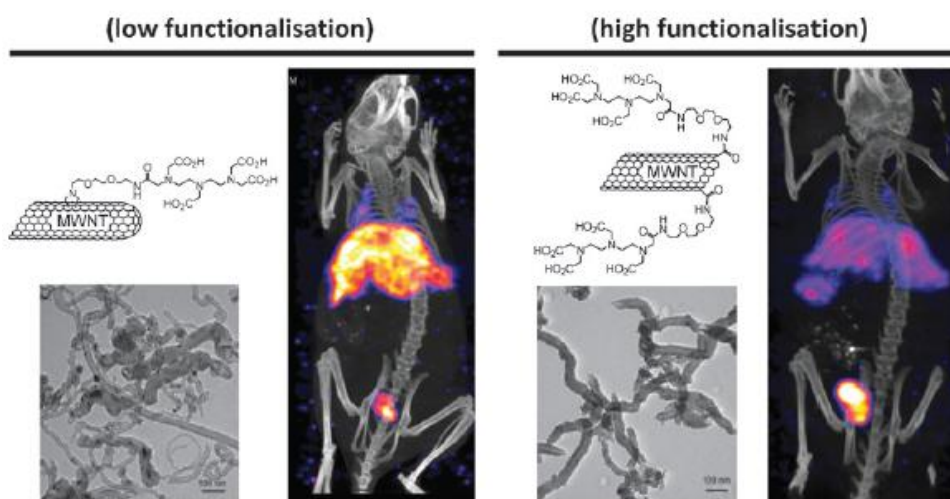
Fig. 22 - TEM images of functionalized MWCNTs and single photon emission computed tomography images of a mices injected with radiolabelled functionalized CNTs: (a) low functionalization level and (b) low functionalization level. The yellowish areas corresponds to higher CNT accumulation (Adapted from [322]).

Afterwards, the smaller and less mobile CNTs that were not trapped in the lungs are uptake by the liver and spleen (CNT1 and CNT2) with similar critical trapping size (0.1 μm) (by hepatic artery route) [315]. CNTs with small length size and stiffness (CNT2), or stiff and as small as 2 μm (critical particle size of Kupffer cells and sinusoidal cells [315]) (CNT1) are easily phagocyted in these organs, preferentially in the liver (Kupffer cells of 15-20 μm in size represent about 50% of all the macrophages [315], Fig. 21c). Also, less rigid filaments can bend and tangle forming clews with small diameters that may be engulfed by phagocytes [306]. On the other hand, big agglomerates (>20 μm) or highly stiff individual CNTs longer than 2 μm (Fig. 23) probably guide to frustrated phagocytosis [306-308] in these organs, eliciting a biochemical cascade that triggers the formation of scar tissues (i.e. cancer).
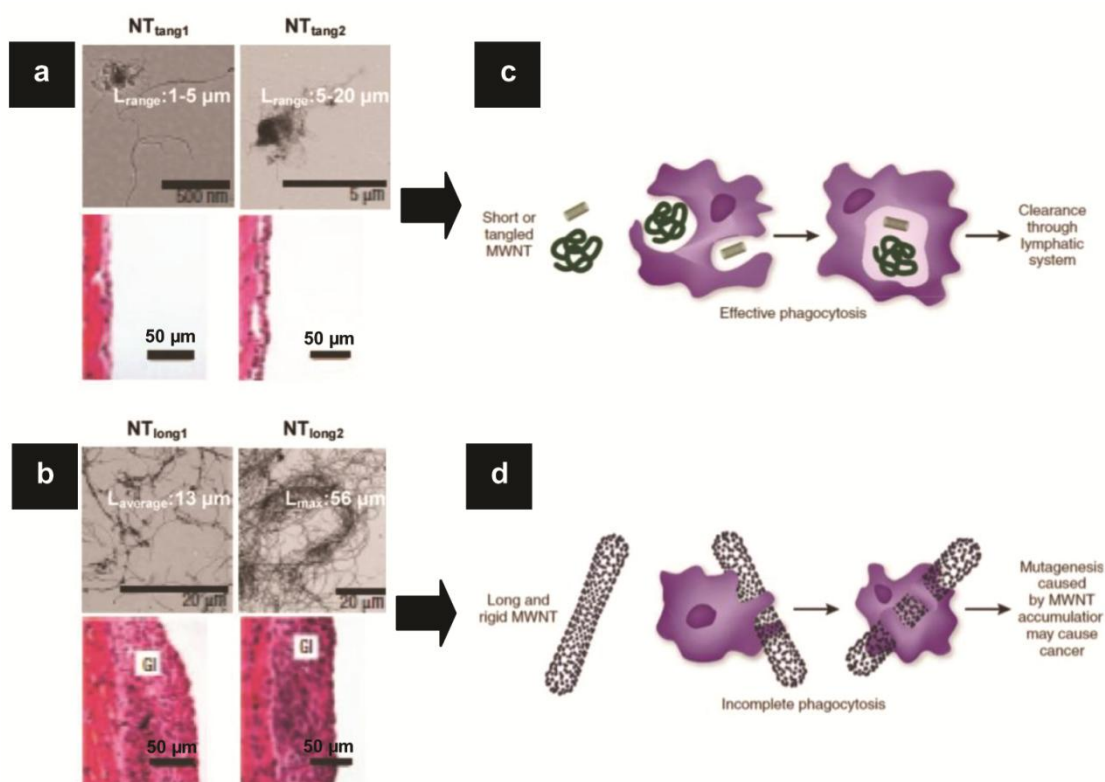
Fig. 23 - TEM images and histological images of granulamatous inflammation (GI) in mice (scale bar of 50 μm) of intraperitoneally instilled (a) tangled (CNT$_{tang1}$ and CNT$_{tang2}$) and (b) long CNTs (CNT$_{long1}$ and CNT$_{long2}$) (adapted from [308]). Effect of CNT structure on phagocytosis success: (c) short and tangled CNTs with low aspect ratio can be easily engulfed and digested, while (d) rigid and long CNTs are not cleared and thus accumulate in tissues promoting carcingenesis (adapted from [306]).

However, the CNT cellular uptake via endocytosis which includes the phagocytosis is not universal. There is some controversy about the mechanisms in which CNT enter cells. In the case of functionalised SWCNTs, it has been reported that nanotubes enter the cells via the endocytosis mechanism which includes the phagocytosis [323]. Conversely, others considering MWCNTs,

which can be beyond the size limit of an endocytosis pathway, suggested a endocytosis-independent mechanism [199, 324, 325]. Accordingly to Kostarelos et al. *in vitro* studies, individual or bundles of functionalized MWCNTs were able to enter the cells even under endocytosis-inhibiting conditions by a mechanism independent of the functional groups and cell type [199]. So, it was suggested that this new endocytosis-independent mechanism is one considering a conformational change of the lipid bilayer membrane of cells following CNT entry into the intracellular space [199, 325]. Regarding this, CNT may also enter phagocyte cells by direct penetration mechanisms at the cell membrane also called "piercing" or "nanosyringe" mechanisms, referred above.

Alternatively, the CNT agglomerates that are dragged to the kidney by renal artery route, having the lowest critical trapping size (0.03 µm) and the lowest macrophage concentration, are hardly eliminated and start to accumulate. Generally, non functionalised tubes were retained in organs for long time, up to 90 days, presenting an average clearance rate of less than 1 µg.day^{-1} [303, 304]. Nonetheless, the tissue accumulation depends on the route of administration. Hence, more studies exploring other routes are required.

Summarizing, it can be attested that the control of the CNT morphology is crucial for the lymphatic and urinary clearance mechanisms. Pristine short <2 µm and thin <30 nm CNTs have their potential toxicity highly depressed by having the ability to pass through the fenestras of the organs and by being engulfed by phagocytes. Nevertheless, the chemical functionalisation of CNT becomes essential to restrict the formation of big aggregates (>20 µm), to accelerate the digestion process accomplished by phagocytes and to increase the CNT mobility in physiological serums.

References

[1]. Dresselhaus M, Endo M. Relation of carbon nanotubes to other carbon materials. In: Dresselhaus M, Dresselhaus G, Avouris P, editors. Carbon nanotubes: Synthesis, Structure, Properties and Applications. Germany: Springer; 2001.

[2]. Bundy FP, Bassett WA, Weathers MS, Hemley RJ, Mao HU, Goncharov AF. The pressure-temperature phase and transformation diagram for carbon; updated through 1994. Carbon. 1996;34(2):141-53.

[3]. Mildred SD. Fifty years in studying carbon-based materials. Phys Scr. 2012;2012(T146):014002.

[4]. Kroto HW, Heath JR, O'Brien SC, Curl RF, Smalley RE. C 60: buckminsterfullerene. Nature. 1985;318(6042):162-3.

[5]. Iijima S. Helical microtubules of graphitic carbon. Nature. 1991;354(6348):56-8.

[6]. Iijima S, Ichihashi T. Single-shell carbon nanotubules of 1-nm diameter. Nature. 1993;363(6430):603.

[7]. Ge M, Sattler K. Observation of fullerene cones. Chem Phys Lett. 1994;220(3–5):192-6.

[8]. Novoselov KS, Geim AK, Morozov SV, Jiang D, Zhang Y, Dubonos SV, et al. Electric field effect in atomically thin carbon films. Science 2004;306(5696):666-9.

[9]. Berger C, Song Z, Li X, Wu X, Brown N, Naud C, et al. Electronic Confinement and Coherence in Patterned Epitaxial Graphene. Science. 2006;312(5777):1191-6.

[10]. Geim AK, Novoselov KS. The rise of graphene. Nat Mater. 2007;6(3):183-91.

[11]. Baker RTK, Barber MA, Harris PS, Feates FS, Waite RJ. Nucleation and growth of carbon deposits from the nickel catalyzed decomposition of acetylene. J Catal. 1972;26(1):51-62.

[12]. Rodriguez NM, Chambers A, Baker RTK. Catalytic Engineering of Carbon Nanostructures. Langmuir : the ACS journal of surfaces and colloids. 1995;11(10):3862-6.

[13]. Martin-Gullon I, Vera J, Conesa JA, González JL, Merino C. Differences between carbon nanofibers produced using Fe and Ni catalysts in a floating catalyst reactor. Carbon. 2006;44(8):1572-80.

[14]. Dresselhaus MS, Dresselhaus G, Jorio A. Unusual properties and structure of crbon nanotubes. Annu Rev Mater Res. 2004;34(1):247-78.

[15]. PJF H. Carbon Nanotube Science: Synthesis, Properties and Applications. UK: Cambridge University Press; 2009.

[16]. Saito R, Fujita M, Dresselhaus G, Dresselhaus MS. Electronic structure of chiral graphene tubules. Appl Phys Lett. 1992;60(18):2204-6.

[17]. Pierson HO. Pyrolotic graphite. Handbook of carbon, graphite, diamond and fullerenes: properties, processing and applications. USA: Noyes publications; 1993.

[18]. Lee C, Wei X, Kysar JW, Hone J. Measurement of the Elastic Properties and Intrinsic Strength of Monolayer Graphene. Science. 2008;321(5887):385-8.

[19]. Paris O, Loidl D, Peterlik H. Texture of PAN- and pitch-based carbon fibers. Carbon. 2002;40(4):551-5.

[20]. Krishnan A, Dujardin E, Ebbesen TW, Yianilos PN, Treacy MMJ. Young's modulus of single-walled nanotubes. Phys Rev B. 1998;58(20):14013-9.

[21]. Teo KB, Singh C, Chhowalla M, Milne WI. Catalytic Synthesis of Carbon Nanotubes and Nanofibers. Encycl Nanosci Nanotechnol. 2004;1(1):665-86.

[22]. Wong EW, Sheehan PE, Lieber CM. Nanobeam Mechanics: Elasticity, Strength, and Toughness of Nanorods and Nanotubes. Science. 1997;277(5334):1971-5.

[23]. Naito K, Tanaka Y, Yang J-M, Kagawa Y. Flexural Properties of PAN- and Pitch-Based Carbon Fibers. J Am Ceram Soc. 2009;92(1):186-92.

[24]. Kuilla T, Bhadra S, Yao D, Kim NH, Bose S, Lee JH. Recent advances in graphene based polymer composites. Prog Polym Sci. 2010;35(11):1350-75.

[25]. Wang M-S, Golberg D, Bando Y. Tensile Tests on Individual Single-Walled Carbon Nanotubes: Linking Nanotube Strength with Its Defects. Adv Materials. 2010;22(36):4071-5.

[26]. Yu M-F, Lourie O, Dyer MJ, Moloni K, Kelly TF, Ruoff RS. Strength and Breaking Mechanism of Multiwalled Carbon Nanotubes Under Tensile Load. Science. 2000;287(5453):637-40.

[27]. Sruti AN, Jagannadham K. Electrical Conductivity of Graphene Composites with In and In-Ga Alloy. J Electron Mater. 2010;39(8):1268-76.

[28]. Chen J-H, Jang C, Xiao S, Ishigami M, Fuhrer MS. Intrinsic and extrinsic performance limits of graphene devices on SiO2. Nat Nanotechnol. 2008;3(4):206-9.

[29]. Avouris P. Graphene: Electronic and Photonic Properties and Devices. Nano Lett. 2010;10(11):4285-94.

[30]. Balandin AA, Ghosh S, Bao W, Calizo I, Teweldebrhan D, Miao F, et al. Superior Thermal Conductivity of Single-Layer Graphene. Nano Lett. 2008;8(3):902-7.

[31]. Arai Y. Structure and properties of pitch-based carbon fibers. Nippon Steel Tech Rep. 1993;59(0).

[32]. Sun X, Liu Z, Welsher K, Robinson J, Goodwin A, Zaric S, et al. Nano-graphene oxide for cellular imaging and drug delivery. Nano Res. 2008;1(3):203-12.

[33]. Cherukuri P, Bachilo SM, Litovsky SH, Weisman RB. Near-Infrared Fluorescence Microscopy of Single-Walled Carbon Nanotubes in Phagocytic Cells. J Am Chem Soc. 2004;126(48):15638-9.

[34]. Lacerda L, Pastorin G, Wu W, Prato M, Bianco A, Kostarelos K. Luminescence of Functionalized Carbon Nanotubes as a Tool to Monitor Bundle Formation and Dissociation in Water: The Effect of Plasmid-DNA Complexation. Adv Funct Mater. 2006;16(14):1839-46.

[35]. Han J. Structures and Properties of Carbon Nanotubes. In: Meyyappan M, editor. Carbon nanotubes Science and Applications. USA: CRC Press; 2005.

[36]. Bolotin KI, Sikes KJ, Jiang Z, Klima M, Fudenberg G, Hone J, et al. Ultrahigh electron mobility in suspended graphene. Solid State Commun. 2008;146(9–10):351-5.

[37]. Beenakker CWJ. Colloquium: Andreev reflection and Klein tunneling in graphene. Rev Mod Phys. 2008;80(4):1337-54.

[38]. Geim AK, MacDonald AH. Graphene: Exploring Carbon Flatland. PhysToday. 2007;60(8):35-41.

[39]. Chico L, Benedict LX, Louie SG, Cohen ML. Quantum conductance of carbon nanotubes with defects. Phys Rev B. 1996;54(4):2600-6.

[40]. Zhu W, Bower C, Zhou O, Kochanski G, Jin S. Large current density from carbon nanotube field emitters. Appl Phys Lett. 1999;75(6):873-5.

[41]. Falvo MR, Clary GJ. Bending and buckling of carbon nanotubes under large strain. (Cover story). Nature. 1997;389(6651):582.

[42]. Oberlin A, Endo M, Koyama T. Filamentous growth of carbon through benzene decomposition. J Cryst Growth. 1976;32(3):335-49.

[43]. Endo M, Takeuchi K, Igarashi S, Kobori K, Shiraishi M, Kroto HW. The production and structure of pyrolytic carbon nanotubes (PCNTs). J Phys Chem Solids. 1993;54(12):1841-8.

[44]. Dai H, Rinzler AG, Nikolaev P, Thess A, Colbert DT, Smalley RE. Single-wall nanotubes produced by metal-catalyzed disproportionation of carbon monoxide. Chem Phys Lett 1996;260(3–4):471-5.

[45]. Terrones M, Grobert N. Controlled production of aligned-nanotube bundles. Nature. 1997;388(6637):52.

[46]. Andrews R, Jacques D, Rao AM, Derbyshire F, Qian D, Fan X, et al. Continuous production of aligned carbon nanotubes: a step closer to commercial realization. Chem Phys Lett. 1999;303(5–6):467-74.

[47]. Dupuis A-C. The catalyst in the CCVD of carbon nanotubes—a review. Prog Mater Sci. 2005;50(8):929-61.

[48]. Anna M, Albert GN, Esko IK. The role of metal nanoparticles in the catalytic production of single-walled carbon nanotubes—a review. J Phys: Condens Matter. 2003;15(42):S3011.

[49]. Height MJ, Howard JB, Tester JW, Vander Sande JB. Flame synthesis of single-walled carbon nanotubes. Carbon. 2004;42(11):2295-307.

[50]. Chhowalla M, Teo KBK, Ducati C, Rupesinghe NL, Amaratunga GAJ, Ferrari AC, et al. Growth process conditions of vertically aligned carbon nanotubes using plasma enhanced chemical vapor deposition. J Appl Phys. 2001;90(10):5308-17.

[51]. Dillon AC, Mahan AH, Parilla PA, Alleman JL, Heben MJ, Jones KM, et al. Continuous Hot Wire Chemical Vapor Deposition of High-Density Carbon Multiwall Nanotubes. Nano Lett. 2003;3(10):1425-9.

[52]. Lee CJ, Kim DW, Lee TJ, Choi YC, Park YS, Lee YH, et al. Synthesis of aligned carbon nanotubes using thermal chemical vapor deposition. Chem Phys Lett. 1999;312(5–6):461-8.

[53]. Hofmann S, Ducati C, Kleinsorge B, Robertson J. Direct growth of aligned carbon nanotube field emitter arrays onto plastic substrates. Appl Phys Lett. 2003;83(22):4661-3.

[54]. Gan B, Ahn J, Zhang Q, Yoon SF, Rusli, Huang QF, et al. Branching carbon nanotubes deposited in HFCVD system. Diam Relat Mater. 2000;9(3–6):897-900.

[55]. Nikolaev P, Bronikowski MJ, Bradley RK, Rohmund F, Colbert DT, Smith KA, et al. Gas-phase catalytic growth of single-walled carbon nanotubes from carbon monoxide. Chem Phys Lett. 1999;313(1–2):91-7.

[56]. Kitiyanan B, Alvarez WE, Harwell JH, Resasco DE. Controlled production of single-wall carbon nanotubes by catalytic decomposition of CO on bimetallic Co–Mo catalysts. Chem Phys Lett. 2000;317(3–5):497-503.

[57]. Wang Y, Wei F, Luo G, Yu H, Gu G. The large-scale production of carbon nanotubes in a nano-agglomerate fluidized-bed reactor. Chem Phys Lett. 2002;364(5–6):568-72.

[58]. Hata K, Futaba DN, Mizuno K, Namai T, Yumura M, Iijima S. Water-assisted highly efficient synthesis of impurity-free single-walled carbon nanotubes. Science (New York, NY). 2004;306(5700):1362-4.

[59]. Zhao B, Futaba DN, Yasuda S, Akoshima M, Yamada T, Hata K. Exploring Advantages of Diverse Carbon Nanotube Forests with Tailored Structures Synthesized by Supergrowth from Engineered Catalysts. ACS nano. 2008;3(1):108-14.

[60]. Cantoro M, Hofmann S, Pisana S, Scardaci V, Parvez A, Ducati C, et al. Catalytic Chemical Vapor Deposition of Single-Wall Carbon Nanotubes at Low Temperatures. Nano Lett. 2006;6(6):1107-12.

[61]. Wagner RS, Ellis WC. Vapor-liquid-solid mechanism of single crystal growth. Appl Phys Lett. 1964;4(5):89-90.

[62]. Gorbunov A, Jost O, Pompe W, Graff A. Role of the catalyst particle size in the synthesis of single-wall carbon nanotubes. Appl Surf Sci. 2002;197–198(0):563-7.

[63]. Baker RTK, Gadsby GR, Terry S. Formation of carbon filments from catalyzed decomposition of hydrocarbons. Carbon. 1975;13(3):245-6.

[64]. Baker RTK. Catalytic growth of carbon filaments. Carbon. 1989;27(3):315-23.

[65]. Klinke C, Bonard J-M, Kern K. Formation of Metallic Nanocrystals from Gel-like Precursor Films for CVD Nanotube Growth: An in Situ TEM Characterization. J Phys Chem B. 2004;108(31):11357-60.

[66]. Hofmann S, Sharma R, Ducati C, Du G, Mattevi C, Cepek C, et al. In situ Observations of Catalyst Dynamics during Surface-Bound Carbon Nanotube Nucleation. Nano Lett. 2007;7(3):602-8.

[67]. Yazyev OV, Pasquarello A. Effect of Metal Elements in Catalytic Growth of Carbon Nanotubes. Phys Rev Lett. 2008;100(15):156102.

[68]. Shi Z, Lian Y, Zhou X, Gu Z, Zhang Y, Iijima S, et al. Mass-production of single-wall carbon nanotubes by arc discharge method. Carbon. 1999;37(9):1449-53.

[69]. Ducati C, Alexandrou I, Chhowalla M, Robertson J, Amaratunga GAJ. The role of the catalytic particle in the growth of carbon nanotubes by plasma enhanced chemical vapor deposition. J Appl Phys. 2004;95(11):6387-91.

[70]. Zhu L, Hess DW, Wong C-P. Monitoring Carbon Nanotube Growth by Formation of Nanotube Stacks and Investigation of the Diffusion-Controlled Kinetics. J Phys Chem B. 2006;110(11):5445-9.

[71]. Hasegawa K, Noda S. Moderating carbon supply and suppressing Ostwald ripening of catalyst particles to produce 4.5-mm-tall single-walled carbon nanotube forests. Carbon. 2011;49(13):4497-504.

[72]. Boellaard E, de Bokx PK, Kock AJHM, Geus JW. The formation of filamentous carbon on iron and nickel catalysts: III. Morphology. J Catal. 1985;96(2):481-90.

[73]. Mattevi C, Wirth CT, Hofmann S, Blume R, Cantoro M, Ducati C, et al. In-situ X-ray Photoelectron Spectroscopy Study of Catalyst−Support Interactions and Growth of Carbon Nanotube Forests. J Phys Chem C. 2008;112(32):12207-13.

[74]. Fan S, Chapline MG, Franklin NR, Tombler TW, Cassell AM, Dai H. Self-oriented regular arrays of carbon nanotubes and their field emission properties. Science (New York, NY). 1999;283(5401):512-4.

[75]. Lee YT, Park J, Choi YS, Ryu H, Lee HJ. Temperature-Dependent Growth of Vertically Aligned Carbon Nanotubes in the Range 800−1100 °C. J Phys Chem B. 2002;106(31):7614-8.

[76]. Wood RF, Pannala S, Wells JC, Puretzky AA, Geohegan DB. Simple model of the interrelation between single- and multiwall carbon nanotube growth rates for the CVD process. Phys Rev B. 2007;75(23):235446.

[77]. Moulijn JA, van Diepen AE, Kapteijn F. Catalyst deactivation: is it predictable?: What to do? Appl Catal, A. 2001;212(1–2):3-16.

[78]. Endo M, Koyama S, Matsuda Y, Hayashi T, Kim Y-A. Thrombogenicity and Blood Coagulation of a Microcatheter Prepared from Carbon Nanotube−Nylon-Based Composite. Nano Lett. 2004;5(1):101-5.

[79]. Hafner JH, Cheung C-L, Oosterkamp TH, Lieber CM. High-Yield Assembly of Individual Single-Walled Carbon Nanotube Tips for Scanning Probe Microscopies. J Phys Chem B. 2001;105(4):743-6.

[80]. Robertson J. Realistic applications of CNTs. Mater Today. 2004;7(10):46-52.

[81]. Britto PJ, Santhanam KSV, Rubio A, Alonso JA, Ajayan PM. Improved Charge Transfer at Carbon Nanotube Electrodes. Adv Materials. 1999;11(2):154-7.

[82]. Bekyarova E, Davis M, Burch T, Itkis ME, Zhao B, Sunshine S, et al. Chemically Functionalized Single-Walled Carbon Nanotubes as Ammonia Sensors†. J Phys Chem B. 2004;108(51):19717-20.

[83]. Portney N, Ozkan M. Nano-oncology: drug delivery, imaging, and sensing. Anal Bioanal Chem. 2006;384(3):620-30.

[84]. Postma HWC, Teepen T, Yao Z, Grifoni M, Dekker C. Carbon Nanotube Single-Electron Transistors at Room Temperature. Science. 2001;293(5527):76-9.

[85]. Robertson J. Growth of nanotubes for electronics. Mater Today. 2007;10(1–2):36-43.

[86]. Bianco A, Kostarelos K, Prato M. Applications of carbon nanotubes in drug delivery. Curr Opin Chem Biol. 2005;9(6):674-9.

[87]. LaVan DA, McGuire T, Langer R. Small-scale systems for in vivo drug delivery. Nat Biotechnol. 2003;21(10):1184-91.

[88]. Leroux F, Méténier K, Gautier S, Frackowiak E, Bonnamy S, Béguin F. Electrochemical insertion of lithium in catalytic multi-walled carbon nanotubes. J Power Sources. 1999;81–82(0):317-22.

[89]. Supronowicz PR, Ajayan PM, Ullmann KR, Arulanandam BP, Metzger DW, Bizios R. Novel current-conducting composite substrates for exposing osteoblasts to alternating current stimulation. Journal of biomedical materials research Part A. 2002;59(3):499-506.

[90]. Zhang L, Webster TJ. Nanotechnology and nanomaterials: Promises for improved tissue regeneration. Nano today. 2009;4(1):66-80.

[91]. Li W, Liang C, Qiu J, Zhou W, Han H, Wei Z, et al. Carbon nanotubes as support for cathode catalyst of a direct methanol fuel cell. Carbon. 2002;40(5):791-4.

[92]. Bonard JM, Salvetat JP, Stöckli T, Forró L, Châtelain A. Field emission from carbon nanotubes: perspectives for applications and clues to the emission mechanism. Appl Phys A. 1999;69(3):245-54.

[93]. Chang CW, Okawa D, Majumdar A, Zettl A. Solid-State Thermal Rectifier. Science. 2006;314(5802):1121-4.

[94]. Welsher K, Liu Z, Daranciang D, Dai H. Selective Probing and Imaging of Cells with Single Walled Carbon Nanotubes as Near-Infrared Fluorescent Molecules. Nano Lett. 2008;8(2):586-90.

[95]. Pradhan B, Batabyal SK, Pal AJ. Functionalized carbon nanotubes in donor/acceptor-type photovoltaic devices. Appl Phys Lett. 2006;88(9):093106-3.

[96]. Tenent RC, Barnes TM, Bergeson JD, Ferguson AJ, To B, Gedvilas LM, et al. Ultrasmooth, Large-Area, High-Uniformity, Conductive Transparent Single-Walled-Carbon-Nanotube Films for Photovoltaics Produced by Ultrasonic Spraying. Adv Materials. 2009;21(31):3210-6.

[97]. Wu Z, Chen Z, Du X, Logan JM, Sippel J, Nikolou M, et al. Transparent, Conductive Carbon Nanotube Films. Science. 2004;305(5688):1273-6.

[98]. Serp P, Corrias M, Kalck P. Carbon nanotubes and nanofibers in catalysis. Appl Catal, A. 2003;253(2):337-58.

[99]. Harrison BS, Atala A. Carbon nanotube applications for tissue engineering. Biomaterials. 2007;28(2):344-53.

[100]. Stevens MM. Biomaterials for bone tissue engineering. Mater Today. 2008;11(5):18-25.

[101]. Clarke B. Normal Bone Anatomy and Physiology. Clin J Am Soc Nephrol. 2008;3(Supplement 3):S131-S9.

[102]. Seeley R, Stephens T, Tate P. Anatomy & Physiology. 8th ed. Boston: McGraw-Hill; 2008.

[103]. Legeros RZ LJ. Dense Hydroxyapatite. In: Hench LL WJ, editor. An introduction to bioceramics. USA: World Scientific; 1993.

[104]. Martini F. Fundamentals of Anatomy & Physiology. 7th ed. Philippines: Perason Education Inc.; 2005.

[105]. Caetano-Lopes J, Canhao H, Fonseca JE. Osteoblasts and bone formation. Acta Reumatol Port. 2007;32(2):103-10.

[106]. http://www.studyblue.com/notes/note/n/anatomy-test-2-integumentary-system/deck/1138766.

[107]. Del Fattore A, Teti A, Rucci N. Bone cells and the mechanisms of bone remodelling. Front Biosci, Elite Ed. 2012;4:2302-21.

[108]. Martonosi AN. Animal electricity, Ca2+ and muscle contraction. A brief history of muscle research. Acta Biochim Pol. 2000;47(3):493-516.

[109]. Burr HS, Northrop FSC. Evidence for the existence of an electro-dynamic field in living organisms. Proc Natl Acad Sci 1939;25(6):284.

[110]. Yasuda I. On the piezoelectric activity of bone. J Jpn Orthop Surg Soc. 1954;28:267-71.

[111]. Bassett CAL, Becker RO. Generation of electric potentials by bone in response to mechanical stress. Science. 1962;137(3535):1063-4.

[112]. Yasuda I. Piezoelectric effects in collagen. Jpn J Appl Phys. 1964;3(2).

[113]. Hastings GW, Mahmud FA. Electrical effects in bone. J Biomed Eng. 1988;10(6):515-21.

[114]. Bassett C. Fundamental and practical aspects of therapeutic uses of pulsed electromagnetic fields (PEMFs). Crit Rev Biomed Eng. 1989;17(5):451-529.

[115]. Griffin M, Bayat A. Electrical stimulation in bone healing: critical analysis by evaluating levels of evidence. Eplasty. 2011;11:e34.

[116]. Brighton C. Current concepts review: the treatment of non-unions with electricity. J Bone Jt Surg. 1981;63A(5):847-51.

[117]. Noda M, Johnson DE, Chiabrera A, Rodan GA. Effect of electric currents on DNA synthesis in rat osteosarcoma cells: Dependence on conditions that influence cell growth. J Orthopaed Res. 1987;5(2):253-60.

[118]. Cain CD, Adey WR, Luben RA. Evidence that pulsed electromagnetic fields inhibit coupling of adenylate cyclase by parathyroid hormone in bone cells. J Bone Miner Res. 1987;2(5):437-41.

[119]. Ozawa H, Abe E, Shibasaki Y, Fukuhara T, Suda T. Electric fields stimulate DNA synthesis of mouse osteoblast-like cells (MC3T3-E1) by a mechanism involving calcium ions. J Cell Physiol. 1989;138(3):477-83.

[120].   McElhaney JH, Stalnaker R, Bullard R. Electric fields and bone loss of disuse. J Biomech. 1968;1(1):47-52.

[121].   Lavine L, Lustrin I, Shamos M, Moss M. The influence of electric current on bone regeneration in vivo. Acta Orthop. 1971;42(4):305-14.

[122].   Bassett C, Valdes MG, Hernandez E. Modification of fracture repair with selected pulsing electromagnetic fields. J Bone Jt Surg, Am Vol. 1982;64(6):888-95.

[123].   Silver IA, Murrills RJ, Etherington DJ. Microelectrode studies on the acid microenvironment beneath adherent macrophages and osteoclasts. Exp Cell Res. 1988;175(2):266-76.

[124].   Duncan R, Misler S. Voltage-activated and stretch-activated Ba^{2+} conducting channels in an osteoblast-like cell line (UMR 106). Febs Lett. 1989;251(1):17-21.

[125].   Zayzafoon M. Calcium/calmodulin signaling controls osteoblast growth and differentiation. Journal of cellular biochemistry. 2006;97(1):56-70.

[126].   Levin M. Bioelectromagnetics in morphogenesis. Bioelectromagnetics. 2003;24(5):295-315.

[127].   Bezanilla F. The voltage sensor in voltage-dependent ion channels. Physiol Rev. 2000;80(2):555-92.

[128].   Loza J, Stephan E, Dolce C, Dziak R, Simasko S. Calcium currents in osteoblastic cells: dependence upon cellular growth stage. Calcif Tissue Int. 1994;55(2):128-33.

[129].   Grimnes S, Martinsen G. Bioimpedance and Bioelectricity Basics. UK: Academic Press; 2008.

[130].   Clapham DE. Calcium Signaling. Cell. 2007;131(6):1047-58.

[131].   Chesnoy-Marchais D, Fritsch J. Voltage-gated sodium and calcium currents in rat osteoblasts. J Physiol. 1988;398(1):291-311.

[132].   Caffrey J, Farach-Carson M. Vitamin D3 metabolites modulate dihydropyridine-sensitive calcium currents in clonal rat osteosarcoma cells. J Biol Chem. 1989;264(34):20265-74.

[133].   Guggino SE, Lajeunesse D, Wagner JA, Snyder SH. Bone remodeling signaled by a dihydropyridine-and phenylalkylamine-sensitive calcium channel. Proc Natl Acad Sci 1989;86(8):2957-60.

[134].   Yamaguchi D, Hahn T, Iida-Klein A, Kleeman C, Muallem S. Parathyroid hormone-activated calcium channels in an osteoblast-like clonal osteosarcoma cell line. cAMP-dependent and cAMP-independent calcium channels. J Biol Chem. 1987;262(16):7711-8.

[135].   Peterson BZ, DeMaria CD, Yue DT. Calmodulin Is the Ca2+ Sensor for Ca2+-Dependent Inactivation of L-Type Calcium Channels. Neuron. 1999;22(3):549-58.

[136].   ZuÈhlke RD, Pitt GS, Deisseroth K, Tsien RW, Reuter H. Calmodulin supports both inactivation and facilitation of L-type calcium channels. Nature. 1999;399(6732):159-62.

[137].   Oancea E, Meyer T. Protein Kinase C as a Molecular Machine for Decoding Calcium and Diacylglycerol Signals. Cell. 1998;95(3):307-18.

[138]. Dupont G, Houart G, De Koninck P. Sensitivity of CaM kinase II to the frequency of Ca2+ oscillations: a simple model. Cell Calcium. 2003;34(6):485-97.

[139]. Tran Q-K, Black D, Persechini A. Intracellular coupling via limiting calmodulin. Sci Signal. 2003;278(27):24247.

[140]. Zayzafoon M. Calcium/calmodulin signaling controls osteoblast growth and differentiation. J Cell Biochem. 2006;97(1):56-70.

[141]. Madgwick S, Levasseur M, Jones KT. Calmodulin-dependent protein kinase II, and not protein kinase C, is sufficient for triggering cell-cycle resumption in mammalian eggs. J Cell Sci. 2005;118(17):3849-59.

[142]. Kahl CR, Means AR. Regulation of Cell Cycle Progression by Calcium/Calmodulin-Dependent Pathways. Endocr Rev. 2003;24(6):719-36.

[143]. Coultrap SJ, Bayer KU. CaMKII regulation in information processing and storage. Trends Neurosci. 2012;35(10):607-18.

[144]. Persechini A, Stemmer PM. Calmodulin Is a Limiting Factor in the Cell. Trends Cardiovas Med. 2002;12(1):32-7.

[145]. Ermak G, Davies KJA. Calcium and oxidative stress: from cell signaling to cell death. Mol Immunol. 2002;38(10):713-21.

[146]. Trump B, Berezesky I. Calcium-mediated cell injury and cell death. FASEB J. 1995;9(2):219-28.

[147]. Orrenius S, Zhivotovsky B, Nicotera P. Regulation of cell death: the calcium–apoptosis link. Nat Rev Mol Cell Biol. 2003;4(7):552-65.

[148]. Leitgeb N, Cech R, Schröttner J. Electromagnetic field spectral evaluation problems in exposure assessment. Radiat Prot Dosim. 2007;124(2):124-9.

[149]. Soong H, Parkinson W, Bafna S, Sulik G, Huang S. Movements of cultured corneal epithelial cells and stromal fibroblasts in electric fields. Invest Ophth Vis Sci. 1990;31(11):2278-82.

[150]. Supronowicz PR, Ajayan PM, Ullmann KR, Arulanandam BP, Metzger DW, Bizios R. Novel current-conducting composite substrates for exposing osteoblasts to alternating current stimulation. J Biomed Mater Res. 2002;59(3):499-506.

[151]. Kim IS, Song JK, Zhang YL, Lee TH, Cho TH, Song YM, et al. Biochim. Biophys. Acta, Mol. Cell Res. Biochimica et Biophysica Acta (BBA) - Molecular Cell Research. 2006;1763(9):907-16.

[152]. Genovese JA, Spadaccio C, Rivello HG, Toyoda Y, Patel AN. Electrostimulated bone marrow human mesenchymal stem cells produce follistatin. Cytotherapy. 2009;11(4):448-56.

[153]. Meng S, Zhang Z, Rouabhia M. Accelerated osteoblast mineralization on a conductive substrate by multiple electrical stimulation. J Bone Miner Metab. 2011;29(5):535-44.

[154]. Ercan B, Webster TJ. The effect of biphasic electrical stimulation on osteoblast function at anodized nanotubular titanium surfaces. Biomaterials. 2010;31(13):3684-93.

[155]. Shao S, Zhou S, Li L, Li J, Luo C, Wang J, et al. Osteoblast function on electrically conductive electrospun PLA/MWCNTs nanofibers. Biomaterials. 2011;32(11):2821-33.

[156]. Hartig M, Joos U, Wiesmann H-P. Capacitively coupled electric fields accelerate proliferation of osteoblast-like primary cells and increase bone extracellular matrix formation in vitro. Eur Biophys J. 2000;29(7):499-506.

[157]. Brighton CT, Wang W, Seldes R, Zhang G, Pollack SR. Signal Transduction in Electrically Stimulated Bone Cells. J Bone Jt Surg. 2001;83(10):1514-23.

[158]. McLeod KJ, Donahue HJ, Levin PE, Fontaine M-A, Rubin CT. Electric fields modulate bone cell function in a density-dependent manner. J Bone Miner Res. 1993;8(8):977-84.

[159]. Chang WH-S, Chen L-T, Sun J-S, Lin F-H. Effect of pulse-burst electromagnetic field stimulation on osteoblast cell activities. Bioelectromagnetics. 2004;25(6):457-65.

[160]. Zhang X, Zhang J, Qu X, Wen J. Effects of Different Extremely Low-Frequency Electromagnetic Fields on Osteoblasts. Electromagn Biol Med. 2007;26(3):167-77.

[161]. Tsai M-T, Li W-J, Tuan RS, Chang WH. Modulation of osteogenesis in human mesenchymal stem cells by specific pulsed electromagnetic field stimulation. J Orthopaed Res. 2009;27(9):1169-74.

[162]. Jansen J, van der Jagt O, Punt B, Verhaar J, van Leeuwen J, Weinans H, et al. Stimulation of osteogenic differentiation in human osteoprogenitor cells by pulsed electromagnetic fields: an in vitro study. Bmc Musculoskel Dis. 2010;11(1):188.

[163]. O'Connor B, Charlton H, Currey J, Kirby D, Woods C. Effects of electric current on bone in vivo. Nature. 1969;204:252-4.

[164]. Bassett C, Andrew L. Pulsing electromagnetic fields: A new method to modify cell behavior in calcified and noncalcified tissues. Calcif Tissue Int. 1982;34(1):1-8.

[165]. Isaacson BM, Bloebaum RD. Bone bioelectricity: What have we learned in the past 160 years? JBiomed Mater Res A. 2010;95A(4):1270-9.

[166]. Hassler CR, Rybicki EF, Diegle RB, Clark LC. Studies of Enhanced Bone Healing via Electrical Stimuli Comparative Effectiveness of Various Parameters. Clin Orthop Relat Res. 1977;124:9-19.

[167]. Berridge MJ, Lipp P, Bootman MD. The versatility and universality of calcium signalling. Nat Rev Mol Cell Biol. 2000;1(1):11-21.

[168]. Brighton CT, Friednberg ZB, Mitchell EI, Booth RE. Treatment of Nonunion with Constant Direct Current. Clin Orthop Relat Res. 1977;124:106-23.

[169]. PATERSON D. Treatment of nonunion with a constant direct current. A totally implantable system. Orthop Clin North Am. 1984;15(1):47-59.

[170]. Brighton CT PS. Treatment of recalcitrant non-union with a capacitively coupled electrical field. A preliminary report. J Bone Jt Surg. 1985;67(4):577-85.

[171]. Lavine L, Grodzinsky A. Electrical stimulation of repair of bone. J Bone Jt Surg, Am Vol. 1987;69(4):626.

[172]. HECKMAN JD, INGRAM AJ, LOYD RD, LUCK JVJ, MAYER PW. Nonunion Treatment with Pulsed Electromagnetic Fields. Clin Orthop Relat Res. 1981;161:58-66.

[173]. Bassett C, Mitchell S, Gaston S. Treatment of ununited tibial diaphyseal fractures with pulsing. J Bone Jt Surg, Am Vol. 1981;63:511-23.

[174]. Navarro M, Michiardi A, Castaño O, Planell JA. Biomaterials in orthopaedics. J R Soc, Interface. 2008;5(27):1137-58.

[175]. Jacobs JJ, Gilbert JL, Urban RM. Current Concepts Review - Corrosion of Metal Orthopaedic Implants*. J Bone Jt Surg. 1998;80(2):268-82.

[176]. Puleo DA, Huh WW. Acute toxicity of metal ions in cultures of osteogenic cells derived from bone marrow stromal cells. J Appl Biomater. 1995;6(2):109-16.

[177]. Patel N. The US and western european markets for bone graft substitutes. Report#M525,Medmarket diligence. 2005.

[178]. Hench L, Best S. Ceramics, glassses and glass-ceramics. In: Ratner B, Hoffman A, Schoen F, Lemons J, editors. Biomaterials Science: an introduction to materials in medicine. USA: Elsevier Academic Press; 2004.

[179]. Bohner M. Resorbable biomaterials as bone graft substitutes. Mater Today. 2010;13(1–2):24-30.

[180]. Moore WR, Graves SE, Bain GI. Synthetic bone graft substitutes. ANZ Journal of Surgery. 2001;71(6):354-61.

[181]. Stevens MM, George JH. Exploring and Engineering the Cell Surface Interface. Science. 2005;310(5751):1135-8.

[182]. Dorozhkin SV. Bioceramics of calcium orthophosphates. Biomaterials. 2010;31(7):1465-85.

[183]. Legeros R, Legeros J. Dense Hydroxyapatite. In: Hench L, Wilson J, editors. An introduction to bioceramics. USA: World Scientific; 1993.

[184]. Daculsi G, LeGeros RZ, Heughebaert M, Barbieux I. Formation of carbonate-apatite crystals after implantation of calcium phosphate ceramics. Calcif Tissue Int. 1990;46(1):20-7.

[185]. Ripamonti U. Osteoinduction in porous hydroxyapatite implanted in heterotopic sites of different animal models. Biomaterials. 1996;17(1):31-5.

[186]. Tamai N, Myoui A, Tomita T, Nakase T, Tanaka J, Ochi T, et al. Novel hydroxyapatite ceramics with an interconnective porous structure exhibit superior osteoconduction in vivo. J Biomed Mater Res. 2002;59(1):110-7.

[187]. Tadic D, Epple M. A thorough physicochemical characterisation of 14 calcium phosphate-based bone substitution materials in comparison to natural bone. Biomaterials. 2004;25(6):987-94.

[188]. White AA, Best SM, Kinloch IA. Hydroxyapatite–Carbon Nanotube Composites for Biomedical Applications: A Review. Int J Appl Ceram Tec. 2007;4(1):1-13.

[189]. Lopes MA, Silva RF, Monteiro FJ, Santos JD. Microstructural dependence of Young's and shear moduli of P2O5 glass reinforced hydroxyapatite for biomedical applications. Biomaterials. 2000;21(7):749-54.

[190]. Lopes MA, Knowles JC, Santos JD, Monteiro FJ, Olsen I. Direct and indirect effects of P2O5 glass reinforced-hydroxyapatite composites on the growth and function of osteoblast-like cells. Biomaterials. 2000;21(11):1165-72.

[191]. Lopes MA, Santos JD, Monteiro FJ, Ohtsuki C, Osaka A, Kaneko S, et al. Push-out testing and histological evaluation of glass reinforced hydroxyapatite composites implanted in the tibia of rabbits. J Biomed Mater Res. 2001;54(4):463-9.

[192]. Spear R, Cameron R. Carbon nanotubes for orthopaedic implants. Int J Mater Form. 2008;1(2):127-33.

[193]. Kostarelos K, Bianco A, Prato M. Promises, facts and challenges for carbon nanotubes in imaging and therapeutics. Nat Nanotechnol. 2009;4(10):627-33.

[194]. Liu Z, Tabakman S, Welsher K, Dai H. Carbon nanotubes in biology and medicine: In vitro and in vivo detection, imaging and drug delivery. Nano Res. 2009;2(2):85-120.

[195]. Liu Z, Davis C, Cai W, He L, Chen X, Dai H. Circulation and long-term fate of functionalized, biocompatible single-walled carbon nanotubes in mice probed by Raman spectroscopy. P Natl Acad Sci. 2008;105(5):1410-5.

[196]. Cherukuri P, Gannon CJ, Leeuw TK, Schmidt HK, Smalley RE, Curley SA, et al. Mammalian pharmacokinetics of carbon nanotubes using intrinsic near-infrared fluorescence. P Natl Acad Sci. 2006;103(50):18882-6.

[197]. Lacerda L, Pastorin G, Gathercole D, Buddle J, Prato M, Bianco A, et al. Intracellular Trafficking of Carbon Nanotubes by Confocal Laser Scanning Microscopy. Adv Mater. 2007;19(11):1480-4.

[198]. Heller DA, Baik S, Eurell TE, Strano MS. Single-Walled Carbon Nanotube Spectroscopy in Live Cells: Towards Long-Term Labels and Optical Sensors. Adv Mater. 2005;17(23):2793-9.

[199]. Kostarelos K, Lacerda L, Pastorin G, Wu W, Wieckowski S, Luangsivilay J, et al. Cellular uptake of functionalized carbon nanotubes is independent of functional group and cell type. Nat Nanotechnol. 2007;2(2):108-13.

[200]. Akasaka T, Watari F, Sato Y, Tohji K. Apatite formation on carbon nanotubes. Mater Sci Eng, C. 2006;26(4):675-8.

[201]. Beuvelot J, Bergeret C, Mallet R, Fernandez V, Cousseau J, Baslé MF, et al. In vitro calcification of chemically functionalized carbon nanotubes. Acta Biomater. 2010;6(10):4110-7.

[202]. Usui Y, Aoki K, Narita N, Murakami N, Nakamura I, Nakamura K, et al. Carbon Nanotubes with High Bone-Tissue Compatibility and Bone-Formation Acceleration Effects. Small. 2008;4(2):240-6.

[203]. Jamilpour N, Fereidoon A, Rouhi G. The Effects of Replacing Collagen Fibers with Carbon Nanotubes on the Rate of Bone Remodeling Process. J Biomed Nanotechnol. 2011;7(4):542-8.

[204]. Zhao B, Hu H, Mandal SK, Haddon RC. A Bone Mimic Based on the Self-Assembly of Hydroxyapatite on Chemically Functionalized Single-Walled Carbon Nanotubes. Chem Mater. 2005;17(12):3235-41.

[205]. Edmonds D. Electricity and Magnetism in Biological Systems. USA: Oxford University Press; 2001.

[206]. Guiseppi-Elie A. Electroconductive hydrogels: Synthesis, characterization and biomedical applications. Biomaterials. 2010;31(10):2701-16.

[207]. Facca S, Lahiri D, Fioretti F, Messadeq N, Mainard D, Benkirane-Jessel N, et al. In Vivo Osseointegration of Nano-Designed Composite Coatings on Titanium Implants. ACS nano. 2011;5(6):4790-9.

[208]. Li X, Liu H, Niu X, Yu B, Fan Y, Feng Q, et al. The use of carbon nanotubes to induce osteogenic differentiation of human adipose-derived MSCs in vitro and ectopic bone formation in vivo. Biomaterials. 2012;33(19):4818-27.

[209]. Cho J, Boccaccini A, Shaffer MP. Ceramic matrix composites containing carbon nanotubes. J Mater Sci. 2009;44(8):1934-51.

[210]. Kagan VE, Konduru NV, Feng W, Allen BL, Conroy J, Volkov Y, et al. Carbon nanotubes degraded by neutrophil myeloperoxidase induce less pulmonary inflammation. Nat Nanotechnol. 2010;5(5):354-9.

[211]. Nunes A, Bussy C, Gherardini L, Meneghetti M, Herrero MA, Bianco A, et al. In vivo degradation of functionalized carbon nanotubes after stereotactic administration in the brain cortex. Nanomedicine : nanotechnology, biology, and medicine. 2012;7(10):1485-94.

[212]. Kane AB, Hurt RH. Nanotoxicology: The asbestos analogy revisited. Nat Nanotechnol. 2008;3(7):378-9.

[213]. Ajayan PM, Tour JM. Materials science: nanotube composites. Nature. 2007;447(7148):1066-8.

[214]. Zhao L, Gao L. Novel in situ synthesis of MWNTs-hydroxyapatite composites. Carbon. 2004;42(2):423-6.

[215]. Kónya Z, Zhu J, Niesz K, Mehn D, Kiricsi I. End morphology of ball milled carbon nanotubes. Carbon. 2004;42(10):2001-8.

[216]. Sarkar SK, Youn MH, Oh IH, Lee BT, editors. Fabrication of CNT-reinforced HAp composites by spark plasma sintering. Mater Sci Forum; 2007: Trans Tech Publ.

[217]. Xu G-H, Zhang Q, Huang J-Q, Zhao M-Q, Zhou W-P, Wei F. A Two-Step Shearing Strategy To Disperse Long Carbon Nanotubes from Vertically Aligned Multiwalled Carbon Nanotube Arrays for Transparent Conductive Films. Langmuir : the ACS journal of surfaces and colloids. 2009;26(4):2798-804.

[218]. Lahiri D, Singh V, Keshri AK, Seal S, Agarwal A. Carbon nanotube toughened hydroxyapatite by spark plasma sintering: Microstructural evolution and multiscale tribological properties. Carbon. 2010;48(11):3103-20.

[219]. Li H, Zhao N, Liu Y, Liang C, Shi C, Du X, et al. Fabrication and properties of carbon nanotubes reinforced Fe/hydroxyapatite composites by in situ chemical vapor deposition. Composites, Part A. 2008;39(7):1128-32.

[220]. Peigney A, Laurent C, Dobigeon F, Rousset A. Carbon nanotubes grown in situ by a novel catalytic method. J Mater Res. 1997;12(03):613-5.

[221]. Li A, Sun K, Dong W, Zhao D. Mechanical properties, microstructure and histocompatibility of MWCNTs/HAp biocomposites. Mater Lett. 2007;61(8–9):1839-44.

[222]. White AA, Kinloch IA, Windle AH, Best SM. Optimization of the sintering atmosphere for high-density hydroxyapatite–carbon nanotube composites. J R Soc, Interface. 2010;7(Suppl 5):S529-S39.

[223]. Peigney A, Rul S, Lefèvre-Schlick F, Laurent C. Densification during hot-pressing of carbon nanotube–metal–magnesium aluminate spinel nanocomposites. J Eur Ceram Soc. 2007;27(5):2183-93.

[224]. Balázsi C, Shen Z, Kónya Z, Kasztovszky Z, Wéber F, Vértesy Z, et al. Processing of carbon nanotube reinforced silicon nitride composites by spark plasma sintering. Compos Sci Technol. 2005;65(5):727-33.

[225]. Inam F, Yan H, Peijs T, Reece MJ. The sintering and grain growth behaviour of ceramic–carbon nanotube nanocomposites. Compos Sci Technol. 2010;70(6):947-52.

[226]. Neil DX, Edward GX. The dependence of transversely isotropic elasticity of human femoral cortical bone on porosity. J Biomech. 2004;37(8):1281-7.

[227]. Hench LL. Bioceramics: From Concept to Clinic. J Am Ceram Soc. 1991;74(7):1487-510.

[228]. Weaver JK. The Microscopic Hardness of Bone. J Bone Jt Surg. 1966;48(2):273-88.

[229]. Evans FG, Vincentelli R. Relations of the compressive properties of human cortical bone to histological structure and calcification. J Biomech. 1974;7(1):1-10.

[230]. Saha S, Williams PA. Electric and dielectric properties of wet human cortical bone as a function of frequency. Biomed Eng. 1992;39(12):1298-304.

[231]. Hench L, Best S. Ceramics, glasses and glass-ceramics. In: Ratner B, Hoffman A, Schoen F, Lemons J, editors. Biomaterials Science: an introduction to materials in medicine. USA: Elsevier Academic Press; 2004.

[232]. Gittings JP, Bowen CR, Dent ACE, Turner IG, Baxter FR, Chaudhuri JB. Electrical characterization of hydroxyapatite-based bioceramics. Acta Biomater. 2009;5(2):743-54.

[233]. Ravaglioli A, Krajewski A. Bioceramics: Materials, Properties and Applications. London: Chapman and Hall; 1992.

[234]. Hench L, Kokubo T. Properties of bioactive glasses and glas-ceramics. In: Black J HG, editor. Handbook of Biomaterials Properties. London: Chapman and Hall; 1998.

[235]. Nagai M, Shibuya Y, Nishino T, Saeki T, Owada H, Yamashita K, et al. Electrical conductivity of calcium phosphate ceramics with various Ca/P ratios. J Mater Sci. 1991;26(11):2949-53.

[236]. Mariappan CR, Yunos DM, Boccaccini AR, Roling B. Bioactivity of electro-thermally poled bioactive silicate glass. Acta Biomater. 2009;5(4):1274-83.

[237]. Lopes MA, Monteiro FJ, Santos JD. Glass-reinforced hydroxyapatite composites: fracture toughness and hardness dependence on microstructural characteristics. Biomaterials. 1999;20(21):2085-90.

[238]. Lopes MA, Monteiro FJ, Santos JD. Glass-reinforced hydroxyapatite composites: Secondary phase proportions and densification effects on biaxial bending strength. J Biomed Mater Res. 1999;48(5):734-40.

[239]. Mata D OF, Ferro M, Gomes PS, Fernandes MH, Lopes MA, Silva RF. Multifunctional carbon nanotube/bioceramics modulate the directional growth and activity of osteoblastic cells. J Biomed Nanotechnol.Submitted.

[240]. Kokubo T. A/W glass ceramic: processing and properties. In: Hench L, Wilson J, editors. An introduction to bioceramics. USA: World Scientific; 1993.

[241]. Kokubo T, Ito S, Shigematsu M, Sanka S, Yamamuro T. Fatigue and life-time of bioactive glass-ceramic A-W containing apatite and wollastonite. J Mater Sci. 1987;22(11):4067-70.

[242]. Xu JL, Khor KA, Sui JJ, Chen WN. Preparation and characterization of a novel hydroxyapatite/carbon nanotubes composite and its interaction with osteoblast-like cells. Mater Sci Eng, C. 2009;29(1):44-9.

[243]. Lei T, Wang L, Ouyang C, Li N-F, Zhou L-S. In Situ Preparation and Enhanced Mechanical Properties of Carbon Nanotube/Hydroxyapatite Composites. Int J Appl Ceram Tec. 2011;8(3):532-9.

[244]. Meng YH, Tang C, Tsui C, Chen D. Fabrication and characterization of needle-like nano-HA and HA/MWNT composites. J Mater Sci: Mater Med. 2008;19(1):75-81.

[245]. Zhan G-D, Kuntz JD, Wan J, Mukherjee AK. Single-wall carbon nanotubes as attractive toughening agents in alumina-based nanocomposites. Nature materials. 2002;2(1):38-42.

[246]. Shi S-L, Liang J. Effect of Multiwall Carbon Nanotubes on Electrical and Dielectric Properties of Yttria-Stabilized Zirconia Ceramic. J Am Ceram Soc. 2006;89(11):3533-5.

[247]. Tatami J, Katashima T, Komeya K, Meguro T, Wakihara T. Electrically Conductive CNT-Dispersed Silicon Nitride Ceramics. J Am Ceram Soc. 2005;88(10):2889-93.

[248]. Hussain M, Kabir M, Sood A. On the cytotoxicity of carbon nanotubes. Curr Sci. 2009;96(5):664-73.

[249]. Yehia HN, Draper RK, Mikoryak C, Walker EK, Bajaj P, Musselman IH, et al. Single-walled carbon nanotube interactions with HeLa cells. J Nanobiotechnol. 2007;5(8):1-8.

[250]. Dumortier H, Lacotte S, Pastorin G, Marega R, Wu W, Bonifazi D, et al. Functionalized Carbon Nanotubes Are Non-Cytotoxic and Preserve the Functionality of Primary Immune Cells. Nano letters. 2006;6(7):1522-8.

[251]. Pulskamp K, Diabaté S, Krug HF. Carbon nanotubes show no sign of acute toxicity but induce intracellular reactive oxygen species in dependence on contaminants. Toxicology letters. 2007;168(1):58-74.

[252]. Shvedova A, Castranova V, Kisin E, Schwegler-Berry D, Murray A, Gandelsman V, et al. Exposure to Carbon Nanotube Material: Assessment of Nanotube Cytotoxicity using Human Keratinocyte Cells. Journal of Toxicology and Environmental Health, Part A. 2003;66(20):1909-26.

[253]. Cui D, Tian F, Ozkan CS, Wang M, Gao H. Effect of single wall carbon nanotubes on human HEK293 cells. Toxicology letters. 2005;155(1):73-85.

[254]. Manna SK, Sarkar S, Barr J, Wise K, Barrera EV, Jejelowo O, et al. Single-Walled Carbon Nanotube Induces Oxidative Stress and Activates Nuclear Transcription Factor-κB in Human Keratinocytes. Nano letters. 2005;5(9):1676-84.

[255]. Raja PMV, Connolley J, Ganesan GP, Ci L, Ajayan PM, Nalamasu O, et al. Impact of carbon nanotube exposure, dosage and aggregation on smooth muscle cells. Toxicology letters. 2007;169(1):51-63.

[256]. Casey A, Herzog E, Lyng FM, Byrne HJ, Chambers G, Davoren M. Single walled carbon nanotubes induce indirect cytotoxicity by medium depletion in A549 lung cells. Toxicology letters. 2008;179(2):78-84.

[257]. Wick P, Manser P, Limbach LK, Dettlaff-Weglikowska U, Krumeich F, Roth S, et al. The degree and kind of agglomeration affect carbon nanotube cytotoxicity. Toxicology letters. 2007;168(2):121-31.

[258]. Kam NWS, O'Connell M, Wisdom JA, Dai H. Carbon nanotubes as multifunctional biological transporters and near-infrared agents for selective cancer cell destruction. Proceedings of the National Academy of Sciences of the United States of America. 2005;102(33):11600-5.

[259]. Magrez A, Kasas S, Salicio V, Pasquier N, Seo JW, Celio M, et al. Cellular toxicity of carbon-based nanomaterials. Nano letters. 2006;6(6):1121-5. Epub 2006/06/15.

[260]. Hirano S, Kanno S, Furuyama A. Multi-walled carbon nanotubes injure the plasma membrane of macrophages. Toxicology and applied pharmacology. 2008;232(2):244-51.

[261]. Simon-Deckers A, Gouget B, Mayne-L'hermite M, Herlin-Boime N, Reynaud C, Carriere M. In vitro investigation of oxide nanoparticle and carbon nanotube toxicity and intracellular accumulation in A549 human pneumocytes. Toxicology. 2008;253(1-3):137-46. Epub 2008/10/07.

[262]. Bottini M, Bruckner S, Nika K, Bottini N, Bellucci S, Magrini A, et al. Multi-walled carbon nanotubes induce T lymphocyte apoptosis. Toxicology letters. 2006;160(2):121-6. Epub 2005/08/30.

[263]. Cheng C, Muller KH, Koziol KK, Skepper JN, Midgley PA, Welland ME, et al. Toxicity and imaging of multi-walled carbon nanotubes in human macrophage cells. Biomaterials. 2009;30(25):4152-60. Epub 2009/05/29.

[264]. Ding L, Stilwell J, Zhang T, Elboudwarej O, Jiang H, Selegue JP, et al. Molecular characterization of the cytotoxic mechanism of multiwall carbon nanotubes and nano-onions on human skin fibroblast. Nano letters. 2005;5(12):2448-64. Epub 2005/12/15.

[265]. Flahaut E, Durrieu MC, Remy-Zolghadri M, Bareille R, Baquey C. Investigation of the cytotoxicity of CCVD carbon nanotubes towards human umbilical vein endothelial cells. Carbon N Y. 2006;44(6):1093-9.

[266]. Wu W, Wieckowski S, Pastorin G, Benincasa M, Klumpp C, Briand J-P, et al. Targeted Delivery of Amphotericin B to Cells by Using Functionalized Carbon Nanotubes. Angewandte Chemie International Edition. 2005;44(39):6358-62.

[267]. Sato Y, Yokoyama A, Shibata K-i, Akimoto Y, Ogino S-i, Nodasaka Y, et al. Influence of length on cytotoxicity of multi-walled carbon nanotubes against human acute monocytic leukemia cell line THP-1 in vitro and subcutaneous tissue of rats in vivo. Mol Biosyst. 2005;1(2):176-82.

[268]. Koyama S, Endo M, Kim Y-A, Hayashi T, Yanagisawa T, Osaka K, et al. Role of systemic T-cells and histopathological aspects after subcutaneous implantation of various carbon nanotubes in mice. Carbon. 2006;44(6):1079-92.

[269]. Fraczek A, Menaszek E, Paluszkiewicz C, Blazewicz M. Comparative in vivo biocompatibility study of single- and multi-wall carbon nanotubes. Acta biomaterialia. 2008;4(6):1593-602.

[270]. Warheit DB, Laurence BR, Reed KL, Roach DH, Reynolds GAM, Webb TR. Comparative Pulmonary Toxicity Assessment of Single-wall Carbon Nanotubes in Rats. Toxicological Sciences. 2004;77(1):117-25.

[271]. Lam C-W, James JT, McCluskey R, Hunter RL. Pulmonary Toxicity of Single-Wall Carbon Nanotubes in Mice 7 and 90 Days After Intratracheal Instillation. Toxicological Sciences. 2004;77(1):126-34.

[272]. Shvedova AA, Kisin ER, Murray AR, Gorelik O, Arepalli S, Castranova V, et al. Vitamin E deficiency enhances pulmonary inflammatory response and oxidative stress induced by single-walled carbon nanotubes in C57BL/6 mice. Toxicology and applied pharmacology. 2007;221(3):339-48.

[273]. Yang S-T, Wang X, Jia G, Gu Y, Wang T, Nie H, et al. Long-term accumulation and low toxicity of single-walled carbon nanotubes in intravenously exposed mice. Toxicology letters. 2008;181(3):182-9.

[274]. Tong H, McGee JK, Saxena RK, Kodavanti UP, Devlin RB, Gilmour MI. Influence of acid functionalization on the cardiopulmonary toxicity of carbon nanotubes and carbon black particles in mice. Toxicology and applied pharmacology. 2009;239(3):224-32.

[275]. Erdely A, Hulderman T, Salmen R, Liston A, Zeidler-Erdely PC, Schwegler-Berry D, et al. Cross-Talk between Lung and Systemic Circulation during Carbon Nanotube Respiratory Exposure. Potential Biomarkers. Nano letters. 2008;9(1):36-43.

[276]. Liu Z, Cai W, He L, Nakayama N, Chen K, Sun X, et al. In vivo biodistribution and highly efficient tumour targeting of carbon nanotubes in mice. Nature nanotechnology. 2006;2(1):47-52.

[277]. Chou C-C, Hsiao H-Y, Hong Q-S, Chen C-H, Peng Y-W, Chen H-W, et al. Single-Walled Carbon Nanotubes Can Induce Pulmonary Injury in Mouse Model. Nano letters. 2008;8(2):437-45.

[278]. Fraczek A, Menaszek E, Paluszkiewicz C, Blazewicz M. Comparative in vivo biocompatibility study of single- and multi-wall carbon nanotubes. Acta biomaterialia. 2008;4(6):1593-602. Epub 2008/07/01.

[279]. Poland CA, Duffin R, Kinloch I, Maynard A, Wallace WA, Seaton A, et al. Carbon nanotubes introduced into the abdominal cavity of mice show asbestos-like pathogenicity in a pilot study. Nature nanotechnology. 2008;3(7):423-8.

[280]. Takagi A, Hirose A, Nishimura T, Fukumori N, Ogata A, Ohashi N, et al. Induction of mesothelioma in p53+/- mouse by intraperitoneal application of multi-wall carbon nanotube. The Journal of toxicological sciences. 2008;33(1):105-16. Epub 2008/02/28.

[281]. Muller J, Huaux F, Fonseca A, Nagy JB, Moreau N, Delos M, et al. Structural defects play a major role in the acute lung toxicity of multiwall carbon nanotubes: toxicological aspects. Chemical research in toxicology. 2008;21(9):1698-705. Epub 2008/07/19.

[282]. Porter DW, Hubbs AF, Mercer RR, Wu N, Wolfarth MG, Sriram K, et al. Mouse pulmonary dose- and time course-responses induced by exposure to multi-walled carbon nanotubes. Toxicology. 2010;269(2-3):136-47. Epub 2009/10/28.

[283]. Lacerda L, Ali-Boucetta H, Herrero MA, Pastorin G, Bianco A, Prato M, et al. Tissue histology and physiology following intravenous administration of different types of functionalized multiwalled carbon nanotubes. Nanomedicine : nanotechnology, biology, and medicine. 2008;3(2):149-61.

[284]. Ma-Hock L, Treumann S, Strauss V, Brill S, Luizi F, Mertler M, et al. Inhalation toxicity of multiwall carbon nanotubes in rats exposed for 3 months. Toxicological sciences : an official journal of the Society of Toxicology. 2009;112(2):468-81. Epub 2009/07/09.

[285]. Lacerda L, Soundararajan A, Singh R, Pastorin G, Al-Jamal KT, Turton J, et al. Dynamic Imaging of Functionalized Multi-Walled Carbon Nanotube Systemic Circulation and Urinary Excretion. Adv Materials. 2008;20(2):225-30.

[286]. Kagan VE, Tyurina YY, Tyurin VA, Konduru NV, Potapovich AI, Osipov AN, et al. Direct and indirect effects of single walled carbon nanotubes on RAW 264.7 macrophages: Role of iron. Toxicol Lett. 2006;165(1):88-100.

[287]. Pulskamp K, Diabaté S, Krug HF. Carbon nanotubes show no sign of acute toxicity but induce intracellular reactive oxygen species in dependence on contaminants. Toxicol Lett. 2007;168(1):58-74.

[288]. Hirano S, Kanno S, Furuyama A. Multi-walled carbon nanotubes injure the plasma membrane of macrophages. Toxicol Appl Pharmacol. 2008;232(2):244-51.

[289]. Simon-Deckers A, Gouget B, Mayne-L'Hermite M, Herlin-Boime N, Reynaud C, Carrière M. In vitro investigation of oxide nanoparticle and carbon nanotube toxicity and intracellular accumulation in A549 human pneumocytes. Toxicology. 2008;253(1–3):137-46.

[290]. Wu W, Wieckowski S, Pastorin G, Benincasa M, Klumpp C, Briand J-P, et al. Targeted Delivery of Amphotericin B to Cells by Using Functionalized Carbon Nanotubes. Angew Chem, Int Ed. 2005;44(39):6358-62.

[291]. Baik KY, Park SY, Heo K, Lee K-B, Hong S. Carbon Nanotube Monolayer Cues for Osteogenesis of Mesenchymal Stem Cells. Small. 2011;7(6):741-5.

[292]. Xiaoming L, Hong G, Motohiro U, Yoshinori S, Tsukasa A, Shigeaki A, et al. Maturation of osteoblast-like SaoS2 induced by carbon nanotubes. Biomed Mater. 2009;4(1):015005.

[293]. Shimizu M, Kobayashi Y, Mizoguchi T, Nakamura H, Kawahara I, Narita N, et al. Carbon Nanotubes Induce Bone Calcification by Bidirectional Interaction with Osteoblasts. Adv Materials. 2012;24(16):2176-85.

[294]. Balani K, Anderson R, Laha T, Andara M, Tercero J, Crumpler E, et al. Plasma-sprayed carbon nanotube reinforced hydroxyapatite coatings and their interaction with human osteoblasts in vitro. Biomaterials. 2007;28(4):618-24. Epub 2006/09/30.

[295]. Hahn BD, Lee JM, Park DS, Choi JJ, Ryu J, Yoon WH, et al. Mechanical and in vitro biological performances of hydroxyapatite-carbon nanotube composite coatings deposited on Ti by aerosol deposition. Acta biomaterialia. 2009;5(8):3205-14. Epub 2009/05/19.

[296]. Xu JL, Khor KA, Sui JJ, Chen WN. Preparation and characterization of a novel hydroxyapatite/carbon nanotubes composite and its interaction with osteoblast-like cells. Materials Science and Engineering: C. 2009;29(1):44-9.

[297]. Bai Y, Neupane MP, Park IS, Lee MH, Bae TS, Watari F, et al. Electrophoretic deposition of carbon nanotubes–hydroxyapatite nanocomposites on titanium substrate. Materials Science and Engineering: C. 2010;30(7):1043-9.

[298]. Facca S, Lahiri D, Fioretti F, Messadeq N, Mainard D, Benkirane-Jessel N, et al. In vivo osseointegration of nano-designed composite coatings on titanium implants. ACS nano. 2011;5(6):4790-9. Epub 2011/05/20.

[299]. Wang W, Zhu Y, Watari F, Liao S, Yokoyama A, Omori M, et al. Carbon nanotubes/hydroxyapatite nanocomposites fabricated by spark plasma sintering for bonegraft applications. Appl Surf Sci. 2012;262(0):194-9.

[300]. Mei F, Zhong J, Yang X, Ouyang X, Zhang S, Hu X, et al. Improved Biological Characteristics of Poly(l-Lactic Acid) Electrospun Membrane by Incorporation of Multiwalled Carbon Nanotubes/Hydroxyapatite Nanoparticles. Biomacromolecules. 2007;8(12):3729-35.

[301]. Yadav SK, Bera T, Saxena PS, Maurya AK, Garbyal RS, Vajtai R, et al. MWCNTs as reinforcing agent to the Hap–Gel nanocomposite for artificial bone grafting. Journal of Biomedical Materials Research Part A. 2010;93A(3):886-96.

[302]. Sitharaman B, Shi X, Walboomers XF, Liao H, Cuijpers V, Wilson LJ, et al. In vivo biocompatibility of ultra-short single-walled carbon nanotube/biodegradable polymer nanocomposites for bone tissue engineering. Bone. 2008;43(2):362-70.

[303]. Deng X, Jia G, Wang H, Sun H, Wang X, Yang S, et al. Translocation and fate of multi-walled carbon nanotubes in vivo. Carbon. 2007;45(7):1419-24.

[304]. Yang S-t, Guo W, Lin Y, Deng X-y, Wang H-f, Sun H-f, et al. Biodistribution of Pristine Single-Walled Carbon Nanotubes In Vivo†. J Phys Chem C. 2007;111(48):17761-4.

[305]. Singh R, Pantarotto D, Lacerda L, Pastorin G, Klumpp C, Prato M, et al. Tissue biodistribution and blood clearance rates of intravenously administered carbon nanotube radiotracers. Proc Natl Acad Sci USA. 2006;103(9):3357-62.

[306]. Kostarelos K. The long and short of carbon nanotube toxicity. Nat Biotechnol. 2008;26(7):774-6.

[307]. Stone V, Donaldson K. Nanotoxicology: signs of stress. Nat Nanotechnol. 2006;1(1):23-4.

[308]. Poland CA, Duffin R, Kinloch I, Maynard A, Wallace WA, Seaton A, et al. Carbon nanotubes introduced into the abdominal cavity of mice show asbestos-like pathogenicity in a pilot study. Nat Nanotechnol. 2008;3(7):423-8.

[309]. Porter AE, Gass M, Muller K, Skepper JN, Midgley PA, Welland M. Direct imaging of single-walled carbon nanotubes in cells. Nat Nanotechnol. 2007;2(11):713-7.

[310]. Elgrabli D, Floriani M, Abella-Gallart S, Meunier L, Gamez C, Delalain P, et al. Biodistribution and clearance of instilled carbon nanotubes in rat lung. Part Fibre Toxicol. 2008;5:20.

[311]. Babior B. Oxidants from phagocytes: agents of defense and destruction. Blood. 1984;64(5):959-66.

[312]. Sbarra AJ, Karnovsky ML. The Biochemical Basis of Phagocytosis: I. Metabolic changes during the ingestion of particles by polymorphonuclear leukocytes. J Biol Chem. 1959;234(6):1355-62.

[313]. Allen BL, Kichambare PD, Gou P, Vlasova II, Kapralov AA, Konduru N, et al. Biodegradation of Single-Walled Carbon Nanotubes through Enzymatic Catalysis. Nano Lett. 2008;8(11):3899-903.

[314]. Liu X, Hurt RH, Kane AB. Biodurability of single-walled carbon nanotubes depends on surface functionalization. Carbon. 2010;48(7):1961-9.

[315]. Freitas R. Nanomedicine Volume IIA: biocompatibility. USA: Landes Bioscience; 2003.

[316]. Li C, Chou T-W. Elastic moduli of multi-walled carbon nanotubes and the effect of van der Waals forces. Compos Sci Technol. 2003;63(11):1517-24.

[317]. Robertson DH, Brenner DW, Mintmire JW. Energetics of nanoscale graphitic tubules. Phys Rev B. 1992;45(21):12592-5.

[318]. Salvetat J-P, Briggs GAD, Bonard J-M, Bacsa RR, Kulik AJ, Stöckli T, et al. Elastic and Shear Moduli of Single-Walled Carbon Nanotube Ropes. Phys Rev Lett. 1999;82(5):944-7.

[319]. Sánchez-Portal D, Artacho E, Soler JM, Rubio A, Ordejón P. Ab initio structural, elastic, and vibrational properties of carbon nanotubes. Phys Rev B. 1999;59(19):12678-88.

[320]. Lacerda L, Herrero MA, Venner K, Bianco A, Prato M, Kostarelos K. Carbon-Nanotube Shape and Individualization Critical for Renal Excretion. Small. 2008;4(8):1130-2.

[321]. Miot-Noirault E, Faure L, Guichard Y, Montharu Jrm, Le Pape A. Scintigraphic in vivo assessment of the development of pulmonary intravascular macrophages in liver disease*: Experimental study in rats with biliary cirrhosis. CHEST Journal. 2001;120(3):941-7.

[322]. Bianco A, Kostarelos K, Prato M. Making carbon nanotubes biocompatible and biodegradable. Chem Commun. 2011;47(37):10182-8.

[323]. Shi Kam NW, Jessop TC, Wender PA, Dai H. Nanotube Molecular Transporters: Internalization of Carbon Nanotube−Protein Conjugates into Mammalian Cells. J Am Chem Soc. 2004;126(22):6850-1.

[324]. Pantarotto D, Briand J-P, Prato M, Bianco A. Translocation of bioactive peptides across cell membranes by carbon nanotubes. Chem Commun. 2004(1):16-7.

[325]. Lopez CF, Nielsen SO, Moore PB, Klein ML. Understanding nature's design for a nanosyringe. Proc Natl Acad Sci USA. 2004;101(13):4431-4.

[326]. Liang C, Li H, Wang L, Chen X, Zhao W. Investigation of the cytotoxicity of carbon nanotubes using hydroxyapatite as a nano-matrix towards mouse fibroblast cells. Mater Chem Phys. 2010;124(1):21-4.

Chapter II

CVD synthesis of carbon nanofibers (CNFs) and vertically-aligned MWCNTs

II.1 Introduction

Following the prerequisites for biomedical applications of carbon nanofibers (CNFs) and carbon nanotubes (CNTs) synthesis, different approaches to obtain dimensionally-controlled and catalyst-free materials were investigated in the present chapter. Two catalyst-supported chemical vapour deposition (CVD) production methods, hot-filament e thermal CVD, were studied. Here, the preparation of the catalyst-substrate and the growth parameters constitute key requisites to produce materials with depressed potential hazards to living organisms, and therefore to decide their clinical fate.

Section II.2 reports the first attempt to synthesize carbon filaments: the growth of (CNFs) on wet-chemically etched Ni metal foils using a hot-filament (HFCVD) reactor. Here, the pre-treatment of the catalyst-substrate was primarily focused. Several acid solutions and oxidizing etching solutions were tested to convert the smooth metal foil into a rough surface with nano-sized protrusions, used to catalyse the growth of CNFs.

In order to improve the control of the growth kinetics and to avoid carbon by-products, copper, having lower carbon solubility than nickel, was afterwards choosen as catalyst. Section II.3 is a description of a HFCVD parametric study of the synthesis conditions of CNFs on etched Cu metal foils. The substrates were treated by a fixed hydrogen peroxide based chemical solution (also found the best performance etching procedure in the work of section II.2). Pure and vertically aligned filaments were obtained with a scarcely control of the morphology.

The above HFCVD synthesis route of CNFs was selected owed to its simplicity and cost-effectiveness as it is applied directly on metals. However, it revealed critical drawbacks: excess of contaminants (from metallic filament and chamber components) and poor growth yield. Therefore, an alternative approach was explored using a different reactor and a different substrate with nanometric metallic particles as catalytic templates. Section II.4 focuses the production of carbon nanotubes CNTs in a dedicated thermal CVD system that was fully designed by the PhD candidate. The CNTs were grown on Si/SiO2 substrates coated with a Al2O3/Fe (diffusion barrier/catalyst) bilayer. The intent was to synthesize exclusively "clean" CNTs for biomedical applications. A complete parametric study of the growth substrate preparation and the growth parameters was accomplished. Milligram scale production of CNTs applying a semi-continuous setting and a stacked growth mode is described.

II.2. Wet-etched Ni foils as active catalysts towards carbon nanofiber growth

D. Mata[a], M. Ferro[a], A.J.S. Fernandes[b], M. Amaral[a,b], F.J. Oliveira[a], P.M.F.J. Costa[a], R.F. Silva[a]

[a]CICECO, Glass and Ceramics Eng. Dept., Univ. of Aveiro, Portugal
[b]I3N, Physics Dept., Univ. of Aveiro, Portugal

Abstract

A study of wet chemical etching treatments for nickel foils and the growth parameters for carbon nanostructures on them using hot-filament chemical vapour deposition (CVD) is described. Catalytically-active protrusions were produced on the Ni foils with sizes and densities in the range ~24-42 nm and ~202-314 P.μm^{-2}, respectively. These protrusions are found to have a key role in the growth process as they determine the yield and morphology of the carbon deposits. It is shown that well-shaped, nanosized protrusions are required to achieve high yield growth of hollow-herringbone carbon nanofibers (CNFs) with an in-plane crystallite size of ~23 nm. Good correlation was seen between the statistical distributions of the protrusion size (sp) and the CNF diameters (df) depicting sp/df ratios close to unity. This work sheds light on the mechanisms behind CVD growth on metal foils.

1. Introduction

Carbon-based nanofilaments, which include nanotubes (CNTs) and nanofibers (CNFs), have emerged as promising 1D-multifunctional structures for advanced technological applications [1,2]. Specifically, the outstanding set of physico-chemical properties showed by these structures [3,4] make them the vanguard graphite materials for integration into the next generation of polymeric [5], ceramic [6] and metallic [7] composites. CNFs are graphitic filaments with diameters commonly ranging from 1 to 200 nm and lengths in the range of several micrometers to millimetres. In resemblance to other carbon nanostructured materials, it is common practice to classify the CNFs in terms of the orientation angle of the graphene walls (or platelets) to the filament axis. Consequently, those with graphene walls arranged at different angles and showing a narrow void channel are known as hollow-herringbone. When the channel is absent and the platelets are almost perpendicular to the main axis, the usual denomination is solid-herringbone [8,9].

In order to commercially exploit CNFs-based composites it is vital that the filaments be assembled in high volumes and at low cost. In this respect, the use of metal foils, acting simultaneously as substrate and catalyst, can be assumed as a potentially advantageous route. Firstly, they are inexpensive when compared to other widely used substrates (Si, quartz, etc.). Second, if surface treatment processes can be understood and controlled, they may be reused numerous times. Third, employing metal foils avoids the need for an extra catalyst-addition step meaning that the growth procedures become simpler and more expedite (compared to sol-gel or floating catalyst techniques, for instance). Finally, foil methods could eventually provide better diameter control over the carbon nanostructures formation (the catalyst active sites, a.k.a. protrusions, can not coalesce easily during growth in contrast to scattered colloidal metal particles [8-11]).

The high catalytic activity of transition metal foils towards filamentous carbon deposition from hydrocarbons pyrolysis was earlier demonstrated [12-18]. Recently, there have been several reports of CNFs growth directly on metal foils performed in materials ranging from pure metals (Ni [19], Cu [20]) to alloys (stainless steel [11,21,22], Inconel$^{©}$ [23]). Highly-dense ensembles of vertically aligned carbon nanostructures ("forests") have been obtained on alloy substrates containing at least one of the transition metals known to be catalytically active (e.g. Ni, Co, Fe) [22,23]. Surprisingly, less commonly used metal catalysts may also lead to forests growth on foil substrates. In fact, one recent study reports the growth of well aligned bamboo-like CNTs on pure Cu foils at 800ºC, using ethanol as the carbon precursor [20].

Unlike catalyst thin films, dispersed particles and other widely used approaches for the growth of CNFs, in the case of metal foils the surface needs to be carefully prepared in order to generate arrays of catalytically active spots [8]. Pertinently, there is evidence that using surfaces treated with wet-chemical etching before growth can maximise the production of CNFs [21,22]. In these, it is claimed that the key factor lies on the initial size and shape of the catalyst-protrusions generated by the etching procedure. Unfortunately, the mechanisms guiding the formation of these

crucial catalytic protrusions are not well understood. Thus, to achieve better control of CNFs growth on metal foils, it is necessary to perform exhaustive studies on the conditions that dominate the generation of the catalytically-active protrusions.

In this work, wet-etching procedures have been devised to optimise the surface of Ni foil substrates for subsequent chemical vapour deposition growth of CNFs. It is shown how the surface pre-treatment controls the formation of the nanoprotrusions responsible for the nucleation of CNFs. The catalyst protrusions formation and the growth mechanism of CNFs on Ni foils are also discussed.

2. Experimental details

2.1 Catalyst metal foils preparation

Square metal foils ($10\times10\times1$ mm^2) of polycrystalline Ni (high purity: 99.99%, Goodfellow) were used as the combined catalyst and supporting material for the CNFs growth process. The metal foils were firstly polished with SiC mats (grades P220, P600, P1200) and diamond suspensions (grain sizes 1 and 6 μm), to normalize the as-received foils surface, and then ultrasonically cleaned in acetone and ethanol baths.

Several wet-chemical etching (CE) procedures were performed on the metal surfaces prior to the hot-filament chemical vapour deposition (HF-CVD) growth. The CE treatments [24] used acid solutions (HCl, HNO$_3$, H$_2$SO$_4$, HF) and other oxidising etchants (H$_2$O$_2$ 30%, CH$_4$O) for varied periods of time (1-20 min), and were carried out in an ultrasonic thermostatic bath kept at 15 ºC. The constant temperature was achieved with a continuous water flow circuit between the ultrasonic bath and a heater. Immediately prior to the CVD deposition, the etched substrates were cleaned with distilled water and again ultrasonically cleaned with acetone and ethanol. To ensure reproducibility of the CE treatments (redox potentials may change with extended storage time), fresh solutions were prepared for every new procedure.

2.2. HF-CVD deposition settings

CNFs were grown using a CH$_4$-Ar-H$_2$ gas mixture. The following conditions (optimized after a set of preliminary experiments) were constant throughout the set of growth runs: Ar/H$_2$ (v/v) = 3, CH$_4$/H$_2$ (v/v) = 1, total gas flow = 50 sccm, tungsten (W) filaments/substrate distance = 10 mm, filament temperature = 2300 ºC and deposition time = 15 min. The total pressure (5, 10 kPa) and substrate temperature (650, 800 ºC) were varied in order to observe their effect on the CNFs formation.

In a standard growth run, the reactor chamber was initially pumped down to 0.2 Pa. Afterwards, the CE foils were loaded and exposed to a Ar-H$_2$ continuous flow, maintained at the work pressure. The substrate foils and reaction chamber were then heated to 400 ºC by four W

filaments (Ø 250 μm). These filaments were always carburized for 30 min prior to the sample loading. Next, the foils were taken to the deposition temperature by the substrate heater (25 °C·min^{-1} of heating rate). Filaments and substrate temperatures were measured by a two-colour pyrometer (Raytec Marathon MR) and a K-type thermocouple touching the backside of the substrate, respectively. The Ar flow was used to dilute the CH_4/H_2 ratio and to set up the total gas flow. After the growth step, the CH_4 flow was cut off and the samples were cooled down to room temperature.

2.3. Characterization techniques

Scanning electron microscopy (SEM, Hitachi S4100) analyses were carried out to help deciding on suitable CE treatments for HF-CVD growth. The CE foils selected by SEM were then further observed by atomic force microscopy (AFM, Digital Instruments Multimode IIIa) to assess topographical features.

Deposited carbon nanostructures morphology, structure and composition were characterized by high-resolution scanning electron microscopy (HR-SEM, Hitachi SU70) assisted by energy dispersive spectroscopy (EDS, Bruker Quantax 400). High-resolution transmission electron microscopy (HR-TEM, JEOL 2200FS) and μ-Raman spectroscopy at 325 nm (Jobin Yvon HR800) and 514.5 nm (Jobin Yvon T64000) were also used. The Raman spectra were collected at room temperature in the frequency range of 50-3500 cm^{-1}. All SEM and TEM images were analysed using the freeware Image J program suite.

3. Results and discussion

3.1. Surface preparation

The carbon nucleation sites on Ni foils are supposedly located on surface defects such as protrusions or atomic step-edges [25,26] and intersections of bulk defects with the surface (e.g. grain boundaries [27], vacancies and dislocations [28]). Commonly, these cover only a small fraction of the total surface area. Wet-etching treatments were therefore performed before the growth step as a surface preparation method to maximise the density of active sites for CNFs nucleation. Fig. 1 shows a set of SEM micrographs of the Ni foils surface for several combinations of etchants and etching times.

This chart is arranged by increasing etching force (from bottom to top and from left to right) with the changes in surface roughness and/or density of topographic features easily observed from the sequence of images. The stronger etching conditions lead to micro-scale modifications (delimited by an orange line in Fig. 1) whereas the weaker ones to a kind of nano-scale surface patterning (delimited by a blue line in Fig. 1). Medium-strength CE results in intermediate submicro-scale etched regions (delimited by a yellow line in Fig. 1). Considering this noticeable distribution of the surface

characteristics, three representative Ni foils were selected for a more comprehensive investigation (designated by C1, C2 and C3 in Fig. 1). SEM micrographs and AFM scans of the selected samples are shown in Figs. 2 and 3, respectively.
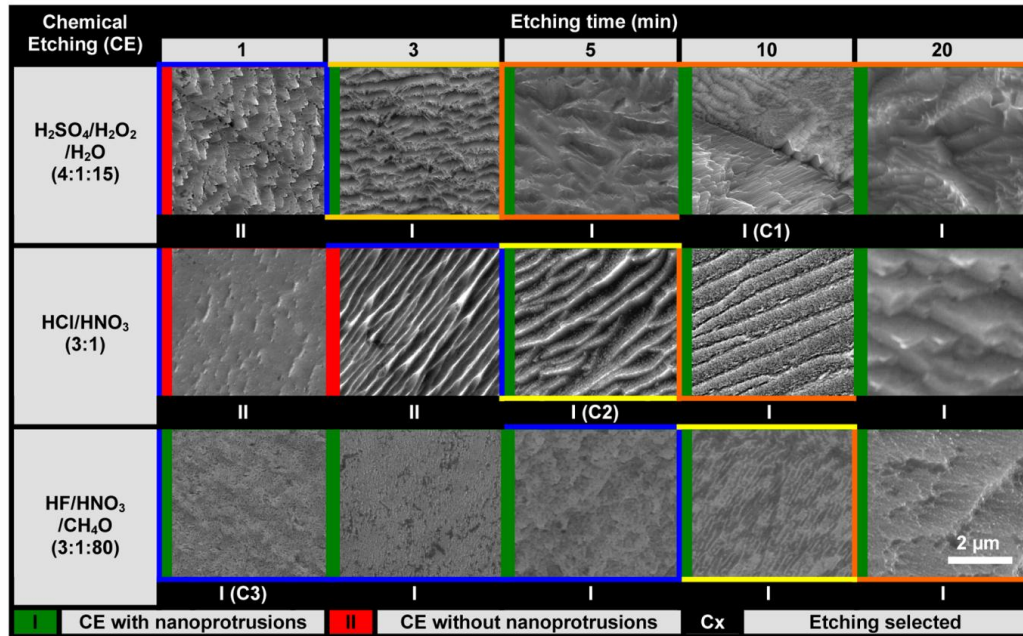
Fig. 1 - SEM map of the Ni foil surfaces obtained from the various wet-chemical etching procedures used. The correlation between the formation of protrusions on Ni foils and the etching force employed is visible.

The microscopy data reveals that nano-sized protrusions with similar dimensions (on the same order of magnitude) and with a Gaussian-like distribution are consistently observed for the selected samples (more details in Table 1).

Table 1 - Surface features of the three selected wet-chemical etched Ni foils.

Chemical Etching (CE)	R_q (nm)	Grain Size (μm)	Protrusions shape	Protrusions size (nm)	Protrusions density (P.μm^{-2})
C1: $H_2SO_4/H_2O_2/H_2O$ (4:1:15), 10 min	323±13		Rounded with nano-steps	29 ± 5	271±29
C2: HCl/HNO_3 (3:1), 5min	271±88	77±15	Irregular	42 ± 8	202±58
C3: $HF/HNO_3/CH_4O$ (3:1:80), 1 min	24±1		Rounded/Irregular	24 ± 7	314±35

However, the morphology and spatial arrangement of the nanoprotrusions differs from C1 to C3. The comparison of Figs. 2a and 2c shows a clear discrepancy between the C1 and C2 surfaces, with the former containing rounded bulges and periodical surface step-edges (height ~118±28 nm; length ~143±34 nm) while the latter mostly includes irregularly shaped protrusions and micro-scaled steps. On the other hand, the C3 sample treatment (Fig. 2e) produced surfaces without steps and

fairly well-uniform protrusions (better shaped than C2 but less regular than C1). Here, it is important to stress that the characteristics just described are directly derived from the CE treatments and should not be considerably influenced by the subsequent steps involving a reducing H_2 flow. As it is widely known, the H_2 role is critical to convert the CE oxidized foil surface into a catalytically active metal towards CNFs growth. In the present work, the foil reduction was done during the heating and growth stages resorting to gas mixtures poor in H_2 (Ar/H_2 (v/v) = 3) to avoid excessive coarsening and deforming of the protrusions [29].
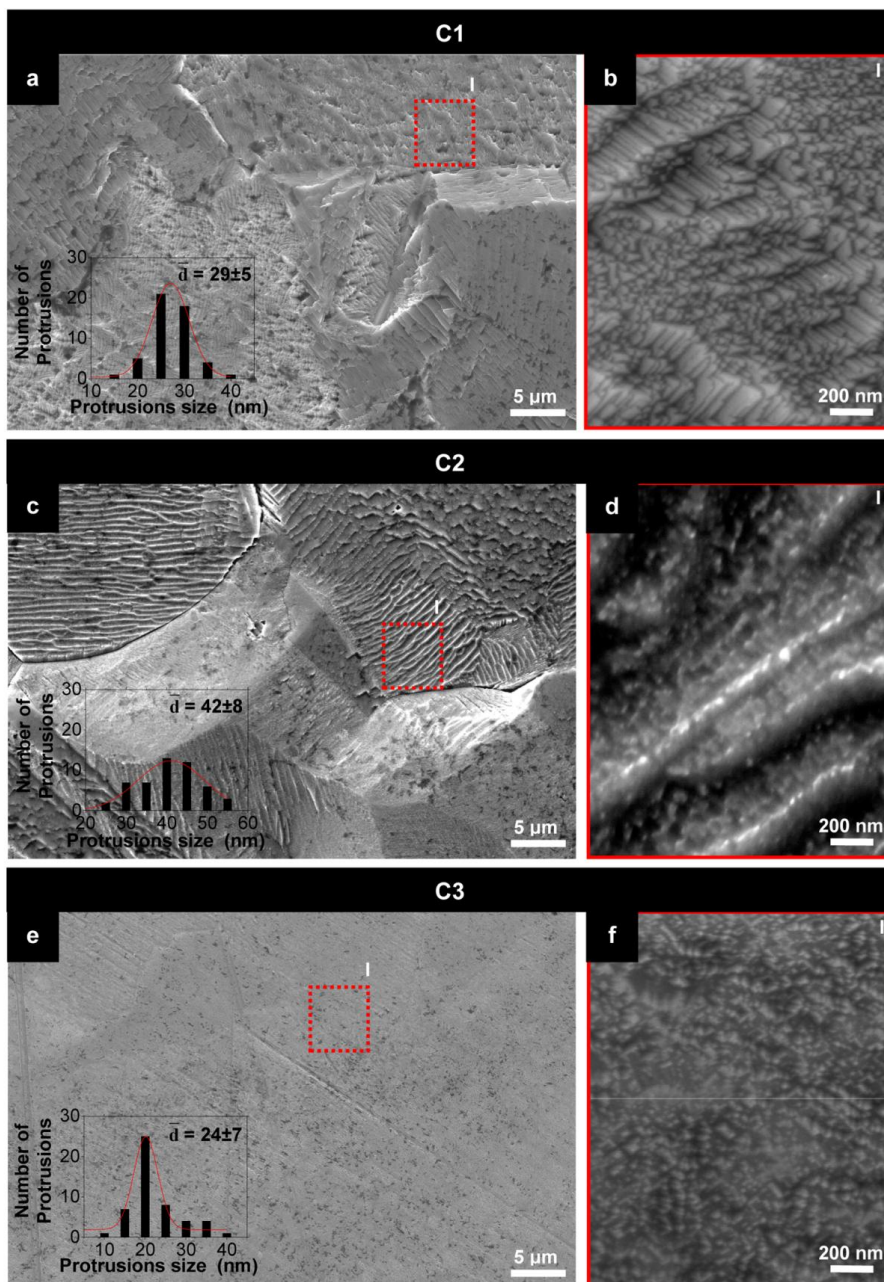
Fig. 2 - SEM images of the three selected etched foils shown in Fig.1. (a) C1; (c) C2; (e) C3. (a, c and e) Low magnification of the C1, C2 and C3 surfaces, respectively, with the plots of statistical size distributions for the nanoprotrusions included.

(b, d and f) Magnification of the regions marked in (a), (c) and (e), respectively, showing the different nanosized characteristics of the surfaces.

Besides the nanoprotrusions, the overall configuration of the surface and its surface roughness value Rq (root means square roughness, rms) differs for each CE. Despite C1 possessing the rougher surface, a much larger Rq standard deviation is observed for the C2 etching (cf. Table 1). This is indicative of higher surface irregularity due to the abundant presence of positive and negative micro-scaled curvatures such as those depicting grain boundaries (see Figs. 3a-d). Several grains and respective boundaries can be seen in Fig. 2a and 2c. From these and the AFM characterisation, the foils grain size exposed by the CE treatment is 77±15 μm. Due to their high interfacial energy and relatively weak bonding, grain boundaries are also considered as active sites for the precipitation of new phases from the metal foil.
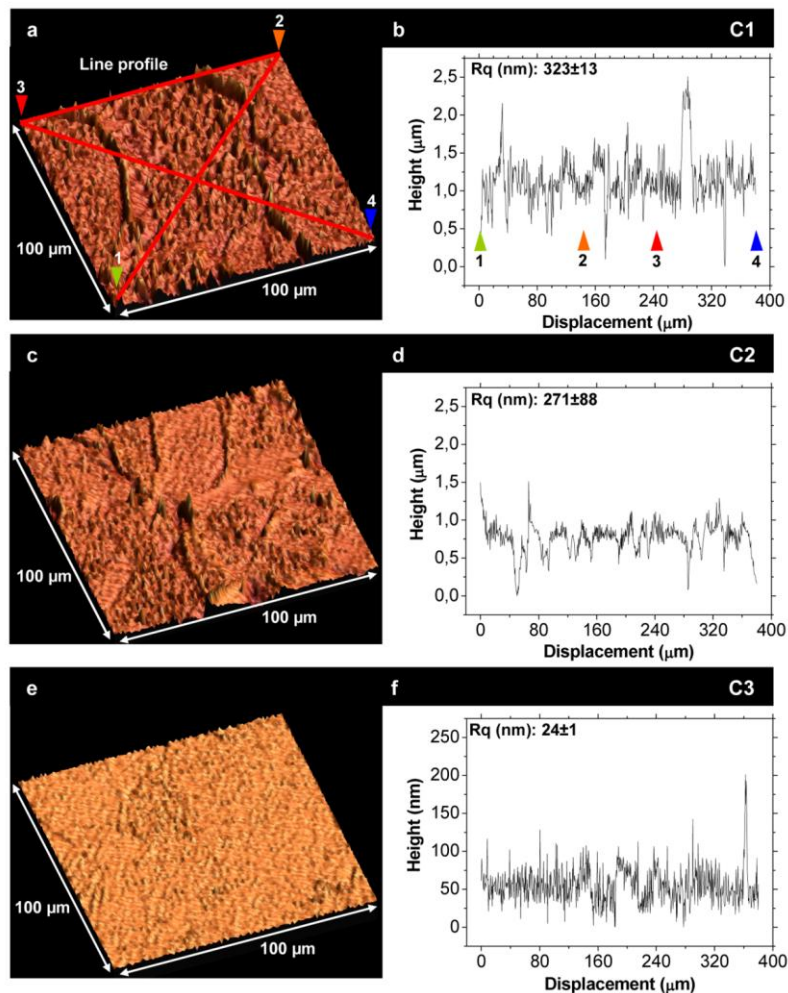
Fig. 3 - (a, c, and e) 3D-images of the surface topography taken by AFM for the three selected foils. (b, d, and f) Line profiles of (a), (c) and (e), respectively, illustrating the differences in protrusions height.

3.2. *CNFs growth*

The three etched metal foil samples (C1, C2 and C3) analysed in the previous section were further used to study the growth of CNFs by HF-CVD. In addition to the intrinsic characteristics of the nano-protrusions formed by chemical etching (CE), other factors may affect the yield and morphology of the carbon products obtained via HF-CVD. Of these, growth parameters can be decisive because of two main reasons: 1) both temperature and pressure influence the thermodynamics and kinetics of CH_4 adsorption and decomposition and, consequently, C_xH_y species dissolution, diffusion and precipitation rates at the Ni protrusions; 2) the reactive atmosphere plays an important role in the reshaping and physical/chemical stability of the protrusions.

3.2.1. *Optimising the CNFs growth yield*

The CNFs products from the set of HF-CVD runs performed, where only the total pressure and substrate temperature were varied, are shown in Fig. 4 as a SEM micrograph matrix. Those products highlighted with I (a, c and g) presented the highest yields, with the metal foil totally covered by a CNFs film. This was obtained for low pressures (5 kPa). In addition, uniform films were only grown for low temperatures (650 ºC), excepting for C2 etching, which is clearly seen in Figs. 4a,c.

High temperature promotes the endothermic decomposition of CH_4 on the metal surface, which is necessary for the heterogeneous catalysis. Furthermore, C_xH_y species dissolution, diffusion and precipitation mechanisms at the Ni protrusions are thermally activated. However, if the temperature is excessive, the dissolution rate of C species is faster than the diffusion and precipitation ones, leading to accumulation of carbon at the metal surface and loosening of their catalytic ability [30]. The chamber pressure has a similar contribution to CNFs growth: higher pressures lead to faster dissolving rates of carbon species, resulting in a less effective process [31].

According to this, in the case of metal foil substrates, where a large catalytic area is exposed to the reacting gases, it is important to use low temperatures and pressures to reduce the number of microscopic processes making the CNFs growth kinetics more deterministic. An evidence of this is the deposition rate decrease of amorphous carbon (a-C) films on metal surfaces at less severe CVD conditions [32]. Fig. 5, particularly the micrographs 5d-f, shows that the simultaneous growth of CNFs and an a-C layer can take place, forming a hybrid material. This means that the a-C film formed has enough porosity for the C_xH_y species diffusion through the layer. Similar results were reported by Chinthaginjala *et al.* [33].

Beyond the induced method described above, a non-induced method for active sites formation can occur in the course of CVD deposition. This method concerns the partial rupture of

the oxidized (Ni_xO_y) and/or carburized (metastable rombohedral-Ni_3C) metal surface along the defect sites, grain boundaries and small features where stress is maximized.
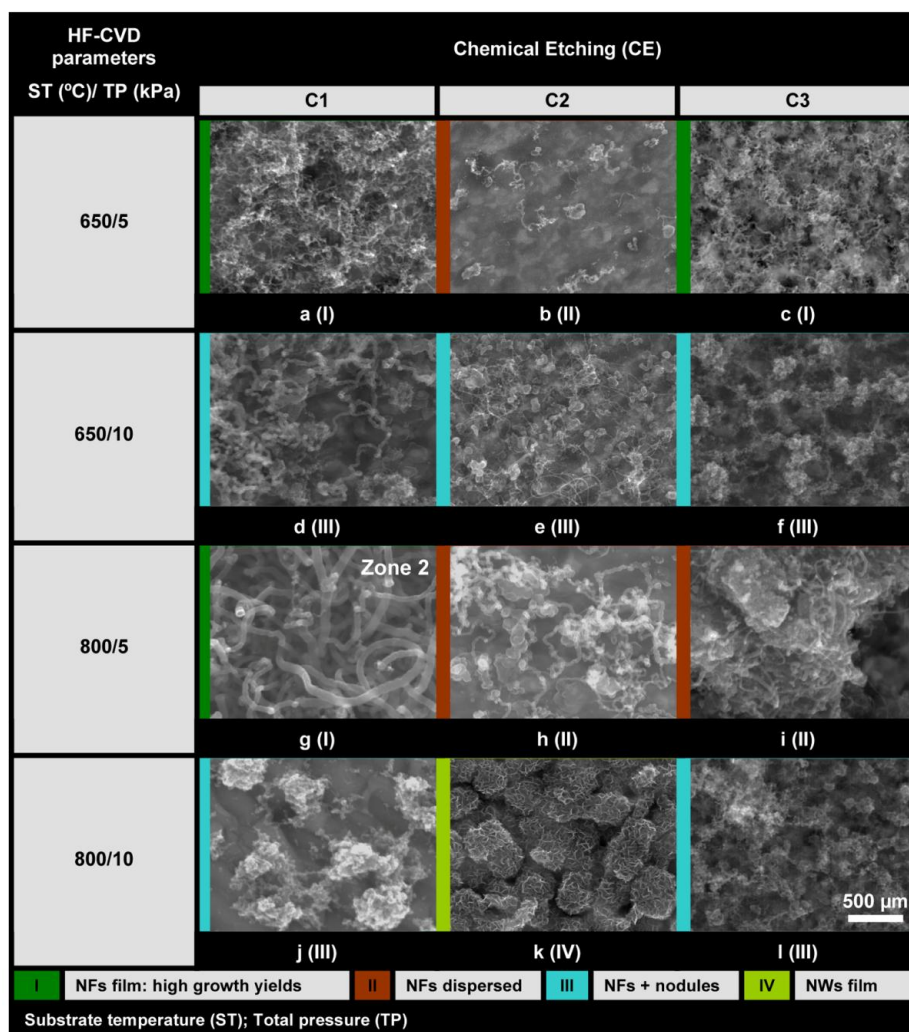
Fig. 4 - SEM map of the carbon deposits as a function of the CVD parameters and wet-chemical etching procedures (C1, C2 and C3) used. The correspondence of different products with growth and etching parameters is clear.

These phenomena were reported earlier. Baker *et al.* [16] showed that the anomalous higher catalytic activity of the FeO compared to the metallic Fe is due to the contribution of the oxidized species for the *in situ* formation of a sponge-like Fe catalyst. Additionally, Sacco *et al.* proposed an initial mechanism for the growth of filamentous carbon over α-Fe (a.k.a. ferrite) foils based on the surface rupture caused by the Fe_3C (a.k.a. cementite) precipitation [34]. Both phenomena highly increase the surface area that is related to the detachment of irregular metallic particles from the foil surface and further exposition of fresh metal underneath. Afterwards, the newly created sites can be active, due to dissociative adsorption, to grow filaments and/or sites for carbon deposition [11]. Surface rupture becomes more expressive at high temperatures (800 ºC) or

high pressures (10 kPa) inducing the growth of CNFs on the new active sites, just as it can be observed in Figs. 6a-d.
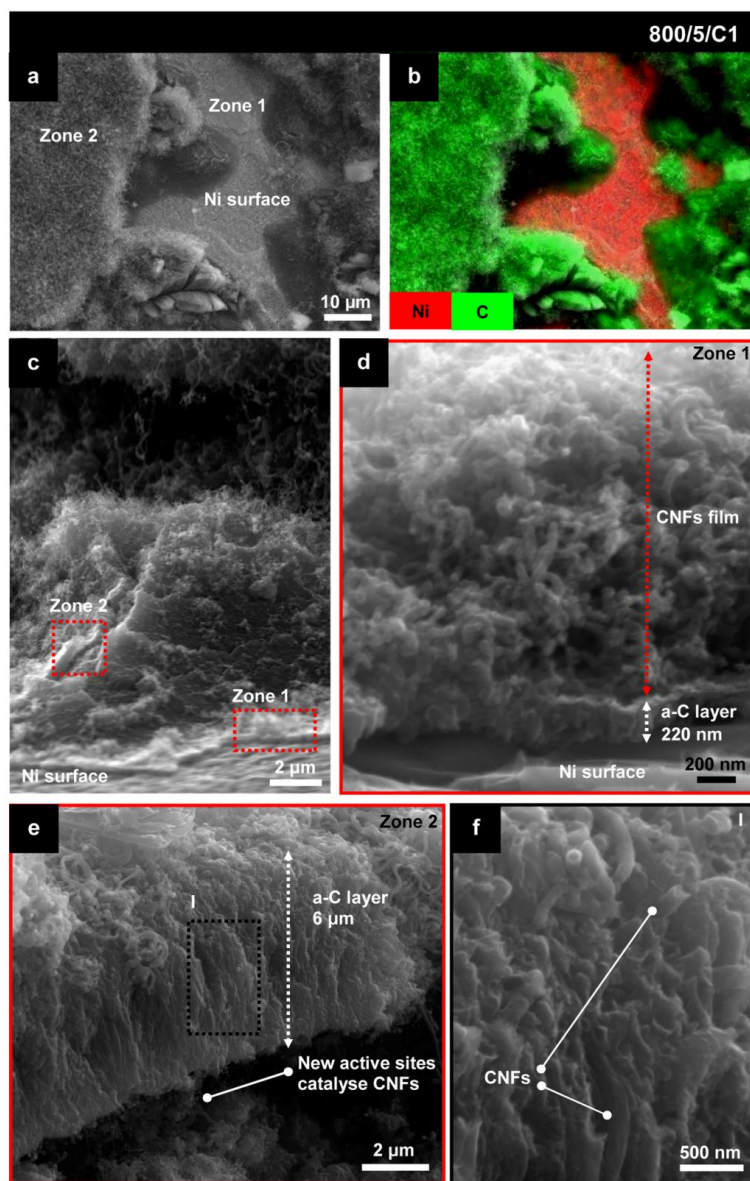
Fig. 5 - SEM images of carbon structures grown on C1 substrates (at 800°C and 5 kPa): (a) top-view showing the bare Ni foil surface and two different growth zones (zone 1: regular surface; zone 2: irregular surface due to foil rupture); (b) EDS map of (a) showing the non-uniform C distribution. C in green and Ni in red.; (c) tilted-view showing the same zones of (a) and (b); (d) cross-sectional view of zone 1 in (a) where the formation of a thin a-C layer and CNFs is obvious; (e) cross-sectional view image of zone 2 in (a) revealing the deposition of an outer a-C layer with CNFs imbedded; (f) magnification of the highlighted area testifying the presence of the CNFs/a-C hybrid material.

Particularly, at 800 °C/5 kPa (Figs. 5a,c and Fig. 6c), two distinctive growth zones on the C1 metal surface are visible. In zone 1 it is admitted that a uniform and dense CNFs film was grown due to the protrusions created by CE. Conversely, in zone 2, a combinatorial contribution is

postulated: CE protrusions and surface rupture on grain boundaries. The carbon deposits content vary in each zone, as given by EDS mapping (Fig. 5b).
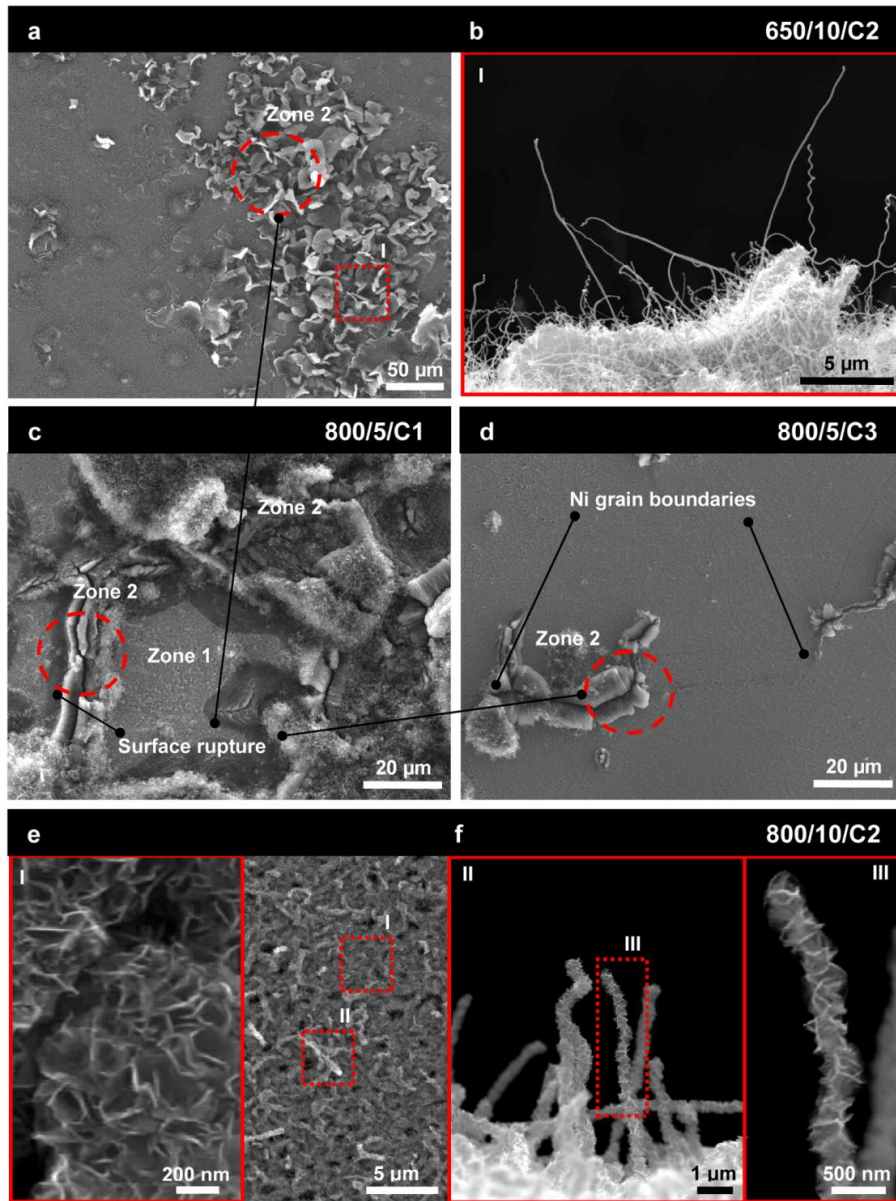
Fig. 6 - SEM images of relevant phenomena occurring on etched Ni foils: (a) C2 surface rupture due to the oxide film reduction at 650 ºC and 10 kPa; (b) growth of CNFs on the new active sites of (a); (c) C1 surface rupture at 800 º C and 5 kPa. This took place preferentially on grain boundaries where stress is maximized; (d) C3 surface rupture showing similar but less severe damage than for C1; (e) deposition of an uniform CNWs film alongside with CNFs on C2 substrates at 800 ºC and 10 kPa; (f) magnified images of the CNFs/CNWs hybrid material in (e) showing the graphene flakes on the side-walls of the CNFs.

The carbon content increases from pure metal foil to zone 2, where the surface rupture occurs. This observation puts in evidence that much thicker C-layers, although more amorphous,

were deposited in zone 2 than in zone 1, as illustrated by Figs. 5d,e, respectively. Additionally, the Ni signal can be seen in pure metal and zone 1, in an indistinguishable form, and no signal is detectable in zone 2. The absence of catalyst particles in CNFs tips or walls denotes a base-growth mechanism.

The surface morphology of the different CE pre-treated samples after deposition at 650 ºC/5 kPa is shown in Figs. 4a-c. The sparse growth of CNFs on the surface treated by C2 highlights the effect of the protrusions shape on the growth yield achieved, demonstrating that irregular faceted protrusions (Fig. 2d) do not catalyze uniform CNFs films growth.

In Fig. 4, the C1 etched samples lead to the best results. For example, at high temperature and low pressure, 800 ºC/5 kPa, only C1 substrates give high growth yield of CNFs (Fig. 4g). Well-shaped nanoprotrusions are produced by C1 and C3 etchings, but these are more regularly distributed and with nano-steps for the case of C1, as discussed above (Fig. 2). It is acknowledged that the step sites are preferential locations for the heterogeneous catalytic reactions including C atoms adsorption [35]. Moreover, the surface rupture contribution in C1 (Fig. 6c) is higher than in the C3 (Fig. 6d), at 800 ºC. Thus, new active sites for CNFs nucleation and growth result from the rupture. This effect is probably due to the thicker oxide film formation on the surface, as a result of the use of concentrated hydrogen peroxide (H_2O_2), and further H_2 reduction that promotes the rupture.

3.2.2. *Optimising the CNFs morphology*

In Fig. 7 it can be seen that either high temperature (800 ºC) or high pressure (10 kPa) can contribute for the CNFs diameter increase, with the first being a major influence.
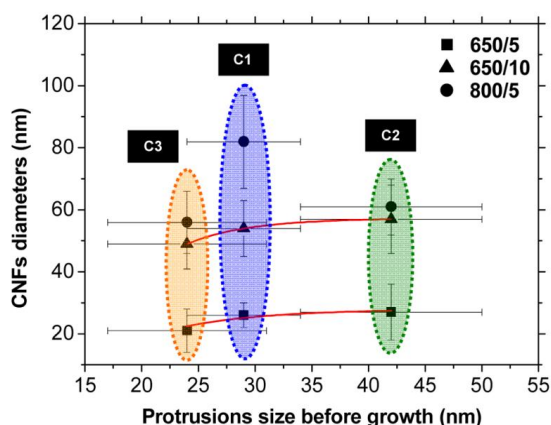
Fig. 7 - Plot illustrating the correlation between the initial protrusion size and the CNFs diameter.

Both parameters are intimately related with surface phenomena– protrusions morphology (size, shape and reshaping) and surface rupture – and growth kinetics that dictate the CNFs

diameter. Overall, the CNFs diameters have a noticeable correlation with the protrusions size for less austere CVD conditions (650 °C/5 kPa), i.e. controlled growth. Similar results had been reported already [36-38]. For these growth parameters, the ratio between the initial protrusions size (s_p) and fibre diameter (d_f) approaches unit values (1.12 to 1.56, according to Fig. 7 data).

The correlation between the protrusion size and the CNFs diameter distributions in C1 and C2 substrates is well supported by the comparison between the catalyst histograms of Figs. 2a,c, that are commensurate with the fibres histograms seen in Figs. 8a,b, respectively. In the case of the C3 substrates, the broadening of the fibres diameters distribution showed in Fig. 8c demonstrates that the C3 protrusions suffer a slight reshaping before the CNFs nucleation.
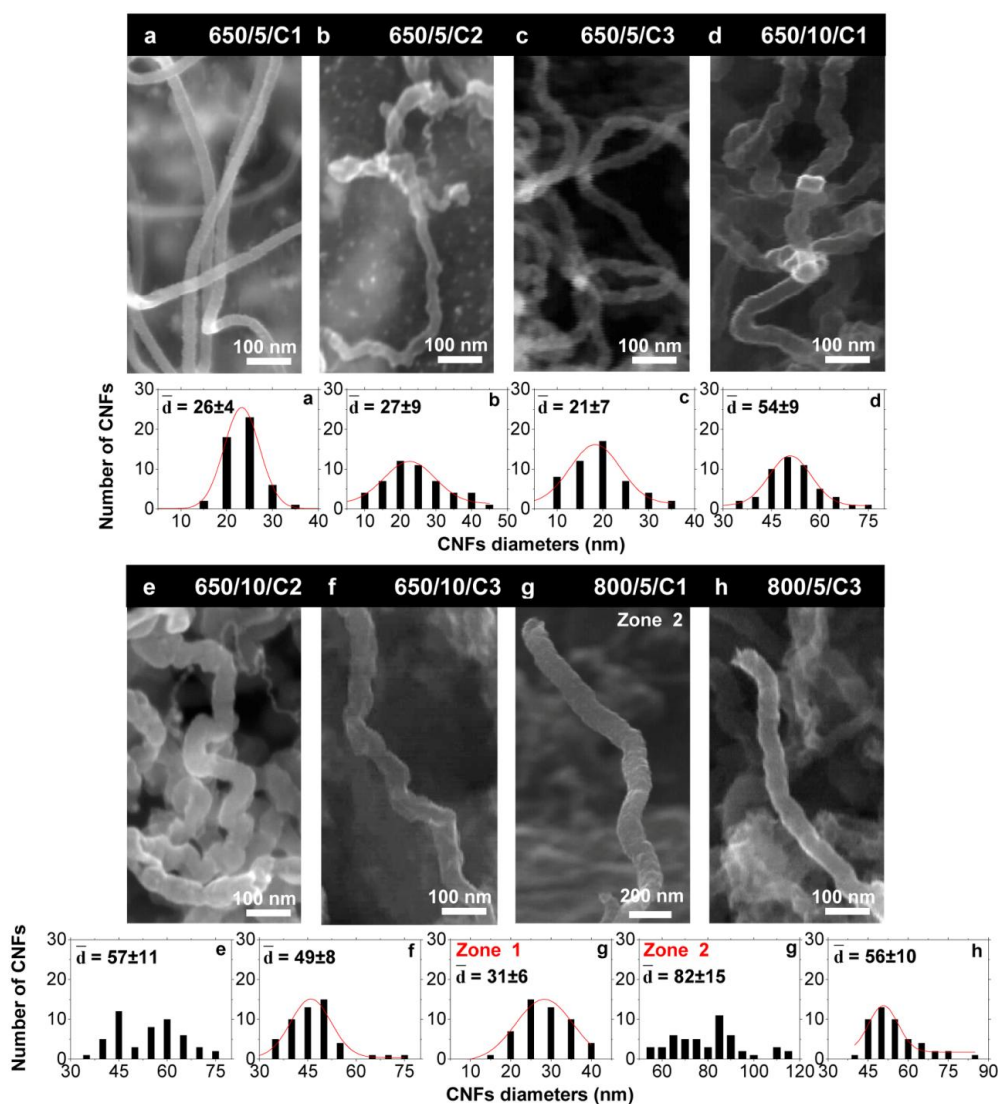
Fig. 8 - SEM images illustrating representative CNFs morphologies for several growth runs (temperature/pressure/foil). Below each image is the corresponding diameter size distribution. (a) 650/5/C1; (b) 650/5/C2; (c) 650/5/C3; (d) 650/10/C1; (e) 650/10/C2; (f) 650/10/C3; (g) 800/5/C1; (h) 800/5/C3.

The results above demonstrate the preservation of the CE features during the CVD growth for the less severe conditions. However, for high temperature (800 ºC), the s_p/d_f ratio achieved is decreased to 0.35. It was suggested that, in the case of Ni particles, high temperatures (T ≥ 700 ºC) induce an increase of the filament diameters [36,37]. This is attributed to sintering processes of highly-reactive nanometer size Ni particles which, when close to their melting temperatures, drastically increase their surface diffusion (e.g. particles of 5 nm are predicted to melt in the range 900-1100 ºC, accordingly to the Gibbs-Thomson effect) [38-40]. Additionally, during the growth step, the catalyst melting temperature diminishes due to the eutectic formation, but it is hard to know by how much because data is not available on *in-situ* measurements of the C concentration in Ni particles. Despite this, extended sintering processes are unlikely to occur in metal foils substrates because, instead of "free particles", nano-sized protrusions (24-42 nm) are formed showing high bonding forces with the substrate. This strong protrusion-substrate interaction increases the energy barrier for long-distance surface diffusion. Nevertheless, the temperature increase may enhance the short-distance diffusion of Ni from the protrusion top to the bottom, resulting in an increase of the curvature radius, i.e. flattening. This mechanism decreases the protrusion surface area where the CNFs nucleation and growth take place. Depending on the CE and the CVD conditions the flattening can be total (no CNFs growth) or partial (less sharp protrusions: CNFs diameters increase).

The diameters increase is also possibly related to the surface rupture phenomenon, which produces irregular active sites with a wide range of sizes. This effect originates CNFs with diameters having a wide size distribution (Fig. 8g – histogram of zone 2). Thinner CNFs with narrower diameters distribution were grown in uniform zone 1 (Fig. 8g – histogram of zone 1). Additionally, at 800 ºC/ 5 kPa, the C3 etched sample exhibits a weaker rupture tendency than the C1 (Fig. 8g – histogram of zone 2). Consequently, CNFs show a lower diameter average size and a narrower distribution for the C3 etching (Fig. 8h).

Also, when comparing the CNFs growth on C3 protrusions at 650 ºC (Fig. 8c) and 800 ºC (Fig. 8h), in the first case a uniform CNFs film comes out, but at high temperature, strong reshaping (before CNFs nucleation) or total protrusions collapse, resulted on the CNFs growth only in the grain boundary where the surface rupture takes place explaining the higher average CNF diameter at 800 ºC. Similar results (not shown) were observed for the C2 protrusions. Comparing the size of the protrusions obtained by each CE pre-treatment, smaller protrusions catalyse thinner CNFs, as depicted by the red line fitting in Fig. 8.

At high pressure (10 kPa), the less controllable growth and the surface rupture give rise to a broader diameter size distribution and a shift to higher values (Figs. 8d,e,f), comparing to lower pressure value runs (5 kPa). Moreover, the density of nano-sized protrusions has an important influence in the morphology of CNFs concerning the orientation. It was found that aligned filaments forests grow in the absence of plasma-assistance only due to the high particles densities (~ 6.2×10^3 P.µm^{-2}) [41]. Here, it can be observed a random growth mode in all samples (Fig. 4). The low density of nucleation sites (202-314 P.µm^{-2}, in Table I) is responsible for the lack of CNFs

packing since they will not be affected by the Van der Waals forces that promote aligned growth [8].

3.2.3. *Graphitic structure of CNFs*

In Fig. 9 is depicted the TEM images of the samples with the highest growth yields. Hollow-herringbone fibres were preferentially grown for all CVD parameters and CE procedures. The angle between the fibre axis and the graphene layers is about ~31º, as it is showed in the HRTEM image (Fig. 9b - II). Additionally, the lattice spacing between the graphene planes, is about ~3.5 Å, higher than for the 3D graphite (~3.4 Å). This increase in the interlayer distance is due to the uncorrelated 2D graphene layers stacking that give rise a turbostratic structure.
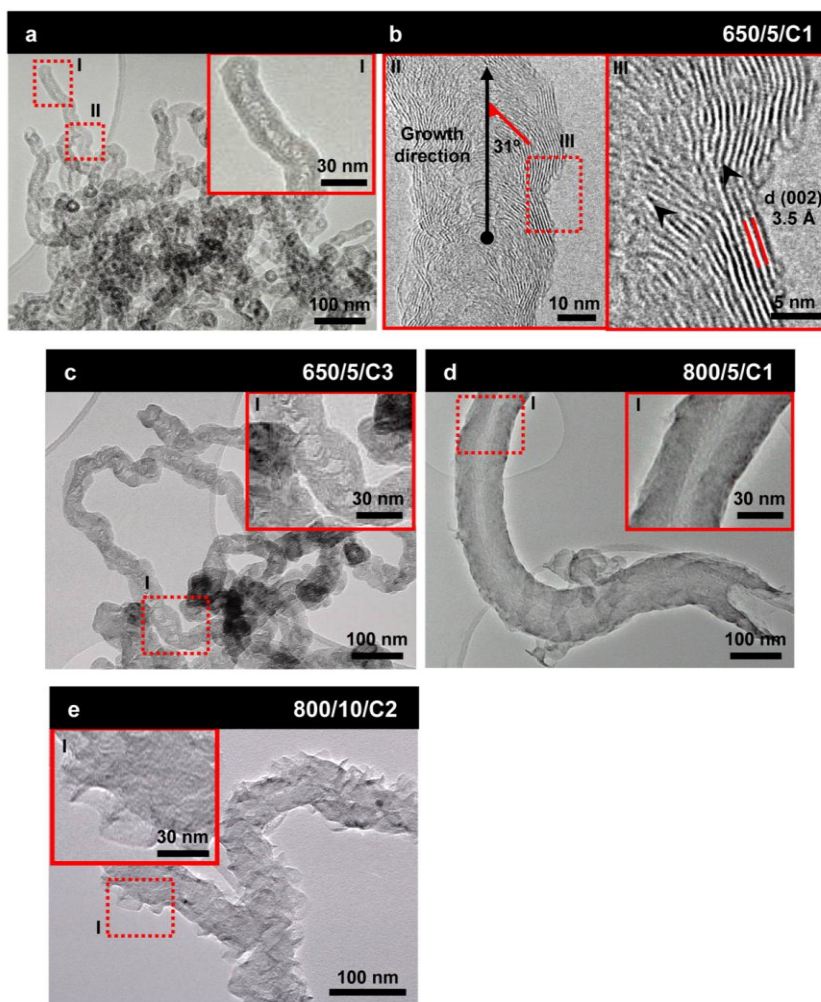
Fig. 9 - TEM images of selected CNF samples. The first four images correspond to the samples showing the best CNFs growth yields and the latter to the CNFs/CNWs hybrid material. The small arrows in the HRTEM image (b.III) symbolize the graphene sheets orientation. (a,b) 650/5/C1; (c) 650/5/C3; (d) 800/5/C1); (e) 800/10/C2.

Here, the disordering and defect incorporation in the lattice are commonly observed for the given CVD conditions. Baird *et al.* found that hydrocarbons decomposition rates over Ni foils dictate the nature of the deposited carbon. Higher graphitised filaments were synthesized from slower reactions such as obtained from the pyrolysis of saturated gases (e.g. methane and propane) [42]. Additionally, recent *in-situ* studies carry out by Hofmann *et al.* [43] point out that the cause for the C lattice disordering deals with the higher incorporation rate of a new C atom into the existing graphene sheet on Ni surface compared to the defect repair rate to anneal out defects while they are still near the growth front.

Accordingly to this, here, the best graphitised CNFs grown on Ni foils were obtained for lower temperature (650 ºC) and pressure (5 kPa), where the C incorporation rate is more controllable (Figs. 9a,b). Audier *et al.* [18] report similar results showing the formation of hollow fibres with diameters less than 10 nm by catalytic decomposition of CH_4 over Ni foils at 600 and 650ºC. On the other hand, at higher temperatures, 700 and 800 ºC, the reaction rates become too high for the filaments growth, instead, only carbon shells (i.e. metal particles surrounded by layers of carbon) were produced. Yet, the shells showed higher graphitization level than the structures obtained at lower temperatures. Therefore, it can be stress out that apart from the growth kinetics the high temperature makes easily the annealing of defects and the C network organization. Hence, the pressure effect in the CNFs graphitisation mechanism is more baneful than the temperature, showing more irregular surfaces (Fig. 8).

Additionally, protrusions shape and size have an important role in the structure of the catalyzed products. The graphene layers are precipitated parallel to the surface of the faceted catalyst protrusion, and hence the angle between the stacked layers and the filament axis is determined by the shape and reshaping (or dynamics) of the catalyst during the growth stage [8,26,43].

Fig. 9 shows that C1 protrusions nucleate the best graphitised CNFs films for 650 ºC/5 kPa and 800 ºC/5 KPa growth conditions. The reasons for this are appointed to be the best well-shaped form with nano-steps and the best resistance to the flatting mechanism.

Micro-Raman spectroscopy was used to further confirm the CNFs structure. Fig. 10 shows the Raman data alongside with fitting curves. All spectra were baseline corrected by linear background removal and then normalized to the maximum intensity of each spectrum, all peaks having been fitted with a Lorentzian line-shape.

Generally, graphite-based materials exhibit typical first and second order spectra. In Fig. 10, using a laser excitation energy (E_L) of 2.41 eV (514.5 nm), at low wavenumbers range it can be seen a strong peak around ~1580 cm^{-1} (G-band: E_{2g} stretching mode), an additionally band at ~1350 cm^{-1} (D-band: disorder-induced phonon mode arising from the effect of finite particle size or lattice distortion) and a weak band around ~1618 cm^{-1} (D'-band: graphite in-plane disorder). At high wavenumbers, common position bands at 2700 cm^{-1} (2D or G'-band: overtone of D mode), at 2945 cm^{-1} (D+G-band: combination mode) and at 3250 cm^{-1} (2D'-band: overtone of D' mode) can also be noticed [44-47]. Fig. 10 reveals that all samples show asymmetric G-bands. The shoulder at higher

frequency (D'-band) is typical of defective graphite-like structures like multi-walled CNTs (MWCNTs) and CNFs [47]. On the other hand, the G-band splitting G^+/G^- and the low frequency radial breathing modes (RBM) (results not shown) are not detected in our samples. These two features are typical of small diameter filaments as single-walled CNTs (SWCNTs), double-walled CNTs (DWCNTs) and some MWCNTs synthesized by arc techniques [44], but not of CNFs.

Additionally, Raman analysis at 3.81 eV (325 nm) was accomplished in order to evaluate the presence of a-C films on the samples. Ferrari and al. proved that Raman active sp^3 vibrations on a-C films are undetectable with visible excitation, UV laser lines being required to raise its Raman signature in the form of a band at ~1060 cm^{-1} (T-band). In fact, within the visible excitation range, resonant coupling with sp^2 π-states very much increases the Raman yield, masking weaker contributions from other carbon structures [48]. Thus, the T-band evidences the presence of sp^3 coordinated structures, most likely from co-grown a-C.

An estimation of the filaments structural crystallinity/graphitisation was obtained by the following parameters: full width at half maximum of G'-band ($FWHM_{G'}$) and I_D/I_G integrated intensity ratios. The I_D/I_G ratio has been used to correlate the structural order of graphitic materials to the graphite in-plane crystallite size (L_a). An increased I_D/I_G value is generally attributed to the presence of structural defects and disordered carbons like a-C films [44,46]. Since it is known that the D-band is dispersive ($d\omega_D/dE_L$ ~53 $cm^{-1}.eV^{-1}$) and changes its intensity with E_L, so is the I_D/I_G ratio, being smaller for higher E_L values. Further studies were accomplished by Cançado *et al.* [49] to achieve a general expression for L_a in the visible range (Eq. (1))

$$L_a \text{ (nm)} = (2.4 \times 10^{-10})\lambda_l^4 \left(\frac{I_D}{I_G}\right)^{-1} \qquad (1)$$

where λ_l (nm) is the laser line wavelength. All L_a calculations were accomplished using the equation above.

Fig. 10 shows 650 ºC/5 kPa/C1 and 650 ºC/5 kPa/C2 samples having analogous structure orders with similar sp^2 domains sizes, L_a ~23 nm and 20 nm, respectively. Thought, it can be asserted that C1 protrusions catalyse more crystalline CNFs for the same growth conditions. At 800 ºC/5 kPa/C1, a thicker a-C film is deposited than in 650 ºC/5 kPa/C1 and 650 ºC/5 kPa/C2 samples, as can be attested by the higher intensity of the T-band in the UV spectra. As a result, the signal of the CNFs was concealed by the a-C layer, giving a lower L_a ~11 nm. An evidence of this is that the D-band intensity becomes higher than the G-band. In addition, the D' and 2D' bands, characteristic of graphitic-like compounds, are no longer clear in the spectra. Nonetheless, since a CNFs film previously developed over the metal foil, the crystallinity of the CNFs at 800 ºC can not be precisely assessed by this method.

The second-order Raman was used here to shore up the results of the first-order. The broadening of the principal double resonance mode, G', typically denotes higher lattice disorder [50]. The $FWHM_{G'}$ values in Fig. 10 corroborate the first-order spectra results. While 650 ºC/5

kPa/C1 and 650 ºC/5 kPa/C2 samples show similar FWHM$_{G'}$ values, ~71 and ~70 respectively, the 800 ºC/5 kPa/C1 sample shows a much higher value of ~90.

The G'-band profile is also known to be a function of stacking order occurring along the *c* axis, since its Raman signature changes from a single-peak (turbostratic graphite) to two-peaks (crystalline graphite) [51]. For all samples in this work, the G'-bands were fitted only with one curve, which is indicative that the filaments have a turbostratic structure, which is also corroborated by SEM and TEM observations (Figs. 8 and 9).
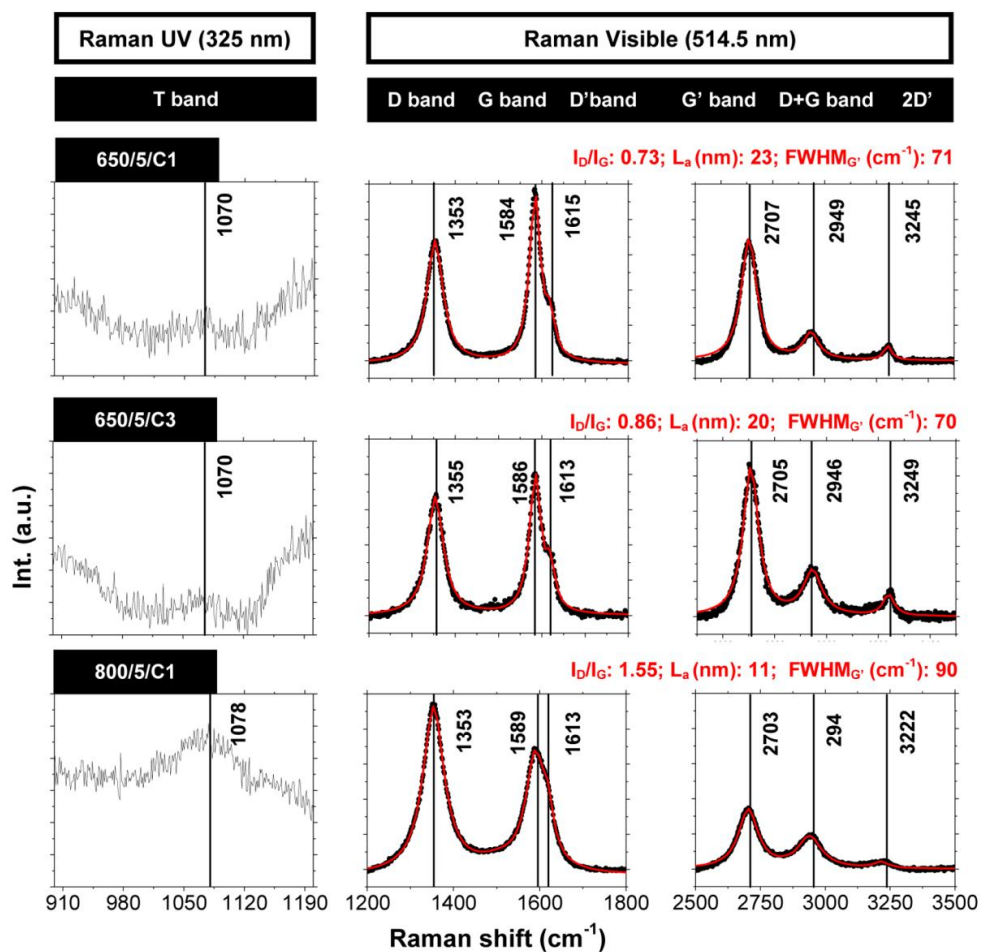
Fig. 10 - Micro-Raman UV (325 nm) and Visible (514.5 nm) spectra of the samples with the best CNFs growth yields. The red line corresponds to the fitting of the experimental data.

3.3. *Other carbon structures*

Fig. 4 denotes that other carbon forms, like nodular structures and carbon nanowalls (CNWs), were deposited on metal foils. The growth of these structures happens preferentially on submicro/micro-sized and/or irregular protrusions. These sites do not efficiently catalyze filaments.

Instead, carbon adsorption occurs on the metal surface leading to the protrusion encapsulation by carbon (onion formation) or promote the growth of other carbon forms [11,43,52] .

For high pressure, 10 kPa, all CE procedures, except the C2 at high temperatures, promote the growth of dispersed CNFs alongside with carbon nodular structures (highlighted with (III) in Fig. 4). This carbon agglomeration occurs preferentially in high carbon concentration conditions on the sites referred above.

At 800 ºC/10 kPa, the C2 etching produced a uniform film of petal-like graphitic nanoflakes, more commonly referred as CNWs, revealing a peculiar bulgy morphology due to the surface features mimicking (Figs. 4k and 6e).

CNWs have been grown with and without bias and in the presence or absence of a metal catalyst. It was found that the most important requirement for CNWs growth is the presence of surface defects on the sub-micron scale [53,54]. Here, becomes clear that C2 sub-micro etching, showing protrusions more irregular than C1 and C3, produce the surface features needed for the high growth yield of CNWs. Moreover, in Fig. 6f it can be seen CNWs on the side-walls of CNFs grown forming CNFs/CNWs hybrids. Fig. 9e shows the TEM image of the detailed structure of the hybrid. The respective inset of the Fig. 9e depicts the carbon nano-flakes morphology. A recent work shows similar results by growing CNWs on SWCNTs by HF-CVD, using CH_4 as precursor at 700 ºC [55].

3.4. *Suggested growth model*

Historically, the account of CVD-promoted growth of carbon filaments concerns the following steps [15,56]: (1) adsorption of the precursor gas on the catalyst surface; (2) dissociation of the precursor molecules; (3) carbon species dissolution and diffusion (in the bulk [17] or on the surface [14] of the catalyst particle); (4) carbon supersaturation and graphite-like structure precipitation from the top or bottom of the catalyst particle; (5) metal particle reshaping and successive carbon incorporation into the growing structure.

In view of the above results, a model that may explain the formation of the various carbon structures grown on chemically etched Ni foils is suggested. The mechanism outlined is strongly guided by the outcome of the experiments performed at 5 kPa. As shown in the diagram of Fig. 11, three main steps are proposed:

- Step 1, depicts the Ni foils after pre-treatment via CE procedures. Nanoprotrusions having regular (corresponding to protrusions optimal for CNF growth, P_{CNF}) and irregular (those responsible for the production of amorphous carbon layer, P_{a-C}) shapes were formed on the metal surface.

- Step 2, concerns two simultaneous thermodynamic processes occurring at both 650 ºC and 800 ºC, i.e. a-C deposition and nucleation/growth of CNFs. These processes involve the diffusion of C adatoms (C_{CH4}) along the polycrystalline Ni surface which takes place on the steps edges, through the subsurface and bulk [57]. In Fig. 11, below the surface drawings, evidence supporting the nucleation of CNFs on regular nanoprotrusions (P_{CNF}) is given (I and II). Concurrently, an irregular

thin a-C layer has started to deposit preferentially on sites with low carbon solubility such as irregular micro-sized protrusions (P_{a-C}), flat surfaces and grain boundaries.
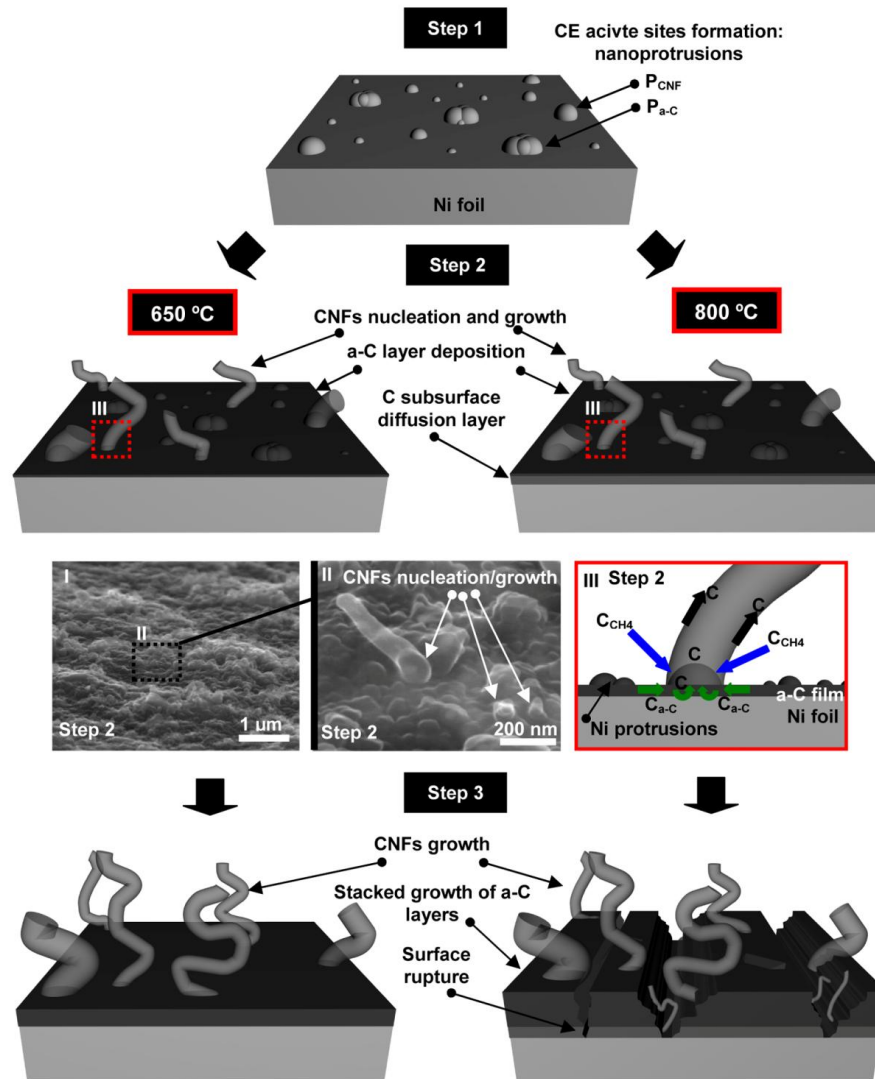
Fig. 11 - Schematic representation of the CNFs base-growth mechanism on Ni foils. Step 1, nanoprotrusions formation by CE procedures; Step 2, thin a-C film deposition, CNFs nucleation/growth and subsurface/bulk C diffusion; Step 3 a-C film and CNFs growth. At 800 ºC, surface rupture forms fresh active sites that will catalyse the growth of new fibres.

The a-C deposition is probably faster than the CNF nucleation because the low C solubility on the referred sites makes possible the direct deposition on the surface without the precipitation step. Thus, the P_{CNF} become partially imbedded in the thin a-C layer. In truth, this does not inhibit the CNFs nucleation because the a-C is microporous. Since there is no effective barrier to access the nanoprotrusion, the P_{CNF} is likely to rapidly become supersaturated due to the concerted interaction with the reactive gas, CH_4 (C_{CH4}), and the deposited a-C layer (C_{a-C}), as illustrated in diagram III. The carbon concentration gradient at the P_{CNF} is assumed as the driving force for the bulk and

surface diffusion [58]. Once the highly concentrated solute carbon is transported to the Ni_{fcc} side-planes of the faceted P_{CNF}, it starts to precipitate on a colder zone and form a graphene layer [59]. Logically, this will diminish the carbon concentration at that zone leading to a new gradient and subsequent formation of an additional graphene layer. The continued repetition of these steps eventually results in the formation of a CNF. Invariably, the all process follows the so-called base-growth since the catalytically active nanoprotrusions are firmly attached to the substrate foil. However, as the SEM image in Fig 11 – II shows the protrusions can still elongate in the same direction of the graphene layer-Ni interface growth due to Ni atoms diffusion. Finally, a word on the noticeable differences that are seen dependent on the temperature employed. At 800 ºC, significant subsurface/bulk carbon diffusion in the Ni foil is observed because of the increased rate of Ni-C bonds breakage and subsequent C diffusion into favourable locations on the Ni lattice (e.g. interstitials and vacancies). At 650 ºC, the energy input is smaller which leads to lower rates. Therefore, the C layer remains mostly superficial.

- Step 3, suggests how the formation of the a-C layer proceeds alongside with the CNFs growth ultimately creating a dense microporous film with imbedded fibres. Depending on the a-C layer thickness, the C_xH_y species continue to reach the metal surface (via CH_4) which promotes continued growth of the fibres together with the staked a-C layers. Additionally, the a-C layer is expected to grow also from the very first C deposit (outer layer) which was found that can act as catalyst [60]. Moreover, specifically at 800 ºC, both a-C layers deposited at high rate and severe surface rupture of the foil take place. This will expose new active sites from which the growth of CNFs was observed.

4. Conclusions

Wet-chemical etching procedures have been investigated to optimise the conversion of flat Ni foils into surfaces with catalytically active protrusions for nanostructured carbon growth by HF-CVD. It was found that the protrusions size and shape are key factors in the production of CNFs, particularly in what concerns yield and fibre morphology. Accordingly, ~30 nm round-shape protrusions can lead to the formation of films of hollow-herringbone CNFs following the base-growth model. In addition, under constant pressure (5 kPa) and temperature (650 ºC), the CNFs diameter distribution is clearly mirrored in the protrusions size distribution (which is manipulated via the pre-treatment etching steps). At these relatively mild conditions, the growth kinetics of nanostructured carbon can be controlled over a large area of the activated metal foil. Higher pressures and temperatures result in surface rupture and subsequent generation of non-optimal protrusions. These will be responsible for the formation of thick (> 6 μm) amorphous carbon layers as well as the excessive production of other carbonaceous products such as nodular structures, CNWs films and CNFs/CNWs hybrids.

Acknowledgements

References:

[1].   Jorio A, Dresselhaus G, Dresselhaus MS (Eds.). Carbon nanotubes: advanced topics in the synthesis, structure, properties and applications. Berlin: Springer-Verlag; 2008.

[2].   Ajayan PM, Tour JM. Materials science - Nanotube composites. Nature 2007;447:1066-8.

[3].   Al-Saleh MH, Sundararaj U. A review of vapor grown carbon nanofiber/polymer conductive composites. Carbon 2009;47(1):2-22.

[4].   Wei C, Srivastava D. Nanomechanics of carbon nanofibers: Structural and elastic properties. Appl Phys Lett 2004;85(12):2208-10.

[5].   Qian D, Dickey EC, Andrews R, Rantell T. Load transfer and deformation mechanisms in carbon nanotube-polystyrene composites. Appl Phys Lett 2000;76(20):2868-70.

[6].   Zhan GD, Kuntz JD, Wan J, Mukherjee AK. Single-wall carbon nanotubes as attractive toughening agents in alumina-based nanocomposites. Nat Mater 2002;2(1):38-42.

[7].   Kuzumaki T, Ujiie O, Ichinose H, Ito K. Mechanical characteristics and preparation of carbon nanotube fiber-reinforced Ti composite. Adv Eng Mater 2000;2(7):416-8.

[8].   Teo KBK, Singh C, Chhowalla M, Milne WI. Encyclopedia of Nanoscience and Nanotechnology 2003;X:1-22.

[9].   Dresselhaus MS, Dresselhaus G, Alvouris Ph (Eds.). Carbon nanotubes: synthesis, structure, properties and applications. New York: Springer-Verlag; 2001.

[10].   Dupuis AC. The catalyst in the CCVD of carbon nanotubes – a review. Progr Mater Sci 2005;50:929-61.

[11].   Wall RLV, Hall LJ. Carbon nanotube synthesis upon stainless steel meshes. Carbon 2003;41:659-72.

[12].   Robertson SD. Carbon formation from methane pyrolysis over some transition metal surfaces - I. nature and properties of the carbon formed. Carbon 1970;8:365-8.

[13].   Endo M, Koyama T, Hishiyama Y. Structural improvement of carbon-fibers prepared from benzene. Jap J Appl Phys 1976;15(11):2073-6.

[14].   Oberlin A, Endo M, Koyama T. Filamentous growth of carbon through benzene decomposition J. Crystal Growth 1976;32(3):335-49.

[15].   Baker RTK, Barber MA, Harris PS, Feates FS, Waite RJ. Nucleation and growth of carbon deposits from the nickel catalyzed decomposition of acetylene. J Catal 1972;26:51-62.

[16].   Baker RTK, Alonzo JR, Dumesic JA, Yates DJC. Effect of the surface state of iron on filamentous carbon formation. J Catal 1982;77: 74-84.

[17].   Baker RTK, Catalytic growth of carbon filaments. Carbon 1989;27(3): 315-23.

[18]. Audier M, Oberlin A, Oberlin M, Coulon M, Bonnetain L. Morphology and crystalline order in catalytic carbons. Carbon 1981;19:217-24.

[19]. Reddy NK, Meunier JL, Coulombe S. Growth of carbon nanotubes directly on a nickel surface by thermal CVD. Mater Lett 2006;60:3761-5.

[20]. Peng X, Koczkur K, Chen A. Synthesis of well-aligned bamboo-like carbon nanotube arrays from ethanol and acetone. J Phys D: Appl Phys 2008;41:095409.

[21]. Park D, Kim YH, Lee JK. Synthesis of carbon nanotubes on metallic substrates by sequential combination of PECVD and thermal CVD. Carbon 2003;41:1025-9.

[22]. Baddour CE, Fadlallah F, Nasuhoglu D, Mitra R, Vandsburger L, Meunier JL. A simple thermal CVD method for carbon nanotube synthesis on stainless steel 304 without the addition of an external catalyst. Carbon 2008;47:313-47.

[23]. Talapatra S, Kar S, Pal SK, Vajtai R, Ci L, Victor P, et al. Direct growth of aligned carbon nanotubes on bulk metals. Nature Nanotechn 2006;1:112-6.

[24]. Petzow G. Metallographic etching: techniques for metallography, ceramography, plastography. USA: ASM; 1999.

[25]. Grenga HE, Lawless KR. Active sites for heterogeneous catalysis. J Appl Phys 1972;43(4):1508-14.

[26]. Helveg S, Cartes CL, Sehested J, Hansen PL, Clausen BS, Nielsen JR, et al. Atomic-scale imaging of carbon nanofibre growth. Nature 2004;427:426-9.

[27]. Siegel D, Hamilton J. Computational study of carbon segregation and diffusion within a nickel grain boundary. Acta Materialia 2005;53:87-96.

[28]. Cratty LE, Granato AV. Dislocations as "active sites" in heterogeneous catalysis. J Chem Phys 1957;26(1):96-7.

[29]. Nessim GD, Hart AJ, Kim JS, Acquaviva D, Oh J, Morgan CD, et al. Tuning of vertically-aligned carbon nanotube diameter and areal density through catalyst pre-treatment. Nano Lett 2008;8(11):3587-93.

[30]. Li WZ, Wen JG, Ren ZF. Effect of temperature on growth and structure of carbon nanotubes by chemical vapour deposition. Appl Phys A 2002;74:397-402.

[31]. Li WZ, Wen JG, Tu Y, Ren ZF. Effect of gas pressure on growth and structure of carbon nanotubes by chemical vapour deposition. Appl Phys A 2001;73:259-64.

[32]. Li WN, Ding YS, Suib SL, DiCarlo JF, Galasso FS. Controlling the growth of CVD carbon from methane on transition metal substrates. Surf Coating Tech 2005;190:366-71.

[33]. Chinthaginjala JK, Thakur DB, Seshan K, Lefferts L. How carbon-nano-fibers attach to Ni foam. Carbon 2008;46:1638-47.

[34]. Sacco A, Thacker P, Chang TN, Chiang ATS. The initiation and growth of filamentous carbon from α-iron in H_2, CH_4, H_2O, CO_2 and CO gas mixtures. J Catal 1984;85: 224-36.

[35]. Nørskov JK, Bligaard T, Logadottir A, Bahn S, Hansen LB, Bollinger M, et al. Universality in Heterogeneous Catalysis. J Catal 2002;209: 275-8.

[36]. Paillet M, Jourdain V, Poncharal P, Sauvajol JL, Zahab A, Meyer JC, et al. Versatile synthesis of individual single-walled carbon nanotubes from nickel nanoparticles for the study of their physical properties. J Phys Chem B 2004;108:17112-8.

[37]. Kukovitsky EF, L'vov SG, Sainov NA, Shustov VA, Chernozatonskii LA. Correlation between metal catalyst particle and carbon nanotube growth. Chem Phys Lett 2002;355:497-503.

[38]. Moisala A, Nasibulin AG, Kauppinen EI. The role of metal nanoparticles in the catalytic production of single-walled carbon nanotubes – a review. J Phys: Condens Matter 2003;15:S3011-35.

[39]. Qi Y, Çagin T, Johnson WL, Goddard WA. Melting and crystallization in Ni nanoclusters: the mesoscale regime. J Chem Phys 2001;115(1):385-94.

[40]. Buffat P, Borel JP. Size effect on the melting temperature of gold particles. Phys Rev A 1976;13(6):2287-98.

[41]. Futaba DN, Hata K, Namai T, Yamada T, Mizuno K, Hayamizu Y, et al. 84% catalyst activity of water-assisted growth of single walled carbon nanotube forest characterization by a statistical and macroscopic approach. J Phys Chem B 2006;110:8035-8.

[42]. Baird T, Fryer JR, Grant B. Carbon formation on iron and nickel foils by hydrocarbon pyrolysis – reactions at 700 ºC. Carbon 1974;12:591-602.

[43]. Hofmann S, Sharma R, Ducati C, Du G, Mattevi C, Cepek C, et al. In situ observations of catalyst dynamics during surface-bound carbon nanotube nucleation. Nano Lett. 2007;7(3)602-8.

[44]. Dresselhaus MS, Dresselhaus G, Saito R, Jorio A. Raman spectroscopy of carbon nanotubes. Phys Reports 2005;409:47-99.

[45]. Zhang HB, Lin GD, Zhou ZH, Dong X, Chen T. Raman spectra of MWCNTs and MWCNTs-based H_2-adsorbing system. Carbon 2002;40:2429-36.

[46]. Antunes EF, Lobo AO, Corat EJ, Trava-Airoldi VJ, Martin AA, Veríssimo C. Comparative study of first- and second-order Raman spectra of MWCNT at visible and infrared laser excitation. Carbon 2006;44:2202-11.

[47]. Lee S, Kim TR, Ogale AA, Kim MS. Surface and structure modification of carbon nanofibers. Synthetic Met 2007;157:644-50.

[48]. Ferrari AC, Robertson J. Resonant Raman spectroscopy of disordered, amorphous, and diamondlike carbon. Phys Rev B 2001;64:075414.

[49]. Cançado LG, Takai K, Enoki T, Endo M, Kim YA, Mizusaki H, et al. General equation for the determination of the crystallite size L_a of nanographite by Raman spectroscopy. Appl Phys Lett 2006;88:163106.

[50]. Lee YJ. The second order Raman spectroscopy in carbon crystallinity. J Nucl Mater 2004;325:174-9.

[51]. Cançado LG, Takai K, Enoki T, Endo M, Kim YA, Mizusaki H, et al. Measuring the degree of stacking order in graphite by Raman spectroscopy. Carbon 2008;46:272-5.

[52]. Lin M, Tan JPY, Boothroyd C, Loh KP, Tok ES, Foo YL. Direct observation of single-walled carbon nanotube growth at the atomistic scale. Nano Lett. 2006;6(3):449-52.

[53]. Dikonimos Th, Giorgi L, Giorgi R, Lisi N, Salernitano E, Rossi R. DC plasma enhanced growth of oriented carbon nanowall films by HFCVD Diam Relat Mater 2007;16:1240-3.

[54]. Chen CC, Chen CF, Lee IH, Lin CL. Fabrication of high surface area graphitic nanoflakes on carbon nanotubes templates. Diam Relat Mater 2005;14:1897-1900.

[55]. Saito T, Chiba H, Ito T, Ogino T. Growth of carbon hybrid materials by grafting on pre-grown carbon nanotube surfaces. Carbon, doi:10.1016/j.carbon.2009.12.005

[56]. Wagner RS, Ellis WC. Vapor-liquid-solid mechanism of single crystal growth. Appl Phys Lett 1964;4(5):89-90.

[57]. Yazyev OV, Pasquarello A. Effect of metal elements in catalytic growth of carbon nanotubes. Phys Rev Lett 2008;100(15):156102.

[58]. Holstein WL. The role of ordinary and soret diffusion in the metal-catalysed formation of filamentous carbon. J Catal 1995;152:42-51.

[59]. Rodriguez NM, Chambers A, Baker RTK. Catalytic engineering of carbon nanostructures. Langmuir 1995;11:3862-6.

[60]. Phillips J, Shiina T, Nemer M, Lester K. Graphitic structures by design. Langmuir 2006;22:9694-9703.

II.3. Self-assembled cones of aligned carbon nanofibers grown on wet-etched Cu foils

D. Mata[a], M. Amaral[a,b], A.J.S. Fernandes[b], F.J. Oliveira[a], P.M.F.J. Costa[a], R.F. Silva[a]

[a]CICECO, Glass and Ceramics Eng. Dept., Univ. of Aveiro, Portugal
[b]I3N, Physics Dept., Univ. of Aveiro, Portugal

Abstract

Hot-filament chemical vapour deposition (HF-CVD) was used to grow aligned carbon nanofibers (CNFs) directly on Cu foils. Fast wet-chemical etching procedures based on hydrogen peroxide (H_2O_2) were found to have a key role on the formation of selective active substrates for the growth process. Here, a comprehensive mechanism is presented. Additionally, it is shown that nano-sized protrusions ~8 nm with round shape and high density ~1.7×10^3 μm^{-2} were decisive for the growth of aligned hollow-herringbone CNFs following the base-growth model. CNFs with heights of ~1 μm and diameters around ~8 nm show narrow diameter size distribution with remarkable correlation to the protrusion size distribution. The fibres were organised in cone-shape configurations with a cone density of ~22 μm^{-2} and a cone angle of 90 º. An activation energy for the CNF growth of E_{act} ~0.90±0.16 eV was extracted from the Arrhenius plot showing that the process kinetics is governed by C diffusion in bulk Cu.

1. Introduction

Carbon nanotubes (CNTs) and nanofibers (CNFs) show exciting physical-chemical properties and are expected to act as the ultimate nanofilament reinforcements in advanced composites [1]. Considering that their growth mechanisms are ruled by the behaviour of transition metal catalysts, it is evident that understanding and engineering these constitutes a key issue towards mass production [2].

For decades catalytically-active metal foils have been explored to grow carbon filaments and films by chemical vapour deposition (CVD) [3-5]. Still, the growth kinetics of tailored morphologies such as vertically-aligned carbon nanofilaments (a.k.a. "forests") is not yet well understood. Important steps towards high growth yields of forests on stainless-steel foils were recently reported [6-9]. The successful production of filaments directly on these substrates may be explained by the presence of highly dense and well dispersed protrusions of monoelemental active metals and solid solutions in a non-catalytic matrix.

Copper foils may be used for direct growth of vertically-aligned CNFs [10]. However, the catalytic activity of Cu is limited or non-existent due to the poor dissociative chemisorption of hydrocarbons [11,12]. The assumption of Cu inertness has been based on its fully filled 3d-orbitals which prevent the establishment of covalent bonds with hydrocarbon molecules [13]. Since the binding energy of carbon species to Cu is small, these can not interact long enough to form graphitic-like structures [14]. Additionally, Cu has low C solubility, making difficult further C diffusion required for precipitation in graphitic form [15,16].

Nonetheless, it was proposed that Cu catalysts can grow better structured carbon fibres, such as CNTs, with narrow chirality distributions [17]. Moreover, it appears that the low catalytic activity of Cu may be an advantage to reach an improved selective growth of forests directly on metal foils [18]. Unfortunately, detailed considerations about the growth mechanism of forests on Cu foils have been neglected.

Commonly, the approaches to grow forests directly on Cu metal foils employ time-consuming catalyst preparation steps such as the deposition of buffer layers (e.g. TiN and ITO) and the use of extra catalyst sources (e.g. ferrocene) [19]. For cost-effective mass production of carbon nanofilaments, it would be most advantageous if these elaborate pre-growth steps could be avoided. The development of new low-cost catalysts and simple surface activation treatments for bulk production of high-quality nanofilaments with controlled morphology is particularly crucial for the future development of advanced carbon-containing composites [6]. Thus, further growth studies involving wet-etched metal foils are necessary. Recently, we introduced an expeditious etching approach to form dense ensembles of round-shaped and catalitically-active nanoprotrusions in Ni foils [20]. The strong nanoprotrusions-substrate interactions enabled us to synthesise pure carbon nanostructures (i.e. free from metal particles) with improved diameter control (the ratio of the average protrusion size to the average CNF diameter was close to one).

In the present work, wet-chemical procedures for metal foils of Cu have been tailored to optimize the CVD-growth of CNFs. These are produced in forests which, furthermore, self-assemble into higher-order conical structures. The surface topology of the activated Cu surfaces was thoroughly evaluated to understand the influence of the nanoprotrusions in the CNF growth mechanism.

2. Experimental details

Metal foils ($10\times10\times1$ mm^2) of polycrystalline Cu (purity: 99.9%, Goodfellow) were used as the combined catalyst and supporting materials for the CNF growth process. The foils were polished and wet-chemically etched (CE) prior to the growth. In the latter step a combination of aqueous solutions of ammonium (NH$_4$OH 25 w/v%, Riedel-de Haën) and hydrogen peroxide (H$_2$O$_2$ 30 w/v%, Paureac) were applied for varied periods of time (1-20 min) [21]. Further details of metal foils preparation and CE procedures are reported elsewhere [20].

High-resolution scanning electron microscopy (HR-SEM, Hitachi SU70) analyses were carried out to help deciding on suitable CE treatments for hot-filament chemical vapour deposition (HF-CVD) growth. The CE foils selected by SEM were then further observed by atomic force microscopy (AFM, Digital Instruments Multimode IIIa) to assess topographical features.

CNFs were grown using a CH$_4$-Ar-H$_2$ gas mixture. The following conditions were constant throughout the set of growth runs: CH$_4$/(Ar+H$_2$) (v/v) = 0.25, total gas flow = 50 sccm, tungsten (W) filaments/substrate distance = 10 mm, filament temperature = 2300 ºC and deposition time = 15 min. The CH$_4$/H$_2$ (v/v) ratio (0.29 - 2), total pressure (5, 10 kPa) and substrate temperature (650-850 ºC) were varied to evaluate their effect on the CNF formation. For a full description of the experimental set-up for carbon deposits production see [20].

Deposited carbon nanostructures morphology, structure and composition were characterized by HR-SEM assisted by energy dispersive spectroscopy (EDS, Bruker Quantax 400). High-resolution transmission electron microscopy (HR-TEM, JEOL 2200FS) and μ-Raman spectroscopy at 325 nm (Jobin Yvon HR800) were also used. The Raman spectra were collected at room temperature in the wavenumber range of 1000-2000 cm^{-1}. All SEM and TEM images were analysed using the freeware Image J program suite.

3. Results and discussion

3.1. *Catalytic protrusion formation*

In a previous work it was showed that nano-sized protrusions formed by CE are found to have a key role in the growth process as they determine the yield and morphology of the carbon deposits [20]. Taking this into account, a similar strategy was applied here to convert the flat as-received Cu foils into surfaces with high density of catalytically active protrusions for CNF growth.

Fig. 1 depicts the SEM micrographs of the Cu foils surface for different etching times. All the low magnification micrographs show micro-scale patterning.

Chemical Etching (CE)	Etching time (min)				
	1	3	5	10	20
NH₄OH/H₂O₂/ H₂O (1:1:1)	I	I (C1)	I	II	II

I	CE with nanoprotrusions	II	CE without nanoprotrusions	C1	Etching selected
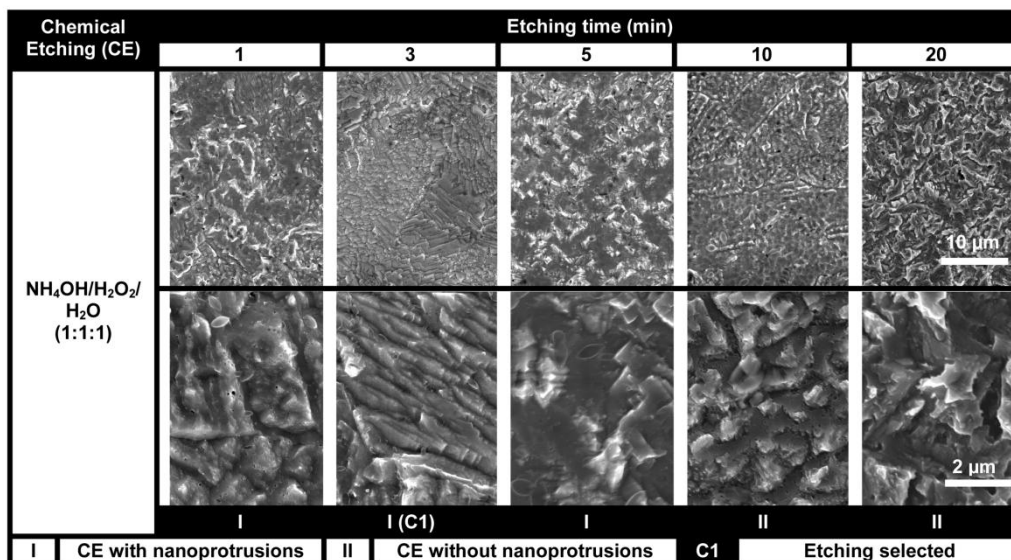
Fig. 1 - SEM map of the wet-chemical etched Cu foils depicting the surface features dependence on the etching time. A stepped morphology is visible for the etching time of 3 min (C1).

At high magnification, a noteworthy stepped morphology is observed for the etching time of 3 min (designated by C1 in Fig. 1). Further morphological and topographical features of C1, obtained by SEM and AFM characterisations, respectively, are present in Fig. 2. Periodical submicro-sized step edges with terraces width of 579±140 nm and steps height of 306±82 nm (projected sizes taken from the SEM images) were formed, as showed in Fig. 2b. The smooth surface of the terraces is different from that of the steps. Detailed observations of the latter (Fig. 2c) show nano-sized protrusions (i.e. kinks and step-adatoms clusters) with two dissimilar diameter size ranges and statistical distributions. At the magnification of Fig. 2c some fairly regular protrusions are depicted with wide size range (37±11 nm) and broad Gauss-like distribution (Fig. 2d). On the other hand, the higher magnification of Fig. 2e shows remarkable rounded protrusions with smaller diameters 8±2 nm and narrower Gauss-like distribution (Fig. 2f) covering the entire step edge. These rounded nanoprotrusions, showing regular spatial arrangement and high density $\sim 1.7 \times 10^3$ μm^{-2}, hold high prospects to catalyse aligned CNFs. This value is comparable to $\sim 6.2 \times 10^3$ μm^{-2}, obtained with thin film preparation techniques [22].

Complementary, AFM topographical analyses of C1 is illustrated in Figs. 2g,h. It shows a rough surface with Rq (root means square roughness, rms) of 215±6 nm and an overall uniform surface, which is corroborated by SEM micrograph in Fig 2a.

Conceptually, metal surfaces can be modelled as a set of terraces, steps (or ledges), kinks, adatoms, etc., according to the Terrace Ledge Kink (TLK) model [23]. Then the etching or

dissolution of metal surfaces can be considered in terms of the preferential motion of such different surface defects.
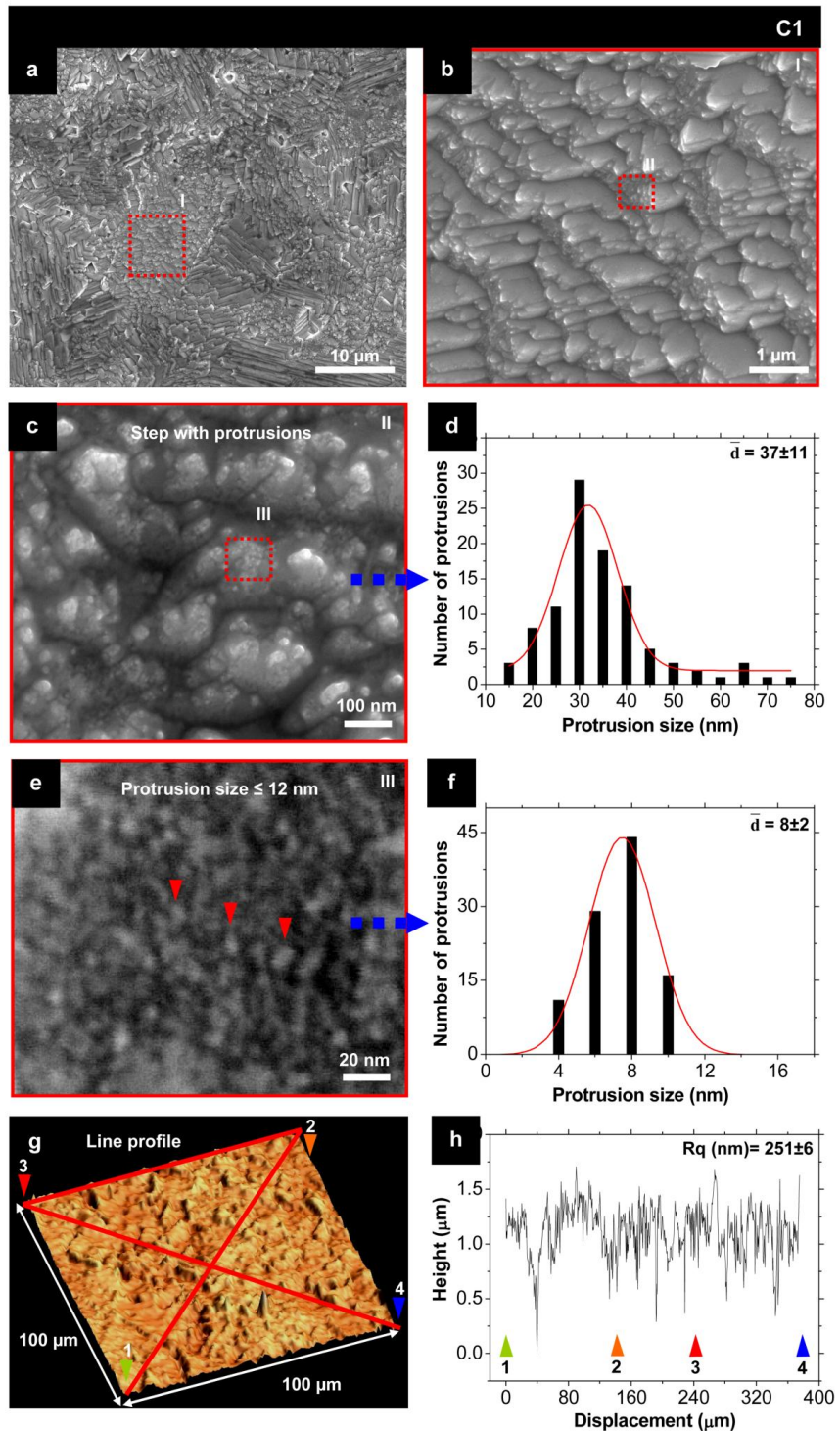
Fig. 2 - SEM images and AFM topographic images of C1. (a) Low magnification SEM micrograph of the etched surface showing high uniformity. (b) Magnification of the periodical step edges formed on the etched surface (c-f) High magnification

of the nano-sized protrusions produced on the step-edges and respective plots of statistical size distribution. (g) 3D AFM image of the surface topography and respective line profile (h).

For normalised surfaces, the etching rates control the interactions between the moving steps which lead to the tailoring of step edge morphology [24-26]. Huang et al. [24] proposed a dynamic step-step repulsion model for the etching kinetics and morphologies, where the nature of the etching was assumed more relevant than the exact crystallographic structure of the surface. It was found that, in a fast step etching regime of Si(111) surfaces, atomically smooth terraces are formed and all the sites along the step edges are etched with approximately equal probability (i.e. the probability of nucleating new defects on the step edge is comparable to, or faster, than the rate of their etching).

Similar hierarchical morphologies were formed on C1 surface, as shown previously in Figs. 2b, 2c and 2e. Therefore, it appears reasonable the extrapolation of the dynamic etching models proposed above to metal surfaces. As a result, the formation of the surface features, including the nano-sized protrusions, can be related to fast oxidative reactions catalyzed by strong oxidizing agents, preferentially on atomic step edges of Cu [26-28].

The enhanced performance of hydrogen peroxide (H_2O_2) based treatments was previously demonstrated in Ni foils [20]. The high growth yields on H_2O_2 treated substrates resulted in the patterning of well-shaped protrusions and step edges similar to those obtained here. Combining the strong oxidizing effect of concentrated H_2O_2 (30 w/v%) with an oxidizing agent of Cu (pure acid or acid-precursor compounds), a fast oxidative reaction takes place on the Cu surface. The present H_2O_2–assisted Cu oxidation mechanism is described in three steps according to the sketch showed in Fig. 3:

Step 1
Spontaneously decomposition of H_2O_2 in H_2O
(Formation of O_2^{2-}(aq))
(eqs. 1 and 2)

O_2^{2-} (aq)

Step 3
Catalysed decomposition of H_2O_2
(Cu^{2+}(aq) catalytical effect)
(eqs. 6 and 7)

Step 2
Oxidation of Cu
(eqs. 3-5)

Cu^{2+}(aq)
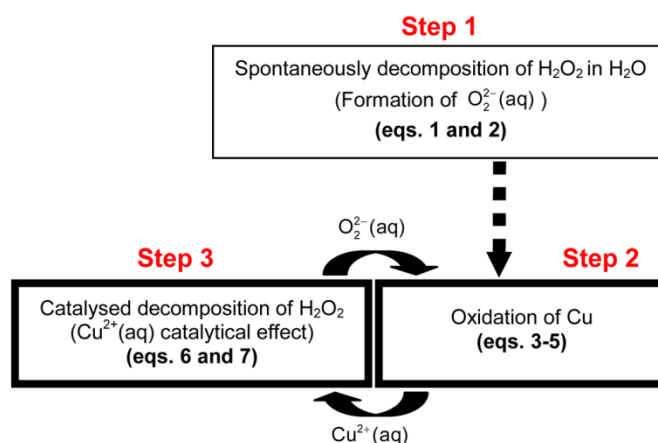
Fig. 3 - Schematic illustration of the etching mechanism of Cu foils assisted by H_2O_2.

- Step 1 concerns the spontaneous decomposition of H_2O_2 in H_2O (ΔH_f (1) = - 98.2 KJ.mol^{-1}) [29] forming highly concentrated O_2 in solution, according to:

$$2H_2O_2(aq) \rightarrow 2H^+(aq) + 2OH^-(aq) \uparrow + O_2(g) \uparrow \quad \Delta H_f(1) \qquad (1)$$

$$4OH^-(aq) \uparrow + O_2(g) \uparrow \leftrightarrow 2O_2^{2-}(aq) \uparrow + 2H_2O(l) \qquad (2)$$
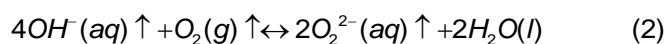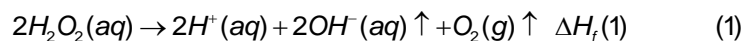
- Step 2 suggests the oxidation of Cu by $O_2^{2-}(aq)$. Firstly, the decomposition of ammonium hydroxide (NH$_3$ (aq)) results in nitric acid (HNO$_3$) (eq. 3), known as a strong oxidizing agent of Cu. Afterwards, the concentration of Cu^{2+} ions increases in solution due to the oxidation of Cu (eq. 4). The presence of these ions was detected by a change in the colour of the solution, from colourless to dark blue, due to the formation of copper-ammonia complex ions (eq. 5).

$$NH_3(aq) + 4O_2^{2-}(aq) \uparrow + H_2O(l) \rightarrow HNO_3(aq) \uparrow + O_2(g) + 4OH^-(aq) + 4e^- \qquad (3)$$

$$Cu(s) + 4HNO_3(aq) \uparrow \rightarrow Cu^{2+}(aq) \uparrow + 2NO_3^-(aq) + 2NO_2(g) + 2H_2O(l) \qquad (4)$$

$$Cu^{2+}(aq) + 4NH_3(aq) \rightarrow Cu(NH_3)_4^{2+}(aq) \ (dark \ blue \ color) \qquad (5)$$
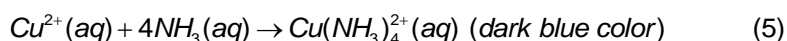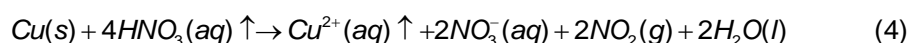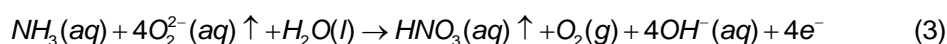
- Step 3, describes the catalysed decomposition of H$_2$O$_2$ in the presence of Cu^{2+} ions surrounding the Cu surface (Cu^{2+} catalytical effect) by a metal-catalysed oxidation (MCO) mechanism, accordingly to eqs. 6 and 7:

$$H_2O_2(aq) + 2Cu^{2+}(aq) \uparrow \rightarrow O_2(g) \uparrow + 2Cu^+(aq) \uparrow + 2H^+(aq) \ \Delta H_f(2) \qquad (6)$$

$$H_2O_2(aq) + 2Cu^+(aq) \uparrow \rightarrow 2OH^-(aq) \uparrow + 2Cu^{2+}(aq) \ \Delta H_f(3) \qquad (7)$$
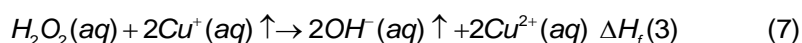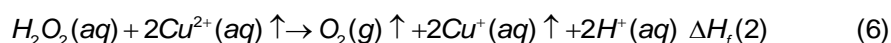
The enthalpy of the catalysed decomposition of H$_2$O$_2$ is lower than that of the spontaneous one ($\Delta H_f(2) + \Delta H_f(3) < \Delta H_f(1)$). By increasing the $O_2^{2-}(aq)$ concentration in solution, according to eq. 2, further oxidation of Cu occurs and a new cycle starts over again, repeating steps 2 and 3 (Fig. 3).

The combination of H$_2$O$_2$ with HNO$_3$ instead of NH$_3$(aq) was not used to prepare the substrates for CNF growth because it was found that HNO$_3$ alone has an excessive etching force, giving oversized protrusions on Cu surface (results not shown).

3.2. CNF forest growth

As stated in the introductory section, Cu has a low catalytic activity comparing to other metals. To overcome this, hot tungsten filaments were used to depress the energy barrier for the C species formation and further chemisorption on the substrate surface.

Also, Cu surfaces were tailored by the previously described etching procedure to become selectively active. If the surface was fully covered by nano-sized protrusions, probably C-layers would have formed alongside with CNFs, as observed in our previous report for Ni [20]. Instead, the C1 treatment converted the flat Cu foil into a surface with hierarchical morphology of non-catalytic sites (smooth terraces) with well dispersed and highly dense catalytic protrusions sites on the steps. These nucleation sites are well recognised as preferential locations for the heterogeneous catalytic reactions including C atoms adsorption [30-32]. Moreover, high temperatures (700-900 ⁰C) are needed to activate the nano-sized protrusions of Cu [18,33,34]. The use of a saturated gas as C precursor, such as CH_4, was intentionally selected to achieve a better growth control (needs more energy to decompose).

Using this strategy, several HF-CVD runs were accomplished as depicted in Fig. 4. The left-hand upper matrix gives the values of the three main growth parameters (substrate temperature; total pressure and CH_4/H_2 ratio) used to optimise the growth yields of CNFs. The right-hand side table resumes the obtained carbon deposit morphologies.

The best growth conditions, labelled as II and III, result in full covering of the metal with aligned CNFs. The shifting to more severe growth conditions compared to those previously obtained for Ni foils (650 ⁰C/5 kPa) [20] is explained by the lower catalytic activity of Cu (see section 1). Additionally, the C species concentration in the reactor when Cu foils are used is probably lower than with Ni, for the same conditions. This might be explained by different CH_4 dissociation mechanisms involved during the growth: on the surface of the W filaments, for Cu; and simultaneously on highly active Ni surface and W filaments, for Ni [35]. Therefore, the concentration limit of C species necessary for the filaments growth (N_C) on Cu, is obtained for conditions that promote the C species formation.

A compilation of representative SEM micrographs of the grown carbon products is given in Figs. 4a to 4g. For all growth combinations, excepting the one labelled as IV in the matrix of Fig. 4, the carbon deposits are formed by two layers of carbon, as it is shown in Fig. 4a. The CNF forests are firstly grown (Figs. 4b to 4d) followed by a simple C-layer (Fig. 4e) or a hybrid C-layer (Figs. 4f and 4g). Particularly, at low temperatures (650 ⁰C) or low pressures (5 kPa), conditions IV, the morphologies of the carbon deposits are similar to the ones formed on Ni foils [20], as it is exhibited in Fig. 4g.

Being the CNF forests films the focus of the present study, further characterisation was accomplished to understand the influence of temperature substrate and CH_4/H_2 ratio on their growth yield, morphology and graphitic structure. Fig. 5 shows the variation of the carbon product

heights with substrate temperature and CH_4/H_2 ratio. In Fig. 5a, the maximum value for the CNF forest height is obtained at 800 ⁰C, corresponding to 1.27 µm.

	1st Layer	2nd Layer
I	Dispersed aligned CNFs	C-layer
II	Film of aligned CNFs	C-layer
III	Film of aligned CNFs	C-layer + C nodular structures
IV	–	C layer + randomly CNFs

Best growth conditions for aligned CNF films
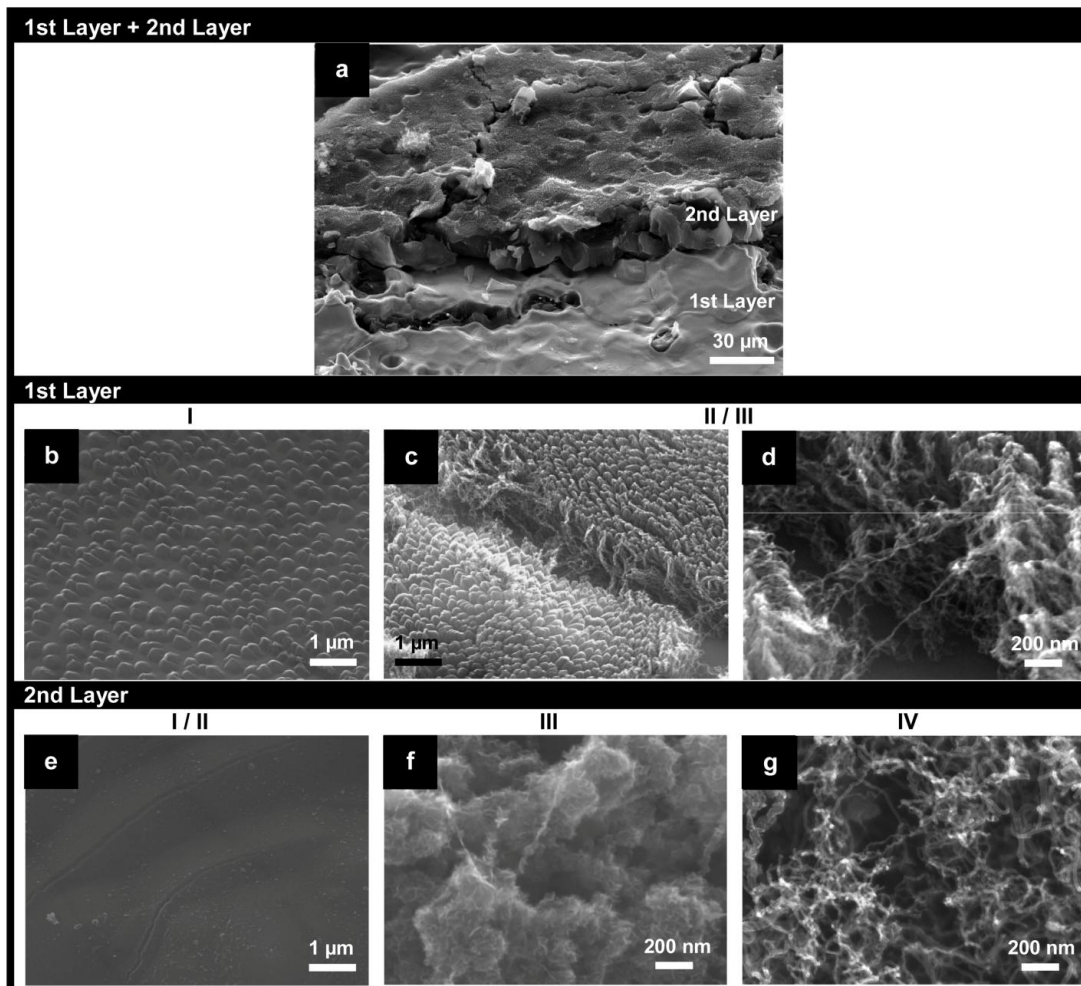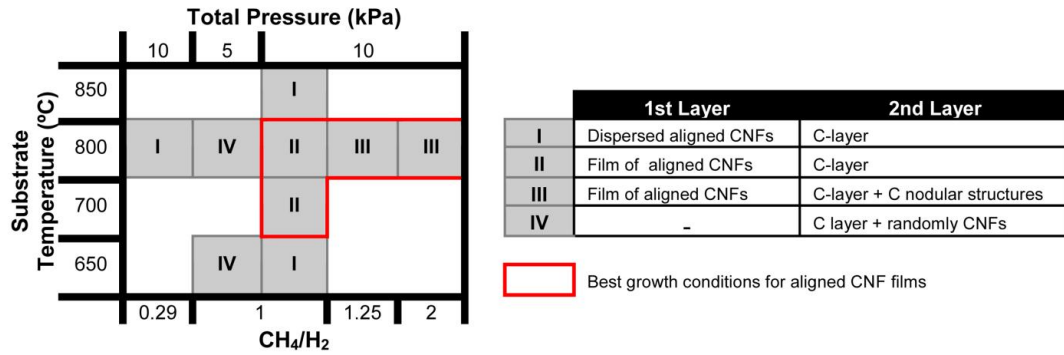
Fig. 4 - Matrix of the CVD parameters and respective table of the carbon deposits grown on C1 substrates. (2a-g) Representative SEM images of the carbon deposits.

The substrate temperature has a key role in the CNF growth as C species adsorption, dissolution, diffusion and precipitation mechanisms on the Cu protrusions are thermally activated. At 850 ºC, the dissolution rate of C species is probably faster than the diffusion and precipitation ones, leading to accumulation of amorphous carbon (a-C) at the surfaces of the nano-sized protrusions and loosening of their catalytic ability [36,37]. On the other hand, for T<800 ºC, the yield drops reaching the minimum at 650 ºC. For these conditions, growth is limited by the activation barrier for the diffusion of C species on the surface of the protrusion [38]. Furthermore, it can be seen in Figs. 4c,d that a continuous film of CNFs is only obtained at 700 ºC and 800 ºC (condition II), reinforcing the idea that the growth is restricted for the extremes of the temperature range studied.

The influence of the CH_4/H_2 on the carbon product heights is depicted in Fig. 5b. Here, the $CH_4/(Ar+H_2)$ ratio was set at 0.25 to ensure that the CH_4 concentration was kept constant during all growth runs. The upper limit of the CNF height is obtained at $CH_4/H_2 = 1$. For atmospheres poorer in H_2, the yield decreases due to fast poisoning of the protrusion (quicker a-C encapsulation) caused by the weak H_2 etching effect [39]. Consequently, smaller open area at the top of the protrusion allows a smaller intake of C species. Using atmospheres rich in H_2, the decreasing in the yield can be provoked by two different reasons. Firstly, a slight coarsening and deforming of the protrusions probably occur during the heating and growth stages, making them less active for the growth [39,40]. Secondly, the etching effect of the H_2 during the growth is perhaps too strong, removing the needed C species amount for the graphite-like structure formation on the highly dense protrusions patterning [39]. Fig. 4b shows this effect, where only a dispersed growth of CNF forests can be seen.
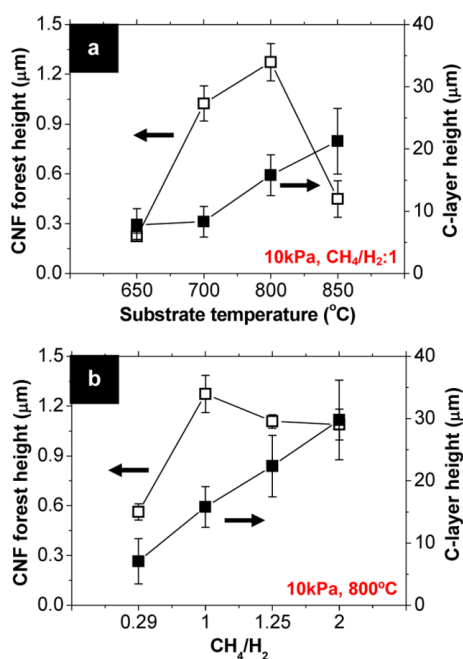
Fig. 5 - Plot showing the influence of the substrate temperature and CH_4/H_2 ratio on the C layers height.

In the case of the C-layer (2nd layer), much thicker deposits than the CNF layer were obtained for all growth conditions. Additionally, it can be seen a linear increasing of their height with the substrate temperature and the CH_4/H_2 ratio. Similar results were obtained by Li et al. [12]. The dissimilar behaviour of the C-layer, when compared to the CNF layer, is explained by different growth mechanisms. The former shows a mechanism independent of the physical/chemical stability of nano-sized protrusions (further details can be seen in section 3.6).

3.3. *CNF forest morphology*

Fig.6 shows a set of SEM micrographs regarding the morphology of the CNF forests of the sample with the highest growth yield, i.e. CH_4/H_2=1/800ºC/10kPa.

A general view of the carbon deposits is given in Fig. 6a, where it can be seen the CNF forests film covered by the C-layer. The magnified top view of zone I1 shows the CNF forest covering all the surface of the Cu foil (Fig. 6b). Additionally, some evidence of grain-boundary traces below the CNF forest is showed. The uniformity of the forest on these particular sites makes evident that neither surface rupture takes place nor new active sites were exposed. In a previous work, using higher catalytic active Ni foils in the same growth conditions, a wide diameter size range of CNFs was formed due to the surface rupture [20]. This comparison indicates that the use of less catalytic active foils gives the path to improve the growth kinetics.

At higher magnification, Fig. 6c, it can be seen that CNFs are organised in a morphology resembling cone figures. The tilted images focusing on the CNF forests give further details about the morphology (Figs. 6d-f). Good film uniformity and alignment can be seen on the entire area, as well as, a remarkable narrow diameter size range.

Fig. 7 compares in detail the morphologies of the C-layer and the CNF forests. In Fig. 7b it is clearly exhibited the interface between the CNF forest (1st layer) and the C-layer (2nd layer), making noticeable the different nature. Though, it can be also seen the C-layer is formed by several layers in a stacked cone-shaped morphology. For more comprehensive investigation of the two cone-based morphologies these layers were separated. They were detached from the Cu substrate by a simple transfer process using a C tape (double-sided adhesive). Firstly, the top C-layer was easily separated from CNF forests using the tape (weak adhesion forces were seen between the two layers). Consequently, the remaining CNF forests film was removed from the substrate using the same technique.

Fig. 7c shows that the 1st layer corresponds to only one layer of aligned CNFs that are organised in a cone-shaped arrangement. The weak Van der Waals interaction forces between CNFs lead to their alignment [41]. Additionally, the very same interaction forces are probably responsible for the fibers self-assembling in cone-shaped figures as dissimilar growth occurs simultaneously in various front directions. These multi-directional growth fronts result from the hierarchical morphology of the etching surface. As described in section 3.1, the small protrusions

totally cover the larger irregular ones at the step edges. CNF growth from these small protrusions along different directions and their interaction result in cone shapes.
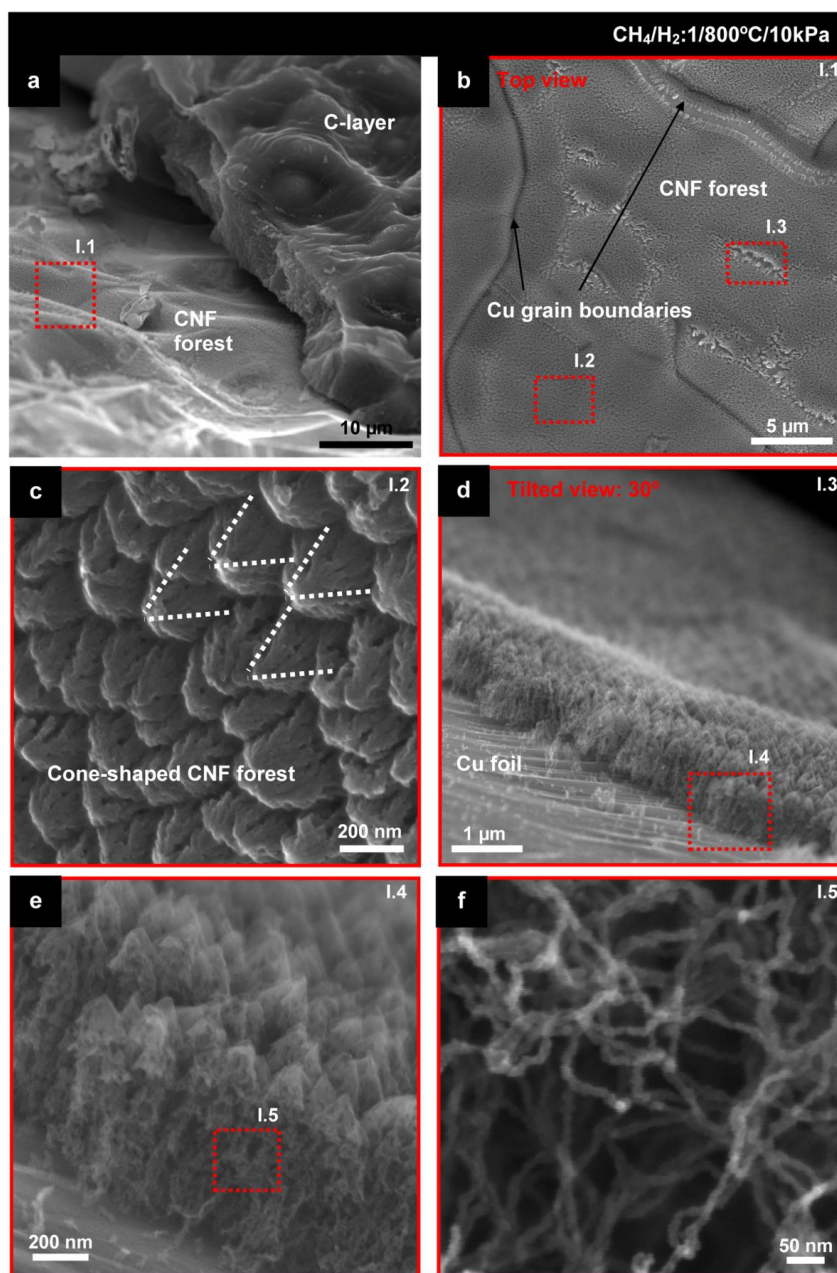
Fig. 6 - SEM images of the CNF forests deposited with the best growth yield conditions (CH$_4$/H$_2$:1;800ºC;10kPa): (a) low magnification image of the carbon deposits; (b) top-view showing the Cu surface totally covered by the CNF forest film; (c) magnification of the CNF forest showing cone-shape figures; (d and e) tilted-view showing the uniformity of the CNF forest; (f) high magnification of (e) depicting the CNF small diameters and narrow diameter size range.

On the other hand, the 2nd layer (Fig. 7d) is constituted by stacked C nanoparticles (CNPs). This hierarchical disposition gives rise to a nanostructured C layer formation completely different

from the a-C layer formed in Ni foils for similar growth conditions [20]. Both nano-sized structures have low average diameters size and narrow Gauss-like distributions.

Fig. 8 shows the dependence of the cone-shaped CNF forests morphology on the substrate temperature and CH_4/H_2 ratio. Four morphological characteristics were analysed: fiber outer diameter; ratio between the initial protrusions size (s_p) and fiber outer diameter (d_f); density and apex angle of cones. According to Figs. 8a and 8b the diameters slightly increase for higher temperatures and poor atmospheres of H_2. This tendency is caused by the excessive C species concentration on the protrusions proximity, leading to the thickening of the fibers diameters by decorating C forms. Subsequently, more irregular surfaces are evidenced by the standard deviation increasing.
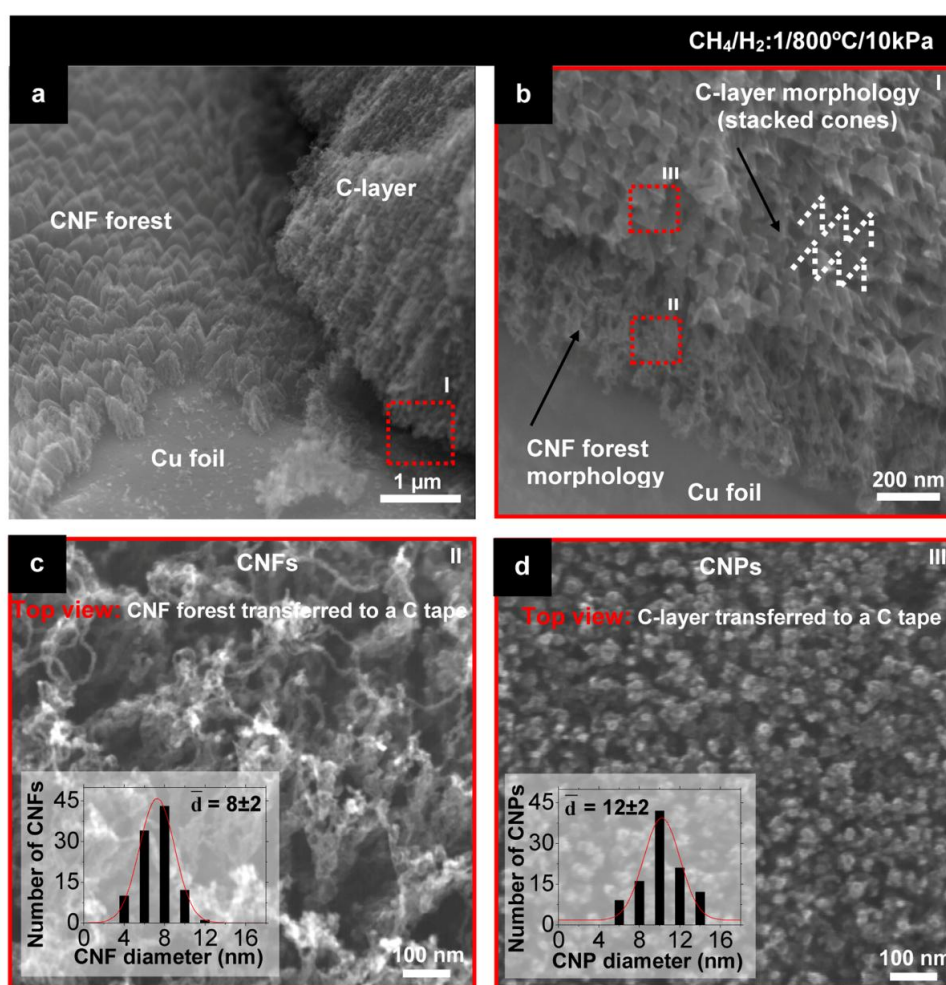
Fig. 7 - SEM images of the C layers deposited with the best growth yield condition revealing the different morphologies: (a) low magnification image showing the cone-shaped CNF forest under the C-layer. (b) cross-sectional view of (a) depicting a notable interface between the two C-layers (the top layer shows also a cone-shaped morphology); (c and d) high magnification of the transferred C layer proving the different morphologies (with respective plots of statistical size distributions).

A marked correlation of the CNF outer diameters and the initial protrusions size is observed for all growth conditions. Figs. 8a,b show s_p/d_f values close to the unity (0.89 to 1.33). A particular result was obtained for $CH_4/H_2=1/800ºC/10kPa$ showing a s_p/d_f ratio of 1 that is supported by the respective histograms matching (Fig.2f and Fig. 7c).

In Figs. 8c-d is showed the influence of the substrate temperature and the CH_4/H_2 ratio on the density and apex angle of the CNF cones. Generally, a greater influence of the temperature is observed. The best cone density, 32 ± 4 µm^{-2}, is obtained at $CH_4/H_2=1/800ºC/10kPa$, according to the best growth conditions. Additionally, for CH_4/H_2 superior to 1 it can be seen a tendency to achieve less uniform densities. Figs. 8e-f illustrate the low and high density cone structures. Overall, the cones have an apex angle in the range of 90-100º as those depicted in Fig. 8g.
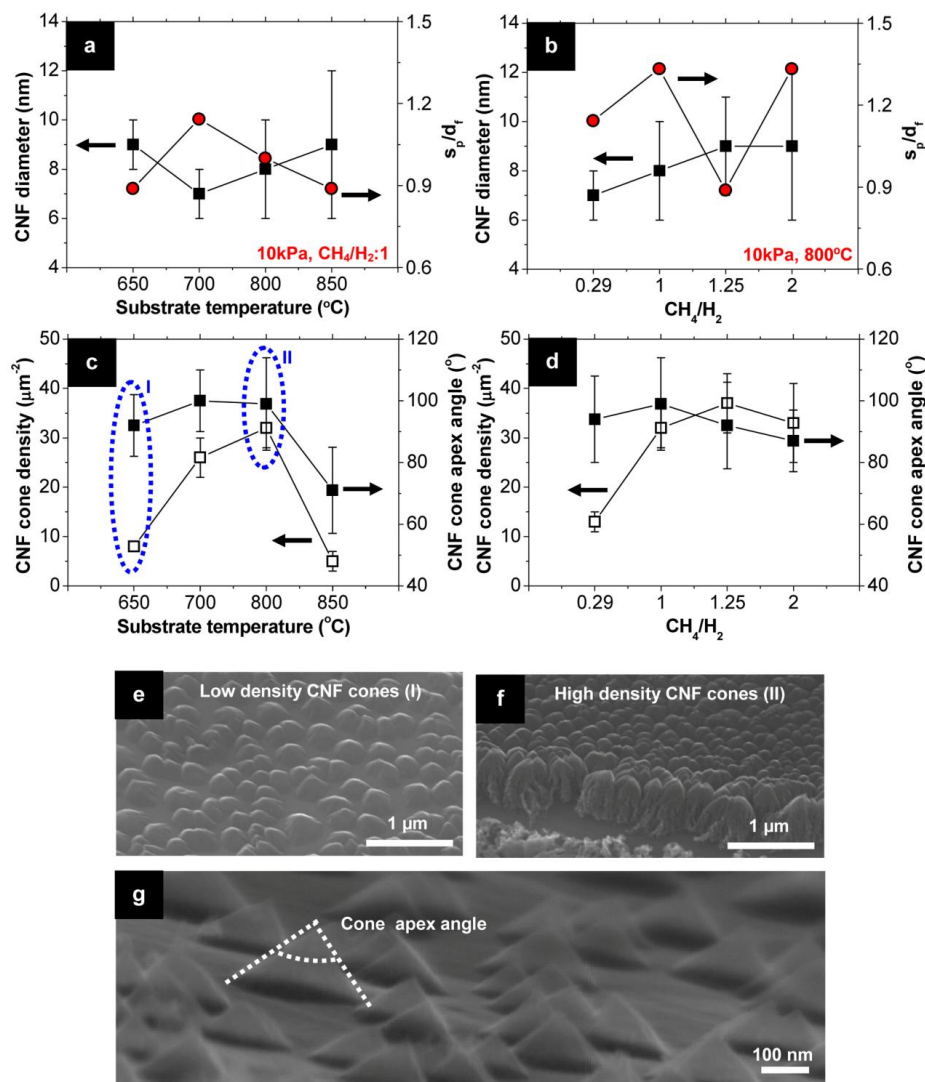
Fig. 8 - Plots illustrating the dependence of the s_p/d_f ratio and CNF forest morphology on the substrate temperature and CH_4/H_2 ratio. (e and f) Representative images of CNF forests with different cones densities. (g) High magnification image of the cone figures with the sketched cone apex angle.

Comparing the Figs. 5 and 8c-d, it is observed that the growth parameters have a similar influence on CNFs height and cone density. This might indicate that the two morphological characteristics are correlated. In the case of the faster growth kinetics, all the catalytic nanoprotrusions are active for the nucleation of CNFs and for longer time which leads to longer and denser CNFs. These two features promote the interaction of neighbouring fibers guiding the formation of more perfect and denser cone figures. On the contrary, for extreme substrate temperatures and low CH_4/H_2 ratio, the cone density decreases (Figs. 8c-d). The substrate temperature is assumed to control the activation of the nanoprotrusions and the growth processes. On the other hand, the overage C species, for CH_4/H_2 superior to 1, conducts to less uniform cone density as they promote a faster poisoning of the nanoprotrusions on more active surface sites.

3.4. *Protrusion size preservation*

Surprisingly, even the Cu nano-sized protrusions showing a very small diameter (~8 nm, Fig. 2f) present at 800 ℃ ($T/T_{m(bulk)}$= 0.79) good resistance to flattening. This feature is associated to the s_p/d_f ratio: the CNF diameter (d_f) mirrors the initial protrusion size (s_p), therefore s_p/d_f ~1 means that the protrusions keep their initial size. Comparable s_p/d_f ratio were obtained previously on Ni foils having nano-sized protrusions in the 24-42 nm range, but only for less austere CVD conditions (650 ℃/5 kPa, $T/T_{m(bulk)}$= 0.53) [20]. This means that the energy barrier for short-distance diffusion of Cu from the protrusion top to the bottom, that would result in an increase of the curvature radius, is higher than that for the Ni protrusions.

The energy values involved on protrusions evolution are greatly dependent on their physical-state. It is recognised that the melting temperature (T_m) of the catalyst metal protrusions, prior to the nucleation and growth steps, can be depressed significantly by the Gibbs-Thomson effect for protrusions with radius, r, smaller than 10 nm, according to:

$$T_m = T_{m(bulk)} - \frac{2T_{m(bulk)}}{\Delta H_f r \rho_s}\left[\sigma_{sl} + \left(1 - \frac{\rho_s}{\rho_l}\right)\sigma_l\right] \qquad (8)$$

where $T_{m(bulk)}$ is the bulk melting point of the metal, ΔH_f is the latent heat of fusion, ρ_s and ρ_l are the densities of solid and liquid metal, respectively, σ_{sl} is the solid-liquid interfacial energy and σ_l is the surface energy of liquid [42]. The main differences in these quantities concern the ΔH_f (13.05 kJ mol^{-1} and 17.48 kJ mol^{-1}, respectively for Cu and Ni), the $T_{m(bulk)}$ (1083℃ for Cu and 1453℃ for Ni) and the protrusion radius (average radius of 4nm for Cu and 15nm for Ni [20]). Hence, theoretically, the T_m of a Cu protrusion is much lower than that of a Ni one. However, taking into account only the Gibbs-Thomson effect (size effect of metal particles), the experimental data is not in agreement with the theory.

Beyond the Gibbs-Thomson effect described above, it is known that the T_m can also be depressed by the C solubility in the metal during the nucleation and growth steps (when the C species are present in the reactor). *In-situ* observations accomplished by Krivoruchko et al. [43] proved that C solubility is, in fact, more important than the Gibbs-Thomson effect of metallic particles in depressing T_m. It was observed that metal particles of 10-150 nm (in this range the Gibbs-Thomson is not significant), embedded in an a-C layer have anomalously supersaturation in C (50 at.%), presenting liquid (for particles of 10-50 nm) or liquid-surface and solid-core (for particles of 50-150 nm) behaviour at 600-700 ºC. Similar observations were reported recently [44,45]. The slightly differences of the physical state of the particles for the two set of sizes is explained by the increase of the C solubility for particles smaller than 10 nm in an exponential manner (size effect of metal-C particles) [30], according to:

$$S = S_0 \exp\left(\frac{2\sigma V}{kTr}\right) \qquad (9)$$

where S and S_0 are solubilities in the particle and bulk material respectively, defined as the ratio of the amounts of solute and solvent, σ is the surface tension and V is the volume of a metal molecule. These observations were valid only for VIII group transition metals, including Ni, having intrinsic high C solubility and ability to form metal-C eutectics.

Concerning this, previous results that showed 15 nm radius sized protrusions of Ni being supersaturated due to the concerted interaction with the reactive gas, CH_4, and the deposited a-C layer (protrusions were embedded in the a-C layer), increase the possibility of a semi-liquid state at 800 ºC, leading to easily reshaping [20]. In the case of Cu, the Cu-C eutectic is almost neglected due to the low C solubility [15,16]. For instance, the C solubility (at.%) at $T_{m(bulk)}$ = 1084 ºC is $\sim 2 \times 10^{-4}$, much less than in Ni ~ 3 [46]. Additionally, it was showed before that the CNFs do not grow alongside with the C-layer forming a hybrid instead, a clear interface separating the two layers was observed. This suggests that Cu protrusions are not embedded in C films, making the supersaturation possibility more difficult to occur. Therefore, it can be postulated that Cu protrusions being in the solid state due to their low intrinsic C solubility show enough resistance to the flattening mechanisms. Though, here the temperature influence on the dynamics of steps and kinks is not underestimated [47].

3.5. *CNF forest graphitic structure*

In Figs. 9a,b there are depicted representative TEM images of the carbon structures grown at the best conditions (CH_4/H_2=1/800ºC/10kPa). The HRTEM picture of a CNP that appear in the 2nd layer (C-layer), showed in Fig. 9c, denotes a typical carbon-onion structure, where the C core is encapsulated by well defined graphitic shells and resulted from the graphitization of the surrounding less organised carbon clusters [48,49]. Concerning the CNF structure (1st layer), a

118

hollow-herringbone arrangement was obtained for all CVD parameters (Figs. 9d,e). Additionally, the in-plane spacing of the graphene structures is about ~3.5 and ~3.8 Å, for CNPs and CNFs, respectively, lower than the 3D graphite (~3.4 Å). This evidences that the grown products show turbostratic structure due to the uncorrelated 2D graphene layers stacking.

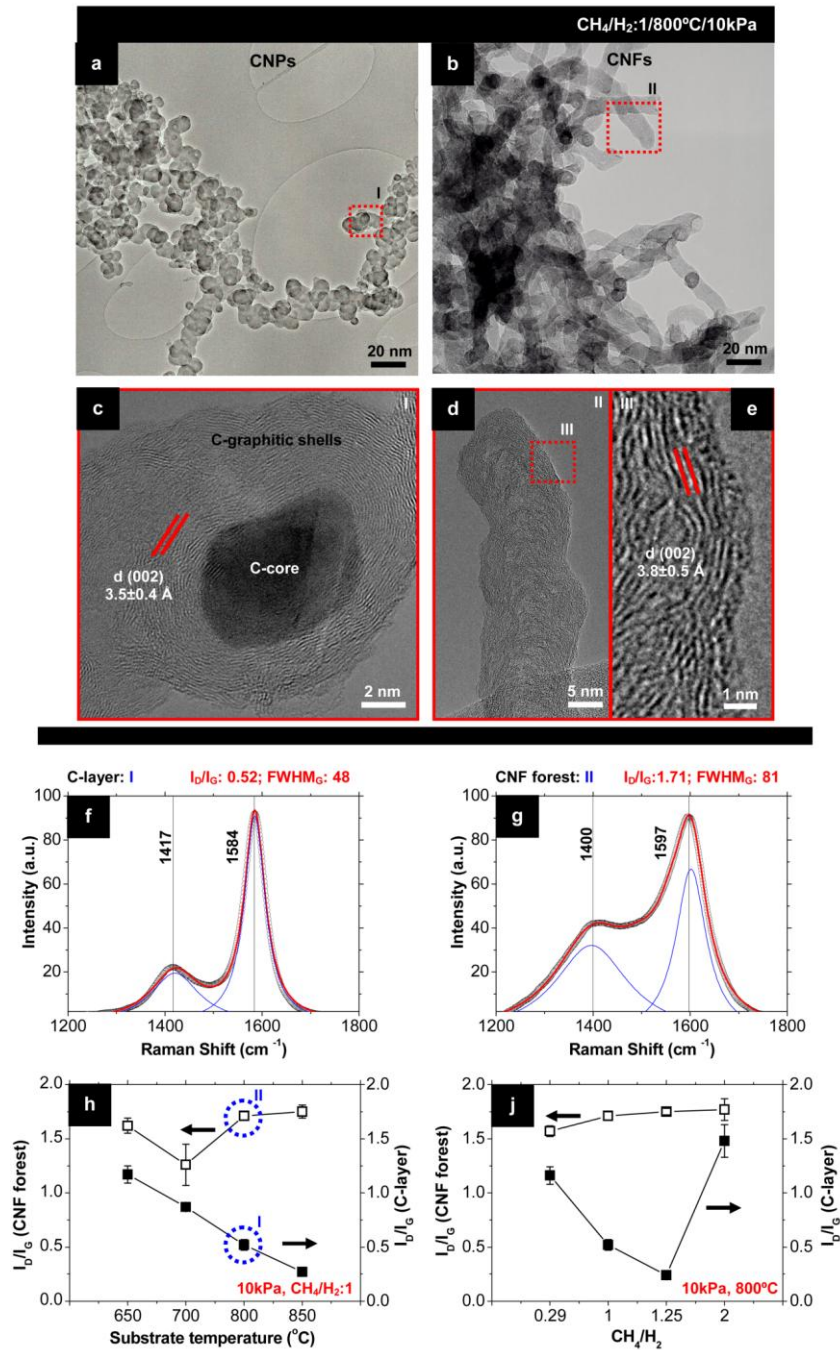**Fig. 9 -** (a-e) TEM images of the different C layers deposited with the best growth yield condition. (c-e) HRTEM images depicting the graphene sheets orientations and the lattice spacing between the sheets. (f and g) Representative .micro-Raman UV (325 nm) spectra of the two different C layers. (h and j) Plots showing the influence of the substrate temperature and CH_4/H_2 ratio on the I_D/I_G ratios.

Micro-Raman spectroscopy at 3.81 eV (325 nm) was further accomplished in order to evaluate the influence of the substrate temperature and CH_4/H_2 ratio on the structure of the grown C products. All spectra were baseline corrected by linear background removal and then normalized to the maximum intensity of each spectrum, all peaks having been fitted with a Lorentzian line-shape. Before the measurements the two layers were isolated. The top C-layer was directly analysed and the CNF forests film was exposed by elimination of the C-layer with a C tape.

Representative first-order Raman spectra of the grown structures for the best growth conditions are presented in Figs. 9f,g. The red solid line corresponds to the fitting (obtained from the Lorentzian curves showed at blue solid line) of the experimental data represented with small rings. Typical graphite-based spectra profiles are obtained using UV excitation 3.81 eV (325 nm): it can be seen at low wavenumbers a broad peak around ~ 1417 cm^{-1} (D-band: arising from lattice disorder) and at higher wavenumbers a strong peak at ~1584 (G-band: E_{2g} stretching mode of the graphitic crystalline structure). Previously, the use of a lower laser excitation energy (E_L) of 2.41 eV (514.5 nm) gave the following band positions for CNF films at ~ 1353 cm^{-1} (D-band) and ~ 1585 cm^{-1} (G-band) [19]. The D-band shifts to higher wavenumbers results from its dispersive excitation response for higher E_L ($d\omega_D/dE_L$ ~53 cm^{-1}.eV^{-1}) [50]. As shown, the two spectra display shifts of ~47-64 cm^{-1}, according to the theoretical prediction. Moreover, the G-band of the CNF forests has its position significantly shifted for higher wavenumbers by ~17 cm^{-1} due to small crystallite size domains (La) [51]. Similar results were found for thick disorder a-C films [20].

Concerning the profile of the spectra, it can be observed that the G-band of C-layer shows high symmetry, which means neither a right shoulder (D'-band: graphite in-plane disorder) nor a splitting (G$^+$, G$^-$) are found [50]. On the other hand, the G-band of CNFs shows a significant asymmetry for lower wavelengths, resulted from the overlap of the D-band, giving evidence of a more imperfect structure. Overall, the smaller D-band and the lower full width at half-maximum (FWHM) of G-band from the C-layer indicate bigger sp^2 crystallite domain sizes in the graphite-like structure than in the CNF forests, which is corroborated by HRTEM observations (Figs. 9c,e).

The assessment of the structural graphitisation of the C products was obtained by the I_D/I_G integrated intensity ratios. An increased I_D/I_G value is generally attributed to the presence of structural defects and disordered carbons [50]. Figs. 9h,i show that CNF structure is more dependent on the substrate temperature than on the CH_4/H_2 ratio. The catalytic Cu protrusions give the best graphitized structures at 700 ºC with a I_D/I_G ratio of ~1.26 (Fig. 9h). At lower temperatures, the annealing of defects is reduced and the low diffusion rates of the C species results in less organised graphitic stacked forms [52]. At higher temperatures, the reaction rates become too high for the filaments growth, overcoming the benign annealing effect of the temperature, thus giving more disordered structures.

Fig. 9i shows the CNF structure order decreasing with the CH_4/H_2 ratio. For poor H_2 atmospheres the weak etching effect of H_2 in the protrusion faceted front allows the excess deposition of C species. This will interfere with the ordinary parallel graphene layers precipitation and originates the deposition of disordered carbon on the outer walls of the grown structure.

Applying rich H_2 atmospheres the best graphitised CNF structures (I_D/I_G ~1.57) were obtained, proving the positive effect of H_2 and the preservation of the protrusions morphological features even for more severe etching conditions.

Figs. 9h,i show dissimilar effects of the substrate temperature and the CH_4/H_2 ratio in the graphitic structure of CNPs compared to the CNFs. The CNPs graphene planes order increases almost linearly with the substrate temperature. Recent *in situ* observations showed similar results [53]. It was demonstrated that a linear acceleration effect of the temperature in the propagation rate of graphitised areas takes place on Ni particles embedded in thin a-C layers. Fig. 9i shows that at 800 ºC the increasing C species concentration up to CH_4/H_2 = 1.25 can be easily organised in graphene planes. Though, for higher C amounts, the excessive C has disordered structure becoming evident that the network refinement effect of the temperature is insufficient.

Summarizing, it can be stated that the growth mechanism of carbon filaments, based on metal protrusions, is more sensitive to the deposition parameters than those of the other carbon structures that are protrusion independent. This is put in evidence by the better graphitized structure of CNPs compared to the CNFs.

3.6. CNF growth mechanism

Figs. 10a,b show the SEM micrograph and EDS mapping of the carbon deposits, respectively. The carbon deposits were transferred to a C tape to assess the presence of metal particles (high compression force was applied to transfer all the C deposits at once). No Cu particles were seen on the C deposits back-side in the detection limit of the detector (the regular red spots corresponds to the background pattern of the Cu signal). This is explained by the strong interaction protrusions-substrate foil making possible the easy remotion of free-particle C structures from the grown substrate. From this result, important issues were taken into account concerning the growth mechanisms of each C-layer.

A base-growth mode is assumed for CNFs, according to the absence of metal particles in the walls and tips of the structures. This is in agreement to previous results [20]. Additionally, assuming the solid state of the Cu protrusions during the CNF nucleation and growth steps, a Vapour-Solid-Solid (VSS) mechanism [54] is also allied, concerning the following steps: (1) adsorption and dissociation of the precursor gas on the W filaments surface (vapour state); (2) carbon species adsorption, dissolution and diffusion on/in the Cu protrusions (solid state); (3) carbon supersaturation and graphite-like structure precipitation from the bottom of the catalyst protrusion; (4) successive carbon incorporation into the growing structure (solid state).

In the case of the C-layer formed by CNPs we postulate that the stacked particles are also formed by a Vapour-Solid-Solid (VSS) mechanism, based on related works on carbon species growth [48,49]: (1) adsorption and dissociation of the precursor gas on the W filaments surface (vapour state); (2) adsorption of C species or/and precipitation of disordered C clusters on the surface of the carbon film; (3) the partially closed C clusters may collide and adhere to each other

(i.e. coalesce) forming compact C particles (solid state); (4) other open C clusters continue to grow on the compact C particles forming concentric layers; (5) graphitisation of the concentric layers on the surface of the C particles (solid state).
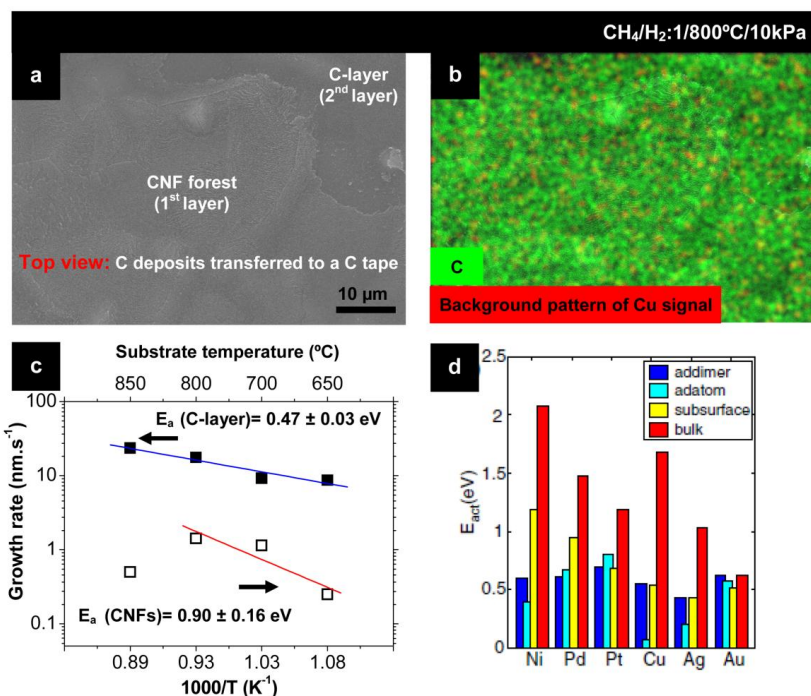
Fig. 10 - (a) SEM top-view image of the transferred C structures deposited with the best growth yield condition. (b) EDS map of (a) showing the absence of Cu particles on the two C layers (C in green and Cu in red). (c) Arrehenius plot for the growth rates of CNFs and C-layer, providing the activation energies of 0.9 eV and 0.47 eV, respectively. (d) Diffusion barriers of monoatomic and diatomic carbon for different metals, data adapted from Yazyev [17].

In Fig. 10c it is displayed the Arrhenius plot that correlates the growth rate of each carbon layer with the substrate temperature in the range of 650-850 ºC, allowing the estimation of activation energy values (E_a). The growth rate measurements were obtained from the average heights of the C-layers. For CNFs, growth at high temperatures (850 ºC) deviates from the linear behaviour due to poisoning of nanoprotrusions, as discussed in section 3.2. Similar results were already reported [38]. In the case of the C-layer the growth rate follows the Arrhenius law in the temperature range studied. The extracted E_a values for CNFs and C-layer were $E_{a\ (CNFs)}$ ~0.90±0.16 eV and $E_{a\ (C-layer)}$ ~0.47±0.03 eV. The $E_{a\ (CNFs)}$, almost twice the value of C-layer, corroborates its slower growth kinetics, denoting dissimilar growth mechanisms. In order to understand the meaning of these values further detailed comprehension of the mechanisms is presented.

In HF-CVD method, the filaments make possible the CH_4 dehydrogenation on their surface creating reactive C species in the gas phase (step 1). The E_a for CH_4 dehydrogenation on W filaments in the temperature range of 927-2327 ºC was estimated to be around 0.44 eV [55]. An eventual adsorption and dissociation of CH_4 molecules on Cu (alternative to step 1) is not

favourable: the activation energy values for the dissociative chemisorption energy of CH_4 on clean and oxidized Cu (100) surfaces are 2.08 eV and 1.3 eV, respectively, exceeding the present $E_{a\ (CNFs)}$ [56].

Beyond the dehydrogenation of the precursor gas, it has been postulated that the diffusion of the C species (step 2) is the rate-limiting step for CNF growth [57-60]. Some works report the estimation of E_a for the C filaments growth on VIII transition metals and found it close to bulk C diffusion in the metals [57,58]. On the contrary, other works pointed out the surface C diffusion as the rate-limiting step rejecting the bulk diffusion possibility [59,60]. Values for bulk diffusion activation energy given in the histogram of Fig. 10d (adapted from [17]) are slightly higher than $E_{a\ (CNFs)}$ ~0.90 eV. However, a closer value of $E_{a\ (Cu-bulk)} = 0.914$ eV is reported by Fuks et al. [61]. Additionally, the histogram shows that atomic C species diffusion on the surface have activation energies lower than 0.5 eV ($< E_{a\ (CNFs)}$ ~0.90 eV), thus bulk diffusion in step 2 would limit the CNF growth rate. Dissolution of C in Cu is disregarded as controlling step as its activation energy presents a smaller E_a value (0.36 eV) [16]).

In the case of the C layer growth, the energy barrier should be at the gas/film interface as the dehydrogenation of the precursor gas occurs at a fixed temperature on the W filaments. It is known that carbonaceous substrates can act as catalysts for the deposition of carbon [62,63]. The experimental value here obtained of $E_{a\ (C-layer)}$ ~0.47 eV, is most likely due to other complex heterogeneous reactions involving the C species and the C film, first on the cone-shaped CNFs and subsequently on the precipitated CNPs. Coltrin et al. estimated E_a values in the range of 0.09-0.32 eV and 0.44-4.95 eV, respectively for direct and inverse surface reactions involving C species [64]. Comparing with the experimental $E_{a\ (C-layer)}$ it is reasonable to assume that the limiting step is the chemisorption of C species [64] on the solid carbon surface having dangling bonds (0.44 eV).

Summarizing, in the HF-CVD process CNF growth starts by hydrocarbons dissociation mainly at the W filaments and not at the Cu catalyst, which is known to have weak chemisorption and dissociation propensity. However, the relatively high temperatures helped on this limitation, as also on C dissolution in copper protrusions. Then, the aligned CNF film (1st layer) starts to grow (1st growth stage) in a multi-step mechanism controlled by C diffusion in the bulk Cu. Though, the life-time of the catalyst is too short, due to an increasing number of C species in the protrusion front, leading to C encapsulation. Consequently, a 2nd growth stage emerges with a C-layer formation (2nd layer) in a faster manner over the CNF film that can act as a catalyst. This stage is controlled by C species chemisorption on the C film. This top layer is formed by stacked films of CNPs that grow in the same ordered manner of the substrate. In addition, the former layers of CNPs may act as a barrier to the C species assessment on the protrusion surface, contributing to the shortening of the 1st growth stage.

4. Conclusions

Aligned carbon nanofibers (CNFs) have been successfully grown on Cu foils in a wide range of temperatures (650-850ºC) using the HFCVD technique. This indicates that Cu, known usually as inactive, is able to catalyse carbon filaments if a suitable growth strategy is demarcated. Here, the strategy combines two conditions:

(1) Conversion of the flat Cu foil (non catalytically active) into a surface with a hierarchical morphology showing different catalytic activities: smooth terraces (non-catalytic sites) with very small size (s_p ~8 nm) well dispersed protrusions (higher catalytic sites) on the steps. This avoids the co-growth of a-C layers and generally promotes the selective growth on metal foils. Here, fast etching by H_2O_2 is the key factor for Cu surface preparation.

(2) Use of W filaments for the dissociative chemisorption of the C precursor gas. This overcomes the lack of catalytic activity of the Cu foils.

The CNF film shows a cone-shape configuration with a maximum height ~1 μm whose individual fibers have average diameters (d_f) are close to the protrusion size (s_p/ d_f ~1). This denotes that the protrusion morphology has been preserved during the nucleation and growth of CNFs.

The CNF growth mechanism comprises a sequence of steps:

(1) Hydrocarbons dissociation at the W filaments.

(2) Adsorption, dissolution and diffusion of C in the Cu protrusions. Bulk diffusion is assumed to control the process kinetics as the overall activation energy (E_a = 0.90 eV) is similar to known $E_{a\ (C\text{-}bulk\ Cu)}$ = 0.914 eV.

(3) Carbon supersaturation and graphite-like structure precipitation to form CNFs following a base-growth mode.

Afterwards, the CNF growth ceases due to Cu protrusions poisoning by C excess and the overage C species starts to condensate over the fibers as a thick nanostructured C-layer formed by carbon nanoparticles (CNPs).

Acknowledgements

References:

[1]. Ajayan PM, Tour JM. Materials science - nanotube composites. Nature 2007;447:1066-8.

[2]. Jorio A, Dresselhaus G, Dresselhaus MS (Eds.). Carbon nanotubes: advanced topics in the synthesis, structure, properties and applications. Berlin: Springer-Verlag; 2008.

[3].   Baker RTK, Barber MA, Harris PS, Feates FS, Waite RJ. Nucleation and growth of carbon deposits from the nickel catalyzed decomposition of acetylene. J Catal 1972;26:51-62.

[4].   Endo M, Koyama T, Hishiyama Y. Structural improvement of carbon-fibers prepared from benzene. Jap J Appl Phys 1976;15(11):2073-6.

[5].   Audier M, Oberlin A, Oberlin M, Coulon M, Bonnetain L. Morphology and crystalline order in catalytic carbons. Carbon 1981;19:217-24.

[6].   Baddour CE, Fadlallah F, Nasuhoglu D, Mitra R, Vandsburger L, Meunier JL. A simple thermal CVD method for carbon nanotube synthesis on stainless steel 304 without the addition of an external catalyst. Carbon 2008;47:313-47.

[7].   Hansen VM, Latorre N, Royo C, Romeo E, Bordejé EG, A. Monzón. Development of aligned carbon nanotubes layers over stainless steel mesh monoliths. Catal Today 2009;147S:S71–5.

[8].   Abad MD, López JCS, Murcia AB, Golovko VB, Cantoro M, Wheatley AEH, Fernández A, et al. Catalytic growth of carbon nanotubes on stainless steel: Characterization and frictional properties. Diam Relat Mater 2008;17:1853-7.

[9].   Karwa M, Iqbal Z, Mitra S. Scaled-up self-assembly of carbon nanotubes inside long stainless steel tubing. Carbon 2006;44:1235-42.

[10].   Peng X, Koczkur K, Chen A. Synthesis of well-aligned bamboo-like carbon nanotube arrays from ethanol and acetone. J Phys D: Appl Phys 2008;41:095409.

[11].   Chen X, Narayan J. Effect of the chemical nature of transition-metal substrates on chemical-vapor deposition of diamond. J Appl Phys 1993;74(6):4168-72.

[12].   Li WN, Ding YS, Suib SL, DiCarlo JF, Galasso FS. Controlling the growth of CVD carbon from methane on transition metal substrates. Surf Coating Tech 2005;190:366-71.

[13].   Hammer B, Morikawa Y, Nørskov JK. CO Chemisorption at Metal Surfaces and Overlayers. Phys Rev Lett 1996;76:2141-4.

[14].   Deng WQ, Xu X, Goddard WA. A Two-Stage Mechanism of Bimetallic Catalyzed Growth of Single-Walled Carbon Nanotubes. Nano Lett 2004;4(12)2331-5.

[15].   Deck CP, Vecchio K. Prediction of carbon nanotube growth success by the analysis of carbon–catalyst binary phase diagrams Carbon 2006;44:267-75.

[16].   Lopez GA, Mittemeijer EJ .The solubility of C in solid Cu. Scripta Mater 2004;51:1-5.

[17].   Yazyev OV, Pasquarello A. Effect of metal elements in catalytic growth of carbon nanotubes. Phys Rev Lett 2008;100(15):156102.

[18].   Zhou W, Han Z, Wang J, Zhang Y, Jin Z, Sun X, et al. Copper Catalyzing Growth of Single-Walled Carbon Nanotubes on Substrates. Nano Lett 2006;6(12):2987-90.

[19].   Céspedes JG, Thomasson S, Teo KBK, Kinloch IA, Milne WI, Pascual E, Bertran E. Efficient diffusion barrier layers for the catalytic growth of carbon nanotubes on copper substrates. Carbon 2009;47:613-21.

[20]. Mata D, Ferro M, Fernandes AJS, Amaral M, Oliveira FJ, Costa PMFJ, Silva RF. Wet-etched Ni foils as active catalysts towards carbon nanofiber growth. Carbon 2010;48(10):2839-54.

[21]. Petzow G. Metallographic etching: techniques for metallography, ceramography, plastography. USA: ASM; 1999.

[22]. Futaba DN, Hata K, Namai T, Yamada T, Mizuno K, Hayamizu Y, et al. 84% catalyst activity of water-assisted growth of single walled carbon nanotube forest characterization by a statistical and macroscopic approach. J Phys Chem B 2006;110:8035-8.

[23]. Stranski IN. Zur Theorie des Kristallwachstums. Z Phys Chem 1927;136:259-78.

[24]. Huang YC, Flidr J, Newton TA, Hines MA. Dynamic repulsion of surface steps flow etching: controlling surface roughness with chemistry. J Chem Phys 1998;109(12)5025-35.

[25]. Flidr J, Huang YC, Newton TA, Hines MA. Extracting site-specific reaction rates from steady state surface morphologies: Kinetic Monte Carlo simulations of aqueous Si(111) etching. J Chem Phys 1998;108(13)5542-53.

[26]. Suggs DW, Bard AJ. Scanning tunneling microscopic study with atomic resolution of the dissolution of Cu(100) electrodes in aqueous chloride media. J Phys Chem 1995;99: 8349-55

[27]. Vogt MR, Lachenwitzer A, Magnussen OM, Behm RJ. In-situ STM study of the initial stages of corrosion of Cu(100) electrodes in sulfuric and hydrochloric acid solution. Surf Sci 1998;399:49-69.

[28]. Li WH, Ye JH, Li SFY, Nichols RJ. In situ scanning tunneling microscopy investigation of restructuring and anodic dissolution of Cu(111) electrode in sulphuric acid solution. Surf Sci 2000;449:207-17.

[29]. Hess WT. Kirk-Othmer Encyclopedia of Chemical Technology. 4th ed. New York: Wiley; 1995.

[30]. Moisala A, Nasibulin AG, Kauppinen EI. The role of metal nanoparticles in the catalytic production of single-walled carbon nanotubes – a review. J Phys: Condens Matter 2003;15:S3011-35.

[31]. Nørskov JK, Bligaard T, Logadottir A, Bahn S, Hansen LB, Bollinger M, et al. Universality in Heterogeneous Catalysis. J Catal 2002;209: 275-8.

[32]. Lukas S, Vollmer S, Witte G, Wöll C. Adsorption of acenes on flat and vicinal Cu (111) surfaces: step induced formation of lateral order. J Chem Phys 2001;114(22):10123-30.

[33]. Takagi D, Homma Y, Hibino H, Suzuki S, Kobayashi Y. Single-Walled Carbon Nanotube Growth from Highly Activated Metal. Nano Lett 2006;6(12): 2642-5.

[34]. O'Byrne JP, Li Z, Tobin JM, Larsson JA, Larsson P, Ahuja R, Holmes JD. Growth of carbon nanotubes from heterometallic palladium and copper catalysts. J Phys Chem C 2010;114(18):8115-9.

[35]. Beebe TP, Goodman DW, Kay BD, Yates JT. Kinetics of the activated dissociative adsorption of methane on the low index planes of nickel single crystal surfaces. J Chem Phys 1987;87(4):2305-15.

[36]. Li WZ, Wen JG, Ren ZF. Effect of temperature on growth and structure of carbon nanotubes by chemical vapour deposition. Appl Phys A 2002;74:397-402.

[37]. Reilly PTA, Whitten WB. The role of free radical condensates in the production of carbon nanotubes during the hydrocarbon CVD process. Carbon 2006;44:1653-60.

[38]. Ducati C, Alexandrou I, Chhowalla M, Amaratunga GAJ, Robertson J.Temperature selective growth of carbon nanotubes by chemical vapor deposition. J Appl Phys 2002;92(6):3299-3303.

[39]. Okita A, Suda Y, Oda A, Nakamura J, Ozeki A, Bhattacharyya K, et al. Effects of hydrogen on carbon nanotube formation in CH4/H2 plasmas. Carbon 2007;45:1518-26.

[40]. Nessim GD, Hart AJ, Kim JS, Acquaviva D, Oh J, Morgan CD, et al. Tuning of vertically-aligned carbon nanotube diameter and areal density through catalyst pre-treatment. Nano Lett 2008;8(11):3587-93.

[41]. Fan S, Chapline M, Franklin N, Tombler T, Cassell A, Dai H. Self-oriented regular arrays of carbon nanotubes and their field emission properties. Science 1999;283: 512-4.

[42]. Buffat P, Borel JP. Size effect on the melting temperature of gold particles. Phys Rev A 1976;13(6):2287-98.

[43]. Krivoruchko OP, Zaikovskii VI. A new phenomenon involving the formation of liquid mobile metal–carbon particles in the low-temperature catalytic graphitisation of amorphous carbon by metallic Fe, Co and Ni. Mendeleev Commun 1998;8(3):97-9.

[44]. Anton R. On the reaction kinetics of Ni with amorphous carbon. Carbon 2008;46:656-62.

[45]. Gorbunov A, Jost O, Pompe W, Graff A .Solid–liquid–solid growth mechanism of single-wall carbon nanotubes. Carbon 2002;40:113-8.

[46]. ASM Handbook: Alloy Phase Diagrams, 10th ed, ASM International; 1992; Vol. 3.

[47]. Kodambaka S, Khare SV, Petrova I, Greene JE. Two-dimensional island dynamics: Role of step energy anisotropy. Surface Science Rep 2006;60:55-77.

[48]. Saito Y, Yoshikawa T, Inagaki M, Tomita M, Hayashi T. Growth and structure of graphitic tubules and polyhedral particles in arc-discharge. Chem Phys Lett 1993;204(3):277-82.

[49]. Zhang QL, O'Brien SC, Heath JR, Liu Y, Curl RF, Kroto HW, et al. Reactivity of Large Carbon Clusters: Spheroidal Carbon Shells and Their Possible Relevance to the Formation and Morphology of Soot. J Phys Chem 1986;90(4)525-8.

[50]. Dresselhaus MS, Dresselhaus G, Saito R, Jorio A. Raman spectroscopy of carbon nanotubes. Phys Reports 2005;409:47-99.

[51]. Nemanich RJ, Solin SA. First and second-order Raman scattering from finite-size crystals of graphite. Phys Rev B 1979;20(2):392-401.

[52]. Hofmann S, Sharma R, Ducati C, Du G, Mattevi C, Cepek C, et al. In situ observations of catalyst dynamics during surface-bound carbon nanotube nucleation. Nano Lett. 2007;7(3)602-8.

[53]. Anton R. On the reaction kinetics of Ni with amorphous carbon. Carbon 2008;46:656-62.

[54]. Raty JY, Gygi F, Galli G. Growth of Carbon Nanotubes on Metal Nanoparticles: A Microscopic Mechanism from Ab Initio Molecular Dynamics Simulations. Phys Rev Lett 2005;95(9):096103-6.

[55]. Winters HF. Activated, dissociative chemisorption of methane on tungsten. J Chem Phys 1975;62(6):2454-60.

[56]. Alstrup I, Chorkendorff I, Ullmann S. The interaction of CH_4 at high temperatures with clean and oxygen precovered Cu(100). Surf Sci 1992;264(1):95-102.

[57]. Baker RTK, Harris PS, Thomas RB, Waite RJ. Formation of filamentous carbon from iron, cobalt and chromium catalyzed decomposition of acetylene. J Catal 1973;30(1):86-95

[58]. Bartsch K, Biedermann K, Gemming T, Leonhardt A On the diffusion-controlled growth of multiwalled carbon nanotubes J Appl Phys 2005;97:114301-7.

[59]. S. Hofmann, Csányi G, Ferrari AC, Payne MC, Robertson J Surface Diffusion: The Low Activation Energy Path for Nanotube Growth Phys Rev Lett 2005;95: 036101-4.

[60]. Helveg S, Cartes CL, Sehested J, Hansen PL, Clausen BS, Nielsen JR, et al. Atomic-scale imaging of carbon nanofibre growth. Nature 2004;427:426-9.

[61]. Fuks D, Mundim KC, Malbouisson LAC, Berner A, Dorfman S, Ellis DE. Carbon in copper and silver: diffusion and mechanical properties. J Mol Struct 2001;539:199-214.

[62]. Muradov N, Smith F, T-Raissi A. Catalytic activity of carbons for methane decomposition reaction. Catal Today 2005;102:225-33.

[63]. Lee E, Lee S, Han G, Lee B, Lee T, Jun J, et al. Catalytic decomposition of methane over carbon blacks for CO_2-free hydrogen production. Carbon 2004;42:2641-8.

[64]. Coltrin M, Dandy D. Analysis of diamond growth in subatmospheric dc plasma-gun reactors. J Appl Phys 1993;74(9):5803:20

II.4. Upscaling potential of the CVD stacking growth method to produce dimensionally-controlled and catalyst-free multi-walled carbon nanotubes

D. Mata[a], R.M. Silva[a], A.J.S. Fernandes[b], F.J. Oliveira[a], P.M.F.J. Costa[a], R.F. Silva[a]

[a]CICECO, Glass and Ceramics Eng. Dept., Univ. of Aveiro, 3810-193 ,Portugal

[b]I3N, Physics Dept., Univ. of Aveiro, 3810-193, Portugal

Abstract

Multi-walled CNTs (MWCNTs) with structural characteristics optimised for bio-applications have been produced using a catalyst-supported chemical vapour deposition (CVD) method. The upscale potential of the process was demonstrated by combining classical semi-continuous and stacked growth modes. The vertically aligned MWCNT films thus obtained were multi-layered with five continuous strata of well-structured nanotubes. Following gentle disentanglement, the stacks were converted to individual MWCNTs with short dimensions (a final length and diameter of ~1.2 µm and ~12 nm) and almost catalyst-free (<0.04%). Overall, our process produces dispersed, bio-tailored MWCNTs with an output growth-yield 20 times higher than a standard CVD setup and exempt of complex or destructive post-growth steps of purification and separation. These constitute key steps towards the mass-production of MWCNTs with low toxicological risks, an essential prerequisite for biomedical applications.

1. Introduction

Two decades ago, carbon nanotubes (CNTs) became accountable for co-triggering the nanoscience and nanotechnology revolution worldwide. A couple of years later, the boom in the nanomedicine field occurred in the following sectors: drug delivery, *in vitro* diagnosis, biomaterials and *in vivo* imaging [1,2].

CNTs, nanometer-sized in diameter, and made of one rolled up graphene sheet - single-walled (SWCNTs) - or several concentric sheets - multi-walled (MWCNTs), have cached increasing enthusiasm in nanomedicine due to their low cost, supreme electrical, mechanical and optical properties [3-5]. Pioneering solutions based on CNTs have been designed to endorse significant advances in the sectors referred above [3-5].

Besides the benefits, CNTs have potential toxicological risks. There are escalating concerns regarding hazards of CNTs in human body due to their apparent similarities to asbestos and other carcinogenic fibres [6,7]. To date, significant discrepancy in the toxicological profile of CNTs is found due to the lack of standard experimental protocols which limits comparative studies across research groups [6,7]. Nonetheless, several studies clearly identified two common factors that are responsible for the toxic behaviour of pristine CNTs [8-13]. Firstly, the residual amount of metals used to produce CNTs can act as catalyst to oxidative stress in cells, leading to toxicity [8,9]. Secondly, CNTs may present high biopersistency due to their nonbiodegradability, hydrophobicity and morphology [8,10-13]. Large CNT agglomerates >20 μm in diameter, resulting from their feeble dispersion [10], and long >10 μm and thick >50 nm individual CNTs [11-13] cannot be totally engulfed by macrophages, inducing inflammation and granuloma lesions [7,10-12].

A lot of effort has been made to overcome the weak dispersion of hydrophobic CNTs on physiological mediums by charging the CNT side-walls with functional groups [4,5]. Yet, the production of gram quantities of biologically safer CNTs is still a challenge [4,14,15]. Accordingly to a meta-analysis presented in the Section I.3.3, a safer CNT for biomedical applications must be highly pure with small length and diameter sizes, typically below 2 μm and 30 nm, respectively. So, to produce CNTs-based materials of pharmaceutical and clinical relevance it is mandatory to control the growth process of safer CNTs.

Chemical vapour deposition (CVD) methods have emerged as the most promising approach for mass production of CNTs, as they offer the highest degree of growth control and upscaling potential. Among several known CVD methods, the catalyst-supported CVD (e.g. "super growth") provides superior prospects to produce safer CNTs for biomedical applications when compared to fluidised bed reactors [15]. The former method produces carbon structures with higher vertical alignment, VACNTs (a.k.a. CNT forests), with a greater control of morphologies, namely diameter and length sizes, and with a much higher purity up to 99.98% [16]. Indeed, the success of this method in producing CNTs for biomedical purposes depends mostly on a strict control of the metal catalyst particles regarding two main factors. Firstly, the diameter size of the catalyst particles and their adhesion strength to the substrate dictate the outer diameter and the amount of

metal impurities of the grown CNT, respectively [17,18]. Secondly, the stability of the catalyst particles during the nucleation and growth stages highly influences not only the growth kinetics, i.e. the length size of the tube, but also the crystallinity of the CNT structure and the amount of carbonaceous impurities on their walls [19,20].

However, the catalyst-supported CVD is a non-continuous method due to the catalyst film preparation step that ends by decreasing the output yield. This has been claimed as the main drawback of the super-growth when compared to the fluidised bed approach. Having this in mind, the reusing of the catalyst particles by applying a stacked-growth mode can be strategically applied to grow short CNT for biomedical applications. Using a strongly bonded catalyst-substrate system and a controlled kinetics regime [21], several highly pure MWCNTs layers with similar morphologies can grow in a multi-layer form up to 5 mm-long [22] or theoretically to meter-long [23].

Taking this into account, an expeditious catalyst method preparation was previously developed regarding metal foils acting as combined catalyst and substrate having strong bonds [17,18]. Carbon filaments with controlled morphologies and almost catalyst-free were obtained. Unfortunately, a thick nanostructured C-layer was formed over the carbon filaments which prevented the employment of the stacked-growth process. Alternatively, the Fe-Al$_2$O$_3$ system also shows strong bonds, due to charge transfer from the Fe to the surface oxygen atoms [24] or to the Fe-O bonds at the Fe-Al$_2$O$_3$ interface [25], and high growth control of CNTs [16].

The present work focuses on the high output production of biologically safer VACNTs on Fe-Al$_2$O$_3$-Si substrates by a semi-continuous process that combines an advantageous experimental set-up and a stacked-growth mode. The substrate annealing conditions were thoroughly assessed to maximize the adhesion strength of the Fe particle-Al$_2$O$_3$ substrate, and fully characterised by high-resolution scanning electron microscopy (HR-SEM) and atomic force microscopy (AFM). The preservation of these interactions and further optimisation of the growth kinetics guaranteed the strict control over large areas of the CNT diameters and lengths suitable for biomedical purposes. Also, it was shown by scanning transmission electron microscopy (STEM) and micro-Raman spectroscopy that the processing steps successfully convert stacked CNT forests into individualized CNTs without damage to their structure.

2. Experimental details

2.1. Substrate preparation

Polished p-type Si (100) wafers of 5 cm in diameter with a 200 nm oxide layer of SiO$_2$ (Siegert Consulting) were used as substrates. A bilayer of Al$_2$O$_3$-Fe was magnetron sputtered on the Si substrates with a base pressure <10^{-4} Pa. Films of Al$_2$O$_3$ (10 nm) were first deposited using a RF power supply and a reactive Ar (purity ≥99,9999%, Praxair)-O$_2$ (purity ≥99,999%, Praxair) gas mixture with 3% of O$_2$. Here, the combined oxide layers act as diffusion barriers, avoiding the

formation of catalytic inactive iron silicides [26]. Then, a DC power supply and an inert Ar atmosphere were used to deposit 0.5, 1 and 2 nm thick Fe catalyst films (Fe(0.5), Fe(1) and Fe(2), respectively) (purity ≥ 99.99%, Goodfellow).

The use of a balanced magnetron system combined with low deposition rates, 0.2 Å.s^{-1} and 0.4 Å.s^{-1}, for Al$_2$O$_3$ and Fe, respectively, ensured a good uniformity of thicknesses on the entire Si wafer surface with a statistical coefficient of variation of < 20%. Finally, the wafers were cut into 5 x 5 mm^2 samples for the growth studies.

The thickness and deposition rate of the films were evaluated *ex situ* by spectroscopic ellipsometry (Jobin Yvon Auto SE working with an incidence angle of 70⁰ in the range of 440-850 nm). Also, the characterisation of the morphology and topography of the particles obtained by *in situ* annealing steps in the hot-wall thermal CVD reactor were carried out by HR-SEM (Hitachi SU70 working at 15 keV, resolution of 1 nm) and AFM (Digital Instruments Multimode IIIa working in tapping mode), respectively. The annealed samples were kept under vacuum to avoid the excessive change of the particles morphology by oxidation.

2.2. CNT forest growth

CNT forest growth was carried out in a hot-wall thermal CVD reactor using a C$_2$H$_2$ (purity ≥99.6%, 300 ppm of H$_2$O, Praxair)-H$_2$ (purity ≥99,999%, ≤2 ppm of H$_2$O, Praxair)-Ar (purity ≥99,9999%, ≤0.5 ppm of H$_2$O, Praxair) gas mixture at atmospheric pressure. The reactor consists of a 5 cm inner diameter quartz tube housed inside a furnace, equipped with mass flows, electrovalves and a PC control station for automatic operation.

In a typical growth run, the substrates were placed in a quartz boat and loaded into the cold zone of the reactor, with the furnace already heated at the temperature of set-point. The reactor tube was then pumped down to ~ 3 Pa and subsequently filled up with Ar to reach the atmospheric pressure. Afterwards, the quartz boat was pushed to the centre of the hot zone using a stainless steel arm, allowing a fast heating. Then, a two stepped annealing process was initialised. Firstly, in an inert flow of Ar (1000 sccm), followed by a treatment in a reductive flow of Ar/H$_2$ (v/v) = 0.4 (700 sccm). Subsequently, the Ar and H$_2$ flows were adjusted and the C$_2$H$_2$ was added for the CNTs synthesis. After the growth step, the C$_2$H$_2$ and H$_2$ flows were cut off and the quartz tube was flushed with Ar flow to remove the reactive gases. Finally, the quartz boat was pulled to the cold zone for a fast cooling down to room temperature in around 2 min. The furnace and the empty quartz boat were then purged with O$_2$ in the hot-zone during 10 min to burn out the carbon residuals, becoming the system, after that, ready for a new growth run.

The time of the first and second annealing steps were varied between 5 to 15 min and 0.5 to 5 min, respectively, to assess the morphological and topographical evolution of the catalyst particles. Moreover, for a constant total flow of 510 sccm and growing time of 15 min, the reaction temperature (650-870ºC) and the gas ratios (C$_2$H$_2$/H$_2$ (v/v) = 0.03-0.2; Ar/H$_2$ (v/v) = 0.25-9) were varied to evaluate their effect on the CNT yield and structure. Additionally, the total flow (210-910

sccm) and the growth time (0.08 to 120 min) were varied to investigate the CNT yield over large areas and the growth kinetics, respectively.

In a stacked-growth process, growth-etching cycles were accomplished as follows. After the typical growth step, the samples were oxidized at 350 ºC (burning temperature of amorphous C) under a constant air flux for 5 min. Then, the tube was pumped down to ~ 5 Pa, filled with Ar and then the samples were pushed again to the hot zone for a new growth step which included a pre-treatment step with a flow of Ar/H_2 (v/v) = 0.4 (700 sccm), for 1 min, to reactivate the oxidized catalyst.

The CNT morphology and structure were characterized by HR-SEM, high-resolution transmission electron microscopy (HR-TEM, JEOL 2200FS working at 200 keV, resolution of 0.1 nm) and micro-Raman spectroscopy at 532 nm (Jobin Yvon T64000), respectively. The Raman spectra were collected at room temperature in the wavenumber range of 1000–2000 cm^{-1}.

The purity of the samples was assessed by energy dispersive spectroscopy (EDS, Bruker Quantax 400) and by using a transmitted electron detector for the model SU-70 Hitachi HR-SEM for acquiring bright field STEM. A more quantitative investigation using termogravimetric analyses (TGA, Setsys Setaram working under a O_2 flow of 200 sccm at 10ºC.min^{-1}), elemental analysis inductively coupled plasma atomic emission spectroscopy (ICP-AES, Jobin Yvon Activa-M) and X-ray photon spectroscopy (XPS, VG Scientific ESCALAB 200A spectrometer using a non-monochromatized AlKα radiation of 1486.6 eV) was also performed.

For the HR-TEM observations the grown materials were suspended in 2-propanol (≥99.8%, Sigma). Then, some drops were placed on lacey-carbon Cu grids (Agar Scientific) and dried afterwards at 100ºC under vacuum (1 Pa) for 45h to remove the solvent residues inside the nanostructures.

2.3. Disentanglement of stacked CNT forests

The stacked forests were first gently scratched from the substrate using a plastic spatula and then immersed in 2-propanol. Afterwards, the big blocks in suspension were high-speed sheared at 20,500 rpm for 15 min (IKA T25-Ultra-Turrax) to separate the layers and disentangle the CNT bundles. Then, small bundles were softly sonicated at room temperature during 60 min (Selecta, working at 60 kHz, 200 W) to produce well individualised CNTs in suspension. The morphology evaluation of the CNTs mounted on lacey-carbon Cu grids was accomplished by STEM.

3. Results and discussion

3.1. *Key factors for growing biologically safer CNTs by catalyst-supported CVD*

According to the meta-analysis presented in section I.3.3, a safer pristine CNT is defined as a tube structure with a length and diameter below 2 μm and 30 nm, respectively.

3.1.1. *Predicting the Fe particle diameters*

In previous works, it was shown the existence of a remarkable correlation between distributions of the filament diameter and catalyst particle size [17,18]. Thus, it is relevant to predict the Fe particle size to produce safer CNTs.

For metal films, it is known that the film thickness and the annealing temperature are particularly important to control the film restructuring into particles [27]. Considering this, a critical Fe particle diameter (C_{pd}) can be predicted using a thermodynamic model, proposed by Sanjabi et al. [28]. Here, it is assumed that during the annealing step only α-Fe (bcc) is present, since it is stable up to 900 ºC [29]. The C_{pd} value corresponds to the minimum stable particle diameter where the total Gibbs free energy change for Fe nanoparticle formation comparing to that of a nanofilm, *ΔG*, is zero. It is calculated as follows,

$$\Delta G = G_p(D) - G_f(t) \qquad (1)$$

$G_p(D)$ is the total Gibbs free energy for the nucleation of a spherical Fe particle of diameter *D*, from liquid Fe. And, $G_f(t)$ is the total Gibbs free energy of the nanofilm of thickness *t*. Thus, *ΔG* is given by

$$\Delta G = \pi D^3 \left[\left(\frac{-g_p(D)}{6V_s} + \frac{Y_{sl}(D)}{D} \right) - \left(\frac{-g_f(t)}{6V_s} + \frac{Y_{sl}(t)}{3t} \right) \right] \qquad (2)$$

where $g_p(D)$ and $g_f(t)$ are the size-dependent molar volume Gibbs free energy of the particle and film, respectively. $Y_{sl}(D)$ and $Y_{sl}(t)$ are the size-dependent solid-liquid interface energy of the particle and the film, respectively. V_s is the molar volume [30,31].

Fig. 1a shows that for a constant annealing temperature the C_{pd} increases with the thickness of the sputtered Fe film, as it is expected. The temperature used for the calculations of ΔG corresponds to the optimum temperature to grow CNTs, that is, 770ºC (Section 3.1.3). Typically, the annealing temperature is the same as the growth temperature to turn the process more prompt. For the temperature range of 650-870ºC the C_{pd} (G_p=0) increases with increasing

134

annealing temperature, but not significantly ~ 31% (Fig. 1b). The C_{pd} corresponds to the diameter of a α-Fe particle of D≈11d (671 atoms, six shells [32]), where d is the atomic diameter [28].
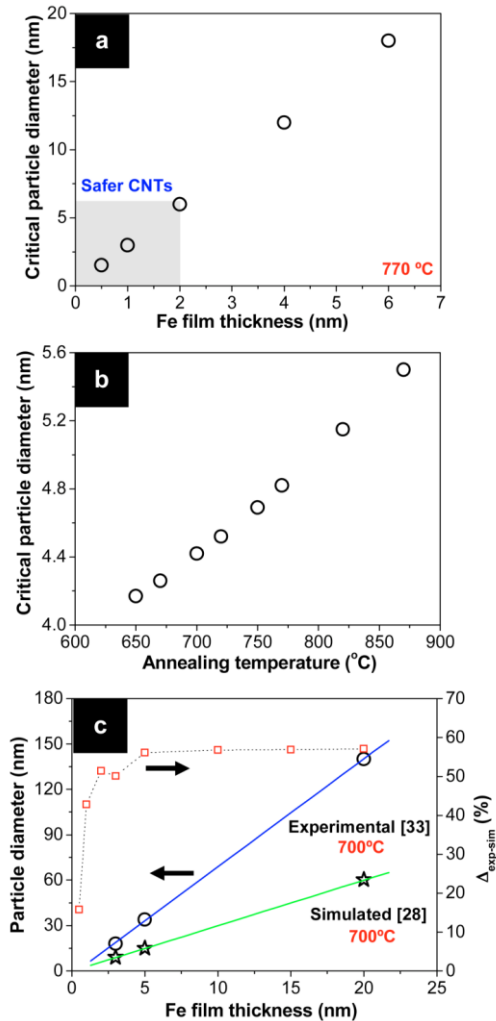
Fig. 1 - (a and b) Plots showing the influence of the Fe film thickness and annealing temperature in the critical particle diameter (P_{cd}) of Fe_{bcc} particle, under vacuum conditions. The parameters for Fe_{bcc} in Eq. 2 are: melting entropy of bulk (S_{mb})= 7.63 J.mol^{-1}.K^{-1} [30]; melting enthalpy of bulk (H_{mb})= 13812 J.mol^{-1} [30]; melting temperature of bulk (T_{mb})= 1811 K [30]; molar volume (V_s)= 7.01x10^{-6} m^3.mol^{-1} [31]; atomic diameter (d)= 2.82x10^{-10} m [30]; lattice packing factor (P_L)= 0.68 [30]; surface packing factor (P_S)= 0.83 [30]; surface-to-volume coordination number ratio (q)= 0.25 [28]; shape factor (α)= 1 [28]. (c) Plot comparing the simulated diameters of Fe particle and those obtained experimentally by [33], at 700 ºC under vacuum conditions.

Fig. 1c compares the diameters (C_{pd}) of Fe particle simulated using Eq. 2 [28] and those obtained experimentally [33], for an annealing temperature of 700ºC under high vacuum (C_{pd} are approximately the same for 770ºC). It is observed an increasing difference between the experimental and the simulated values, $\Delta_{exp-sim}$ (%), with the increasing Fe thickness. The higher experimental values are related to the Ostwald ripening that consists on larger particles that

continued to grow at the expense of smaller ones nearby showing higher mobility [34]. For a higher metal amount the density of the particles is higher, increasing the probability of ripening between neighbour particles. For example, the annealing at 770 ºC of a 2 nm thick film (C_{pd}= 5.7) is expected to give an experimental average particle diameter ≥ 11.6 nm ($\Delta_{exp-sim}$= 51%). Nonetheless, in a realistic experimental setting the commonly used reductive H_2 atmospheres have a great contribution in the particle size distribution by enhancing the Ostwald ripening and surface diffusion mechanisms [35].

Bearing this in account, Fe films of Fe(0.5), Fe(1) and Fe(2) were used to ensure the production of small catalyst particles < 30 nm for the growth of safer CNTs (gray area in Fig. 1a).

3.1.2. *Controlling the Fe particle coarsening and Fe/Al$_2$O$_3$ adhesion strength*

To depress the Ostwald ripening or simple surface migration some strategies have been devised by others. Concerning the physical interactions, a sandwich arrangement Al_2O_3/Fe/Al_2O_3 [36] or a slightly rough surface [37], for example, helps on the particles stabilisation.

In the present work, the sputtering deposition of the Al_2O_3 layer was optimised (results not shown) to obtain a slightly roughed surface in a one step process. Fig. 2a shows the cross-sectional SEM image of a 100 nm Al_2O_3 layer, deposited on the Si/SiO$_2$ (200 nm) substrate, deliberately thick for better showing of the surface features.
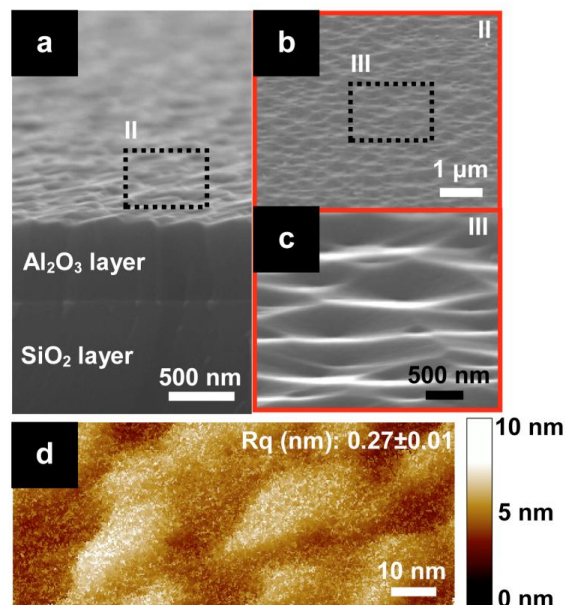

Fig. 2 - SEM images and AFM topographic images of the Al$_2$O$_3$ layer on the Si/SiO$_2$ substrate: (a) cross-sectional image of the Al$_2$O$_3$ layer; (b) tilted-view showing the regularity of the craters; (c) high magnification image of (b) showing in detail the morphology; (d) 3D AFM image of the surface topography.

At low-magnification, the 30º tilted Al_2O_3 surface presents regular craters with diameters of 240±77 nm that help to prevent the mobility of the nanoparticles (Fig. 2b). A detailed observation of this morphology is given by the high magnification image of Fig. 2c. The influence of the thickness of the Al_2O_3 film on the CNT yield is reported by Chakrabarti et al. [37]. The results showed that the yields did not vary significantly with the thickness, and the maximum yield value was achieved for a 10 nm thick film. Thus, in the present work, this value was kept constant at 10 nm. Typical AFM topographical analysis of a 10 nm thick Al_2O_3 film is depicted in Fig. 2d. It shows a smoother surface than the 100 nm thick film, with a R_q (root mean square roughness, rms) of 0.27±0.01 nm.

Besides the physical interactions, it was shown that chemical Fe-O bonds at the Fe/Al_2O_3 interface restrict the mobility of particles [25]. Hence, the H_2-reduction effect of the annealing treatment should be weak to preserve the interfacial oxygen of the Fe/Al_2O_3 interface and to avoid excessive coarsening of the Fe particle [35]. But, at same time, the reducing effect should be strong enough to break the Fe film and, at least, partially reduce the oxidised particles to become catalytic active at the growth front [25,38].

Concerning this balance and the semi-continuous growth (see Fig. 6 of section I.1.2) the time and annealing atmosphere and annealing time were optimised for Fe(0.5), Fe(1) and Fe(2) films. Three *in situ* treatment approaches, T1, T2 and T3, were studied in the hot-wall reactor at atmosphere pressure: Ar (T1); Ar/H_2 mixture (T2) and Ar + Ar/H_2 mixture (T3). The two-step treatment, T3, starts with Ar flow of 1000 sccm for 5 min (T1) followed by treatment T2.

Fig. 3a shows a set of SEM micrographs of the three types of as-sputtered films alongside with the T2 and T3 treated ones. For treatment T1 the samples were fast heated, by being quickly pushed to the hot-zone in a few seconds, and then exposed to the less reducing atmospheres of Ar (1000 sccm) for 5, 10 and 15 min. For all the treatments there were no apparent changes to the surface, showing a smooth morphology like the as-sputtered films (results not shown). These results reveal that Ar atmospheres, at temperatures as high as 770ºC, promote minor coarsening of the metal films, thus, prevent successful annealing treatments.

On the other hand, when a reductive H_2 flow was introduced into the reactive zone, treatment T2, the thin Fe films de-wetted on Al_2O_3 due to the higher surface energy of the Fe film when compared to the substrate ($\gamma(Fe)= 2.12$ $J.m^{-2}$ and $\gamma(Al_2O_3)= 0.155$ $J.m^{-2}$) [39,40]. Then, isolated nano-sized particles are formed (Fig. 3a) driven by minimization of the total free energy [41].

In treatment approaches using more reductive atmospheres, T2 and T3, the Ar and H_2 flows were kept constant at 200/500 sccm and the treatment time was varied from 0.5 to 5 min. The study of T3 was accomplished having in mind a semi-continuous approach for CNTs growth. As for T1 and unlike conventional TCVD methods where the pre-heating is achieved by heating the furnace, the substrates are quickly pushed to the hot-zone. This heating step does not visibly affect the surface since as was seen above, even after 15 min of treatment T1 there are no significant changes. This is a standard procedure that allows for enough time to carefully place the quartz boat in the right position inside the reactor without greatly affecting the CVD process.

Comparing the morphology of the particles after 5 min of T2 and T3 treatments it can be seen that they are nearly of the same size but the ones obtained for T2 have slightly lower density which means that the Fe film did not fully de-wet into particles (Fig. 3a).

The bubble colour graphics in Figs. 3b and 3c compares the efficiency of active catalyst particles for the CNT growth. The average values are discriminated by colour and diameter of the bubble, and the black contour represents the upper limit of the standard deviation. For a correct comparison of values it should be consider the colour and the outer diameter of the bubble. The CNT heights obtained with treatment T3 are higher than the ones obtained with T2 for all treatment durations. It can also be seen that, for all the film thicknesses, the best growth yields using the T2 were achieved for longer treatment times (3 min) when comparing to T3 treated ones (1min). Moreover, for T3 treatments longer than 1 min the growth yields are larger for the thicker Fe films. These observations prove that in the semi-continuous growth process, the pre-heating (T1) of the Fe film helps to maximise the following etching effect of the H_2 treatment (T2).
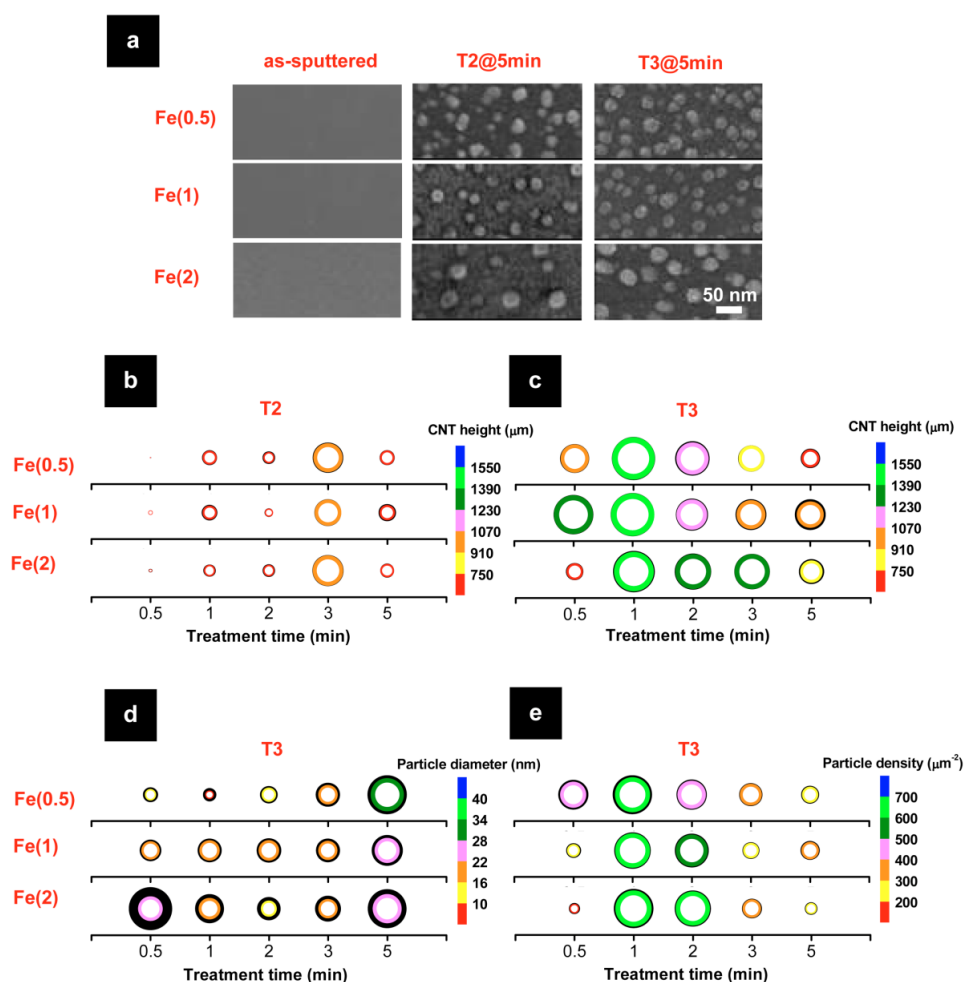
Fig. 3 - (a) SEM images of the as-sputtered Fe(0.5), Fe(1) and Fe(2) films and annealed with the T2 and T3 treatments for 5 min. (b and c) Bubble colour graphics showing the influence of the T2 and T3 annealing times on the CNT height. (d and e) Bubble colour graphics illustrating the dependence of the diameter and density of the particles on T3 annealing time.

138

For the three films subjected to treatment T3, the particle diameter and density evolution with the treatment time are presented in Figs. 3d and 3e, respectively.
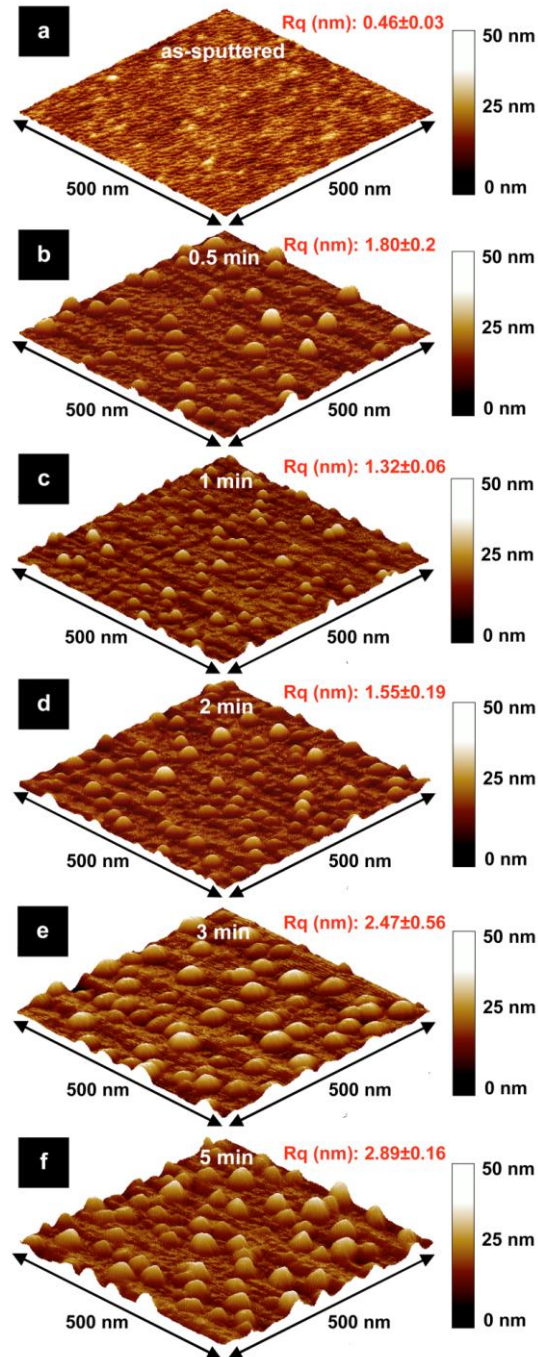
Fig. 4 - 3D AFM images evolution of the Fe particle topography with the T3 annealing time for Fe(1): (a) as-sputtered; (b) 0.5 min; (c) 1 min; (d) 2 min; (e) 3 min; (f) 5 min.

Overall, round particles show regular spatial arrangement with diameter sizes and densities in the range of 10-30 nm and 172-635 μm^{-2}, respectively. The diameters of the particles increase

for thicker Fe films and for longer treatments, having a minimum for 1 min. The evolution of particles density with treatment time shows the opposite trend of the diameter size, Fig. 3e.

AFM topographical analysis of Fe(1) film treated by T3 were done to further understand the effect of the H_2 exposition time on the formation of the Fe particle (Figs. 4, 5 and 6). The 3D AFM images in Fig. 4 illustrate the increasing roughness of the Fe film with the H_2 exposition time.

Complementary, side views of AFM scans of the treated substrates are shown in Fig. 5a. Overall, the Fe particles present similar geometry. Though, the presence of artefacts due to the curvature radius of the AFM tip of ~10 nm cannot be neglected, the line profile of an individual particle gives approximately a cone trunk geometry with a top diameter smaller than the one of the bottom (Fig. 5b). EDS spectra were taken on the substrate (Al_2O_3 top layer) and the particle (inset of Fig. 5c) to prove that the analysed particle is in fact Fe (Fig. 5c).
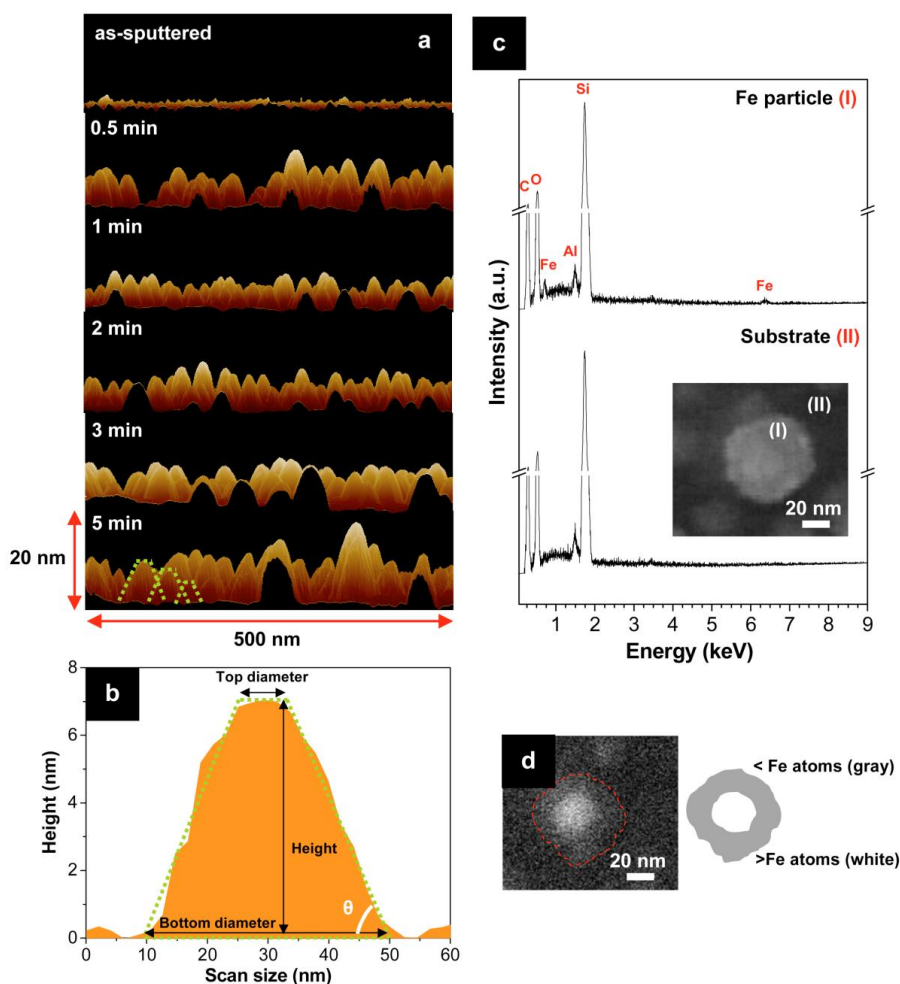
Fig. 5 - (a) Cross-sectional AFM images of the Fe particle to assess their geometry evolution with the T3 annealing time for Fe(1). (b) Scan profile of an isolated Fe particle depicting a cone trunk geometry; (c) EDS spectra of (b) and Al_2O_3 substrate; (d) backscattered image of (b).

The respective backscattered image of the particle (Fig. 5d) provides the element contrast information. The gray area does not correspond entirely to an oxide layer because its thickness is expected to be much thinner ~2-4 nm [42]. Thus, it is assumed that the centre part (white area) has a higher number of Fe atoms than the surrounding part (gray area) which confirms the proposed cone-shaped geometry.

The evolution of the height and the d_{top}/d_{bottom} ratio of the particle with the H_2 exposition time are depicted in the graphic of Fig. 6a. Overall, it can be seen that there is an increase of the height of the particles, most likely due to the short-distance diffusion of Fe atoms from the bottom to the top. Moreover, two behaviours are observed. Up to 3 min of H_2 exposition, the slight increase of the height and the d_{top}/d_{bottom} ratio reveals that particles become slightly flat (i.e. increase of the curvature radius) [35]. On the other hand, for 5 min the significant increase of the particle height and the decrease of the d_{top}/d_{bottom} ratio indicate that the particles become sharper and bigger (Fig. 6a). AFM images of Fig.s 4 and 5a help to visualize these behaviours.
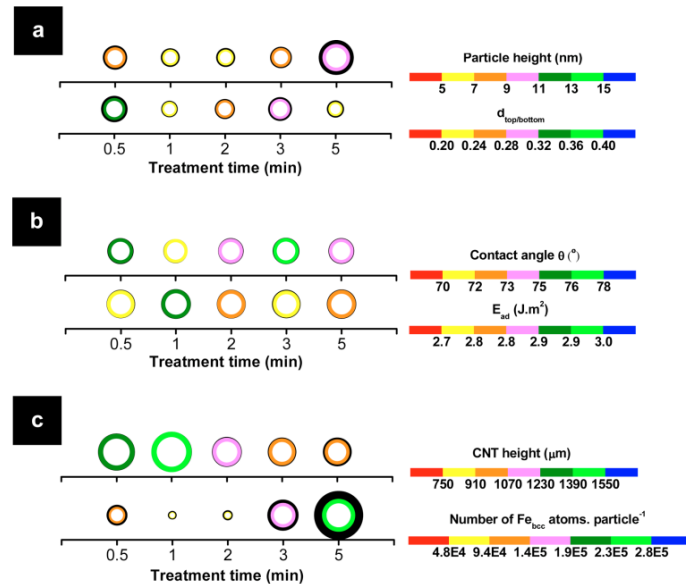
Fig. 6 - Bubble colour graphics illustrating the influence of the T3 annealing time on the characteristics of Fe particle for Fe(1): (a) d_{top}/d_{bottom} ratio and height; (b) contact angle and adhesion energy (E_{ad}); (c) number of atoms per particle and its correlation with the growth results of Figure 3c.

Fig. 6b shows the variation of the contact angle θ (illustrated in Fig. 5b) and the respective E_{ad} with treatment time. The measured angles in the range of 72-76º (108-104º) are larger than the AFM tip angle which indicates that the line profiles are real and not merely artefact. The adhesion energy (E_{ad}) between the Fe particle and the Al_2O_3 substrate was calculated by the Young-Dupre equation [41],

$$E_{ad} = \gamma_{np}(1 + \cos\theta) \qquad (3)$$

where θ is the contact angle of the solid Fe particle, in degrees, and γ_{np} is the surface energy of the particles. Additionally, since the E_{ad} ($J.m^{-2}$) is calculated at the annealing and growth temperature of 770 °C, the $\gamma_{np}(T)$ was determined as follows,

$$\gamma_{np}(T) = \gamma_{np}(T_0) + (T - T_0)\frac{\delta\gamma_{np}}{\delta T}\bigg|_{T_0} \qquad (4)$$

where T_0 is the melting temperature, in Celsius degrees. For Fe the $\gamma_{np}(T_0)$ and $(T-T_0)\frac{\delta\gamma_{np}}{\delta T}\bigg|_{T_0}$ are 1.88 $J.m^{-2}$ and -0.00043 $J.m^{-2}.°C^{-1}$, respectively [41].

The Fe/Al_2O_3 system has a E_{ad} in the range of 2.73-2.92 $J.m^{-2}$ (Fig. 6b), much higher than the Fe/SiO_2 system of 0.8 $J.m^{-2}$ [41]. Additionally, in general, the E_{ad} decreases with H_2 exposition time (Fig. 6b). Surprisingly, for 5 min it can be seen a slight increase of E_{ad}. This can be explained by the sharpening of the particles, as described above, which decreases the θ angle. However, the ripening mechanism becomes significant above 3 min of exposure, leading to the increase of the number of Fe atoms per particle (Fig. 6c). Therefore, it is expected the reduction of the interfacial oxidation states Fe^{2+} and Fe^{3+} for longer H_2 exposition and the decrease of the E_{ad}.

To prove this, the growth results of Fig. 3c for 1 nm thick Fe films were plotted together with the number of Fe atoms per particle (Fig. 6c). For the same growth condition, there is an inverse correlation between the CNT height and the number of Fe atoms per particle (size of the particle), as reported in [43]. Accordingly, the smallest starting particles have the highest growth yield (T3: 1min) (Fig. 6c). However, the particles obtained using T3: 2min, with a similar starting particle size to that of T3: 1min, presents much lower growth yield. This indicates that for annealing times above 1 min the particles start to lose their interfacial oxygen that leads to the increase of their initial size when exposed to C_2H_2 during the growth step and, ultimately, to the decrease of the growth yield. Similar results were reported by others [35].

Summarizing, the treatment T3: 1min presenting the highest ability to produce nano-sized catalyst particles was used into the following CNT growth studies.

3.1.3. Optimizing the CNT growth parameters

The growth of CNTs in a horizontal hot-wall reactor involves complex interactions between the homogeneous gas-phase and heterogeneous surface reactions [44]. Recently, Ma et al. proposed a simple CNT growth model using these reactors, a gas mixture of C_2H_2-Ar and Fe catalyst particles [43]. Concerning the C_2H_2 pyrolysis, it was found that the C_4H_4 species is the main gas-phase product and has an important contribution to the CNT growth process. Thus, C_2H_2 and C_4H_4 species are the main carbon sources involved in the surface reactions [43]. These

species are firstly adsorbed and dissociated on active sites of the Fe particle surface accordingly to the following equations,

$$C_2H_2 + S(s) => C_2(s) + H_2 \qquad (5)$$

$$C_4H_4 + S(s) => C_4(s) + 2H_2 \qquad (6)$$
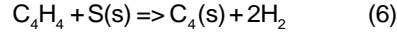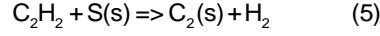
where $S(s)$ is the active site on the Fe catalyst particle, and C_2 and C_4 are the Fe-C solid solutions. The rates of the reactions above can be determined by,

$$q = \sqrt{\frac{RT}{2\pi W_i}} \frac{A^*}{\rho_0} \gamma_T \, [C_xH_x][S(s)] \qquad (7)$$

where R is the radius of catalyst particles and CNTs, T is the temperature, W_i is the molar mass of the ith species, A^* is the fraction of substrate surface covered by Fe particle, ρ_0 is the density of active sites (cm^{-2}) and γ_T is the ratio between the carbon atoms entering into the Fe particle and the carbon atoms colliding on the Fe particle. Carbon diffuses in the Fe lattice forming the C_2 and C_4 solutions and ends up precipitating in the form of CNTs as follows,

$$C_2(s) => 2C\,(CNT) \qquad (8)$$

$$C_4(s) => 4C\,(CNT) \qquad (9)$$
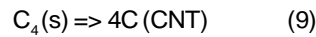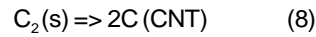
The carbon precipitation rate is converted to the CNT growth rate (GR_{CNT}) per Fe particle [43,45] accordingly to

$$GR_{CNT} = \frac{(2q_{c_2} + 4q_{c_4})V_c}{\frac{\pi}{4}\rho_{Fe\,particle}(d^2_{outer} - d^2_{inner})} \qquad (10)$$

where q_{c2} and q_{c4} are the reaction rates of C_2 and C_4, respectively, V_c is the atomic volume of carbon ($cm^3.mol^{-1}$), ρ is the density of Fe particle (cm^{-2}), d_{outer} and d_{inner} are the outer and inner diameters of the CNT.

Previous reports by others showed that higher growth temperature in the range of 750-950ºC results in combined high quality and yield of CNTs [46]. Concerning this and the maximisation of the catalyst particles lifetime, a set of preliminary experiments were accomplished at moderate temperature, 770 ºC. The CNT heights for each CVD condition were plotted in a colour

mapped graphic in Fig. 7a. Each height value corresponds to a (x,y) position without physical significance. The largest CNT height was obtained for the partial pressure p_{C2H2} and p_{H2} of 2 and 19.6 kPa, respectively (condition A, black dot in Fig. 7a). This condition was further optimised to obtain high outputs with high crystallinity over large areas. Therefore, and according to Eqs. 5-10, the growth temperature, the p_{C2H2} and p_{H2}, and the total flow (influence of the γ_T ratio) were varied around that of condition A.
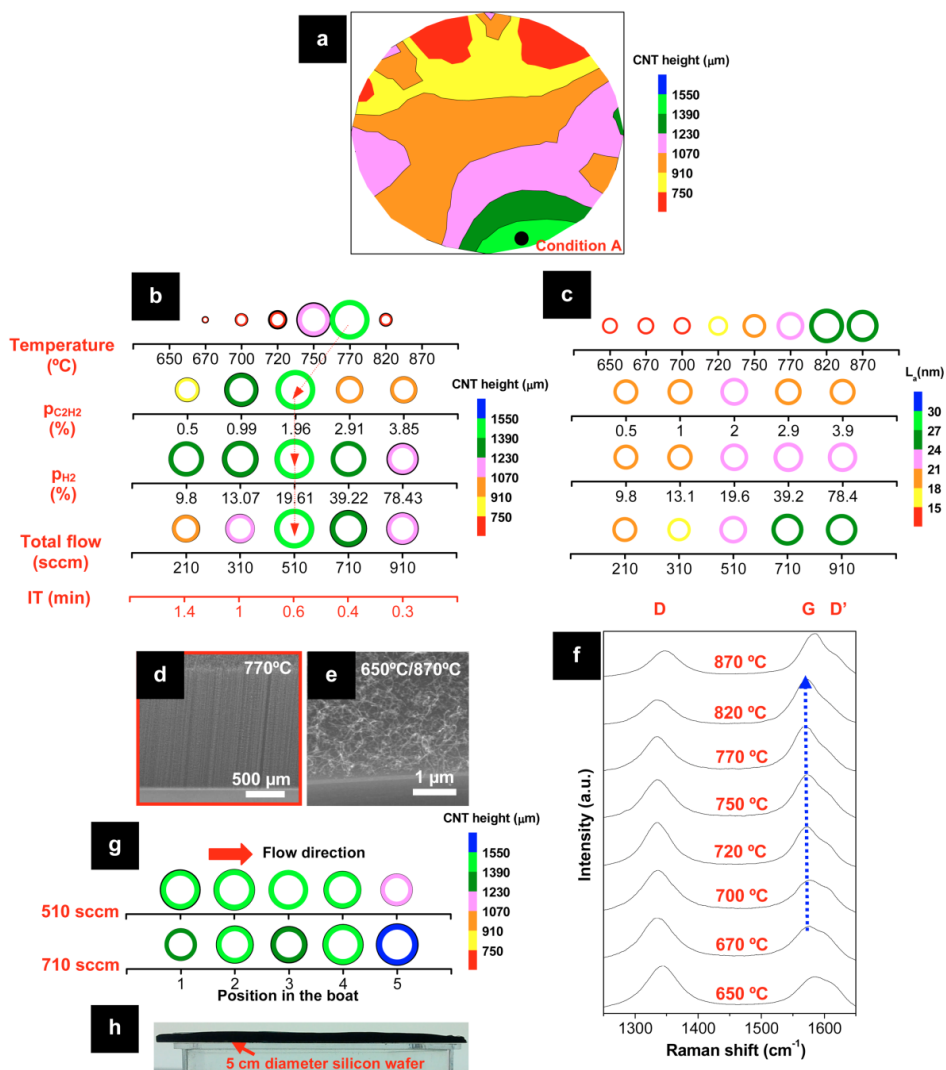
Fig. 7 - (a) Colour mapped graphic compiling the CNT height data of preliminary growth studies. The best growth condition found was the condition A represented with a black dot. (b and c) Bubble colour graphics illustrating the influence of the varied growth parameters around that of condition A on the CNT yield and crystallinity, estimated by the graphite in-plane crystallite size (L_a), using a Fe(1). (d and e) Representative SEM images of CNT forests grown at different temperatures. (f) Visible micro-Raman spectra evolution, taken at the top of the CNT forests, with the growth temperature variation. (g) Bubble colour graphic showing the variation of the CNT height with the position in a 15 cm long boat for two different total flows. (h) Cross-sectional photography of a millimetre-long CNT forest grown with condition A on a 5 cm wafer showing the uniformity of the height over large areas.

The evaluation of the CNT structure crystallinity was assessed by micro-Raman using a laser excitation energy (E_l) of 2.33 eV (532 nm). The spectra were baseline corrected by linear background removal and then normalised to the maximum intensity of each spectrum, all peaks having been fitted with a Lorentzian line-shape. The CNT crystallinity was estimated by calculating the graphite in-plane crystallite size (L_a) using the Cançado's equation as follows [47].

$$L_a \text{ (nm)} = (2.4 \times 10^{-10}) \lambda_l^4 \left(\frac{I_D}{I_G} \right)^{-1} \qquad (11)$$

Figs. 7b and 7c compile the influence of the growth parameters referred above on the GR_{CNT} and crystallinity, respectively, using a 1 nm thick Fe film. The optimal condition obtained for each growth parameter studied was selected, considering the best balance between GR_{CNT} and crystallinity, and was then maintained constant for the optimisation of the following parameters. The selected pathway is marked by red arrows in Fig. 7b. Surprisingly, the best growth condition found was the condition A already established in preliminary experiments. Nonetheless, it is important to note the influence of each growth parameter. Overall, the temperature, p_{C2H2} and total flow parameters have major roles in the yield and crystallinity of the CNTs.

Fig. 7b shows the variation of the CNT height with the temperature. The upper limit of the CNT height is achieved at 770 ºC. The respective SEM image of the forest is illustrated in Fig. 7d. For the extremes of the temperature range the yield drops and only randomly oriented CNTs are observed (Fig. 7e). The model proposed by Ma et al. suggests an optimum growth temperature at 700 ºC using C_2H_2-Ar gas mixtures [43]. This proves that the dissolution and diffusion (including in the bulk) mechanisms are fully activated at 700 ºC [43]. In the present work, the excess of H_2 and the total amount of H_2O present in the system (3-15 ppm) contribute to a more efficient elimination of carbonaceous deposits [48]. As a consequence, the optimum growth temperature can shift to slightly higher temperature values.

At lower temperatures (<770ºC) the amount of [C_4H_4] is not significant [43] and the carbon [C_2] at the surface of the Fe particle seems too low due to the etching effect of H_2. Consequently, this gives lower q_{c2} and q_{c4}, thus lowering GR_{CNT}. At high temperatures, 820 and 870ºC, the pyrolysis of the C_2H_2 molecules cannot be neglected [43]. At 800-850ºC the contribution of C_4H_4 to the CNT growth increases ~6% when comparing to the optimised growth temperature, 700ºC [43]. At high temperature, the excess intake of C_4 probably poisons the catalyst particles and the CNT height decreases.

The evolution of the CNT structure crystallinity with the growth temperature is depicted in Fig. 7f. The spectra show that all samples present asymmetric strong peaks around ~1580 cm^{-1} (G band: E_{2g} stretching mode of the graphitic crystalline structure). The shoulder at higher wavenumbers around ~1618 cm^{-1} (D'-band: graphite in-plane disorder) is typical of defective graphite-like structures such as multi-walled CNTs (MWCNTs) [49]. For lower wavenumbers it is shown another band around ~1350 cm^{-1} is shown (D band: arising from lattice disorder). These

bands show a notorious trend with the growth temperature evolution. For increasing temperatures the intensity of the D and D' bands decrease and the G band increases. The intensity of G band becomes higher than D band at 720 ºC. Also, it is interesting to note the increase of the deviation of G band to lower wavenumbers (dashed dark blue line) for increasing temperature in the range of 670-820ºC which is related to the increase of the structure order [50]. This gives full evidence of the CNT crystallinity increasing with the growth temperature, as it was found earlier [46]. These observations are well supported by calculating the graphite in-plane crystallite size (L_a) using the Eq. 11. The graphic in Fig. 7c shows the increasing of the sp^2 domain size with the increasing growth temperature reaching a maximum at 820 ºC. More organised graphitic stacked forms are obtained at higher temperatures due to the annealing of defects [19]. Also, at higher temperatures, the excess of C species in the gas-phase leads to the formation of disordered carbons like a-C on the CNT side-walls that provoke the increase of the I_D/I_G ratio [17,19]. At 870 ºC, the amount of these deposits overcomes the benign annealing effect of the temperature, thus giving more disordered structures and smaller L_a.

The previous temperature studies suggest that the maximization of the GR_{CNT} in a H_2-containing growth atmosphere deals with the commitment between the amounts [C_2] and [C_4] and the H_2 etching effect on the active sites of the Fe particle. Considering this, and the fact that C_2H_2 is a source of C and H_2 (Eq. 5) it is relevant to optimise the p_{C2H2}. Thus, the p_{C2H2} was varied around that of condition A to find the best p_{C2H2} to grow CNTs at 770ºC under a constant H_2-containing atmosphere (p_{H2}= 19.6 kPa). Fig. 7b shows that the highest CNT height is obtained at p_{C2H2}= 2 kPa (condition A). For p_{C2H2}< 2 kPa it can be seen that the growth yield decreases with the p_{C2H2} decreasing. For these conditions the [C_2H_2] and [C_4H_4] on the surface of the Fe particle apparently are too low decreasing the [C] species entering into the Fe particle. Moreover, for p_{C2H2}> 2 kPa the CNT height also decreases. In this case, the excess of C species decreases the fraction of vacant active sites leading to a fast poisoning of the Fe particle. Additionally, these C deposits formed on the CNT-particle interface and CNT side-walls can induce the formation of turbostractic structures resulted from the uncorrelated 2D graphene layers stacking. Noting, the curve in the graphic of Fig. 7c shows that the CNT height is mirrored by the L_a value, as discussed above.

To help on the control of the etching of a-C impurities the p_{H2} (extra H_2 flow source) was also optimised. Fig. 7b shows that the p_{H2} was varied around that of condition A and the p_{C2H2} was kept at 2 kPa. There is no significant variation in the GR_{CNT} and L_a values (Figs. 7b and 7c). The highest GR_{CNT} is still obtained for the H_2 partial pressure used for condition A.

Bearing in mind the TCVD reactors, a dynamic flow passing over the substrates widely affect the CNT growth, in accordance to its flow regime. The Reynolds number of the quartz tube filled with a C_2H_2-H_2-Ar gas mixture was calculated as follows [51],

$$Re = \frac{\rho_m u_m d_{inner}}{\mu_m} \qquad (12)$$

146

where ρ_m is the density (kg. m^{-3}), u_m is the mass flux (m.s^{-1}) , d_{inner} is the inner diameter of the quartz tube (m) and μ_m is the dynamic viscosity (kg.m^{-1}.s^{-1}). The density of the gas mixture is determined as

$$\rho_m = \sum_{i=1}^{n} \rho_i \alpha_i \qquad (13)$$

where ρ_i and α_i are the density and volume fraction of the ith gas phase, respectively. Moreover, the dynamic viscosity of the gas mixture is obtained by the Wilke's equation [52] as follows,

$$\mu_m = \frac{\sum_{i=1}^{n} \mu_i}{1 + \sum_{\substack{j=1 \\ j \neq i}}^{n} \frac{X_j}{X_i} \phi_{ij}} \qquad (14)$$

and Wilke's parameter, ϕ_{ij}, was corrected by Saxena's equation to high temperature range [53] according to

$$\phi_{ij} = \frac{\mu_i M_j}{\mu_j M_i} \frac{50M_i + 33M_j}{33M_i + 50M_j} \phi_{ji} \qquad (15)$$

where μ_i, X_i and M_i are the dynamic viscosity, mole fraction and molecular mass of the ith phase, respectively. For the total flow range studied the Re varied from 0.88 to 3.82 which indicates a laminar flow regime. This allows a better control of the growth kinetics in larger areas. Similar values were compiled by Moisala et al. for hot-wall reactors [20].

The curve in the graphic of Fig. 7b shows the influence of the total flow or the interaction time (IT, red scale in Fig. 7b) on the CNT height. Here, IT is defined as the time that a new flow front needs to cross the boat length of 15 cm in the flow direction. The P_{C2H2} and P_{H2} were kept at 2 and 19.6 kPa, respectively, according to condition A. The maximum of GR_{CNT} is once more obtained for the condition A. It seems that 0.6 min is the interaction time that gives the best balance between the formation of C species (Eqs. 5 and 6) and their precipitation (Eqs. 8 and 9) and the H_2 etching effect to keep active the Fe particle, resulting in uniform CNT forest over the entire substrate surface. For condition A, and a substrate of 5 x 5 mm^2 with a catalyst particle density of 6 x 10^{10} cm^{-2}, obtained for Fe(1), a new flow front collides with 7 x 10^4 particles perpendicular to the flow direction in 7.3 x 10^{-6} s. For IT>0.6 min C_2H_2 and C_4H_4 contact with active sites of Fe particle for longer times leading to an excess of C species that, ultimately, lead to the fast poisoning of the active sites and to the decrease of CNT growth rate. Consequently, less organised structures are obtained for lower total flows as is suggested by the decrease of L_a for smaller total flows, Fig. 7c. For IT< 0.6 min the total flow is too large to allow the hydrocarbon molecules to have sufficient time to interact with the Fe particle originating a decrease of the CNT growth rate. The graphic of Fig. 7c illustrates the increase of L_a for larger total flows because of the easily drag out of excess C species from the surrounding environment of the particles. This effect is depicted in Fig. 7g that

shows the variation of the CNT height with the sample position in a 15 cm long quartz boat for two different total flows: 510 and 710 sccm. Numbers 1 to 5 correspond to the position of five substrates of 5 x 5 mm^2 with a 1 nm thick Fe film disposed along the boat with a distance between them of ~3 cm. It is worth reminding that data from Fig. 6e in the Section I.1.2 shows that the furnace temperature is constant for the length of the boat. Ma et al. show that there is a drop of the mole fraction of C_2H_2 and C_4H_4 species when they interact with the catalytic surface [43]. Thus, for larger total flow (lower IT) the CNT height is smaller and increases from position 1 to 5 (coefficient of variation of 9%). This means that the C species at the first samples were not fully consumed and are accounted in the CNT growth process on the substrates further away. For smaller total flows the CNT height decreases with the increasing distance to the flow entrance due to the fast consumption of the C species on each substrate (coefficient of variation of 10%). If the p_{C2H2} decreases from the position 1 to 5 it means that the reaction probability (γ_T) also decreases as well as the CNT height in the same direction. Fig. 7g shows that for the first four positions in the quartz boat (length of ~ 10 cm) the CNT heights are more uniform using a total flow of 510 sccm (condition A) than 710 sccm. As result, a nearly uniform CNT forest can grow on a total area equivalent to a 5 cm diameter wafer cut in two parts and disposed on the quartz boat at the positions 1 to 4 (length of ~10 cm). A representative cross-sectional photography of CNT forest grown on one of the parts of the wafer it is shown in Fig. 7h. Thus, by controlling the interaction time between the C species and the Fe particle it is possible to make the best use of the available C species and them achieve a better control of the CNT height over large growth areas. Though, for the highest total flow the removal of C is probably too much and the L_a decreases (Fig. 7c). Additionally, the increasing of the CNT structure disorder can be also due to the increased turbulence of the gas flow, as the larger Re number implies.

Besides the influence of the growth parameters on the CNT yield, the starting Fe film thickness has also an important contribution. The film thickness dictates the size of the catalyst particles, as shown in Section 3.1.1, and consequently the surface density of active sites [43] that influence the carbon uptaking and etching equilibrium on their surfaces. For an easier viewing of this effect, the CNT yield data of the Fe(0.5), Fe(1) and Fe(2) films were plotted in colour mapped graphics depicted in Figs. 8a-c. Each map was created by plotting the CNT heights resulted from a parametric study equivalent to the one showed in Fig. 7b for the Fe(1) (corresponds to the map in Fig. 8b). By comparing the colours of the maps it becomes evident that the yield data of Fe(1) and Fe(2) are analogous and superior to Fe(0.5) for the studied conditions. In addition, Fe(1) presents a wider range of growth conditions that give higher CNT yields than Fe(2) - bigger light green area. Also, it can be observed that the dark and light green areas have the same position in the maps which means that the best growth conditions found are reproducible irrespective of the film thicknesses.
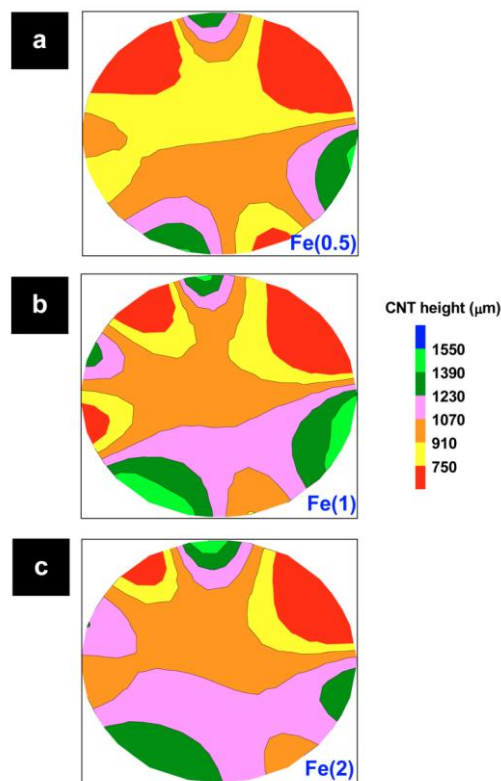
Fig. 8 - Colour mapped graphic compiling the data studies of the growth parameters for Fe(0.5), Fe(1) and Fe(2) films.

3.2. Upscaling potential of the catalyst-supported CVD method to produce safer CNTs

3.2.1. CNTs with tailored morphologies

CNT length widely influences its toxicological profile (see Section I.3.3). Hence, to produce safer CNTs it is essential to further investigate the growth kinetics and mechanism.

The growth kinetics of CNT forests can be limited by diffusion of gases molecules through the CNT film, as adopted from the Deal-Grove model by Zhu et al. [54] (dashed light blue line in Fig. 9a), or by a decaying reaction rate of the catalyst particles, following a radioactive decay-like model proposed by Hata and coworkers [55] (dotted green line in Fig. 9a). Both curves were obtained at 750 ºC under very similar growth conditions, but there is an important difference in the two experimental procedures. Zhu et al. used an interrupted growth mode with efficient etching steps combining H_2O and H_2 between CNT growth steps [54]. This strategy allowed the etching of amorphous carbon existing at the CNT-catalyst interface. Therefore, under these conditions the CNT growth is merely limited by the Knudsen diffusion of gases through the densely packed CNT films. Conversely, in a standard growth run accomplished by Hata et al. [55], even using H_2O as etching agent, the poisoning of the catalyst with amorphous carbon took place leading to the loss of the catalyst reactivity and its decay.
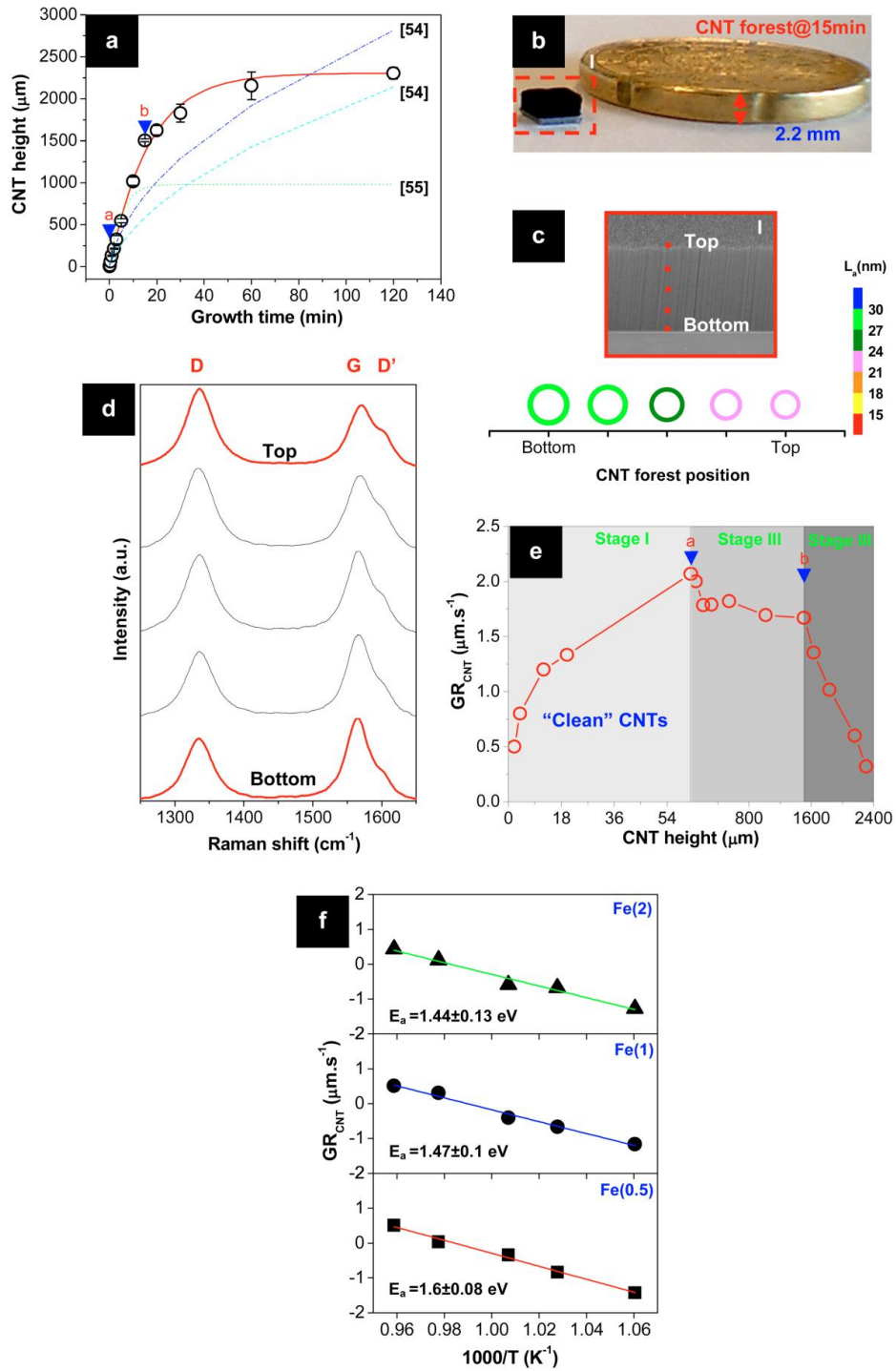
Fig. 9 - (a) Plot showing the CNT forest height as a function of the growth time. The solid red line corresponds to the best fit of Eq. 6 to the experimental data points obtained for the best growth yield condition (condition A) on 1 nm thick Fe film. The dashed light and dark blue lines corresponds to the Zhu's data at 750ºC (B= 5.09 x 10^4 $\mu m^2.min^{-1}$; A= 714 μm) and 770ºC (B= 7.9 x 10^4 $\mu m^2.min^{-1}$; A= 552 μm) [54] and the dotted green line represents the Futaba's data at 750 ºC (β= 207 $\mu m.min^{-1}$; τ_0= 4.74 min) [55], respectively. (b) Photograph comparing the height of the millimetre-long CNT forest of (a) grown for 15 min on a Si substrate to a 2.2 mm height EUR 20c coin. (c) Bubble colour graphic showing the CNT in-plane crystallite size

evolution along the cross-sectional direction of the CNT forest of (b) and respective (d) visible micro-Raman spectra. (e) Plot depicting the evolution of the growth rate with the CNT height, obtained by using the data of (a). (f) Arrehenius plot for the growth rates of CNT forests grown on Fe(0.5), Fe(1) and Fe(2) films with condition A, providing the activation energies of 1.6±0.08 eV, 1.47±0.1 eV and 1.44±0.13 eV, respectively.

In the present work, the experimental data obtained at 770ºC with the best growth condition, A, and using a 1 nm thick Fe film is well fitted by Hata's model with a R^2 = 0.996 (solid red line in Fig. 9a). According to this model the time evolution of the CNT height is expressed as follows,

$$h_{CNT} = \beta\tau_0(1 - e^{-t/\tau_0}) \qquad (16)$$

where h_{CNT} is the height of the CNT forest (µm), t is the growth time (min), β is the initial growth rate corresponding to the linear rate (µm.min^{-1}) and τ_0 is the catalyst lifetime.

For the growth condition used the fitting parameters β and τ_0 were 139 µm.min^{-1} (2.32 µm.s^{-1}) and 16.6 min, respectively. Additionally, the theoretical maximum height obtained for this growth condition is given by $h_{CNTmax} = \beta\tau_0$ = 2304 µm which is in excellent agreement with the experimental value of 2300 µm. Comparing this value with h_{CNTmax}= 2800 µm, obtained by the curve of Zhu et al. [54] at 770 ºC (dashed-dotted dark blue line in Fig. 9a), also the best growth temperature achieved, it can be denoted the good kinetics of growth condition A because the catalyst is active for a long time with a behaviour similar to that of a purely diffusion limited growth. This is also confirmed by the increase of 2.5 times of our catalyst lifetime when compared to the best value reached by Hata [55]. This means that our growth condition has a good commitment between the carbon flux into the particle and the etching effect of the H_2 on its surrounding. A typical photography compares a CNT forest on a Si substrate grown with condition A for 15 min to a 2.2 mm height EUR 20c coin (Fig. 9b).

Raman spectra were taken along the cross-sectional direction of the CNT forest of Fig. 9b to further investigate the growth kinetics. The respective inset SEM image of Fig. 9c illustrates the acquisition positions of the spectra. The L_a size and corresponding evolution of D, G and D' bands are shown in Figs. 9c and 9d, respectively. It can be seen that the CNT crystallinity improves from the top to the bottom position, a fact also reported by others [56]. This occurs due to the accumulation of carbonaceous impurities at unsaturated CNT side-walls, also responsible for the deterioration of the CNT quality over growth time, accordingly to a full comprehensive investigation by Yasuda et al. [56].

Therefore, in view of the fact that the mass transfer during the growth process involves obligatory the C species collision through the CNT forest to reach the catalyst particles [57] it is reasonable to assume that the exposition time and growth conditions determine the amount of carbonaceous impurities at the CNT surface [56]. This assumption is well supported by the growth rate evolution with CNT height depicted in Fig. 9e. Initially (stage I, light grey area), the growth rate

of CNTs increases with the CNT height up to 62 μm (30 s). A short exposition time to C species results on almost a-C free CNT walls ("clean" CNTs) that helps to maximize the surface diffusion of chemisorbed C species on the CNT walls, according to Louchev et al [57]. This path of mass transfer has a great contribution to the growth even at the earlier stages ($h_{CNT} \approx d_{particle}$) due to the low activation energy E_a= 0.13 eV [57].

Above 30s (stage II, dim grey area), the forest began to get "dirty" acting the C deposits, stacking layers and particles [56], as barriers to the diffusion of new C species on the CNT surface. The growth rate starts to decrease slowly until reaching 1500 μm height (15 min) and then falls abruptly up to h_{CNTmax} (stage III, dark grey area). This is consistent with recent modelling studies [23]. It was found that MWCNT forests with similar density to those of the present work start to have some diffusion limitations above 1 mm height, but strong limitations occur only above 1 m long, accordingly to the classic Knudsen theory [23]. Regarding these observations it is reasonable to suppose that C species accumulation on the CNT side-walls end up by limiting the growth kinetics, according to the decay mechanism described above, not only due to the poisoning of the Fe particle [55] but also to a lack of C influx at the catalyst.

In order to better understand the CNT growth kinetics the associated activation energies were calculated for each Fe film thickness. Fig. 9f shows the Arrhenius plots of the growth rate obtained for the temperature range of 670-770ºC. Activation energies of $E_{a(Fe0.5)}$= 1.6±0.08, $E_{a(Fe1)}$= 1.47±0.1 and $E_{a(Fe2)}$= 1.44±0.13 eV were extracted from the slope of the linear correlation between the $\ln(GR_{CNT})$ and the reciprocal growth temperature.

More comprehensive information on the growth mechanism of MWCNTs from C_2H_2 decomposition on Fe catalyst was given by recent *in situ* HRTEM observations [58]. This indicates that carbon density is homogeneous at all ends and therefore, it is most likely that C atoms supplied on the open surface area of the Fe particle diffuses in its bulk rather than on its surface, and precipitates at the opposite side. This is in agreement with several works, compiled in [59], postulating that the C diffusion in the bulk of the Fe particle is the rate-limiting step of the CNT growth process.

The C bulk diffusion to form filamentous carbon can occur at 627 ºC in either a carbide, metallic or oxide Fe depending on the P_{H2}, P_{O2} and P_C of the gas mixture used, accordingly to Sacco et al. [60]. Here, the presence of oxidised states on the open surface area of the Fe particle, not in the Fe-Al_2O_3 interface, as proved before, can be unnoticed because of the efficient co-reducing effect of the H_2 and C_2H_2 [61]. Also, it is consistent to think that nano-sized Fe particle during the growth step at 670-770ºC showing C solubility above 0.75 wt.% are present in the γ-Fe phase or as Fe_3C [29]. The activation energies for the C diffusion in the bulk of these phases are ~1.52 eV [62] and ~1.79 eV [63], respectively. This means that for the growth condition A, and accordingly to the activation energies shown in Fig. 9f, the γ-Fe phase plays a major role in determining the GR_{CNT} as earlier observed by others [59,64]. Yet, for C-richer atmospheres the Fe_3C is the main phase involved in the CNT growth [58,61].

Beyond the CNT length, the outer diameter size and number of walls has an important influence on the CNT toxicological profile (see Section I.3.3). Inset SEM images of Figs. 10a-c show the CNTs with small diameters in the 14-16 nm range.
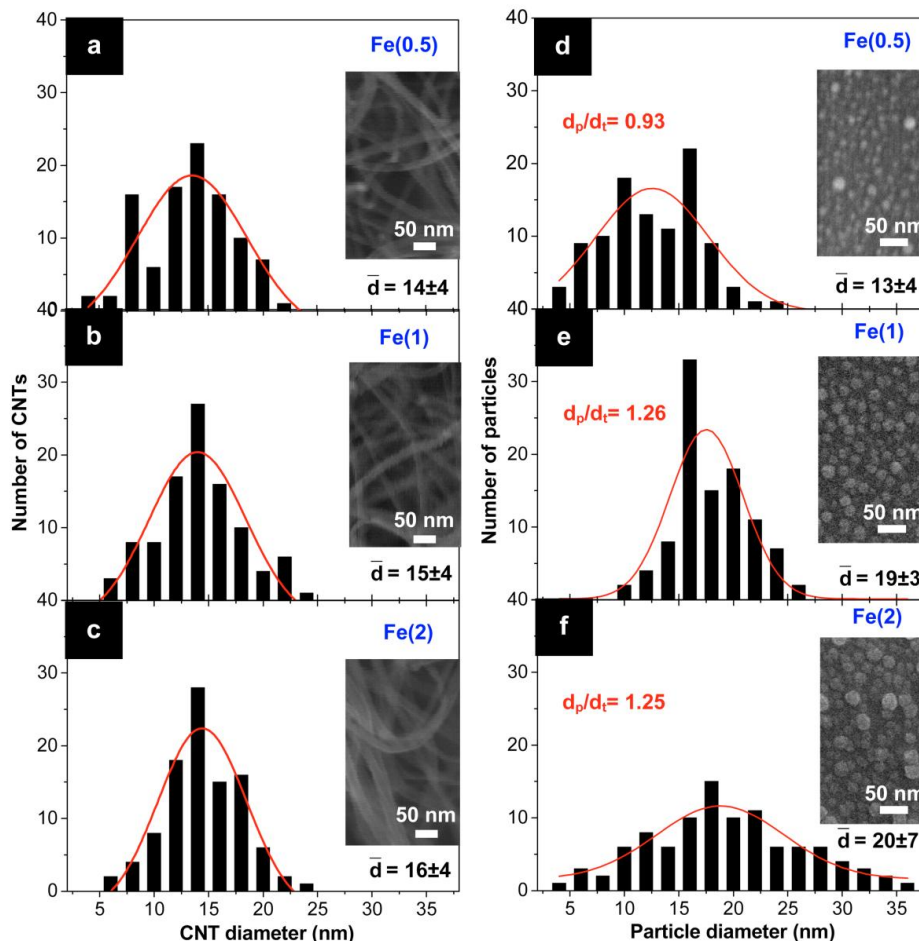
Fig. 10 - Plots showing the statistical size distribution of the (a-c) outer diameter of millimetre-long CNTs grown with condition A and the (d-f) initial Fe particle bottom diameter obtained by T3: 1 min annealed Fe(0.5), Fe(1) and Fe(2) films.

These diameter sizes are in accordance with the ones showed in a previous study reporting similar experimental conditions [65]. MWCNTs with almost constant outer diameters of ~ 14 nm were grown on 0.5, 1 and 2 nm thick Fe films [65]. The respective narrow diameter size distributions following Gauss-like curves are given for the three Fe film thicknesses in Figs. 10a-c. Figs. 10d-f show the diameter size distributions and the insets images are SEM micrographs of the particles obtained for the Fe(0.5), Fe(1) and Fe(2) films under condition T3: 1min (Section 3.1.2). It can be seen that the Fe(0.5) and Fe(1) films show narrower Gauss-like distributions than the thicker film. Also, the thinner film gives a slight deviation of the distribution to smaller diameters when compared to the Fe(1), as it was expected.

Comparing the diameter distributions of the CNT and the particle it can be seen there is a good correlation for the Fe(0.5) film. Additionally, the d_p/d_t (initial particle bottom diameter/tube outer diameter) ratios of the three Fe films differ from the unit varying slightly in the range 0.93-1.26, particularly for Fe(1) and Fe(2) films.

The respective high resolution TEM images of the CNT structures are presented in Figs. 11a-f.
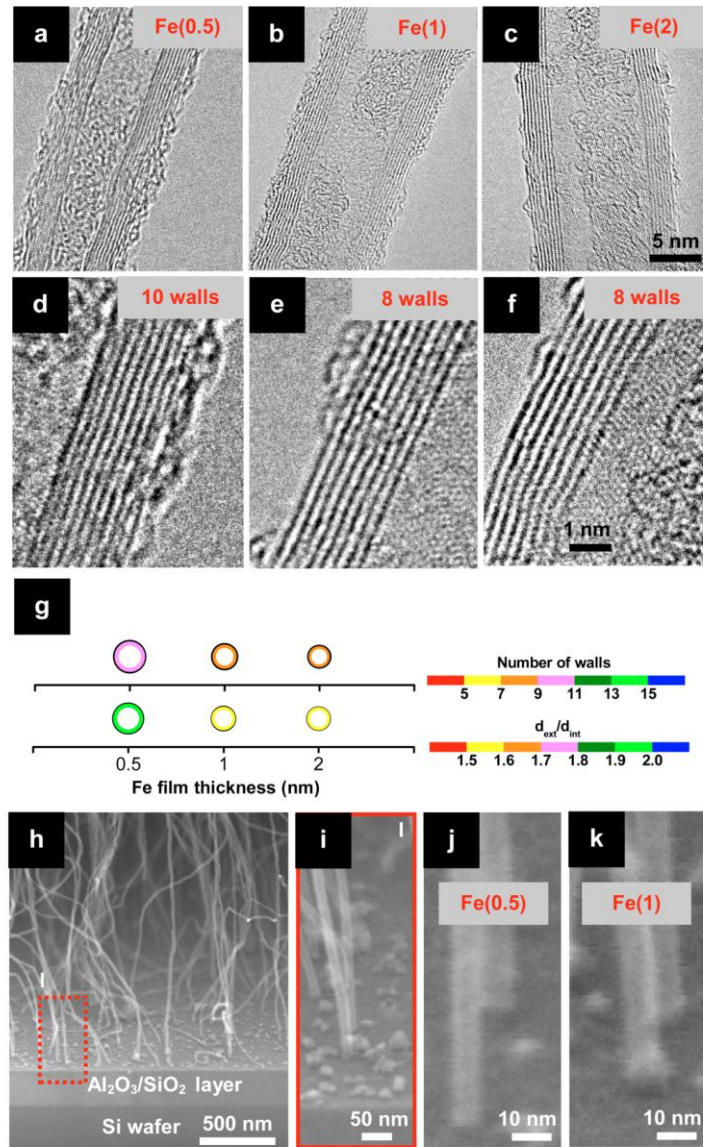
Fig. 11 - (a-f) HRTEM images of the millimetre-long CNTs grown on Fe(0.5), Fe(1) and Fe(2) films with condition A. (g) Bubble colour graphic showing the variation of the number of walls and diameter ratio d_{ext}/d_{int} with the Fe film thickness. (h) Representative cross-sectional SEM image of a millimetre-long CNT forest grown on Fe(1). (i) High magnification of (h) showing the base-growth mechanism. Magnification of the CNT-Fe particle interfaces of (j) Fe(0.5) and (k) Fe(1) films.

Surprisingly, Fig. 11g shows that the number of walls and d_{outer}/d_{inner} ratio decreases for increasing Fe thicknesses in an inverse trend of that found in [16]. This discrepancy can be explained by considering not only the diameter of the catalyst particle but also the significant role of the flux of C atoms on controlling the number of C walls of the grown CNT structure [66]. Conventionally, a MWCNT nucleates and begins to grow in the axial and radial directions due to the addition of C clusters to the open end of the graphene structure [67,68] or/and to the interface of this structure and the catalyst particle [58,66]. Also, it is expected that the tube thickens by wall growth on already grown inner-wall templates from the centre (inner C wall) to the periphery (outer C wall) [68]. Yet, this is only a hypothesis since *in situ* observations can not show the detailed growth process due to the extremely fast C incorporation into the CNT structure that ends by giving the insight that all C walls have the same growth rate [58]. For example, the estimation of the flux of C atoms into a CNT grown on a 1 nm thick Fe film is ~3.1×10^7 C atoms.s^{-1}. This was calculated for the present growth rate of 139 µm.min^{-1} and an eight-walls CNT with an outer diameter of 15 nm that has ~ 1.3×10^7 C atoms.µm^{-1}.

To further investigate this, the cross-sectional SEM image of a CNT forest grown on a 1 nm thick film is presented in Fig. 11h. The vertical alignment of the CNTs can be seen, most likely due to van-der-Wall (vdW) forces induced by the close-packed arrangement. Moreover, at high magnification it can be seen the good dispersion of Fe particle attached to the Al_2O_3 layer indicating the CNT base-growth mechanism (Fig. 11i). This mechanism results from the preservation of the high adhesion strength of Fe-Al_2O_3 system as described in Section 3.1.2.

Detailed observations of the catalyst particles at the bottom of individual CNTs grown from Fe(0.5) and Fe(1) films are given in Figs. 11j and 11k, respectively. Considering, the thickening mechanism described above, the inner diameter of the CNT, i.e. the first C wall or graphene cylinder, is defined here as the diameter of nucleation (d_n). For small particles ($\bar{d}$ ~13 nm, for Fe(0.5)) the d_n is small, thus, the inner diameter of CNT is also small. Since there are enough [C] atoms, new C walls start to grow resulting on the tube thickening until reaching the same diameter of the bottom diameter of the Fe particle (Fig. 11j).

On the other hand, bigger particles ($\bar{d}$ ~19 and 20 nm, for Fe (1) and Fe (2), respectively) have larger d_n than the smaller ones giving CNTs with larger inner diameters. Moreover, since the particles have bigger diameters more [C] atoms are needed to grow CNTs with the same length. Thus, the [C] atoms become mislaid in thickening the tube and the number of C layers decreases, being the size of the outer diameter a value between the d_n and the bottom diameter of the Fe particle, as it is depicted in the SEM micrograph of Fig. 11k. This corroborates with the results reported in [69], where, for bigger particles, the P_{C2H2} must double to achieve a d_p/d_t ratio closer to unity. Thus, the growth of CNTs with diameters smaller than the starting catalyst particle ones is possible because accordingly to in situ observations the extensive reshaping of the particles during the growth step is more important than the initial particle diameter in determining the outer and inner diameters of the final CNT structure [19].

Briefly, Fe(1) films are more promising than Fe(0.5) and Fe(2) to grow safer CNTs with small outer diameters and low number of C walls.

3.2.2. Almost catalyst-free CNTs

The SEM micrographs in Figs. 12a,b (white arrows illustrate the movements) show the detachment of the CNT forests from the grown substrate having a Fe(1) film. The high magnification image of the CNT-substrate interface (Fig. 12c) shows that short segments of the removed CNT are still attached to the substrate. Concerning the base-growth mode this means that the metal particles also remain attached to the Al_2O_3 substrate.
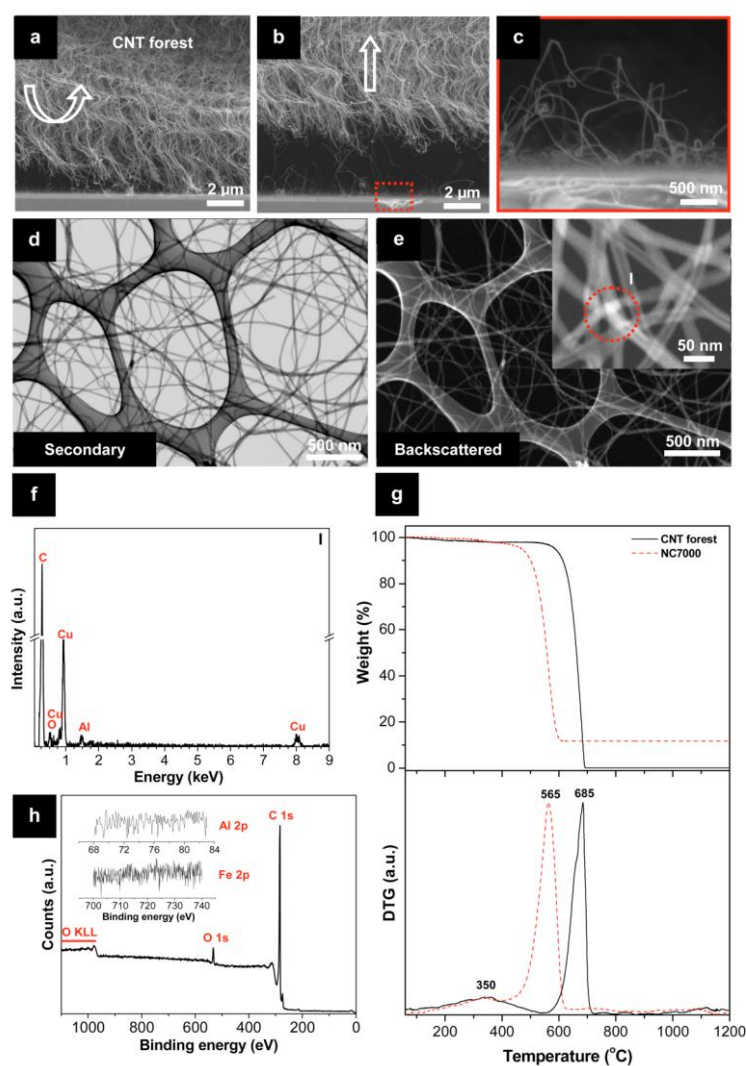

Fig. 12 - (a-c) SEM images sequence of the detachment movements of a millimetre-long CNT forest grown on Fe(1) film with condition A. (d and e) Bright and dark filed STEM images of the disentangled CNT of (a). (f) EDS spectrum of the area marked in the inset image of (e). (g) TGA weight loss and derivative weight for the milimeter-long CNT forest (solid black

line) of (a) and the commercial NC7000 tubes (dashed red line). (h) XPS wide-scan spectra of the CNT forest of (a) alongside with the inset high-resolution scans of Al2p and Fe2p peaks.

In order to evaluate the purity of the CNT forests, the tubes were firstly observed by STEM with bright field images (secondary electrons) and respective dark filed images (backscattered electrons), as it is shown in the micrographs of Figs. 12d and 12e, respectively. The last type of SEM images are an expeditious practice to reveal the existence of heavy elements like Fe as they are brighter than light ones such as C. Lower magnification images given by Figs. 12d and 12e show no trace of metal impurities but a more detailed observation of a higher magnification image depicted in the inset of Fig. 12e shows small white spots (highlighted with a red dot line). These are not Fe metal particles as it is confirmed by the EDS spectrum signature in Fig. 12f, but only several intercepted CNTs. Nevertheless, some Fe traces from the catalyst may still present but, below the detection limit of the EDS detector.

To further confirm the purity of the CNT forests more quantitative analyses were accomplished and results were compared to those of commercially available MWCNTs (NC7000, Nanocyl). The respective thermogravimetric analyses (TGA) are presented in Fig. 12g. Firstly, the profiles show that the CNT forests (solid black line) and the commercial available ones (dashed red line) have similar amounts of a-C ~3 wt.%, that burn at 350ºC. Yet, the CNT forests are more graphitised than the NC7000 ones since the former burn at higher temperature 685 ºC and 565 ºC, respectively. Moreover, the NC7000 tubes have a residue of 11.6 wt.% and no measurable residue was observed above 700 ºC for the CNT forests which mean that the latter ones are much purer. To confirm the high purity of our material, a XPS survey scan of its surface is given in Fig. 12h where it is shown a total inexistence of contaminants. The high-resolution spectra in the energy range of Fe and Al does prove the absence of these elements (inset of Fig. 12 h).

Further investigation of the residuals was performed by ICP-AES analyses (Table 1) to quantify the elements that might be involved in the growth process.

Table 1 - Qualitative and quantitative analyses of the impurities of the pristine CNT samples.

Element	CNT forest (wt.%)	NC7000 (wt.%)
Si	0.12	<0.1
Al	0.021	1.1
Fe	0.036	0.26
Co	-	0.13
Ni	-	0.0019
Total	0.18[a]	1.59
	NMR[b]	11.7
	[a] ICP-AES [b] TGA NMR- no measurable residue	

There is a significant discrepancy between the TGA and ICP values for NC7000. This is probably due to the incomplete digestion of Al_4C_3, reported by Paiva et al. as the main impurity [70]. In the case of the VACNTs the residues of Si and Al may result from the scratching movements on the substrate surface when collecting the CNT forests. This also implies that some Fe traces may be forcibly removed during the scratching procedure. Even though, it is clear that the amount of metals present on the commercial sample is around one order of magnitude higher than that found in the CNT forest.

3.2.3. Maximizing the outputs of safer CNTs

The catalyst-supported growth method optimised here allows the production of highly pure CNTs with tailored morphologies. However, short CNTs are needed in high outputs which may compromise the scalability of this method.

To overcome this, the standard growth procedure (Fig. 13a) was strategically switched to a stacked growth mode (Fig. 13b). Typically, in a single growth run, several CNT stacking layers vertically lined up are formed by repeating growth cycles on catalyst particles attached to the substrate, i.e. base growth mode, in such way that the former layers are lifted up by the latter layer that is in contact with the substrate [71-75]. In this respect, the density, the diameters and the purity of CNTs across layers are only guaranteed for catalyst-substrate systems with high adhesion energy (e.g. Fe-Al_2O_3) [72,74] that allow the unchanged catalyst particles to be kept attached to the substrate.

Besides the diameters and purity degree, it is compulsory to preserve the CNT growth rate across the multi-layers to produce high outputs of safer CNTs. Depending on the CVD conditions the growth rates may be constant [73,74] with the increasing number of layers or be decreased due to reaction-driven catalytic deactivation or diffusion-limited transport across the CNT arrays [71,72]. It was shown that using condition A the catalyst reactivity starts to decay only above 30 s of growth time, Section 3.2.1. This means that short times, 4 s (stage I, light gray area of Fig. 9e), gives safer CNT forests of 2 μm height with a constant growth rate of 0.5 μm.s^{-1} for increasing number of layers (Figs. 13b and 13c).

To make a proper use of the grown 5-layer film (Fig.13d) the layers must be separated. This process has been shown to be straightforward due to the non contiguous growth of CNTs between adjacent layers [71-75]. To improve the separation of layers, the growth cycles have been efficiently replaced by growth-etching cycles using H_2O as a weak oxidiser [71,72]. The selective H_2O etching of each CNT layer removes the excess of carbon impurities at the CNT-catalyst interfaces through oxidisation and partially oxidises the catalyst particles [48], changing probably the active sites on their surfaces. As a result, the nucleation of the next CNT layer under the former one, on the new active sites, induces a slight disruption of the CNT alignment, usually seen by marked lines [71,72].
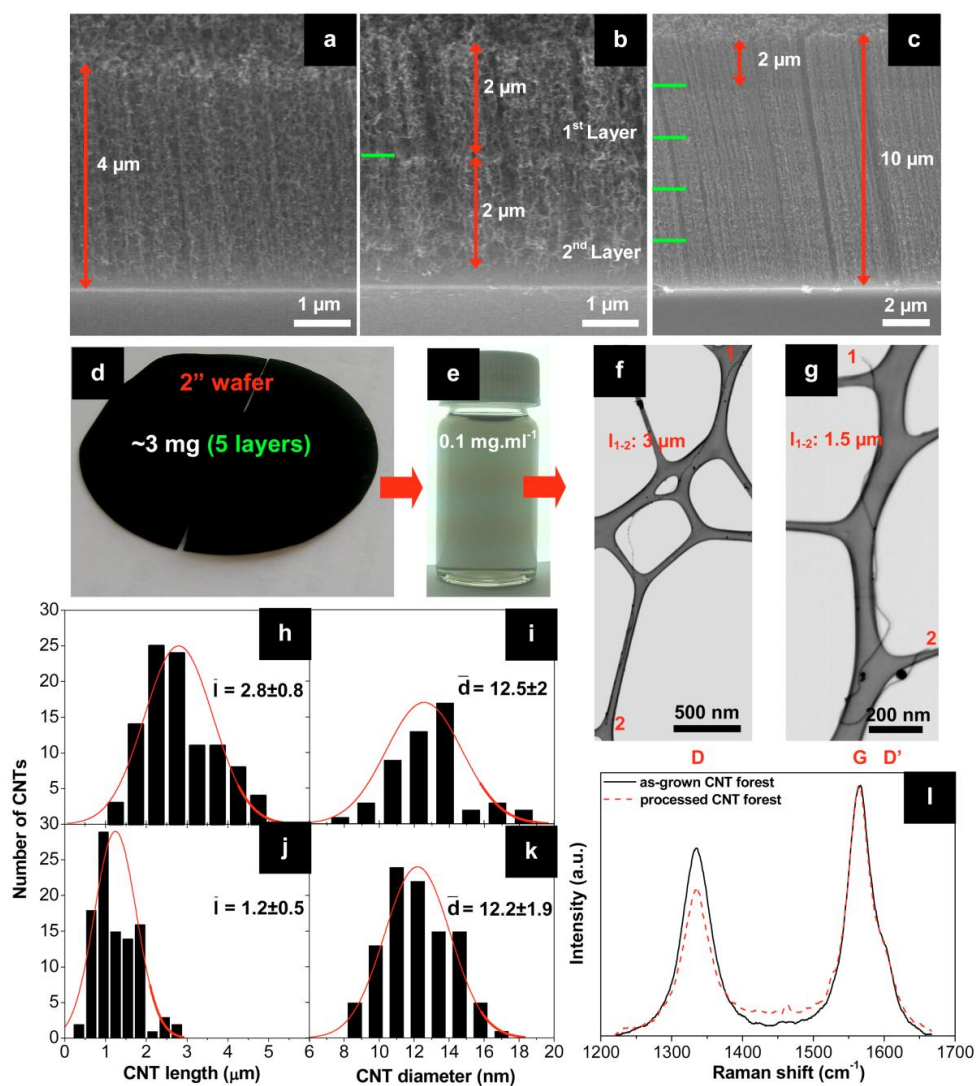
Fig. 13 - SEM images of a CNT forest grown on a Fe(1) film with condition A by (a) a standard and (b and c) a stacked growth mode (interfacial lines at green). (d) Photographs of a 5-layer forest grown on a 5 cm diameter wafer and respective (e) 2-propanol suspension of the processed CNT forest. STEM images of processed CNT forests, (f) standard and (g) 5-layer, and corresponding statistical distributions of length and diameter sizes for (h,i) a standard and (j,k) 5-layer. (i) Visible micro-Raman spectra of the as-grown CNT forest (solid black line) and processed material (dashed red line).

In the present work, the oxidising effect of H_2O was surrogated by an oxidation under an constant air flux at 350 ºC (position P3 of the furnace, see Fig. 6e in the Section I.1.2). The cyclic growth-etching steps (see Section 2.2 for more details) give layers of rather aligned CNT with fairly distinct interfacial lines between layers (green solid lines in Figs. 13b and 13c). Yet, these lines seem to be sufficiently demarked to permit the separation and disentanglement of these short CNT layers of ~2 µm (see Section 2.3 for more detail). Theoretically, two identical tubes with outer diameter sizes of 15 nm and 2-2000 µm long, aligned parallel to each other with a separation gap in the range of 70-200 nm (Fig. 11h), have vdW forces in the range of 4-43 Pa [76]. Thus, by

applying a shear force of 96 Pa the tubes should be fully disentangled. This force was calculated for the ultra-turrax equipment working at 20500 rpm and using 2-propanol as dispersing medium (viscosity of 2.07 mPa.s^{-1}, at 25°C). Fig. 13e shows a representative well dispersed CNT suspension in 2-propanol obtained from big blocks of CNT forests scratched from the substrate.

The disentanglement degree and morphology of standard and 5-layer CNT forests were evaluated by STEM observations of at least 100 CNTs in each case. Overall, the processed CNTs, standard (Fig.13f) and 5-layer (Fig. 13g), are well individualised with narrow Gauss-like distributions of lengths and diameters presented in Figs. 13h,i and Fig. 13j,k, respectively. The average CNT length obtained for the disentangled 5-layer CNT film of ~1.2 μm corresponds to the length size of each CNT layer of ~2 μm. This length reduction of ~30-40% was also seen in the standard CNT forest (~2.8 μm instead of ~4 μm) revealing that it is linked to the disentanglement process. Hence, it is proved that the 5-layer CNT film was efficiently separated at the interfacial lines between layers. Also, by comparing the average diameters and distributions of Figs. 10c (as-grown CNTs), 13i and 13k it can be stressed out that the CNT diameters were preserved across the multi-layer film and they were not damaged by the processing route. This was showed by the Raman spectra of Fig. 13l preformed to the as-grown CNT forest (solid black line) and the respective processed one (dashed red line) giving similar L_a values of 29.4 and 31.6 nm, respectively. The slight increase of L_a can be related to the elimination of C deposits on the CNT walls during the processing steps, as observed earlier by Xu et al. [76].

Considering a 5-layer forest and the semi-continuous process, it should be noted that the CNT output per day of work is increased by 20 times. Eventually, if there is any diffusion limitation of C species, it only occurs above 1 mm height CNT forests [23] which means that one growth run would yield 500 layers of 2 μm height.

4. Conclusions

High output yields (milligrams per day) of biologically safer MWCNTs were successfully grown on 5 cm diameter Si-Al$_2$O$_3$-Fe wafers by hot-wall CVD combining a semi-continuous setting and a stacked growth mode.

By adjusting the CVD growth parameters it was possible to control the length of CNTs below 2 μm and to determine the outer diameter (14-16 nm) and number of C layers (7-10 layers) by tuning the thickness of the Fe catalyst film (0.5-2 nm).

For a stacked growth on 5 cm diameter wafers coated with 1 nm thick Fe films the growth rate of ~0.5 μm.s^{-1} was constant for the increasing number of grown layers obtained by cyclic growth-etching steps. As result, almost amorphous carbon free CNTs, i.e. "clean" CNTs, with length of ~1.2 μm was conserved across the multi-layer film as well as the CNT diameter of ~12 nm. This average diameter is close to the catalyst particle diameter (d_p/d_t ~1.26) that is attached to the substrate. This is in accordance with the demonstrated base-growth mechanism. The strong Fe-Al$_2$O$_3$ bonds ensure the high purity degree of the CNTs with metals content <0.04%.

Furthermore, it was found that the processed MWCNTs are more crystalline and purer (by one order of magnitude) than the commercial ones produced in fluidized bed reactors.

By fully automating the cyclic growth-etching steps in the semi-continuous setting and using large deposition areas, the output yields can easily ascend to kilograms per day. Also, by making further adjusts in the thickness of the catalyst film and in the C flux it is possible to produce as well safer SWCNTs. Furthermore, CNT post-growth treatments of purification and morphology separation that are not only complex and expensive but also destructive can be then avoided.

In conclusion, the present results open a scale-up prospective for the catalyst-supported CVD method. Particularly for bioapplications, where the CNT purity and morphology are decisive to their clinical fate, the proposed method is very attractive among other available mass production ones.

Acknowledgements

References:

[1]. Mazzola L. Commercializing nanotecnology. Nat Biotechnol 2003;21(10):1137-43.

[2]. Wagner V, Dullaart A, Bock AK, Zweck A. The emerging nanomedicine landscape. Nat Biotechnol 2004;24(10):1211-7.

[3]. Lu F, Gu L, Meziani MJ, Wang X, Luo PG, Veca LM et al. Advances in bioapplications of carbon nanotubes. Adv Mater 2009;21:139-52.

[4]. Liu Z, Tabakman S, Welsher K, Dai H .Carbon nanotubes in biology and medicine in vitro and in vivo detection, imaging and drug delivery. Nano Res 2009;2:85-120.

[5]. Kostarelos K, Bianco A, Prato M. Promises, facts and challenges for carbon nanotubes in imaging and therapeutics. Nat Nanotechnol 2009;4:627-33.

[6]. Zhao Y, Xing G, Chai Z .Are carbon nanotubes safe? Nat Nanotechnol 2008;3:191-2.

[7]. Kane AB, Hurt RH .The asbestos analogy revisited. Nat Nanotechnol 2008;3:378-9.

[8]. Firme CP, Bandaru PR. Toxicity issues in the application of carbon nanotubes to biological systems. Nanomed-Nanotechnol 2010;6:245-56.

[9]. Pulskamp K, Diabaté S, Krug HF .Carbon nanotubes show no sign of acute toxicity but induce intracellular reactive oxygen species in dependence on contaminants. Toxicol Lett 2007;168:58-74.

[10]. Wick P, Manser P, Limbach L, Dettlaff-Weglikowska U, Krumeich F, Royh S et al. The degree and kind of agglomeration affect carbon nanotube cytotoxicity. Toxicol Lett 2007;168:121-31.

[11]. Stone V, Donaldson K .Signs of stress. Nat Nanotechnol 2006;1:23-4.

[12]. Kostarelos K .The long and short of carbon nanotube toxicity. Nat Biotechnol 2008;26(7):774-6.

[13]. Kobayashi N, Naya M, Ema M, Endoh S, Maru J, Mizuno K, et al. Biological response and morphological assessment of individually dispersed multi-wall carbon nanotubes in the lung after intratracheal instillation in rats. Toxicology 2010;276:143-53.

[14]. Grobert N. Carbon nanotubes - becoming clean. Nicole Grobert Mater Today 2007;10:28-35.

[15]. Seah CM, Chai SP, Mohamed AR. Synthesis of aligned carbon nanotubes. Carbon 2011;49:4613-35.

[16]. Zhao B, Futaba DN, Yasuda S, Akoshima M, Yamada T, Hata K .Exploring advantages of diverse carbon nanotube forests with tailored structures synthesized by supergrowth from engineered catalysts. ACS Nano 2009;3(1):108-14.

[17]. Mata D, Ferro M, Fernandes AJS, Amaral M, Oliveira FJ, Costa PMFJ, Silva RF. Wet-etched Ni foils as active catalysts towards carbon nanofiber growth. Carbon 2010;48:2839-54.

[18]. Mata D, Amaral M, Fernandes AJS, Oliveira FJ, Costa PMFJ, Silva RF. Self-assembled cones of aligned carbon nanofibers grown on wet-etched Cu foils. Carbon 2011;49:2181-96.

[19]. Hofmann S, Sharma R, Ducati C, Du G, Mattevi C, Cepek C, et al. In situ observations of catalyst dynamics during surface-bound carbon nanotube nucleation. Nano Lett 2007;7(3):602–8.

[20]. Moisala A, Nasibulin AG, Kauppinen EI. The role of metal nanoparticles in the catalytic production of single-walled carbon nanotubes – a review. J Phys: Condens Matter 2003;15:S3011-35.

[21]. Zhu L, Xu J, Xiao F, Jiang H, Hess DW, Wong CP. The growth of carbon nanotube stacks in the kinetics-controlled regime. Carbon 2007;45:344-8.

[22]. Li Q, Zhang X, DePaula RF, Zheng L, Zhao Y, Stan L, et al. Sustained growth of ultralong carbon nanotube arrays for fiber spinning. Adv Mater 2006;18: 3160-63.

[23]. Xiang R, Yang Z, Zhang Q, Luo G, Qian W, Wei F et al. Growth deceleration of vertically aligned carbon nanotube arrays: catalyst deactivation or feedstock diffusion controlled? J Phys Chem C 2008;112: 4892-6.

[24]. A. Arranz A, Perez-Dieste V, Palácio C. Growth, electronic properties and thermal stability of the Fe/Al$_2$O$_3$ interface. Surf Sci 2002;521:77-83.

[25]. Sato H, Hori Y, Hata K, Seko K, Nakahara H, Saito Y. Effect of catalyst oxidation on the growth of carbon nanotubes by thermal chemical vapor deposition. J Appl Phys 2006;100;1043211-6.

[26]. Simmons JM, Nichols BM, Marcus MS, Castellini OM, Hamers RJ, Eriksson MA. Critical oxide thickness for efficient single-walled carbon nanotube growth on silicon using thin SiO$_2$ diffusion barriers. Small 2006:2(7) 902-9.

[27]. Carey JD, Ong LL, Silva SRP. Formation of low-temperature self-organized nanoscale nickel metal islands. Nanotechnology 2003;14:1223-7.

[28]. Sanjabi S, Faramarzi A, Momen MH, Barber ZH. Thermodynamics approach of the formation of Ni catalyst particles for carbon nanotubes growth. J Phys Chem Solid 2008;69:1940-4.

[29]. ASM handbook: alloy phase diagrams. USA: ASM International; 1992.

[30]. Safaei A. Cohesive energy and physical properties of nanocrystals. Philos Mag 2011;91(10):1509-39.

[31]. Lu XG, Selleby M, Sundman B. Assessments of molar volume and thermal expansion for selected bcc, fcc and hcp metallic elements. CALPHAD 2005;29:68-89.

[32]. Besley NA, Johnston RL, Stace AJ, Uppenbrink J. Theoretical study of the structures and stabilities of iron clusters. J Mol Struct 1995;341:75-90.

[33]. Quintana C, Menéndez JL, Huttel Y, Lancin M, Navarro E, Cebollada A. Structural characterization of Fe (110) islands grown on α-Al2O3 (0001). Thin Solid Films 2003;434:228-38.

[34]. Klinke C, Bonard JM, Kern K. Formation of metallic nanocrystals from gel-like precursor films for CVD nanotube growth: an in situ TEM characterization J Phys Chem B 2004;108(31): 11357-60.

[35]. Nessim GD, Hart AJ, Kim JS, Acquaviva D, Oh J, Morgan CD, et al. Tuning of vertically-aligned carbon nanotube diameter and areal density through catalyst pre-treatment. Nano Lett 2008;8(11):3587-93.

[36]. Zhong G, Iwasaki T, Robertson J, Kawarada H. Growth kinetics of 0.5 cm vertically aligned single-walled carbon nanotubes. J Phys Chem B 2007; 111(8) 1907-10.

[37]. Chakrabarti S, Kume H, Pan L, Nagasaka T, Nakayama Y. Number of walls controlled synthesis of millimeter-long vertically aligned brushlike carbon nanotubes. J Phys Chem C 2007;111(5):1929-34.

[38]. Moulijn JA, Diepen AE, Kapteijn F. Catalyst deactivation: is it predictable? What to do? Appl Catal A-Gen 2001;212: 3-16.

[39]. Sun C, Berg JC Effect of moisture on the surface free energy and acid–base properties of mineral oxides. J Chromatogr A 2002;969: 59-72.

[40]. Vitos L, Ruban AV, Skriver HL, Kollar. The surface energy of metals. J Surf Sci 1998;411:186-202.

[41]. Wang Y, Luo Z, Li B, Ho PS, Yao Z, Shi L et al. Comparison study of catalyst nanoparticle formation and carbon nanotube growth: support effect. J Appl Phys 2007;101:124310-8.

[42]. Martin JE, Herzing AA, Yan W, Li X, Koel BE, Kiely CJ, et al. Determination of the oxide layer thickness in core-shell zerovalent iron nanoparticles. Langmuir 2008;24: 4329-34.

[43]. Ma H,Pan L, Nakayama Y. Modelling the growth of carbon nanotubes produced by chemical vapour deposition. Carbon 2011;49:854-61.

[44]. Huttinger KJ .CVD in hot wall reactors- the interaction between homogeneous gas-phase and heterogeneous surface reactions. Chem Vap Deposition 1998;4(4)151-8.

[45]. Lysaght AC, Chiu KSW. Modeling of the carbon nanotube chemical vapor deposition process using methane and acetylene precursor gases. Nanotechnology 2008;19:1656071-8.

[46]. Lee C, Park J, Huh Y, Lee JY. Temperature effect on the growth of carbon nanotubes using thermal chemical vapor deposition. Chem Phys Lett 2001;343:33-8.

[47]. Cançado LG, Takai K, Enoki T, Endo M, Kim YA, Mizusaki H, et al. General equation for the determination of the crystallite size La of nanographite by Raman spectroscopy. Appl Phys Lett 2006;88:163106.

[48]. Yamada T, Maigne A, Yudasaka M, Mizuno K, Futaba DN, Yumura M, Iijima S, Hata K. Revealing the secret of water-assisted carbon nanotube synthesis by microscopic observation of the interaction of water on the catalysts. Nano Lett 2008;8(12):4288-92.

[49]. Jorio A, Pimenta MA, Filho AGS, Saito R, Dresselhaus G, Dresselhaus MS. Characterizing carbon nanotube samples with resonance Raman scattering New J Phys 2003;5:139.1-17.

[50]. Nemanich RJ, Solin SA. First and second-order Raman scattering from finite-size crystals of graphite. Phys Rev B 1979;20(2):392–401.

[51]. Massey BS. Mechanics of fluids. New York: Taylor and Francis. 1979:129-134.

[52]. Wilke CR. A viscosity equation for gas mixtures J Chem Phys 1950;18(4):517-9.

[53]. Saxena SC, Narayanan TKS. Multicomponent viscosities of gaseous mixtures at high temperatures. Ind Eng Chem Fund 1962;1(3):191-5.

[54]. Zhu L, Hess DW, Wong CP. Monitoring carbon nanotube growth by formation of nanotube stacks and investigation of the diffusion-controlled kinetics J Phys Chem B 2006;110: 5445-9.

[55]. Futaba DN, Hata K, Yamada T, Mizuno K, Yumura M, Iijima S. Kinetics of water-assisted single-walled carbon nanotube synthesis revealed by a time-evolution analysis. Phy Rev Lett 2005; 95:056104 1-4.

[56]. Yasuda S, Hiraoka T, Futaba DN, Yamada T, Yumura M, Hata K. Existence and kinetics of graphitic carbonaceous impurities in carbon nanotube forests to assess the absolute purity. Nano Lett 2009;9(2) 769-773.

[57]. Louchev OA, Sato Y, Kanda H Growth mechanism of carbon nanotube forests by chemical vapour deposition. Appl Phys Lett 2002;80(15) 2742-4.

[58]. Yoshida H, Takeda S, Uchiyama T, Kohno H, Homma Y. Atomic-scale in-situ observation of carbon nanotube growth from solid state iron carbide nanoparticles. Nano Lett 2008;8(7):2082-6.

[59]. Kim KE, Kim KJ, Jung WS, Bae SY, Park J, Choi J, Choo J. Investigation on the temperature-dependent growth rate of carbon nanotubes using chemical vapor deposition of ferrocene and acetylene. Chem Phys Lett 2005;401:459-64.

[60]. Sacco A, Thacker P, Chang TN, Chiang ATS. The initiation and growth of filamentous carbon from α-iron in H2, CH4, H2O, CO2 and CO gas mixtures. J Catal 1984;85:224-36.

[61]. Sharma R, Moore E, Rez P, Treacy MMJ. Site-specific fabrication of Fe particles for carbon nanotube growth. Nano Lett 2009;9(2):689-94.

[62]. Holstein WL. The roles of ordinary and soret diffusion in the metal-catalyzed formation of filamentous carbon. J Catal 1995;152:42-51.

[63]. Schneider A, Inden G. Carbon diffusion in cementite (Fe3C) and Hägg carbide (Fe5C2). CALPHAD 2007;31:141-7.

[64]. Jung YJ, Wei B, Vajtai R, Ajayan PM, Homma Y, Prabhakaran K, et al. Mechanism of selective growth of carbon nanotubes on SiO2/Si patterns Nano Lett 2003;3(4):561-4.

[65]. O. A. Nerushev, Dittmar S, Morjan RE, Rohmund F, Campbell EEB. Particle size dependence and model for iron-catalyzed growth of carbon nanotubes by thermal chemical vapor deposition. J Appl Phys 2003;93(7):4185-90.

[66]. Wood RF, Pannala S, Wells JC, Puretzky AA, Geohegan DB. Simple model of the interrelation between single- and multiwall carbon nanotube growth rates for the CVD process. Phys Rev B 2007;75:235446.

[67]. Kwon YK, Lee YH, Kim SG, Jund P, Tománek D, Smalley RE. Morphology and stability of growing multiwall carbon nanotubes. PRL 1997;79(11):2965-8.

[68]. Charlier JC, Iijima. S, Growth mechanisms of carbon nanotubes. In: Carbon nanotubes: synthesis, structure, properties, and applications. Dresselhaus MS, Dresselhaus G, Avouris Ph, Eds. Berlin: Springer-Verlag; 2008. pp. 55–81.

[69]. Cheung CL, Kurtz A, Park H, Lieber CM. Diameter-controlled synthesis of carbon nanotubes. J Phys Chem B 2002;106:2429-33.

[70]. Paiva MC, Simon F, Novais RM, Ferreira T, Proença MF, Xu W, e tal. Controlled functionalization of carbon nanotubes by a solvent-free multicomponent approach. *ACS Nano*, 2010;4(12):7379–86.

[71]. Patole SP, Park JH, Lee TY, Lee JH, Patole AS, Yoo JB. Growth interruption studies on vertically aligned 2-3 wall carbon nanotubes by water assisted chemical vapor deposition. App Phys Lett 2008;93:114101-3.

[72]. Zhu L, Xiu Y, Hess DW, Wong CP. Aligned carbon nanotube stacks by water-assisted selective etching. Nano Lett 2005; 5(12):2641-6.

[73]. Li X, Cao A, Jung YJ, Vajtai R, Ajayan PM. Bottom-up growth of carbon nanotube multilayers: unprecedented growth. Nano Lett 2005; 5(10):1997-2000.

[74]. Iwasaki T, Zhong G, Aikawa T, Yoshida T, Kawarada H. Direct evidence for root growth of vertically aligned single-walled carbon nanotubes by microwave plasma chemical vapor deposition. J Phys Chem B 2005;109(42):19556-9.

[75]. Pinault M, Pichot V, Khodja H, Launois P, Reynaud C, Mayne-L'Hermite M. Evidence of sequential lift in growth of aligned multiwalled carbon nanotube multilayers. Nano Lett. 2005;5(12):2394-8.

[76]. Xu GH, Zhang Q, Huang JQ, Zhao MQ, Zhou WP, Wei F. A two-step shearing strategy so disperse long carbon nanotubes from vertically aligned multiwalled carbon nanotube arrays for transparent conductive films. Langmuir 2010;26(4):2798-2804.

166

Chapter III

In vitro/*in vivo* biocompatibility and biodegradability of MWCNTs

III.1. Introduction

CNT biopersistency in human body is a real concern when bioapplications are envisaged. The CNT biopersistency depends on the morphology, biodegradability and biodispersibility. While the first parameter was addressed in the previously Chapter II, the latter two are investigated in the present section. To modulate these two parameters and also the CNT biocompatibility, a double functionalization of CNTs was designed. The *in vitro* human MG63 osteoblastic response on the functionalized materials and the *in vivo* biocompatibility, biodegradability and biodispersibility profiles of the materials subcutaneously implanted in rats, were evaluated and shown in the present chapter.

III.2. Doubly functionalized carbon nanotubes for bone tissue engineering: *in vitro*/*in vivo* biocompatibility and biodegradability

D. Mata[a], M. Amaral[a,b], A.J.S. Fernandes[b], B. Colaço[c], A. Gama [c], M.C. Paiva[d], P.S. Gomes[e], R.F. Silva[a], M.H. Fernandes[e]

[a]CICECO, Materials and Ceramic Eng. Dept., Univ. of Aveiro, 3810-193 Aveiro ,Portugal

[b]I3N, Physics Dept., Univ. of Aveiro, 3810-193 Aveiro ,Portugal

[c]Dept. of Veterinary Sciences, Center for the Study of Animal Sciences (CECA), ECAV, Univ. of Trás-os-Montes e Alto Douro, 5000-801 Vila Real, Portugal

[d]Institute for Polymers and Composites/I3N, Univ. of Minho, 4800-058 Guimarães, Portugal

[e]Laboratory for Bone Metabolism and Regeneration, Faculty of Dental Medicine, Univ. of Porto, 4200-465 Porto, Portugal

(Biomaterials, submitted)

Abstract

The risk-benefit balance for carbon nanotubes (CNTs) dictates their clinical fate. To take a step forward in this crossroad it is compulsory to modulate the CNT *in vivo* biocompatibility and biodegradability via chemical functionalization.

CNT membranes were doubly functionalised combining a Diels-Alder cycloaddition reaction to generate cyclohexene followed by a mild oxidisation to yield carboxylic acid groups (-COOH). *In vitro* proliferation and osteogenic differentiation of human osteoblastic cells were maximized on functionalized CNT membranes (*p,f*-CNTs). The *in vivo* subcutaneously implanted materials showed higher biological reactivity, thus inducing a slighter intense inflammatory response relatively to non-functionalized CNT membranes (*p*-CNTs), but still showing a reduce cytotoxicity profile. Moreover, the *in vivo* biodegradation of CNTs was superior for *p,f*-CNTs membranes, mediated by oxidation-induced myeloperoxidase (MPO) in neutrophils and macrophages inflammatory milieus. This put evidences for the biodegradability faculty of doubly functionalized CNTs, which potentially avoids long-term tissue accumulation and triggering of acute toxicity.

On the whole, the proposed double functionalization was accounted for the improved CNT biological response as referred to biocompatibility and biodegradability profiles. Therefore, CNTs can be considered to be used in bone tissue engineering without noteworthy toxicological threats.

Keywords: Carbon, Bone graft, Biocompatibility, Biodegradation, Bone tissue engineering

1. Introduction

Pioneering solutions based on carbon nanotubes - single-walled (SWCNTs) and multi-walled (MWCNTs) - have been widely explored to endorse relevant breakthroughs in bone tissue engineering upmost demands of scaffolding, drug delivering, cell tracking and sensing, and *in situ* control of cell proliferation and differentiation [1-3]. Moreover, the outstanding idea that all of these functionalities could be accumulated in a unique multifunctional CNT-based smart bone graft triggered a huge excitement in the bone tissue engineering field.

Despite the enthusiasm for CNT-engineered biomedical products, the CNT potential toxicological risks made, so far, some of their applications unrealistic to clinic. CNT toxicity is still a controversial topic, while some studies have shown biocompatibility with cells and tissues [4], others have demonstrate their toxic effect [5]. This discrepancy is explained by variations in the experimental protocols across research groups, namely: CNT physical-chemical characteristics (structure, morphology, purity, functionalization), preparation methods (concentration, dispersion) and route of administration [6]. Indeed, up to now, studies clearly show that metal impurities, morphology, hydrophobicity and non-biodegradability dictate the *in vitro* and *in vivo* toxicological profiles of CNTs [6, 7]. Transition-metal impurities used in CNT production processes induce cell toxicity by acting as catalyst to oxidative stress [8]. Also, the CNT morphology is crucial for the success of the clearance, either through urinary and/or lymphatic mechanisms [9-11]. Small pristine (i.e. non-functionalized) CNTs have their potential toxicity highly depressed by having the ability to be excreted through *fenestrae* of the organs and by being engulfed and digested by phagocytes [10, 11]. Yet, purifying and shortening pristine CNTs just solve part of their toxicological risks.

Chemical functionalization becomes essential to reduce hydrophobicity and biopersistency [12]. Chemical charging of CNTs restricts the formation of big agglomerates and increases the CNT mobility in physiological serums and ultimately avoid their accumulation into cell, tissues and organs [10]. Furthermore, covalent type functionalization might help to design biodegradable and bioresorbable CNTs under *in vivo* scenarios of material accumulation and retention [12]. *In vitro* studies revealed that the level and type of the chemical groups covalently bonded to CNTs dictate their cleavage/oxidation rate in simulated oxidative phagolysosome mediums containing acidic hydrolase enzymes (lysozymes), hydrogen peroxide and superoxide anions [13, 14]. The carboxylic group (-COOH) is the most efficient to produce biodegradable CNTs due to the uppermost level of induced damage, originating active sites at two neighboring C atoms due to C-C bond breaking [14]. Carboxylic groups are commonly added to highly reactive ends and at defect sites of CNTs by means of strong acidic oxidation procedures [15]. Notwithstanding, the intrinsic CNT properties are also affected due to the breakage and π-disruption [16].

Sidewall cycloadditions (e.g. 1,3 dipolar and [4+2] Diels-Alder) have emerged as a promising alternative to acidic oxidations in biomedical applications, due to the superior balance between preservation of intrinsic properties and maximization of CNT biodegradability [12, 17, 18].

Cycloaddition reactions to CNTs involve the covalent bonding of cycloadducts to two adjacent sp^2 C atoms of the CNT hexagonal lattice. In these bonding, the cycloadduct disrupts the sp^2 C-C structure into sp^3 geometry at two neighboring C atoms, weakening but not breaking the C lattice. Cycloaddition reactions of 1,3 dipolar groups were ascribed to the longitudinal unzipping of CNTs, observed under ultra-high vacuum scanning tunneling microscopy conditions, as described by Paiva et al. [19]. Soon after, Bianco's group found other external stimuli that were able to cut or degrade 1,3 dipolar functionalized CNTs, in an *in vivo* harsh oxidative milieu [20].

Overall, cycloadditon reactions become promising functionalization strategies to tune the biocompatibility and biodegradability of CNTs. This gives a new perspective on translation of CNTs into the clinics. While 1,3 dipolar cycloadditons have been widely studied following the pioneering work of Bianco's group for bioapplications [21], the [4+2] Diels-Alder cycloaddition route has received less attention. Yet, both show similar potential to functionalize CNTs [22] and to render them biocompatible and biodegradable.

A Diels-Alder based functionalization with potential for biomedical purposes was proposed by Proença et al. [22]. The covalent functionalization starts by bonding the "anchor" group (hydrophobic group) resulting from the [4+2] Diels-Alder cycloaddition of 1,3 butadiene, followed by a soft oxidation of the alkene group with $KMnO_4$, to generate carboxylic groups (hydrophilic group). Each group has specific functionalities. The hydrophobic group controls the solubility (steric stabilization) and biodegradation, altogether with minor damage to the CNT intrinsic properties; and the hydrophilic group promotes the solubility (electrostatic stabilization), the bonding of active biomolecules (e.g. proteins, carbohydrates, nucleic acids) and gives negative electrical charge CNT surfaces. The latter functionalities granted by the carboxylic groups also govern the CNT interfacing with bone tissue [23]. Regarding the surface polarity, those negatively charged have shown superior *in vitro* and *in vivo* performances in osteoblastic cells adhesion/proliferation and acceleration of bone bonding than positively charged ones [24].

The present work focuses on the *in vitro* and *in vivo* evaluation of the toxicological profile of multi-walled carbon nanotubes (MWCNTs) membranes functionalized by the Diels-Alder cicloaddition reaction of 1,3 butadiene. The CNT membranes were fully characterized considering the functionalization yield, functional groups recognition, surface charge, wettability and roughness. Due to the relevance and promising applications of Diels-Alder functionalized CNTs in bone tissue-related applications, *in vitro* testing was conducted with human osteoblastic-like cells to assess their viability/proliferation. The *in vivo* experiments of subcutaneous implantation of CNTs in rats aimed to address their biocompatibility and biodegradation.

2. Materials and methods

2.1. *CVD production of VACNTs*

Vertically aligned CNTs (VACNTs) were synthesised by an optimised catalyst-supported chemical vapour deposition (CVD) technique [9], as sketched in Fig. 1a. Prior to the synthesis step, the 2 inch diameter p-type Si/SiO$_2$ wafer (Siegert Consulting) substrates for the CNT growth were coated with a bilayer of Al$_2$O$_3$ (10 nm)/Fe (1 nm), by magnetron sputtering. Then, the Fe film was converted into nano-sized particles (~20 nm) with a round shape morphology and a uniform density (~10^{10} particles.m^{-2}) by means of an *in situ* annealing, inside the CVD reactor, at 770ºC, under a reductive gas flow of H$_2$/Ar (500/200 sccm) (Fig. 1a). Subsequently, the H$_2$ and Ar flows were adjusted to 400 and 100 sccm respectively, and the C$_2$H$_2$ flow (10 sccm) was added for 15 min to yield the Fe-catalysed growth of VACNTs with diameter and length sizes of ~15 nm and ~1.5 mm, respectively, on large areas (Figs. 1a to 1c). The ability of this method to grow dimensionally-controlled CNTs avoids post-synthesis processes of cutting and selection, becoming highly advantageous to produce biologically safe CNTs for biomedical purposes [9].

2.2. *Purification and functionalization of CNTs*

Large VACNTs blocks were removed from the Si substrate using a polymeric spatula and then dispersed in ethanol/water (3:1) suspensions. Subsequent mechanical mixing steps of high-speed shearing (IKA T25-Ultra-Turrax, working at 20500 rpm) and sonication (Selecta, working at 60 kHz, 200 W) steps for 15 min and 60 min, respectively, were applied to disentangle the bundles of tubes. Ultimately, the suspension of CNTs was frieze dried (Labconco, LYPH Lock 4.5, Kansas City, MO), at -30ºC under vacuum for 96h, to obtain a final fluffy CNT powder with minimal agglomeration and maximum specific surface area, designated here as CNTs (Figs. 1d and 1e). Both features are favorable to improve the yield of the subsequent purification and functionalization processes.

CNT purification was performed in an open graphite crucible inside a graphite furnace, at 1900 ºC for 8 h. This process was done under highly pure Ar (purity> 99.9999%) atmosphere a fixed flow of 20 sccm to drag-out vaporized impurities.

CNTs were functionalised using a double functionalization method based on the Diels-Alder cycloaddition reaction of 1,3-butadiene (Bu), forming cyclohexene at the CNTs surface, as described elsewhere [22]. The alkene formed was further oxidized under mild conditions to form carboxylic acid groups (COOH) (Fig. 2a). Approximately 70 mg of CNTs were suspended in a solution of equal weight of sulfolene (≥98%, Sigma-Aldrich) in 20 ml of diglyme (≥99.5%, Sigma-Aldrich), in a round-bottom flask. The suspension was heated to 150 ºC to induce the slow decomposition of sulfolene, generating sulphur dioxide and Bu. The end of the sulfolene decomposition was detected when a filter paper soaked with an aqueous solution of potassium

dichromate, placed at the top of the condenser, no longer changed the colour from orange to blue/green. The reaction proceeded for 24 hours, the CNTs were collected by filtration using a 0.22 µm pore size polycarbonate membrane (Millipore) and carefully cleaned to eliminate the solvent. This process was done by sonication in ethanol (≥99.9%, Sigma) for 5 min followed by washing with ethyl ether (≥98%, Sigma). The solid was then vacuum dried at 100ºC for 48 h.

The alkene functional groups of the Diels-Alder functionalized CNTs were further converted into carboxylic acid groups (COOH) by oxidation with a 0.1 M aqueous solution of $KMnO_4$ (≥99%, Sigma-Aldrich) at room temperature. After oxidation, the CNTs were filtered, washed with distilled water and dried at 100ºC in the vacuum oven for 5h.
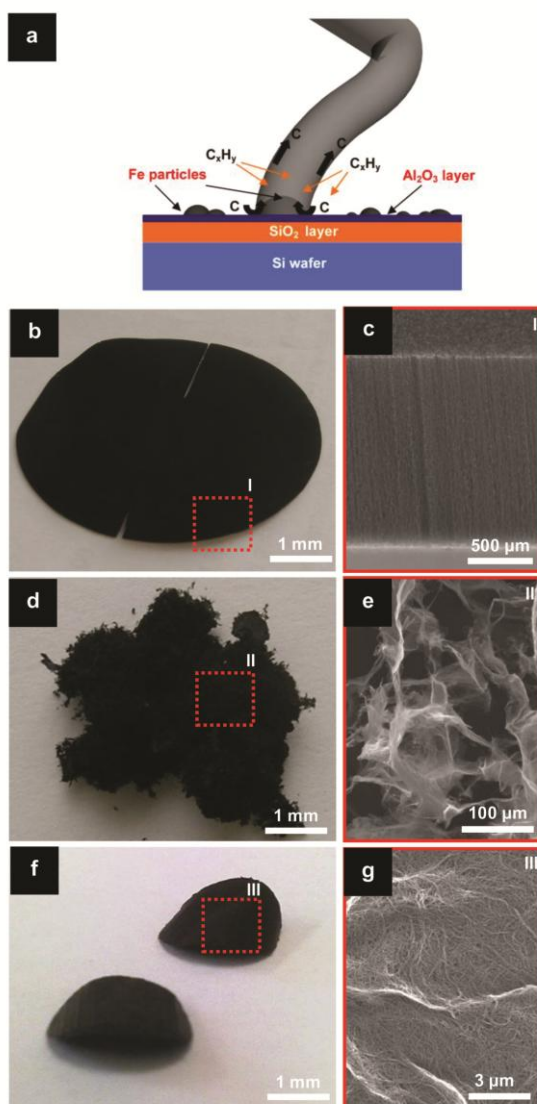

Fig. 1 - (a) Schematic image of the catalyst-supported CVD growth method of CNTs. (b-g) Photographs and respective SEM micrographs of the key steps of the preparation route of CNT membranes: (b,c) as-grown vertically aligned CNTs; (d,e) frieze-dried CNTs; (f,g) CNT membranes.

2.3. Preparation of CNT membranes

CNTs were re-suspended in isopropyl alcohol (≥99.8%, Sigma-Aldrich) with a concentration of 0.1 g.l^{-1} by the two-step mechanical mixing method described in section 2.2. Afterwards, the CNT suspension was dropped in a cylindrical mould of 10 mm of diameter placed on a 0.22 μm pore size disc filter (hydrophobic PTEF, Millipore), to produce CNT membranes by vacuum filtration. This was accomplished by a rotary vacuum pump connected to the filter-Büchner funnel-Kitasato flask setting. For each CNT membrane of 10 mm of diameter (Figs. 1f and 1g), about 4 ml of suspension was used. After filtration, the membranes were dried in an oven at 80ºC for 15 min. The membranes were sterilized by UV radiation for 12 h prior to the biological testing.

2.4. Characterization of CNT membranes

Acid-base titration. The acid-base characterization of the CNTs was carried out by base titration under similar conditions to those described by Gorgulho et al. [25]. Approximately 100 mg of CNTs were suspended in a HCl solution (0.01 M) so that all the titrations started at a pH ~ 2. The suspension was stirred under inert atmosphere (Ar) during 15 min. The potentiometric titration started with the addition of 2 mL of a 0.1 M NaOH (aq) solution, continuing with the addition of 0.01 mL/min aliquots until reaching pH = 11. The electrode was protected with a dialysis membrane, previously neutralized.

Fourier transform infrared spectroscopy (FTIR). Infrared spectroscopy (Bruker, IFS 55) was applied to inspect the chemical groups on the sidewalls of the CNTs. The spectra were collected by a golden gate attenuated total reflectance (ATR) configuration using a diamond tip with a resolution of 4 cm^{-1} in the wavenumber range of 400-4000 cm^{-1}.

Electron microscopy. High resolution scanning microscopy (HR-SEM, Hitachi SU70 working at 15 keV with a resolution of 1 nm) was used to analyse the microstructure of the CNT membranes. Scanning transmission electron microscopy (STEM), performed with a transmitted electron detector coupled to the HR-SEM equipment, was applied to observe the global position of the organic deposits of the CNTs. For more detailed examination of the CNT sidewalls, a high-resolution transmission electron microscopic (HR-TEM, JEOL 2200FS working at 200 keV, resolution of 0.1 nm) was accomplished. STEM and HRTEM samples were prepared by suspending CNTs in isopropyl alcohol (≥99.8%, Sigma-Aldrich) and dropping the suspension on lacey-carbon Cu grids (Agar Scientific), and drying afterwards in a vacuum oven at 100ºC for 30 h to reduce contamination.

μ-Raman spectroscopy. The CNT containing tissues were inspected by Raman spectroscopy. For that, a Jobin Yvon HR800 (Horiba, Japan) micro-Raman apparatus was used in the backscattering configuration. The selected 532nm laser line was provided by a Nd:YAG DPSS laser (Ventus, Laser Quantum, UK). The spectra were acquired using a 1800 l/mm grating, while the Rayleigh rejection was accomplished by edge filtering allowing Raman acquisition from 50cm-

1. In order to optimize the collection conditions, a 100x objective (spot size ~1μm, NA=0.85, Olympus, Japan) was used, focusing the laser excitation onto the sample and collecting the backscattered Raman radiation into the spectrometer to be further detected by a Peltier cooled (223K) CCD sensor. The spectrometer was operated in the confocal mode, setting the iris to 300μm, while the acquisition time was set to 45 seconds with 5 accumulations. The laser power was monitored in order to avoid any damage by local overheating, always keeping the radiation level below 0.2mW/μm2. Each spectrum was averaged from the data collected at three randomly selected spots. The in-plane crystallite size (L_a) of CNTs was estimated by measuring the ratio of the integral area of the D-band and G-band (Cançado's equation [26]).

Thermogravimetric analyses (TGA)*.* CNT impurities of amorphous carbon and inorganic types were quantified by thermogravimetry (Setsys Setaram) in N_2 (TG_{N2}) and O_2 (TG_{O2}) atmospheres, respectively. The samples were heated at 10 ºC/min under a constant gas flow of 200 sccm.

Specific surface area analyses (BET). Quantitative measurements of the chemical fuctionalization were performed by BET analyses (Micromeritics Gemini 2370 V5). For accurate measurements, the samples were firstly dried in an oven for 24h at 80ºC. Eight partial pressures were applied to further calculate the surface area after degassing the samples in N_2 at 120ºC for at least 2 h.

DC electrical conductivity measurements. Conductivity measurements of CNTs were accomplished to investigate on the level of π-disruption promoted by the chemical fuctionalization. Disc-shaped CNT membranes of 10 mm in diameter and 14±3 μm thick were prepared by vacuum filtration. Following a Van der Pauw configuration, for of each sample, four copper wires were fixed with a high conductive silver glue (RS, $\sigma > 1 \times 10^5$ Ω.m^{-1}) to two pairs of diametrically opposite contact positions. While the current was passing between one pair of contacts the voltage was measured along the other pair, perpendicular to the first pair. The I-V data was acquired by a computer-controlled 16-bit high-speed board (National Instruments DAQPad-6015) with a stepped applied voltage of 0.5 V in the range of -10V to 10V at 1s time intervals at room temperature.

X-ray photoelectron spectroscopy (XPS). Quantitative and qualitative examination of the organic chemical groups were accomplished by XPS (VG Scientific ESCALAB 200A). The spectra were acquired using a non-monochromatized AlKα radiation (1486.6 eV, 300 W) working at 15 keV, with a step size of 0.10 eV and a dwell time of 1s.

Contact angle analyses. A sessile drop technique assisted by a video-based software interface (DataPhysics OCA 20) was used to measure the contact angle of the CNT membranes. For this, the CNT membranes were previously fixed on a glass slice and clean three times with distilled and deionized water, followed by overnight drying in an oven at 80ºC. For a typical contact angle measurement, a drop of 1 ml of distilled and deionized water was gently dropped on the surface of the membrane using a micrometric syringe. At this point, the drop starts to be recorded over time by a CCD-camera. A single video frame was then selected to calculate the contact angle. This frame corresponds to the instant of the water drop stabilization just after the contact with the

surface of the membrane. A Laplace-Young mathematical function, suitable for the measurement of high contact angles, was used to fit the contour line of the drop. No less than 5 drops were analysed.

Zeta potential (ZP) analyses. The polarity and density of electrical charges of the CNTs were estimated in a Zeta-meter equipment (Malvern, Zetasizer Nano Series) in an electrolyte aqueous solution of 0.01M of KCl. The experiments were performed in quintuplicate at pH:7, adjusted with 0.001 M HCl and 0.001 M NaOH solutions, and the ZP was calculated according to Smoluchowski's equation [27].

Surface roughness measurements. The average surface roughness (R_a) and the peak count (R_{pc}) parameters of the membranes were determinate using a profilometer (Perthometer Mahr M1), an average of 5 acquisitions was done for each sample.

2.5. *Evaluation of the biological behavior – in vitro testing*

Human osteoblastic-like cells (MG63 cells, ATCC number CRL-1427™) were cultured in α-Minimal Essential Medium (α-MEM), supplemented with 10% fetal bovine serum, 50 µg.ml^{-1} ascorbic acid, 50 µg.ml^{-1} gentamicin and 2.5 µg.ml^{-1} fungizone, at 37ºC, in a humidified atmosphere of 5% CO_2 in air. For sub-culturing, the cell layer (at around 70-80% confluence) was detached with trypsin – EDTA solution (0.05% trypsin, 0.25% EDTA), for 5 minutes, at 37ºC and a single cell suspension was prepared in complete supplemented culture medium. Cells were cultured ($5x10^4$ cells.cm^{-2}) on the surface of *p*-CNTs and *p,f*-CNTs membranes, for 4 days. Colonized membranes were evaluated for cell adhesion and morphology by confocal laser scanning microscopy (CLSM) and scanning electron microscopy (SEM) and for cell viability/proliferation (MTT and LDH assays) and alkaline phosphatase activity.

CLSM observation. Cells grown over the samples were fixed (3.7% methanol-free formaldehyde, 15 minutes), at 6 hours of culture in order to analyse the cell adhesion process. Cells were following permeabilized with 0.1% Triton, and incubated with bovine serum albumin (Sigma Aldrich), 10 mg.ml^{-1} in PBS, for 1 hour, in order to block non-specific interactions. Cytoskeleton filamentous actin (F-actin) was visualized by treating permeabilized cells with Alexa Fluor® 488-conjugated phalloidin (Invitrogen), 1:100 in PBS, for 20 minutes. Cells were counterstained with propidium iodide (Sigma Aldrich), 10 mg.ml^{-1} in PBS, for 5 minutes. Stained samples were mounted in Vectashield® (Vector laboratories) and examined in a Leica SP5 AOBS (Leica Microsystems®) microscope.

SEM observation. Samples were fixed (1.5% glutaraldehyde in 0.14M sodium cacodylate buffer, pH 7.3, 10 minutes), and dehydrated in graded alcohols and critical-point dried. Previously to SEM observation, samples were sputter-coated with gold and analyzed in a FEI Quanta 400FEG ESEM.

MTT assay. The MTT (3-(4,5-Dimethylthiazol-2-yl)-2,5-diphenyltetrazolium) assay is based in the ability of mitochondrial dehydrogenase to reduce the MTT to a dark blue formazan product.

MTT (0.5 mg.ml^{-1}) was added to each well, and the colonized membranes were incubated for 3 hours at 37ºC. Following, the formazan salts were dissolved in dimethylsulphoxide (DMSO) and the absorbance (A) was determined at λ = 600 nm on an Elisa reader (Synergy HT, Biotek).

LDH assay. The lactate dehydrogenase (LDH) assay is based on the reduction of NAD by the action of LDH released to the medium. The resulting reduced NAD (NADH) is utilized in the stoichiometric conversion of a tetrazolium dye. Determination of the total LDH was performed in the colonized membranes using the *In vitro* toxicology assay kit lactate dehydrogenase based (Sigma-Aldrich; St. Louis, MO), according to the manufacturers' instructions. The amount of LDH leakage to the medium was normalized by total LDH, and calculated as follows: LDH leakage % = LDH medium / total LDH x 100.

ALP activity. ALP activity was evaluated in cell lysates (0.1% Triton X-100, 5 min) by the hydrolysis of *p*-nitrophenyl phosphate in alkaline buffer solution (pH~10.3; 30 min, 37 ºC) and colorimetric determination of the product (*p*-nitrophenol) at 400 nm in an ELISA plate reader (Synergy HT, Biotek). ALP activity was normalized to total protein content (quantified by Bradford's method) and expressed as nmol/min.mg$_{protein}^{-1}$.

2.6. *Evaluation of the biological behavior – in vivo testing*

The study was performed in accordance with the authorization of the Local Ethical Committee and observed the technical standards of protection of experimental animals, according to the Portuguese (Decree No. 1005/92) and European (Directive 2010/63) legislations.

Sixteen male Wistar rats, 95 – 105 days old (Harlan Laboratories, Germany) were used for subcutaneous implantation of prepared *p*-CNTs and *p,f*-CNTs membranes. Animals were housed in groups of 2 in type II cages, with water and food given ad libitum. Four implantation periods were evaluated: 3 days, 1, 3, and 7 weeks. General anesthesia was induced with the intraperitoneal (IP) injection of xylazine (10mg/kg) and ketamine (90mg/kg). The rats were monitored to ensure that an appropriate surgical plane of anesthesia was maintained throughout surgical manipulation. An IP injection of tramadol (10mg/Kg) was given for post-operative analgesia. The skin around the dorsum midline was shaved and disinfected with povidone-iodine solution and each animal was placed in a ventral position. Four small longitudinal incisions (~2 cm) were made on the dorsum, close to the midline, and a subcutaneous pocket was bluntly dissected at each incision with blunt tweezers. A single membrane was placed in each pocket. A total of eight membranes per experimental group, per time point, were implanted (four rats per time point). Following, each incision was closed with simple interrupted absorbable 4/0 sutures (Vicryl Rapide® - polyglatin 910, Ethicon, Livingston, UK). Each animal received a subcutaneous injection of tramadol (10mg.Kg^{-1}) at 12, 24 and 36h after surgery for continued post-operative analgesia. Animals were monitored daily for any complications or abnormal behavior.

Histological preparation. After euthanasia, segments of the subcutaneous tissue including the areas of the implanted samples were retrieved and excised and processed for histological

observation. Harvested specimens were fixed in 10% neutral buffered formalin. Tissues were embedded in paraffin and thin sections were cut and stained with haematoxylin and eosin to evaluate the tissue response to implanted *p*-CNTs and *p,f*-CNTs. Specimens were characterized by optic microscopy.

Peroxidase histochemistry. All samples collected 48 hours after implantation were immediately frozen on -20ºC and cut in the horizontal plane on a cryostat (HM520 Microm) into 5-µm sections. Peroxidase activity was demonstrated using DAB (*3,3'-diaminobenzidine)* (Merck®) as the enzyme substrate. The incubating medium consisted in one DAB buffer tablet dissolved in 10 ml distilled water (pH 6.85) and 40 µl of 3% H_2O_2. The sections were incubated with DAB (pre-heated to 37ºC) for 10 minutes, then washed thoroughly in distilled water, counterstained with hematoxylin, dehydrated and mounted with Entellan (Merck®) for evaluation by light microscopy.

3. Results and Discussion

3.1. *Doubly functionalized CNT membranes characterization*

As stated in the introductory section, doubly functionalized CNTs were designed with chemical groups to maximize their biodegradability and biocompatibility. CNTs were functionalized starting by a Diels-Alder reaction to form a chain of 1,3-butadiene cycloadducts (hydrophobic groups, highlighted in green in the sketch of Fig. 2a) following by an oxidation of the end alkene groups to produce carboxylic groups (hydrophilic groups, highlighted in red in the sketch of Fig. 2a).

3.1.1. *Assessment of hydrophobic 1,3 butadiene cycloadded groups*

Covalently bonded chains of cycloadducts with highly dense arrangement on the CNT outer sidewalls are designated here as an organic coating. To evaluate the uniformity and thickness of this coating, STEM and HRTEM analyses were performed (Figs. 2b-e). The low magnification STEM images of Figs. 2b and 2c clearly shows uniformly coated *p,f*-CNTs at long-range and clean p-CNT, both free of metallic impurities. Further details on the CNT sidewalls are given by high resolution TEM images (Figs. 2d and 2e). Fig. 2d shows clean walls free of metallic nanoparticles and amorphous carbon. On the other hand, Fig. 2e confirms the uniformity of a ~2 nm thick organic coating on the *p,f*-CNT sidewalls.

The TEM images also shown both CNT types with high structural organization presenting carbon walls perfectly aligned with the tube's axis (Figs. 2d and 2e). The structural crystallinity (L_a), listed in Table 1, corroborates these observations by showing high values and no significant change of crystallite size with the organic coating. This gives evidences for the non-destructive nature and high efficiency of the purification and functionalization methods.
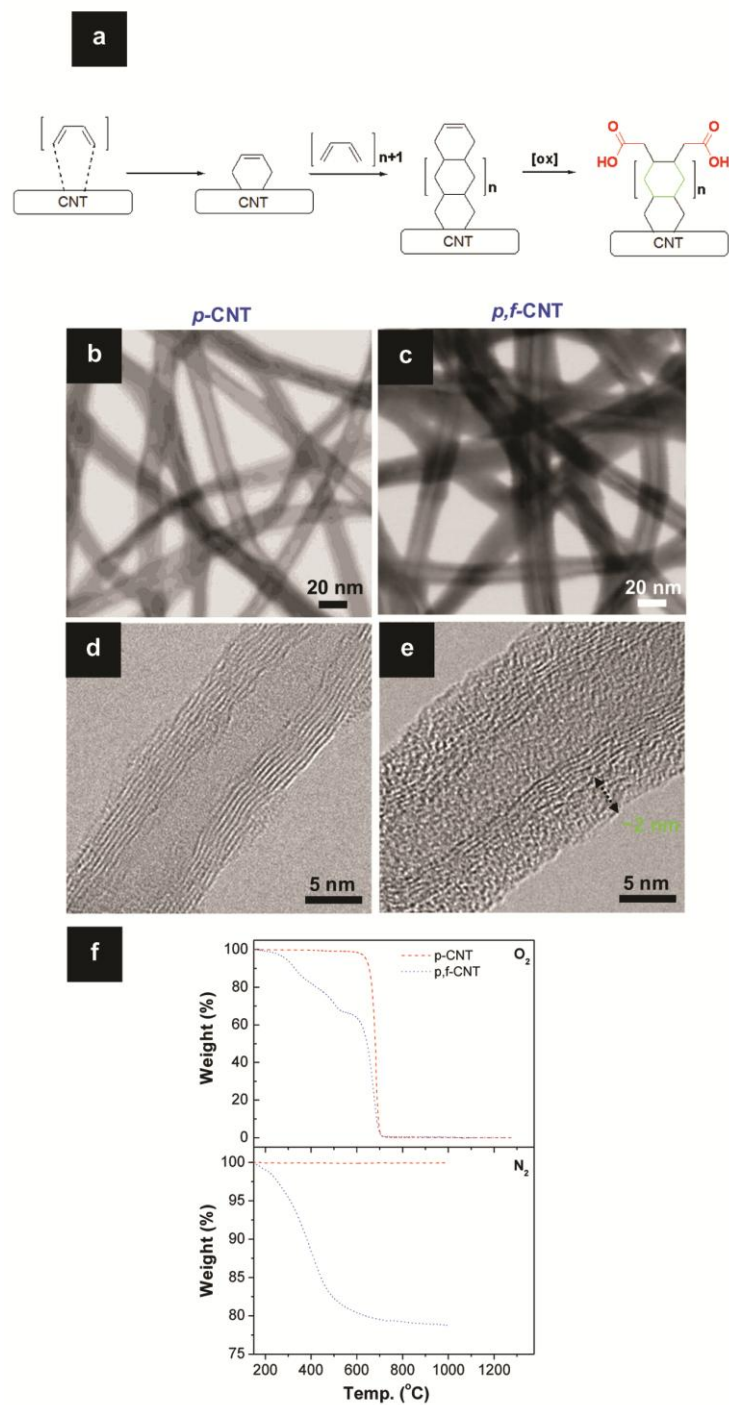
Fig. 2 - (a) Sketch of the doubly functionalized CNTs showing the aromatic chain (hydrophobic group, at green color) and the carboxylic groups (hydrophilic groups, at orange color). (b and c) STEM images of the p-CNTs and p,f-CNTs samples. (c and d) Respective HRTEM images of (b and c). (f) TG_{O2} and TG_{N2} curves of the samples of (b and c).

To further demonstrate this, TG_{O2} and TG_{N2} curves were presented in Fig. 2f. TG_{O2} depict non-measurable residues for both samples that are suggestive of the absence of inorganic impurities. Also, the oxidation temperatures of both samples are close, of 681ºC and 695ºC, proving the

preservation of the CNT structure when submitted to the functionalization process. Below the oxidation temperature, the *p,f*-CNTs suffer from partial weight losses due to gradual elimination of organic groups [22]. The respective TG_{N2} confirms the large grafting of an organic coating by yielding a weight loss of ~21% (Fig. 2f). The TG_{N2} curve of the *p*-CNTs reveals that the sample is almost free of amorphous carbon since no weight loss was detected up to 1000ºC (Fig. 2f). These results are in accordance with the STEM and TEM observations (Figs. 2b-e).

Surface area and electrical conductivity values presented in Table 1 also indicate the significant deposition yield of the organic coating on the CNT sidewalls by giving a reduction of ~40 % and ~70 % , respectively.

Table 1 - Physical-chemical and morphological characteristics of *p*-CNTs and *p,f*-CNTs.

Sample	Structural cristallinity L_a (nm)	Electrical conductivity (S.m^{-1})	Surface area (m^2.g^{-1})	Zeta potential (mV)	Contact angle (º)	Surface roughness R_a (µm)	Peak counts R_{Pc} (peaks.mm^{-1})
p-CNT	31±1	$1 \times 10^4 \pm 1 \times 10^3$	203±9	-34±4	135±4	3±0.6	5±1
p,f-CNT	36±6	$3 \times 10^3 \pm 9 \times 10^2$	122±3	-50±5	123±3	1.7±0.2	9±1
p- purified *f*- functionalized							

3.1.2. *Assessment of hydrophilic carboxylic groups*

Fig. 3a depicts the acid-base characteristics of the functionalized materials evidencing their acidic character.
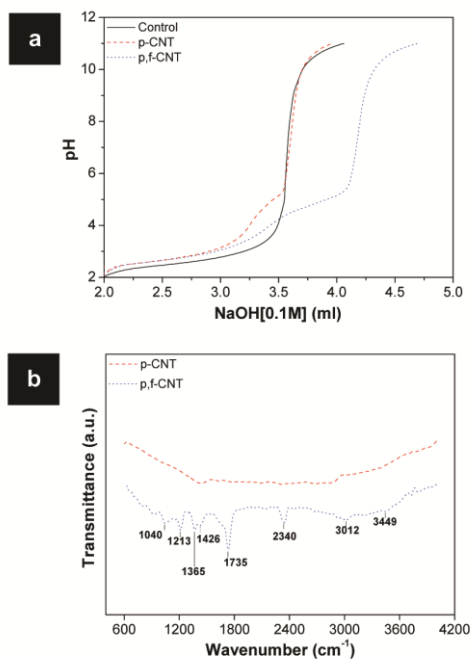

Fig. 3 - (a) Acid-base titration curves of the *p*-CNTs and *p,f*-CNTs samples. (b) Respective FTIR spectra of the samples in (a).

The control and the aqueous suspension of *p*-CNTs reached a neutral pH:7 at a lower concentration of NaOH compared to *p,f*-CNTs, the former requiring ~ 3.6 ml and the latter ~ 4.2 ml of NaOH solution. The identification of these acidic groups was accomplished by FTIR (Fig. 3b). The spectrum of the *p,f*-CNT sample reveals the presence of carboxylic (COOH) functional groups with typical signature peaks for carbonyl (C=O) at 1735 cm^{-1}, for hydroxyl (-OH) at 3449 cm^{-1} (H-bonded), at 1365 cm^{-1} for O-H bending, and at 1212 cm^{-1} for C-O stretching [28, 29]. The peak at 1040 cm^{-1} may be attributed to S=O stretching associated to sulfonic acid groups [30]. Adsorbed CO_2 molecules were also detected at 2340 cm^{-1} [31], but only on the reactive surface of the *p,f*-CNT samples. Both p-CNT and p,f-CNT samples present small peaks at 3012 and 1426 cm^{-1} that may be attributed to C-H stretching in aryl-H type of bonds and saturated C-H deformations, respectively.

Further evidence for the acidic nature of the functionalized CNTs was obtained by XPS.
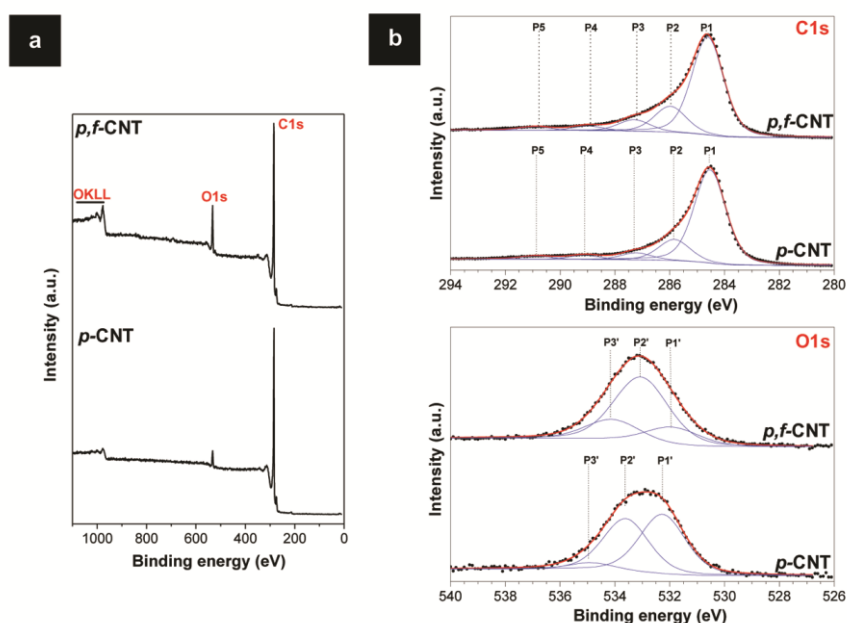
Fig. 4 - XPS analyses of the *p*-CNTs and *p,f*-CNTs samples: (a) survey spectra; (b) High resolution spectra and fitting curves of the C1s and O1s bands.

Fig.4a depicts the survey spectra showing the typical C1s and O1s peaks, the latter clearly more intense for the *p,f*-CNT, corresponding to twice the O:C ratio relative to *p*-CNT (Table 2). This observation is consistent with the FTIR analyses presented previously (Fig. 3b). The shape of the high-resolution C1s spectra is characterized by a main component peak corresponding to the sp2 carbon of the graphite-like lattice and a strong tailing toward higher binding energy (Figure 4b).

Table 2 - XPS elemental composition of the *p*-CNTs and *p,f*-CNTs samples.

Samples	C1s (%)					O1s (%)			O:C
	P1	P2	P3	P4	P5	P1'	P2'	P3'	
p-CNT	71.4 (284.6eV)	18 (285.8eV)	5.1 (287.3eV)	3.0 (289.1eV)	2.5 (290.9eV)	46.1 (532.3eV)	45.6 (533.6eV)	8.3 (534.8eV)	0.045
p,f-CNT	68.2 (284.6eV)	18.5 (286eV)	7.5 (287.3eV)	3.3 (288.9eV)	2.5 (290.9eV)	14.6 (531.9eV)	62.6 (533.1eV)	22.8 (534.1eV)	0.093

Four additional peaks were necessary to obtain a good fit, that may be assigned to C-O (~286 eV), >C=O (~287.5 eV), -COO (~288.5 eV), and the higher energy shakeup peaks due to $\pi \rightarrow \pi^*$ electron transitions. The peaks resulting from curve deconvolution are present in both types of CNT, showing higher intensity for the *p,f*-CNT relative to *p*-CNT. The detailed information of the peak areas obtained by deconvoluting the C1s and O1s peaks is presented in Table 2. The high resolution O1s spectrum obtained for *p*-CNTs could be deconvoluted into two main component peaks centred at approximately 532 and 533.8 eV, typically corresponding to O-C=<u>O</u> and <u>O</u>-C=O, respectively. These component peaks are still present in the O1s deconvolution for *p,f*-CNTs (slightly shifted) and an additional intense peak centred at 533 eV, that may be assigned to C-OH [29]. Inspection of Table 2 confirms that *p,f*-CNT samples have higher concentration of carboxylic groups (peaks P4 and P3') than the *p*-CNT samples. These XPS observations corroborate with the FTIR analysis.

Surfaces supplied with -OH or -COOH groups are expected to be both negatively charged (δ-) due to their high tendency to ionize by losing the H$^+$ ion [32]. Also, it can be assured that *p,f*-CNTs have higher density of electrical charge than the *p,f*-CNTs due to the higher level of the referred groups, according to the data already shown. Zeta potential and wettability measurements were carried out to verify the chemical analysis results obtained. Table 1 confirms that *p,f*-CNTs samples exhibit higher negative potentials than purified ones, -50 and -34 mV, respectively. Similar observations were previously observed in isopropyl alcohol [33]. Moreover, the wettabilitty measurements are in accordance with the zeta potential values by showing *p,f*-CNTs samples with an average contact angle of 123º, lower than 135º of the *p*-CNTs.

3.1.3. *Topographical features*

Fig. 5 depicts representative SEM micrographs of the p-CNTs and p,f-CNTs. membranes. Overall, they have rough surfaces (Table 1) resulted from the arrangement of rough areas of micrometer-sized positive and negative protrusions interspaced by smooth areas of horizontally disposed nano-rough tubes (Figs. 5a-c). Yet, distinct topographic features are seen between the two types (Figs. 5a and 5b). Particularly, the p,f-CNTs membrane presents higher linear frequency of local positive protrusions, given by the peak count parameter R_{pc} (Table 1), and lower surface roughness Ra, which indicates a more homogeneous surface topography.
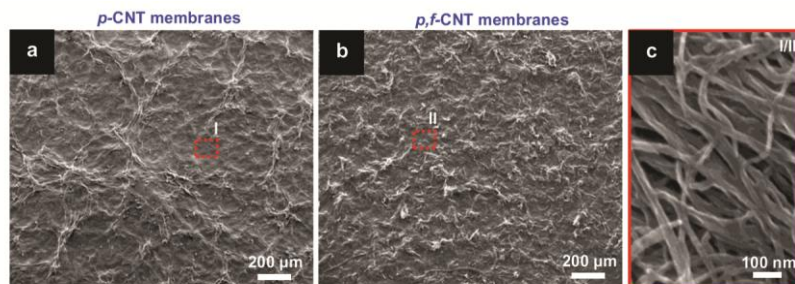
Fig. 5 - (a and b) SEM images showing the topography of the *p*-CNTs and *p,f*-CNTs samples. (c) High resolution image of the nano-rough CNT network (smooth area).

3.2. *In vitro human osteoblastic cell response on doubly functionalized CNT membranes*

Adhesion of MG-63 osteoblastic cells to *p*-CNTs and *p,f*-CNTs membranes was evident soon after plating, as seen by the progressive cytoplasmic expansion and gradual acquisition of an elongated morphology (Fig. 6a). However, cell spreading was clearly improved on the functionalized membranes where a significant percentage of cells exhibited an elongated morphology, compared to the rounded appearance of most cells on *p*-CNT (Fig. 6a). Differences on the cell morphology subsist at 4 days of culture. Still, SEM images showed that cells were able to adapt to the irregular surface topography of both membranes and to establish intimate interactions via cytoplasmic expansion (Fig. 6a).

Results for cell compatibility tests are given in Fig. 6b. Cell viability/proliferation, assessed by the MTT assay, increased throughout the culture time in both membranes. MTT reduction values were higher on *p,f*-CNT, particularly at day 4, suggesting an enhanced cell viability and/or growth rate on the functionalized samples. The LDH released to the medium was higher on *p*-CNT membrane, evidencing signs of cellular toxicity, namely membrane integrity, which might explain the lower MTT reduction values compared to those on *p,f*-CNT samples. Cells synthesized ALP, an early osteoblastic marker, however present higher enzyme activity on *p,f*-CNT membranes.

Literature reports addressing the cytocompatibility of CNTs-containing materials reveal divergent results, ranging from a dose-dependent impairment of the cellular metabolic activity/proliferation, to the absence of cytotoxicity, and even to the enhancement of cellular function, as recently reviewed [34]. Regarding the response to osteoblastic cells, a general trend for a biocompatible profile is verified. Appropriate cellular adhesion and early proliferation has been reported in studies involving several osteoblastic cell systems, i.e. in SaOS2 cells seeded over SWCNTs films prepared by different techniques and reporting different degrees of purity [35], MWCNTs sheets [36], and compact MWCNTs constructs [37], in rat osteoblastic-like cells (MC3T3-E1 cell line) cultured over MWCNTs-covered culture plates [38], and human mesenchymal stem cells (hMSCs) cultured on a thin layer of SWCNTs [39] or monolayer patterns of CNTs [40]. Concerning the functional activity, increased alkaline phosphatase activity, osteoblastic gene

expression and calcium deposition were seen in SaOS2 grown over compact MWCNTs [37] or CNTs grown from anodized titanium alloys [41], and the interaction of hMSCs with MWCNTs substrates lead to an induction of the expression of osteogenic markers [42].
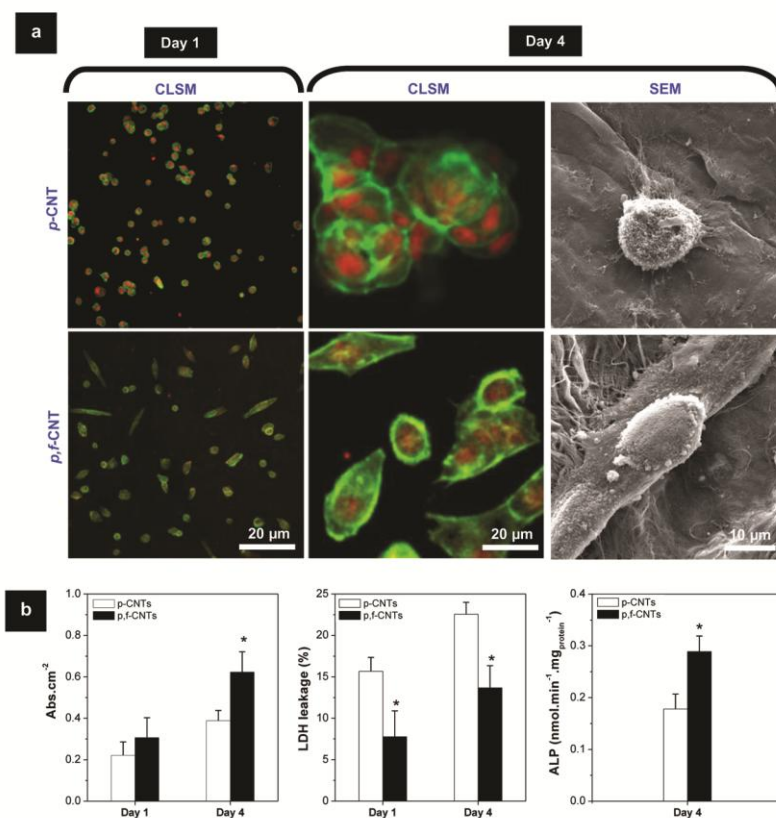
Fig. 6 - Behaviour of MG63 osteoblastic cells over p-CNTs and p,f-CNTs membranes cultured for 1 and 4 days: (a) CLSM images of cells stained for F-actin cytoskeleton (green) and nucleus (red) and SEM images; (b) cell viability/proliferation (MTT assay), LDH leakage and ALP activity. *Significantly different from *p*-CNTs membranes.

On the whole, data strongly suggest that two key parameters, surface roughness and surface energy density, have rendered the modulation of the *in vitro* biocompatible profile of CNTs interfacing osteoblastic cells. Suitable cell adhesion and early proliferation observed over CNTs surfaces might be, at least, in part related to the nanoscale roughness profile. It has been shown that such nanoscale features are able to tune osteogenesis by a cell membrane distortion mechanism. As suggested recently, the increased tension over actin filaments, derived from the bloated cytosolic expansion, may determine cellular events that converge to an enhanced osteogenesis via the activation of Rho-family GTPase signaling [43]. Beyond the distortion-induced phenomenon, CNT surfaces are also able to interfere with biomolecules distribution, including that of talin, α-actinin, filamin and vinculin [44]. These focal adhesion proteins greatly determine early and late adhesion events and seem to temper the subsequent cell proliferation process [45].

Related to this, increased expression of focal adhesion proteins was reported on CNTs substrates [46].

The surface roughness parameters evaluated for the membranes (Table 1) are not sensitive to nanoscale features. However, the R_{pc} value for the p,f-CNT (9 peaks.mm^{-1}) portraits more anchorage sites to cells, with dimensions in the range 20-50 μm (Fig. 6a), than the corresponding value for the p-CNTs. Thus, the topography of the former (Fig. 5b) turn them friendlier for cell adhesion and proliferation [47]. In addition, the modifications introduced within the CNTs surface energy by functionalization may determine the success of the early adhesion and cell proliferation/differentiation events. For example, hMSCs grown over oxygen-functionalized (negatively charged) SWCNTs monolayers showed improved morphology and enhanced osteogenic commitment, as compared to non-functionalized substrates [42]. Both the p-CNT and p,f-CNT are negatively charged, but they presented significant differences in the zeta potential values, which is expected to influence the composition, exchange events and stability of the protein layer that quickly forms on the reactive surface of the CNTs membranes, with a relevant role in the elicited cell response [48, 49].

Overall, CNTs substrates contribute for an appropriate proliferation and osteoblastic differentiation, yet, doubly functionalized CNTs membranes evidenced clear improved cell response.

3.3. *In vivo biocompatibility and biodegradability of doubly functionalized CNT membranes subcutaneously implanted in rats*

The *in vivo* biological response to functionalized and non-functionalized membranes was evaluated following subcutaneous implantation in Wistar rats for 1, 3 and 7 weeks. At the necropsy, no macroscopic signs of significant inflammatory reaction or cellular exudate were found around the implanted membranes, for the assayed time points. Histopathological analysis revealed that both MWCNTs membranes triggered an inflammatory response, characterized by the presence of a chronic immuno-inflammatory infiltrate and associated encapsulated granulation tissue, broadly identified following 1 week post implantation. With increased implantation time, at 3 and 7 weeks, a denser inflammatory infiltrate was attained, despite that a slight milder response was verified with the implantation of non-functionalized MWCNTs (Fig. 7 and Table 3).

Table 3 - Histological analysis of the tissue reactions associated with the subcutaneous implantation of p-CNT and p,f-CNT samples.

Timeframe	Sample	Thickness (μm)[a]	MØ[b]	Giant cells[b]	Lymphocytes[b]	Degradation[b]
Day 7	p-CNT	35-90	1	2	1	0/1
	p,f-CNT	44-133	2	2	1	1/2
Day 21	p-CNT	75-136	2	2	1	0/1
	p,f-CNT	105-166	3	3	1	2
Day 49	p-CNT	73-148	2	2	1	0/1
	p,f-CNT	172-250	3	3	2	3

[a]Minimum-Maximum
[b]Scoring system: 0-Absent; 1-Reduced; 2-Moderate; 3-Marked (adapted from Macleod et al., 2005)

Nevertheless, the attained trifling inflammatory response for both MWCNTs membranes did not result in neutrophil infiltration, cell necrosis, or the presence of cell debris – processes associated with the development of an adverse biological response – thus supporting the reduced cytotoxicity profile of the tested materials [50].

These results come in line with previously published reports addressing the *in vivo* biological response to pristine CNTs.
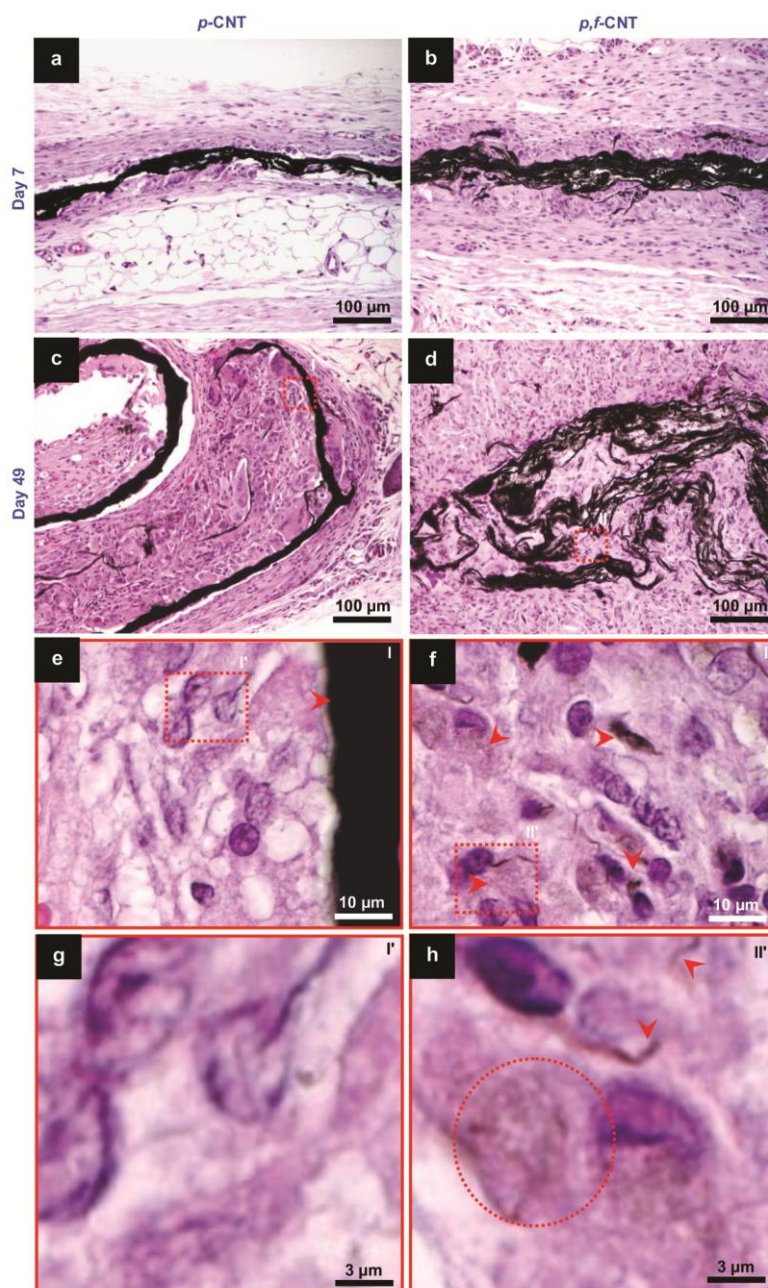

Fig. 7 - Hematoxylin and eosin-stained sections of subcutaneous implanted membranes in Wistar rats, at 7 and 49 days post-operatively: (a-d) low magnification micrographs; (e-h) high magnification micrographs at 49 days (CNTs ropes highlighted by red arrows and individualized CNTs by a dotted red circle).

Current insights tend to support the idea that highly pure and crystalline CNTs are broadly nontoxic and only activate a milder inflammatory response, as detailed in recent reviews [7]. Subcutaneous or intramuscular implantation of both SWCNTs and MWCNTs in rodents seems to induce a minor infiltration of inflammatory cells associated with CNTs encapsulation [51], as verified in this report. Still, biological output seems to be major dependent on the particularities of the CNTs physic-chemical profile [1].

The intraperitoneal or subcutaneous grafting of distinct size MWCNTs suspensions revealed a minor response for shorter and smaller CNTs, while the administration of longer fibers, induced a high grade and reactive inflammatory response [11]. Apart from CNTs size (i.e., diameter and length) their degree of purity also seems to be a determining factor affecting tissue response. The presence of impurities in MWCNTs was found to induce the activation of a severe immune-inflammatory reaction – manifested by marked follicular dystrophy and alopecia - following subcutaneous implantation of sampled CNTs powder in mice or rats; while purified MWCNTs revealed minor cell infiltration and slight granulomatous reaction [52]. Our results regarding the subcutaneous implantation of a relative high dose (4 mg per animal) of highly pure and crystalline unfunctionalized MWCNTs in a membrane form are in line with published literature supporting the adequate biological response with only trifling inflammation and encapsulation, following 7 weeks of implantation.

The biological response to functionalized CNTs is far less scarce in the literature. Despite that most studies are focused on the response following systemic administration and little is known regarding local tissue implantation, published data seems to trail the idea that functionalization improves the biological profile of CNTs [53]. In our work, functionalized MWCNTs membranes implanted subcutaneously induced a slighter intense inflammatory response, in comparison to non-functionalized MWCNTs membranes. This distinct biological behavior might be related to the fact that, while *p*-CNTs membranes were broadly undegraded following 7 weeks of implantation, signs of degradation and loss of structural integrity could be easily identified in *p,f*-CNTs membranes, right after the first week of implantation, and were found to increase progressively with the implantation time (Fig. 7). At high magnification, implanted *p*-CNTs seem to retain the structural integrity (Figs. 7e and 7g) while *p,f*-CNTs revealed an advanced cell-mediated degradation process (Figs. 7f and 7h). Small fibrillar remains of *p,f*-CNTs can be identified, dispersed throughout the inflammatory infiltrate area (Fig. 7f, labelled by red arrows), at the same time that phagocytes seem to uptake and digest the fibrilar debris, as evidenced by the intracellular accumulation of thinner *p,f*-CNTs fibrils (Fig. 7h, dotted red circle). A faster degradation of functionalized CNTs within the biological environment has been recently addressed in distinct literature reports outreaching their improved biosafety profile. Accordingly, carboxylated and nitrogen doped MWCNTs were found to be hastily degraded by oxidative peroxidases and hydrogen peroxide, in a layer-by-layer exfoliation mechanism facilitated by side wall defects [54]. Furthermore, CNTs with carboxylated surfaces, unlike unmodified CNTs, underwent degradation in a simulated phagolysosomal assay, revealing both longitudinal splitting as well as oxidative degradation of the side walls [14]. *In vitro* assays with

living cells also tend to support the biodegradation of functionalized CNTs in a process mediated by oxidative enzymes commonly found in phagocytic cells of the immune system. Human neutrophils were found to completely degrade functionalized carbon nanotubes following 12 hours of incubation, in a process mediated by myeloperoxidase (MPO) and NADPH oxidase [55]. Interestingly, functionalized-CNTs incubated with human macrophages were negligible degraded after 6 hours of incubation and following 12 hours, only around 13% of degradation was verified by infrared spectroscopy [55]. Attained results support the idea that peroxidase activity may be a determinant of the biodegradation of CNTs [12], as macrophages contain far less levels of MPO than neutrophils [56], and thus are expected to induce a significantly slower biodegradation of functionalized CNTs.

In order to endorse the neutrophils-mediated activity in p,f-CNTs degradation, we evaluated the tissue response to CNTs membranes implanted for 72 hours, valuing the identification of peroxidases in tissue sections (Fig. 8).
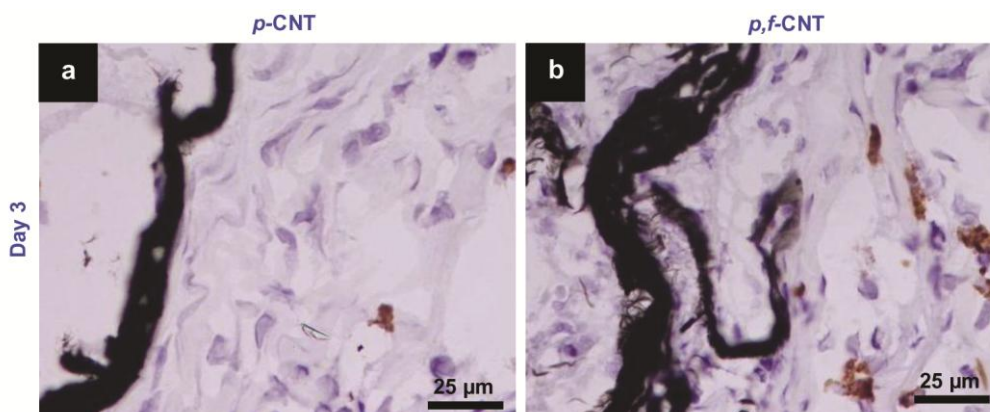
Fig. 8 - Sections of the histochemical staining for peroxidase activity of subcutaneous implanted membranes in Wistar rats, at 3 days post-operatively.

Neutrophils recruitment and activation can only be disclosed during the acute phase response triggered by material implantation, usually lasting for a few days [56]. Following, the persistence of the implanted material leads to a chronic phase, largely characterized by the presence of differentiating monocytes, macrophages and lymphocytes [56, 57], as that attained in histopathological sections of the 1, 3 and 7 weeks implantation time. The 72 hours time point was chosen in order to minimize the effect of the surgical trauma in short-term experiments, still enclosing the transition from the acute to the chronic phase response and thus, being able to disclose the effect of the early neutrophilic recruitment and activation [58, 59]. Attained tissue sections revealed a typical staining corroborating peroxidase activity, generally dispersed throughout the immune-inflammatory infiltrate area, but particularly concentrated at the region neighboring the implanted membranes (Figs. 8a and 8b). Qualitatively, *p,f*-CNTs implantation seemed to induced an intense peroxidase staining, as comparing to *p*-CNTs implantation,

corroborating the idea that neutrophilic peroxidases are determinant in the individualization and degradation of functionalized CNTs (Figs. 8a-d).

Figs. 9a and 9b show micro Raman spectra acquisition areas taken on subcutaneously implanted p-CNT and p,f-CNT membranes.

Fig. 9 - Optical images of the implanted (a) p-CNT and (b) p,f-CNT membranes with respective magnified images of the acquisition area of the Raman analysis as inset. (c and d) μ-Raman spectra of the materials of (a) and (b) for implanted

times of 0, 7 and 49 days. (e and f) Respective integral intensities and FWHM measurements of the D- and G-bands of the Raman data of (c) and (d).
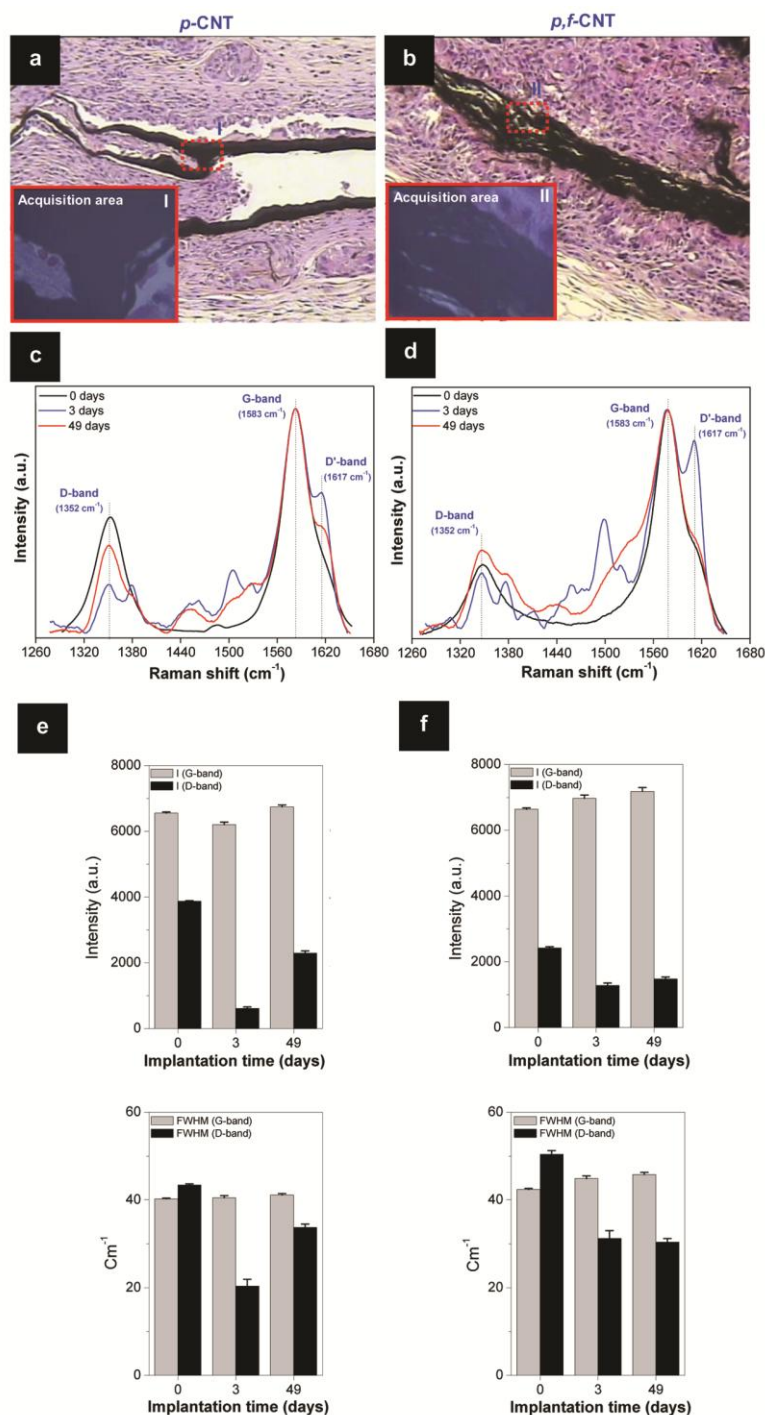
In samples analyzed immediately after implantation (Figs. 9c and 9d), spectra are dominated by the standard main features in CNTs at ~1350cm^{-1} (D band), ~1580cm^{-1} (G band) and a right shoulder at ~1620cm^{-1} (D' band). While the G band is associated to the main C-C tangential E$_{2g}$vibration mode, D and D' are disorder induced double-resonance (DR) Raman bands. In fact, whereas the D band comes from the breathing modes of sp^2 rings, D' is due to an intravalley DR mechanism, both bands being activated by local defects [60].

Compared to the *p*-CNT, the *p,f*-CNT reveal a decrease in the D band intensity before contact with the biological medium (Figs. 9c and 9d). This mode originates on the presence of defects on sp^2 C rings. The functional groups attached to the C rings seem to have a damping effect on such vibrations, reducing the D band intensity. This damping is also observed for the exposed *p*- and *p,f*-CNT, presenting a reduction of the D band intensity after 7 days of implantation (Figs. 9c and 9d). There is evidence for the presence of other species with characteristic Raman bands at 1380, 1505 and 1618cm^{-1} that may be adsorbed or covalently bonded to the MWCNT, both for *p*-CNT and *p,f*-CNT, with higher intensity for the latter. The functional groups on the *p,f*-CNT may react with the biological material, and that is evidenced by the persistent changes induced on the D and G modes after 49 days of exposure to the biological medium. After this long exposure period the *p*-CNT show an increase of the D band intensity, indicating a partial recovery of their original structure, while the *p,f*-CNT present a nearly unchanged D band relative to the material exposed for 7 days. After 49 days of implantation the Raman spectra of both types of nanotubes reveal a considerable intensity decrease for the frequencies associated to the bonded/adsorbed molecules, but this reduction is less pronounced for the *p,f*-CNT. In fact the *p,f*-CNT present a small increase of the G band intensity and width, and the bands at 1380 and 1505 cm^{-1}, observed under *in vivo* conditions, coalesce with the D and G bands, respectively. This may be an indication either that the biological molecules are stably bonded to the *p,f*-CNT surface or that a CNT structural amorphization might occur to some extension.

Functionalized MWCNTs were observed to disperse much better in biological milieus (Figs. 7a-d), therefore increasing the available surface for reaction or adsorption of other molecules. The increase in surface availability or opening of the membrane may be a direct consequence of the MWCNT chemical modification, or may be due to physical changes of the *p,f*-CNT under stress induced by *in vivo* biochemical conditions. Recent studies showed that the MWCNT functionalized by the Diels-Alder cycloaddition reaction used in the present work may unzip the outer MWCNT layer, forming functionalized graphene nanoribbons (*f*-GNR). This effect was observed in solution by the application of ultrasounds for a short period of time, and may be triggered under different types of stresses. It was observed under scanning tunneling microscopy conditions, for MWCNTs functionalized by another type of cycloaddition reaction, the 1,3 dipolar addition of azomethine yilides [19]. Also, it was recently proved that this functionalization boost the *in vivo* biodegradation

of MWCNTs [20]. As so, there is strong evidence that cycloaddition reactions are able to tune CNT degradation by either longitudinal opening or simple cutting. If this biodegradation phenomenon is observed, the new formed semi-opened structures would be able to extend and flatten the surface available for interaction with biological environments depressing the intrinsic toxicological risks of the starting CNT needle-like materials.

4. Conclusions

The biocompatibility and biodegradability profiles of doubly functionalized CNT membranes were successfully studied by *in vitro* and *in vivo* assays.

In vitro suitable cell adhesion was observed onto *p*-CNT and *p,f*-CNT membranes due to the nanoscale roughness profile. Yet, the surface energy was also determinant in the success of the early adhesion event. In line with this, cell spreading was clearly improved on the functionalized membranes. The enhanced cell spreading on *p,f*-CNT substrates also contributes for an appropriate proliferation and osteogenic differentiation, supported by higher MTT reduction values and ALP activity values in the *p,f*-CNT membranes than the *p*-CNT ones.

In vivo subcutaneously implanted CNT membranes in Wistar rats revealed that both materials triggered a chronic immuno-inflammatory infiltrate and associated encapsulated granulation tissue, but without neutrophil infiltration or cell necrosis. This supports the reduced cytotoxicity profile of the tested materials. Owed to their higher biological reactivity, *p,f*-CNT membranes induced a slighter intense inflammatory response relatively to *p*-CNT membranes. Also, signs of degradation and loss of structural integrity were identified in *p,f*-CNT membranes, but not in the *p*-CNT membranes. It was demonstrated that the *in vivo* biodegradation of *p,f*-CNT was mediated by oxidative milieus containing neutrophilic and macrophages peroxidases following 7 weeks of implantation.

In vitro and *in vivo* data suggest that CNTs display an adequate profile for biological interaction, especially in bone tissue related applications. Though, CNTs functionalization provides new opportunities to modulate the interaction between these materials and biological environments, holding a strong promise as novel systems for drug delivery, or just systems with improved biocompatibility and biodegradability. Regarding the latter, observations put forward that cycloaddition reactions have a high balance between preservation of intrinsic properties and maximization of CNT *in vivo* biodegradability, thus presenting superior appetency to functionalize CNTs for biomedical purposes than conventional acidic functionalizations. Future work, including studies exploring other live tissues and a careful morphological evaluation of the CNT membranes, will be carried out to confirm this idea and to propose a biodegradation mechanism.

Acknowledgements

References

[1].   Harrison BS, Atala A. Carbon nanotube applications for tissue engineering. Biomaterials. 2007;28(2):344-53.

[2].   Tran PA, Zhang L, Webster TJ. Carbon nanofibers and carbon nanotubes in regenerative medicine. Adv Drug Delivery Rev. 2009;61(12):1097-114.

[3].   Shimizu M, Kobayashi Y, Mizoguchi T, Nakamura H, Kawahara I, Narita N, et al. Carbon Nanotubes Induce Bone Calcification by Bidirectional Interaction with Osteoblasts. Adv Mater 2012;24(16):2176-85.

[4].   Dumortier H, Lacotte S, Pastorin G, Marega R, Wu W, Bonifazi D, et al. Functionalized Carbon Nanotubes Are Non-Cytotoxic and Preserve the Functionality of Primary Immune Cells. Nano Lett. 2006;6(7):1522-8.

[5].   Shvedova A, Castranova V, Kisin E, Schwegler-Berry D, Murray A, Gandelsman V, et al. Exposure to Carbon Nanotube Material: Assessment of Nanotube Cytotoxicity using Human Keratinocyte Cells. J Toxicol Environ Health, Part A. 2003;66(20):1909-26.

[6].   Cui H-F, Vashist SK, Al-Rubeaan K, Luong JHT, Sheu F-S. Interfacing Carbon Nanotubes with Living Mammalian Cells and Cytotoxicity Issues. Chem Res Toxicol. 2010;23(7):1131-47.

[7].   Firme ICP, Bandaru PR. Toxicity issues in the application of carbon nanotubes to biological systems. Nanomed Nanotech Biol Med. 2010;6(2):245-56.

[8].   Pulskamp K, Diabaté S, Krug HF. Carbon nanotubes show no sign of acute toxicity but induce intracellular reactive oxygen species in dependence on contaminants. Toxicol Lett. 2007;168(1):58-74.

[9].   Mata D, Silva R, Fernandes A, Oliveira F, Costa P, Silva R. Upscaling potential of the CVD stacking growth method to produce dimensionally-controlled and catalyst-free multi-walled carbon nanotubes. Carbon. 2012;50(10):3585-606.

[10].   Lacerda L, Soundararajan A, Singh R, Pastorin G, Al-Jamal KT, Turton J, et al. Dynamic Imaging of Functionalized Multi-Walled Carbon Nanotube Systemic Circulation and Urinary Excretion. Adv Mater 2008;20(2):225-30.

[11]. Poland CA, Duffin R, Kinloch I, Maynard A, Wallace WA, Seaton A, et al. Carbon nanotubes introduced into the abdominal cavity of mice show asbestos-like pathogenicity in a pilot study. Nat Nanotechnol. 2008;3(7):423-8.

[12]. Bianco A, Kostarelos K, Prato M. Making carbon nanotubes biocompatible and biodegradable. Chemical Chem Commun. 2011;47(37):10182-8.

[13]. Allen BL, Kichambare PD, Gou P, Vlasova II, Kapralov AA, Konduru N, et al. Biodegradation of Single-Walled Carbon Nanotubes through Enzymatic Catalysis. Nano Lett. 2008;8(11):3899-903.

[14]. Liu X, Hurt RH, Kane AB. Biodurability of single-walled carbon nanotubes depends on surface functionalization. Carbon. 2010;48(7):1961-9.

[15]. Ziegler KJ, Gu Z, Peng H, Flor EL, Hauge RH, Smalley RE. Controlled Oxidative Cutting of Single-Walled Carbon Nanotubes. J Am Chem Soc. 2005;127(5):1541-7.

[16]. Kim YJ, Shin TS, Choi HD, Kwon JH, Chung Y-C, Yoon HG. Electrical conductivity of chemically modified multiwalled carbon nanotube/epoxy composites. Carbon. 2005;43(1):23-30.

[17]. Kumar I, Rana S, Cho JW. Cycloaddition Reactions: A Controlled Approach for Carbon Nanotube Functionalization. Chem Eur J. 2011;17(40):11092-101.

[18]. Lee Y-S, Marzari N. Cycloaddition Functionalizations to Preserve or Control the Conductance of Carbon Nanotubes. Phys Rev Lett. 2006;97(11):116801.

[19]. Paiva MCao, Xu W, Fernanda Proença M, Novais RM, Lægsgaard E, Besenbacher F. Unzipping of Functionalized Multiwall Carbon Nanotubes Induced by STM. Nano Lett. 2010;10(5):1764-8.

[20]. Nunes A, Bussy C, Gherardini L, Meneghetti M, Herrero MA, Bianco A, et al. In vivo degradation of functionalized carbon nanotubes after stereotactic administration in the brain cortex. Nanomedicine : nanotechnology, biology, and medicine. 2012;7(10):1485-94.

[21]. Bianco A, Kostarelos K, Partidos CD, Prato M. Biomedical applications of functionalised carbon nanotubes. Chem Commun. 2005(5):571-7.

[22]. Proen, a MF, Ara, jo RF, Paiva MC, Silva CJR. The Diels-Alder Cycloaddition Reaction in the Functionalization of Carbon Nanofibers. J Nanosci Nanotechnol. 2009;9(10):6234-8.

[23]. Stevens MM. Biomaterials for bone tissue engineering. Mater Today. 2008;11(5):18-25.

[24]. Kobayashi T, Nakamura S, Yamashita K. Enhanced osteobonding by negative surface charges of electrically polarized hydroxyapatite. J Biomed Mater Res. 2001;57(4):477-84.

[25]. Gorgulho HF, Mesquita JP, Gonçalves F, Pereira MFR, Figueiredo JL. Characterization of the surface chemistry of carbon materials by potentiometric titrations and temperature-programmed desorption. Carbon. 2008;46(12):1544-55.

[26]. Cancado LG, Takai K, Enoki T, Endo M, Kim YA, Mizusaki H, et al. General equation for the determination of the crystallite size L[sub a] of nanographite by Raman spectroscopy. Appl Phys Lett. 2006;88(16):163106-3.

[27]. Hiemenz P, Rajagopalan R. Principles of Colloid and Surface and Chemistry. New York: Marcel Dekker; 1997.

[28]. Peng H, Alemany LB, Margrave JL, Khabashesku VN. Sidewall Carboxylic Acid Functionalization of Single-Walled Carbon Nanotubes. J Am Chem Soc. 2003;125(49):15174-82.

[29]. Zhou J-H, Sui Z-J, Zhu J, Li P, Chen D, Dai Y-C, et al. Characterization of surface oxygen complexes on carbon nanofibers by TPD, XPS and FT-IR. Carbon. 2007;45(4):785-96.

[30]. Xing R, Liu N, Liu Y, Wu H, Jiang Y, Chen L, et al. Novel Solid Acid Catalysts: Sulfonic Acid Group-Functionalized Mesostructured Polymers. Adv Funct Mater. 2007;17(14):2455-61.

[31]. Chong CS, Ishak I, Mahat RH, Amin YM. UV-VIS and FTIR spectral studies of CR-39 plastics irradiated with X-rays. Radiat Meas. 1997;28(1–6):119-22.

[32]. Hu H, Yu A, Kim E, Zhao B, Itkis ME, Bekyarova E, et al. Influence of the Zeta Potential on the Dispersability and Purification of Single-Walled Carbon Nanotubes. J Phys Chem B. 2005;109(23):11520-4.

[33]. D. M, J. OF, M. F, P.S. G, M.H. F, M.A. L, et al. J Biomed Nanotechnol. 2013:*Submitted*.

[34]. Uo M, Akasaka T, Watari F, Sato Y, Tohji K. Toxicity evaluations of various carbon nanomaterials. Dent Mater J. 2011;30(3):245-63.

[35]. Kalbacova M, Kalbac M, Dunsch L, Hempel U. Influence of single-walled carbon nanotube films on metabolic activity and adherence of human osteoblasts. Carbon. 2007;45(11):2266-72.

[36]. Akasaka T, Yokoyama A, Matsuoka M, Hashimoto T, Abe S, Uo M, et al. Adhesion of human osteoblast-like cells (Saos-2) to carbon nanotube sheets. Bio-Med Mater Eng. 2009;19(2):147-53.

[37]. Xiaoming L, Hong G, Motohiro U, Yoshinori S, Tsukasa A, Shigeaki A, et al. Maturation of osteoblast-like SaoS2 induced by carbon nanotubes. Biomed Mater 2009;4(1):015005.

[38]. Terada M, Abe S, Akasaka T, Uo M, Kitagawa Y, Watari F. Development of a multiwalled carbon nanotube coated collagen dish. Dent Mater J. 2009;28(1):82-8.

[39]. Tay CY, Gu H, Leong WS, Yu H, Li HQ, Heng BC, et al. Cellular behavior of human mesenchymal stem cells cultured on single-walled carbon nanotube film. Carbon. 2010;48(4):1095-104.

[40]. Park SY, Namgung S, Kim B, Im J, Kim JY, Sun K, et al. Carbon Nanotube Monolayer Patterns for Directed Growth of Mesenchymal Stem Cells. Adv Mater. 2007;19(18):2530-4.

[41]. Sirinrath S, Chang Y, Xingcheng X, Brian WS, Thomas JW. Greater osteoblast functions on multiwalled carbon nanotubes grown from anodized nanotubular titanium for orthopedic applications. Nanotechnology. 2007;18(36):365102.

[42]. Baik KY, Park SY, Heo K, Lee K-B, Hong S. Carbon Nanotube Monolayer Cues for Osteogenesis of Mesenchymal Stem Cells. Small. 2011;7(6):741-5.

[43]. Arnsdorf EJ, Tummala P, Kwon RY, Jacobs CR. Mechanically induced osteogenic differentiation – the role of RhoA, ROCKII and cytoskeletal dynamics. J Cell Sci. 2009;122(4):546-53.

[44]. Lim JY, Dreiss AD, Zhou Z, Hansen JC, Siedlecki CA, Hengstebeck RW, et al. The regulation of integrin-mediated osteoblast focal adhesion and focal adhesion kinase expression by nanoscale topography. Biomaterials. 2007;28(10):1787-97.

[45]. Cox BD, Natarajan M, Stettner MR, Gladson CL. New concepts regarding focal adhesion kinase promotion of cell migration and proliferation. J Cell Biochem. 2006;99(1):35-52.

[46]. Holt BD, Short PA, Rape AD, Wang Y-l, Islam MF, Dahl KN. Carbon Nanotubes Reorganize Actin Structures in Cells and ex Vivo. ACS Nano. 2010;4(8):4872-8.

[47]. Choi C-H, Hagvall SH, Wu BM, Dunn JCY, Beygui RE, "Cj" Kim C-J. Cell interaction with three-dimensional sharp-tip nanotopography. Biomaterials. 2007;28(9):1672-9.

[48]. Verma A, Stellacci F. Effect of Surface Properties on Nanoparticle–Cell Interactions. Small. 2010;6(1):12-21.

[49]. Lynch I, Dawson KA. Protein-nanoparticle interactions. Nano Today. 2008;3(1–2):40-7.

[50]. Anderson JM. Biological responses to materials. Annu Rev Mater Res. 2001;31(1):81-110.

[51]. Firme Iii CP, Bandaru PR. Toxicity issues in the application of carbon nanotubes to biological systems. Nanomed Nanotech Biol Med. 2010;6(2):245-56.

[52]. Koyama S, Endo M, Kim Y-A, Hayashi T, Yanagisawa T, Osaka K, et al. Role of systemic T-cells and histopathological aspects after subcutaneous implantation of various carbon nanotubes in mice. Carbon. 2006;44(6):1079-92.

[53]. Koyama S, Kim YA, Hayashi T, Takeuchi K, Fujii C, Kuroiwa N, et al. In vivo immunological toxicity in mice of carbon nanotubes with impurities. Carbon. 2009;47(5):1365-72.

[54]. Liu Z, Cai W, He L, Nakayama N, Chen K, Sun X, et al. In vivo biodistribution and highly efficient tumour targeting of carbon nanotubes in mice. Nat Nanotechnol. 2006;2(1):47-52.

[55]. Zhao Y, Allen BL, Star A. Enzymatic Degradation of Multiwalled Carbon Nanotubes. J Phys Chem A. 2011;115(34):9536-44.

[56]. Kagan VE, Konduru NV, Feng W, Allen BL, Conroy J, Volkov Y, et al. Carbon nanotubes degraded by neutrophil myeloperoxidase induce less pulmonary inflammation. Nat Nanotechnol. 2010;5(5):354-9.

[57]. Bianco A, Kostarelos K, Prato M. Making carbon nanotubes biocompatible and biodegradable. Chem Commun 2011;47(37):10182-8.

[58]. Franz S, Rammelt S, Scharnweber D, Simon JC. Immune responses to implants – A review of the implications for the design of immunomodulatory biomaterials. Biomaterials. 2011;32(28):6692-709.

[59]. Coleman DL, King RN, Andrade JD. The foreign body reaction: A chronic inflammatory response. J Biomed Mater Res. 1974;8(5):199-211.

[60]. Marion L, Haugen E, Mjör IA. Methodological assessments of subcutaneous implantation techniques. J Biomed Mater Res. 1980;14(4):343-57.

[61]. Anderson JM. Chapter 4 Mechanisms of inflammation and infection with implanted devices. Cardiovasc Pathol. 1993;2(3, Supplement):33-41.

[62]. Frank O, Tsoukleri G, Riaz I, Papagelis K, Parthenios J, Ferrari AC, et al. Development of a universal stress sensor for graphene and carbon fibres. Nat Commun. 2011;2:255.

Chapter IV

MWCNT/Glass/HA bone grafts: processing, physicochemical characterisation and *in vitro* biocompatibility

IV.1. Introduction

In the present section a great effort was placed to produce CNT/Glass/HA composites with adequate microstructural, mechanical, thermal, electrical and, most important, biological characteristics to apply as non-metallic conductive bone grafts in the electrotherapy of skeletal tissue. Here, the major goal was to obtain composites with functional properties. The level of CNT individualization in the composites was controlled to yield percolation thresholds at low CNT loadings, to avoid the deterioration of the biological behaviour of the matrix, and to improve, or at least prevent, the damage of the mechanical properties relatively to those of the matrix. The inclusion of CNT agglomerates in the composite microstructure increased the contact area between CNTs and bone cells, giving rise to other functionalities, such as cell orientation, and enhanced adhesion assigned to the CNT nano-topography.

Briefly, the powder processing step and the consolidation step were fully optimised to: (1) homogeneously distribute the CNTs in the ceramic matrix; (2) control the size of the CNT agglomerates, below the biologically safe diameter sizes (<20 μm); (3) minimize contaminant sources; (4) preserve the intrinsic CNT properties; and (5) minimize CNT losses.

Section IV.1 depicts the sintering strategies for the CNT/Glass/HA composites, at fixed 4.4 vol.% CNT loading, comprising reactive-bed pressureless sintering and pressure-assisted sintering methods. The sintering conditions were optimised towards prevention of HA dehydroxylation and subsequent CNT loss by oxidation.

Section IV.2 describes the functionalization-free powder processing route of CNT/Glass/HA composites, at fixed 4.4 vol.% CNT loading, with minor contaminant levels and damage to CNTs, integrating aligned biologically safe CNT agglomerates (<3 μm). The *in vitro* biological characterization of the composites was evaluated, with particular interest on the effects of the CNT agglomerates on cell orientation and functional activity.

Section IV.3 express a detailed investigation on the mechanical and functional properties of CNT/Glass/HA composites with CNT loading ranging from 0 to 4.4 vol.%. Detailed 2D and 3D microstructures of the composites were analysed. Further assessment of the contribution of the CNT loading-percolation and porosity level in the microstructure-properties correlation was accomplished.

IV.2. Sintering strategies for smart electroconductive carbon nanotube/glass/hydroxyapatite bone grafts

D. Mata[a], F.J. Oliveira[a], N.M. Ferreira[a,b], R.F. Araújo[c], A.J.S. Fernandes[b], M.A. Lopes[d], R.F. Silva[a]

[a]CICECO, Materials and Ceramic Eng. Dept., Univ. of Aveiro, 3810-193 Aveiro ,Portugal

[b]I3N, Physics Dept., Univ. of Aveiro, 3810-193 Aveiro, Portugal

[c] Centre of Chemistry, Univ. of Minho, 4710-057 Braga, Portugal

[d] CEMUC, Metallurgical and Materials Eng. Dept., Faculty of Eng., Univ. of Porto, 4200-465 Porto, Portugal

Abstract

Electroconductive bone grafts have been design to control bone regeneration. Contrary to polymeric matrices, the translation of the carbon nanotube (CNT) electroconductivity into oxide ceramics is challenging due to the CNT oxidation during sintering.

Sintering strategies involving reactive-bed pressureless sintering (RB+P) and hot-pressing (HP) were optimized towards prevention of CNT oxidation in glass/hydroxyapatite (HA) matrices. Both showed CNT retentions up to 80%, even at 1300ºC, yielding an increase of the electroconductivity in ten orders of magnitude relatively to the matrix. The RB+P CNT compacts showed higher electroconductivity by ~170% than the HP ones due to the lower damage to CNTs of the former route. Even so, highly reproducible conductivities with statistical variation bellow 5% and dense compacts up to 96% were only obtained by HP. These sintering strategies offer new insights in the sintering of electroconductive bioactive ceramics with unlimited geometries for *in situ* electrical stimulation of bone.

Keywords: Carbon nanotubes, Ceramic matrix composite, Reactive sintering, Hot pressing, Electroconductive bone graft

1. Introduction

Calcium phosphate (CaP) bioceramics have been widely used in bone surgery as synthetic grafts for over more than three decades [1-3]. Their success is owed to the chemical resemblance with the mineral component of the natural bone [3]. Though, all of these family-related CaPs present poorer mechanical properties than natural bone [3]. At load bearing sites, this represents a concern giving the loss of the material structural integrity at the first stage of the new bone growth. To improve this, CaPs are usually reinforced with other phases, for example: P_2O_5-bioglass reinforced hydroxyapatite - Glass/HA. Besides the improved mechanical properties [4], this composite shows higher bioactivity [5] than single phase HA. Other attractive phases, as carbon nanotubes (CNTs), have been recognised to strengthen CaP ceramics [6] due to the high biocompatibility with bone tissue [7], bioactivity [8], low cost and outstanding mechanical properties [9]. Despite great efforts, the mechanical properties of the composites are usually only marginally better than those of the ceramic alone.

Beyond the attractive mechanical properties, CNTs present ultimate electrical conductivity [9] allowing obtaining electroconductive biomaterials at low percolation thresholds (P_c), without damaging the biological profile of the CaP matrix. Moreover, non-metallic CNTs establish a breakthrough in the production of high electroconductive biomaterials to work under electrical stimulation routines, free of corrosion related toxicological risks.

Great effort has been placed on such biomaterials, considered a new generation of "smart" materials, that are able to control particular responses of excitable tissues [10]. CNT-polymeric substrates have been used to stimulate neuronal [11] and bone tissue [12]. Yet, polymers present much lower bone grafting qualities than CaPs. These ceramics are also dielectric [13], but studies investigating the use of CNTs to improve their electrical properties are not found. By combining the biological profile and mechanical strength of the Glass/HA ceramic, with the morphology and electrical conductive of the CNTs, a superior multi-functional bone graft is proposed - CNT/Glass/HA, inspired in the respective apatite-like phase and the collagen type I fibers of the natural bone.

Contrary to polymeric composites, the translation of the CNT properties into bulk ceramics is not straightforward. Particularly for oxide matrices, a major concern deals with the sintering step at high temperatures. In H_2O-free atmospheres, at 680-1080ºC, the HA phase begins to lose the structural OH groups, i.e. the dehydroxylation occurs [14]. The release of oxygen-containing groups from the matrix, above the oxidising temperature of the CNTs, at 500-600 ºC, may fully oxidise or severely damage them. This becomes a real concern when the maximisation of the CNT electrical properties is envisaged.

Concerning this, the selection of a suitable sintering route is the first challenge to overcome in the processing of CNT-HA formulations. Such composites have been consolidated by pressureless or pressure-assisted sintering techniques [6]. When compared to the later ones, the former, has the advantage of being less destructive to CNTs [15] and of not being geometrically

limited or an expensive technique. The main disadvantages of the absence of pressure are the lack of full densification and total prevention of the dehydroxylation and subsequent oxidizing reactions in most CNT-HA systems [16]. Even tough, a recent work reports a pressureless sintering via with a good balance of CNT loading and densification [17]. There was however no data on the electrical characterisation of the composites or on the crystallinity of the CNT structure in the processed materials.

This work focuses on the optimisation of the sintering route of highly electroconductive CNT/Glass/HA synthetic bone grafts. The powders were consolidated under reductive atmospheres by different routes: simple pressureless sintering (P); reactive powder bed under pressureless sintering (RB+P); hot pressing (HP). To assess the efficiency of the sintering routes, the loading and structural crystallinity of CNTs, after sintering alongside with the compressive strength and electrical conductivity of the composites, were thoroughly investigated. Also, the balance of CNT loading and densification were maximised to preserve the mechanical properties of the matrix and achieve a 3D electron transporting network.

2. Materials and Methods

2.1. *Preparation of CNT/Glass/HA powders*

P_2O_5-glass (65 P_2O5, 15CaO, 10CaF$_2$, 10Na$_2$O mol%) and HA powders were lab-prepared from high purity (>98%) grade reagents: the glass was formed at 1450 °C for 90 min in a platinum crucible then rapidly cooled to room temperature; HA was synthesised by a conventional precipitation method. Full description of these processes was reported previously [4,5]. The Glass and HA materials were then individually planetary milled in ethanol (≥99.9%, Sigma) with agate jar and balls until reaching a particle diameter size of $D_{0.5}$= 3.1±1.6 μm and $D_{0.5}$= 2.2±1.1 μm, respectively. Subsequently, Glass/HA powders with 2.5 wt% of glass were planetary co-milled/mixed in the same conditions for 24h, having a final particle diameter size of $D_{0.5}$= 1.8±1.4 μm.

MWCNTs (NC7000) were provided by Nanocyl with the characteristics presented in Table 1. The CNTs were functionalised by a Diels-Alder cycloaddition reaction of 1,3-butadiene upon heating at 150ºC for 7 days. Further details of the process are presented elsewhere [18].
Isopropyl alcohol (≥99.8%, Sigma), used previously [4,5], was also applied for thorough mixing the composite powder with a fixed CNT loading of 2.5 wt% (4.4 vol.%) - CNT/Glass/HA composites. The powders were processed by a two-stepped method combining high-speed shearing for 30 min (IKA T25-Ultra-Turrax, working at 20,500 rpm) and sonication during 60 min (Selecta, working at 60 kHz, 200 W). After fast solvent evaporation under vaccum at 80ºC, to avoid phase separation, the dried powders were crushed in an agate mortar and sieved to less than 75 μm.

2.2. *Sintering routes*

For pressureless sintered (P) powders, disc-shaped samples with a diameter of 5.5± 0.1 mm diameter and thickness of 1.2±0.1 mm were prepared by isostatic pressing at 300 MPa. Green compacts were further fired in a open Al_2O_3 crucible inside a graphite furnace under vacuum (3 Pa) or Ar (70 kPa, purity> 99.9999%), as follows: heating rate of 4 °C.min^{-1} with a fixed dwelling time of 60 min at 1300 °C, followed by cooling at rate of 10 ºC.min^{-1} to room temperature. When using a reactive-bed pressureless sintering (RB+P) approach, only Ar atmospheres were applied, and the open crucible was replaced by a closed graphitic crucible filled with a bed of HA + carbon black (≥ 99.5%, Degussa) powder mixture. The degree of HA dehydroxylation was controlled by varying the sintering temperature (1200, 1300 ºC), the total amount of the powder (5-30 g) and the carbon loading (10-50 wt.%). The diameter and thickness of P and RB+P sintered compacts were in the range of 4.5-5 mm and 1-1.1 mm.

For hot-pressing (HP), the powder mixture was placed in a 2 cm diameter graphite die and preliminary pressed at fixed pressure of 30 MPa. Then, the chamber was pumped down to ~3 Pa, and subsequently, the samples were fired by the following HP cycle: heating rate of 10 °C.min^{-1} with a fixed dwelling time of 60 min at temperature ranging from 1000-1300ºC, followed by cooling at rate of 10 ºC.min^{-1} to room temperature. The final compacts are disc-shaped samples 20 mm in diameter and 3±1 mm thick. Finally, the discs were cut into parallelepiped of 2.5 × 2.5 × 4.5 mm^3 for further investigation.

2.3. *Characterization techniques*

Termogravimetric analyses (TGA, Setsys Setaram) were performed under a constant flow of 200 sccm at 10ºC.min^{-1} with two types of atmospheres, N_2 (TG$_{N2}$) and O_2 (TG$_{O2}$). While the first one was used to quantify the level of amorphous carbon and functional groups of the CNT outer walls, the latter was applied to assess the CNT loading before and after sintering. Advantageously, the TG$_{O2}$ analysis allowed the precise determination of the CNT weight loss at known oxidation temperature (Table 1). The appearance of the disc-shaped samples was recorded to further confirm the CNT loading.

To confirm the functionalisation level, specific surface area measurements (BET, Micromeritics Gemini) were also performed. Eight partial pressures were applied to further calculate the surface area after degassing the samples in N_2 at 120ºC for at least 2 h.

Micro-Raman spectroscopy (Jobin Yvon T64000) was conducted at 532 nm in the wavenumber range of 1000-2000 cm^{-1} to assess the structural crystallinity of CNTs before and after sintering. The CNT crystallinity was estimated by calculating the graphite in-plane crystallite size (L_a) using the Cançado's equation [19].

The phase composition of sintered composites was assessed by X-ray diffraction (X'PERT-MPD Philips) working with a CuKα$_1$ radiation (λ= 0.154056 nm), from 5 to 80º with a stepped size of

0.02º. The Gazzara and Messier method [20] was applied for phase quantification by considering the heights of the most representative planes of each phase.

Fourier transform infrared spectroscopy (FTIR, Mattson 7000 galaxy series) were applied to investigate the H_2O peaks of HA phase. The spectra were collected with a resolution of 4 cm^{-1} in the wavenumber range of 400-4000 cm^{-1} in transmittance mode.

The experimental and theoretical densities of sintered composites were respectively obtained by geometric measurements and by the rule of mixtures by considering the following phases: HA (d= 3.16 $g.cm^{-3}$ [21]), β-TCP (d= 3.07 $g.cm^{-3}$ [21]),TTCP (d= 3.05 $g.cm^{-3}$ [21]), α-TCP (d= 2.86 $g.cm^{-3}$ [21]), Bioglass (d= 2.7$g.cm^{-3}$ [22]) and MWCNT-NC7000 (d= 1.66 $g.cm^{-3}$ [23]).

High resolution scanning microscopy (HR-SEM, Hitachi SU70 working at 15 keV with a resolution of 1 nm) was used to analyse the microstructure of polished and chemically etched surfaces. The samples were firstly polished with SiC papers (grades P1000, P1200, P2500, P4000) followed by a 50 nm sized silica finishing. The chemical etching was accomplished with 0.01 M HNO_3 for 10-60s, with two etching strength, to show the CNT locations in the microstructure and reveal the grains. The grain size was determined by Heyn's method, according to the ASTM E112-196 .

Scanning transmission electron microscopy (STEM) performed, with a transmitted electron detector coupled to the HR-SEM equipment, was used to evaluate the morphological features of purchased CNTs and the chemical-physical interactions of CNTs and Glass/HA dried powders. High-resolution transmission electron microscopy (HR-TEM, JEOL 2200FS working at 200 keV, resolution of 0.1 nm) analysis were accomplished to evaluate the structure of purchased CNTs.
DC electrical conductivity measurements of CNTs were accomplished to investigate on the level of π-disruption. Disc-shaped CNT membranes of 10 mm in diameter and 14±3 μm thick were prepared by vacuum filtration. Following a Van der Pauw configuration, for of each sample, four copper wires were fixed with a high conductive silver glue (RS, $\sigma > 1 \times 10^5$ $\Omega.m^{-1}$) to two pairs of diametrically opposite contact positions. While the current was passing between one pair of contacts the voltage was measured along the other pair, perpendicular to the first pair. The I-V data was acquired by a computer-controlled 16-bit high-speed board (National Instruments DAQPad-6015) with a stepped applied voltage of 0.5 V in the range of -10V to 10V at 1s time intervals at room temperature.

For the ceramic samples, the DC electrical conductivity measurements at room temperature were performed in two different apparatus: a Keithley 617 programmable electrometer with a stepped applied voltage of 0.5 V in the range of 0-100 V for dielectric samples; ISO-TECH IPS-603 programmable power supply with a stepped applied voltage of 0.1 V in the range of 0-1 V for conductive samples. For the parallelepiped HP samples the copper wires were fixed directly to both ends of each sample. For the disc-shaped P and RB+P samples, the contact diameter was reduced to 2.2 mm by masking the sample and evaporating a Au/Pd film on each side of the sample.

Compressive tests were carried out in a Zwick/Roell Z020 equipment with a load cell of 2 kN and a constant displacement rate of 0.3 mm.min^{-1}. All mechanical and electrical tests were performed with five specimens for each condition.

3. Results and Discussion

3.1. *Green powders characterisation*

For biomedical applications, a careful morphological characterisation of the purchased MWCNTs is relevant [24]. Table 1 compiles the physical-chemical and morphological characteristics of Nanocyl-NC7000 CNTs.

Table 1 - Physical-chemical and morphological characteristics of as-received and functionalised Nanocyl-NC7000.

Sample	Length (μm)[a]	Diameter (nm)[a]	Number of walls[a]	Oxidation temperature (°C)[b]	Inorganic impurities (wt.%)[b]	Amorphous carbon impurities (wt.%)[c]	COOH groups (wt.%)[c]	Surface area (m^2.g^{-1})	Structural cristallinity, L_a (nm)[d]	Electrical conductivity (S.m^{-1})
r-CNT	3±2	10±2	7±2	562±2	12±1	3±1	-	256±7	18.2±0.4	3x10^3±9x10^2
f-CNT				570±2	8±1		15±3	181±2	17.9±0.6	1.2x10^3±5x10^2

r - raw
f - functionalised
[a]HRTEM measurements
[b]TGA, O_2 flow
[c]TGA, N_2 flow
[d]Micro-Raman (532 nm)

The low magnification STEM image of Fig. 1a shows CNTs with uniform morphologies. From higher magnifications of isolated CNTs as those shown in Figs. 1b and 1c, it was possible to estimate average values of length, diameter and number of carbon walls obtained after analysing of 50 CNTs (Table 1).

CNTs were used as-purchased with an average level of inorganic impurities of 12 wt.% that decreases to 8 wt.% after functionalisation (Table 1). The reduction of impurities could be explained by manipulation in solvents.

TG_{N2} measurements were also used to quantify CNT functional groups, previously identified as carboxilic (COOH) groups [18]. The functionalisation procedure applied here provided the maximum level of functional groups of 18 wt% (Table 1). Additionally, the surface area measurements show a decrease of ~30 % which is indicative of the presence of deposits on the CNT sidewalls, as it is shown in Table 1.

The presence of this functional groups did not significantly changed the structural cristallinity (L_a) of the CNTs (Table 1). The almost preserved CNT cristallinity is also proved by the thermal stability of the materials with respective oxidation temperatures of 570 and 562°C, obtained from the TG_{O2} analysis (Table 1). The existence of a residual π-disruption was translated into a 2.5-fold conductivity loss (Table 1). This is not a significant reduction when compared to a 25-fold loss obtained by commonly used acidic oxidisations [25]. In this way, the Diels Alder cicloadditon is probably one of the most suitable covalent reactions to functionalise CNTs with minor damage to produce high electroconductive composites. This was already recognised in the literature [26].
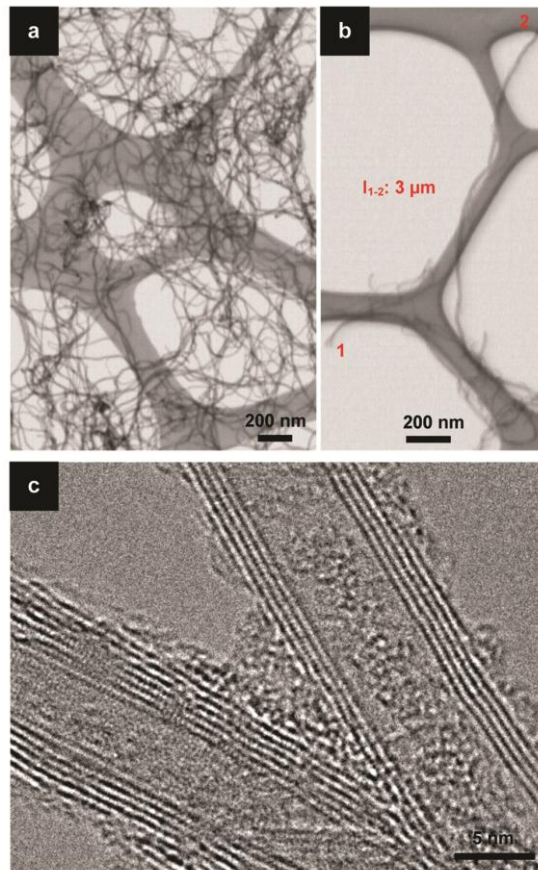
Fig. 1 - Structural and morphological features of as-received MWCNTs: (a) STEM low-magnification view showing the homogeneity of the CNT diameters; (b) representative STEM high magnification image of an individualised CNT showing a length size of 3 µm; (c) HRTEM image showing in detail the number of C walls and the amorphous carbon deposits.

Fig. 2 shows the morphological characterization of green compacts and processed CNT/Glass/HA powders. The initial CNT loading was 2.5 wt% (4.4 vol%), where only 2.2 wt% (3.9 vol.%) are pure phase CNTs. The % CNT loss due to the processing steps was irrelevant ~0.3 wt% (of 2.2 wt%). STEM image of Fig. 2a depicts CNT networks decorated with Glass/HA particles. This chemical bonding could be induced by hydrogen bonds between the carbonyl group of the COOH group of the CNTs with the OH groups of HA [27].

Besides the CNT-HA interactions, these charged groups maximise the disentanglement and dispersion of CNTs in polar solvents [18], such as isopropyl alcohol. To evaluate this, the 30º tilted views of the fracture surface of green compacts of Glass/HA (Figs. 2b-d) and CNT/Glass/HA (Figs. 2e-g) were compared. At low magnification, the ceramic matrix alone (Fig. 2b) is much smoother than the CNT containing sample (Fig. 2e), as expected. The detailed morphological analysis shows the compact ceramic powders of Fig. 2d being totally covered and intimately connected to CNTs in Fig. 2g.
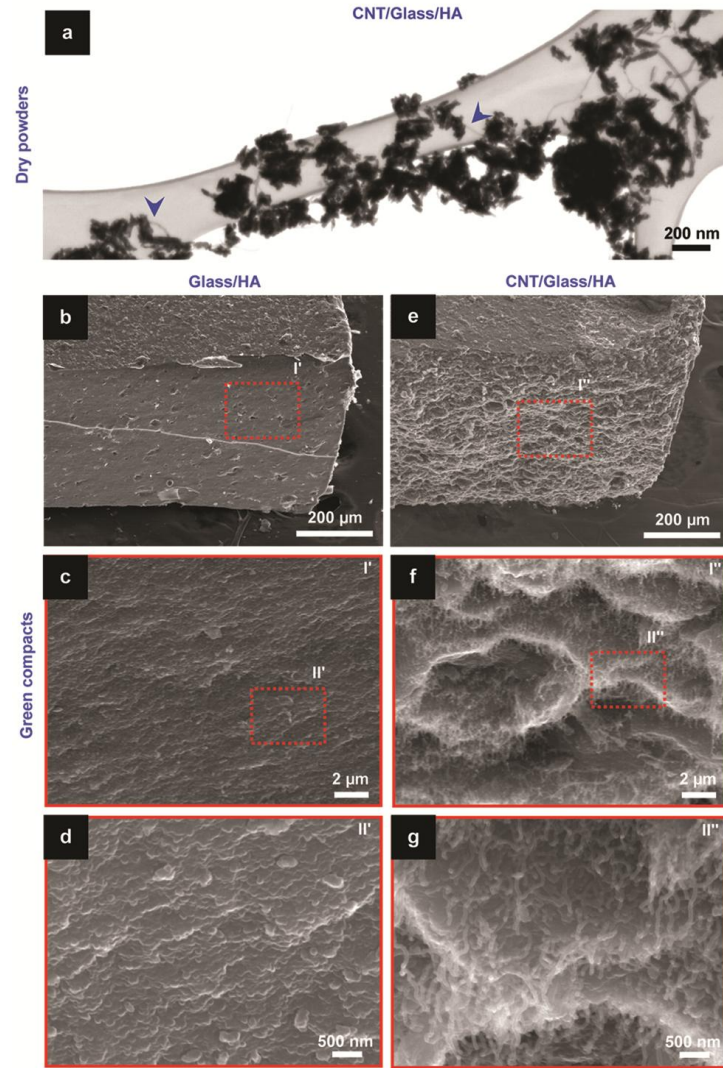
Fig. 2 - Morphological characterisation of the pre-sintered Glass/HA and CNT/Glass/HA materials: (a) STEM image of dry powders of CNT/Glass/HA showing the interactions between functionalised CNTs (highlighted with blue arrows) and ceramics; SEM images at three magnification views of the fracture surface of isostatically pressed green compacts of (b,c,d) Glass/HA and (e,f,g) CNT/Glass/HA.

3.2. *HA dehydroxylation and CNT oxidation at high temperatures*

Fig.3 shows the TG_{O_2} of functionalised CNTs and green powders of Glass/HA. The differential thermogravimetric curve (DTG) of the latter clearly show two weight loss ranges, typically of HA [14]: 100-530 °C - adsorbed H_2O; 660-1100°C - structural H_2O, i.e. dehydroxylation. At the first stages of dehydroxylation HA structure is converted to a similar one, but with hydrogen vacancies (V_x) resulting in an unstable phase, oxyhydroxyapatite (OHA), accordingly to

$$Ca_{10}(PO_4)_6(OH)_{2(s)} \leftrightarrow Ca_{10}(PO_4)_6(OH)_{2-2x}O_xV_{x(s)} + {}_xH_2O_{(g)} \qquad (1)$$

210
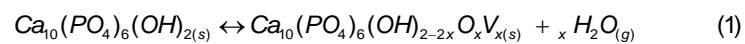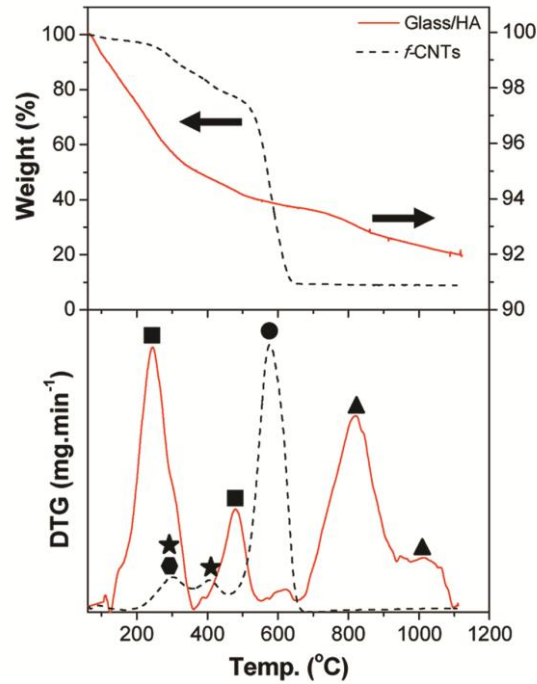
Fig. 3 - TG_{O_2} and respective DTG of functionalised CNTs (dashed black line) and Glass/HA matrix (solid red line). (CNT$_S$: ● CNTs, ◕ amorphous carbon, ★ COOH groups; Glass/HA: ■ adsorbed H_2O; ▲ structural H_2O).

When OHA is fully dehydroxylated it becomes oxyapatite (OA, $Ca_{10}(PO_4)_6O$), which is decomposed in a mixture of TTCP, TCP (β-TCP and α-TCP) and CaO [3,14]. The TG curve of Fig. 3 shows that oxyapatite phase is obtained at 1100ºC with a corresponding weight loss of 2.17 wt.%, which is in accordance with data from reference [14].

The release of structural H_2O becomes a shortcoming when CNT containing powders are processed, specially at low loadings (2.2wt%), because this carbon phase can be oxidised in the range of 400-600ºC (Fig. 3), as follows

$$C_{(s)} + H_2O_{(g)} \leftrightarrow CO_{(g)} + H_{2(g)} \qquad (2)$$
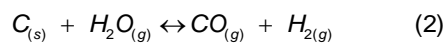
Regarding this, CNT/Glass/HA powders should be consolidated in reductive sintering atmospheres that might fully prevent the HA dehydroxylation. However, this is not straightforward because H_2O-free atmospheres accelerate HA dehydroxylation by favouring the forward reaction of eq. 1 [28]. To fully understand this, Glass/HA powders were firstly investigated alone. Two reductive atmospheres - Ar and vacuum - were used to sinter the ceramic powders in a graphite furnace. Here, the temperature used was 1300 ºC, accordingly to the optimised sintering cycle of this system [4,5].

XRD spectra of Fig. 4a show differences in phase composition of the sintered samples.

211
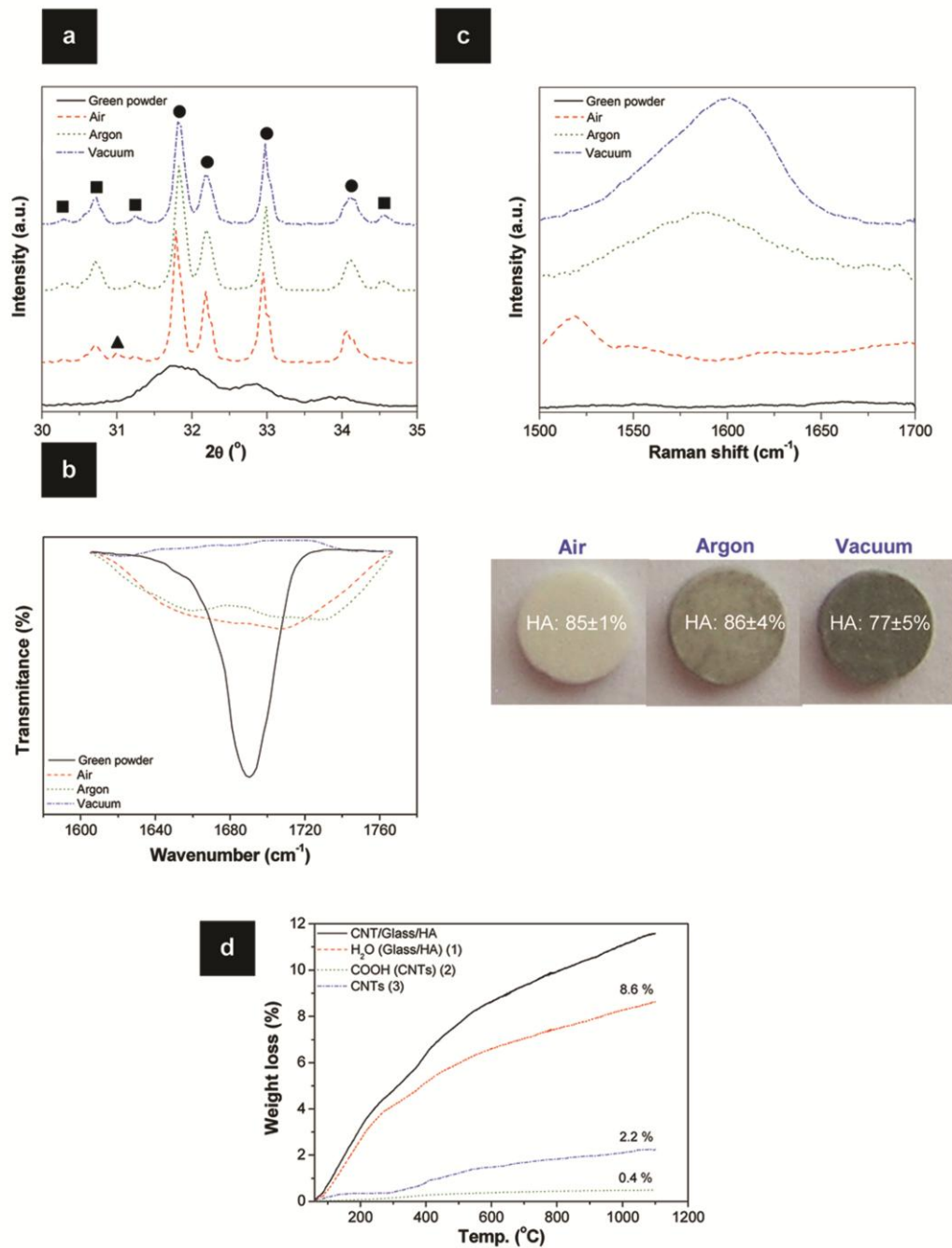
Fig. 4 - (a) XRD spectra of green Glass/HA powders and P sintered under air, Ar and vacuum conditions at 1300ºC (● HA; ▲ β-TCP; ■ α-TCP) (b) FTIR spectra of the H_2O-band of the (a) powders. (c) micro-Raman spectra of the graphitic G-band of the (a) powders (representative photographs of the sintered samples are shown as insets); (d) TG$_{Ar}$ weight loss curves of CNT/Glass/HA powders with the respective deconvolution to assess the contribution of each component: (1) H_2O of the Glass/HA; (2) COOH of the CNTs; (3) CNTs.

The fraction of HA is similar for air and Ar atmospheres, but decreases for the vacuum condition. This occurs since eq.1 has a product in the gas phase, the H_2O, thus, the vacuum condition promote the fast elimination of H_2O by strong suction forces, favouring the forward reaction of eq.

212

1. FTIR analysis shown in Fig. 4b corroborates this by showing stronger H_2O peak at ~1685 cm^{-1} [29] for the air and Ar sintered samples than for the vacuum ones.

At the same time, the H_2O released from the hydroxyapatite decomposition reacts with the graphite elements of the furnace producing CO (eq. 2). This gas is the carbon vehicle that leads to its precipitation inside the samples during sintering (eq. 3), accordingly to

$$CO_{(g)} \leftrightarrow C_{(s)} + \frac{1}{2}O_{2(g)} \qquad (3)$$
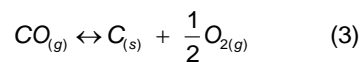
The presence of carbon in the samples was evaluated by collecting the micro-Raman spectra (Fig. 4c) in the region of the G-band at ~1580 cm^{-1} (typical feature of graphitic materials). The spectra show an increase content of carbon in the samples for the following sintering conditions: air<Ar<Vacuum. The appearance of the sintered samples shown in the inset photographs of Fig. 4c confirms this phenomenon by presenting an increase darkening with the increase carbon content.

Briefly, the above results suggest that Ar atmospheres should have higher appetency to preserve the CNTs than sintering under vacuum. To verify this, TG_{Argon} studies were performed with free powders of CNT/Glass/HA having high reactivity (Fig. 4d). For a detailed investigation of the CNT oxidation under these conditions, the total weight loss of the composite powder was deconvoluted to assess the contribution of each component: (1) H_2O of the Glass/HA; (2) COOH of the CNTs; (3) CNTs. Curve (1) was calculated with reference to the curve of Glass/HA powder in Ar. The second contribution, curve (2), was determined with the TG data of the raw and functionalised CNTs and by adjusting the values to the maximum of CNT fraction in the powder composite (2.2 wt.%). Finally, curve (3) was obtained by subtracting the TG curve of Glass/HA to CNT/Glass/HA and adjusting the result to the amount of amorphous carbon (3 wt.%, Table 1), followed by a subtraction of the curve 2.

Fig. 4d shows that the main weight loss contribution is attributed to the H_2O elimination form the ceramic matrix with a final value of 8.6%, close to 8.05% obtained for the TG performed in air (Fig. 3). This proves the similar thermal decomposition of the ceramic powders in Ar, as shown previously (Figs. 4a-c).

Surprisingly, the curve of weight loss of CNTs starts to increase significantly in the range of 300-400ºC reaching the maximum of 2.2 wt% at 1100ºC which means that they were totally oxidised, according to eq. 2. The abrupt increase of weight loss can be associated to the combined oxidisation of the adsorbed H_2O and the oxygen containing functional groups (COOH). The last case becomes evident in Fig. 4d, where it can be seen that the CNT and COOH curves presenting similar shape and starting to increase at the same temperature ~300ºC.

Nevertheless, compacted pellets should have a different thermal behaviour to high reactive free powders. For more realistic insights, compacted powders were P sintered under Ar

atmosphere (see section 2.2). As expected, the sintering gives a CNT weight loss of 1.78 %, around 20 % lower than for the free powders.

3.3. *Sintering strategies for high electroconductive CNT/Glass/HA composites*

3.3.1. *Reactive bed pressureless sintering (RB+P) route*

As demonstrated by White et al. [17], the retention of HA and CNT in the final composite can be achieved by simply shifting the equilibrium of reaction H_2O+C (eq. 2), according to Le Chatelier's principle. Gas flows containing $CO+H_2+H_2O$ mixtures running in a tube furnace were found to be the most successful [17]. A simpler approach concerns the formation of a $CO+H_2+H_2O$ atmosphere inside a sealed crucible by using a high reactive HA+C powder bed, as follows: (1) free powder of HA of the bed having higher reactivity than the compact powder (see section 3.2) starts by decomposing to form H_2O vapor (eq.1); (2) H_2O reacts with solid C powder of the bed to produce $CO+H_2$ gas mixtures (eq.2); (3) $CO+H_2$ gas intimately contacts the compact pellets and locally retains CNTs (by forming carbon, eq. 2 and eq. 3) and the H_2O (eq. 2) needed to prevent HA dehydroxylation. RB+P sinterig studies were performed at 1200 ºC and 1300ºC. The lower temperature was also investigated in an attempt of achieving a better balance between CNT loading and densification.

Following the thermodynamics of the eq. 2, the respective equilibrium constants (K) at 1200 ºC and 1300ºC are 500 and 1000, respectively. These values were calculated using the Factsage 6.1 software. Concerning Le Chatelier's rule, the backward reaction of eq. 2 is promoted when the reaction quotient (Q) is higher than the equilibrium one, Q>K. This can be achieved by increasing either CO, H_2 or both species. Having this in mind, HA+C reactive bed compositions were strategically selected to obtain a narrow range of partial pressures of CO (P_{CO}, where $P_{CO}=P_{H2}$) that follows the condition of Q>K. As shown in Fig. 5a, for each temperature, four P_{CO} conditions were used where three of them respect the condition Q>K. For these calculations it was assumed that the crucible was completely sealed and the powders were fully reacted. Also, it is relevant to highlight that these values are theoretical being relative to equilibrium conditions, yet they give the closest perspective to the experimental conditions.

Fig. 5b shows the variation of porosity and HA content of Glass/HA and CNT/Glass/HA samples with the sintering temperature and sintering atmosphere composition (P_{CO}). In respect to HA fraction, the values for both sample compositions are almost independent of the temperature used falling in the narrow range of 80-100%. Overall, the porosity of the CNT composite decreases with the increasing of the sintering temperature from 25-30% to 20-25%, but for the matrix alone the porosity did not significantly varied (10-15%).

Concerning the influence of the atmosphere composition, it can be seen that the HA fraction variation is close for both samples type. Though, in Glass/HA samples the HA phase was not totally retain due to two competitive reactions. Firstly, the matrix alone have a larger amount of

HA than the CNT/Glass/HA samples, thus, the produced H_2O from the $CO+H_2$ mixture it becomes insufficient to fully retain the HA phase (increase of HA retention for higher P_{CO} values). Secondly, since there is no CNTs to retain in the Glass/HA samples, the solid carbon formed locally by the high reductive CO (eq.2 and eq.3) may accelerate the HA decomposition, as reported elsewhere [30] (increase of HA retention for lower P_{CO} values). Considering this balance, the Glass/HA samples present a maximum HA retention at similar P_{CO} value than the CNT/Glass/HA samples for both sintering temperatures (Fig. 5b).
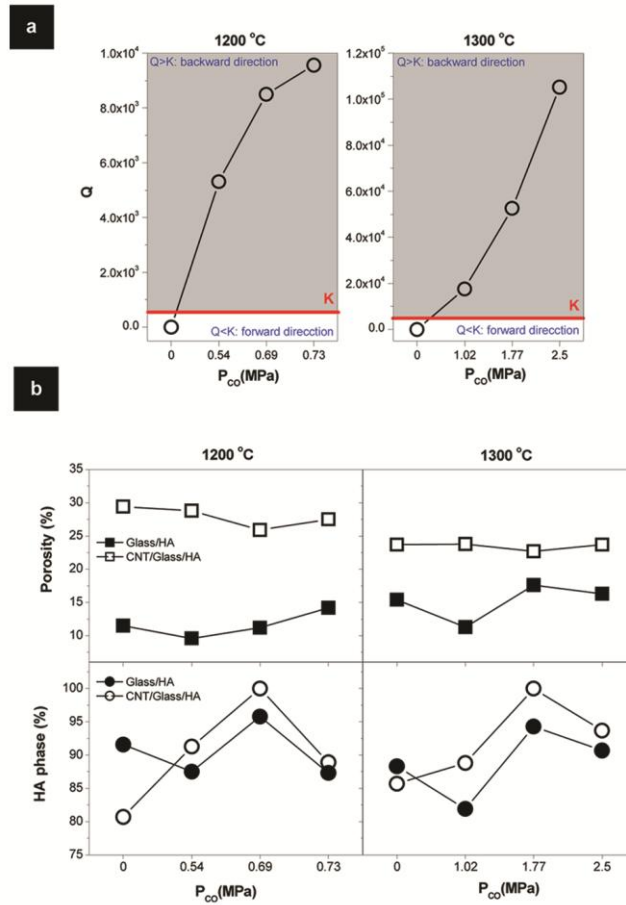
Fig. 5 - (a) Plot showing the influence of the RB+P atmosphere composition (P_{CO}) on the direction tendency of the $C+H_2O$ reaction (eq. 2) by comparing the respective equilibrium constant (K) and the reaction quotient (Q) at 1200°C and 1300°C. (b) plots showing the dependence of the porosity and HA phase of the Glass/HA and CNT/Glass/HA sintered by P+RB at 1200°C and 1300°C on the P_{CO} of the sintering atmosphere.

For the CNT/Glass/HA samples, the HA content increases with P_{CO} up to a maximum value of 100% for both sintering temperatures. Interestingly, the full HA dehydroxylation suppression was achieved when Q values were approximately twofold and threefold the K values at 1200°C and 1300°C, respectively (Fig. 5a). For higher values of Q the atmosphere becomes probably too reductive, accelerating the HA decomposition.

Overall, the porosity of the Glass/HA samples varies with P_{CO} in the same trend of the HA fraction. The higher HA decomposition is resulted from a higher carbon impurities content which promotes a subsequent decrease in the porosity due to the carbon incorporation in the microstructure. For CNT/Glass/HA samples the porosity varies with P_{CO} with an opposite trend of the HA fraction. Particularly in CNT/Glass/HA samples, this occurs because the higher HA content promotes higher CNTs retention and subsequent lower porosity. This can be easily evaluated by visual observation of the appearance of the samples. Fig. 6a shows a colour mapped ternary graph of the phase composition of CNT/Glass/HA samples (highlighted with red dots), sintered at 1200 and 1300ºC, plotted as a function of their appearance, following a three colour grade: white outer layer and light grey inner; uniformly dark grey; uniformly black.

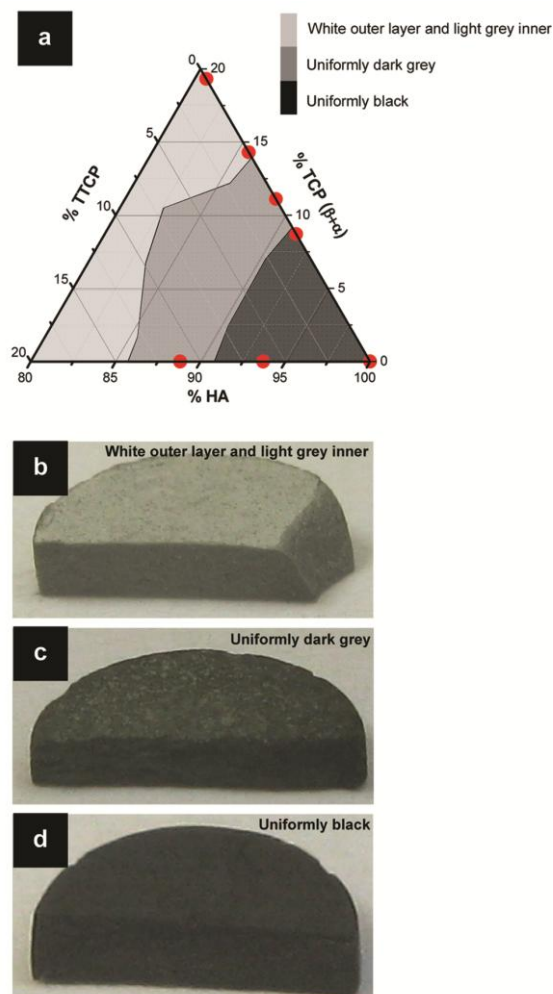**Fig. 6 -** (a) Colour mapped ternary graphic illustrating the influence of the phase composition (represented with red dots) on the appearance of CNT/Glass/HA samples fired by P+RB. (b) representative photographs of (a).

Representative photograph images of the three situations are shown in Figs. 6b-d. It is evident in Fig. 6a that the darkening of the samples increases with the increasing HA fraction due to the large

amount of unreacted CNT loading. Concerning the extreme conditions, the two points in the light grey area corresponds to compositions of lower HA fraction obtained for sintering atmospheres where $P_{CO}= 0$, using a 100% HA reactive bed. In this condition, only H_2O is produced which induced the CNT oxidation across the sample, especially at the surface, where a white layer can be seen (Fig. 6b). In the other extreme, for samples with HA content higher than 91%, the four points in the black area, the CNT loading is enough to give uniformly black samples, Fig.6d.

3.3.2. *Sintering efficiency of P, RB+P and hot pressing (HP) routes*

Regarding the purpose of the present work, the balance of CNT loading and densification should be maximised to preserve the mechanical properties of the matrix and to have a high electroconductive composite. Despite the successful retention of HA and CNT, the porosity of RB+P sintered samples is still quiet high (Fig. 5b), negatively affecting their physical properties. To overcome this, pressure-assisted routes are usually applied with high success, achieving porosity values below 4% for CNT/HA composites [6]. Also, it was found that the applied pressure has a similar role to the reactive bed in supressing HA dehydroxylation [16]. Although, the mechanisms involved in the phase retention are different for the two sintering processes. In RB+P sintering the mechanism is guided by a local chemical equilibrium while a purely kinetic mechanism is concerned in HP sintering [16]. Considering these potentialities, the hot pressing route was also investigated.

Figs. 7 and 8 summarize data regarding the morphology, CNT structural crystallinity and physical properties of Glass/HA and CNT/Glass/HA samples consolidated at 1300ºC by three different routes: pressureless sintering in Ar (P); reactive bed pressureless sintering in a $P_{CO}= 1.77$ MPa atmosphere (RB+P); hot pressing at 30 MPa (HP).

Fig. 7a denotes that the reactive bed sintered CNT/Glass/HA samples have improved their HA retention by ~16% and significantly decreased the CNT loss by ~75 % relatively to the P sintering route. Yet, their porosity only improved ~7 %. The final porosity of the composites is not only dependent of the CNT elimination by H_2O oxidation as it is shown in section 3.3.1, in fact, it is resulted from the balance between CNT elimination and CNT retention.

The low densification of RB+P CNT/Glass/HA samples of ~76% is caused by the high level of CNT in the final composite (CNT loss of ~20%) that are seen as physical obstacles to the sintering and densification process [23]. This corroborates sintering studies showed by White et al. under different $CO+H_2$-based atmospheres [17]. It was shown densifications of 82, 86 and 95 % with a respective CNT loss of 54, 62, 88 % [17]. These results also indicate that the present RB+P route is more efficient to preserve CNTs than the gas mixture flow route used by White et al. [17], probably due to the higher values of P_{CO} that allowed a higher penetration depth of CO gas in the samples. Additionally, Glass/HA samples had an improvement of the porosity of 18 %, probably due to the local formation of carbon impurities, according to eq. 3. The low porosity of pressureless sintered Glass/HA samples is due to presence of the glass phase [4]. It forms a liquid phase that

promotes the particles rearrangement during the sintering process and accelerates densification (classic model of Kingery [31]). Figs. 7b-e show representative low magnified SEM images of the microstructures to illustrate the porosity of the samples.
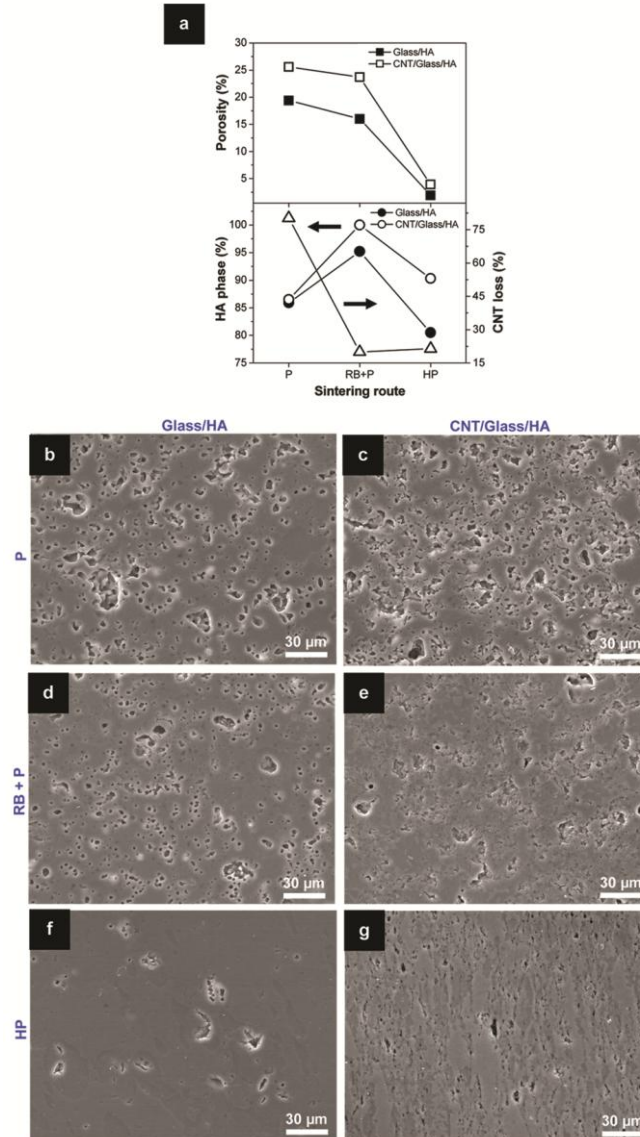
Fig. 7 - (a) plots showing the dependence of the porosity, HA phase and CNT loss of Glass/HA and CNT/Glass/HA consolidated samples at 1300ºC on the applied sintering route (P, RB+P and HP). (b-g) SEM images of (a) at low magnifications.

For the HP Glass/HA and CNT/Glass/HA samples the porosity decreased abruptly by ~88% and ~84 % when comparing with RB+P sintering, as show Figs. 7d-g. However, the HA and CNT retention by the applied pressure was less efficient than the reactive bed approach which results in a decrease of HA of ~10% and an increase of CNT loss of 7%.

Micro-Raman spectra of Fig. 8a compare the structural crystallinity of post-sintered CNTs and the starting functionalised materials. Data was processed as described in section 3.1. In the wavenumbers range of 1200-1800 cm^{-1} all spectra show typical signatures of MWCNT phases: one asymmetric strong peak at ~1580 cm^{-1} corresponding to G-band (E_{2g} stretching mode of the graphitic crystalline structure, square symbol) with a shoulder at higher wavenumbers ~1618 cm^{-1}, the D'-band (graphite in-plane disorder, circle symbol); D band (arising from lattice disorder, triangle symbol) at lower wavenumbers ~1350 cm^{-1}. Other peaks related to the Glass/HA matrix are also seen in the range of 300-1000 cm^{-1} wavenumbers corresponding to the internal vibration modes of the PO_4^{3-} tetrahedral [32].

Fig. 8a shows that all processed CNTs have higher structural crystallinity than the starting material.
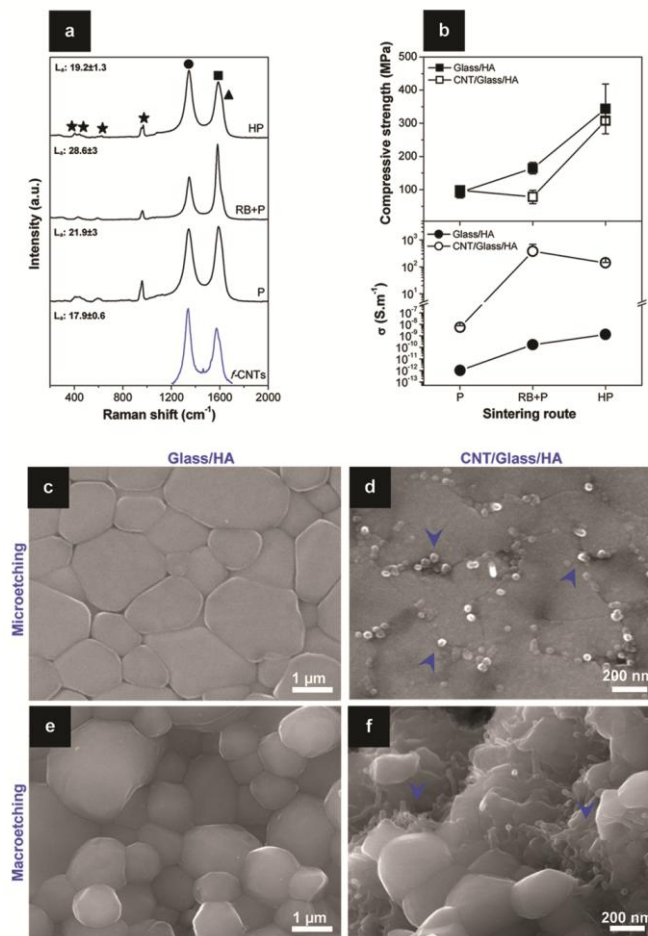
Fig. 8 - (a) Micro-Raman spectra of functionalised CNTs and post-sintered CNTs by P, RB+P and HP (CNTs: ● D-band, ■ G-band, ▲ D'-band; Glass/HA: ★ PO_4^{3-} bands). (b) plot illustrating the influence of the sintering route of (a) on the electrical conductivity and compressive strength of Glass/HA and CNT/Glass/HA samples. (c-f) SEM images of microetched and macroetched samples of (c) showing, respectively, the 2D and 3D intergranular disposition of CNTs.

This might be explained by the combined action of the functional groups loosening at high temperature and the oxidation of amorphous carbon by H_2O molecules. As it was shown in Fig. 4d,

all functional groups are fully eliminated at 1100ºC. By losing these deposits, it is expected that the post-sintered CNTs have L_a values closer to the raw materials with higher values than to the functionalised ones (Table 1). The L_a values could be even higher when the amorphous carbon is eliminated [24]. This might occur by oxidation at 350ºC (Fig. 3) promoted by H_2O resulted from the HA of the matrix or from the reactive bed (see section 3.3.1). Evidences of the amorphous carbon elimination can be seen in the spectra signature by the decrease of the D-band and the narrowing of G-band. Comparing the spectra of P and RB+P samples (Fig. 8a) it becomes obvious that the last samples present less amorphous carbon. This is explained by the different amounts of H_2O that, ultimately, dictates the efficiency of the oxidation reaction. The P samples generate less H_2O than RB+P because in the first case it results only from the HA decomposition and in the latter also from the reactive powder bed.

Fig. 8a shows that HP samples have a minor change of the CNT structural crystallinity, with a spectrum signature similar to the raw (not shown) and functionalised CNTs. Though, the L_a value of HP CNTs is closer to the raw CNTs than the functionalised, as expected. Surprisingly, despite of the HA dehydroxylation (Fig.7a) there is no improvement of the CNT structural crystallinity, in contrast to the conventional sintering. This is explained by the fast driving out of the entrapped H_2O vapour by the combined applied pressure and vacuum, resulting in an incomplete oxidation of the amorphous carbon.

Fig. 8b shows the respective electrical conductivity and compressive strength of the final composites. The results are in accordance with the morphological characterization of Fig. 7. The CNT/Glass/HA RB+P sintered samples have their compressive strength decreased by ~20% relatively to the P sintered ones due to the high CNT loading. In these partially densified composites the load bearing ability of the matrix is much decreased and CNTs may act as microstructural defects, accelerating the propagation of cracks leading to the detereoration of the mechanical properties. On the other hand, the Glass/HA samples have mechanical strength increased by ~80% due to the lower porosity and higher retention of HA phase, the highest mechanical performance CaP phase [33].

The electrical conductivity of both types of samples, Glass/HA and CNT/Glass/HA, increases when sintered in the presence of a reactive bed, Fig.8b. The higher conductivity in the Glass/HA samples is caused by the thermal diffusion of the carbon of the reactive bed giving an increase of two orders of magnitude relatively to the P route. For the CNT/Glass/HA, it can be seen an exceptional increase of ten orders of magnitude due to the high level of CNT retention.

For almost fully dense HP samples the compressive strengths highly increased with respect to the RB+P sintered samples, as expected. The Glass/HA and CNT/Glass/HA samples exhibited an increase of ~108% and 293 %, respectively. Additionally, it is shown in Fig. 8b that the compressive strengths of hot pressed Glass/HA and CNT/Glass/HA compacts are close within a 10% window. The electrical conductivity of the Glass/HA samples increased around tenfold when compared to the RB+P samples due to the higher carbon level resulted from a fast C diffusion under pressure from the graphite die. For the hot pressed CNT/Glass/HA samples the electrical

conductivity decreases in 56% when comparing with the RB+P samples. Of relevance, this value is only an trend due to the high statistical coefficient of variation of the conductivity values for RB+P samples of 82% compared to 5% for HP samples. The lower reproducibility of the RB+P route might be attributed to an inhomogeneous CNT retention due to an extended dispute of neighbour samples for the local $CO+H_2$ atmosphere. The conductivity decrease can be explained by the lower structural crystallinity of ~34% and lower CNT loading of ~1.7%. As shown in section 3.1, the electrical conductivity of CNTs is highly sensitive to the structural crystallinity. This indicates that porosity has an inferior influence in the electrical conductivity of the composite than the CNT crystallinity and loading, nevertheless, these two features affect the 3D electron transporting network.

To understand of how this CNT network is organised in the microstructure a more detailed analysis was accomplished. Figs. 8c-f show the microstructure of polished surfaces of HP Glass/HA and CNT/Glass/HA samples chemically wet-etched with two different etching strengths: microetching and macroetching. Top view of microetched polished samples clearly show the cross-sectional profile of CNTs (highlighted with blue arrows) placed in the grain boundaries (Figs. 8c and d). To further reveal the 3D position of CNTs, respective 30º tilted macroetched surfaces were also shown (Figs. 8e and f). The composites have predominantly CNTs located at the grain boundaries corroborating the 2D observations.

3.4. *Optimisation of HP temperature*

Concerning the influence of the temperature on the CNT elimination at 1300ºC (see section 3.3.2), in the present section, the temperature was varied bellow the upper limit condition, 1300ºC, to achieve the best compromise between densification and CNT loading.

Fig. 9a shows that increasing HP temperature decreases CNT retention but, surprisingly, augments HA fraction. This trend is opposite to the one found in the RB+P route where both phases are as a generally rule preserved together. This is an evidence that CNT elimination in HP is governed by the combined destructive action of temperature and pressure [15] and not by simple H_2O oxidation. Other evidence that H_2O does not take a relevant role in the CNT elimination is given by the negligible variation of the CNT crystallinity with the HP temperature. The respective average value of L_a= 18.8 ±0.5 is close to the value of the CNTs before sintering (Table1). These observations are justified by the key role of the applied pressure and vacuum in the H_2O elimination, previously discussed in section 3.3.2.

The HA retention increasing with the HP temperature increasement probably results from the decrease of the reducing effect of the vacuum atmosphere (Fig. 4). For a constant dwell time, the higher temperatures give higher densification kinetics resulting in shorter periods of time with open porosity. Consequently, the fast elimination of H_2O by vacuum action decreases, allowing more HA retention. The release of some H_2O from the HA structure at the close porosity sites may permits the formation of a local H_2O-rich atmosphere that end by helping on the HA retention [28].

Interestingly, it can be also seen the decomposition evolution of oxyapatite phase, i.e. fully dehydroxylated HA, with temperature. Under 1200ºC, only β-TCP phase is present, at 1200ºC, a mixture of β-TCP and α-TCP is formed and above 1300ºC all β-TCP is converted to α-TCP, in accordance with the literature [14].
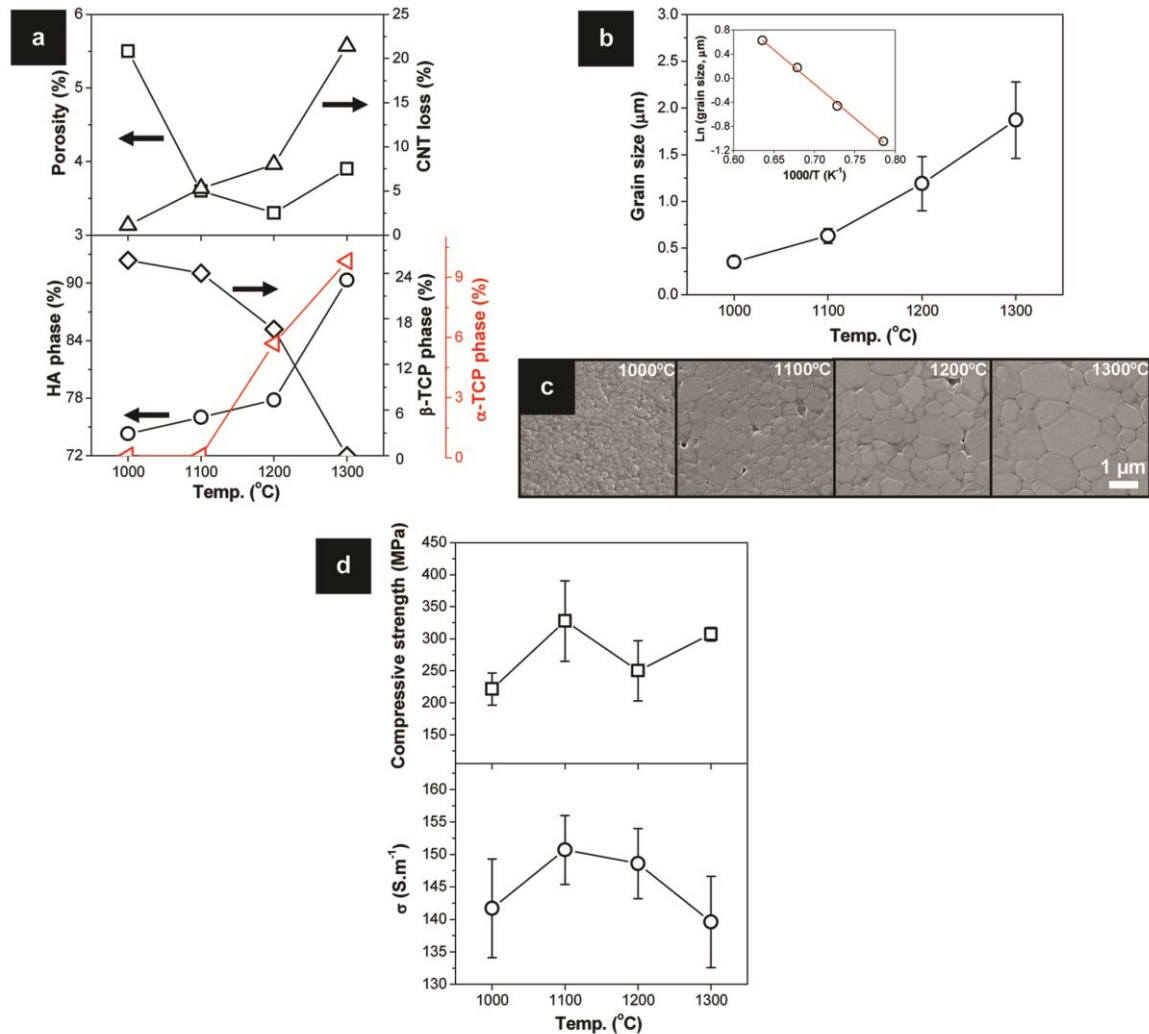
Fig. 9 - (a) plots showing the temperature dependence of the porosity, CNT loss and phase composition of CNT/Glass/HA samples consolidated by HP on the temperature. (b) plot depicting the influence of the HP temperature on the grain size (Arrhenius plot is shown as inset). (c) representative SEM images of (b). (d) plot illustrating the effect of the HP temperature on the electrical conductivity and compressive strength of CNT/Glass/HA samples.

The porosity of the composite varies with temperature following a typical profile except at extremely high temperatures, as shown in Fig. 9a. At 1300ºC, the porosity increase resulting from the CNT elimination overcomes the porosity decrease by densification, giving a final increase of porosity. At temperatures lower than 1300ºC there is an abrupt decrease of CNT loss to below ~8%. The use of temperatures around 1200ºC combines high CNT retention in composites with the lowest porosity.

In Fig. 9b is depicted the grain size dependence on the temperature along with the inset Arrhenius plot. It can be observed the grain increase following an exponential low with a activation energy of ~0.97±0.004 eV. This value is much higher than those previously found for pure Glass/HA systems (0.01-0.14 eV) [4]. This indicates that CNTs act as physical barriers to preliminary grain-to-grain contact to form columns and subsequent grain growth. Representative SEM micrographs of CNT/Glass/HA samples are shown in Fig. 9c. A maximum grain size of 1.9 ±0.4 μm was achieved at 1300 ºC (Fig. 9c) around ~24% smaller than the Glass/HA samples of 2.5±0.8 μm (Fig. 8c). Yet, the regions with high density of CNTs as the one shown in Fig. 8d present a much lower grain size of 0.7±0.4 μm which corresponds to a 3.5-fold grain reduction. Similar grain growth restriction of similar magnitude, tenfold, was reported by others [23].

Overall, the properties dependence in the HP temperature (Fig. 9c) mirror the microstructural evolution. The maximum value of electrical conductivity of ~150 S.m^{-1} is obtained at 1100 ºC due to the maximised balance between CNT retention and densification (Fig. 9a). Comparable conductivity of 200 S.m^{-1} was achieved with Nanocyl-NC7000 at similar loading of 4.65 vol.% for 95% dense samples using the SPS method [34]. Here, it is proved that CNT loading has a higher influence in the electrical conductivity than porosity due to the long-range CNT connecting through intergranular locations. HP samples at 1000ºC presenting higher porosity have larger electrical conductivity than those processed at 1300ºC. A similar behaviour was presented by the high porous RB+P samples howsoever having high conductivity (Figs. 7a and 8b).

Comparing the average conductivity of these partially densified samples (Fig. 8b) with the HP sample at 1100 ºC (Fig. 9c) it is evident that the structural crystallinity of the CNTs has also an important contribution to the final electrical conductivity. HP samples have ~25 % more CNTs than the RB+P samples but the respective structure crystallinity of the CNTs is ~57 % lower which resulted in an effective electrical conductivity reduction of ~60 %.

The highest mechanical strength samples were obtained at 1100ºC (Fig. 9c). This performance was resulted from the best combination of porosity, CNT loss, grain size and HA retention. Also, by comparing the compressive strength at 1100ºC and 1300ºC of composites with similar porosity it becomes clear that the fraction of the secondary phase α-TCP has also a relevant contribution (Fig. 9a). At 1300ºC, the amount of α-TCP phase becomes significant to strengthen the HA, by putting HA lattice under stress due to the higher occupied volume of α-TCP compared to HA [4], and not due to the intrinsic properties of the α-TCP itself [33].

4. Conclusions

High electroconductive CNT/Glass/HA bone grafts with conductivities in the range of 140-640 S.m^{-1} were successfully produced with just 2.5 wt% of CNTs by reactive bed pressureless sintering (RB+P) and hot pressing (HP). Both sintering routes were optimised towards CNT preservation through two mechanisms: by preventing the HA dehydroxylation in RB+P samples to ultimately avoid CNT oxidation. Following this, reactive powder beds of HA+C were used to form

CO+H$_2$ atmospheres at positive pressure to shift the equilibrium of reaction of H$_2$O+C, according to the Le Chatelier's principle. Phase retentions of 100% and 80% were achieved for HA and CNT by using an atmosphere of P$_{CO}$= 1.77 MPa; by simply adjusting the HP temperature. For HP samples, the entrapped H$_2$O from the HA dehydroxylation did not oxidise the CNTs due to the fast dragging out by the combined applied pressure and vacuum. The optimal balance of CNT loss and densification of ~5 % and ~96% was found at 1100ºC.

Non-metallic electroconductive bone grafts offer new exciting possibilities in bone regeneration strategies by delivering *in situ* electrical stimulus to cells and control the bone formation rate. Hopefully, conductive smart materials might turn the *in situ* bone electrotherapy of clinical relevance by decreasing the postoperative healing times.

Acknowledgements

References:

[1]. Jarcho M, Bolen CH, Thomas MB, Bobick J, Kay JF, Doremus RH. Hydroxylapatite synthesis and characterization in dense polycrystalline form. J Mater Sci 1976;11:2027-35.

[2]. Akao M, Aoki H, Kato K. Mechanical properties of sintered hydroxyapatite for prosthetic. J Mater Sci 1981;16:809-12.

[3]. LeGeros RZ, LeGeros JP. Dense Hydroxyapatite. In: Hench LL, Wilson J, editors. An Introduction to Bioceramics, Singapore: World Scientific; 1993, p.145.

[4]. Lopes MA, Monteiro FJ, Santos JD. Glass-reinforced hydroxyapatite composites: secondary phase proportions and densification effects on biaxial bending strength. J Biomed Mater Res 1999;48:734-40.

[5]. Lopes MA, Knowles JC, Santos JD, Monteiro FJ, Olsen I. Direct and indirect efects of P$_2$O$_5$ glass reinforced-hydroxyapatite composites on the growth and function of osteoblast-like cells. Biomaterials 2000;21:1165-72.

[6]. Lahiri D, Ghosh S, Agarwal A. Carbon nanotube reinforced hydroxyapatite composite for orthopedic application: A review. Mater Sci Eng C 2012;32:1727-58.

[7]. Usui Y, Aoki K, Narita N, Murakami N, Nakamura I, Nakamura K, et al. Carbon nanotubes with high bone-tissue compatibility and bone-formation acceleration effects. Small 2008;4:240-6.

[8]. Akasaka T, Watari F, Sato Y, Tohji K. Apatite formation on carbon nanotubes. Mater Sci Eng C 2006;26:675-8.

[9]. Harris PJF. Carbon nanotube science - synthesis, properties an applications. 2nd ed. Cambridge: Cambridge University Press; 2009.

[10]. Navarro M, Michiardi A, Castaño O, Planell JA. Biomaterials in orthopaedics. J R Soc Interface 2008;5:1137-58.

[11]. Hu H, Ni Y, Mandal SK, Montana V, Zhao B, Haddon RC, Parpura V. Polyethyleneimine functionalized single-walled carbon nanotubes as a substrate for neuronal growth. J Phys Chem B, 2005;109:4285-9.

[12]. Supronowicz PR, Ajayan PM, Ullmann KR, Arulanandam BP, Metzger DW, Bizios R. Novel current-conducting composite substrates for exposing osteoblasts to alternating current stimulation. J Biomed Mater Res 2002;59:499-506.

[13]. Gittings JP, Bowen CR, Dent ACE, Turner IG, Baxter FR, Chaudhuri JB. Electrical characterization of hydroxyapatite-based bioceramics. Acta Biomaterialia 2009;5:743-54.

[14]. Wang T, Dorner-Reisel A, Muller E. Thermogravimetric and thermokinetic investigation of the dehydroxylation of a hydroxyapatite powder. J Eur Ceram Soc. 2004;24:693-8.

[15]. Peigney A, Rul S, Lefevre-Schlick F, Laurent C. Densification during hot pressing of carbon nanotube–metal–magnesium aluminate spinel nanocomposites. J Eur Ceram Soc 2007;27:2183-93.

[16]. Rapacz-Kmita A, Paluszkiewicz C, Slosarczyka A, Paszkiewicz Z. FTIR and XRD investigations on the thermal stability of hydroxyapatite during hot pressing and pressureless sintering processes. J Mol Struct 2005;744–747:653-6.

[17]. White AA, Kinloch IA, Windle AH, Best SM. Optimization of the sintering atmosphere for high-density hydroxyapatite–carbon nanotube composites J. R. Soc. Interface 2010;7:S529-39.

[18]. Proença MF, Araújo RF, Paiva MC, Silva CJR. The Diels-Alder cycloaddition reaction in the functionalization of carbon nanofibers. J. Nanosci. Nanotechnol. 2009; 9: 6234-8.

[19]. Cançado LG, Takai K, Enoki T, Endo M, Kim YA, Mizusaki H, et al. General equation for the determination of the crystallite size La of nanographite by Raman spectroscopy. Appl Phys Lett 2006;88:163106-1–6.

[20]. Gazzara CP, Messier DR. Determination of content of SisN4 by X-ray diffraction analysis. Am Ceram Soc Bull 1977;56:777-80.

[21]. Kalita SJ, Bhardwaj A, Bhatt HA. Nanocrystalline calcium phosphate ceramics in biomedical engineering. Mater Sci Eng C 2007;27:441-9.

[22]. Hench LL. Biomaterials: a forecast for the future. Biomaterials 1998;19:1419-23.

[23]. Inam F, Yan H, Peijs T, Reece MJ. The sintering and grain growth behaviour of ceramic–carbon nanotube nanocomposites. Compos Sci Tech 2010;70:947-52.

[24]. Mata D, Silva RM, Fernandes AJS, Oliveira FJ, Costa PMFJ, Silva RF. Upscaling potential of the CVD stacking growth method to produce dimensionally-controlled and catalyst-free multiwalled carbon nanotubes. Carbon 2012;50:3585-606.

[25]. Rinzler AG, Liu J, Dai H, Nikolaev P, Huffman CB, Rodríguez-Macías FJ, et al. Large-scale purification of single-wall carbon nanotubes: process, product, and characterization. Appl Phys A 1998;67:29-37.

[26]. Lee YS, Marzari N. Cycloaddition functionalizations to preserve or control the conductance of carbon nanotubes. PRL 2006;97:116801-4.

[27]. Zhang X, Li YB, Zuo Y, Guo-L GY, Mu YH, Li H. Morphology, hydrogen-bonding and crystallinity of nano-hydroxyapatite/polyamide 66 biocomposites. Composites: Part A 2007;38:843-8.

[28]. Wang PE, Chaki TK. Sintering behavior and mechanical properties of hydroxyapatite and dicalcium phosphate. J Mater Sci Mater Med 1993;4:150-8.

[29]. Panda RN, Hsieh MF, Chung RJ, Chin TS. FTIR, XRD, SEM and solid state NMR investigations of carbonate-containing hydroxyapatite nano-particles synthesized by hydroxide-gel technique. J Phys Chem Solid 2003;64:193-99.

[30]. Jacob KD, Reynolds DS, Hill WL. Reduction of tricalcium phosphate by carbon effect of silica and alumina on the reaction. Ind Eng Chem 1962:1;1126-32.

[31]. Kingery WD. Densification during sintering in the presence of a liquid phase. I. theory. J Appl Phys 1959;30(3):301-6.

[32]. Cuscó R, Guitián F, Aza S, Artús L. Differentiation between hydroxyapatite and β-tricalcium phosphate by means of μ-Raman spectroscopy. J Eur Ceram Soc 1998;18:1301-5.

[33]. Liang L, Rulis P, Ching WY. Mechanical properties, electronic structure and bonding of α- and β-tricalcium phosphates with surface characterization. Acta Biomaterialia 2010;6:3763-71.

[34]. Inam F, Yan H, Reece MJ, Peijs T. Dimethylformamide: an effective dispersant for making ceramic–carbon nanotube composites. Nanotechnology 2008;19:195710-5.

226

IV.3. Multifunctional carbon nanotube/bioceramics modulate the directional growth and activity of osteoblastic cells

D. Mata[a], F.J. Oliveira[a], M. Ferro[a], P.S. Gomes[b], M.H. Fernandes[b], M.A. Lopes[c], R.F. Silva[a]

[a]CICECO, Materials and Ceramic Eng. Dept., Univ. of Aveiro, 3810-193 Aveiro ,Portugal
[b]Laboratory for Bone Metabolism and Regeneration, Faculty of Dental Medicine, Univ. of Porto, 4200-465 Porto, Portugal
[c]CEMUC, Metallurgical and Materials Eng. Dept., Faculty of Eng., Univ. of Porto, 4200-465 Porto, Portugal

Abstract

Biomaterials can still be reinvented to become simple and universal bone regeneration solutions. Following this roadmap, a bone graft of carbon nanotube(CNT)/glass/hydroxyapatite (HA) with controlled CNT agglomeration state was designed with multifunctionalities able to stimulate the bone cell phenotype.

The preparation route, the mechanical and electrical behavior and the *in vitro* profiles of degradation and osteocompatibility were described. A non-destructive dynamic route was found to have a higher influence than the Diels-Alder functionalization one on controlling the CNT agglomerate state in the ceramic-matrix composite. Biologically safe CNT agglomerates, with diameter sizes below 3 µm homogenously distributed, were obtained in non-functionalized and functionalized composites. Yet, the lowest CNT damage and the highest mechanical and electrical properties were found for the non-functionalized materials. Even though that these composites present higher degradation rate at pH:3 than the ceramic matrix, the CNT agglomerates are released with safe diameter sizes. Also, non-functionalized composites allowed cellular adhesion and modulated the orientation of the cell growth, with a proliferation/differentiation relationship favoring osteoblastic functional activity.

Findings offer further contributions for bone tissue engineering by showing that multifunctional bone grafts with high electroconductivity, and integrating CNT agglomerates with maximized interfacing area, allow the *in situ* control of bone cell functions.

1. Introduction

The roadmap for biomaterials to become simple and universal bone regeneration solution includes "smart" bone grafts that have been designed with new functionalities able to stimulate specific bone cell responses [1]. Regarding the well-known beneficial effects of endogenous electrical signals in natural bone [2,3], electron conductivity emerges as an exciting functionality. Electron currents can be delivery *in situ* to damaged bone site by external fields that are expected to be confined on highly electroconductive materials [4]. The simple external control over the level and duration of electrical stimulation allows the subsequent tuning of the *in situ* regeneration rate of the new bone tissue. Such promising candidates for non-metallic conductive smart bone grafts, to work under electrical stimulation routines without corrosion related toxicological risks, are the carbon nanotube (CNT) reinforced composites, highly conductive at low electrical percolation thresholds [5-7]. Those use either flexible polymers [5] or bioactive glass/hydroxyapatite (HA) [6] as matrices. Of relevance, the latter bioceramic-based ones have been shown promising *in vitro/vivo* biocompatibility profiles, according to data compiled by Lahiri et al. [7].

Other equally exciting functionalities of the CNT composites can be explored by simply controlling the CNT agglomerates since they increase the interfacing area between contiguous CNTs and bone tissue. CNT agglomerates having nano-topography may facilitate control of cell orientation, migration and also enhance cell adhesion and proliferation [8,9]. Moreover, CNT agglomerates could be supplemented with functional groups able to anchor bioactive molecules (e.g. bone morphogenic proteins - BMPs) and drugs (e.g antibiotics) that can be then controllably delivered *in situ* to the fractured site by an electro-stimulated release [10].

CNT agglomerates should have controlled diameter sizes due to toxicological issues. Flexible individualized CNTs with length sizes as small as 2 µm are biologically safe through being internalized/trafficked within cells with no detected cell apoptosis and by being easily excreted by the renal route and/or by lymphatic route [11-14]. On the other hand, cells/macrophages, struggle to internalize/engulf highly stiff and long individualized CNTs [15] or big CNT agglomerates. Still, less rigid 20 µm maximum sized CNT agglomerates are biologically safe by being engulfed/digested by polymorphonuclear phagocytes (PMNs) [16] and mononuclear phagocytes such as Kupffer cells and sinusoidal cells [17] (of 15-30 µm in size, representing about 50% of all macrophages in living organisms [18]), or simply by interface with tissues without acute toxic responses [19,20].

Even so, the control of the CNT agglomerate state in composites is not straightforward because CNTs have high tendency to agglomerate due to strong van der Waals and hydrophobic interactions [21]. Particularly for biocomposites, this becomes even harder. Most of the dispersion agents (e.g. triton X-100, sodium dodecyl sulfate - SDS) successfully used to disperse CNTs alone or in ordinary composites are not suitable since they are unconcerned to contamination [22,23]. Inorganic impurities might be retained in the consolidated ceramic-matrix composites affecting negatively their biological profile.

Taking this into account, the processing of biocomposites with controlled CNT agglomeration state becomes a major challenge since it should contemplate the conjugation of the following requisites: (1) minor introduction of contaminants; (2) preservation of the CNT structure and intrinsic properties; (3) homogeneous distribution of CNTs in the ceramic matrix.

Having these requisites in consideration, pure solvents are probably the best processing route to control the CNT agglomeration state and achieve nearly stable CNT-ceramic suspensions for composites preparation with low level of contaminants and negligible change of CNT structure/properties [24]. Non-aqueous polar solvents can be successfully used with maximum CNT concentration limits in the range of 0.001-0.095 g.l^{-1} [25], depending on the sign and strength of the charge on their outer walls resulted from the interactions with the solvent [26,27].

To maximize the control of the CNT agglomeration state and the powder interactions in polar solvents, CNTs can be charged by means of chemical functionalization. The covalent approach, yielding less organic deposits on the CNT walls than the non-covalent polymeric grafting [28], promotes lower interference during sintering. These organic deposits are not fully eliminated during the calcination step, usually performed at relatively low temperature in order to limit CNT oxidation. As a result of this, the organic groups will burn during the sintering process, facilitating CNT oxidation, and contributing to increase the porosity that, ultimately, deteriorates the composite properties.

Sidewall functionalization, such as the cycloaddition reactions, allows a controlled addition of organic deposits with minor damage to CNT structure and change of the intrinsic electrical conductivity [29]. Particularly, the one developed by Proença et al. [30], the Diels-alder cycloaddition of 1,3-butadiene has proved the efficient stabilization of CNTs in polar solvents by steric and electrostatic interactions.

The present work focuses on the preparation route, properties and biological evaluation of multifunctional CNT/Glass/HA bone grafts with controlled CNT agglomeration. All processing steps were fully optimized to preserve the CNT structure and to minimize the level of contaminants. The influence of the mechanical dispersion multi-steps and the CNT functionalization on the CNT agglomeration state and distribution homogeneity in the matrix was assessed. The translation of the CNT functionalization effects into the mechanical and electrical properties of the hot-pressed composites was also investigated. Further evaluation of the *in vitro* degradation and *in vitro* osteoblastic cytocompatibility of CNT/Glass/HA composites was accomplished.

2. Experimental details

2.1. *CNT purification and functionalization*

MWCNTs (NC7000) were provided by Nanocyl supplier. Raw CNTs have average length and diameter sizes of ~3 μm and ~20 nm, respectively [6], and a content of inorganic contaminants of ~12wt.% (Table 1). CNTs were purified by a high temperature annealing process in an open

graphite crucible inside a graphite furnace working under a highly pure Ar atmosphere (purity> 99.9999%), as follows: heating rate of 10 °C.min^{-1} with a fixed dwelling time of 8 h at temperature ranging from 1500-1900 ºC, followed by cooling at rate of 10 ºC.min^{-1} to room temperature. The carried gas flow was kept constant at 20 sccm to drag-out vaporized impurities from the furnace. CNTs were functionalised by a Diels-Alder cycloaddition reaction of 1,3-butadiene, generated *in situ* from sulfolene (≥98%, Sigma-Aldrich), upon heating at 150ºC for 7 days in diethylene glycol dimethyl ether (≥99.5%, Sigma-Aldrich). The alkene functional groups on their outer CNT walls were further converted into carboxylic acid groups (COOH) by means of oxidation with a 0.1 M aqueous solution of $KMnO_4$ solution (≥99%, Sigma-Aldrich) at room temperature. Further details of the process can be found elsewhere [30].

2.2. *Preparation of CNT/Glass/HA composites*

Glass/HA powders containing 2.5 wt% of P_2O_5-glass (65 P_2O5, 15CaO, 10CaF$_2$, 10Na$_2$O mol%) with a final particle diameter size of $D_{0.5}$= 1.8±1.4 µm were prepared as detailed previously [6]. CNT/Glass/HA composite powders were mixed with 2.5 wt% of CNTs (4.4 vol.%) by a non-destructive process in alcohol suspensions following 5 main steps. The CNTs start to be processed alone with a concentration of 1.8 g.l^{-1} in ethanol (≥99.9%, Sigma-Aldrich) and isopropyl alcohol (≥99.8%, Sigma-Aldrich) suspensions for comparison: (1) high-speed shearing (HSS) for 15 min (IKA T25-Ultra-Turrax, working at 20,500 rpm) with a shearing force of 96 Pa (calculated according to [18]) to uniformize the CNT agglomerate size by eliminating big agglomerates; (2) soft sonication (S) (Selecta, working at 60 kHz, 200 W) with time varying in the range of 5-120 min to obtain mixtures of individualized CNTs and controlled size agglomerates. Afterwards, the Glass/HA powders were added to the CNT suspension and (3) sonicated (S) for 15 min to deagglomerate soft ceramic clusters and to initiate the interactions of individual CNT-HA particles. The composite powders were then mixed by (4) a high-speed shearing (HSS) for 15 min with the same conditions of the initial CNT suspension. In order to avoid phase separation, the composite powders were dried by a (5) fast evaporation combining heating at 80 ºC and vacuum under a magnetic shearing (MS) until a consistent slurry was obtained. Subsequently, the slurry was slowly evaporated in an oven at 60 ºC for 24 h. Finally, the dried powders were crushed in an agate mortar and sieved to less than 75 µm.

The CNT/Glass/HA composite powders were consolidated by hot-pressing (HP) at fixed pressure of 30 MPa for 60 min at 1100ºC. The detailed description of the sintering process was presented elsewhere [6]. The final compacts are disc-shaped samples with two dimensions: 20 mm and 50 mm in diameter, and 15±1 mm and 10±1 mm thick, respectively. The smaller discs were cut into slices of 1±0.05 mm for bending testing and also into parallelepiped form of 2.5×2.5×4.5 mm^3 for compression testing and electrical measurements. On the other hand, the bigger discs were used to determine the dynamic Young's and shear modules. These discs were also used for the *in vitro* experiments. For the degradation testing the discs were crushed and sieved to obtain

granules of 250-500 µm, while for the cell cultures the discs were cut into square slices of 5×5×1 mm^3, ground and polished (P4000). Before the *in vitro* testing, the materials were ultrasonically cleaned in ethanol and sterilized by autoclaving.

2.3. *Characterization of materials*

2.3.1. *Assessment of CNT purification and functionalization*

Quantitative analyses of the CNT amorphous carbon and inorganic impurities were performed by thermogravimetry (TG, Setsys Setaram) in N_2 (TG$_{N2}$) and O_2 (TG$_{O2}$) atmospheres, respectively, under a constant flow of 200 sccm at 10ºC.min^{-1}. The level of inorganic impurities was also measured by inductively coupled plasma atomic emission spectroscopy (ICP-AES, Jobin Yvon Activa-M).

The functional groups of the CNT outer walls were quantified by TG$_{N2}$ and specific surface area measurements (BET, Micromeritics Gemini 2370 V5). For both analyses, samples of the same batch were firstly dried for 24h at 60ºC. Eight partial pressures were applied to further calculate the surface area after degassing the samples in N_2 at 120ºC for at least 2 h.

Qualitative analyses of the CNT purification and functionalization treatments were performed by: (1) DC electrical conductivity measurements of disc-shaped CNT membranes, 10 mm in diameter and 170±30 µm thick, following a Van der Pauw configuration, reported previously [6]; (2) high-resolution transmission electron microscopy (HR-TEM, JEOL 2200FS working at 200 keV, resolution of 0.1 nm) to identify organic deposits on the CNT sidewalls. The samples were prepared by suspending CNTs in isopropyl alcohol and dropping the suspension on lacey-carbon Cu grids (Agar Scientific) and drying afterwards at 100ºC under vacuum ~1 Pa for 30 h to reduce contamination; (3) electron energy loss spectroscopy (EELS, resolution of 1 eV - full width at half maximum (FWHM) of the zero loss peak) to detect the oxygen element of the chemical groups and their effect on CNT π- and σ-bands; (4) Selected-area Electron Diffraction (SAED) patterns were recorded with a camera length of 60 cm using an accelerating voltage of 200 keV.

2.3.2. *CNT crystallinity evaluation*

The structural crystallinity of CNTs, the in-plane crystallite size (L_a) and the c-axis crystallite size (L_c), were estimated by micro-Raman spectroscopy (at 532 nm in the wavenumber range of 1000-2000 cm^{-1}, Jobin Yvon T64000) and X-ray diffraction analyses (XRD, CuKα$_1$ radiation, λ= 0.154056 nm, from 5 to 80º, with a step size of 0.02º, X'PERT-MPD Philips), respectively. For quantitative analyses, all spectra were baseline corrected by linear background removal and fitted with a Lorentzian line-shape. While the L_a was calculated by measuring the ratio of the integral area of the D-band and G-band and using the Cançado's equation [31], the graphite

c-axis crystallite size (L_c) was determined by analysing the integral area of the (002) peak from XRD and applying the Scherrer's equation [36].

2.3.3. *Evaluation of the CNT stabilization and agglomeration state in solvents and the morphology and physical-chemical characteristics of hot-pressed composites*

Zeta potential (ZP) measurements (Malvern, Zetasizer Nano Series) were accomplished to assess the powders stabilization in alcohol solvents. Measurements of CNTs alone and sieved (<75 µm) CNT/Glass/HA powders were performed in triplicate at natural pH and the ZP was calculated according to Smoluchowski's equation [33].

Optical microscopy (Nikon microphot) assisted by a coupled camera (Infinity 1-3C-NS) was used to analyze the CNT morphology and distribution homogeneity in the final hot-pressed composites, and to investigate the influence of the mechanical multi-step treatments and functionalization on the morphology of the CNT agglomerates in 0.1 g.l^{-1} suspensions. The agglomeration state was evaluated by an "instantaneous freezing", just after each mixing treatment. This was obtained by an ultra-fast vacuum suction of the CNT suspension when dropped in a 0.22 µm pore size disc filters (hydrophilic polycarbonate, Millipore) placed on a Büchner funnel/Kitasato flask connected to a rotary vacuum pump. The membranes were then collected for optical observation.

UV spectroscopy (UV-3100 Shimadzu) measurements were performed to evaluate the effect of the sonication treatment on the CNT disentanglement process in 0.05 g.l^{-1} suspensions. Complementary size distribution profiles of CNTs and CNT/Glass/HA composites were obtained by a laser diffraction equipment (Coulter LS230). Aqueous powder suspensions of 0.1 g.l^{-1} were stabilized with an aqueous-based surfactant with a concentration of 2 g.l^{-1} (nanosperse AQ, Nanolab).

For a more detailed morphological investigation of the CNTs alone with concentration of 0.1 g.l^{-1} and of the CNT/Glass/HA green powders, a scanning transmission electron microscopy (STEM) performed with a transmitted electron detector coupled to a high resolution scanning microscope (HR-SEM, Hitachi SU70) was used.

HR-SEM (working at 15 keV with a resolution of 1 nm) was used to analyse the microstructure of polished and fracture surfaces. The samples were ground with SiC papers (grades P1000, P1200, P2500, P4000). The experimental and theoretical densities of sintered composites were respectively obtained by the Archimedes method in ethylene glycol and by the rule of mixtures considering the phases identified previously [6].

The surface characteristics of the hot-pressed ceramics were carried out on P4000 polished samples, previously washed with 70% alcohol for 15 min followed by ionized water, and oven dried overnight.

The surface roughness (arithmetic average roughness – Ra) of the sample was measured using Etamic GMBH profilometer with a diamond tip feeler (Hommel Werke) according to DIN 4768.

Zeta potential analyses were performed using an EKA - Electro Kinetic Analyzer (Anton Paar). Each parallelepiped sample of 20x20x0.5 mm^3 was measured at least eight times, at fixed conditions of pH of 7.4, adjusted with 1 mM KCl and NaOH solutions, pressure and temperature of 40 kPa and 27 ºC.

Wettability measurements of the samples were done using the OCA 15 Optical Contact Angle System (Data Physics). These measurements were carried out following the sessile drop method, using an Axsymmetric Drop Shape Analysis–Profile (ADSA-P) software. The analysis was performed with ultra-pure water (Merck, Germany 1.01262.1000) and the drop size was 4μl, and no less than 10 drops was done.

2.3.4. *Electrical and mechanical properties of hot-pressed composites*

DC electrical conductivity measurements contemplated the use of samples with copper wires directly fixed to both surface extremities. The tests were performed at room temperature in two different apparatus: (1) a Keighley 617 programmable electrometer with a stepped applied voltage of 0.5 V in the range of 0-100 V for dielectric samples; (2) a ISO-TECH IPS-603 programmable power supply with a stepped applied voltage of 0.1 V in the range of 0-1 V for conductive samples.

The mechanical properties assessed were: (1) the dynamic Young's and shear moduli, by an impulse excitation of vibration method, according to ASTM C1259-96; (2) the compressive and bending strengths, using a Zwick/Roell Z020 equipment with a load cell of 2.5 kN under a constant displacement rate of 0.3 mm.min^{-1} and 1 mm.min^{-1}, respectively. The bending strength values were determined by a piston on three ball test, according to ASTM F394-78; (3) Vickers micro-hardness, conducted in a micro-indenter (type M, Shimadzu) on 50 nm polished samples with a 3 N applied load (15 indentations for each specimen); (4) the fracture toughness (KIC), by the Niihara's indentation method considering Palmqvist radial cracks [34]. All mechanical and electrical tests were performed with five specimens for each condition.

2.4. *In vitro degradation testing*

The degradation testing was performed according to the International Standard ISO 10993-14 "Biological evaluation of medical devices- Part 14: Identification and quantification of degradation products from ceramics". Two sets of experiments were performed at different pH values. The first set was conducted at pH 3.0 using citric acid and it is referred as extreme solution testing, and the second one was performed at pH 7.4 using Tris-HCl solution, referred to as simulation solution testing. A ratio of 5g of granules/100 mL of testing solution was used. The

samples were incubated for 24 and 72h, at 37 ºC, and containers agitated at 2 Hz using a circular movement; triplicate samples were used. At these time points, the solid and liquid phases were separated by filtering (0.22 mm). The solid samples were then washed in deionised water and dried in an oven to constant weight. A relative weight loss percentage (W_L) after a certain time of immersion, t, of the samples was calculated from the following equation: $W_L \% = (W_0-W_t)/W_0 \times 100$, where W_0 and W_t stand for initial and final weight after a specific immersion time, respectively. Quantitative analyses of Na, Ca, Fe and Co elements in the liquid phase was performed by atomic absorption spectroscopy (AAS, GBC Avanta).

2.5. *In vitro biological evaluation*

Human osteoblastic-like cells (MG63 cells, ATCC number CRL-1427™) were cultured in α-Minimal Essential Medium (μ-MEM), supplemented with 10% fetal bovine serum, 50 µg.ml^{-1} ascorbic acid, 50 µg.ml^{-1} gentamicin and 2.5 µg.ml^{-1} fungizone, at 37ºC, in a humidified atmosphere of 5% CO_2 in air. For sub-culturing, the cell layer (at around 70-80% confluence) was detached with trypsin – EDTA solution (0.05% trypsin, 0.25% EDTA; 5 minutes, 37ºC), and the cell suspension was used in the cell response studies.

Cells were cultured (5×10^4 cells.cm^{-2}) over the p-CNT/Glass/HA composites, for 1 and 4 days. Colonized samples were evaluated for cell morphology and pattern of cell growth by confocal laser scanning microscopy (CLSM) and scanning electron microscopy (SEM), and for cell viability/proliferation (MTT and LDH assays) and alkaline phosphatase (ALP) activity. Parallel experiments were performed on standard cell culture plates and over Glass/HA composites.

SEM and CLSM observations. For SEM observation, samples were fixed (1.5% glutaraldehyde in 0.14*M* sodium cacodylate buffer, pH=7.3, 10 min), dehydrated in graded alcohols, critical-point dried, sputter-coated with an Au/Pd thin film (SPI Module Sputter Coater equipment), and observed in a High resolution (Schottky) Environmental Scanning Electron Microscope (Quanta 400 FEG ESEM). For CLSM assessment, samples were fixed (3.7% paraformaldehyde, 15 min). Cell cytoskeleton filamentous actin (F-actin) was visualized by treating the cells with Alexa Fluor 488 Phalloidin (1:20 dilution in PBS, 1 h) and counterstaining with propidium iodide (1 µg/ml, 10 minutes) for cell nuclei labelling. Labelled cultures were mounted in Vectashield® and examined with a Leica SP2 AOBS (Leica Microsystems) microscopy.

MTT assay. The MTT (3-(4,5-Dimethylthiazol-2-yl)-2,5-diphenyltetrazolium) assay is based in the ability of mitochondrial dehydrogenase to reduce the MTT to a dark blue formazan product. MTT (0.5 mg/ml) was added to each well, and cultures were incubated for 3 hours at 37ºC. Following, the formazan salts were dissolved in dimethylsulphoxide (DMSO) and the absorbance (A) was determined at λ = 600 nm on an Elisa reader (Synergy HT, Biotek). Results were expressed as A.cm^{-2}.

LDH assay. The lactate dehydrogenase (LDH) assay is based on the reduction of NAD by the action of LDH released to the medium. The resulting reduced NAD (NADH) is utilized in the

stoichiometric conversion of a tetrazolium dye. Determination of the total LDH was performed using the *In vitro* toxicology assay kit lactate dehydrogenase based (Sigma-Aldrich; St. Louis, MO), according to the manufacturers' instructions. The amount of LDH leakage to the medium was normalized by total LDH, and calculated as follows: LDH leakage % = LDH medium / total LDH x 100.

ALP activity. ALP activity was evaluated in cell lysates (0.1% Triton X-100, 5 min) by the hydrolysis of *p*-nitrophenyl phosphate in alkaline buffer solution (pH~10.3; 30 min, 37 ºC) and colorimetric determination of the product (*p*-nitrophenol) at 400 nm in an ELISA plate reader (Synergy HT, Biotek). ALP activity was normalized to total protein content (quantified by Bradford's method) and was expressed as $nmol/min.mg_{protein}^{-1}$.

Statistical analysis. Three independent experiments were performed; in each experiment, three replicas were accomplished for the biochemical assays and two replicas for the qualitative assays. Results are presented as mean ± standard deviation (SD). Groups of data were evaluated using a two-way analysis of variance (ANOVA) and no significant differences in the pattern of the cell behaviour were found. Statistical differences between Glass/HA and CNT/Glass/HA composites were assessed by Bonferroni's method. Values of $p \leq 0.05$ were considered statistically significant.

3. Results and discussion

3.1. *Non-destructive purification and functionalization of CNTs*

Fig.1a shows the SEM image of raw CNT (r-CNT) powders with high level of contaminant particles easily detected by electron charging bright particles. These particles are of Al and have a wide range of sizes from 100 nm to 2 μm with platelet-like geometries, as shown in the STEM image and EDS map insets of Fig. 1a. The local EDS spectrum of r-CNTs (Fig. 1b) also indentifies traces of Si, Fe and Co. The metallic impurities corresponds to small catalyst particles (5-20 nm), commonly used in CNT synthesizes, disposed on the top of the large Al particles (Fig. 1c).

The XRD spectrum of the TGA_{O2} ash residues of r-CNTs shows that these contaminants are combined mainly in the oxide and silicate phases (inset in Fig. 1c). This information was further used to select the temperature of the purification process (1900 ºC), which should be higher than the higher melting temperature (T_m) of the identified impurities, in this case the range of 1377-1597 ºC that includes the iron oxide or metallic iron phases [35]. This process proves to be highly efficient resulting in purified CNTs (p-CNT) almost free of contaminants, as shows the respective SEM micrographs and EDS spectrum (Figs. 1d-f).

Large portion of Al-transition metals contaminants were fully melted and incorporated inside the graphite at the bottom of the crucible, acting as a getter, by liquid-phase diffusion. This phenomenon is shown in the sequence of images of the bottom of the graphite crucible (Figs. 1g-i).

Before purification, the crucible was empty with a clean bottom (Fig. 1g). Then, after the purification treatment, the bottom appearance changed to a metallic-glowing one (Fig. 1h).
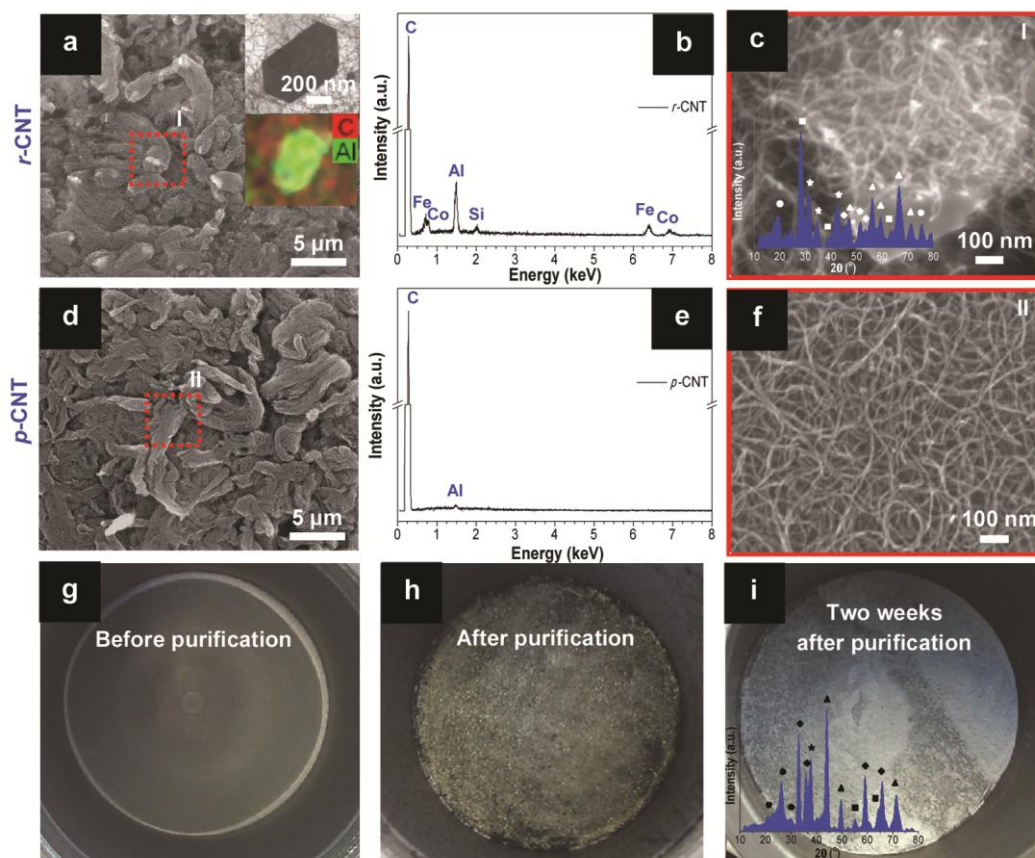

Fig. 1 - Low magnification SEM image of (a) *r*-CNTs (STEM image and EDS map of an Al particle as insets). (b) EDS spectra of the CNT impurities of (a). (c) High magnification view showing the small sized metallic particles of the *r*-CNTs in (a) (XRD spectrum of the impurities as inset, ■SiO$_2$, ★FeSO$_3$, ◆Al$_2$SiO$_4$, ●Al$_2$O$_3$, ▲Al$_3$Co). (d-f) Respective data for *p*-CNTs at 1900ºC/8h being almost free of impurities. Sequence of photographs of the bottom of the graphite crucible: (g) before the purification treatment; (h) after the treatment and (i) two weeks after the treatment showing the collected impurity powder (XRD spectra of the impurities as inset, ■SiO$_2$, ★FeSO$_3$, ◆Al$_2$SiO$_4$, ● Fe$_2$Al$_4$Si$_5$O$_{18}$, ▲Al$_3$Co).

Surprisingly, two weeks after the treatment the glowing bottom of the crucible was replaced by a greyish powder contaminant (Fig. 1i). The powder was formed by a re-oxidation of the Al-transition metals solid solutions inside the bulk graphite under ambient conditions. This oxidation was followed by a volume change that forced the exudation of contaminants from the graphite walls. The XRD spectra (inset of Fig. 1i) shows that the greyish powder is mainly oxide and silicate phases of Al, Si, Fe and Co, with similar phase composition of the contaminants at the starting powder (inset of Fig. 1c).

The reduction by one order of magnitude of the inorganic impurities led to CNTs with increased surface area of ~15 % but a decreased electrical conductivity of more than one order of

magnitude (Table 1). The conductivity loss is explained by a decrease of Al, Fe and Co electroconductive impurities in ~80%, ~73% and ~72%, respectively, according to elemental quantitative ICP-AES analyses. EDS spectrum of Fig. 1e corroborates these observations by showing almost impurity-free CNTs.

To assess the effects of purification and functionalization steps on the CNT structure, HRTEM analyses were performed (Figs. 2a-f). Fig. 2a shows a typical HRTEM image of the raw materials and the respective SAED pattern as inset. The SAED ring pattern, typical of a polycrystalline material, can be ascribed to the contribution of several MWCNTs (analysed area as inset, Fig. 2a) with typical planes indexed to CNT bundle structures [36]. The pattern also shown carbon structures free of metal particles with the absence of dot patterns.

HRTEM micrographs of the purified CNTs give full evidence of the efficiency of the temperature on the elimination of amorphous carbon deposits (Figs. 2a-d). Much cleaner sidewalls can be seen in the purified CNTs at 1900ºC (Figs. 2c and 2d) comparatively to the raw material (Figs. 2a and 2b). Purified and functionalized CNTs (Figs. 2e and 2f) also present intact sidewalls as those of the purified CNTs (Figs. 2c and 2d), although uniformly coated with a ~4 nm thick organic layer. These observations prove that the adopted purification and functionalization processes are intrinsically non-destructive to CNTs, as unlike the commonly used acid treatments to both purify and functionalize CNTs in a single step [37].

Complementary characterization was accomplished to support these observations (Table1).

Table 1 - Physical-chemical and morphological characteristics of *r*-CNTs, *p*-CNTs and *p,f*-CNTs.

Sample	Oxidation temperature (ºC)[b]	Inorganic impurities (wt.%)[b]	Amorphous carbon impurities (wt.%)[c]	COOH groups (wt.%)[c]	Surface area (m².g⁻¹)	Structural cristallinity, L_a (nm)[d]	Structural cristallinity, L_c (nm)[e]	Electrical conductivity (S.m⁻¹)
r-CNT	562±2	12±1	3±1	-	256±7	18.2±0.4	1.5±0.02	3x10³±9x10²
p-CNT	651±2	1.1±2	NM	-	299±3	31.8±1.8	3.1±0.2	1.6x10²±1.8x10¹
p,f-CNT	650±2	0.8±2	NM	9±1	247±1	34.5±0.3	1.43±0.03	1.3x10²±3.5x10¹

r - raw
p - purified at 1900ºC/8h
f - functionalised
[b]TGA, O_2 flow
[c]TGA, N_2 flow
[d]Micro-Raman (532 nm)
[e]XRD
NM - non measurable

According to data of Fig. 2g, the high temperature annealing not only is non-destructive, but also allowed a refinement of the CNT structure. This is confirmed by a 16% increase of the temperature for the onset CNT oxidation (Fig. 2g). These observations are in agreement with the literature [38]. Moreover, both in-plane (L_a) and c-axis (L_c) crystallite sizes increase by ~74% and ~110%, respectively, with the increasing purification temperature (Fig. 2g). The increased crystallinity can be also associated with the elimination of amorphous carbon deposits on the CNT sidewalls [11]. The absence of any measurable deposits by TG_{N2} further corroborates this (Table 1).
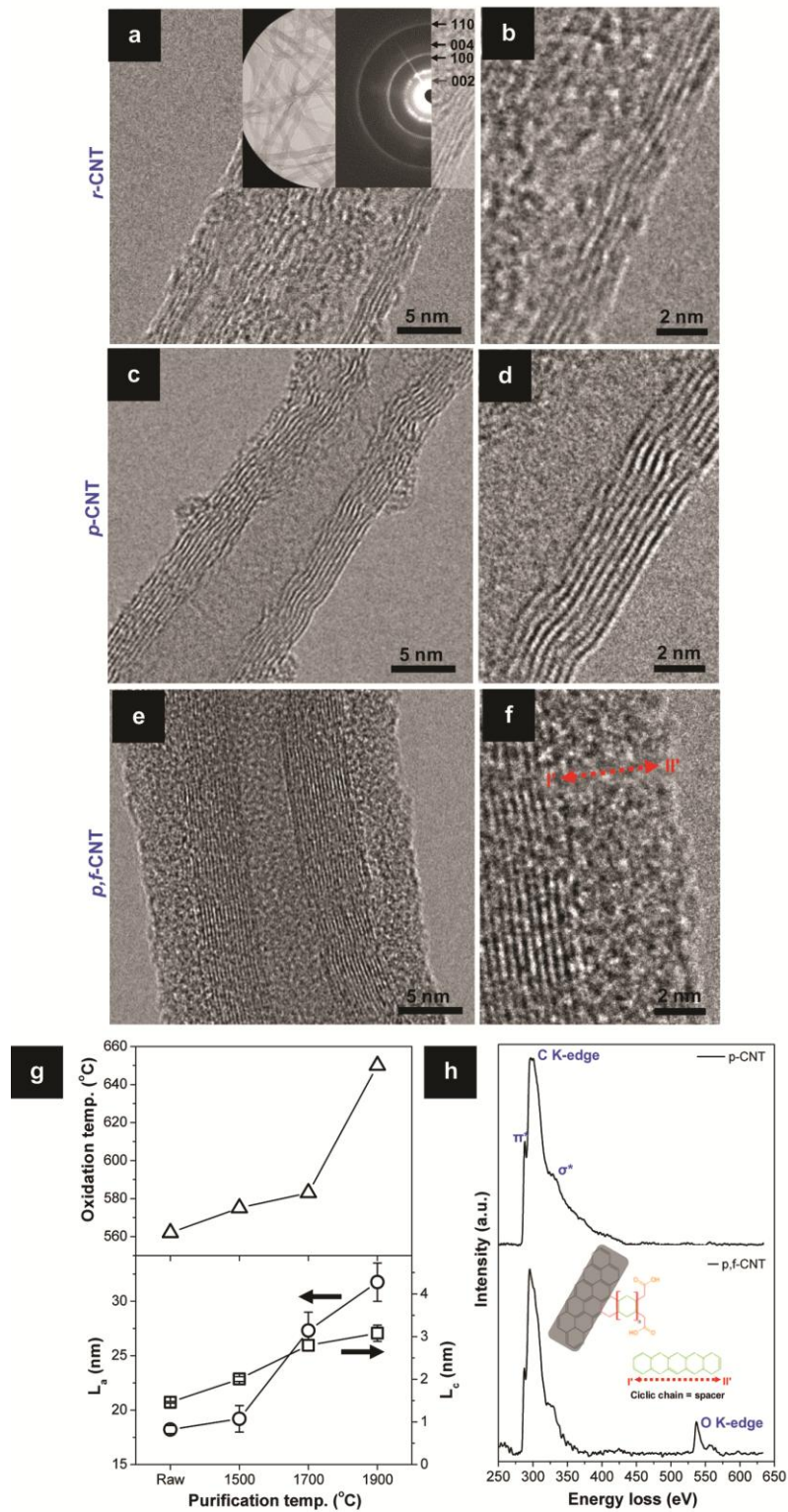
Fig. 2 - HRTEM images of the (b and c) *r*-CNT (SAED pattern and respective analysed area image as insets), (d and e) *p*-CNTs at 1900ºC/8h and (e and f) *p,f*-CNT. (g) Plot showing the influence of the purification temperature on the oxidation temperature, in-plane crystalline size (L$_a$) and c-axis crystalline size (L$_c$) of the CNT structure. (h) EELS spectra of the *p*-CNT and *p,f*-CNT showing the differences in the level of oxygen containing groups on the CNT sidewalls (schematic image of the sidewall chemical functionalization as inset).

TG$_{N2}$ data of *p,f*-CNTs indicates a reaction yield of ~ 9% of functional groups (Table 1). Of interest, the L$_a$ crystallinity of the CNTs was not affected by the 4 nm thick organic layer (Figs. 2e and 2f), according to previous observations [6], but the L$_c$ was decreased by ~54%, relatively to the *p*-CNT condition (Table 1). Also, the functionalization decreased the surface area of CNTs by ~17% and slightly decreased the electrical conductivity by ~19% (Table 1), as was previously shown [6]. The organic layer corresponds to the ciclic chains used to sterically stabilize the CNTs, highlighted in green in the inset sketch of Fig. 2h. In order to guarantee this, the cycloaddition was active until an ciclic chain with a length size superior to ~0.336 nm was formed, this being the range of the van der Waals attraction predicted for two crossed MWCNTs [21]. Additionally, the organic layer thickness was kept the thinnest possible to minimize the interference with the following sintering cycle, at any case much thinner than the non-covalent polymer grafting deposits of 4-14 nm obtained by Kong et al. [28].

One alkene group allocated to the ends of the ciclic chain are converted into two electron donor carboxylic groups (COOH) groups by means of oxidation (inset sketch of Fig. 2h), as previously recognised [30]. The oxygen containing groups can also be identified by EELS (Fig. 2h). The O k-edge peaks at 537 eV and 557 eV is negligible for the *p*-CNT samples but it are clearly seen in the *p,f*-CNTs.

3.2. *Processing route of CNT/Glass/HA composites with controlled CNT agglomerates*

3.2.1. *Selection of the dispersion solvent*

The selection for the best dispersion solvent between ethanol (EtOH) and isopropyl alcohol (iPrOH), commonly applied in bioceramic processing [39], was done accordingly to the universal solubility parameters of Hansen [40]: (a) hydrogen bonding component (δ_h); (b) polar component (δ_p); (c) dispersion component (δ_d). The plotting of these parameters (Fig. 3a) for some commonly used solvents to disperse CNTs (red dots: (1) DMF [25,41]; (2) Benzyl alcohol - BnOH [24]; (3) Chloroform [25,41]; (4) N-methylpyrrolidone - NMP [41,42]) can be advantageously used as references to select other solvents applied in bioceramic processing (blue dot: (5) water - H$_2$O; (6) gray dot: EtOH, (7) green dot: iPrOH). The 3D graph of Fig. 3a shows that the contribution of each Hansen parameter in the CNT dispersion is not evident, a fact also mentioned by others [25]. Both solvents (2) and (4), efficiently disperse CNTs but present divergent parameters. Nonetheless, a pattern is visible, showing that solvents with low polarity, δ_p~6 MPa$^{1/2}$ (1,3,4), low hydrogen bonds, δ_h<15 MPa$^{1/2}$ (1,2,3,4) and high dispersibility, δ_d>15 MPa$^{1/2}$ (1,2,3) have their solubility efficiency maximised. This corroborates the optimised Hansen parameter found for SWCNTs of δ_p= 7.5 MPa$^{1/2}$, δ_h=7.6 MPa$^{1/2}$, δ_d= 17.8 MPa$^{1/2}$ [43]. Considering this, the Hansen parameter of iPrOH ((7): δ_p= 6.1 MPa$^{1/2}$, δ_h= 16.4 MPa$^{1/2}$; δ_d= 15.8 MPa$^{1/2}$) indicates that this alcohol has higher efficiency to disperse CNTs than EtOH ((6): δ_p= 8.8 MPa$^{1/2}$, δ_h= 19.4 MPa$^{1/2}$, δ_d= 15.8 MPa$^{1/2}$), as also found by Ham et al. [41].

To further confirm the superiority of the iPrOH solvent over EtOH, a systematic suspension test was accomplished with a constant CNT concentration of 0.1 g.l^{-1} (Fig. 3b).
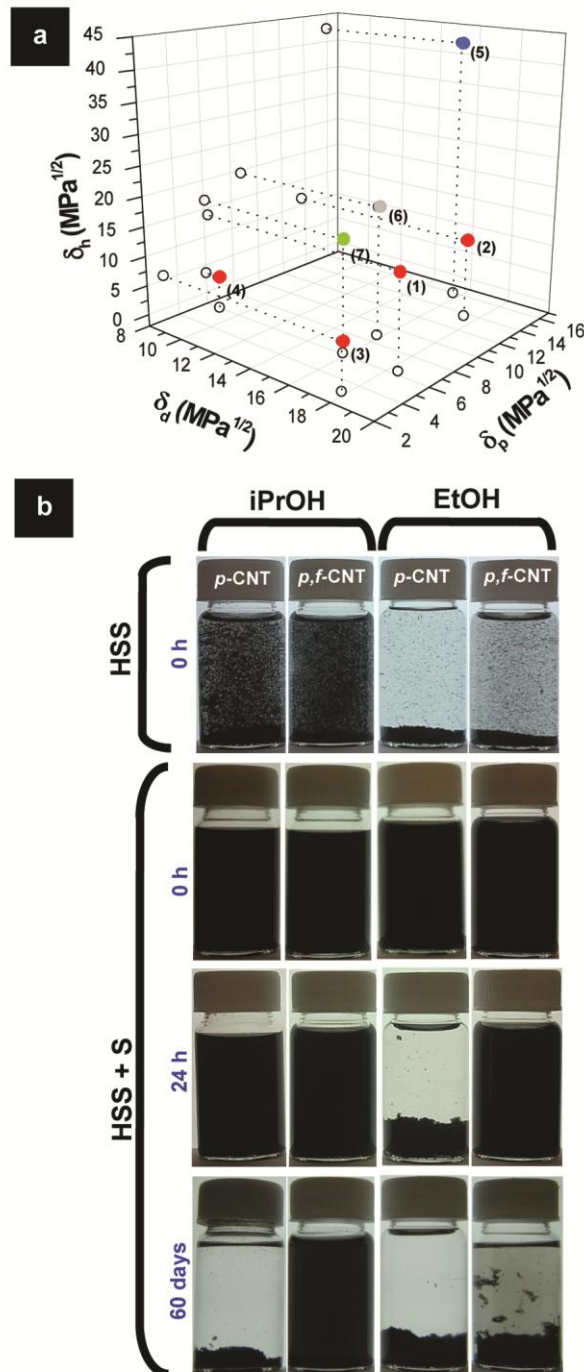

Fig. 3 - (a) 3D scattered plot of the Hansen parameters of pure solvents, commonly used to disperse CNTs and to process bioceramic composites. (b) Photographs of *p*-CNT and *p,f*-CNT suspensions in iPrOH and EtOH under treatments of high speed shearing (HSS) and sonication (S). Evaluation of HSS+S suspensions for resting times of 0 h, 24 h and 60 days.

This value was selected to be higher than the dispersion limits of pure organic solvents 0.001-0.095 g.l^{-1} [19] to better evaluate the effect of the functional groups on the CNT stabilization. The powder suspensions were mixed in the following conditions: (1) high-speed shearing at 20.500 rpm for 15 min (HSS); (2) HSS + sonication for 60 min (S). The time evolution of the HSS+S suspensions (2) was also investigated for 0 h, 24 h and 60 days.

Overall, the iPrOH suspensions present higher CNT stabilisation than EtOH. This can be already seen even for the first HSS step (1) (first row in Fig. 3b). The following step (2) of sonication for 60 min yields uniform black colour suspensions for all conditions (second row in Fig. 3b). The stabilization differences between suspensions become evident for long periods of resting (Fig. 3b). After 24h (HSS+S, 24h), the *p*-CNT in EtOH settled down in the bottom of the flask but not in iPrOH and the same occurred for the *p,f*-CNT in iPrOH, but only after 60 days. These results clearly show that the iPrOH gives more stable CNT suspensions than EtOH and the functional groups extend the CNT stabilisation time (Fig. 3b).

3.2.2. *Control of the CNT agglomeration state across the multi-step processing method*

The CNT agglomerate diameter size was controlled to be below 20 µm, the upper limit size for biologically safe CNT agglomerates (see section 1). This control was accomplished in the chemical functionalization and dynamic processing routes (see section 2.2).

A high shearing treatment (HSS: step 1) were firstly applied to convert the initial wide size range CNT agglomerates into a narrower distribution of agglomerate sizes (distribution curves not shown) below 100 µm. This was traduced in a reduction of the CNT agglomerate average size and variation coefficient of 92% and 30%, respectively, for *p*-CNT, and 85% and 26% for *p,f*-CNT (values calculated from the size distribution curves). The values are suggestive of a neglected influence of the chemical functionalization on the CNT agglomerate sizes.

Sonication processing (S: step 2) was then performed to reduce the CNT agglomerate sizes below 100 µm. Fig. 4a shows the influence of the functional groups and sonication time on the agglomeration state of HSS+S treated CNTs (see section 2.3.3). Without sonication (only the HSS treatment), the *p*-CNT present a less uniform agglomeration size than *p,f*-CNT, as is indicated by the much higher maximum values of the former. But when sonication is applied the differences of the agglomeration state between for the *p*-CNT and *p,f*-CNT are no longer observed even for long sonication times (Fig. 4a). This clearly shows that the sonication attenuates the effect of the functional groups on the CNT agglomeration state. Moreover, the agglomerate average size and variation coefficient decreases by ~45% and ~61%, respectively, for *p*-CNT, and ~54% and ~1% for *p,f*-CNT with the increasing sonication time (Fig. 4a). It is also interesting to note that the sonication treatment was more decisive to obtain final uniform CNT agglomerate size distributions for the *p*-CNT samples than for *p,f*-CNTs. The *p*-CNT morphology evolution with the sonication time is shown in Fig. 4b.
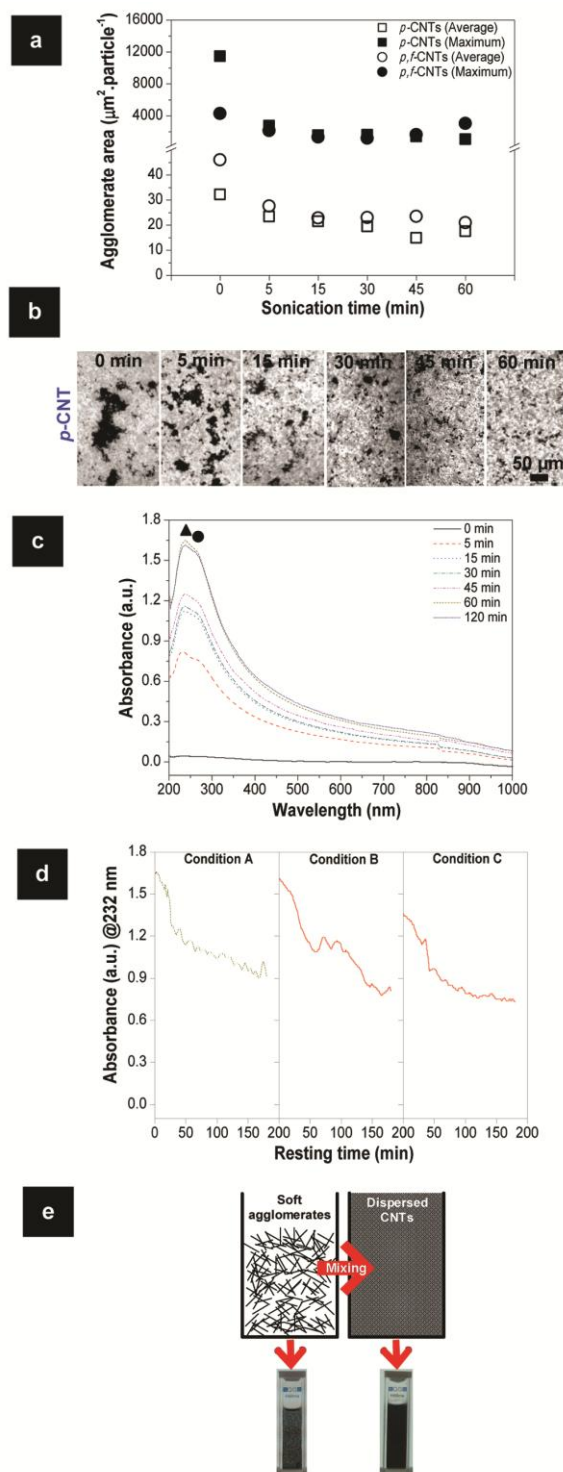
Fig. 4 - (a) Plot depicting the influence of the sonication time on the agglomerate size of *p*-CNT and *p,f*-CNT in iPrOH suspensions. (b) Respective optical images showing the evolution of the *p*-CNT agglomerate morphology with the sonication time. (c) Plot screening the dependence of UV spectroscopy curves of *p*-CNTs in iPrOH with the sonication time (● 232 nm, ▲ 270 nm). (d) Continuous UV spectroscopy measurements of the CNT suspensions stability in iPrOH, in respecting to the 232 nm CNT peak, for resting times up to 3h. Three conditions were evaluated: (1) HSS+S:60min; (2) resuspended by S:5min; (3) resuspended by MS. (e) Schematic image illustrating the effect of the mixing steps on the CNT agglomeration state.

242

The effect of the sonication time on the control of the CNT agglomeration state was further confirmed by UV spectroscopy studies of the p-CNT sample (Fig. 4c). The absorbance of the CNT related peaks at 232 and 270 nm due to 1D van Hove singularities [44], in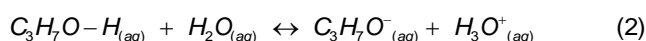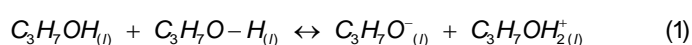crease with the sonication time up to 40-fold as a result of the increasing exfoliation of the CNT agglomerates. Additionally, by comparing the curves of 60 and 120 min (Fig. 4c) it can be seen the loss of effectiveness of sonication in reducing the agglomerate size for periods longer than 60 min. This corroborates the results of similar experiments accomplished by Yu et al [45].

Further investigation on the influence of the dynamic processing route and the chemical functionalization route on the control of the CNT agglomeration state across the multi-step powder processing method, including steps 3 to 5 (see section 2.2), was accomplished.

To thoroughly evaluate the influence of the dynamic processing route on the CNT agglomeration state, uninterrupted UV spectroscopy measurements of p-CNT suspensions, at 232 nm peak, for resting times up to 3h, were accomplished (Fig. 4d). Isopropyl alcohol suspensions were evaluated consecutively under similar conditions used in the powder processing (see section 2.2): (A) HSS+S:60min (step 1 + step 2); (B) condition (A) + S:5min (step 3); (C) condition (B) + magnetic shearing (MS):5min (step 5).

Considering the first condition, the absorbance of the 232 nm peak decreases with the increasing resting with a pronounced reduction after just 30 min (Fig. 4d). Over time, there is a change of the CNT agglomeration state, with individualised CNTs starting to link together leading to an increase of the agglomerate size, forming a swollen structure, also reported by others [41]. Yet, these CNT agglomeration events were not detected by eye, as shown by the uniformly black suspensions over 24h of resting time (Fig. 3b). Moreover, by comparing the curves of condition B and C with the starting condition A (Fig. 4d) it can be reasoned that the big agglomerates formed over the resting time are soft structures that can be easily re-dispersed to an almost full recovery of the CNT agglomeration state when gently stirred by S and MS (Figs. 4d and 4e). Similar observations were reported in benzyl alcohol by Xu et al. [24]. This is explained by the similar polar component (δ_p) of Hansen for benzyl (2) and isopropyl (7) alcohols of 6.3 and 6.1, respectively (Fig. 3a). According to Ham et al., solvents with low polar components are successful in the dispersion of non-functionalized CNTs due to the high hydrophobicity of these materials [41]. The easily re-dispersion of the p-CNT in iPrOH is thus intimately related to the chemical interactions between the CNTs and the iPrOH solvent.

Generally, solid particles are charged by electron transfer [26] or adsorption/desorption of ions [27] between the particle and the solvent medium. Concerning the latter, pure iPrOH (Eq. 1) or aqueous alcohol solution (Eq. 2) ionizes into a protonated alcohol and an alkoxide ion, accordingly to the following,

$$C_3H_7OH_{(l)} + C_3H_7O-H_{(l)} \leftrightarrow C_3H_7O^-_{(l)} + C_3H_7OH^+_{2(l)} \qquad (1)$$

$$C_3H_7O-H_{(aq)} + H_2O_{(aq)} \leftrightarrow C_3H_7O^-_{(aq)} + H_3O^+_{(aq)} \qquad (2)$$

Of interest, the *p*-CNT and *p,f*-CNT samples have negative zeta potentials in iPrOH of -98.9±6.4 mV and -122.7±7.2 mV, respectively. With high potentials is expectable strong repulsive electrostatic forces involving CNT-CNT in iPrOH which might explain the easily re-dispersion of CNTs in this alcoholic medium. These values are in line with those found for carbon black particles in iPrOH suspensions of -71.1 mV [46]. The more negative charges on the *p,f*-CNT compared to the *p*-CNT is explained by the combined contribution of the adsorbed alkoxide ions (Eq.1 and Eq.2) and the negative dipole of the COOH functional groups on the CNT sidewalls.

The uninterrupted UV measurements prove that after setting a CNT agglomeration state, this can be kept almost preserved across the multi-step powder processing method by using a dynamic processing route where all the involved steps are performed under continuous stirring. To support these observations and also investigate the influence of the functionalization route, the morphology and diameter size distribution of the CNT agglomerates was assessed at two crucial conditions (Fig. 5): (A') solo dispersed CNTs in suspension (HSS+S:60min) and (B') sieved final composite powders.

Regarding the condition A', the low magnification STEM images depict uniform agglomerate morphologies with sizes below 5 μm for both samples, *p*-CNT and *p,f*-CNT (Figs. 5a and 5b). At higher magnification, it can be also seen that *p*-CNT and *p,f*-CNT samples (Figs. 5b and 5e) show agglomerates interconnected by well individualised CNTs, forming an organised 3D arrangement.

For a complete picture of the agglomerate size of these two samples, the respective size distribution curves are shown in Figs. 5c and 5f. The *p*-CNT curve is more symmetric than the *p,f*-CNT one which indicates a higher uniformity of the agglomerates sizes. Also, the cumulative volume percentage of agglomerate size <3 μm (of small agglomerates or individualised tubes, see section 2.1), is lower for *p*-CNT than for *p,f*-CNT, 21% and 28%, respectively. This is explained by the higher effectiveness of the functional groups on the CNT disentanglement.

Contrarily to the CNTs alone, the composite powders (condition B') present some differences between them (Figs. 5g-l). Bigger particle aggregates of *p,f*-CNT/Glass/HA comparatively to the *p*-CNT/Glass/HA are seen (Figs. 5g and 5j). This highlights the stronger attractive electrostatic forces in the *p,f*-CNT/Glass/HA powders due to the more negative charge density in *p,f*-CNT. This occurs because the Glass/HA mixture has a zeta potential in iPrOH at natural pH of +21.1±2.1 mV, intermediate between those of the individual constituents of -16.2±2.6 mV for glass and +31.3±1.5 mV for HA (similar value of +22.6 mV were observed by Javidi et al. [47]). Though, the respective high magnified images do not make obvious the differences between the two powders (Figs. 5h and 5k). Both powders dispose a CNT network decorated by ceramic particles intimately attached to individual CNTs.

244
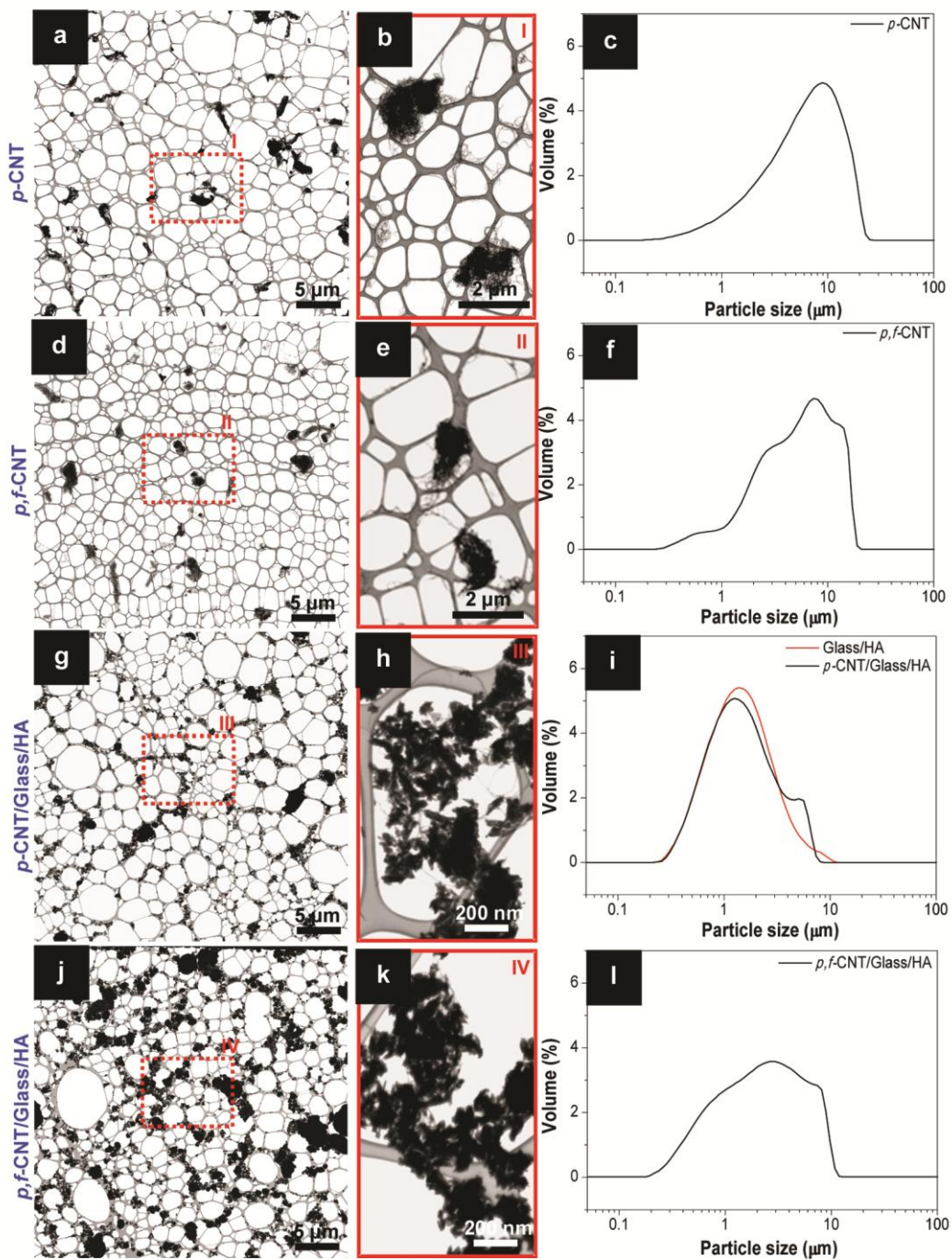
Fig. 5 - STEM micrographs and size distribution plots of HSS+S:60min treated (a,b,c) *p*-CNT and (d,e,f) *p,f*-CNT, and of sieved composite powders (g,h,i) *p*-CNT/Glass/HA and (j,k,l) *p,f*-CNT/Glass/HA powders.

Moreover, the low magnification images of the both type of composite powders also gives clue to a slight reduction of the CNT agglomerates (Figs. 5g and 5j) comparatively to the CNTs alone (Figs. 5a and 5b). This might by endorsed to the disentanglement action of the ceramic powders under shearing forces.

Complementary size distribution measurements of the composite powders (Figs. 5i and 5l) corroborate these STEM observations. The distribution curve of the composite powders is shifted to lower sizes when compared to the curves of solo CNT suspensions (Figs. 5c and 5f). Also, the stronger powder interactions in *p,f*-CNT/Glass/HA over *p*-CNT/Glass/HA become obvious when comparing the centre position of the Glass/HA size distribution band is at 1.4 μm with the composite powders (Figs. 5i and 5l). While the *p*-CNT/Glass/HA powder shows a band centred at a similar position of 1.3 μm, in *p,f*-CNT/Glass/HA the centre was deviated to 2.9 μm. Furthermore, the slight distinction between Glass/HA and *p*-CNT/Glass/HA curves concerns the small right-side band centre at about 5.3 μm in the latter curve. This band probably corresponds to the *p*-CNT (Fig. 5c) which may indicate a minor interaction between CNT and Glass/HA. On the other hand, the *p,f*-CNT/Glass/HA curve show a right-side band shifted to 7.5 μm, a value higher than *p*-CNT/Glass/HA because of the CNTs themselves (Fig. 5f) or due to a higher interaction between the composite powders. The *p,f*-CNT/Glass/HA curve (Fig. 5l) also shows a singularity at 800 nm that results from the small size CNTs presented in Fig. 5f. Furthermore, the higher interactions in the *p,f*-CNT/Glass/HA powders comparing to the *p*-CNT/Glass/HA ones also promote a slightly lower homogeneous green powders in the first case.

3.3. *Effects of functional groups on the CNT structure under high temperature sintering conditions*

The effect of functional groups on the CNT thermal stability was evaluated by TG analysis (Fig. 6a). By comparing the TG_{O_2} curves of the Glass/HA and *p*-CNT/Glass/HA (data not shown) a weight fraction of CNTs of ~2.8 wt% in the green composite powder was determined.

In order to reproduce the inert atmosphere used in hot-pressing, the present TG study was accomplished in N_2 atmospheres. Fig. 6a shows the TG_{N_2} curves of the following powders: (1) *p*-CNT; (2) *p*-CNT; (3) Glass/HA; (4) *p*-CNT/Glass/HA; (5) *p,f*-CNT/Glass/HA. Under inert atmospheres it is expected that *p*-CNT does not oxidise, giving negligible weight loss (curve 1). When the *p*-CNT is incorporated in the *p*-CNT/Glass/HA composite powder it can be seen that ~1.1 wt% CNTs oxidised at 1300ºC (difference of weight losses of curves 3 and 4). The CNT oxidation starts to occur visibly at ~1000ºC (curve 4) by reaction with oxygen containing groups released from the HA dehydroxylation [6]. Below 1000ºC, the curves 3 and 4 present similar profiles (Fig. 6a). Yet, a contradictory behaviour is seen for curves (3) and (5) under 1000ºC. The *p,f*-CNT/Glass/HA powder (curve 5) starts to lose weight at ~ 280ºC due to the breakage of the functional groups, known to start at ~250ºC, as given by curve 2. The total weight loss of organic compounds (CNT+COOH groups) was ~2.53 wt% at 1300ºC (difference of weight losses of curves 3 and 5). The weight fraction of functional groups on the CNT sidewalls is ~9.2 wt%, calculated from curve 2, so a 2.8 wt% CNT containing *p,f*-CNT/Glass/HA powder should fully loose ~0.26 wt% of functional groups.
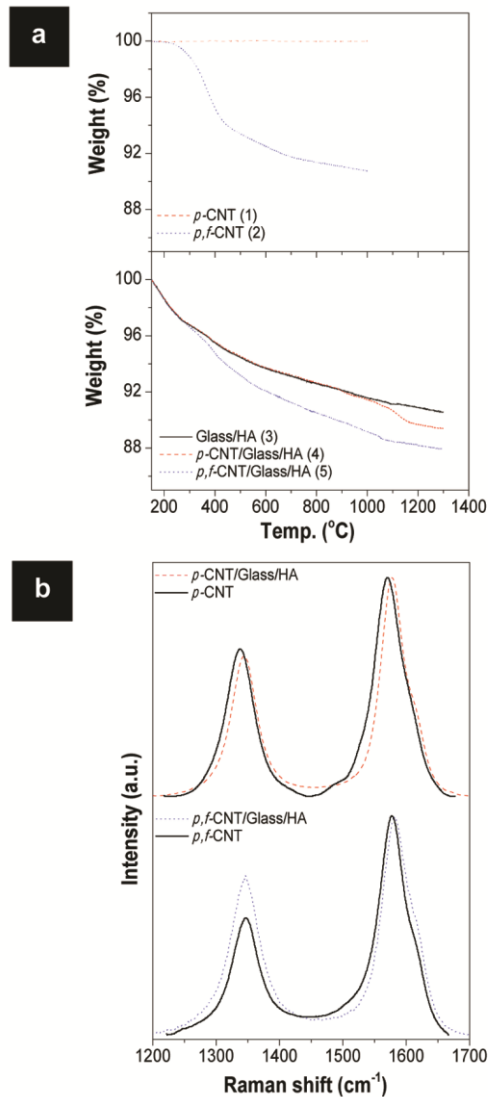
Fig. 6 - (a) TG$_{N2}$ analyses of (1) *p*-CNT, (2) *p,f*-CNT, (3) Glass/HA, (4) *p*-CNT/Glass/HA and (5) *p,f*-CNT/Glass/HA. (b) μ-Raman of the *p*-CNT and *p,f*-CNT alone and incorporated in the hot-pressed ceramic matrix.

This means that for the ~ 2.3 wt% of CNT oxidised at 1300ºC (curve 5), 1.2 wt% loss was caused by reaction with the functional groups that remain on the CNT sidewalls in the temperature range of 600ºC to 1000ºC (curve 2) and 1.1 wt% loss was promoted by reaction with O$_2$ from the HA dehydroxylation above 1000ºC.

The TG experiments with free powders having high reactivity showed that the organic functional groups oxidise the CNT phases at high temperatures. So, this becomes a drawback during the high temperature sintering of the composite powders. Yet, the composite powders are sintered under a constant applied pressure of 30 MPa (see section 2.2), thus these powder compacts should have different reactivity from those used in the TG experiments. A preliminary study showed in fact that during hot-pressing under vacuum, the entrapped H$_2$O from the HA dehydroxylation did not oxidise the CNTs due to the fast dragging out by the combined applied

pressure and vacuum [6]. Nonetheless, the potential CNT oxidation by functional groups linked to impurity-free sidewalls (Figs. 2e and 2f) was not yet evaluated.

Fig. 6b shows the μ-Raman spectra of p-CNTs and p,f-CNTs alone and incorporated in the hot-pressed composites. The results depict a negligible change of the defect-related D-band in the hot-pressed p-CNTs which proves that the processing route is non-destructive to the CNTs. Conversely, the intensity and FWHM of the D-band of the p,f-CNTs in the composite slightly increases after elimination of the functional groups during hot-pressing, indicating that some defects were left in the CNT surface due to oxidative reactions.

3.4. *Effects of functional groups on the morphology and properties of hot-pressed composites*

SEM micrographs of the polished and fracture surfaces of the hot-pressed p-CNT/Glass/HA and p,f-CNT/Glass/HA composites are shown in Figs. 7a-i. The polished surfaces show p-CNT/Glass/HA and p,f-CNT/Glass/HA composites having comparable microstructures with CNT agglomerates homogeneously dispersed in the ceramic matrix (Figs. 7a-c). It can be also seen that the porosity of the two CNT composites is low, similar and close to that of the cortical bone (Table 2). Yet, the presence of CNT agglomerates increases the porosity of the microstructure in comparison to the matrix alone (Table 2).

Table 2 - Mechanical and electrical properties of the cortical natural bone and the synthetic bone grafts of hot-pressed Glass/HA, p-CNT/Glass/HA and p,f-CNT/Glass/HA.

Properties	Cortical bone	Glass/HA	p-CNT/Glass/HA	p,f-CNT/Glass/HA
Porosity (%)	5.4-14.2[a]	1±0.01	7±0.01	7±0.01
Young's Modulus, E (GPa)	6.5-20.7[a,b]	119±4	87±1	n/a
Shear Modulus, G (GPa)	2.2-5.5[a]	47±1	34±2	n/a
Hardness, Hv (GPa)	0.31-0.58[c]	6.8±0.4	3.5±0.2	3.3±0.2
Fracture toughness, K_{IC} (MPa.m.$^{1/2}$)	2-12[d]	1±0.04	1.33±0.19	n/a
Compressive strength (MPa)	100-230[d]	894±78	725±18	749±24
Bending strength, σ_R (MPa)	50-150[b]	236±13	162±10	147±3
Electrical conductivity, σ (S.m^{-1})	5×10^{-3}-6.5×10^{-2}[e]	5×10^{-9}±3×10^{-9}	55±1	24±3
n/a: not assessed [a]Ref. [49] [b]Ref. [50] [c]Ref. [51] [d]Ref. [52] [e]Ref. [53]				

The porosity differences explain the better overall mechanical properties of the Glass/HA samples comparatively to the p-CNT/Glass/HA and p,f-CNT/Glass/HA composites. Still, the mechanical properties of the CNT composites outperform those of the cortical bone, with exception to the fracture toughness (Table 2). Yet, CNTs work as efficient toughening agents in the p-CNT/Glass/HA composites improving the fracture toughness of the Glass/HA matrix by 50%, making it closer to the value of the natural bone (Table 2). The toughening potential of CNTs is well recognised in the literature [48].
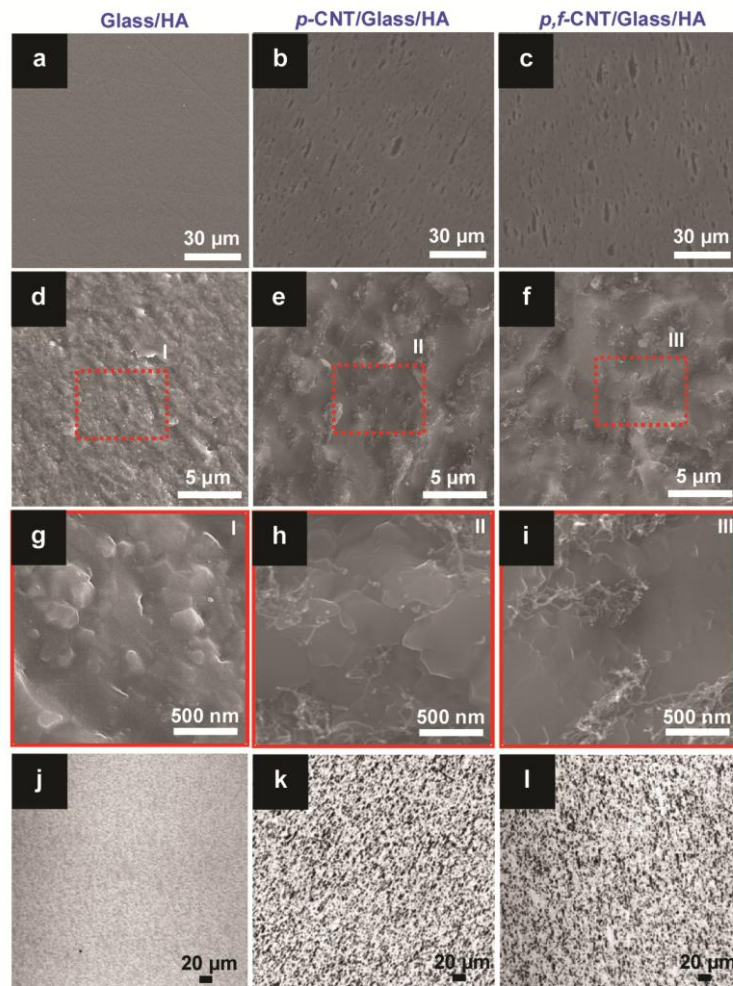
Fig. 7 - SEM images of the polished surfaces of hot-pressed samples of (a) Glass/HA, (b) *p*-CNT/Glass/HA and (c) *p,f*-CNT/Glass/HA. (d-i) Respective SEM micrographs of the fracture surface of (a), (b) and (c). (j-l) Macro-scale optical images of the (a), (b) and (c) samples.

Additionally, the overall mechanical properties of the *p*-CNT/Glass/HA are higher than those of *p,f*-CNT/Glass/HA. The evolution of CNT agglomerates size and distribution inside the composites and identification of closed porosity were studied by analysis of the fracture surfaces shown in Figs. 7d-i. There are no evident differences of closed porosity or of 3D arrangement agglomerates in the two CNT composites. So, the differences of the mechanical performance between the CNT composites can be resulted from the loss of the organic groups on the CNT sidewalls during the hot-pressing. The elimination of these organic groups is followed by the increase of defects in the CNT structure (Fig. 6b) and thus deterioration of the CNT-matrix interface.

At a nano-sized scale (Figs. 7g-i), it is clear that there are individualised CNTs that form interfaces with the matrix. This points towards the existence of a microstructure with a 3D CNT network formed by micro-sized agglomerates together with individualised CNTs, as previously shown by the 2D arrangement in the green composite powders, Figs. 5b,e,h,k. The formation of an

organised 3D CNT network in both CNT composites allowed an increase of the electrical conductivity by ten orders of magnitude relatively to the matrix alone (Table 2). Also, the superior preservation of the *p*-CNTs over the *p,f*-CNTs (Fig. 6b) helps understand the slight electrical conductivity differences of the respective composites (Table 2).

The organisation of the 3D CNT network is thus reproducible at a macro-sized scale (Figs. 7j-l). Overall, the optical micrographs show CNT composites with well distributed agglomerates with diameter sizes below 20 µm (maximum area <320 µm^2), as expressly intended in the introductory section. Though, a more precise quantitative analyses demonstrate that the CNT agglomerates of the *p*-CNT/Glass/HA composites have a marginally higher homogeneity and lower diameter sizes than those of the *p,f*-CNT/Glass/HA composites, 2 and 3 µm respectively. These results are in accordance with the green powder characteristics (Figs. 5g-l).

The results reported in the previous 3.3 and present sections did not show relevant advantages of the functionalization in the composites preparation. In addition, the mechanical and electrical properties of the *p*-CNT/Glass/HA composites were marginally superior to those of *p,f*-CNT/Glass/HA due to the full elimination of the functional groups during the high temperature sintering step. In this context, only the *p*-CNT/Glass/HA composite was further evaluated for its degradation and osteoblastic cytocompatibility.

3.5. *In vitro degradation testing of p-CNT/Glass/HA composites*

Calcium phosphate-based bone grafts when applied *in vivo*, in contact with bone tissue, undergo osteoclastic degradation/reabsorption, accordingly to the bone regeneration cycle, and/or by simple chemical degradation. Alongside with the ceramic matrix degradation, it is expectable the release of CNTs to the living milieu. Once the agglomeration state of the released CNTs dictates their *in vivo* toxicity [16-20], further investigation on the degradation profile of the *p*-CNT/Glass/HA composites and on the agglomeration degree of the released materials becomes particularly relevant when bone regeneration purposes are envisaged. To evaluate this, an *in vitro* acellular degradation test with granule samples of 250-500 µm was performed under two conditions simulating both degradation mechanisms referred above (Fig. 8). An extreme solution with pH:3 that mimics the acid environment produced by osteoclasts [54] and a pH:7.4 solution that better simulates the *in vivo* millieu conditions.

The weight loss was found to be lower at pH:7.4 than at pH:3 after 24 and 72h of immersion (Fig. 8a), as expected, since most calcium phosphate phases are more soluble at low pH [55]. At pH:7.4, no significant differences were observed between the weight loss profile of *p*-CNT/Glass/HA and Glass/HA materials, being the highest degradation achieved after 72h of immersion (Fig. 8a).
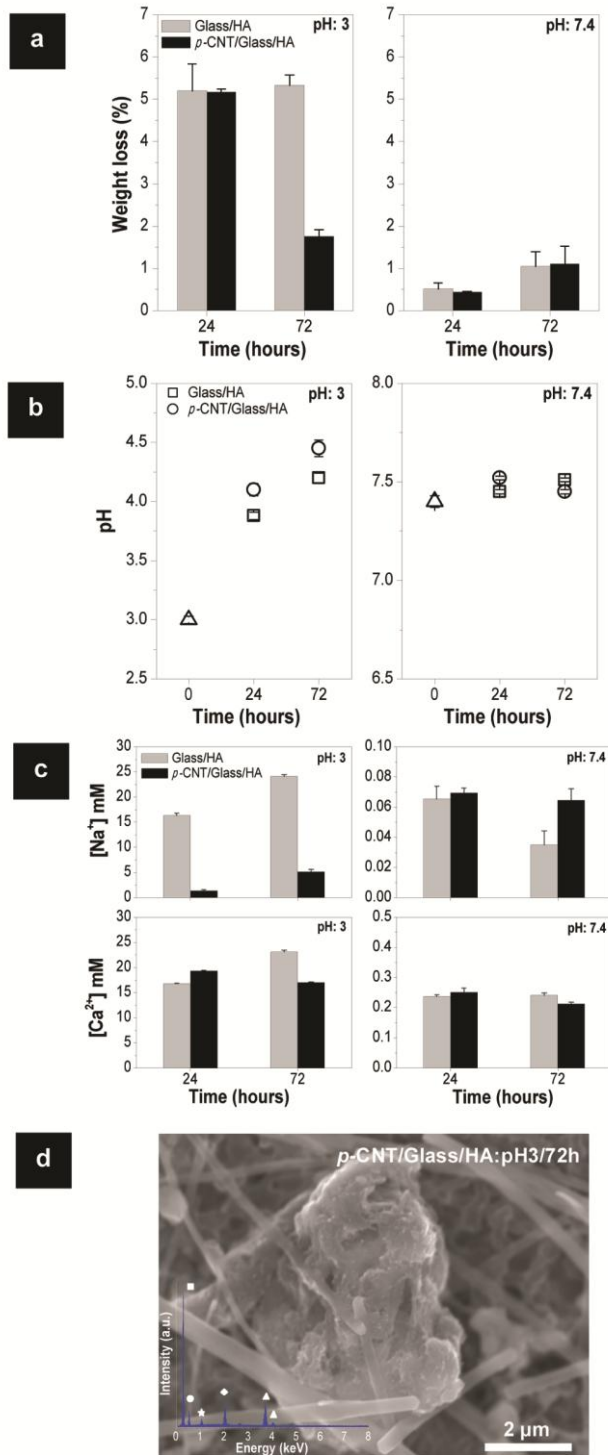
250

Fig. 8 - Plots of *in vitro* degradation tests of Glass/HA and *p*-CNT/Glass/HA samples showing the influence of the immersion time on their (a) weight loss and on the (b) pH and (c) ion concentration profiles of the collected immersion liquid. (d) Representative SEM micrograph of a released CNT agglomerate (EDS spectrum of the agglomerate as inset, ■C, ●O, ★ Na, ◆P, ▲Ca).

After 24h of immersion in the buffer solution of pH:3, both materials presented similar weight loss, but after 72h the composite containing CNT showed less degradation (Fig. 8a).

Despite the similar chemical phase composition of both materials, the presence of some pits in the surface of *p*-CNT/Glass/HA composite may had caused a higher degradation after 72h at pH:3, and by the occurrence of a dissolution-precipitation process originate an apparent reduction in weight loss, ions release and a low pH change (Figs. 8a-c). The pH and calcium release ion profile patterns of Figs. 8b and 8c reflects this degradation behavior.

Regarding the release profile of Na ions (Fig. 8c), the materials behaved slightly different, being the amount released at pH:7.4 much less than at pH:3 for both materials.

By observing the Na profile release mainly at pH:3, it can be speculated that the small sodium ions, presented in the glass liquid phase that was spread through the CNT and HA during the sintering process, may had been entrapped in the CNT channels during the sintering process. This was confirmed by EDS detection of Na on the surface of a CNT agglomerate released from the ceramic matrix, after immersion for 72h at pH:3 (Fig. 8d). Also, metallic impurities such as Fe and Co were not observed either by EDS on the CNT agglomerates or by AAS in the collected immersion liquid (even for high concentrated conditions). Moreover, Fig. 8d shows a released CNT agglomerate with biological safe diameter sizes. The controlled size and high purity of CNT agglomerates makes these composites promising bone grafts to interface with bone tissue.

3.6. Osteoblastic cell response to p-CNT/Glass/HA composites

Fig. 9a shows the results for the viability/proliferation (evaluated by the MTT and LDH assays) and ALP activity of osteoblastic cells cultured over *p*-CNT/Glass/HA composite, compared to those on Glass/HA composite and standard cell culture plate (control). At day 1, MTT reduction values were similar on the three surfaces, showing that comparable number of cells adhered to these substrates (although the Glass/HA composite presented slightly higher values). However, at day 4, cell proliferation on the CNT/Glass/HA composite was lower than that on the Glass/HA surface and control cultures. On the LDH assay, the similar values observed on the two composites suggest that the attached cells were viable on both surfaces. In spite of the lower cell proliferation seen on the *p*-CNT/Glass/HA composite, significantly higher values were found for ALP activity. This enzyme is an important osteoblastic differentiation marker, as it plays a relevant role in the mineralization of the bone collagenous matrix [56].

CLSM images at day 1 (Fig. 9b) show that MG63 cells adhered to the tested surfaces, and exhibited an organized F-actin cytoskeleton with intense staining at the cell boundaries. However, differences were noted on the cell morphology and distribution over the surface. Cells attached to the control surface and to the Glass/HA composite showed a polygonal/elongated morphology and a random distribution, whereas, on the *p*-CNT/Glass/HA composite, cells were more elongated and displayed a tendency for an oriented alignment. Cell division was already visible, at day 1, on the three surfaces.
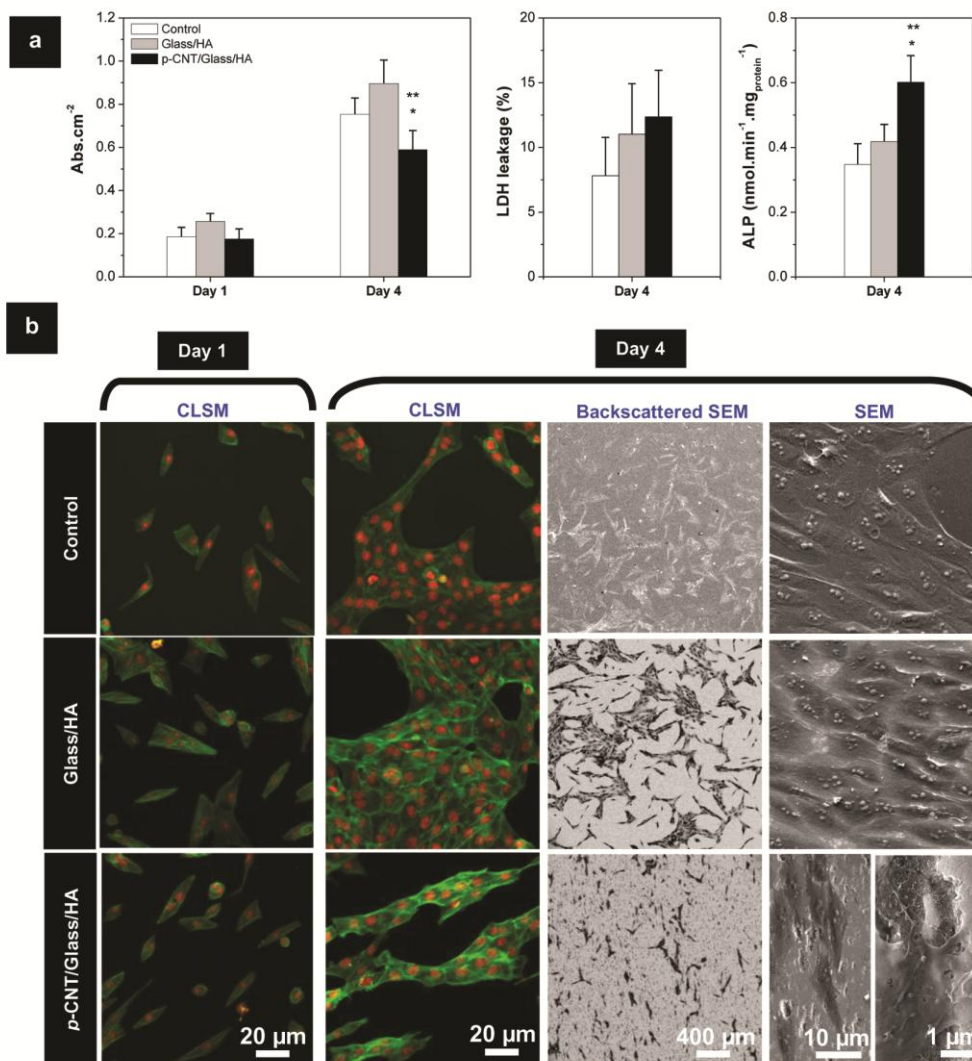
252

Fig. 9 - Behaviour of osteoblastic cells cultured over standard cell culture plates (control), Glass/HA and *p*-CNT/Glass/HA composites. (a) Cell viability/proliferation (MTT and LDH assays) and ALP activity; significantly different from the control (*) and from the Glass/HA composite (**). (b) Representative CLSM images, showing the F-actin cytoskeleton (green) and nucleus (red) of cells at day 1 and 4, and backscattered SEM and SEM images of the cell growth pattern at day 4, depicting intimate cell-CNT interactions.

Cells proliferated throughout the culture time, as shown in the CLSM images at day 4 (Fig. 9b). Cells displayed a healthy behaviour, with a prominent nucleus, a well-developed F-actin cytoskeleton and signs of active on-going proliferation on control cultures and on both composites. However, the pattern of cell growth was clearly distinct, i.e. the cell layer was randomly organized over Glass/HA composite, but revealed a defined oriented alignment over the *p*-CNT/Glass/HA composite. These observations were further confirmed by SEM analyses (Fig. 9b). Cells cultured over the *p*-CNT/Glass/HA composite displayed a tendency to follow the alignment/orientation of the CNT agglomerates on the material surface (Figs. 7b). At high magnification (bottom right in Fig.

9b), an intimate cell-CNT interaction was observed with cells exhibiting a normal morphology with abundant cytoplasm expansions over CNT agglomerates, being fully integrated in the tube´s fibrilar morphology.

Results presented above showed evident differences in the behaviour of osteoblastic cells over the p-CNT/Glass/HA and Glass/HA composites. The inclusion of CNT agglomerates in the Glass/HA matrix endowed the resulting composites with distinct surface properties, namely for roughness, zeta potential and contact angle, as summarized in Table 3. All these parameters affect osteoblastic cell response, as they modulate the interaction of the material surface with proteins, relevant in the cell adhesion process, thus conditioning the subsequent cellular events [56]. The surface characteristics of the CNT composite relatively to the matrix alone - higher roughness, higher hydrophobicity, and higher positively charged - would induce a distinct adhesion profile of the α-MEM medium proteins to the surface of the material, and thus differences on the cell adhesion and proliferation on it [57]. The MTT data for CNT composites (Fig. 9a) evidence that this protein-mediated cell adhesion mechanisms are in a range that do not dictate the cell adhesion and proliferation. Nevertheless, the close cellular interaction with the nanoscale roughness of the CNT clusters on the CNT/Glass/HA composite, as it was evident on high magnification SEM images, might effectively affect the osteogenic differentiation, as suggested by the increased ALP activity found on the CNT composite. Regarding the p-CNT/Glass/HA composite, cell response to CNT-containing materials for bone tissue applications has been addressed in a variety of studies, and results revealed a great variability because of the diverse experimental protocols involved, related to the biomaterial profile and the biological protocols.

Table 3 - Surface characteristics of the hot-pressed Glass/HA and p-CNT/Glass/HA materials.

Sample	Surface roughness, R_a (µm)	Zeta potential (mV)	Contact angle (°)
Glass/HA	0.05±0.01	-25.4±2	61.5±1.6
p-CNT/Glass/HA	0.17±0.03	-1.3±0.3	96.6±3.7

However, CNTs-containing scaffolds broadly show the ability to support cell adhesion, proliferation and osteogenic differentiation [7]. In this context, the results of the present work are in agreement with previous observations. Thus, the specific cellular orientation seen over the p-CNT/Glass/HA composite is in line with some reported information, showing that the distribution of the CNTs seems to play a role on the biological output. Hence, in organized arrays of vertically-aligned MWCNTs, the periodicity and alignment of the CNTs influenced morphology, orientation and proliferation of osteoblastic-like cells [58]. Also, aligned conductive nanofibers of biodegradable poly-DL-lactide (PLA) embedded with MWCNTs were found to greatly enhance the extension and the outgrowth of osteoblastic cells, better than randomly oriented fibers [59]. In addition, aligned CNT networks exhibited the ability to control the directional growth of hMSCs, and to further

enhance cell proliferation and the osteogenic differentiation, in comparison to seeded randomly oriented CNTs network [60]. According to the authors, this process may be mediated by the high cytoskeletal tension accumulated on aligned cells, which thus leads to the activation of selective mechano-transduction pathways [60]. These studies strongly suggest that the spatial organization of the CNTs modulates osteoblastic proliferation and differentiation events. Due to the established inverse relationship between proliferation and differentiation during the development of the osteolastic phenotype [56], the lower cell proliferation but higher ALP activity observed in the present work on the *p*-CNT/Glass/HA composite suggests an inductive effect on the osteoblastic differentiation, compared to that observed over the Glass/HA composite. Increased ALP activity was also observed in MC3T3-E1 pre-osteoblastic cells with the inclusion of MWCNTs in hydroxyapatite coatings, compared to that attained on the bare substrate (titanium alloy) and pure HA coating [61].

4. Conclusions

Multifunctional carbon nanotube/bioceramic bone grafts with controlled CNT agglomeration were processed by an optimized functionalization-free route with minor contaminant levels and damage to CNTs.

The non-functionalized CNT composites presented homogenously dispersed CNT agglomerates with diameter sizes below 3 μm similar to those resulting from Diels-Alder functionalization. The latter improved the CNT stabilization and CNT-ceramic interactions. However, this functionalization was less decisive than the functionalization-free processing route in the final properties of the biocomposite, due to *in situ* oxidation of CNTs during the high temperature sintering.

CNTs worked as efficient toughening agents in non-functionalized composites improving the fracture toughness of the ceramic matrix, making it closer to the one of natural cortical bone. The remaining mechanical and electrical properties of the composite outperformed those of the natural bone. These composites degraded at higher rates in *in vitro* testing than the ceramic matrix, but with releasing of CNTs with biological safe diameter sizes. The CNT/bioceramic composites allowed cell adhesion and proliferation, further enhancing the functional activity and modulating the orientation of the cell growth along the alignment of the CNT agglomerates on the composite surface.

The present highly electroconductive and tough multifunctional bone grafts including biologically safe and impurity-free CNT agglomerates are apt to interface with bone tissue and offer high perspectives to control its regeneration rate by *in situ* electrical stimulation.

Acknowledgements

References:

[1]. Hench LL, Polak JM. Third-generation biomedical materials, Science. 2002;295:1014-1017.

[2]. Friedenberg ZB., Brighton CT. Bioelectric potentials in bone, J. Bone Joint Surg. Am. 1966;48:915-923.

[3]. Fukada E, Yasuda I. On the piezoelectic effect of bone, J. Phys. Soc. Japan. 1957;12:1158-1162.

[4]. Grimnes S, Martinsen OG. Editors, Bioimpedance and Bioelectricity Basics, Academic Press, UK; 2008.

[5]. Supronowicz PR, Ajayan PM, Ullmann KR, Arulanandam BP, Metzger DW Bizios R. Novel current-conducting composite substrates for exposing osteoblasts to alternating current stimulation, J. Biomed. Mater. Res. 2002;A59:499-506.

[6]. Mata D, Oliveira FJ, Ferreira NM, Araújo RF, Fernandes AJS, Lopes MA Silva RF. Sintering strategies for smart electroconductive carbon nanotube/glass/hydroxyapatite bone grafts, Biomed. Mater. *submitted.*

[7]. Lahiri D, Ghosh S, Agarwal A. Carbon nanotube reinforced hydroxyapatite composite for orthopedic application: a review, Mater. Sci. Eng. 2012; C32:1727-1758.

[8]. Zanello LP, Zhao B, Hu H, Haddon RC. Bone cell proliferation on carbon nanotubes, Nano Lett. 2006;6:562-567.

[9]. Meng J, Song L, Meng L, Kong H, Zhu G, Wang C. Using single-walled carbon nanotubes nonwoven films as scaffolds to enhance long-term cell proliferation *in vitro,* J. Biomed. Mater. Res. A. 2006;79:298-306.

[10]. Guiseppi-Elie A. Electroconductive hydrogels: synthesis, characterization and biomedical applications, Biomaterials. 2010;31:2701-16.

[11]. Mata D, Silva RM, Fernandes AJS, Oliveira FJ, Costa PMFJ, Silva RF. Upscaling potential of the CVD stacking growth method to produce dimensionally-controlled and catalyst-free multiwalled carbon nanotubes, Carbon. 2012;50: 3585-3606.

[12]. Mu Q, Broughton DL, Yan B. Endosomal leakage and nuclear translocation of multiwalled carbon nanotubes: developing a model for cell uptake Nano Lett. 2009;9: 4370-4375.

[13]. Lacerda L, Herrero MH, Venner K, Bianco A, Prato M, Kostarelos K. Carbon-nanotube shape and individualization critical for renal excretion. Small. 2008;4:1130-1132.

[14]. Bussy C, Cambedouzou J, Lanone S, Leccia E, Heresanu V, Pinault M, et al. Carbon nanotubes in macrophages: imaging and chemical analysis by X-ray fluorescence microscopy. Nano Lett. 2008;8:2659-2663.

[15]. Stone V, Donaldson K. Signs of stress. Nat. Nanotechnol. 2006;1:23-4.

[16]. Poland C, Duffin R, Kinloch I, Maynard A, Wallace W, Seaton A, et al. Carbon nanotubes introduced into the abdominal cavity of mice show asbestos-like pathogenicity in a pilot study, Nat. Nanotechnol. 2008;3:423-348.

[17]. Schipper ML, Nakayama-Ratchford N, Davis CR, Kam NWS, Chu P, Liu Z, et al. A pilot toxicology study of single-walled carbon nanotubes in a small sample of mice nature. Nat. Nanotechnol. 2008;216-221.

[18]. Freitas RA, Editor, Nanomedicine Volume IIA: Biocompatibility, Landes Bioscience, Texas; 2003.

[19]. Sato Y., Yokoyama A., Shibata K-I., Akimoto Y., Ogino S-I., Nodasaka Y. Influence of length on cytotoxicity of multi-walled carbon nanotubes against human acute monocytic leukemia cell line THP-1 *in vitro* and subcutaneous tissue of rats in vivo. Mol. Bio. Syst. 2005;1:176–182.

[20]. Abarrategi A, Gutiérrez MC, Moreno-Vicente M, Hortigüela MJ, Ramosa V, Lopéz-Lacomba JL, et al. Multiwall carbon nanotube scaffolds for tissue engineering purposes, Biomaterials. 2008;29:94-102.

[21]. Zhbanov AI, Pogorelov EG, Chang YC. Van der Waals interaction between two crossed carbon nanotubes, ACS Nano. 2010;4:5937-5945.

[22]. Dong L, Witkowski CM, Craig MM, Greenwade MM, Joseph KL. Cytotoxicity effects of different surfactant molecules conjugated to carbon nanotubes on human astrocytoma cells, Nanoscale Res. Lett. 2009;4:1517-1523.

[23]. H. Chen, J. Shen, G. Longhua, Y. Chen and D. H. Kim, Cellular response of RAW 264.7 to spray-coated multi-walled carbon nanotube films with various surfactants, J. Biomed. Mater. Res. Part A. 96, 413-421 (2011).

[24]. Xu GH, Zhang Q, Huang JQ, Zhao MQ, Zhou WP, Wei F. A two-step shearing strategy to disperse long carbon nanotubes from vertically aligned multiwalled carbon nanotube arrays for transparent conductive films, Langmuir. 2010;26:2798-2804.

[25]. Cheng Q, Debnath S, Gregan E, Byrne HJ. Ultrasound-assisted SWNTs dispersion: effects of sonication parameters and solvent properties, J. Phys. Chem. C. 2010;114:8821-8827.

[26]. Labib ME, Williams R. The use of zeta-potential measurements in organic solvents to determine the donor - acceptor properties of solid surfaces, J. Colloid Interface Sci. 1984;97:356-366.

[27]. Damodaran R, Moudgil BM. Electrophoretic deposition of calcium phosphates from non-aqueous media, Colloids Surf. A: Physicochem. Eng. Aspects. 1993;80;191-195 ().

[28]. Kong H, Gao C, Yan D. Controlled functionalization of multiwalled carbon nanotubes by *in situ* atom transfer radical polymerization, J. Am. Chem. Soc. 2004;126:412-413.

[29]. Lee YS, Marzari N. Cycloaddition functionalizations to preserve or control the conductance of carbon nanotubes, Phy. Rev. Lett. 2006;97:116801(4).

[30]. Proença MF, Araújo RF, Paiva MC, Silva CJR, The Diels-Alder cycloaddition reaction in the functionalization of carbon nanofibers, J. Nanosci. Nanotechnol. 2009;9:6234-6238.

[31]. Cançado LG, Takai K, Enoki T, Endo M, Kim YA, Mizusaki H, et al. General equation for the determination of the crystallite size La of nanographite by Raman spectroscopy, Appl. Phys. Lett. 2006;88:163106(6).

[32]. Patterson AL, The Scherrer formula for X-ray particle size determination, Phys. Rev. 1939;56:978-982.

[33]. Hiemenz P, Rajagopalan R. Editors, Principles of Colloid and Surface and Chemistry, Marcel Dekker, New York; 1997.

[34]. Niihara K. A fracture mechanics analysis of indentation-induced Palmqvist crack in ceramics, J. Mater. Sci. Lett. 1983;2:221-3.

[35]. *ASM handbook: alloy phase diagrams,* ASM International, USA: 1992.

[36]. Terrones M, Grobert N, Olivares J, Zhang JP, Terrones H, Kordatos K, et al. Controlled productionof aligned-nanotubebundles Nature. 1997;388: 52-5.

[37]. Zhang J., Zou H, Qing Q, Yang Y, Li Q, Liu Z. Effect of chemical oxidation on the structure of single-walled carbon nanotubes, J. Phys. Chem. B. 2003;107:3712-3718.

[38]. Huang W, Wang Y, Luo G, Wei F. 99.9% purity multi-walled carbon nanotubes by vacuum high-temperature annealing, Carbon. 2003;41:2585-2590.

[39]. Lopes MA, Santos JD, Monteiro FJ, Ohtsuki C, Osaka A, Kaneko S. Inoue H. Push-out testing and histological evaluation of glass reinforced hydroxyapatite composites implanted in the tibia of rabbits, J. Biomed. Mater. Res. 2001;54:463-469.

[40]. Hansen CM, Smith A. L. Using Hansen solubility parameters to correlate solubility of C60 fullerene in organic solvents and in polymers, Carbon. 2004;42:1591-1597.

[41]. Ham HT, Choi YS, Chung IJ. An explanation of dispersion states of single-walled carbon nanotubes in solvents and aqueous surfactant solutions using solubility parameters, J. Colloid Interface Sci. 2005;286:216-223.

[42]. Bergin SD, Nicolosi V, Streich PV, Giordani S, Sun Z, Windle AH, et al. Towards solutions of single-walled carbon nanotubes in common solvents, Adv. Mater.2008;20:1876-1881.

[43]. Bergin SD, Sun ZY, Rickard D, Streich PV, Hamilton JP, Coleman JN. Multicomponent solubility parameters for single-walled carbon nanotube-solvent mixtures, ACS Nano.2009;3:2340-2350.

[44]. Kataura H, Kumazawa Y, Maniwa Y, Umezu I, Suzuki S, Ohtsuka Y, et al. Optical properties of single-wall carbon nanotubes, Synth. Met. 1999;103:2555-2558.

[45]. Yu J, Grossiord N, Koning CE, Loos J. Controlling the dispersion of multi-wall carbon nanotubes in aqueous surfactant solution, Carbon. 2007;45:618-623.

[46]. Xu R, Wu C, Xu H. Particle size and zeta potential of carbon black in liquid media, Carbon. 2007;45:2806-2809.

[47]. Javidi M, Bahrololoom ME, Javadpour S, Ma J. Studying surface charge and suspension stability of hydroxyapatite powder in isopropyl alcohol to prepare stable suspension for electrophoretic deposition, Adv. Appl. Ceram. 2009;108:241-248.

[48]. Han GD, Kuntz JD, Wan J, Mukherjee A. K. Single-wall carbon nanotubes as attractive toughening agents in alumina-based nanocomposites, Nat. Mater. 2003;2:38-42.

[49]. Dong NX, Guo XE. The dependence of transversely isotropic elasticity of human femoral cortical bone on porosity, J. Biomech. 2004;37:1281-1287.

[50]. Hench LL, Bioceramics: from concept to clinic, J. Am. Ceram. Soc. 1991;74:1487-1510.

[51]. Weaver JK. The microscopic hardness of bone, J. Bone. Joint Surg. 1966;48:273-288.

[52]. Evans FG, Vincentell R. Relations of the compressive properties of human cortical bone to histological structure and calcification, J. Biomech. 1974;7:1-10.

[53]. Saha S, Williams PA. Electric and dielectric properties of wet human cortical bone as a function of frequency IEEE, Trans. Biomed. 1992;Eng. 39:1298-1304.

[54]. Baron R, Neff L, Louvard D, Courtoy PJ. Cell-mediated extracellular acidification and bone-resorption - evidence for a low ph in resorbing lacunae and localization of a 100-kD lysosomal membrane-protein at the osteoclast ruffled border, J. Cell Biol. 1985;101:2210-2222.

[55]. Dias AG, Gibson IR, Santos JDM, Lopes MA. Physicochemical degradation studies of calcium phosphate glass ceramic in the $CaO–P_2O_5–MgO-TiO_2$ system, Acta Biomater. 2007;3:263-9.

[56]. Aubin J. Mesenchymal Stem Cell and Osteoblast Differentiation. In Bilezikian JP, Raisz LG, Martin TJ. Principles of Bone Biology. Academic Press, USA, 2008. 85-107.

[57]. Nakanishi K, Sakiyama T, Imamura K. On the adsorption of proteins on solid surfaces, a common but very complicated phenomenon. J. Biosc. Bioeng. 2001;91(3):233-244.

[58]. Giannona S, Firkowska I, Rojas-Chapana J, Giersig M. Vertically aligned carbon nanotubes as cytocompatible material for enhanced adhesion and proliferation of osteoblast-Like Cells, J. Nanosci. Nanotechnol. 2007;7:1679-1683.

[59]. Shao S, Zhou S, Li L, Li J, Luo C, Wang J, et al. Osteoblast function on electrically conductive electrospun PLA/MWCNTs nanofibers, Biomaterials. 2011;32:2821-2833.

[60]. Namgung S, Baik KY, Park J, Hong S. Controlling the growth and differentiation of human mesenchymal stem cells by the arrangement of individual carbon nanotubes, ACS Nano. 2011;5:7383-7390.

[61]. Hahn B-D, Lee J-M, Park D-S, Choi J-J, Ryu J, Yoon W-E, et al. Mechanical and *in vitro* biological performances of hydroxyapatite–carbon nanotube composite coatings deposited on Ti by aerosol deposition, Acta Biomater. 2009;5:3205-3214.

IV. 4. Carbon nanotubes-based bioceramic grafts for electrotherapy of bone

D. Mata[a], A.L. Horovistiz[a], M. Ferro[a], N.M. Ferreira[b], M. Belmonte[c], M.A. Lopes[d], R.F. Silva[a], F.J. Oliveira[a]

[a] CICECO, Materials and Ceramic Eng. Dept., Univ. of Aveiro, 3810-193 Aveiro ,Portugal

[b] I3N, Physics Dept., Univ. of Aveiro, 3810-193 Aveiro, Portugal

[c] Institute of Ceramics and Glass, CSIC, Campus Cantoblanco, 28049 Madrid, Spain

[d] CEMUC, Metallurgical and Materials Eng. Dept., Faculty of Eng., Univ. of Porto, 4200-465 Porto, Portugal

Abstract

Bone complexity demands the engineering of new scaffolding solutions for its reconstructive surgery. Emerging bone grafts should offer not only mechanical support but also functional properties to explore innovative bone therapies. Following this, ceramic bone grafts of glass/hydroxyapatite (HA) reinforced with conductive carbon nanotubes (CNTs) - CNT/Glass/HA - were prepared for bone electrotherapy purposes.

Computer-aided 3D microstructural reconstructions and TEM analysis of CNT/Glass/HA composites provided details on the CNT 3D network and further correlation to their functional properties. CNTs are arranged as sub-micrometric sized ropes bridging homogenously distributed ellipsoid-shaped agglomerates. This arrangement yielded composites with a percolation threshold of P_c= 1.5 vol.%. At 4.4 vol.% of CNTs, thermal and electrical conductivities of 1.5 $W.m^{-1}.K^{-1}$ and 55 $S.m^{-1}$, respectively, were obtained, matching relevant requisites in electrical stimulation protocols. While the former avoids bone damaging from Joule's heat generation, the latter might allow the confinement of external electrical fields through the conductive material if used for *in vivo* electrical stimulation. Moreover, the electrically conductive bone grafts have better mechanical properties than those of the natural cortical bone.

Overall, these highly conductive materials with controlled size CNT agglomerates might accelerate bone bonding and maximize the delivery of electrical stimulation during electrotherapy practices.

1. Introduction

Earlier studies have shown that healthy bone tissue has the ability to generate endogenous electric signals that affect its regeneration mechanism [1]. This is achieved by activating voltage-gated Ca^{2+} channels in the plasma membrane of "bone-forming" cells [2, 3]. When bone is ill or fractured these endogenous signals are compromised [4].

Clinical studies have reported that exogenous electrical stimulus delivered to the fractured bone site accelerate the regeneration process by compensating the mislaid endogenous electrical signals found in the healthy bone tissue [4]. Recent findings gave evidences that such process can be regulated *in situ* with preferential stimulation by new "smart" electrical conductive bone grafts. These are able to confine exogenous electrical fields on their surface and delivery it locally to bone cells [5-7]. To guarantee this under electrical stimulation routines, bone grafts should present the following combined requisites: (1) mechanical strength, to keep its structural integrity during the first stages of bone regeneration and, thus, to preserve the electrical percolation and the interconnected porous network [8]; (2) higher electrical conductivity than the surrounding biological environment, at the damaged bone site, forcing electric currents to travel along the easier pathway, the highly conductive graft material [9]; (3) thermal conductivity, to avoid cellular and tissue damage from heat generation due to Joule's effect [10].

Nonetheless, the clinical availability of bone grafts conjugating the above requisites is limited. Some material processing strategies have been applied including the reinforcement of matrices with conductive metallic fillers (e.g. stainless steel fibers [11]). Though, conductive carbon-based fillers such as nanotubes (CNTs) are much more promising candidates than the metallic ones due to the strong depression of corrosion-related toxicological risks under electrical stimulation routines. Also, CNT fillers having high aspect-ratio yield conductive matrices, typically of 100 $S.m^{-1}$, at percolation values as low as 0.6-3.5 vol.% [12, 13]. Furthermore, at this small CNT loading the grafting qualities of the matrices are advantageously preserved [14].

An example of CNT composites that have been applied in bone stimulation are the polymeric based ones [5]. Yet, they have lower bone grafting qualities than well known bioceramics (e.g. calcium phosphates - CaPs). Despite sharing the same dielectric characteristic, research exploring the CNT- CaPs conductivity has been neglected [15]. By combining the biological profile and mechanical strength of the Glass/Hydroxyapatite (HA) ceramic [16, 17], with the morphology and electrical conductive of the CNTs [18], a superior multi-functional bone graft is proposed here - CNT/Glass/HA - inspired in the respective apatite-like phase and the collagen type I fibers of the natural bone [19].

The present work focuses on the study of the effects of the CNT loading in mechanical, electrical and thermal behaviours of hot-pressed CNT/Glass/HA composites. The CNT percolation threshold and properties of the composites were correlated with the 2D and 3D microstructures developed during the confined sintering.

2. Experimental Procedure

2.1. *Sample preparation*

Commercially available CNTs (NC7000, Nanocyl, Belgium) were used in this work for preparing the composites. Due to the presence of impurities (~12 wt.%) from the growth technique used, the CNTs were purified following a non-destructive procedure that involved an annealing at 1900°C for 8h in a flowing Ar atmosphere.

Hidroxiapatite (HA) powder was planetary co-milled with P_2O_5-glass (65 P2O5, 15CaO, 10CaF$_2$, 10Na$_2$O mol%) in 97.5/2.5 proportion in weight, yielding to a final particle diameter size of $D_{0.5}$= 1.8±1.4 μm. CNT/Glass/HA composite powder suspensions were mixed by a two-step process with different volume fractions of CNTs (0, 0.4, 0.9, 1.8, 3, 4.4 and 7.8 vol. %) in isopropyl alcohol (≥99.8%, Sigma-Aldrich). This process contemplates a mechanical approach, not used excessively to avoid damage to CNTs: (1) a high-speed shearing (HSS) for 15 min (IKA T25-Ultra-Turrax, working at 20,500 rpm) followed by (2) a 60 min sonication step (Selecta, working at 60 kHz, 200 W). Afterwards, the composite powders were dried, also by a two-step method to avoid phase separation: (1) fast evaporation, by combining heating at 80 ºC and vacuum under a magnetic shearing until a high viscosity slurry is obtained; (2) slow evaporation, in an oven at 60 ºC for 24 h. Once dried, the powders were crushed in an agate mortar and sieved to less than 75 μm. CNT/Glass/HA composite powders were consolidated by hot-pressing at a fixed pressure of 30 MPa for 60 min at 1100ºC, under vacuum conditions. Cylindrical-shaped samples with 20 mm diameter and 15 ± 1 mm in height were produced and then cut into (1) thinner slices of 1 ± 0.05 mm for bending tests; (2) parallelepipeds of 2.5 × 2.5 × 4.5 mm^3 for compression tests and electrical measurements.

2.2. *Phases, 2D and 3D microstructure*

The phase composition of sintered composites was determined by the Gazzara and Messier method [20]. The X-ray diffraction patterns (X'PERT-MPD, Philips, Netherlands) were collected with a CuKα$_1$ radiation (λ= 0.154056 nm) in 0.02º steps in the interval 2θ 10-80º. Before microstructural characterization, the surfaces were ground, lapped and polished down to 50 nm colloidal silica. Selected samples of all materials were observed by scanning electron microscopy, SEM (SU-70, Hitachi, Japan) and by optical microscopy (Microphot, Nikon, Japan). In order to reveal the distribution of the β-TCP phase in the microstructure of the ceramic composite, a selective chemical etching was performed with 0.56M citric acid for 4 min at room temperature, as previously adopted [21].

Of particular interest concerning the percolation threshold are the size, shape, aspect ratio, volume fraction and distribution of CNTs and CNT agglomerates. These data were obtained from plane sections for all composite and from three-dimensional analysis through in-depth serial

sectioning for the 4.4vol% CNT composite. The experimental procedure and 3-D microstructure reconstruction studies from these consecutive planes were carried out according to the following: (1) controlled polishing of the composite surface with a 50 nm sized silica suspension and a smooth polishing paper, under an applied load of 10 N for 10 min; (2) digital image acquisition of the microstructure; (3) depth marking with a Vickers indenter using a 3 N load; (4) repetition of steps (1) to (3); (5) alignment and stacking of the digital images; (6) rendering for visualization and analysis of CNT agglomerates. The microstructure of the 4.4vol% CNTs composite was characterized after stacking and aligning one hundred consecutive 2-D planar sections using a 3D reconstruction plugin and the freeware Image J. Thus, the reconstructed volume for the sample is approximately 100 × 100 × 50 μm^3. The depth of material (Δh) removed after each polishing cycle was about 0.5 μm and measured using the average size of the diagonals (before - d1 - and after - d2 - polishing) of the square shaped indentation mark and the pyramid angle φ = 136° [23], accordingly to

$$\Delta h = \frac{d1 - d2}{2\tan\left(\dfrac{\varphi}{2}\right)} \qquad (1)$$

2.3. *Mechanical, electrical and thermal properties*

The modulus of rupture was measured using the circular plate geometry with the Ø20x1 mm discs using a load cell of 2.5 kN under a constant displacement rate of 1.0 mm.min^{-1} (Z020, Zwick/Roell, Germany). The biaxial flexural strength values were calculated according to ASTM F394-76: the specimen is supported by 3 ball bearings spaced 120° apart on a 13 mm diameter circle. Loading was applied by a cylinder with a flat loading face with 1.0 mm diameter. For the compressive strength, a cross head speed of 1.0 mm.min^{-1} was used for the 2.5 × 2.5 × 4.5 mm^3 samples.

DC electrical conductivity of the Glass/HA/CNTs composites and Glass/HA matrix were performed on samples of similar dimensions, by fixing copper wires to the smaller faces of the 2.5 x 2.5 x 4.5 mm^3 parallelepipeds. The characterization was performed at room temperature in a programmable electrometer (617, Keithley, USA) with voltage applied in 0.5 V step in the range of 0-100 V for dielectric samples. For the conductive samples a programmable power supply (IPS-603, ISO-TECH, UK) was used by applying a voltage in the range 0-1 V in 0.1 V steps.

The impedance spectroscopy measurements were carried out as a function of the temperature (80-360K), in the frequency range of 40 Hz - 2 MHz using an impedance analyzer (4292A, Agilent, USA).

Thermal diffusivity (α) was determined in Ar atmosphere as a function of temperature, from 298 to 673 K, on 8.8 mm × 8.8 mm square specimens of ~1 mm in thickness by the laser-flash method (Thermaflash 2200, Holometrix Netzsch, USA). The specific heat (Cp) as a function of temperature was estimated by the rule of mixtures from the chemical composition and the heat

capacity data of each phase computed using the HSC Outokumpu code [25]. Thermal conductivity (k) was then calculated from the thermal diffusivity, the density, and the specific heat, using the following expression: $k = \alpha \cdot \rho \cdot Cp$.

3. Results and discussion

3.1. *Purification of CNTs*

The CNTs placed are inside a graphite crucible that allows the exhaust of vapour contaminants while the liquefied ones will deposit at the bottom of the crucible and infiltrate into the porous walls, as is schematically described in Fig. 1a.
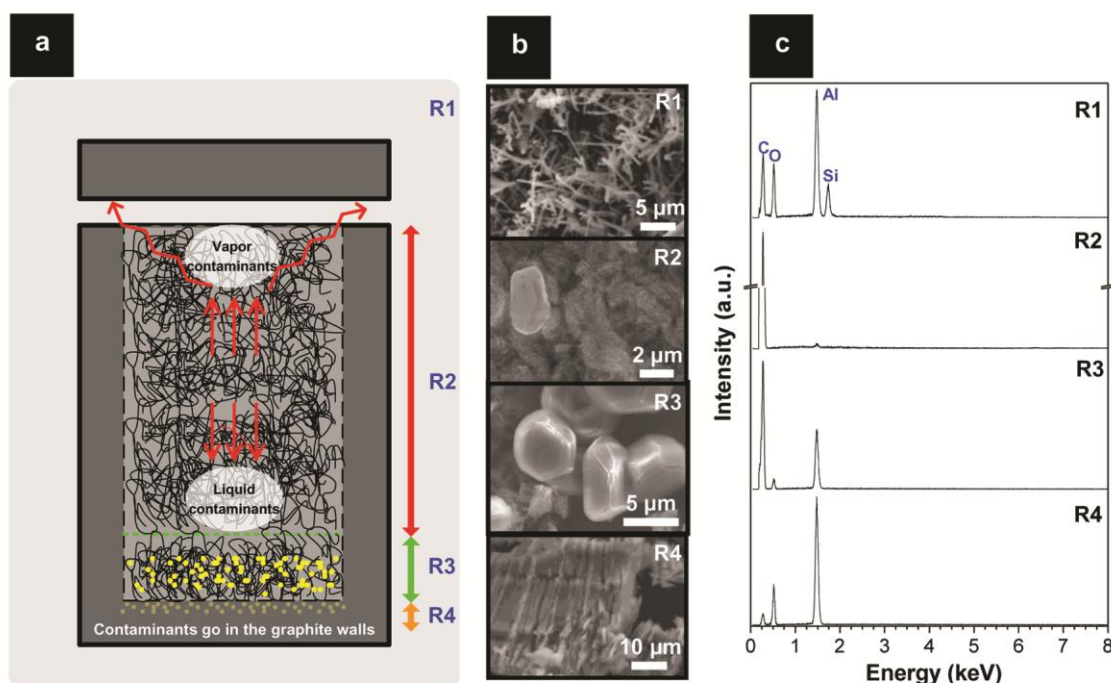
Fig. 1 - (a) Sketch of the graphite dye used to purify CNTs, divided in four main regions, accordingly to the contaminants type. Representative (b) SEM images and (c) EDS spectra of each region.

Different reactions may occur as a function of position, a trend also observed by Tsuchida et al. in a different system [26]. So, according to the reactions/impurity phases, four main regions were identified: (R1) outside the crucible; (R2) top region, inside the crucible; (R3) bottom region, inside the crucible; (R4) bottom region, incorporated into the graphite. SEM micrographs and EDS spectra of the representative solid impurities of each region are shown in Figs. 1b and 1c, respectively. At region R1, needle-like deposits of Al and Si (Fig. 1b-R1 and Fig. 1c-R1) are observed. These structures were formed by evaporation of small-sized silicate impurities, by the

reduction of the phase transition temperatures according to the Gibbs-Thomson effect for particles smaller than 10 nm [27], followed by condensation on the colder sections of the graphite furnace. This is in accordance to similar observations by Schuster et al. [28]. In region R2, CNTs are almost free of contaminants. Nevertheless, carbon rich particles are seen (Fig. 1b-R2 and Fig. 1c-R2) as a result of the high temperature purification of Al and Si containing phases.

In region R3, the CNTs were highly contaminated by partially melted large particles that dropped by gravity to the bottom of the crucible. In this process, the bottom CNTs acted as a filter to physically separate the contaminants from the purified CNTs. Here the remaining Al containing impurities (Fig. 1b-R3) should be fully carburized as the EDS analysis in Fig. 1c-R3 shows. Some residual amounts of Co and Fe were also detected in these particles (not shown).

Region R4 contains a large portion of Al contaminants (Fig. 1b-R4 and Fig.1c-R4) that were fully melted and incorporated inside the graphite at the bottom of the crucible that acted as a getter. After the purification treatment, the bottom appearance changed to a metallic-glowing one. Surprisingly, two weeks after the treatment the glowing bottom of the crucible was replaced by a greyish Al powder contaminant having a laminar morphology (Fig. 1b-R4). The powder was formed by a re-oxidation of the Al and transition metals contaminants inside the solid graphite under ambient conditions. This oxidation was followed by a volume change that forced the exudation of contaminants from the graphite walls.

Briefly, Al, Si and transition metals impurities might be eliminated by an evaporation route (R1) via Ar flow dragging-out and/or by a melting route (R3 and R4) via Al liquid dragging-out and gravitational deposition. Weight measurements in the purified CNTs, token from R2 region, revealed a reduction of impurities of more than 90% relatively to the as-received CNTs. The final high thermal annealed materials presented a carbon purity of >99 wt.%.

3.2. *Phase composition and microstructure*

Data from X-ray diffraction of the starting materials HA and CNTs, of the unreinforced matrix and of the composite materials can be observed in Fig. 2a. The obtained XRD patterns correspond to those reported in Joint Committee on Powder Diffraction Standards (JCPDS) files for HA (JCPDS 72-1243), β-Tricalcium phosphate, β-TCP (JCPDS 09-0169) and CNTs (JCPDS 58-1638). The adopted hot pressing procedure ensured that the maximum density could be obtained at 1100 °C, the selected temperature that guarantees an appropriate balance between HA and β-TCP for bone regeneration applications [29]. As previously reported [30], the liquid sintering process that occurs during the preparation of the materials makes the glass to react with the hydroxyapatite, which is then partially converted in β-TCP phase. The sintering temperature of 1100 °C together with the load used in the densification of the materials prevented the conversion of β-TCP into α-TCP. Comparing the XRD plots, it becomes quite clear that there are almost no changes in the phase composition when the CNTs are added to the matrix, the only crystalline phases detected being HA and β-TCP. There is however a reduction of HA to β-TCP phase

transformation rate with increased CNT content, as is clear from the graphic of Fig. 2b, likely due to the reduction of the effective contact area between the ceramic components.
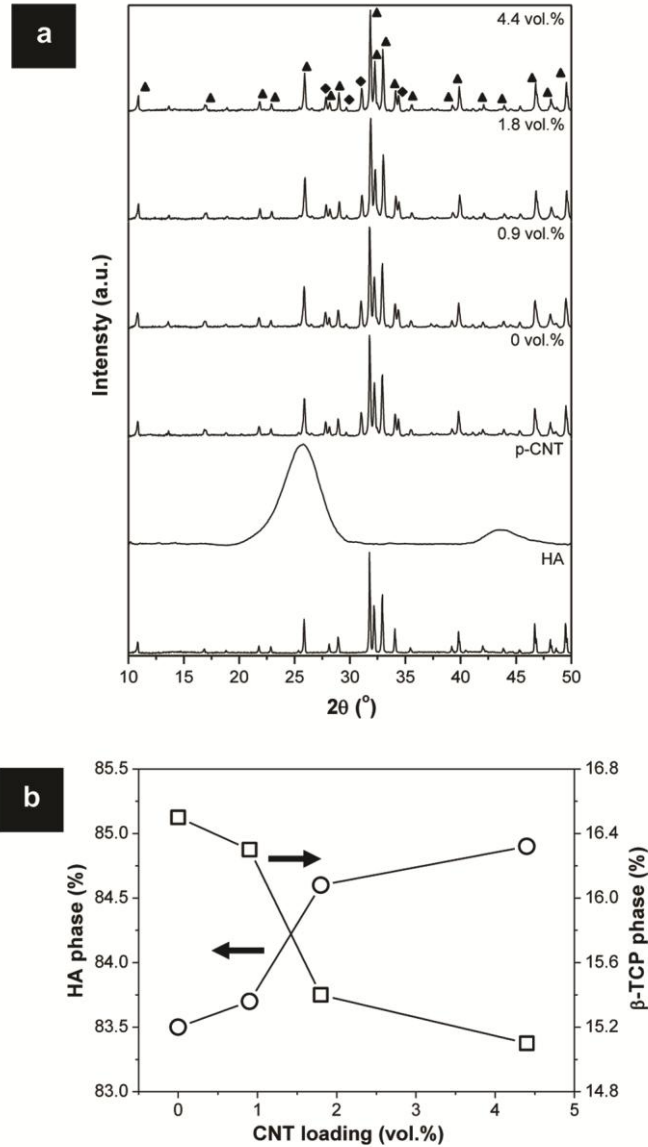
Fig. 2 - (a) XRD spectra of the starting materials and of the hot-pressed composites with different CNT loadings (■ B-TCP, ▲HA). (b) Plot showing the dependence of the phase composition of the consolidated composites on the CNT loading.

The microstructure of the Glass/HA/CNTs composites is illustrated by SEM micrographs of polished and chemical etched surfaces of the 4.4 vol% CNT composite in Fig. 3a. Dense regions are of unreacted HA (I). The porosity shown is mostly due to the preferential leaching of the β -TCP phase (II) [21]. CNT agglomerates are the remaining (III). The location of CNTs in the microstructure is illustrated by the SEM micrographs in Figs 3b-d: (1) CNT ropes present at the pores resulted from leaching of the β-TCP phase (Fig. 3b); (2) CNT agglomerates with preferential

alignment perpendicularly to hot pressing direction, with lengths below 5 µm (Fig. 3c); and (3) individualized CNTs, at HA grain boundaries (Fig. 3d).
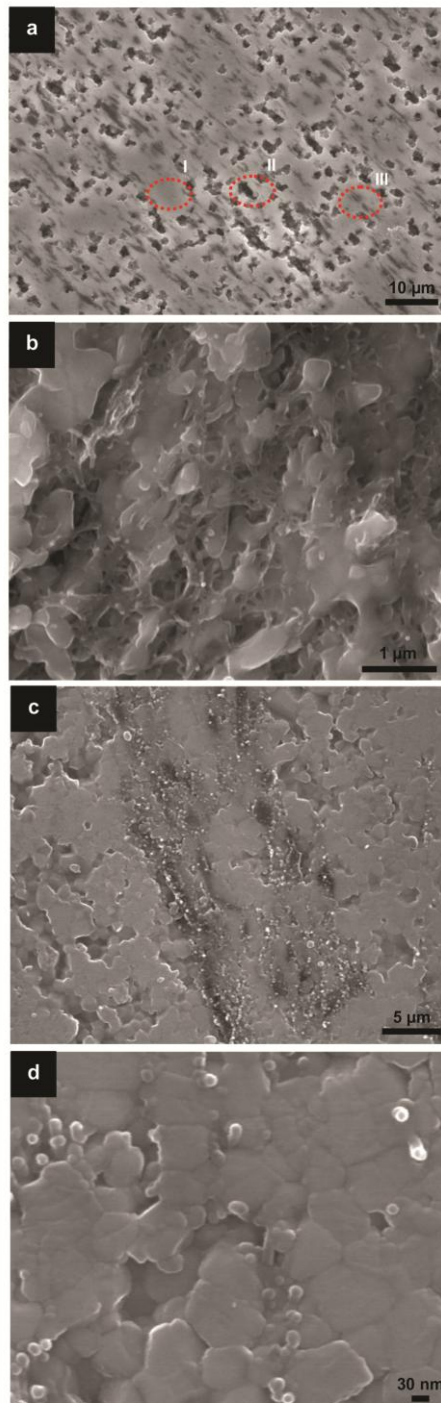

Fig. 3 - SEM micrographs of polished and chemically etched CNT(4.4 vol.%)/Glass/HA surfaces: (a) low magnification image (I - HA; II- β-TCP; III - CNTs); (b-d) high magnification images of the CNT distribution in the ceramic matrix: (b) CNT net at the pores formed by the β-TCP leaching; (c) CNT agglomerates, and (d) individualized CNTs.

This CNTs disposition will contribute for the formation of the 3D network, affecting the mechanical, electrical and thermal properties [30] and of the composites.

3.3. *Mechanical properties of the composites*

The alignment of CNT agglomerates is observed for all the compositions in the optical micrographs of Fig. 4a, where they are visible as dark-contrasted areas. At the scale of visualization, the CNT agglomerates are more evenly distributed in the 4.4 vol% composite, having a somewhat smaller size than in the composites with lower amounts of CNTs. This may reflect the increased interaction between the CNTs and the matrix during processing, helping their distribution throughout the material. The agglomerates of CNTs are well distinguished from the surrounding matrix, appearing as elongated features, their longest axis aligned perpendicularly to the pressing direction.
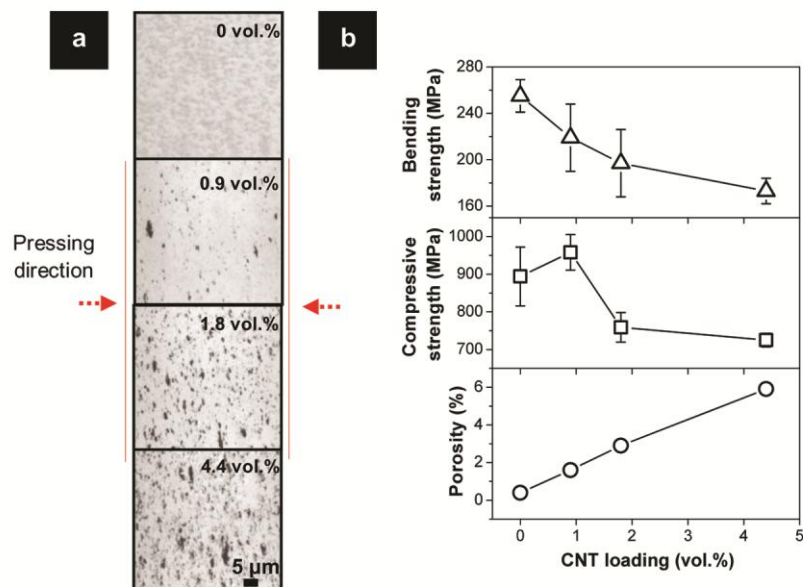
Fig. 4 - (a) Optical micrographs of the CNT/Glass/HA composites with different CNT loadings. (b) Respective porosity and mechanical properties of (a).

The increasing amounts of CNT incorporation raise the porosity from 0.2% for the matrix, to about 6% for the 4.4vol% composite, as is evidenced by the bottom plot of Fig. 4b. The evolution of porosity with CNT content reflects not only the damping effect of the CNTs and the difficulty in transmitting the pressure to the Glass/HA matrix for densification, but also the increased interactions and entanglement of CNT agglomerates that further prevent matrix contiguity from occurring. Such porosity effect is clearly mirrored in the bending strength of the matrix and composites tested, top plot of Fig. 4b, and to some extent in the compressive strength, middle

graph in Fig. 4b. For fully dense materials, CNT mechanical reinforcing is expected, due to toughening by grain bridging or pull-out, crack deflection, and crack branching [31]. This is observed for the compressive strength of the 0.9 vol% CNT composite but, as porosity has an exponentially detrimental effect on the rupture strength of a given material [32], a decrease in the mechanical properties is observed for higher CNT contents. This effect was clearly identified by others for the indentation fracture toughness and bending strength in HA/CNT composites produced under hot pressing, although no information regarding porosity levels was given [33]. Both the compressive and bending strengths of our materials have values that are well within or above cortical bone specifications for adult, healthy individuals [34, 35] and are much larger than those reported in other works [33, 36, 37]. The porosity of the composite with 4.4vol% of CNTs is closer to that of the cortical bone (~5.4%-14.2%) [38] than the one of the Glass/HA matrix alone (1%).

3.4. *3D network of CNTs*

A closer inspection of the microstructure of the composites was done for the more heavily loaded composite, with 4.4 vol% CNTs, using the 3D microstructural reconstruction method described in Section 2.2. Of particular interest is the spatial distribution of the CNT agglomerates, influenced by the confined, hot-pressing assisted densification. The agglomerates have an ellipsoid-shape, depicted in Figs. 5a and 5b and have their main axis preferentially aligned within the pressing plane, although other directions are possible, as is depicted in Fig. 5c. Microstructural parameters relating to these agglomerates are graphically represented in the plots of Fig. 5d, namely typical major axis length (2a) and aspect ratio (AR) as a function of the CNT content. Considering that the matrices of the composites are almost fully dense, with the phase composition given by XRD and taking the porosity values in Fig. 4b, the computed apparent density values for the ellipsoid-shaped CNT bundles are about one half the density of CNTs, within the range 1.2-2 g·cm^{-3}. The calculation is done assuming that all porosity is trapped within the agglomerates thus yielding total agglomerate area fraction up to 10% for the 4.4vol% composite. Of relevance is the total area fraction of those CNT agglomerates that have AR above 1.5 and among these, those that are aligned within Θ= ±20° of the pressing plane, these values being given also in Fig. 5d. The area fraction of aligned with AR ≥ 1.5 is about 8% for the 4.4vol% composite, as shown in Fig. 5d, and this yields a maximum value of aligned CNTs of around 90%, irrespective of the amount of CNTs used. The content of oriented CNTs, also depicted in this graph, is proportionally larger for the 0.9vol% and 1.8vol% composites than for the 4.4vol%, due most likely to a better interaction of CNTs with the ceramic matrix powders in the latter, during the wet processing step of fabrication. This tendency is confirmed by the smaller size and lower AR of the agglomerates in the 4.4vol% composite, relatively to the other composites, as given by the top plot in Fig. 5d. A 3D microstructure reconstruction of the CNT agglomerates in a CNT(4.4 vol.%)/Glass/HA composite is depicted in Fig. 5e.
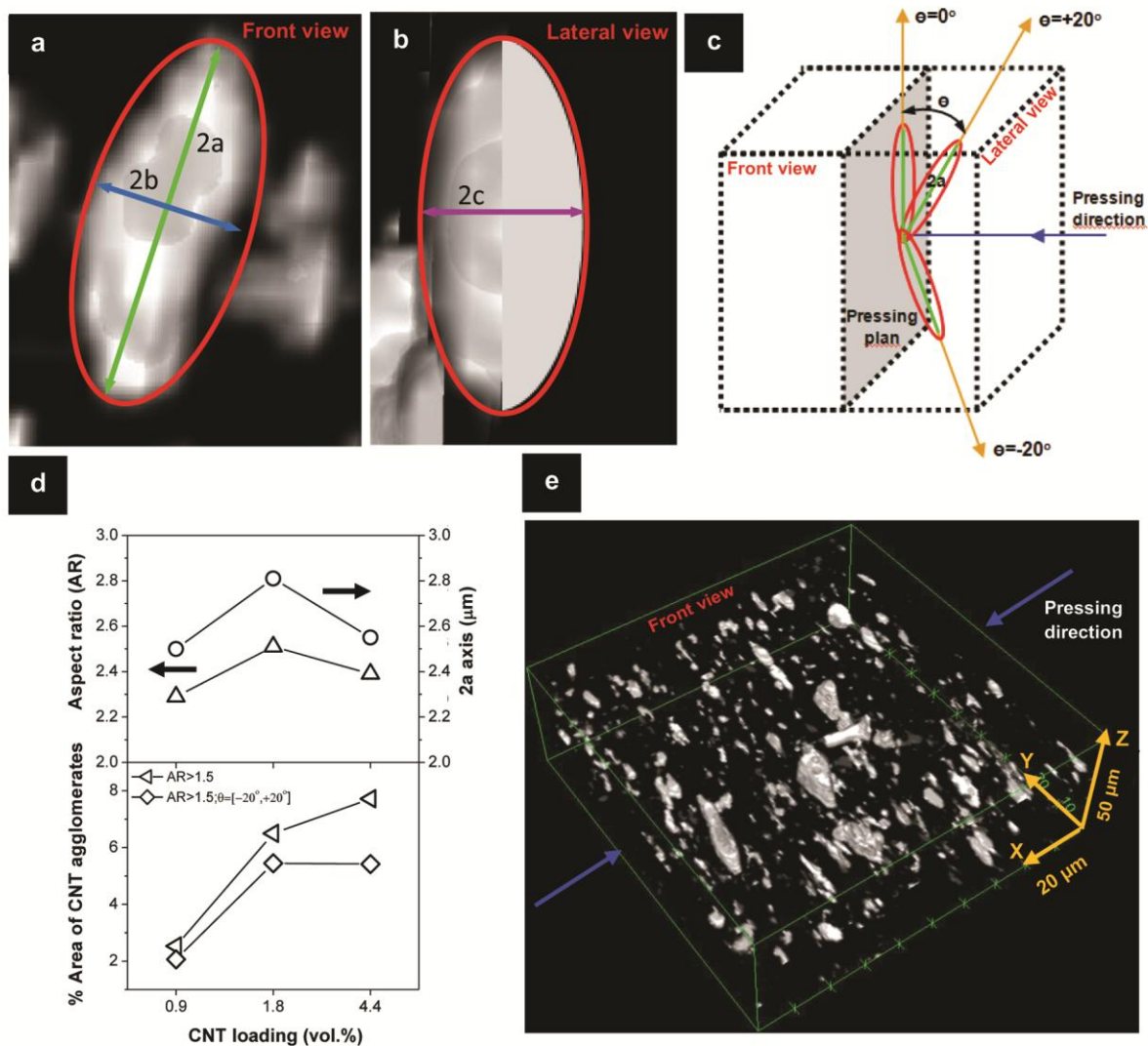
Fig. 5 - (a) Front view and (b) lateral view images of a ellipsoid shaped CNT agglomerate (2a - large axis; 2b=2c - small axes). (c) Sketch image of a CNT/Glass/HA composite volume showing the orientation of a CNT ellipsoid shaped agglomerate relatively to the pressing plan and pressing direction. (d) Plots showing the effects of the CNT loading in the fraction area of CNT agglomerates and in the aspect ratio and 2a axis of individualized agglomerates. (e) 3D microstructure reconstruction of the CNT agglomerates in a CNT(4.4 vol.%)/Glass/HA composite.

Despite most of the CNTs being located in the agglomerates, TEM analysis revealed that there are also CNT bundles and ropes around individual HA grains, as can be observed in Fig. 6.

The low magnification TEM image (Fig. 6a) is sketched in Fig. 6b for easier understanding, revealing the CNT agglomerates (regions I) and the intergrain CNT disposal (region II). CNT bundles of sub-micron size are easily identified at the HA grain triple points (Figs. 6c and 6d), but, more interestingly, at the matrix grain boundaries there are ropes of CNTs connecting those small bundles. Similar microstructures have been reported for other ceramic-matrix systems [13, 31]. The CNT agglomerates, oriented and ellipsoid shaped (Fig. 5e), with a main axis having a few

micrometers, are thus interconnected at a sub-micrometric scale, ensuring that a network of contiguity is effectively established throughout the volume of the material.
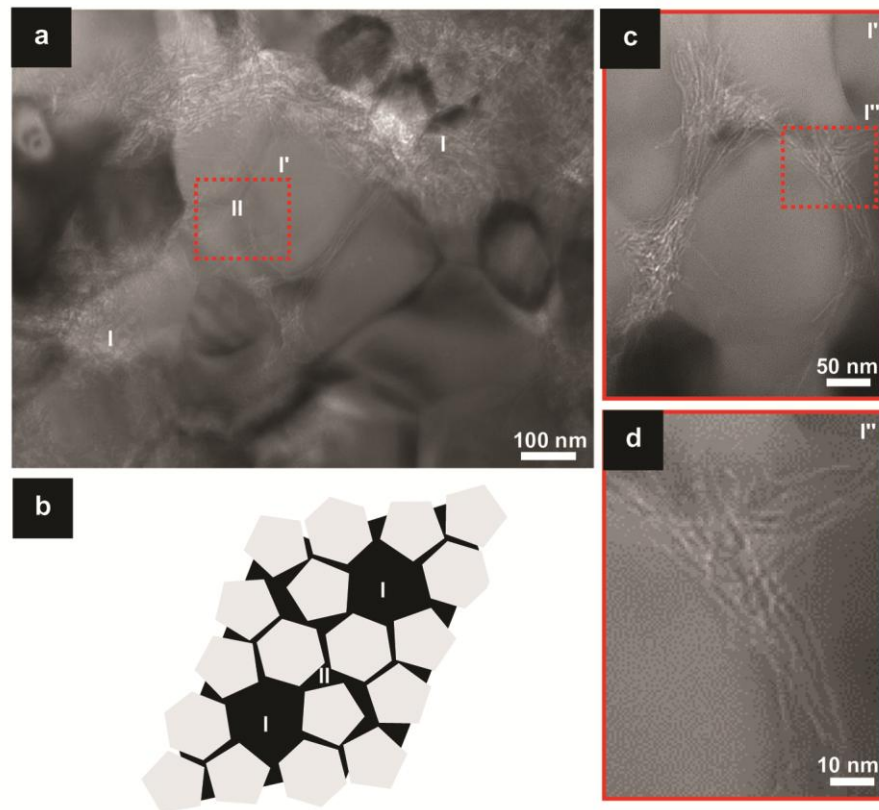
Fig. 6 - TEM micrographs of the CNT (4.4 vol.%)/Glass/HA composite. (a) low magnification image of the microstructure: region I - CNT agglomerates, region II - CNT bundles; (b) sketch image for a microstructure model; (c and d) high magnification images of region II of (a).

3.5. *Electrical percolation threshold*

The foremost condition for obtaining electrically conductive bio-composites is that a CNT 3D network might form, in the present case made of CNT ropes, bundles and large agglomerates, as was above established. The existence of electrical conductivity due to the presence of CNTs in ceramic materials at various loading levels, has been demonstrated by several authors and are reviewed in some works [39]. However, the minimum volume fraction of CNTs that permits this has to be experimentally evaluated since it is a function of the processing conditions. The increase of conductivity with the amount of CNTs in otherwise insulating materials should follow the following scaling law [40]:

$$\sigma = k(p - p_c)^t \qquad (2)$$

where, *p* is the volume fraction of CNTs, p_c is the percolation threshold given as the critical amount of CNTs that gives rise to an abrupt increase in electrical conductivity, and the exponent *t* is a measure of the dimensionality of the system. Both the exponent *t* and the percolation threshold have been attributed different values in various researches and for ceramic composites, typical t exponent and p_c values are within the 1.3-2 range (low values - two dimensional; and high values close to 2 - three dimensional) [13, 40, 41] and 0.6-5.5 vol% range [12, 13, 41-43], respectively. For CNT/ceramic matrix composites densified by hot-pressing, Rul et al. [41] determined experimentally percolation threshold and exponent values of p_c = 0.64vol% and *t* = 1.73, respectively. These parameters were later successfully used by Julian-Gonzalez and co-workers to fit their electrical conductivity data as a function of CNT content in a quite different system prepared under rapid pressure assisted sintering [13]. The scatter of values is usually attributed to differences in the type of CNTs used, their size and aspect ratio. Moreover, CNT dispersion in the ceramic matrix and temperature-inducing oxidation effects also have relevant contributions [44].

In the present work, a sudden increase of five orders of magnitude is recorded in the plot of the electrical conductivity data as a function of CNTs volume fraction, as given in Fig. 7a.
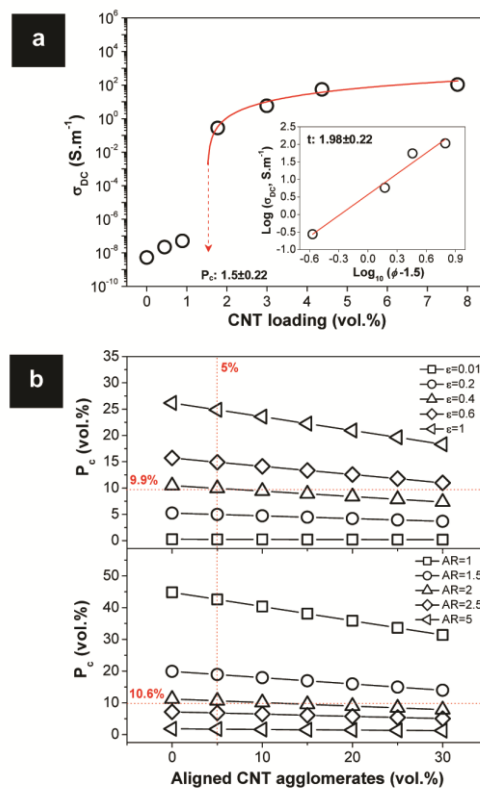
Fig. 7 - (a) DC conductivity plot of the composites as a function of the CNT loading: data points fitted by a electrical percolation curve (highlighted at red) and log-log plot of the conductivity as a function of p-p_c as inset. (b) Plots depicting the evolution of the electrical percolation thresholds (P_c) with the volume fraction of CNT agglomerates (ө=-20⁰,+20⁰; AR >1.5), for agglomerates with varied apparent densities (ε) and aspect ratios (AR).

The lines fitting the data points and those of the inset graph correspond to the application of the scaling law to the experimental results, yielding a percolation threshold of p_c=1.5 vol% and an exponent of t= 1.98. The p_c value is close to those obtained in other ceramic/CNT systems [12, 13] and the exponent value obtained is consistent with electrical conductivity due to a three dimensional network of CNTs. Generally, lower t values mean that the electrical conductivity between CNTs is hindered by insulating barriers that are surpassed only by thermally induced hopping [41, 45] for interparticle distances (IPD) below 10 nm [46].

The individual CNTs have a major contribution to the percolation threshold value of 1.5 vol%, as it is further demonstrated. The percolation model developed by Li and co-workers [46] accounting only for CNT agglomerates is used to proof by contradiction. Making this assumption, the percolation threshold, p_c, is simply given as a function of the volume fraction of those agglomerates (ζ) in the composite and not by the volume of individual CNTs, as follow,

$$P_c = \frac{\varepsilon\pi(2a.2b.2c)}{6\left[\langle\cos^2\theta\rangle(2a+IPD)\right]^3} \qquad (3)$$

where 2a, 2b and 2c are the axes of the ellipsoid-shaped agglomerates, Θ the orientation angle, IPD =10 nm, and ε is the apparent density of the CNT agglomerates. The value of ε is estimated taken the CNT theoretical density, the experimental values for the agglomerates volume content and the Arquimedes density of the composite.

Data regarding the fraction of agglomerates is available and was presented when discussing Figs. 4 and 5. The top plot of Fig. 7b shows the evolution of the percolation threshold with the volume fraction of agglomerates, with average values of AR=2.4, length (2a = 2.55 μm) and orientation (Θ= 20º), as given in Fig. 5d, for different ε of the CNT bundles. For a volume fraction of aligned CNT agglomerates of 5 vol% (Fig. 5d) and crossing it with the apparent density of the agglomerates, ε = 0.4, results a percolation threshold (the horizontal line) of 9.9 vol%. Using the same approach, but varying the aspect ratio of the agglomerates while keeping constant their length (2a = 2.55 μm), apparent density (ε = 0.4) and orientation (Θ= 20º), it gives a p_c of 10.6 vol%, as is graphically described by the bottom plot of Fig. 7b. The effect of the aspect ratio on p_c should be stressed, as for a AR = 1 the CNT content would rise to more than 30 vol% for ε = 0.4. These overestimated values for a hypothetical microstructure where the CNTs are only present as agglomerates show that the experimental percolation threshold of 1.5 vol% of CNTs is really achieved by a 3D network of aligned agglomerates of CNTs bridged by ropes of individual CNTs along the grain boundaries (Fig. 6).

3.6. *Conductivity behaviour in bone stimulation conditions*

To further investigate the influence of the CNT percolation in electrical and phonon conductivity of the composites under simulated *in vivo* bone stimulation conditions, four CNT loads around that of the P_c value (1.5 vol.%) were selected and closer studied: two below P_c (0 and 0.9 vol.%) and two above P_c (1.8 and 4.4 vol.%).

Impedance spectroscopy was used to evaluate the AC conductivity of the unreinforced matrix and of the composites at the body temperature (37 ºC), as shown in Fig. 8a.

Fig. 8 - AC conductivity plot of the Glass/HA and CNT/Glass/HA composites for 0.9, 1.8 and 4.4 vol.% CNT loadings as a function of the (a) signal frequency and (b) temperature.

The Glass/HA matrix follows a purely capacitive or rectifying-like (Schottky) behaviour over the 40-10^5 Hz range of frequencies, as also reported by others for HA [47]. The same was observed for the composites below the percolation threshold. On the other hand, composites with nominal CNT loadings above 1.5 vol%, have a predominantly resistive electrical or metallic-like behaviour, with constant conductivities at all frequencies. That is, the composites behave either as insulating below p_c, or as conducting materials, above p_c. Although a similar trend was found in CNT/ceramic composites [42, 48], the rate limiting conductivity mechanisms in dielectric/CNT composites may vary as a function of the CNTs content, both below and above the percolation threshold [13] and are dependent upon temperature. Nevertheless, the electrical conductivity of the materials of the present work does not vary with temperature, above the body temperature, under a frequency

typical of bone stimulation (40 Hz), Fig. 8b. Moreover, for the CNT/Glass/HA composites above the P_c value, the independence of electrical conductivity on the applied frequency means an increased flexibility on the selection of the best value for the electrical stimulation, since the current values will be kept constant, depending only on the magnitude of the applied voltage.

The CNT percolation also affects the phonon conductivity in the composite, as it is shown in Fig. 9. Composites with CNT contents below P_c, with an interrupted phonon transportation pathway, have lower thermal conductivities than those with CNT loads above the percolation limit where a contiguous CNT pathway exists.

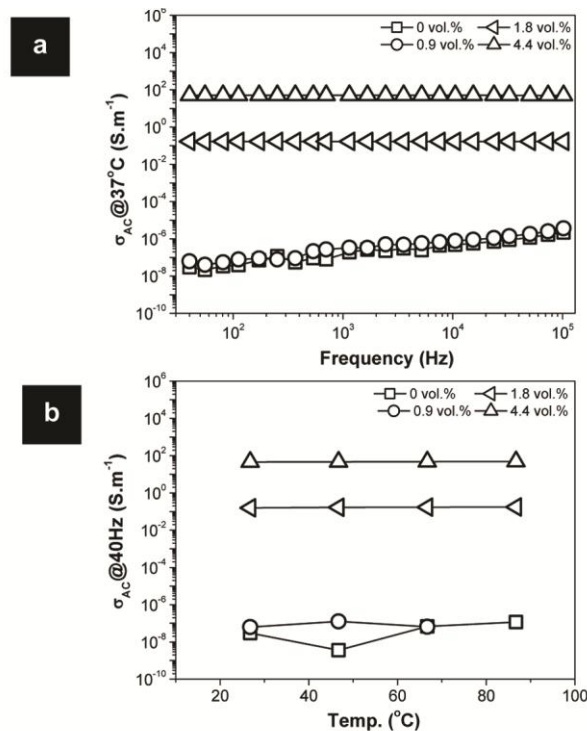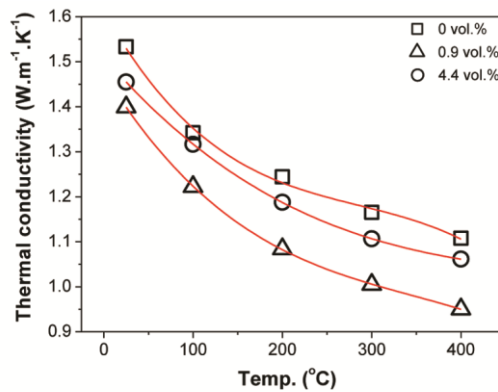**Fig. 9 -** Thermal conductivity plots of the Glass/HA and CNT/Glass/HA composites for 0.9 and 4.4 vol.% CNT loadings as a function of the temperature.

The thermal barriers include the porosity that increases with CNT content but also CNT-CNT and CNT-matrix contacts [49-51]. The balance between these will determine the thermal conductivity, and from the results it becomes evident that the porosity effect overcomes the increased thermal conductivity that arises with CNT loads. Thus the matrix is always more thermally conductive than the CNT composites, both below and above the percolation threshold. Yet, at low temperatures, in the range of 47 to 50°C (Fig. 9), the threshold for bone thermonecrosis [52], the matrix and the CNT composites have approximate values of thermal conductivity, around 1.5 $W.m^{-1}.K^{-1}$. This value should be high enough to dissipate minor Joule's heat generation by micro-currents delivered on the composite-cell/tissue interface during the electrical stimulation protocols [53-55].

4. Conclusions

Highly pure MWCNTs (>99 wt.%) were used to prepare dense CNT/Glass/HA bone grafts with CNT loadings in the range of 0 to 4.4 vol.% (relative density >94%). For this CNT load range, negligible changes in the phase composition of the ceramic matrix were observed, with a typical bi-phasic composition including β-TCP domains uniformly distributed in a HA bed. The CNTs are homogenously distributed in the ceramic matrix, forming a 3D CNT network comprised of sub-

micron sized CNT bundles bridging ellipsoid-shaped CNT agglomerates of average length sizes of 2.6 µm.

There is a close correlation between these microstructural features and the composite properties with major contribution of the porosity level and the CNT loading. Overall, the compressive and bending strengths of the CNT/Glass/HA bone grafts are in the range of 720-960 MPa and 170-220 MPa, respectively. These values are lower than those of the matrix Glass/HA alone, yet, larger than those of the natural cortical bone. High electrically conductive composites were obtained at a percolation threshold of P_c= 1.5 vol.% due to a 3D network of CNTs (dimensionality of the system, t, close to 2). For the 4.4 vol.% there is a conductivity increase of ten orders of magnitude relatively to the bioceramic alone. These composites have higher conductivity than living bone, thus in an *in vivo* scenario, they can be used to locally delivery electrical stimuli through the conductive material to bone tissue. Additionally, the electrical conductivity of CNT/Glass/HA bone grafts has no dependence on the applied frequency signal (at 37 ºC) and on the temperature (at 40 Hz), values typical of *in vivo* bone stimulation conditions. Furthermore, from the thermal conductivity values, it is expected that the thermal dissipation in these composites will be high enough to keep the composite temperatures below the bone thermonecrosis threshold value, while under electrical stimulation.

Throughout the present work, the results obtained indicate that the CNT/Glass/HA bone graft composites have a conjugation of mechanical, electrical and thermal behavior adequate for their use as "smart" materials for clinical bone electrotherapy.

References

[1]. Yasuda I. On the piezoelectric activity of bone. J Jpn Orthop Surg Soc. 1954;28:267-71.

[2]. Bezanilla F. The voltage sensor in voltage-dependent ion channels. Physiol Rev. 2000;80(2):555-92.

[3]. Chesnoy-Marchais D, Fritsch J. Voltage-gated sodium and calcium currents in rat osteoblasts. J Physiol. 1988;398(1):291-311.

[4]. Bassett C. Fundamental and practical aspects of therapeutic uses of pulsed electromagnetic fields (PEMFs). Crit Rev Biomed Eng. 1989;17(5):451-529.

[5]. Supronowicz PR, Ajayan PM, Ullmann KR, Arulanandam BP, Metzger DW, Bizios R. Novel current-conducting composite substrates for exposing osteoblasts to alternating current stimulation. J Biomed Mater Res. 2002;59(3):499-506.

[6]. Ercan B, Webster TJ. The effect of biphasic electrical stimulation on osteoblast function at anodized nanotubular titanium surfaces. Biomaterials. 2010;31(13):3684-93.

[7]. Vila M, Cicuéndez M, Sánchez-Marcos J, Fal-Miyar V, Manzano M, Prieto C, et al. Electrical stimuli to increase cell proliferation on carbon nanotubes/mesoporous silica composites for drug delivery. J Biomed Mater Res Part A. 2013;101A(1):213-21.

[8]. Navarro M, Michiardi A, Castaño O, Planell JA. Biomaterials in orthopaedics. J R Soc Interface. 2008;5(27):1137-58.

[9]. Edmonds D. Electricity and Magnetism in Biological Systems. USA: Oxford University Press; 2001.

[10]. Leitgeb N, Cech R, Schröttner J. Electromagnetic field spectral evaluation problems in exposure assessment. Radiat Prot Dosim. 2007;124(2):124-9.

[11]. Ravaglioli A, Krajewski A. Bioceramics: Materials, Properties and Applications. London: Chapman and Hall; 1992.

[12]. Tatami J, Katashima T, Komeya K, Meguro T, Wakihara T. Electrically Conductive CNT-Dispersed Silicon Nitride Ceramics. J Am Ceram Soc. 2005;88(10):2889-93.

[13]. González-Julián J, Iglesias Y, Caballero AC, Belmonte M, Garzón L, Ocal C, et al. Multi-scale electrical response of silicon nitride/multi-walled carbon nanotubes composites. Compos Sci Technol. 2011;71(1):60-6.

[14]. Misra SK, Ohashi F, Valappil SP, Knowles JC, Roy I, Silva SR, et al. Characterization of carbon nanotube (MWCNT) containing P(3HB)/bioactive glass composites for tissue engineering applications. Acta Biomater. 2010;6(3):735-42.

[15]. Lahiri D, Ghosh S, Agarwal A. Carbon nanotube reinforced hydroxyapatite composite for orthopedic application: A review. Mater Sci Eng C. 2012;32(7):1727-58.

[16]. Lopes MA, Knowles JC, Santos JD, Monteiro FJ, Olsen I. Direct and indirect effects of P2O5 glass reinforced-hydroxyapatite composites on the growth and function of osteoblast-like cells. Biomaterials. 2000;21(11):1165-72.

[17]. Lopes MA, Silva RF, Monteiro FJ, Santos JD. Microstructural dependence of Young's and shear moduli of P2O5 glass reinforced hydroxyapatite for biomedical applications. Biomaterials. 2000;21(7):749-54.

[18]. Harris P. Carbon Nanotube Science: Synthesis, Properties and Applications. UK: Cambridge University Press; 2009.

[19]. Zhao B, Hu H, Mandal SK, Haddon RC. A Bone Mimic Based on the Self-Assembly of Hydroxyapatite on Chemically Functionalized Single-Walled Carbon Nanotubes. Chem Mater. 2005;17(12):3235-41.

[20]. Gazzara CP MD. Determination of content of Si3N4 by X-ray diffraction analysis. Am Ceram Soc Bull 1977;56:777-80.

[21]. Lopes MA, Monteiro FJ, Santos JD. Glass-reinforced hydroxyapatite composites: fracture toughness and hardness dependence on microstructural characteristics. Biomaterials. 1999;20(21):2085-90.

[22]. Schmid B. ImageJ 3D Viewer. 2007 [10th March 2013]; Available from: http://rsbweb.nih.gov/ij/plugins/3d-viewer/.

[23]. Baldissera MR, Rios PR, Hein LRO, Sandim HRZ. Three-dimensional characterization of pores in Ti-6Al-4V alloy. Mater Res. 2011;14(1):102-6.

[24]. Roine A. Outokumpu HSC Chemistry for Windows V. 5.11. In: Research O, editor. Pori, Finland2002.

[25]. Tsuchida T, Hasegawa T, Kitagawa T, Inagaki M. Aluminium nitride synthesis in air from aluminium and graphite mixtures mechanically activated. J Eur Ceram Soc. 1997;17(15–16):1793-5.

[26]. Buffat P, Borel JP. Size effect on the melting temperature of gold particles. Phys Rev A. 1976;13(6):2287-98.

[27]. Schuster JC. A reinvestigation of the thermal decomposition of aluminum carbide and the constitution of the Al-C system. JPE. 1991;12(5):546-9.

[28]. Dorozhkin SV. Bioceramics of calcium orthophosphates. Biomaterials. 2010;31(7):1465-85.

[29]. Lopes MA, Knowles JC, Santos JD. Structural insights of glass-reinforced hydroxyapatite composites by Rietveld refinement. Biomaterials. 2000;21(18):1905-10.

[30]. Zhan G-D, Kuntz JD, Wan J, Mukherjee AK. Single-wall carbon nanotubes as attractive toughening agents in alumina-based nanocomposites. Nat Mater. 2002;2(1):38-42.

[31]. Liu D-M, Fu C-T. Effect of residual porosity and pore structure on the mechanical strength of SiC☐Al2O3☐Y2O3. Ceram Int. 1996;22(3):229-32.

[32]. Meng YH, Tang C, Tsui C, Chen D. Fabrication and characterization of needle-like nano-HA and HA/MWNT composites. J Mater Sci: Mater Med. 2008;19(1):75-81.

[33]. Evans FG, Vincentelli R. Relations of the compressive properties of human cortical bone to histological structure and calcification. J Biomech. 1974;7(1):1-10.

[34]. Hench LL. Bioceramics: From Concept to Clinic. J Am Ceram Soc. 1991;74(7):1487-510.

[35]. Zhao L, Gao L. Novel in situ synthesis of MWNTs-hydroxyapatite composites. Carbon. 2004;42(2):423-6.

[36]. Lei T, Wang L, Ouyang C, Li N-F, Zhou L-S. In Situ Preparation and Enhanced Mechanical Properties of Carbon Nanotube/Hydroxyapatite Composites. Int J Appl Ceram Technol. 2011;8(3):532-9.

[37]. Neil Dong X, Edward Guo X. The dependence of transversely isotropic elasticity of human femoral cortical bone on porosity. J Biomech. 2004;37(8):1281-7.

[38]. Cho J, Boccaccini A, Shaffer MP. Ceramic matrix composites containing carbon nanotubes. Mater Sci Forum. 2009;44(8):1934-51.

[39]. Stauffer D. Introduction to the percolation theory. London and Philadelphia: Taylor & Francis; 1985.

[40]. Rul S, Lefèvre-schlick F, Capria E, Laurent C, Peigney A. Percolation of single-walled carbon nanotubes in ceramic matrix nanocomposites. Acta Mater. 2004;52(4):1061-7.

[41]. Shi S-L, Liang J. Effect of Multiwall Carbon Nanotubes on Electrical and Dielectric Properties of Yttria-Stabilized Zirconia Ceramic. J Am Ceram Soc. 2006;89(11):3533-5.

[42]. Poorteman M, Traianidis M, Bister G, Cambier F. Colloidal processing, hot pressing and characterisation of electroconductive MWCNT-alumina composites with compositions near the percolation threshold. J Eur Ceram Soc. 2009;29(4):669-75.

[43]. White AA, Kinloch IA, Windle AH, Best SM. Optimization of the sintering atmosphere for high-density hydroxyapatite–carbon nanotube composites. J R Soc, Interface. 2010;7(Suppl 5):S529-S39.

[44]. Ahmad K, Pan W, Shi S-L. Electrical conductivity and dielectric properties of multiwalled carbon nanotube and alumina composites. Appl Phys Lett. 2006;89(13):133122-3.

[45]. Li C, Thostenson ET, Chou T-W. Dominant role of tunneling resistance in the electrical conductivity of carbon nanotube--based composites. Appl Phys Lett. 2007;91(22):223114-3.

[46]. Gittings JP, Bowen CR, Dent ACE, Turner IG, Baxter FR, Chaudhuri JB. Electrical characterization of hydroxyapatite-based bioceramics. Acta Biomater. 2009;5(2):743-54.

[47]. Ahmad K, Pan W. Dramatic effect of multiwalled carbon nanotubes on the electrical properties of alumina based ceramic nanocomposites. Compos Sci Technol. 2009;69(7–8):1016-21.

[48]. Miranzo P, García E, Ramírez C, González-Julián J, Belmonte M, Isabel Osendi M. Anisotropic thermal conductivity of silicon nitride ceramics containing carbon nanostructures. J Eur Ceram Soc. 2012;32(8):1847-54.

[49]. Osendi MI, Gautheron F, Miranzo P, Belmonte M. Dense and Homogenous Silicon Nitride Composites Containing Carbon Nanotubes. J Nanosci Nanotechnol. 2009;9(10):6188-94.

[50]. Shenogina N, Shenogin S, Xue L, Keblinski P. On the lack of thermal percolation in carbon nanotube composites. Appl Phys Lett. 2005;87(13):133106-3.

[51]. Eriksson RA, Albrektsson T. The effect of heat on bone regeneration: An experimental study in the rabbit using the bone growth chamber. Int J Oral Surg. 1984;42(11):705-11.

[52]. Ormsby R, McNally T, Mitchell C, Halley P, Martin D, Nicholson T, et al. Effect of MWCNT addition on the thermal and rheological properties of polymethyl methacrylate bone cement. Carbon. 2011;49(9):2893-904.

[53]. Ormsby R, McNally T, Mitchell C, Dunne N. Incorporation of multiwalled carbon nanotubes to acrylic based bone cements: Effects on mechanical and thermal properties. J Mech Behav Biomed Mater. 2010;3(2):136-45.

[54]. Bonnet P, Sireude D, Garnier B, Chauvet O. Thermal properties and percolation in carbon nanotube-polymer composites. Appl Phys Lett. 2007;91(20):201910-3.

Chapter V

In vitro electrical stimulation of human osteoblastic MG63 cells on MWCNT/Glass/HA bone grafts

V.1. Introduction

Conductive bone grafts would accelerate bone healing while electrically stimulated as they might behave as high efficient electron stimuli delivering systems. This, being the foremost idea of the present thesis work, was validated in the present chapter. Human osteoblastic MG63 cells were stimulated *in vitro* by biphasic electrical pulses in a stimulation system designed by the PhD candidate. The time and current density stimulation parameters were optimised. For a comparative study of the stimulation efficiency, the bone cells were stimulated on dielectric and conductive composite samples. To further evaluate the advantages of the conductive samples over the dielectric ones a set of preliminary studies were done, under the same *in vitro* stimulation conditions, including impedance measurements and vibrating voltage probe analysis of the electric field lines distribution interacting with samples.

V.2. Smart electroconductive bioactive ceramics to promote in situ electrostimulation of bone

D. Mata[a], F.J. Oliveira[a], M.A. Neto[a], A.C. Bastos[a], M. Belmonte[b], M.A. Lopes[c], P.S Gomes[d], M.H. Fernandes[d], R.F. Silva[a]

[a]CICECO, Materials and Ceramic Eng. Dept., Univ. of Aveiro, 3810-193 Aveiro (Portugal)
[b]Institute of Ceramics and Glass, CSIC, 28049 Madrid (Spain)
[c]CEMUC, Metallurgical and Materials Eng. Dept., Faculty of Eng., Univ. of Porto, 4200-465 Porto (Portugal)
[d]Laboratory for Bone Metabolism and Regeneration, Faculty of Dental Medicine, Univ. of Porto, 4200-465 Porto (Portugal)

Abstract

Conductive CNT-based "smart" materials accumulate exciting grafting qualities for tuning the *in vitro* cellular phenotype while electrically stimulated.

Biphasic electrical stimulation of human osteoblastic cells was performed *in vitro* on either dielectric bioactive bone grafts or conductive CNT-reinforced composites. The efficiency of the electrical stimuli delivering, as well as the effect of the stimulation in the cellular functions were investigated. Conductive substrates boosted the local increase of the culture medium conductivity and the confinement of the exogenous electrical fields. Hence, bone cells proliferation, DNA content and mRNA expression were maximized on conductive substrates yielding superior stimuli delivering efficiency over dielectric ones. These findings are suggestive that bioactive bone grafts with electrical conductivity are able of a high spatial and temporal control of bone cells stimulation.

Keywords: Carbon, Bone graft, Electrical stimulation, Gene expression, Bone regeneration

1. Introduction

Bone regenerative medicine has noticed huge progress in the past decades driven by the great socioeconomic interest in treating skeletal diseases [1]. While there have been tremendous improvements of synthetic bone grafts materials, most are still incapable of fully repair and regenerate severe bone injuries [2]. The development of solutions followed the routes of complex tissue engineering, involving cell manipulation, and of simpler strategies such as "smart" bone grafts with new functionalities, able of stimulating specific phenotype expressions of osteoblastic cells [2, 3]. One such exciting functionality is to take advantage of the piezoelectric effect of bone. The forces exerted internally on the bone generate electrical signals that are carried to the bone cells, thus helping to regulate their biological functions [4, 5]. These electrical currents found in healthy bone are not expected to exist at the fractured bone site, in case of bone tissue damage or loosening. So, it was thought that the use of exogenous electric fields would mimic the mislaid endogenous electric signals and accelerates bone healing [6].

Externally applied electrical stimuli delivered to the fractured bone site activate voltage-gated Ca^{2+} channels in plasma membranes allowing the regulation of cell functions and the acceleration of bone healing [7, 8]. However, the use of implanted electrodes has drawbacks related to infection risks and damage to the bone upon their removal while the non-invasive techniques, capacitive coupling or inductive, also target unrelated cells. In the latter, the likely activation of voltage-dependent pathway signals in the surrounding tissues may lead to an overloaded concentration of the internal Ca^{2+} concentration in cells causing functional disorders (e.g. oxidative stress, cytotoxicity) and its premature apoptosis [9, 10].

Numerous studies have shown the potential of suitable stimulation protocols in improving cell proliferation and/or differentiation of osteoblastic lineage cells, in a variety of non-conductive [11-17] and conductive [18-21] matrices, compared to non-stimulated conditions. It is expected that conductive bone grafts may be able to confine exogenous electrical fields on their surface and directly deliver current to cells boosting the spatial and temporal control of bone tissue regeneration [18]. The use of metal containing grafts for such purpose is precluded due to corrosion phenomenon that induces cytotoxicity [22]. The characteristics of carbon nanotubes (CNTs), namely the ultimate electrical conductivity in a non-metallic phase and their high aspect-ratio, make them the highest performance filler to obtain highly conductive biomaterials at low percolation thresholds, without damaging the biological profile of the matrix. CNTs were used as mechanical reinforcement of dielectric bone grafts, namely HA (hydroxyapatite) reinforced composites, proving that the mechanical properties, bioactivity and osteointegration were improved relatively to single phase HA even if electrical stimulation was not considered [23, 24]. For electrical functionality to be used, the level of CNT individualization should be enough to allow a low electrical percolation threshold and to improve, or at least avoid, the degradation of the mechanical properties relatively to those of the matrix. The difficulty in doing so means that CNT agglomerates will always be present and that they should be kept within biologically safe diameter sizes (<20 μm) [25]. Their

presence insures, nevertheless, that the contact area between CNTs and bone cells will be larger and may also give rise to other functionalities. In the bundles there will be cell accessible CNTs that having nano-topography may control cells orientation, migration and also enhance cell adhesion and proliferation [26, 27]. Also, CNTs in the bundles could be provided with functional groups able of anchoring bioactive molecules (e.g. bone morphogenic proteins - BMPs) and drugs (e.g antibiotics) that can be then delivered in situ to the fractured site while simultaneously doing electrical stimulation [28].

It was the main motivation of the work presented here to develop and in-vitro test a CNT/HA/Glass composite material having the adequate mechanical, electrical, microstructural and, most important, biological characteristics, to apply as electroconductive bone graft. The available literature describes the osteoblastic cell response to electrical stimulation either on non-conductive or on conductive substrates. However, comparative studies reporting on the efficiency of stimuli delivering on dielectric and conductive substrates are not found. The use of AC impedance spectroscopy and of vibrating voltage probe measurements in α-MEM (minimal essential medium) reveal the converging effects the conductive composite material have on the electric field and current flow paths. Results for the cell viability/proliferation, DNA content and gene expression increase proved that electrical stimulation clearly induced cell growth and differentiation on the electroconductive bio-composite. The results validate the hypothesis that these new biodegradable CNT/HA/Glass bone grafts could be used together with a non-invasive electrical stimulation technique to activate cell growth preferentially in the healing zone of the bone.

2. Experimental

2.1. Characterization of materials

CNT/Glass/HA composite powder suspensions were mixed in isopropyl alcohol by a non-destructive process with volume fractions of 4.4 vol% CNTs, above the electric percolation threshold, and densified by hot pressing at fixed pressure of 30 MPa for 60 min at 1100ºC. Microstructural characterization was carried out on polished surfaces of selected samples by scanning electron microscope, SEM (Hitachi, SU-70). X-ray diffraction (X'PERT-MPD Philips, CuKα1 radiation (λ= 0.154056 nm) with a step size of 0.02º) and Raman spectroscopy (Alpha300 WITec GmbH) were used to identify the different phases present in the Glass/HA matrix and in the 4.4vol% CNTs composite. Raman imaging was performed using an excitation wavelength of 532 nm. For the imaging, 75 points were acquired per line for a total of 75 lines. The scan size was 80 x 80 µm2 and 90 ms of acquisition time per spectrum. Mechanical characterization (biaxial flexural and compressive tests) was carried out using a Zwick/Roell Z020 equipment with a load cell of 2.5 kN, under a constant displacement rate of 0.3 and 1 mm.min-1, respectively. The biaxial flexural strength values were measured using the circular plate geometry with the 20 mm diameter discs, according to ASTM F394-76: the specimen is supported by 3 ball bearings spaced 120° apart on a

13 mm diameter circle. Loading was applied by a cylinder with a flat loading face with 1.0 mm diameter. For the compressive strength, a cross head speed of 1.0 mm.min^{-1} was used for the 2.5 × 2.5 × 4.5 mm^3 samples. Samples of similar dimensions were used to measure the DC electrical conductivity of the Glass/HA and CNT/Glass/HA materials by fixing copper wires to the smaller faces of the 2.5 x 2.5 x 4.5 mm^3 parallelepipeds. The characterization was performed at room temperature in a Keithley 617 programmable electrometer, with voltage applied in 0.5 V steps in the range of 0-100 V for dielectric samples. For the conductive samples, a programmable power supply (ISO-TECH IPS-603) was used by applying a voltage in the range 0-1 V in 0.1 V steps.

For the cell cultures, square slices of 5×5×1 mm^3 were ground and polished (P4000). Before the *in vitro* testing, the materials were ultrasonically cleaned in ethanol and sterilized by autoclaving.

2.2. *Electrical field lines in α-MEM solution*

In order to evaluate the effect of conductive substrates on the electrical behavior the culture medium used in cell proliferation studies, the resistance of α-Minimal Essential Medium (α-MEM) with different conductive samples was measured by electrochemical impedance spectroscopy (EIS) with a Autolab PGstat 302N (Eco Chemie, The Netherlands). A two electrode arrangement was used with spiral platinum electrodes having the solution and the conductive samples between them. The impedance of the electrochemical cell was measured in the 100 kHz to 10 Hz frequency range with 7 points per decade logarithmically distributed; the sinusoidal perturbation was 10 mV rms at open circuit potential (OCP). The effect of different substrate geometry on the current paths was also assessed by measuring the current lines in solution (12 ml μ-MEM) using with a vibrating voltage probe (Figure 3a), under 3mV.cm-1 of applied electrical field and of 100 μA of current. The equipment used was manufactured by Applicable Electronics Inc. (USA) and controlled by the ASET 2.0 program developed by Sciencewares (USA). The vibrating microelectrode was a polymer insulated Pt-Ir microwire with a 20 μm diameter platinum black sphere electrodeposited on the tip. The probe vibrates in 2 orthogonal directions (X and Z) and measures the potential difference between the two ends of the vibration. The potential difference divided by the distance between the extremes of vibration gives the local electric field which can be converted to a local current density by knowing the solution conductivity [29-31].

2.3. *Characterization of the cell stimulation system*

A stimulation system was designed to reproduce the in situ stimuli conditions delivered by capacitive coupling stimulation used in clinics [32, 33, 34]. This system includes three main components: a culture dish electrode assembly (stimulation box, Figs 1a and 1b); a function generator; and a PC control interface (Fig. 1a). The stimulation box has dishes connected in parallel to accommodate a large number of samples. Every branch of the parallel circuit consists of a set of resistors connected in series, R1 to R6 (Fig. 1a): R1- known resistor; R2 = R6 - platinum

coil immersed in a 20 ml electrolyte solution of KCl (0.33M) housed in a 25 ml plastic container (Polyethylene terephthalate - PET, Kartell); R3 = R5 - salt-bridge filled with Agar (cell culture tested - A1296, Sigma Aldrich)/KCl (0.33M) acting as an electrode (Fig. 1b); R4 - culture medium (α-MEM).
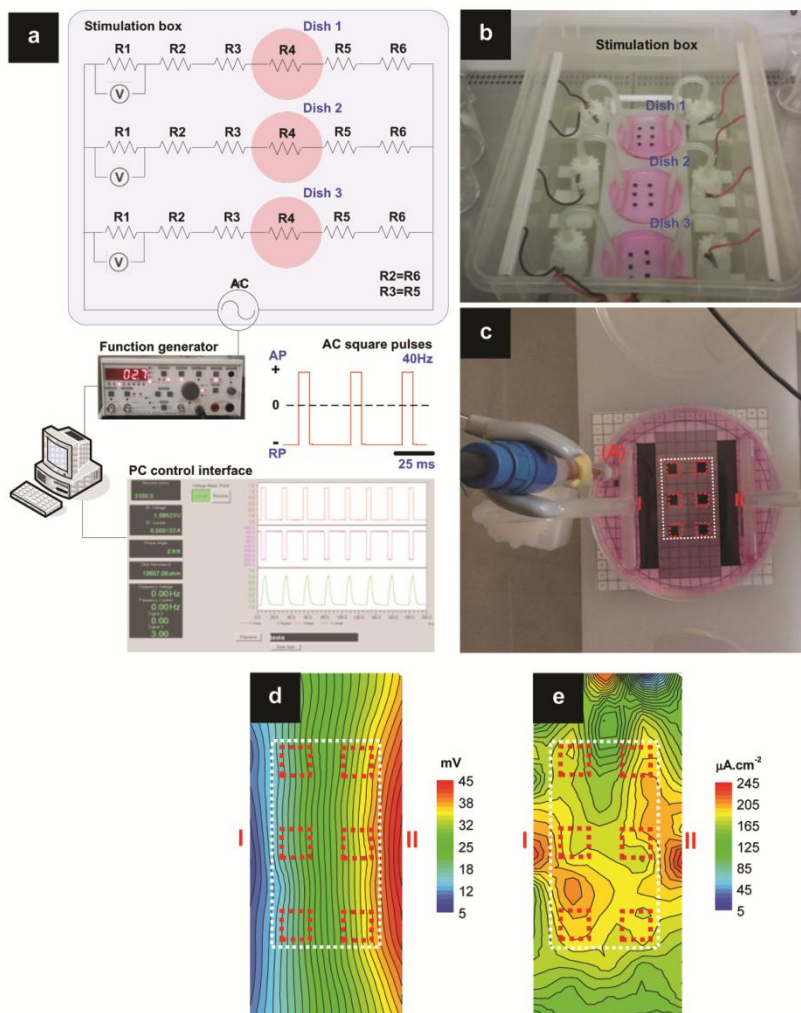

Fig. 1 - (a) Schematic illustration of the electrical stimulation system: stimulation box; function generator, with the respective waveform used (action potentials - AP and resting potentials - RP); and PC control interface. (b) Photograph image of the stimulation box. (c) Magnified photograph image of a culture dish of (b) with parallel disposed salt-bridge electrodes. Color maps of the (d) voltage and (e) current density of the stimulation zone (delineated by a white dotted line).

Advantageously, the conductive electrodes of biological Agar depress the toxicological/contamination risks to cells by avoiding the release of oxidative species typically formed in metallic electrodes and avoid contamination of other non-metallic electrodes. The extremities of the electrodes (R3 and R5) have a "T" configuration with 5 openings disposed along its length size, with 1 mm in diameter and spaced by 1 cm, to ensure a uniform distribution of the

electrical fields and thus a homogeneous stimulation of the samples. Also, the "T" sections of 6 cm in length are smaller than the inner diameter of the culture dish to fit its edge and guarantee the perfect parallelism between electrodes (I and II, Fig. 1c), resembling capacitive coupled electrodes. The maximum number of 6 samples per culture dish was set after obtaining the voltage and current density maps (Figs. 1d and 1e) of the area between the two electrodes (grayish area, Fig. 1c). The maps were obtained in the same conditions of the stimulation experiments using a reference electrode (A) (Fig. 1c) and the equipment described in the previous experimental sections. The area corresponding to the values with the highest uniformity was then selected and used as the stimulation area (delineated with a dotted white line, Figs. 1c-e).

2.4. *MG63 osteoblastic-like Cell culture*

Human osteoblastic-like cells (MG63 cells, ATCC number CRL-1427™) were cultured in α-MEM, supplemented with 10% fetal bovine serum, 50 μg.ml^{-1} ascorbic acid, 50 μg.ml^{-1} gentamicin and 2.5 μg.ml^{-1} fungizone, at 37 ºC, in a humidified atmosphere of 5% CO2 in air. For sub-culturing, the cell layer (at around 70-80% confluence) was detached with trypsin – EDTA solution (0.05% trypsin, 0.25% EDTA; 5 minutes, 37ºC), and the cell suspension was used in the experiments.

Cell culture stimulation: The waveform and magnitude of the applied electrical stimuli were carefully selected based on three major requisites for bone electrical stimulation: the time-current-voltage response of Ca2+ ion channels of osteoblastic-like cells to an action potential [35]; the current threshold applied in clinic to efficiently stimulate bone tissue - 5-20 µA [32]; and the upper limit of current density and electrical field to avoid tissue injury from heat generation - 1-2 mA.cm^{-2} and 10 V.cm^{-1} [33]. Cells were seeded (2x10^4 cells.cm^{-2}) over standard cell culture coverslips, HA/Glass matrix and CNT/HA/Glass composite, and were cultured for 3 days. Subsequently, the cultures were exposed to a daily electrical stimulation to one of the following conditions: (i) 5 μA, 15 min, (ii) 5 μA, 30 min, (iii) 15 μA, 15 min, and (iv) 15 μA, 30 min (Table 1).

Table 1 - *In vitro* electrical stimulation metrics of human osteoblastic cells.

Stimulation conditions		Resistor, R1 (kΩ)	Peak-to-peak voltage (V)	Electrical field (mV.cm^{-1})	Current$_{total}$ (µA)	Current$_{samples}$ (µA)	Current density$_{samples}$ (µA.cm^{-2})
5µA	15 min	3.3	2.7	5.6	100	5±2	65±25
	30 min						
15µA	15 min	1.5	4	15.3	200	15±3	185±30
	30 min						

Symmetrical biphasic square pulses with fixed frequency and duty cycle values of 40 Hz and 20-80% were used, setting action potentials (AP) and resting potential (RP) with fixed periods of 5 and 20 ms. This procedure was repeated during 5 consecutive days. Cultures were characterized 24 h after 1, 3 and 5 electrical stimuli. Non-stimulated cultures were run in parallel.

290

Cell proliferation: DNA and MTT assays: DNA content was analyzed by the PicoGreen DNA quantification assay (Quant-iT™ PicoGreen® dsDNA Assay Kit, Molecular Probes Inc., Eugene), according to manufacturer´s instructions. Cultures were treated with Triton X-100 (0.1%) (Sigma) and fluorescence was measured on an Elisa reader (Synergy HT, Biotek) at wavelengths of 480 and 520 nm, excitation and emission respectively, and corrected for fluorescence of reagent blanks. The amount of DNA was calculated by extrapolating a standard curve obtained by running the assay with the given DNA standard. Results are expressed as percentage from control. The MTT assay was used to assess the cell viability/proliferation. This is based in the reduction of the MTT (3-(4,5-Dimethylthiazol-2-yl)-2,5-diphenyltetrazolium) by viable cells to a dark blue formazan product. MTT (0.5 mg.ml-1) was added to each well, and cultures were incubated for 3 hours at 37ºC. Subsequently, the formazan salts were dissolved in dimethylsulphoxide (DMSO) and the absorbance (A) was determined at λ = 600 nm on an Elisa reader (Synergy HT, Biotek). Results are expressed as percentage from control.

Gene expression: Cultures were assessed by RT-PCR after 5 daily stimuli, for the expression of the housekeeping gene glycerol-3-phosphate dehydrogenase (GAPDH), the transcription factor Runx2 and the osteoblastic genes collagen type I (Col I), alkaline phosphatase (ALP), osteocalcin (OC) and osteoprotegerin (OPG). For that, RNA was extracted with Rneasy® Mini Kit (QIAGEN) according to manufacturer's instructions and was quantified by UV spectrophotometry at 260 nm. Half microgram of RNA was reverse transcribed and amplified (25 cycles) with the Titan One Tube RT-PCR System (Roche), with an annealing temperature of 55ºC. Table 2 shows the primers used in the RT-PCR analysis. After electrophoresis on a 1% (w/V) agarose gel, the bands were analysed by densitometry with ImageJ 1.41 software. Values were normalized to the corresponding GAPDH value of each experimental condition.

Table 2 - Primers used on RT-PCR analysis.

Gene	Forward primer	Reverse primer
GAPDH	CAGGACCAGGTTCACCAACAAGT	GTGGCAGTGATGGCATGGACTGT
Runx2	CAGTTCCCAAGCATTTCATCC	TCAATATGGTCGCCAAACAG
COL1	TCCGGCTCCTGCTCCTCTTA	ACCAGCAGGACCAGCATCTC
ALP	ACGTGGCTAAGAATGTCATC	CTGGTAGGCGATGTCCTTA
OC	CACTCCTCGCCCTATTG	CCCACAGATTCCTCTTCT
OPG	AAGGAGCTGCAGTAGGTCAA	CTGCTCGAAGGTGAGGTTAG

SEM and CLSM observation: For SEM observation, samples were fixed (1.5% glutaraldehyde in 0.14 M sodium cacodylate buffer, pH=7.3, 10 min), dehydrated in graded alcohols, critical-point dried, sputter-coated with an Au/Pd thin film (SPI Module Sputter Coater equipment), and observed under a High resolution (Schottky) Environmental Scanning Electron Microscope (Quanta 400 FEG ESEM). For CLSM assessment, samples were fixed (3.7% paraformaldehyde, 15 min). Cell cytoskeleton filamentous actin (F-actin) was visualized by treating the cells with Alexa Fluor 488 Phalloidin (1:20 dilution in PBS, 1 h) and counterstaining with

propidium iodide (1 µg.ml^{-1}, 10 min) for cell nuclei labelling. Labelled cultures were mounted in Vectashield® and examined under a Leica SP2 AOBS (Leica Microsystems) microscopy.

Statistical analysis: For improving data quality, three independent experiments were performed; in each experiment, three replicas were accomplished for the biochemical assays and two replicas for the qualitative assays. Results are presented as mean ± standard deviation (SD). Groups of data were evaluated using a two-way analysis of variance (ANOVA) and no significant differences in the pattern of the cell behavior were found. Statistical differences between experimental groups were assessed by Bonferroni's method. Values of $p \leq 0.05$ were considered statistically significant

3. Results and discussion

3.1. *Microstructural and mechanical characterization of the bone grafts*

The hot-pressing temperature of 1100 °C used in the preparation of the materials made the glass to react with the hydroxyapatite and then partially converted it into β-TCP (tricalcium phosphate) phase, as depicted in the X-ray diffraction patterns in Figs. 2a and 2b, respectively for the HA/Glass matrix and the 4.4 vol.% CNT/HA/Glass composite. The peaks correspond to those reported in Joint Committee on Powder Diffraction Standards (JCPDS) files for HA (JCPDS 72-1243) and β-tricalcium phosphate, β-TCP (JCPDS 09-0169). Comparing those two plots, it becomes quite clear that there are almost no changes in phase composition when the CNTs are added to the matrix. Arquimedes' density showed that the HA/Glass matrix is almost fully dense. The scanning electron micrographs (SEM) micrographs of polished surfaces of the unreinforced matrix and the 4.4 vol.% CNT composite after immersion in α-MEM, Figs. 2c an 2d, show some well distributed porosity as a result of preferential leaching of the β-TCP phase [36]. This effect is further enhanced in the presence of CNTs, as is clear from the observation of the microstructure of the 4.4 vol.% CNT composite, Fig. 2d. The material surrounding the pore-like defects due to α-MEM preferential attack is less dense, with evidences of micro porosity that is not present in the HA/Glass matrix. Also, from SEM observations only, there are no clearly identifiable zones containing individualized CNTs thereof.

The use of Raman spectroscopy in imaging mode permitted clearly identifying the areas in the dense materials where HA, β-TCP and CNTs are present, as Figs. 2e and 2f illustrate [37]. The image of the unreinforced matrix, Fig. 2e, and the spectra in Fig. 2g help understanding that the pore-like defects are associated to the β-TCP phase location. Also, there is carbon contamination during hot-pressing in graphite dies at temperatures where the HA/Glass matrix is quite chemically active. This contamination is not so clear in the Raman mapping of Fig. 2f, for the 4.4 vol.% CNT composite.
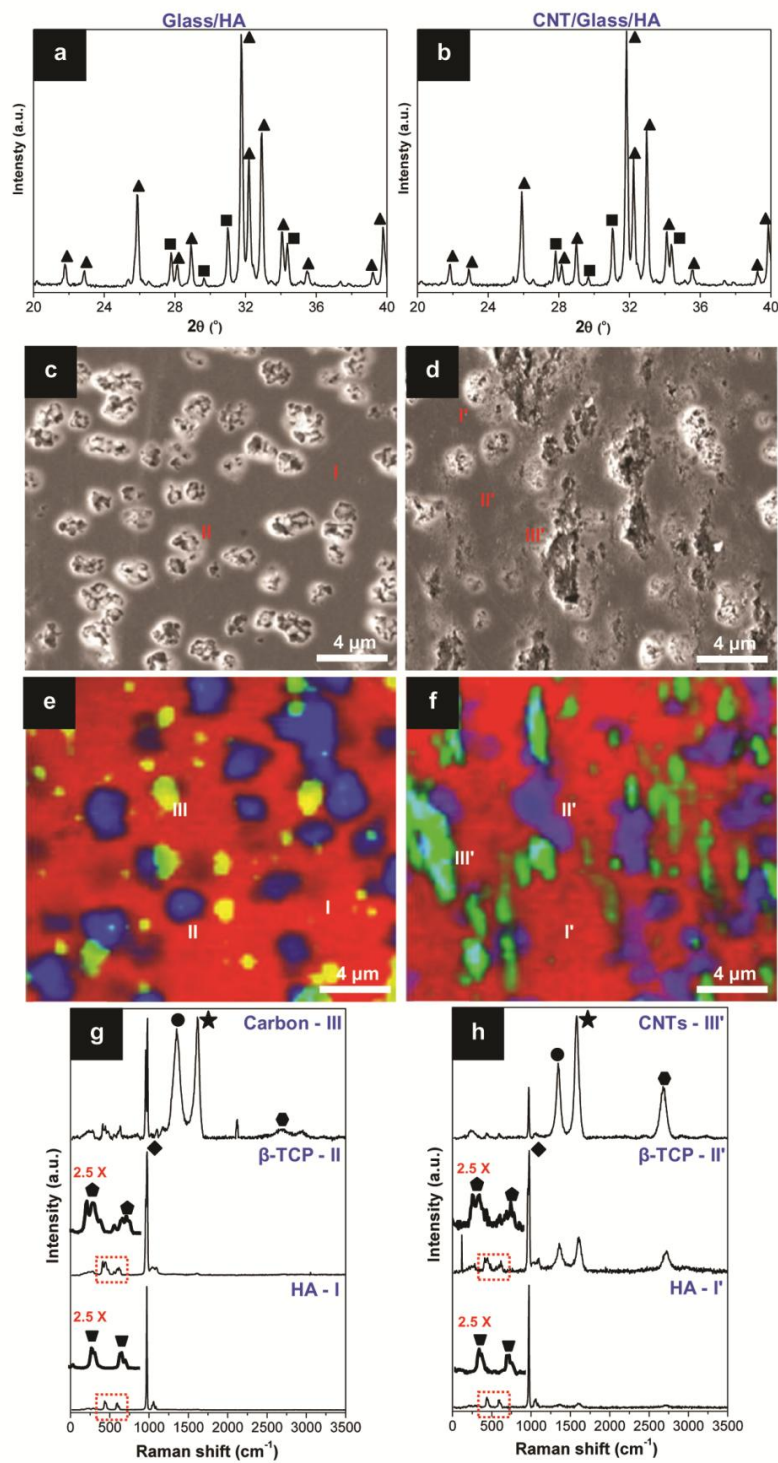
Fig. 2 - XRD spectra of hot-pressed (a) Glass/HA and (b) CNT/Glass/HA compacts. (■ β-TCP, ▲ HA) (c and d) SEM micrographs of (a) and (b). (e and f) Colour Raman maps and respective (g and h) spectra of (a) and (b) (carbon and CNTs: ● D-band, ★ G-band, ⬡ G'(2D)-band; β-TCP: ◆v_1-PO_3^{2-}, ⬟v_2-PO_3^{2-}; HA: ◆v_1-PO_3^{2-}, ▼v_2-PO_3^{2-}).

Combining the code colors in Fig. 2f with the corresponding spectra in Fig. 2h, it becomes clear that CNTs (addressed by the G' (2D) signature and higher G/D ratio) are present mainly as elongated agglomerates but can be identified throughout the matrix, within the resolution limits of

293

the technique. It is worth noting that the observed SEM surfaces are parallel to the pressing direction, this accounting for the pressure induced alignment observed of the CNT large agglomerates in the 4.4 vol.% CNT material (Fig. 2d). The 6% porosity measured in this material by Arquimedes' immersion reflects not only the damping effect of the CNTs and the difficulty in transmitting the pressure to the HA/Glass matrix for densification, but also the increased interactions and entanglement of CNT agglomerates that further prevent matrix contiguity from happening. This porosity is closer to the cortical bone than the Glass/HA matrix alone, that is almost fully dense but still reacts readily with α-MEM, as shown above, Fig. 2c. Nevertheless, both the compressive and bending strength of the produced materials have values that are well within or above cortical bone specifications for adult, healthy individuals with average values of compressive and bending strengths of 700 MPa and 160 MPa, respectively, for the 4.4 vol.% CNT/HA/Glass composite.

3.2. *Bone grafts-α-MEM culture medium interactions*

A key idea of the present work is to make the electrical stimulus to converge through the osteoblasts present at the composite surface in order to tune its cellular functions. Fig. 3a gives the conductivity of the culture medium α-MEM and several biological tissues/organs/milieus together with the new CNT/Glass/HA material (labeled at blue) [34]. It can be seen that the CNT composite has higher conductivity than the *in vitro* culture medium and than any *in vivo* environment. In line with this, it is expectable that this characteristic yields CNTs containing substrates with high potential to increase the local conductivity and to confine electrical fields, making them high efficient electron transport and delivering pathway systems.

To ensure the validity of this hypothesis and the experimental approach used for cell stimulation, a set of preliminary studies were carried out, as follows: (1) by studying the effects on the overall resistivity of α-MEM using immersed conducting and nonconducting samples; and (2) by identifying the current density (electric field) lines on samples of different geometries.

3.2.1. *Neutral conditions*

The electrochemical cells contained α-MEM and 6 or 12 samples (example in Fig. 3b). The impedance of the cell was measured in a two electrode arrangement using 2 platinum spiral electrodes. The variation of the modulus of impedance, |Z|, with the signal frequency is shown in Fig. 3c. The values are normalized to the area of the electrodes. The impedance response shows two regions, one at higher frequencies with constant |Z| and another at frequencies below ~5 kHz where |Z| increases as the frequency decreases. The high frequency region is related to the solution resistance while the second one measures the double layer capacitance at the surface of the Pt electrodes. As so, only the high frequency part is interest to this study.
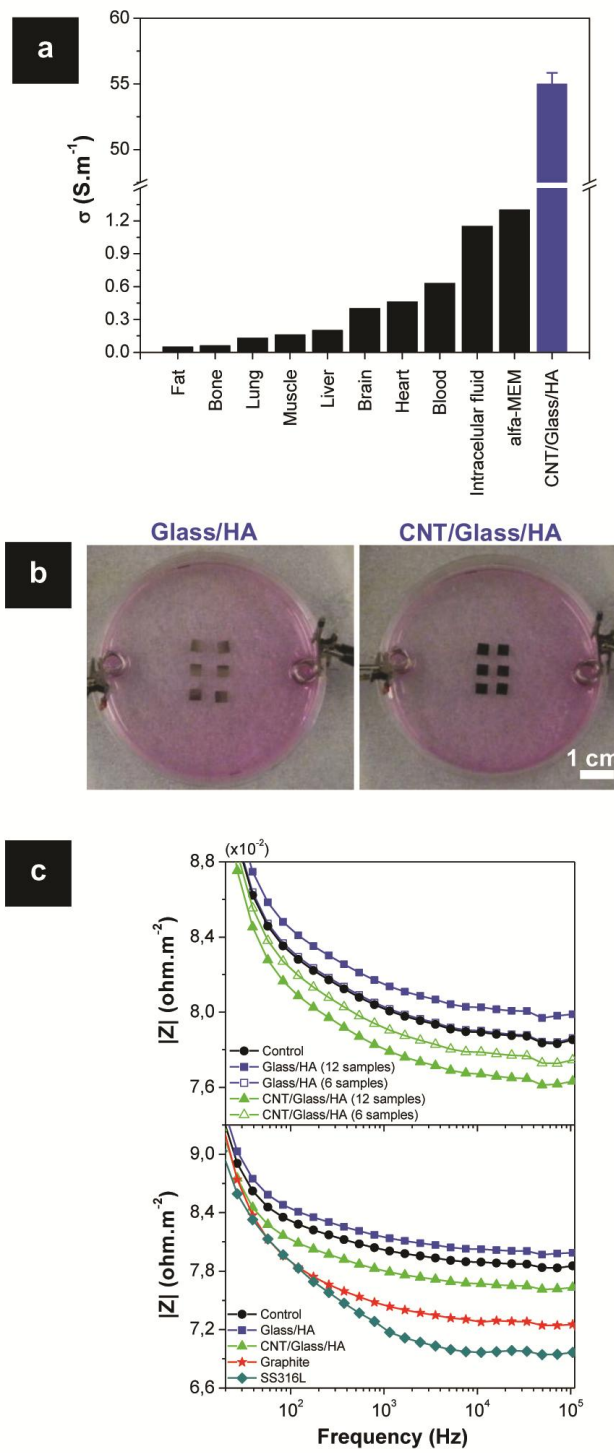
Fig. 3 - (a) Plot comparing the electrical conductivity of biological tissues and milieus, α-MEM and the CNT/Glass/HA composite (highlighted at blue). (b) Photographs of the electrochemical cells with 6 samples immersed in 12 ml of α-MEM and platinum spiral electrodes. (c) Plots showing the dependence of the modulus of impedance |Z| of the electrochemical cells on the signal frequency.

The control curve is simply the resistance of α-MEM. The other curves give the resistance when 6 or 12 samples of either Glass/HA (non-conductive) or CNT/Glass/HA (conductive) were

immersed in solution. It increased with 12 nonconductive samples and decreased when conductive pieces were used, with a decrease proportional to the number of pieces. The same experiment with different materials showed that the more conductive the material is the lower the resistance of the medium.

3.2.2. Electrical stimulation conditions

The current lines in solution near the conductive samples, when placed in an electrochemical cell, were measured by a vibrating voltage probe.
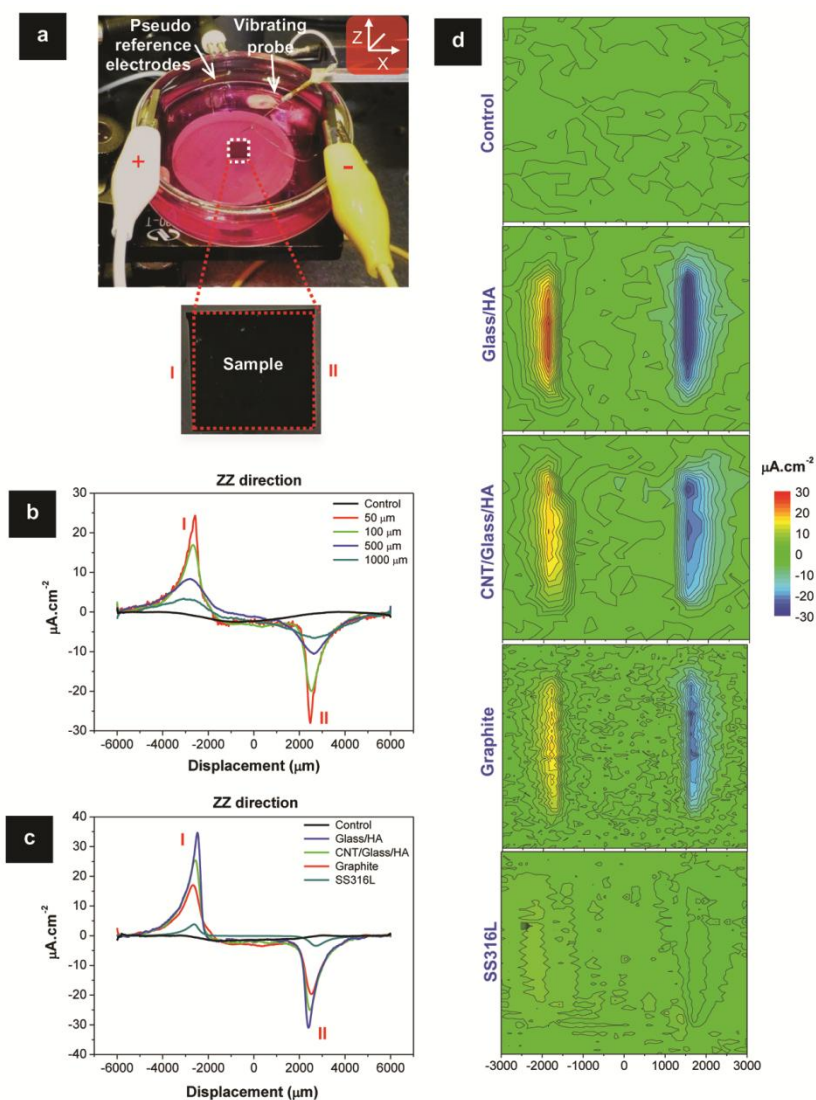
Fig. 4 - (a) Set-up of the vibrating voltage probe measuring system of a electrochemical cell containing one sample immersed in 12 ml of α-MEM and parallel graphite electrodes (b) Plot of the variation of the current density line profile (from I to II labels) in the zz direction with the distance between the surface of the sample and the vibrating probe of (a). (c) Plot showing the influence of the electrical conductivity of the sample on the current density line profiles at a fixed sample-probe distance of 50 µm. (d) Respective color mapped graphic representation of (c).

Fig. 4a depicts the experimental set up with a fixed current running from one electrode plate to the other, both disposed in parallel. Part of the current flows through the sample and the remaining current will diverge, surrounding the sample, because it represents an obstacle to flow. A component of the current normal to the surface could be detected, having a positive sign on the side of the positive electrode because the current lines shift up and negative on the right because the current paths descend, returning to their original path in the solution, as can be seen in Fig. 4b. The closer the line of measurement is to the sample the higher is the measured normal component. A distance of 50 µm provided the highest sensitivity to the normal current, still avoiding the risk of the probe touching the sample. The experiment was repeated with different materials, Figs. 4c and 4d. The decrease of the normal component for higher conductive materials proves that the current is converging through the material in a higher extent for the more conductive materials (steel and graphite), as depicted in the vibrating voltage probe maps showed in Fig. 4d.
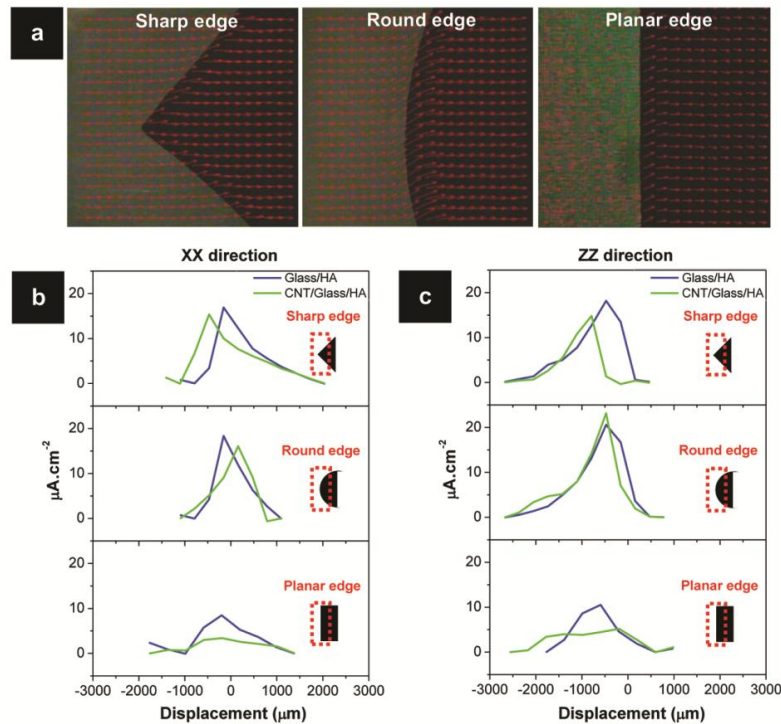
Fig. 5 - (a) Photographs showing the 2D distribution of the current density vectors (I_x, I_z) for CNT/Glass/HA samples with different edge geometries. Respective plots of the variation of the current density line profiles in the (b) xx and (c) zz directions with the edge geometry of Glass/HA and CNT/Glass/HA samples.

The influence of the sample geometry on current distribution was also investigated because CNT/Glass/HA bone grafts may be applied as granules having irregular shapes, thus being important to check if geometry is a factor to consider in the electrical field distribution. The results in Fig. 5 show that no significant differences of the xx and zz components of current density,

Ix and Iz, exist for triangular, round and rectangular shaped samples. Also, the correspondent Ix and Iz values for CNT/Glass/HA and Glass/HA samples are close, still, the former have lower values, corroborating data of Figs. 4c and 4d.

3.3. *Osteoblastic cells proliferation and gene expression: substrate efficiency in in situ stimulus delivery*

MG63 cell line was used to address the potential role of the electroconductivity of the CNT/HA/Glass composite on the osteoblastic cell response under electrical stimulation, and to select an optimized set of conditions for improved cell behaviour. This cell system provides a homogeneous, phenotypically stable and proliferative population that shows many phenotypic features of normal osteoblastic cells including hormonal responsiveness and expression of early and late stage osteogenic genes, being widely used as a osteoblast cell model for *in vitro* research [38]. Cell cultures, performed on standard cell culture coverslips, HA/Glass matrix and CNT/HA/Glass composite were submitted to electrical stimuli of 5 μA/15 min, 5 μA/30 min, 15 μA/15 min or 15 μA/30 min (Table 1), one time a day for up to five consecutive days, and were assessed 24 h after 1, 3 and 5 stimuli for the DNA content, metabolic activity and gene expression of of Runx2, Col I (Collagen type I), ALP (Alkaline Phosphatase), OC (Osteocalcin) and OPG (Osteoprotegerin).

The DNA content on the cultured coverslip and on the two materials, in non-stimulated conditions, increased throughout the culture time. This parameter reflects the number of cells present on the substrates, being an index of the cell proliferation. Under electrical stimulation, DNA content on the CNT/HA/Glass composite was greatly increased after 1 and 3 stimuli (~25 to 60%) and was similar after 5 days of treatments, compared to non-stimulated cultures (Figs. 6a-c). The inductive effect was dependent on the stimulus intensity and duration, and was higher with 15 μA, 30 min (after 1stimulus, ~60%) and 15 μA, 15 min (after 3stimuli, ~62%). Cell response over the dielectric surfaces (coverslip and HA/Glass matrix) was similar under electrical stimulation (Figs. 6a-b). Compared to control, DNA content was slightly increased, similar and significantly lower after 1, 3 and 5 daily treatments. Results for the MTT reduction (Figs. 6d-f), a cell viability/proliferation assay based on the reduction ability of cell mitochondrial dehydrogenases, showed a pattern similar to that observed for the DNA content, in the conductive and dielectric substrates. However, in both types of surfaces, for the inductive effects, the percentage of increase was always higher than that found for the DNA content. Thus, on the CNT/HA/Glass composite, increases of ~40 to 130% were found after 1 and 3 stimuli. Hence, under selected stimulation conditions, both the cell proliferation and the metabolic activity were induced, suggesting the presence of a higher number of cells with increased metabolic activity, compared to non-stimulated conditions. However, these cellular parameters decreased following repeated stimuli. The time-dependent effect of electrical stimulation on cell proliferation was reported previously and appears to depend on the stage of cell differentiation [15, 39].
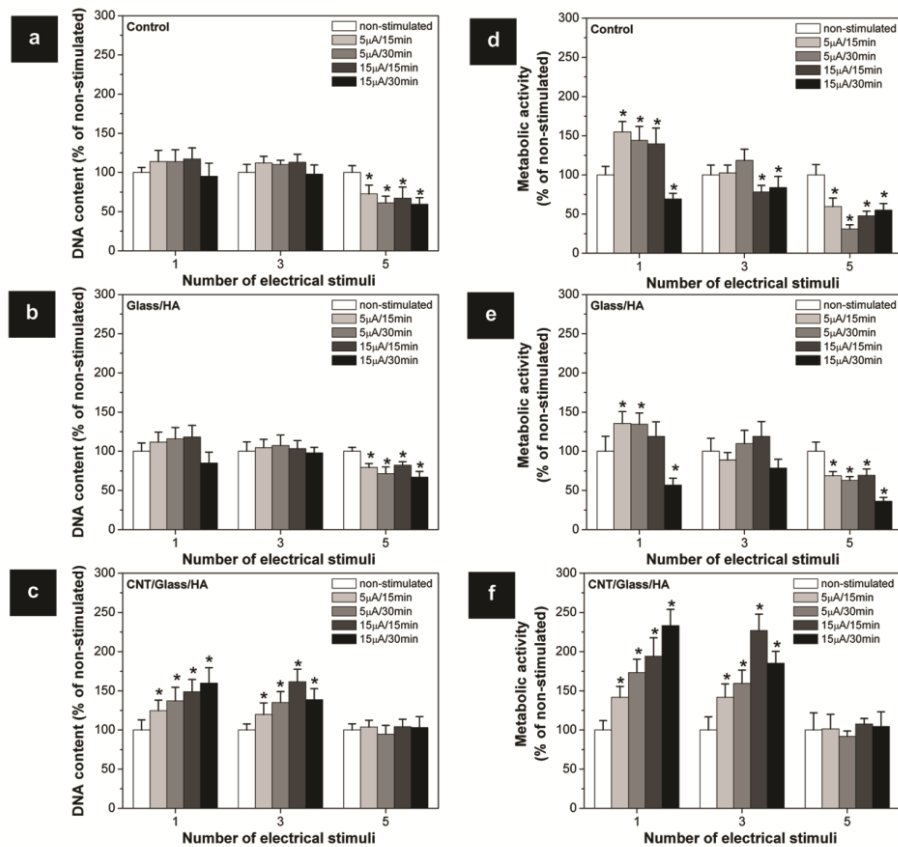
298

Fig. 6 - (a-c) DNA content and (d-f) cell viability/proliferation of osteoblastic cell cultures grown over standard cell culture coverslips, Glass/HA matrix and CNT/Glass/HA composite, and characterized 24h after 1, 3, and 5 daily electrical stimuli, under different stimulation conditions. Results are expressed as percentage of variation from non-stimulated cultures. *Significantly different from non-stimulated cultures.

Results on the mRNA expression after 5 daily treatments (Fig. 7) show that the expression of Runx2 was particularly sensitive to the inductive effects of the electrical stimulation. It was up regulated on the cultures grown over the CNT/HA/Glass composite, and also on those over the HA/Glass matrix. Even in the cultured coverslip, that showed low expression of Runx2 in the non-stimulated cultures, there was a trend for an increase under stimulation conditions. This is an interesting finding, as Runx2 is the earliest transcription factor for osteogenic differentiation and, in addition, it activates the expression of multiple late stage osteoblastic genes [40]. Over the stimulated CNT/HA/Glass composite, there was also increased mRNA expression for ALP and OC, respectively an early and a late stage marker in the osteogenic differentiation pathway. As both molecules have a role in the extracellular matrix mineralization, respectively in the initiation of mineral deposition (ALP) and in the regulation of crystal growth (OC) [41], this observation points to an enhanced osteogenic differentiation under electrical stimulation. No effect was noted on the

mRNA expression for Col 1, the main component of the extracellular matrix, and also for OPG, a key molecule in the interplay between osteoblasts and osteoclasts during bone remodelling [42].
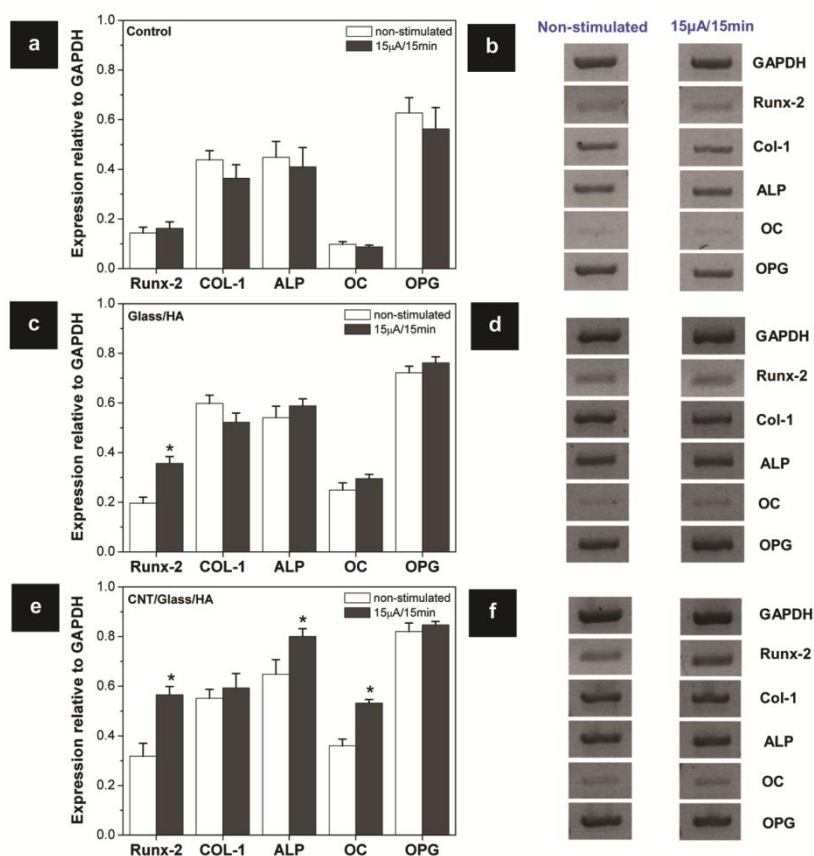

Fig. 7 - Expression of osteoblastic-related genes by cell cultures grown over standard cell culture coverslips, Glass/HA matrix and CNT/Glass/HA composite, and characterized 24h after 5 daily electrical stimuli, under 15 µA, 15 min. Results are expressed as percentage of variation from non-stimulated cultures. Densitometric analysis of the RT-PCR bands normalized to the corresponding GAPDH value (a, c, e) and representative images of the PCR products in the agarose gel (b, d, f) . *Significantly different from non-stimulated cultures.

On CLSM (Fig. 8), non-stimulated and stimulated cells displayed a polygonal/elongated morphology on the HA/Glass matrix and, essentially, an elongated/fusiform appearance on the CNT/HA/Glass composite. In both surfaces, cells exhibited a well-organized F-actin cytoskeleton, with intense staining at the cell boundaries, prominent nucleus and on-going cell division, signs of mechanical integrity and healthy behaviour. Over the CNT/HA/Glass composite, a specific cell orientation was visible already at day 1, and a characteristic aligned cell growth was evident at later culture times, compared to the random pattern of cell growth seen over the Glass/HA matrix. SEM observation provided similar information but, additionally, images showed that the organization of the cell layer over the CNT/HA/Glass composite followed the alignment direction of the CNT agglomerates on the Glass/HA matrix (Fig. 9).
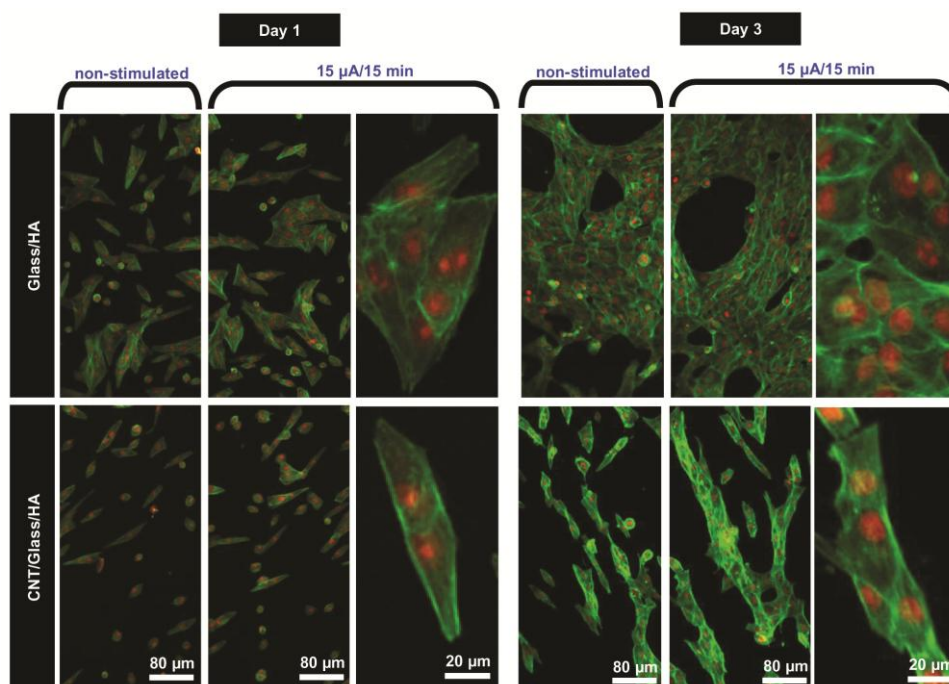
300

Fig. 8 - CLSM appearance of osteoblastic cell cultures grown over Glass/HA matrix and CNT/Glass/HA composite, and observed 24h after 1 and 3 daily electrical stimuli, under different stimulation conditions. Cells were stained for F-actin cytoskeleton (green) and nucleus (red).

This observation is in line with some reported information, showing that aligned CNT networks exhibited the ability to modulate cell morphology and the directional growth of human osteoblastic cells, in comparison to seeded randomly oriented CNT network [40, 43]. Overall, the electrical stimulation did not result in evident effects in the aligned cell organization over the CNT/HA/Glass composite. The distinct cytoskeleton organization over the CNT/HA/Glass and HA/Glass samples is expected to modulate the cell response to the two substrates. The F-actin cytoskeleton, which is highly concentrated just beneath the plasma membrane, provides structural stability and elasticity to the cell undergoing substrate adaptation, but it is also a key player in the cellular mechano-transduction mechanisms modulating complex signalling pathways, such as Rho family GTPases, which affects the overall cell behaviour [44]. Related to this, it has been suggested that the directional cell growth observed in aligned CNTs structures enhances osteogenic differentiation, in comparison to seeded randomly oriented CNTs network, a process possibly mediated by the high cytoskeleton tension accumulated on aligned cells leading to the activation of selective mechano-transduction pathways [40].
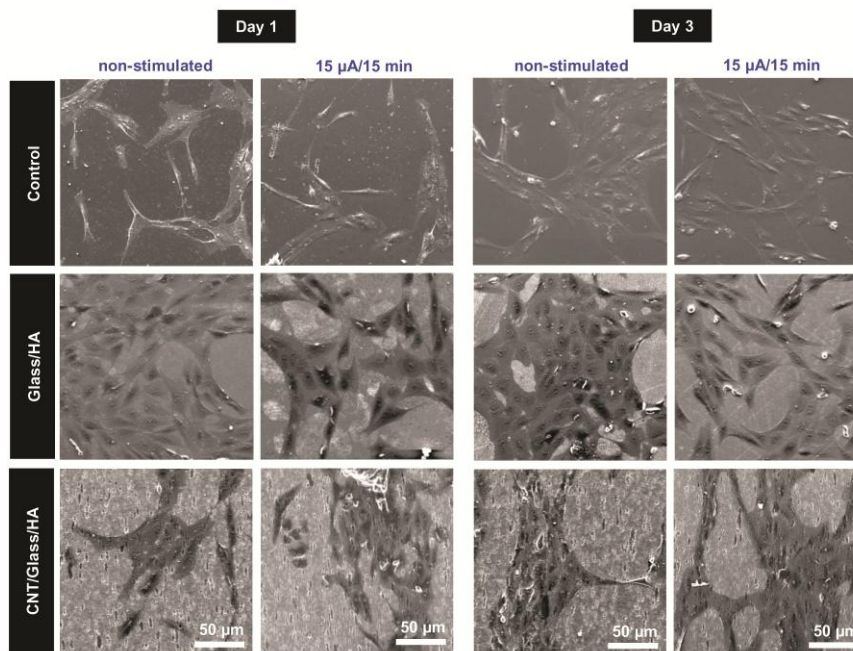
Fig. 9 - SEM appearance of osteoblastic cell cultures grown over standard cell culture cover slips, Glass/HA composite and CNT/Glass/HA composite, and observed 24h after 1 and 3 daily electrical stimuli, under different stimulation conditions.

Results showed that under an appropriate electrical stimulation protocol, the conductive CNT/HA/Glass composite showed significantly improved cell proliferation, metabolic activity and osteoblastic gene expression. The lower inductive effect on cell proliferation but higher expression of relevant osteogenic genes and ALP activity found over the CNT/HA/Glass composite after few stimuli suggest an inductive effect on the osteoblastic differentiation, taking in account the established inverse relationship between proliferation and differentiation during the development of the osteoblastic phenotype [42].

Briefly, cell functional activity was significantly improved on the CNT/HA/Glass composite, which is intimately related with its efficiency in the electrical stimuli delivering to cells. According to section 3.2, conductive substrates increase the local conductivity of the culture medium and render the confinement of the exogenous electrical fields on the surface of the material. Fig. 10 sketches the interaction of the electrical field lines with cells surrounding non-conductive and conductive substrates. In the latter, the electrical field confinement (higher current density) at perpendicular angles to the surface [19] imposes osteoblastic cells in contact to be crossed by the electrical fields. Contrarily, in a dielectric material the external fields are parallel to its surface, so they are not confined, thus a much lower efficiency of stimuli delivering at the sample surface is observed relatively to the conductor material.

Regarding the involved mechanisms, electrical stimulation seems to modulate cell behaviour essentially by altering the intracellular calcium dynamics [44]. Although being a versatile process and likely to depend on the cell type and microenvironmental conditions, the modulation of the intracellular calcium levels in human mesenchymal stem cells seems to be involved in directing

their osteogenic differentiation [44-46]. Associated mechanisms appear to be related with the clustering and activation of cell-surface receptors (e.g. integrins), interaction with G-protein coupled receptors (e.g., PLC - Phospholipase C), ATP (Adenosine 5'- triphosphate) release and activation of ion channels. Regarding the latter, the intracellular calcium can be raised inside osteoblastic cells by Ca^{2+} transport via L-type Ca^{2+} channels [47, 48]. Of interest, it was found that these ion channels preferentially regulate Ca_{2+}-dependent genes and enzymes, such as the Ca2+/calmodulin-dependent protein kinase II (CaMKII) [49], a key pathway towards regulation of osteoblast proliferation/differentiation [50]. In the present work, the high current-voltage thresholds of osteoblastic Ca2+ ion channels give further evidences that cell response to stimuli appears to be L-type $Ca^{2+/}$CaMKII mediated since cell proliferation and metabolic activity were maximized for the high current stimuli conditions (15 µA,15 min). Moreover, compared to Glass/HA, the conductive CNT/Glass/HA composite reveals a higher activation of L-type ion channels (i.e. intracellular Ca^{2+} levels) and further larger efficiency of bone cell stimulation. This may be related to the high efficiency of charge transfer voltage at the substrate-cell interface, related to the high density of electric field lines crossing the cell (Fig. 10), which boosts opening of voltage-gated channels at multi-locations in the cell membrane, and raises action potentials' magnitude.
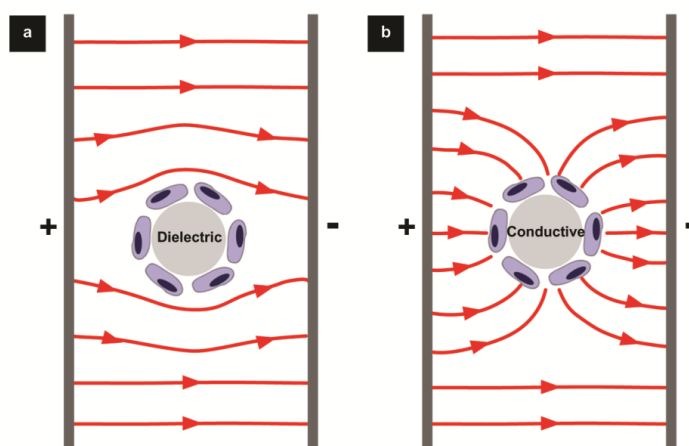
Fig. 10 - Top view schematic images of the electric field (current density) lines distribution of a (a) dielectric and a (b) conductive spherical samples interfacing with osteoblastic cells (elliptical purple sketches) immersed in a homogeneous α-MEM culture medium.

4. Conclusions

In the present study, the conductive CNT/HA/Glass composite showed significantly improved cell functional activity under an appropriate electrical stimulation protocol, compared to the HA/Glass matrix. The cell metabolic activity and DNA content were increased by 130% and 60%, relatively to the non-stimulated condition, after only 3 days of daily stimulation of 15 µA for 15 min. Moreover,the osteoblastic gene expression for Runx2, OC and ALP was enhanced by 80%, 50% and 25%, after 5 days of stimulation. These observations were intimately related to the local

increase of the culture medium conductivity and the confinement of electrical fields on the surface of the conductive material. It is trust that experimental evidences of selective bone cell stimulation on conductive bone grafts will offer new possibilities in non invasive clinic electrotherapies.

.

Acknowledgements

References

[1]. Stevens MM. Biomaterials for bone tissue engineering. Materials Today. 2008;11(5):18-25.

[2]. Navarro M, Michiardi A, Castaño O, Planell JA. Biomaterials in orthopaedics. J R Soc, Interface. 2008;5(27):1137-58.

[3]. Spear R, Cameron R. Carbon nanotubes for orthopaedic implants. Int J Mater Form. 2008;1(2):127-33.

[4]. Bassett CAL, Becker RO. Generation of electric potentials by bone in response to mechanical stress. Science. 1962;137(3535):1063-4.

[5]. Yasuda I. On the piezoelectric activity of bone. J Jpn Orthop Surg Soc. 1954;28:267-71.

[6]. Bassett C. Fundamental and practical aspects of therapeutic uses of pulsed electromagnetic fields (PEMFs). Crit Rev Bioeng. 1989;17(5):451-529.

[7]. Zayzafoon M. Calcium/calmodulin signaling controls osteoblast growth and differentiation. J Cell Biochem. 2006;97(1):56-70.

[8]. Bezanilla F. The voltage sensor in voltage-dependent ion channels. Physiol Rev. 2000;80(2):555-92.

[9]. Orrenius S, Zhivotovsky B, Nicotera P. Regulation of cell death: the calcium–apoptosis link. Nat Rev Mol Cell Biol. 2003;4(7):552-65.

[10]. Ermak G, Davies KJA. Calcium and oxidative stress: from cell signaling to cell death. Mol Immunol. 2002;38(10):713-21.

[11]. Kim IS, Song JK, Zhang YL, Lee TH, Cho TH, Song YM, et al. Biphasic electric current stimulates proliferation and induces VEGF production in osteoblasts. Biochim Biophys Acta, Mol Cell Res. 2006;1763(9):907-16.

[12]. Schwartz Z, Simon BJ, Duran MA, Barabino G, Chaudhri R, Boyan BD. Pulsed electromagnetic fields enhance BMP-2 dependent osteoblastic differentiation of human mesenchymal stem cells. J Orthop Res. 2008;26(9):1250-5.

[13]. Kim IS, Song JK, Song YM, Cho TH, Lee TH, Lim SS, et al. Novel effect of biphasic electric current on in vitro osteogenesis and cytokine production in human mesenchymal stromal cells. Tissue Eng, Part A. 2009;15(9):2411-22.

[14]. Sun L-Y, Hsieh D-K, Yu T-C, Chiu H-T, Lu S-F, Luo G-H, et al. Effect of pulsed electromagnetic field on the proliferation and differentiation potential of human bone marrow mesenchymal stem cells. Bioelectromagnetics. 2009;30(4):251-60.

[15]. Tsai M-T, Li W-J, Tuan RS, Chang WH. Modulation of osteogenesis in human mesenchymal stem cells by specific pulsed electromagnetic field stimulation. J Orthop Res. 2009;27(9):1169-74.

[16]. Hwang SJ, Song YM, Cho TH, Kim RY, Lee TH, Kim SJ, et al. The implications of the response of human mesenchymal stromal cells in three-dimensional culture to electrical stimulation for tissue regeneration. Tissue Eng, Part A. 2011;18(3-4):432-45.

[17]. Hess R, Jaeschke A, Neubert H, Hintze V, Moeller S, Schnabelrauch M, et al. Synergistic effect of defined artificial extracellular matrices and pulsed electric fields on osteogenic differentiation of human MSCs. Biomaterials. 2012;33(35):8975-85.

[18]. Supronowicz PR, Ajayan PM, Ullmann KR, Arulanandam BP, Metzger DW, Bizios R. Novel current-conducting composite substrates for exposing osteoblasts to alternating current stimulation. J Biomed Mater Res. 2002;59(3):499-506.

[19]. Woo DG, Shim M-S, Park JS, Yang HN, Lee D-R, Park K-H. The effect of electrical stimulation on the differentiation of hESCs adhered onto fibronectin-coated gold nanoparticles. Biomaterials. 2009;30(29):5631-8.

[20]. Zhang J, Neoh KG, Hu X, Kang E-T, Wang W. Combined effects of direct current stimulation and immobilized BMP-2 for enhancement of osteogenesis. Biotechnol Bioeng. 2013;110(5):1466-75.

[21]. Vila M, Cicuéndez M, Sánchez-Marcos J, Fal-Miyar V, Manzano M, Prieto C, et al. Electrical stimuli to increase cell proliferation on carbon nanotubes/mesoporous silica composites for drug delivery. J Biomed Mater Res, Part A. 2013;101A(1):213-21.

[22]. Puleo DA, Huh WW. Acute toxicity of metal ions in cultures of osteogenic cells derived from bone marrow stromal cells. J Appl Biomater. 1995;6(2):109-16.

[23]. Facca S, Lahiri D, Fioretti F, Messadeq N, Mainard D, Benkirane-Jessel N, et al. In Vivo Osseointegration of Nano-Designed Composite Coatings on Titanium Implants. ACS Nano. 2011;5(6):4790-9.

[24]. Lahiri D, Singh V, Keshri AK, Seal S, Agarwal A. Carbon nanotube toughened hydroxyapatite by spark plasma sintering: Microstructural evolution and multiscale tribological properties. Carbon. 2010;48(11):3103-20.

[25]. Poland CA, Duffin R, Kinloch I, Maynard A, Wallace WA, Seaton A, et al. Carbon nanotubes introduced into the abdominal cavity of mice show asbestos-like pathogenicity in a pilot study. Nat Nanotechnol. 2008;3(7):423-8.

[26]. Meng J, Song L, Kong H, Zhu G, Wang C, Xu L, et al. Using single-walled carbon nanotubes nonwoven films as scaffolds to enhance long-term cell proliferation in vitro. J Biomed Mater Res, Part A. 2006;79A(2):298-306.

[27]. Correa-Duarte MA, Wagner N, Rojas-Chapana J, Morsczeck C, Thie M, Giersig M. Fabrication and Biocompatibility of Carbon Nanotube-Based 3D Networks as Scaffolds for Cell Seeding and Growth. Nano Lett. 2004;4(11):2233-6.

[28]. LaVan DA, McGuire T, Langer R. Small-scale systems for in vivo drug delivery. Nat Biotechnol. 2003;21(10):1184-91.

[29]. Jaffe LF, Nuccitelli R. An ultrasensitive vibrating probe for measuring steady extracellular currents. The Journal of cell biology. 1974;63(2):614-28.

[30]. Scheffey C. Two approaches to construction of vibrating probes for electrical current measurement in solution. Review of Scientific Instruments. 1988;59(5):787-92.

[31]. Reid B, Nuccitelli R, Zhao M. Non-invasive measurement of bioelectric currents with a vibrating probe. Nature protocols. 2007;2(3):661-9.

[32]. Griffin M, Bayat A. Electrical stimulation in bone healing: critical analysis by evaluating levels of evidence. Eplasty. 2011;11.

[33]. Isaacson BM, Bloebaum RD. Bone bioelectricity: What have we learned in the past 160 years? J Biomed Mater Res, Part A. 2010;95A(4):1270-9.

[34]. Grimnes S, Martinsen G. Bioimpedance and Bioelectricity Basics. UK: Academic Press; 2008.

[35]. Loza J, Stephan E, Dolce C, Dziak R, Simasko S. Calcium currents in osteoblastic cells: Dependence upon cellular growth stage. Calcif Tissue Int. 1994;55(2):128-33.

[36]. Jalota S, Bhaduri SB, Tas AC. In vitro testing of calcium phosphate (HA, TCP, and biphasic HA-TCP) whiskers. J Biomed Mater Res, Part A. 2006;78A(3):481-90.

[37]. Cuscó R, Guitián F, Aza Sd, Artús L. Differentiation between hydroxyapatite and β-tricalcium phosphate by means of μ-Raman spectroscopy. J Eur Ceram Soc. 1998;18(9):1301-5.

[38]. Czekanska E, Stoddart M, Richards R, Hayes J. In search of an osteoblast cell model for in vitro research.

[39]. Jansen J, van der Jagt O, Punt B, Verhaar J, van Leeuwen J, Weinans H, et al. Stimulation of osteogenic differentiation in human osteoprogenitor cells by pulsed electromagnetic fields: an in vitro study. BMC Musculoskeletal Disord. 2010;11(1):188.

[40]. Namgung S, Baik KY, Park J, Hong S. Controlling the Growth and Differentiation of Human Mesenchymal Stem Cells by the Arrangement of Individual Carbon Nanotubes. ACS nano. 2011;5(9):7383-90.

[41]. A A. Mesenchymal stem cell and osteoblast differentiation. In: . Bilezikian JP RL, Martin TJ, editor. Principles of Bone Biology. Academic Press.

[42]. Aubin JE. Mesenchymal stem cell and osteoblast differentiation, in Principles of bone biology In: Bilezikian JP RL, Martin TJ, editor. Principles of bone biology. USA: Academic Press; 2008.

[43]. Giannona S, Firkowska I, Rojas-Chapana J, Giersig M. Vertically aligned carbon nanotubes as cytocompatible material for enhanced adhesion and proliferation of osteoblast-like cells. J Nanosci Nanotechnol. 2007;7(4-5):4-5.

[44]. Titushkin I, Sun S, Shin J, Cho M. Physicochemical control of adult stem cell differentiation: shedding light on potential molecular mechanisms. Biomed Res Int. 2010;2010.

[45]. Sun S, Liu Y, Lipsky S, Cho M. Physical manipulation of calcium oscillations facilitates osteodifferentiation of human mesenchymal stem cells. The FASEB Journal. 2007;21(7):1472-80.

[46]. Titushkin I, Cho M. Modulation of Cellular Mechanics during Osteogenic Differentiation of Human Mesenchymal Stem Cells. Biophys J. 2007;93(10):3693-702.

[47]. Guggino SE, Wagner JA, Snowman AM, Hester LD, Sacktor B, Snyder SH. Phenylalkylamine-sensitive calcium channels in osteoblast-like osteosarcoma cells. Characterization by ligand binding and single channel recordings. J Biol Chem. 1988;263(21):10155-61.

[48]. Chesnoy-Marchais D, Fritsch J. Voltage-gated sodium and calcium currents in rat osteoblasts. J Physiol. 1988;398(1):291-311.

[49]. Peterson BZ, DeMaria CD, Yue DT. Calmodulin Is the Ca2+ Sensor for Ca2+-Dependent Inactivation of L-Type Calcium Channels. Neuron. 1999;22(3):549-58.

[50]. Zayzafoon M. Calcium/calmodulin signaling controls osteoblast growth and differentiation. J Cell Biochem. 2006;97(1):56-70.

Chapter VI

Conclusions and future work

VI.1. General discussion and main conclusions

Thorough the present thesis work, the design of novel conductive biomaterials based on CNTs was accomplished being aware of the CNT potential toxicological risks. The CNT purity and morphology, two major CNT risks, received particular attention. According to latest studies, highly pure CNTs with small length and diameter sizes, typically below 2 μm and 30 nm, respectively, have their potential toxicity highly depressed by avoiding oxidative stress and being easily cleared from the body by the lymphatic and urinary systems. These tube structures are defined here as biologically safe CNTs.

In an attempt to control the purity and morphology, a detailed study of the production process of CNTs was performed. Two processes were exploited, both considering catalyst-supported chemical vapor deposition (CVD) approaches: (1) a hot-filament CVD and metal foils (Ni and Cu) acting simultaneously as substrate and catalyst; and (2) a hot-wall thermal CVD reactor and Si/SiO$_2$ substrates with a magnetron sputtered bilayer of Al$_2$O$_3$/Fe, acting as a diffusion barrier/catalyst. In the first approach, the metal foils were wet-chemically etched to convert the flat surface into catalytic-active protrusions with nano-sized diameters. In the second, the Fe catalytic nanoparticles were formed by breaking the metal film under H$_2$-rich atmospheres at high temperature.

Both approaches contemplated the use of catalyst-substrate systems with strong interactions - (1) metal-metal (of the same material) in the first approach and (2) ceramic-metal (both oxidized forms, Al$_2$O$_3$-Fe$_x$O$_y$) in the second. These interactions guaranteed the settlement of a base growth mechanism, i.e., the catalyst particles remained attached to the substrate, that were accounted to yield catalyst-free carbon filaments with vertical alignment for easier length regulation. In the first approach, an expedite substrate preparation step was successfully applied, but only turbostratic carbon nanofibers (CNFs) were grown with a partial vertical alignment, organized in cone-shape configuration with length and diameter sizes of 1 μm and 8 nm, respectively. The CNFs were grown using a CH$_4$-Ar-H$_2$ gas mixture, under the following optimised conditions: filament temperature= 2300 ºC; substrate temperature= 650-800 ºC; CH$_4$/H$_2$=1; Ar/H$_2$=3; total flow= 50 sccm; total pressure= 5-10 kPa. For the Cu substrates, the optimised growth parameters of pressure and temperature of 10 kPa and 800 ºC, respectively, were more severe than those for the Ni of 5 kPa and 650 ºC. This is explained by the lower carbon solubility of Cu relatively to the Ni.

In the second approach, highly pure (99.96 wt.%) and almost-perfectly vertically aligned CNTs were obtained at a fixed rate of 0.5 μm.s^{-1} with high morphological control of the external diameter (14-16 nm), the number of carbon walls (7-10 walls) and the length size (1-2000 μm), due to not only to the control of the kinetic regime, but also to the engineering of the diameter of the Fe particles. In this case, milligram-amounts of CNTs were produced under a C$_2$H$_2$-Ar-H$_2$ gas mixture, according to the following conditions: furnace temperature= 770 ºC; CH$_4$/H$_2$= 0.1; Ar/H$_2$= 4; total flow= 510 sccm; total pressure= 100 kPa. The different characteristics between the two reactors,

the HFCVD and TCVD, justified the adjustment in the growth parameters of these other 1D carbon filaments, the CNTs. The higher total flow and total pressure in the TCVD reactor, comparatively to the HFCVD, implies a lower CH_4/H_2 and higher Ar/H_2 ratios, for barely the same growth temperature of ~800ºC.

Beyond the morphology and purity, the CNT chemical functionalization it was also considered to regulate its toxicological profile. A double covalent functionalization with high potential for bone tissue engineering was proposed. The functionalization started by bonding the cycloadducts groups (hydrophobic groups) resulting from the [4+2] Diels-Alder cycladdition of 1,3 butadiene, followed by a soft oxidation of the alkene groups with $KMnO_4$, to generate carboxylic (-COOH) groups (hydrophilic groups). The hydrophobic groups were responsible to weakening but not breaking the CNT lattice. Thus, they encouraged the *in vivo* biodegradation of subcutaneously implanted CNTs in mice, mediated by oxidative milieus containing neutrophilic and macrophages peroxidases. Whereas, the negatively charged hydrophilic groups enhanced the *in vitro* adhesion and proliferation/differentiation of MG63 osteoblastic cells and the *in vivo* biodispersion of CNTs. Overall, CNTs do not trigger acute *in vitro* and *in vivo* toxicological responses and have adequate biocompatibility with bone forming cells. As so, CNTs have a satisfactory profile to incorporate CNT-engineering bone grafts to interface with living bone without noteworthy toxicological threats.

The above study pointed out to a high quality standard of biocompatibility, biodispersibility and biodegradability characteristics of CNTs, by controlling the synthesis and functionalization. In paralell, CNT reinforced Glass/Hydroxyapatite (HA) bioceramics were prepared using commercially available MWCNTs (NC7000, Nanocyl) with average diameter and length sizes of 9.5 nm and 1.5 μm. Purification and functionalization routes optimized for the CVD grown CNTs were adopted. The processing of these composites had two main challenges: (1) the disentanglement/mixing step due to the attractive CNT-CNT van der Waal forces; and (2) the consolidation step of the composite powders owed to the CNT oxidation (at 400 ºC) during the dehydroxylation of HA, above 900 ºC.

To overcome the first drawback, the powders were processed by a vigorous continuously mixing route (i.e. dynamic route). Firstly, the CNTs were previously purified and functionalized (p,f-CNTs) using the procedure referred above. This functionalization was found to be a suitable covalent reaction to chemically modify CNTs without changing their pristine properties. In this case, the CNT stabilization in polar solvents (e.g. isopropyl alcohol - iPrOH) was obtained by either steric interactions (cycloadducts groups acting as "physical spacers") and electrostatic interactions (-COOH groups). Besides the guaranteed repulsive CNT-CNT forces in iPrOH, the opposite electrical charge of HA, potential zeta (PZ): +31±2 mV, and purified and functionalized CNTs (p,f-CNTs), PZ: -123±7 mV, would maximized the interaction with the ceramic powders. Yet, barely purified CNTs (p-CNTs) showed high PZ in iPrOH of - 99±6 mV, due to the efficient ionization of the iPrOH and adsorption of negatively charged alkoxide ions (-RO-), a value close to the one of the p,f-CNTs.

However, no significant differences were seen between the non-functionalized p-CNTs and the p,f-CNTs consolidated composites. Both composite green powders showed high CNT-ceramic

interaction being the CNTs decorated with Glass/HA particles ($D_{0.5}$= 1.8 μm). According to this, it was assumed that the dynamic route had a higher influence than the Diels-Alder functionalization on controlling the CNT agglomerate state in the ceramic-matrix composite. Also, the lowest CNT damage and the highest mechanical and electrical properties were found for the non-functionalized materials. Hence, under the selected powder processing conditions, the functionalization step did not show any advantage. Also, the absence of these organic groups is not relevant for the CNT-ceramic interface performance in the final consolidated material because during the high temperature sintering step these functional organic groups were fully eliminated.

Regarding the consolidation challenge, two sintering strategies were optimized towards prevention of CNT oxidation in Glass/HA matrices, at fixed CNT loading of 4.4 vo.%: (1) reactive-bed pressureless sintering (RB+P) and (2) hot-pressing (HP). Both showed CNT retentions up to 80%, even at 1300ºC, yielding an increase of the electroconductivity in ten orders of magnitude relatively to the matrix. The RB+P CNT compacts showed higher electroconductivity by ~170% than the HP ones due to the lower damage to CNTs of the former route. Even so, highly reproducible conductivities with statistical variation bellow 5% and dense compacts up to 96% were only obtained by HP.

Briefly, envisioning the processing of a biocomposite, where its toxicological profile is a key factor, the materials were prepared by an optimised functionalization-free route with minor contaminant levels and damage to CNTs: (1) CNTs were purified at 1900ºC for 8h under highly pure Argon flows in a graphite furnace; (2) powders were vigorous mixed in IPA by shearing and sonication forces for 15 and 60 min, respectively, avoiding damage to CNTs due to the excessive use; and (3) consolidated by hot-pressing under vacuum at mid conditions of 30 MPa and 1100 ºC for 60 min.

Considering the phase composition of the consolidated composites, it was observed a typical bi-phasic composition of the ceramic matrix including β-TCP domains uniformly distributed in a HA bed. No negligible changes in phase composition were detected for a wide range of CNT loadings (0.9-4.4 vol.%). Additionally, for a 4.4 vol.% CNT composite, detailed 3D microstructural recontructions and TEM analysis had shown a interconnected CNT network arranged as homogenously distributed ellipsoid-shaped agglomerates (<3 μm) bridged by sub-micrometric sized ropes.

These CNT ropes, located at the matrix grain boundaries, worked as efficient toughening agents, and thus improved the fracture toughness of the ceramic matrix, making it closer to the one of natural cortical bone. The remaining mechanical properties of the composite outperformed those of the natural bone. Moreover, the 3D CNT arrangement yielded composites with attractive functional properties with a percolation threshold of Pc= 1.5 vol.%. At 4.4 vol.% of CNTs, thermal and electrical conductivities of 1.5 $W.m^{-1}.K^{-1}$ and 55 $S.m^{-1}$, respectively were obtained, matching relevant requisites for the success of electrical stimulation protocols of bone tissue. While the former might avoids bone damaging from Joule's heat generation, the latter allow the confinement of external electrical fields through the conductive material. This confinement of fields and the

increase of conductivity at the damaged bone sites where the filling material (e.g. granules) is applied, are guaranteed owed to the higher conductivity of the material, comparatively to that of the surrounding biological environment, either tissues/organs or interstitial mediums.

As a proof of concept, a comparative biphasic electrical stimulation protocol of human MG63 osteoblastic cells was performed *in vitro* on either dielectric bioactive bone grafts or conductive CNT-reinforced composites, to evaluate the efficiency of the electrical stimuli delivering. Also, the biocompatibility of the materials and the effects of the stimulation protocol in the cellular activity were also investigated.

A stimulation system was designed in the present thesis work to reproduce the in situ stimuli conditions delivered by capacitive coupling stimulation used in clinics. Parallel salt-bridge filled with conductive Agar acting as electrodes were used, resembling capacitive coupled electrodes. The cells received a daily stimulation for five consecutive days. Symmetrical biphasic square pulses with fixed frequency and duty cycle values of 40 Hz and 20-80% were used, setting action potentials (AP) and resting potential (RP) with fixed periods of 5 and 20 ms, while the magnitude of the signal (5 and 15 μA) and the stimulation time (15 and 30 min) were varied.

The waveform and magnitude of the applied electrical stimuli were carefully selected based on three major requisites for bone electrical stimulation: (1) the current threshold applied in clinic to efficiently stimulate bone tissue - 5-20 µA; (2) the upper limit of current density and electrical field to avoid tissue injury from heat generation - 1-2 $mA.cm^{-2}$ and 10 $V.cm^{-1}$; and (3) the time-current-voltage response of Ca^{2+} ion channels of osteoblastic-like cells to an action potential.

To support the biological testing and to validate the experimental approach used for cell stimulation, a set of preliminary studies were carried out in the same conditions of the stimulation protocol (i.e. volume of α-MEM, number of samples per culture plate, parallel electrodes and magnitude of the electric field), as follows: (1) by studying the effects on the overall resistance of α-MEM using immersed conducting and nonconducting samples by impedance measurements (non-stimulated conditions); and (2) by identifying the current density (electric field) lines on samples of different geometries (similar to granule materials) by a vibrating voltage probe technique (stimulation conditions). The first experiment was performed with the composite materials and other materials with different conductivities. It was shown that the resistance of the medium decreased with the increasing conductivity of the immersed material and with number of conductive samples. In the second experiment, a probe vibrating in two orthogonal directions (X and Z), parallel and perpendicular to the electric filed lines, respectively, and measuring the current density in the two directions, showed a decrease of the normal component for higher conductive materials. This proves that the current is converging through the material in a higher extent for the more conductive materials.

Under non-stimulated conditions, the biological studies showed biocompatible CNT-bioceramic composites, denoting suitable cell adhesion, with intimate CNT-cells interactions, and proliferation. These features further enhanced the cellular functional activity and modulated the

314

orientation of the cell growth along the alignment of the 3 μm sized ellipsoid-shaped CNT agglomerates on the composite surface.

Bearing in mind the possibility of the CNT releasing from the matrix to the living milieu, the degradation profile of the CNT composites and the agglomeration degree of the released materials were investigated. Data showed that the composites degraded at higher rates in an *in vitro* acellular testing than the ceramic matrix, but with releasing of CNTs with biologically safe diameter sizes (<3 μm).

Under a proper electrical stimulation protocol, it was clear an enhancement of the cell functional activity for all materials, which proved the beneficial effect of the electrical stimuli. Nevertheless, the conductive CNT/HA/Glass composites showed significantly improved cell response than the dielectric Glass/HA matrix. The cell metabolic activity and DNA content were increased by 130% and 60%, relatively to the non-stimulated condition, after only 3 days of daily stimulation of 15 μA for 15 min. Moreover, the osteoblastic gene expression for Runx2 and ALP (relevant markers of the osteogenic differentiation) was enhanced by 80 % and 25%, after 5 days of stimulation.

These observations may be related to the high efficiency of charge transfer voltage at the substrate-cell interface, owed to the high density of electric field lines (i.e. confinement of electrical fields) crossing the cell because the electric fields meets the surface of a conductor in perpendicular angles. This might boosts the raising of the magnitude of the action potentials and the opening of voltage-gated channels at multi-locations in the cell membrane. Subsequently, this triggers Ca^{2+}/calmodulin-dependent protein kinase II (CaMKII) signalling pathways towards regulation of osteoblast proliferation/differentiation.

Findings of the present thesis work offer further contributions for the potential clinical use of CNTs in bone tissue engineering. Throughout the present work, strategies to control the CNT toxicological profile were actively pursued. Dimensionally-controlled and catalyst-free CNTs were successfully grown by a catalyst-supported CVD method; and their *in vitro*/*in vivo* biocompatibility and *in vivo* biodispersibility and biodegradability were modulated by a double functionalization approach based on [4+2] Diels-Alder cycloadditions.

The incorporation of biologically safe CNTs, with high flexibility and electrical conductivity, in a bioactive and mechanically reinforced Glass/HA matrix, gives rise to an unique bone grafts - CNT/Glass/HA - mimicking the biofunctionalities of the collagen I fibres and apatite-like phase of natural bone tissue, respectively. The CNT/Glass/HA composites integrating impurity-free CNT agglomerates with maximized interfacing area, but with respective diameter sizes below the biologically safe threshold (<20 μm), allowed the *in situ* control of bone cell functions, and thus are apt to interface with bone tissue. Also, these composites have a conjugation of suitable biocompatibility and exciting functional properties, high thermal and electrical conductivities, that make them attractive to turn the non-invasive bone electrotherapies highly selective, by maximizing the confinement of electrical fields at the bone damaged site, and hence offering high perspectives to decrease the postoperative healing times of the patients.

VI.2. Future work

As future work, it would be imperative to proceed with an animal model testing applying the optimised *in vitro* electrical stimulation protocol to further validate the efficiency of the spatial and temporal control of bone stimulation on conductive bone grafts. Furthermore, it might be interesting to explore other equally exciting functionalities offered by the CNT agglomerates of the CNT/Glass/HA composites, if functionalized: (1) by the double functionalization developed in the present work, to improve the biocompatibility; (2) with therapeutic molecules to be delivered by the very same current-voltage electrical signal confined on the surface of the CNT composite, while electrical stimulated; (3) before implantation, by a simple immersion in solutions containing functional moieties, such as anti-microbiotic agents, to avoid infection or stem cell-rich fractions to maximize bone bonding.

VII. Apendix

Table A1 - Toxicity data of solo CNTs.

CNT type	Morphology (nm)/ Purity (%)	Chemical functionalization	Animal model/ cell type	Dosage	Toxicity	Ref.
SW	Ø:5-20/ l:50-300/ 95	-	-/Human epithelial cells (HeLa)	100 mg/l	SWNT dispersions are not inherently cytotoxic to HeLa cells	[249]
SW	Ø:1.4/ l:300-1000/>95	1,3-dipolar cycloaddion reaction, oxidation/ amidation	-/B and T lymphocytes, macrophages	1-10 mg/l	SWCNTs does not modify primary immune cells' viability and functionality *in vitro*.	[250]
SW	Ø:1-2/ l:5000-15000/ >90	-	-/Rat alveolar macrophage cells (NR8383); human alveolar epithelial cells (A549)	5-100 mg/l	SWCNTs possess no acute toxicity in pulmonary epithelial and macrophage cell lines.	[251]
SW	Ø:1.5/ l:1000/ ~97	-	-/Human epidermal keratinocytes (HaCaT)	60-240 mg/l	Exposure of HaCaT cells to SWCNT resulted in accelerated oxidative stress, depletion of total antioxidant reserve and vitamin E and morphological changes in cultured skin cells.	[252]
SW	Ø:0.8-1.2/ l:100-1000/ ~90	-	-/Human embryo kidney cells (HEK293)/	0.78-200 mg/l	SWCNT can inhibit the proliferation of HEK293 cells by inducing cell apoptosis and decreasing cellular adhesive ability.	[253]
SW	Ø:1.4/ l:300-1000/ >95	-	-/Human epidermal keratinocytes (HaCaT); human epithelial cells (HeLa); human alveolar epithelial cells (A549 and H1299)	1-10 mg/l	SWCNT particles show an adverse effect on keratinocytes through an oxidative mechanism leading to NF-̄B activation.	[254]
SW	Ø:0.8-1.2/ l:100-1000/ >99	Acid-treated	-/Rat aortic smooth muscle cells (SMC)	180-220 mg/l	SMC growth inhibition was dependent on SWCNT related parameters such as aggregate/particle, dimensions, dosage and duration of exposure.	[255]
SW	Ø:0.8-1.2/ l:100-1000/ >90	-	-/Human alveolar epithelial cells (A549)	1.56-800 mg/l	SWCNT can induce an indirect cytotoxicity by alteration of cell culture medium (in which they have previously been dispersed) which potentially results in a false positive toxic effect being observed in cytotoxicity studies.	[256]
SW	Ø:20-30/ l:1000-5000/ 85-98	-	-/MSTO-211H cells	7.5-30 mg/l	Critical features that seem to determine SWCNT toxicity are the presence of carboneous material and the degree of CNT dispersion but not the content of entrapped Y and Ni.	[257]
SW	Ø:1.5/ l:150/ ~97	PL-PEG-FA; PL-PEG-FITC	-/Human epithelial cells (A96)	2.5-5 mg/l	Cells remained intact and exhibited normal proliferation behavior when exposed to functionalized SWCNTs..	[258]
SW	Ø:0.8-1.2/ l:100-1000/ 99.5	-	Mouse/-	20 mg/kg	SWNTs exposure can result in accelerated oxidative stress.	[268]
SW	Ø:2-3/ l:30000-50000/ 98.2	-	Mouse/-	4 mg/Kg	The transport of SWNTs from the implant sites to the lymph nodes may suggest undesirable effects related to cytotoxicity.	[269]
SW	Ø:1.4/ l:>1000/ 65	-	Mouse/-	1-5 mg/Kg	There are potential risk associated with inhaling carbon nanotubes.	[270]
SW	Ø:0.8-1.2/ l:100-1000/ >90	-	Mouse/-	0.002-0.01 mg/ml	When SWCNTs reach the lungs, they are much more toxic than carbon black and can be more toxic than quartz, which is considered a serious occupational health hazard in chronic inhalation exposures.	[271]
SW	Ø:1-4/	Acid-treated+PS	Mouse/-	2.5-62.5	Coating of SWCNTs with PS not only	[272]

	l:-/ ~99.7			mg/kg	makes them highly recognizable but also affects macrophage functions in ways similar to those of apoptotic cells.	
SW	Ø:10-30/ l:2000-3000/ >95.4	-	Mouse/-	0.4-10 mg/kg	Only serum biochemical changes and pulmonary inflammation were observed. No obvious cell apoptosis or changes of immunological indicators were induced. The proposed main toxicological mechanism is oxidative stress aroused in liver and lungs. The low toxicity of pristine SWCNTs implicates that SWCNTs could be used as the safe materials for biomedical applications. It also suggests that further chemical functionalization should be taken to improve the dispersion and excretion of SWCNTs.	[273]
SW	Ø:1.1/ l:500-100000/97.6 and 99.4	Acid-treated	Mouse/-	0.3-1.3 mg/Kg	There was no significan ischemia/reperfusion injury in mice exposed to non-functionalized SWCNTs despite significant pulmonary inflammation, suggesting that the combination of acid functionalization and SWCNTs was required to mediate extra-pulmonary toxicity.	[274]
SW	Ø:0.8-1.2/ l:100-1000/91.2	-	Mouse/-	0.4 mg/kg	SWCNTs and MWCNTs deposited in the lung induced an acute lung and systemic effect, which was more pronounced in the MWCNT exposure.	[275]
SW	Ø:1-5/ l:100-300/99.5	PEG	Mouse/-	0.1-2 mg/kg	No obvious toxicity or negative health effects (such as weight loss and fatigue) were observed over monitoring periods of up to several months.	[276]
SW	Ø:1.2-1.5/ l:100-300/85-95	-	Mouse/-	0.5 mg/kg	SWCNTs Induced alveolar macrophage activation, various chronic inflammatory responses, and severe pulmonary granuloma formation.	[277]
MW	Ø:20/ l:1600-18000/>95	-	-/Human alveolar epithelial cells (H596, H446, and Calu-1)	0.002 - 0.2 mg/ml	MWCNTs are less toxic than carbon fibers and nanoparticles, the toxicity of carbon nanotubes increases significantly when carbonyl (CdO), carboxyl (COOH), and/ or hydroxyl (OH) groups are present on their surface.	[259]
MW	Ø:10-50/ l:10000-30000/>95	-	-/Rat alveolar macrophage cells (NR8383); human alveolar epithelial cells (A549)	5-100 mg/l	MWCNTs possess no acute toxicity in pulmonary epithelial and macrophage cell lines.	[251]
MW	Ø:67.4/ l:3000-30000/99.7	-	-/Macrophage cell line (J774.1 and CHO-K1)	10-1000 mg/l	Macrophages bind to MWCNTs via MARCO, and the plasma membrane extends along the MWCNT fibers. In the course of membrane extension, the membranes are injured.	[260]
MW	Ø:44 and 26/ l:1500 and 900/95.76 and 99.92	-	-/Human alveolar epithelial cells (A549)	0.25-100 mg/l	Both nanotubes and nanoparticles are able to rapidly enter into cells, and distribute in the cytoplasm and intracellular vesicles. Their toxicity was globally lower than nanotubes toxicity. Among nanotubes, the length did not influence cytotoxicity, neither the presence of metal catalyst impurities.	[261]
MW	Ø:20-40/ l:1000-5000/>95	-	-/Human T lymphocytes	40 mg/l	CNTs can be harmful to cells in a time- and dose-dependent manner. 40 mg/l of CNTs did not seem to have any toxic effects on the function of T cells, supporting the notion that this amount does not measurably harm the cell.	[262]
MW	Ø:68 / l:2000-164000 and 4000-65000/93.8 and >99	-	-/Human monocyte-derived macrophage	0.31-20 mg/l	Viability assays revealed a dose dependent toxicity for unpurified and purified. Comparable toxicity of unpurified and purified MWNTs with no noticeable toxicity from the residual iron suggests that the nanotubes themselves are the principle cause of cytotoxicity.	[263]
MW	Ø:18/ l: 20000/>99	-	-/Human skin fibroblasts (HSF42); human embryonic lung fibroblasts (IMR-90)	0.06-0.6 mg/l	At high dosage, carbon particles can seriously impact the cellular functions in maintenance, growth, and differentiation. Of these two nanomaterials, MWCNTs appear to induce more stress on the cells than MWCNOs.It is evident from our studies that carbon nanomaterials have a toxic effect on lung and skin cells.	[264]
MW	Ø:1.2-3.2	-	-/Human umbilical vein	0.5-0.9	It revealed no cytotoxic effect according	[265]

	and 0.7-6.3 / l:-/>90 and >80		endothelial cells (HUVEC)	mg/l	to the standards of the method. However, we have observed that for the CNTs having the highest specific surface area, a cytotoxicity effect (decrease of HUVEC viability) seems to appear slowly with increasing the dilution of the suspension.	
MW	Ø:- /l:20000/90	1,3-dipolar cycloaddition + amphotericin B antibiotic (AmB)	-/Human Jurkat lymphoma T cells	1-40 mg/l	Studies revealed that AmB covalently linked to MWCNTs is taken up by mammalian cells without presenting any specific toxic effect.	[266]
MW	Ø:20-40/ l: 220-825/98	Acid treated	-/Human acute monocytic leukemia cells (THP-1)	0.005-0.5 mg/l	Both 220-CNTs and 825-CNTs possess induction activity toward macrophages, although their activities were much lower compared to that of a microbial antigen.	[267]
MW	Ø:10-50 and 50-150 / l:10000-20000/95	-	Mouse/-	20 mg/kg	MWNTs induced the release of the proinflammatory cytokine such as IL8 from cells, resulting in irritation response on the skin.	[268]
MW	Ø:5-20 / l:300-2000/99.5	-	Mouse/-	4 mg/kg	The presence of abundant multinucleated cells attached to the MWCNT agglomerations may suggest undesirable effects related to cytotoxicity.	[278]
MW	Ø:15±5 and 40-50 / l:1000-5000 and 5000-2000 and 13000 and 56000/>99.9	-	Mouse/-	100 mg/l	Long (>20 μm) MWCNTs have the potential to induce an acute inflammatory reaction when injected in the peritoneal cavity of mice. This acute inflammatory response was similar to that induced by long amosite fibers, suggesting that long MWCNTs may exert an asbestos-like activity.	[279]
MW	Ø:100 / l:10000-20000/99.5	-	Mouse/-	3 mg/ml	MWCNT induces mesothelioma along with a positive control, crocidolite (blue asbestos), when administered intraperitoneally to mice.	[280]
MW	Ø:5.9±0.5 and 0.7±0.07 / l:9700±2100 and 11300±3900/ 97.8±0.2 and 98±0.2	-	Mouse/-	10 mg/kg	If MWCNTs reach the lung they are biopersistent, have the capacity to stimulate lung cells to produce TNF-a and induce lung inflammation and fibrosis.	[281]
MW	Ø: 49±13 / l:3860 /99.2	-	Mouse/-	0.1-0.4 mg/Kg	Exposure of mice to MWCNT caused dose- and timedependant pulmonary inflammation and damage, as also rapid development of pulmonary fibrosis.	[282]
MW	Ø: 80 / l:10000-20000 /99.7	-	Mouse/-	0.4 mg/kg	MWCNTs deposited in the lung induced an acute lung and systemic effect.	[275]
MW	Ø: 20-30 / l:500-2000 /94	,3-dipolar cycloaddition and DTPA	Mouse/-	2 mg/kg	Highly functionalized and water dispersible MWCNTs did not accumulate in or injure any tissues on passage. By contrast, non-functionalized pMWCNTs and f-MWCNTs with a low functionalization degree can interact and accumulate in different tissues.	[283]
MW	Ø: 5-15 / l:100-10000 /90	-	Mouse/-	0.1-2.5 mg/l	Inhaled MWCNT produces lesions (inflammation and granuloma formation) in the lung and associated lymph nodes similar to those after intratracheal administration.	[284]
MW	Ø:20-40/ l: 220-825/98	Acdis treated	Mouse/-	1 mg/Kg	No severe inflammatory response such as necrosis, degeneration or neutrophil infiltration was observed around either CNTs throughout the experimental period. These results indicated that macrophages could envelop 220-CNTs more readily than 825-CNTs. The degree of inflammation around 825-CNTs was stronger than that around 220-CNTs since some of the 825-CNTs were not enveloped by macrophages even after 4 weeks.	[267]

[a] The *in vivo* dosages were converted to mg/kg assuming a standard mouse weight of 100 g.

Table A2 - Toxicity data of CNT/HA composites.

CNT type	CNT Loading (wt.%)[a]	Morphology (nm)/ Purity (%)	CNT-HA composite system	Animal model/ cell type/ Administration	Toxicity	Ref.
MW	4	Ø:40-70/ l:500-2000/95	CNT-HA coatings	-/Human osteoblast cells (hFOB 1.19)/-	Unrestricted human osteoblast hFOB 1.19 cell growth and proliferation during cell culture studies demonstrate non-toxicity of HA–CNT coating.	[294]
MW	1-3	Ø:10-15/ l:10000-20000/-	CNT-HA coatings	-/Mouse osteoblast cells (MC3T3-E1)/-	The addition of CNTs to HA could remarkably improve both the mechanical and biological properties of the HA coating.	[295]
MW	1.12	Ø:10-30/ l:1000-10000/>95	CNT-HA free standing compacts	-/Human osteoblast cells (hFOB 1.19)/-	The presence of CNTs in HA has promoted growth and adhesion of osteoblast cells at the early stage of culturing.	[296]
MW	-	Ø:10-40/ l:5000-30000/>93	CNT-HA free standing compacts	-/Mouse osteoblast cells (MC3T3-E1)/-	CNTs-HA coatings not only provide efficient protection of the titanium substrate in SBF, but also have good biocompatibility.	[297]
MW	2	Ø:10-15/ l:1000-15000/>98.5	CNT-HA free standing compacts	-/Mousefibroblast Cells (L929)/-	High level of cells' biocompatibility with CNTs/HA composite powders This proves the composite surface functionalization is not necessary to obtain or increase biocompatibility.	[326]
MW	3	Ø:40-60/ l:500-500000/>95	CNT-HA free standing compacts	Mouse/-/muscle tissue	CNT composite induce little stimulation to the tissue around the sample without arousing strictly inflammatory reaction, indicating that they are anything but toxic and possess better histocompatibility. CNT composites have higher histocompatibility than ZrO$_2$/HA composites.	[221]
MW	4	Ø:20-50/ l:200-2000/>95	CNT-HA coatings	Mouse/-/ femoral bone	CNT addition resulted in the growth of new bone and improved osseointegration.	[298]
MW	27-69	Ø:20-40/ l:10000/80	CNT-HA free standing compacts	Mouse/-/femoral bone	MWCNTs/HA composites possessed the better biocompatibility compared with the pure MWCNTs *in vivo*.	[299]
MW	3	Ø:20-40/ l:-/>95	PLLA/MWCNTs/HA free standing membranes	Mouse/-/muscle tissue	Excellent dual biological functions and satisfied the requirement of the guided tissue regeneration.	[300]
MW	1-5	Ø:20-40/ l:300000-500000/-	MWCNTs/HA/ Gelatin free standing powders	Mouse/-/subcutaneous	Histopathological study of the tissues such as skin, liver, and kidney has hardly shown any evidences of toxicity for lower concentration of MWCNTs in the composite. Some reversible cellular injury in the liver and toxic changes in kidney was observed only at higher concentration (4% of MWCNTs). MWCNT just less than 4% by weight may be used for reinforcing the Hap based composites to improve the biomaterials mechanically and thus can be considered to be used in artificial bone implants without serious toxicological threats.	[301]

[a] Volume fractions were converted to weight fractions assuming a CNT density of 1.75 g.cm^{-3}.